Phone : +90 (312) 201 10 00
Fax : +90 (312) 287 91 88
Adress : MTA 06520 - Ankara - TURKEY
www.mta.gov.tr

162

BULLETIN OF THE MINERAL RESEARCH AND EXPLORATION

2020

BULLETIN OF THE MINERAL RESEARCH AND EXPLORATION

Foreign Edition | 2020 | 162 | ISSN : 0026-4563 E-ISSN : 2651-3048

CONTENTS

Research Articles

BULLETIN OF THE MINERAL RESEARCH AND EXPLORATION

Foreign Edition | 2020 | 162 | ISSN : 0026-4563 E-ISSN : 2651-3048

CONTENTS

Research Articles

LOCATION OF MANAGEMENT
Redaksiyon Kurulu Başkanlığı
Maden Tetkik ve Arama Genel Müdürlüğü
D Block Room Number: 2-3
Çukurambar Mah. Dumlupınar Bulvarı No: 33/A
06800 Çankaya/ANKARA/TURKEY
e-mail: redaksiyon@mta.gov.tr

The translations of Göktaş, Yeşilova and Hozatlıoğlu et al. were made by M. Kerem AVCI. The translation of Canbaz et al. was made by Tandoğan ENGİN. The translation of Aydınçakır et al. was made by Catherine YİĞİT. The translation of Dinçer and Işık was made by Şükrü Sinan DEMİRER

Bull. Min. Res. Exp. is indexed and abstracted in TR Dizin, Emerging Source Citation Index (ESCI), Scopus, The ICI Journals Master List (Copernicus), Directory of Open Access Journals (DOAJ), Clarative Analytics Master List (OAJI), Georef, MIAR, EBSCO and Zoological Record.

The Bulletin of the Mineral Research and Exploration is published in three issues in a year. Each bulletin is printed in Turkish and English languages as two separate issues. The English and Turkish issues of the "Bulletin of the Mineral Research and Exploration" can be obtained from "BDT Department" free of charge, either directly or ordered by adding postage fee from the correspondence address. Typesetting and printing operations are carried out and followed by the Publication Service of the Scientific Documentation and Publicity Department. Typesetting and Print Review: Yaşar ÖZKAN, Tuğba UĞUR. e-mail: bdt@mta.gov.tr

The section of "notes to the authors", format, copyright and other information can be obtained from www.mta.gov.tr as PDF files.

Printed Date: 11.08.2020
PRINTING HOUSE: Kuban Matbaacılık - İvedik Organize Sanayi Matbaacılar Sitesi 1514. Sokak No: 20 Phone: 0312 395 2070 Fax: 0312 395 3723 www.kubanmatbaa.com
PERIODICAL
ISSN: 0026-4563

Bulletin of the Mineral Research and Exploration

http://bulletin.mta.gov.tr

Characterization of iron ore and scale for synthesizing vinyl paint

Mohammed Tayeb ABEDGHARS[a*], Mokhtar GHERS[b], Salah BOUHOUCHE[a] and Belgacem BEZZINA[a]

[a]*Research Center in Industrial Technologies CRTI: P.O. Box 64, Cheraga 16014 Algiers, Algeria*
[b]*Department of Physics, Badji Mokhtar University, Annaba, Algeria*

Research Article

Keywords:
Pigment iron, Scale (calamine), Simultaneous thermal analysis, X-ray diffraction, Spectrophotometry.

Received Date: 12.11.2018
Accepted Date: 17.07.2019

ABSTRACT

Two materials are studied to synthesize a vinyl painting. Iron ore is an iron pigment with an oolithic structure containing phosphorus. The second material is a steel by-product. The raw materials proprieties were studied by chemical, particle size, thermal, XRD and spectrophotometric analysis. The iron contents of the pigment and scale are respectively 53.18% and 73.83%. The grindability of scale is better than that of the pigment. The particle volume distribution is 0.7 to 32 µm for scale and 0.6 to 40 µm for pigment. TGA and DTA tests show that the pigment loses weight with phase dissolution by consuming energy and the scale gains weight with the formation of a new phase when the temperature increases. The SEM of the scale showed a homogeneous structure of iron oxide grains ranging from 1 to 10 µm. XRD analysis shows that the iron in the pigment is in the form of (Fe_2O_3) and FeO (OH)) and very little (Fe_2SiO_4). The iron in the scale is in the form of (FeO, Fe_2O_3 and Fe_3O_4). Spectrophotometric tests show that the two materials have no absorption and their reflection is maximum (100%) in the visible range.

1. Introduction

The red pigments are iron ore deposits. Their operation in the field of paints is dictated by certain technical conditions.

– Scale counts among the fatal productions of secondary materials generated by the steel industry, we find this by-product in different mills. Chen and Yuen (2005) and Umadevi et al. (2013) showed that the scale is formed by oxidation at high temperature during the cooling of the products in continuous cast steel and during the reheating treatment and hot forming.

Pigments are chemical compounds presenting absorption only at certain wavelengths of the visible spectrum. It is this property which makes their color.

– The pigments are mostly in the form of fine dry particles and are almost soluble in all solvents. The first ones used the properties of these compounds, 30.000 years ago in prehistoric caves. Today, artists use pigments such as ocher, yellow and red clay or iron oxide.

There are different types of pigments:

– Nature: Plants, soil, animals, flowers, plants, trees

– Chemical: Obtained by mixing or fusion of various materials

The use of pigments has continued to increase and is widely used in the following applications: toner, paint, coating, ink, plastic, rubber, textile, cosmetic, food and pharmaceutical.

Citation info: Abedghars, M. T., Ghers, M., Bouhouche, S., Bezzina, B. 2020. Characterization of iron ore and scale for synthesizing vinyl paint. Bulletin of the Mineral Research and Exploration 162, 1-9. https://doi.org/10.19111/bulletinofmre.604081

* *Corresponding author: Mohammed Tayeb ABEDGHARS, abedghars@yahoo.fr*

Morvan (2002) showed that the analysis of the particle size of the pigments could influence the properties of final products such as: optical properties, color, shade, opacity, viscosity, shine, durability and sedimentation.

Hematite has a dark red color and a granulometric distribution which are sufficient properties to be used as a chromophore for encapsulation in pigment production and this is demonstrated by Della et al. (2007). Pigments production is still carried out according to the classical mechanical methods. The lands are extracted first manually from careers then cleaned, dried and finely ground. Their purity and fineness of their grinding determine the later possibilities of use as was described by Philip (2010) in Histoire Vivante des Couleurs.

Husband et al. (2006) wrote that pigments are generally powders. The fineness and particle shape can change the color of ground pigment considerably by acting on the proportion of light rays reflected from the surface of grains compared to those crossing.

Particle size effects on:

- *The optical properties*, the size of pigment particles can affect the final aspect of the coated surface, e.g., a painting can be glossy, matt or satiny, depending on particle size. This effect is related to phenomena of diffusion, reflection and refraction of light.

- *The final performance of the coating*, the ease of a pigment applying or paint is determined by the particle size distribution of the coloring elements. The particle size determines the coloring strength or color depth directly.

- *Rheological properties*, e.g., work done by Husband et al. (2006) and Brinke et al. (2007) on the influence of the shape of the pigment particles on the tensile properties in the plane of the kaolin-based coating layers, have shown that the intrinsic viscosity (μ) of particles having the same volume is directly related to their aspect ratio. The viscosity is increased by the presence of finer particles, which allows limiting the sedimentation and flocculation. These two phenomena can notably change the color intensity of a formulation in a meaningful way.

Among the fatal productions of secondary materials generated by the steel industry, we find the scale of different mills. The scale is formed by oxidation at high temperature during the cooling of the products in continuous cast steel and during the heating treatment, and hot forming as illustrated by Umadevi et al. (2013).

Our objective in this preliminary study is to characterize the mixtures for synthesizing of pigment. In this part we will determine the microstructure of two components, the grindability and finally the particle size by laser granulometry. Differential Thermal Analysis (DTA), Thermal Variation of Enthalpy (DSC), X-Ray Diffraction Analysis and Visible Light Spectrophotometer are performed.

2. Materials and Methods

Chemical analysis of the material was carried out by X-Ray Fluorescence spectrometry (XFR). The grinding time depends on the initial state of raw materials. The Determination of the optimal grinding time is required for each component. Control of the grain size is carried out after each grinding session to the mesh 32 microns. The particle size distribution of the two samples is investigated using a laser micro-granulometer - Mastersizer 2000 / Malvern. It works with the sample preparer Hydro MU.

In the study of the contribution of grain size analysis by laser granulometry in the physical characterization of calcareous fillers, Michel and Courard (1986) showed that this laser scattering analysis is an indirect measurement technique commonly used to determine particle size distribution of powdered materials. The principle of the method is as follows.

The optical unit of the particle size analyzer records the diffusion (diffraction, reflection, refraction) of monochromatic radiation by a suspension of particles. Diffusion images are calculated from a diffusion model, according to theoretical particle size distributions. The calculated images and the measured image are adjusted by the least squares method

A device of type TA Instruments SDT.Q.600 is used for the study of the Differential Thermal Analysis (DTA) and the Thermal Variation of the Enthalpy (DSC) of the raw materials.

An amount of scale is gradually added to the natural pigment in the range of (5, 10, 15, 20, 25% and 35%) to optimize the synthetic mixture. According to the experimental procedures cited by Thirion (2016), heating is ensured at 50°C per minute until a temperature of 1100°C in an alumina crucible. The Scanning Electron Microscope (SEM) used in the framework of mineralogical quantization is a microscope type of Quanta 250 with an Analyzer Ametek. The crystallographic structure of our materials was studied using an X-Ray Diffractometer (XRD) – a Rigaku equipped with a copper anticathode tube. Optical transmission measurements at room temperature on our samples (absorption and reflection) were carried out by a UV-Visible-IR spectrophotometer, Brand Agilent type Carry 5000.

3. Results and Discussion

3.1. Chemical Analysis

Both materials consist mainly of iron oxide. Like all minerals, the pigment contains oxides from the dross. The analysis is given by table 1.

Hematite and magnetite in the ore are calculated from the contents of total iron and ferrous iron. By a simplified calculation method, the pigment contains 72.48% of hematite and 3.44% of magnetite.

$$\text{Total Hematite} = (Fe^{T}\text{-}Fe^{+2}) \times 1{,}43 \quad (1)$$

$$\text{Magnetite} = FeO \times \left(\frac{232}{72}\right) \quad (2)$$

$$\text{Hematite combined} = FeO + \left(\frac{232}{72}\right) - FeO \quad (3)$$

Hematite free = Total Hematite – Hematite combined

3.2. Grinding

The choice of particles sizes has consequences for dispersions stabilization modes.

Indeed, the particles of micrometric size are attracted by Van der Waals strength of high intensity and scale comparable to their sizes.

According to Cabane (2003), more generally, the particle shapes have a significant effect on the mechanical properties of aggregated dispersions.

The sampling process conditions and grinding are the same for the two materials, namely:

- Raw materials crushed to less than 160 microns
- Drying at 200°C
- Test taking equal to 10 g ± 0.3
- Screening time: 3 minutes (suction) through a mesh sieve of 32 microns.
- Depression (suction) of 1500 Pascal

We retain the initial results that the scale has a better yield of grindability than the pigment. Grinding of the iron pigment is carried out at 3, 5, 8, 12 and 15 minutes. The results are shown in figure 1. According to the first indications, the scale is not hard and it is easy to grind. For this reason, grinding of the scale LRB is carried out at 1, 2, 3, 4 and 5 minutes. The results are shown in figure 2. We conclude that the optimum time for the grinding of pigment and scale are respectively 5 and 01 minutes.

3.3. Particle Size

As noted above, the particle size affects the optical properties, the final performance of the coating and the rheological properties. The viscosity is increased by the presence of finer particles, which allows limiting the sedimentation and flocculation. These two phenomena can notably change the color intensity of a formulation significantly. According Bohic (2007), the particle size is generally between 0.1 and 50 microns. D_{50} is between 1 and 10 microns. Particle size analysis measured by a laser granulometer (Hydro 2000MU) gave us a volume distribution with particle size between 0.7 and 32 microns for scale and between 0.6 and 40 microns for the pigment. Thus, as can be seen, the average diameters (D_{50}) are 6.31 microns for the scale and 7.97 microns for the pigment milled respectively to 01 and 05 minutes. Their specific areas

Table1- Chemical analysis of iron pigment and calamine.

%	FeT	FeO	CaO	SiO_2	MgO	Al_2O_3	MnO	P_2O_5	ZnO	Fe_2O_3	Fe_3O_4
Pigment	53.18	1.07	0.76	4.23	0.36	2.13	0.64	1.63	0.75	72.48	3.44
Scale	73.83	56.9	0.42	0.14	0.37						

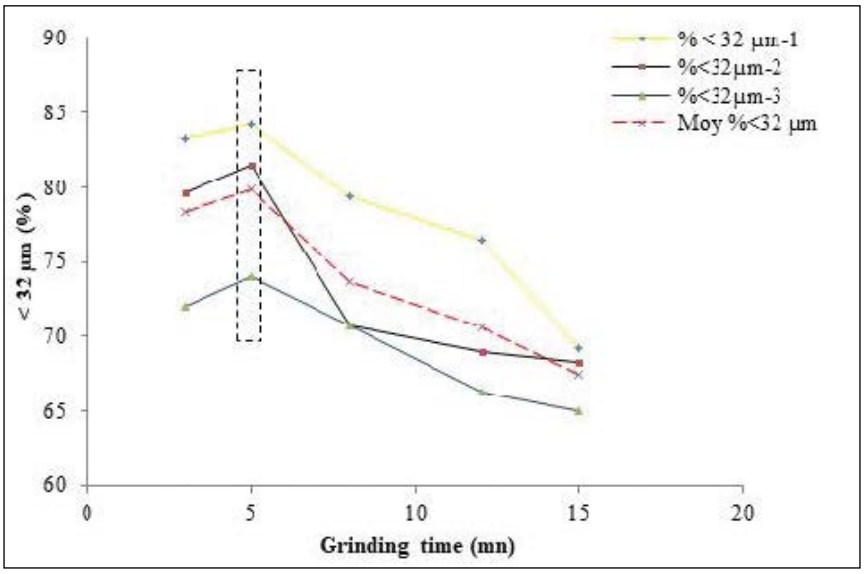

Figure 1- Grindability iron pigment.

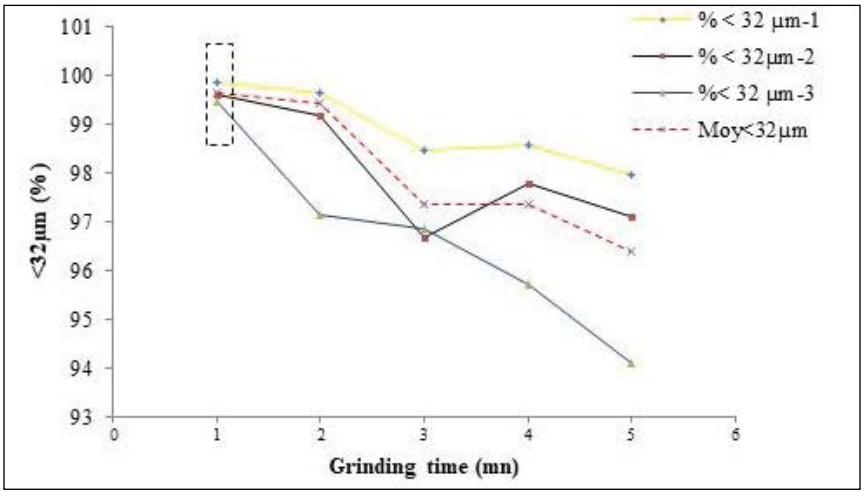

Figure 2- Grindability of the LRB scale.

are 1.6 and 1.5 m^2/g. The grinding is carried out with a laboratory disc mill and it is mostly sufficient for the development of paint with outstanding surface characteristics.

3.4. Simultaneous Thermal Analysis

Simultaneous Thermal Analysis for scale shows an increase in weight (3.602%) between 400 and 1000°C, which is attributed to the oxidation reaction of iron oxides (new phase formation) according to the reaction.

$$3FeO + \frac{1}{2} O_2 = Fe_3O_4 \quad (4)$$

Between 850°C and 1150°C, the system remains stable, according to the reaction.

$$2Fe_3O_4 + \frac{1}{2} O_2 = 3Fe_2O_3 \quad (5)$$

This oxidation is accompanied by weight gain and heat generation (exothermic reaction) respectively of 3.602% and 1.128 W/g (Figure 3).

For iron pigment, this analysis shows a mass loss which is attributed to the evaporation of water formation of iron hydroxides (goethite FeOOH dissolution). This decrease is 11.05% between temperatures 289°C and 349°C. This dissolution is accompanied by absorption of heat (endothermic)

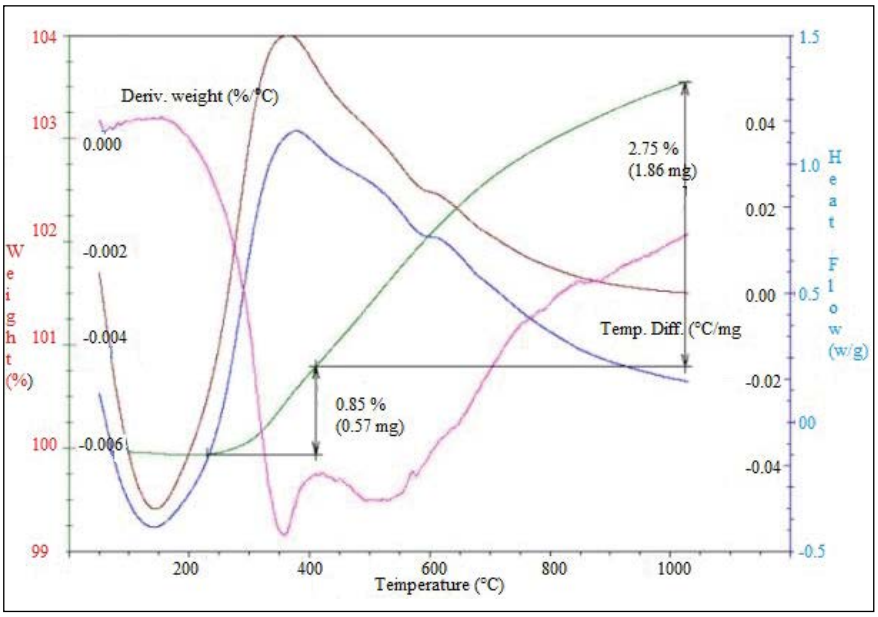

Figure 3- Simultaneous thermal analysis of the scale.

equal to 1.926 W/g as shown in figure 4. Kinetically, according Goss (1987), the transformation of αFeOOH (goethite) to αFe_2O_3 (hematite) during the heating higher than 255°C is evidenced by a loss of weight during the test. The dehydration mechanism involves the elimination of H_2O. Hematite begins to grow starting only from a weight loss of 3.97% when we have the synthetic goethite. The transformation of the product (dehydration) is done starting from the surface towards the inside of the grains by the formation of pores the release of water vapor.

In figure 4, we also noticed that there's a first small endothermic peak corresponding to the fact of a quantity of heat required to evaporate moisture from the pigment at a temperature lower than 200°C. Thermal analysis mixtures synthesized with the addition of (5, 10, 15, 20, 25 and 35%) of scale in the natural iron pigment showed a weight loss fall. This

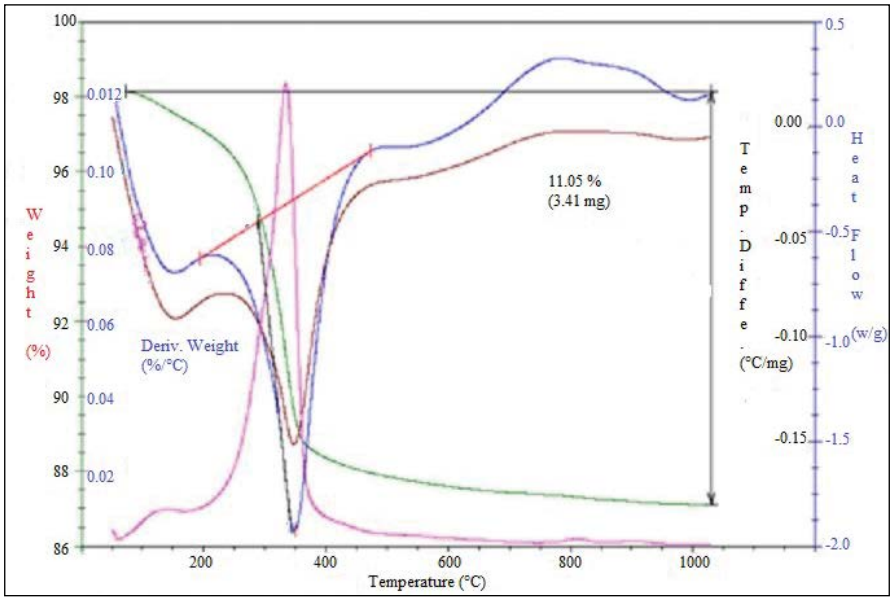

Figure 4- Simultaneous thermal analysis of iron pigment.

phenomenon can be explained by the decrease in the amount of iron pigment in favor of the scale. Loss of weight is proportional to the rate of addition of mill scale, when the injection rate of scale increases, the weight loss decreases. The heat flux takes an increasing polynomial pace, the energy expended for the dissolution of iron hydroxides (goethite dissociation) in the iron pigment is offset by the energy released by the scale (oxidation reactions).

3.5. Scanning Electron Microscope (SEM)

The observation scale milled during 5 min on the SEM showed a homogeneous structure composed of iron oxide grains with sizes and forms ranging from 1 and 10 micrometers (Figure 5a). Chemical analysis on all ranging in observation in the range given by EDS shows the dominant existence of iron with very little of manganese and some traces of silicon and aluminum. Iron is the main component of the steel from which the scale was formed (oxidized iron), manganese is in the chemical composition of the steel. Traces of Si and Al can originate either from the chemical composition of the iron-carbon alloy (steel) or from the powder of the continuous casting.

Exploration picture by scanning electron microscope of red iron pigment shows a grain aggregate rounded formed at least of iron oxide and gangue (Figure 5b). The analysis by EDS shows a predominance of iron with a rather important gangue containing the four predominant oxides in the case of iron ore deposits. Chemical elements forming these four oxides are silicon, calcium, aluminum and magnesium.

3.6. X-ray Diffraction Analysis (XRD)

The X-ray diffractogram (Figure 6) shows that the crystalline phases are mixtures of phases of wustite, magnetite and hematite for calamine. Wustite ($Fe_{0.94}O$) is of cubic structure, magnetite (Fe_3O_4) is orthorhombic and hematite (Fe_2O_3) is of trigonal structure. As for the pigment, the X-Ray Diffractogram (Figure 7) shows that the crystalline phases are also mixtures of 6 phases. These phases are goethite, hematite, fayalite, silica, phosphorus pentoxide, and hausmannite.

3.7. Spectrophotometer Analysis

The analysis of the absorption of light by the materials showed weak and constant absorption in the ultraviolet and visible light domains (Figure 8). In the visible domain (380 to 780 nm), we observe an almost zero absorbance. A coloring substance is most often defined by its ability to absorb light radiation in the visible spectrum of light. The analysis of the reflectance of these materials in the visible range has shown excellent reflectance, note that the curve is on average 120% (Figure 9). We can deduce that the constituents of these materials themselves become sources of radiation that can be added to the total reflected radiation. The incident radiation is totally reflected.

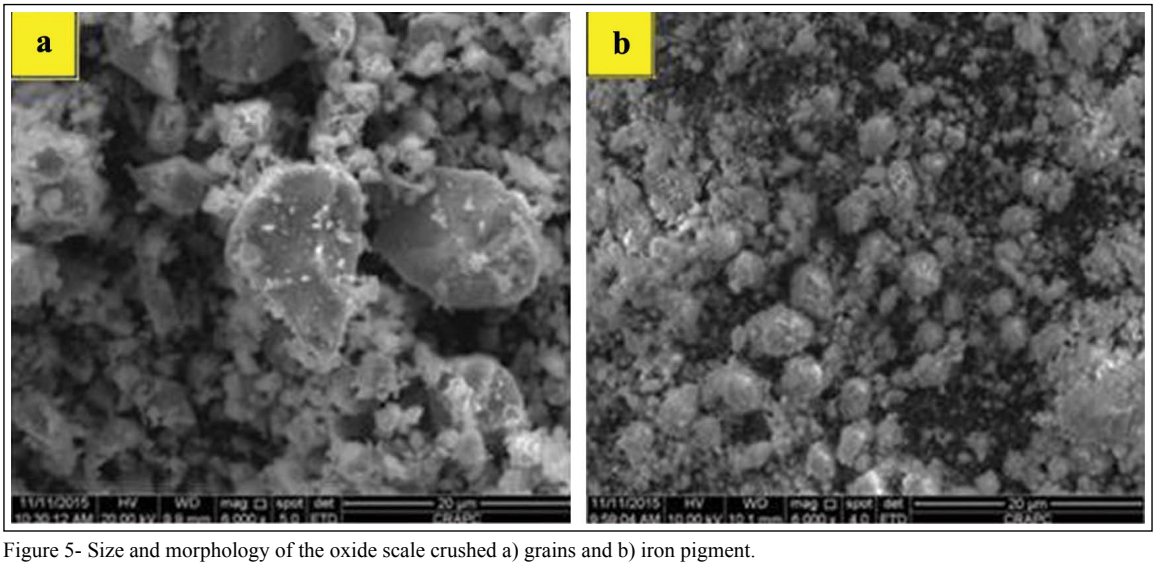

Figure 5- Size and morphology of the oxide scale crushed a) grains and b) iron pigment.

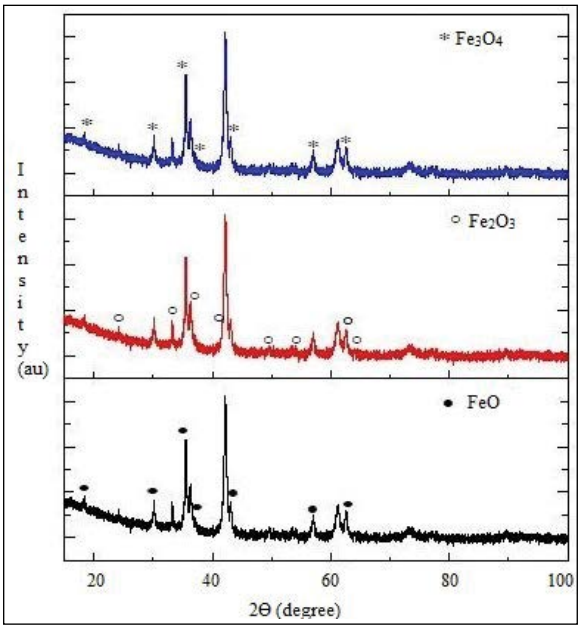

Figure 6- Calamine diffractometer (FeO-Cubic, Fe_2O_3-Orthorhombic and Fe_3O_4-trigonal).

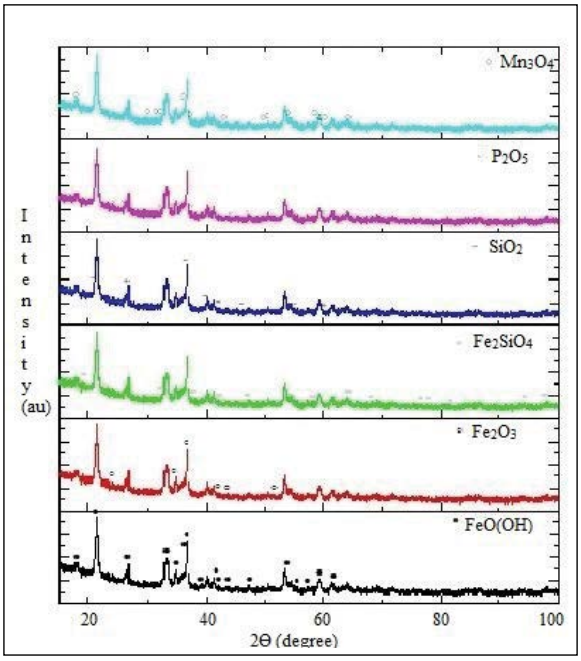

Figure 7- Iron pigment diffractometer (FeOOH, Fe_2O_3, Fe_2SiO_4, Mn_3O_4, SiO_2, P_2O_5).

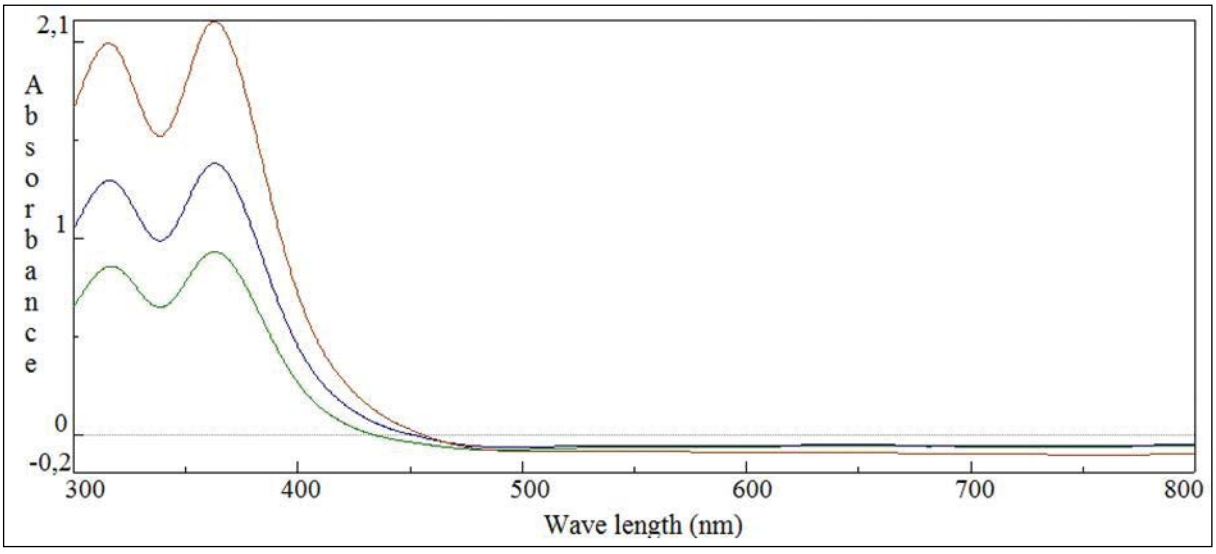

Figure 8- Absorbance of materials.

4. Conclusion

Chemical analysis shows that raw materials contain iron in the form of oxide. The scale has a uniform structure of magnetite. The pigment contains, in addition iron, a siliceous gangue. Calamine, in turn, consists of 98% iron oxides.

Preliminary grinding tests showed that the milling time of the iron pigment is more important than the scale.

The analysis of the particle sizes is carried out by the laser granulometer. It shows a density distribution of particles with a size between 0.7 and 32 µm for

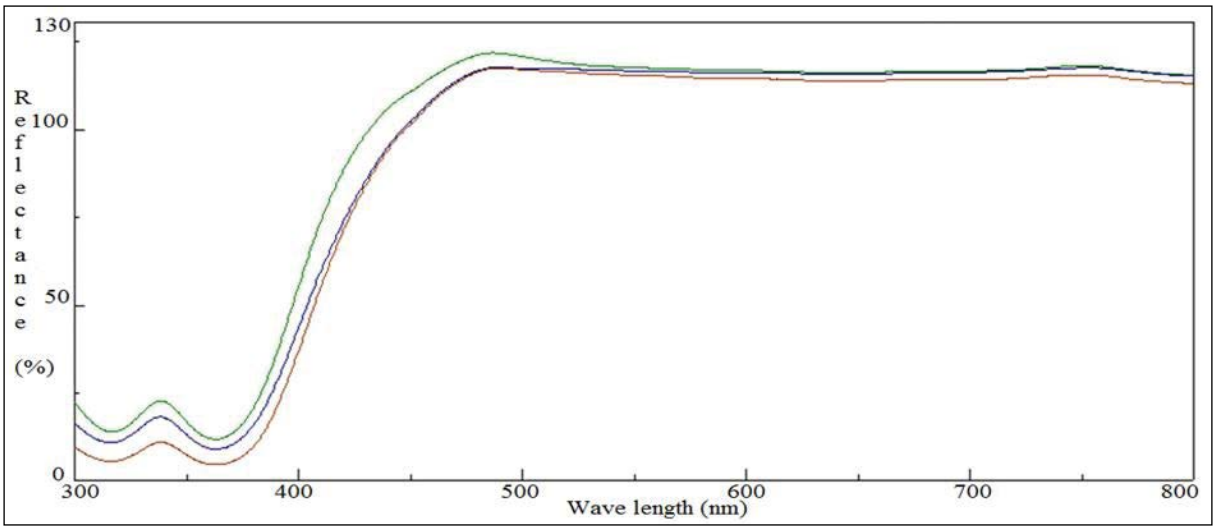

Figure 9- Reflectance of materials.

scale and between 0.6 and 40 µm for the pigment. Means that the average diameters D_{50} are 6.31 µm for the scale and 7.97 µm for the pigment milled respectively at 01 and 05 minutes. Their specific area is 1.6 and 1.5 m^2/g.

Simultaneous Thermal Analysis for calamine shows an increase in weight (3.602%) between 400 and 1000°C, which is attributed to the oxidation reaction of iron oxides (new phases formation).

For iron pigment, this analysis shows a mass loss which is attributed to the evaporation of water formation of iron hydroxides (goethite - FeOOH dissolution).

The observation scale milled during 5 min on the SEM showed a homogeneous structure composed of iron oxide grains with size and forms ranging from 1 µm to 10 µm.

Exploration picture by scanning electron microscope of red iron pigment shows a grain aggregate rounded formed at least iron oxide and gangue.

The X-ray diffractograms show that the crystalline phases are mixtures of phases of wustite, magnetite and hematite for scale. As for the pigment, the X-Ray Diffractograms shows that the crystalline phases are also mixtures of 6 phases. These phases are goethite, hematite, fayalite, silica, phosphorus pentoxide, and hausmannite.

The analysis of the absorption of light by the materials showed weak and constant absorption in the ultraviolet and visible light domains.

The analysis of the reflectance of these materials in the visible range has shown excellent reflectance, note that the curve is on average.

Acknowledgments

This study was carried out as part of the project for the exploitation of mineral resources and the recycling of by-products at the level of the Industrial Technology Research Center (CRTI). The author acknowledges Prof. Mokhtar Ghers for his contributions to the development of this article with his constructive criticism, Prof. Salah Bouhouche for helping develop the statistical analysis and his prestigious advice and Dr. Toufik Chouchane for the financial support of the consumables during the tests carried out in this work.

References

Bohic, M. 2007. Caractérisation de la surface de pigments traités par des polyesters acrylique, thèse de doctorat, école des mines de Paris.

Brinke, A. J. W., A., Bailey, L., B., Henk, Lekkerkerker, H. N. W., Maitland. G. C. 2007. Rheology modification in mixed shape colloidal dispersions. Part I: Pure components. Soft Matter 3, 1145–1162.

Cabane, B. 2003. Formulation des dispersions, Dossier techniques de l'ingénieur, J2 185, p.13.

Chen, R.Y., Yuen, W.Y.D. 2005. Examination of Oxide Scales of Hot Rolled Steel Products, ISIJ International 45(1), 52–59.

Della, V.P., Junkes, J.A., Montedo, O.R.K., Oliveira, A.P.N., Rambo, C.R., Hotza, D. 2007. Synthesis of hematite from steel scrap to produce ceramic pigments. Am Ceram Soc Bull 86 (5), 9101-9107.

Goss, C.J. 1987. The kinetics and reaction mechanism of the goethite to hematite transformation, Mineral Mag 51, 437-451

Husband, J.C. Preston, J.S. Gate, L.F. Storer, A. Creaton, P. 2006. The influence of pigment particle shape on the in-plane tensile strength properties of kaolin-based coating layers. TAPPI J 5(12), 3-8.

Michel, F., Courard, L. 1986. Apport de la granulométrie laser dans la caractérisation physique des fillers calcaires, Septième édition des Journées scientifiques du Regroupement francophone pour la recherche et la formation sur le béton, Toulouse, France 40-49.

Morvan, M. 2002. Fabrice, Elaboration, Caractérisation et développement de nouveaux grades de pigments aluminium, Thèse de doctorat en physico-chimie de la matière condensée, Université de Bordeaux I - France, Ecole doctorale des Sciences Chimiques, p-47, janvier.

Philip, B. 2010. Histoire vivante des couleurs, 5000 ans de peinture racontée par les pigments. Paris, Hazan.

Thirion, V.M. 2016. Spectrométrie de fluorescence X. Circulation et provenance des matériaux dans les sociétés anciennes, Collection Sciences Archéologiques, 9782813001634.

Umadevi, T., Brahmacharyulu, A., Karthik, P., Mahapatra, P.C., Prabhu, M., Ranjan, M. 2013. Recycling of steel plant mill scale via iron ore sintering plant. Journal Ironmaking and Steelmaking, Processes, Products and Applications 39(3), 222-227.

Bulletin of the Mineral Research and Exploration

http://bulletin.mta.gov.tr

Estimation of co-seismic land deformation due to Mw 7.3 2017 earthquake in Iran (12 November 2017) using Sentinel-1 DInSAR

Fatma CANASLAN ÇOMUT[a*], Şule GÜRBOĞA[b] and Tayeb SMAIL[c]

[a]*Disaster and Emergency Directorate of Denizli (AFAD Denizli), Turkey,*
[b]*General Directorate of Mineral Research and Exploration, Turkey*
[c]*Department of Civil Engineering, Blida University, Algeria*

Research Article

Keywords:
Interferometry, DInSAR, 12 November 2017 Iran earthquake.

ABSTRACT

A strong shaking with Mw 7.3 occurred on 12th November 2017 around the Sarpol-e Zahab town in the border area between Iran and Iraq. It has a number of foreshocks and aftershocks increasing the total deformation, cumulatively. In this study, we have investigated how earth surface deformed after such a strong earthquake and its scatters. Because, the deformation inspection are indispensable for the safety of citizens and infrastructures. The best way for monitoring of surface deformation in such a big event is the SAR technique. This system can work effectively during night and day under different weather conditions. The Interferometric SAR (InSAR) allows accurate measurements of surface deformation in mm resolution. There are several methods for the application of SAR techniques and one of them is Differential InSAR (DInSAR) indicating an uplift and subsidence around epicentral area precisely. We preferred to use it for sensitive vertical displacement in the target area. The seismological data from the observatory centers indicate that the recent earthquake sourced from the NW-SE trending, northeast dipping High Zagros Reverse Fault Zone. According to the results, epicentral area has been exposed a vertical displacement with 90 cm uplift and -41 cm subsidence in the northeastern and southwestern block of the fault, respectively.

Received Date: 26.12.2018
Accepted Date: 01.07.2019

1. Introduction

Sarpol-e Zahab earthquake is the largest event after the occurrence of 1909 earthquake around the shaking area (Ambraseys and Melville, 1982). 1909 and recent events sourced from the Zagros fold belt in the Zagros vicinity that has the most of the active faults of Iran. The reason for the seismic activities in this region is the continental collision between the African-Arabian and Eurasian plates (Şengör and Kidd, 1979; Dewey et al., 1986; Dilek et al., 2009; Ghalamghash et al., 2016; Fahim Guilany et al., 2019) (Figure 1). Moreover, the Zagros fold belt is characterized by a folded 12–14 km thick sedimentary cover deposited on the northeastern continental border of the Arabian plate (Falcon, 1974; Colman-Sadd, 1978). From early Mesozoic to Quaternary, the collision creates a compressional tectonic regime where compression has stemmed from subduction of NeoTethyan oceanic crust underneath the Iranian Central Block, and the subsequent collision between the Arabian and Eurasian plates along the Zagros suture zone (Şengör and Kidd, 1979; Dewey et al., 1986; Dilek et al., 2009; Ghalamghash et al., 2016). Naturally, the area experiences the high seismic activity. The convergent motion creates a huge amount of relief differences and elevated mountainous area.

Citation info: Canaslan Çomut, F., Gürboğa, Ş., Smail, T. 2020. Estimation of co-seismic land deformation due to Mw 7.3 2017 earthquake in Iran (12 November 2017) using Sentinel-1 DInSAR. Bulletin of the Mineral Research and Exploration 162, 11-30. https://doi.org/10.19111/bulletinofmre.604026

* *Corresponding author: Fatma CANALAN ÇOMUT, fatma.c.comut@afad.gov.tr*

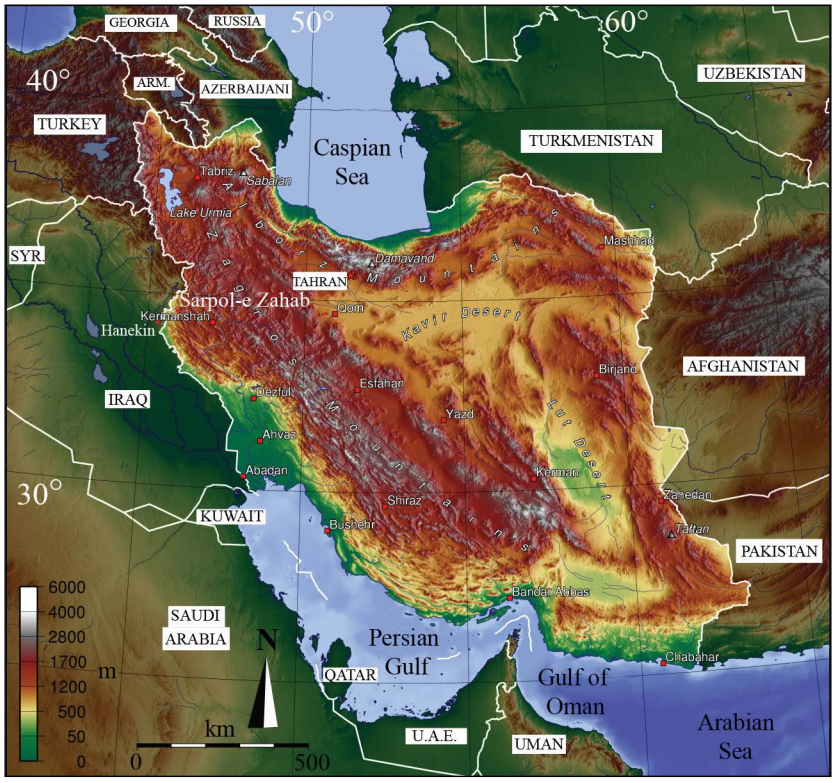

Figure 1- Map of Zagros area showing the location of Sarpol-e Zahab and Hanekin settlements with digital elevation model of the area (Emami et al., 2010).

Comparing two towns in both sides of mountainous area and plateau area of the fold belt, Sarpol-e Zahab is located 618 m in the Iran, and Hanekin is located 200 m above the sea level in the Iraq (Figure 1, Emami et al., 2010). There is approximately 400 km altitude difference in just 50 km distance between these towns. In case of such a big earthquake, an important vertical displacement should be happening and the amount of vertical motion is significant for the deformation in the crust. Newly growing technologies give a chance to determine vertical displacement in cm to mm scale.

Satellite Interferometric Synthetic Aperture Radar (InSAR) is a technique being develop very intensively during last 20 years (Hanssen, 2001). It is famous for giving information about vertical ground motion or deformation of structures in a millimetric scale. When it is compared with the older systems achieving the detection of surface deformation, there are many advantages and disadvantages. One of the advantage is related to high spatial resolution and short temporal range between the measurements. It means the same area is being monitored with high resolution in a more frequent time slices. It will increase the sensitivity of the taken data. On the other hand, the signal could be often lost due to the weather condition, agricultural activity etc. In this case, it could not be possible a solution for the lost data. However, this problem is tried to be solved with improved satellite technologies.

Within new satellite systems of high revisit time as Sentinel-1/2, InSAR has now a huge capacity to provide more reliable and useful information that can be used to offer detection of hazardous movements at the surface, their delineation and spatiotemporal description. This can be applied in practice as within an early warning system to avoid the damages such as identification of slow landslide motions, determination of sinkholes or static risk evaluation for buildings and structures. An approach of detecting risk for infrastructure using InSAR is currently in experimental stage, however the potential is discussed and proved by several works (Thiebes, 2012; Intrieri et al., 2013). The technique that would semi-automatically process a long time series of high quality satellite SAR image. It is used for the recognition of recent movements in a selected area using different approaches such as Permanent Scatterers (Ferretti et al., 2005). This method can be

extended by probabilistic approach in order to provide an estimation of structural deformation in near future, supposing a continuous trend of detected movement. Detected and predicted movements of a structure or earth surface can be evaluated with other data such as geological settings or reference in-situ measurements that would cause a risk of serious damages. A proper interpretation could be applied with an interdisciplinary connection of other experts offering a completeness of the system.

This paper presents a transfer of knowledge about InSAR technology and methodological aspects of InSAR application towards detection of dangerous terrain and structure movements due to Mw 7.3, 12 November 2017 Iran earthquake. We focus on estimating the co-seismic displacements along the line-of-sight LOS direction by mean of interferometry SAR. In order to investigate this issue, we used Interferometric Synthetic Aperture Radar. Presented results are based on the processing of SAR data using Differential InSAR, to highlight the benefits of high resolution SAR sensors for the purpose of deformation monitoring, the datasets are from Sentinel-1 SAR images with 2 different passes, ascending and descending. The main objectives for this work is to detect ground LOS displacement, for the earthquake that struck Iraq-Iran border on 12 November 2017 and its effect on nearby villages.

2. Methodology

Interferometric Synthetic Aperture Radar (InSAR) is a microwave imaging system and belong the system SAR signals contains amplitude and phase components of the same pixel. With this technology it is possible to measure surface movement and estimate the topography (Pritchard, 2006; Kim, 2013). SAR imaging uses amplitude (intensity) of backscattered echoes. Radar sees through clouds – all – weather imagining is possible and doesn't need illumination by the Sun – can image day and night. Surface roughness and slopes control the strength of the backscatter. All full resolution SAR images have both an amplitude component and a phase component; called as "SLC (single look complex)".

The multiplication of master SLC data and a conjugate of slave SLC data generates an interferogram which includes topographic phase effect, atmospheric distortion, baseline errors and noise (Kim, 2013; Netzband et al., 2007; Goudarzi 2010). The calculation of interferogram is done by using the formula given below;

$$\emptyset_{ifgs} = \emptyset_{topo} + \emptyset_{baseline} + \emptyset_{atm} + \emptyset_{def} + \emptyset_{noise} \quad (1.1)$$

where

$\emptyset_{ifgs}$ is interferogram

$\emptyset_{topo}$ is topography phase effect

$\emptyset_{baseline}$ is a baseline error phase

$\emptyset_{atm}$ is an atmospheric phase

$\emptyset_{def}$ is deformation phase

$\emptyset_{noise}$ refers to noise phase contribution.

Instead of noise and baseline error phase, equation (1.1) can be also evaluated as pixel and orbital effect to the interferogram generation. In this way; components of interferometric phase can be defining as (1.2).

$$\Delta\emptyset_{int} = \Delta\emptyset_{orb} + \Delta\emptyset_{topo} + \Delta\emptyset_{atm} + \Delta\emptyset_{pixel} + \Delta\emptyset_{def} \quad (1.2)$$

The phase of an individual interferogram can be divided into five parts:

i. Orbit ($\Delta\emptyset_{orb}$), topography ($\Delta\emptyset_{topo}$) and deformation phase ($\Delta\emptyset_{def}$) are related to the difference distance between the satellite and the ground.

ii. Atmospheric phase $\Delta\emptyset_{atm}$ is related to the difference in the properties of the medium that the radar pulse moves through.

iii. Pixel phase ($\Delta\emptyset_{pixel}$) is related to the change in properties of the pixel on the ground.

A differential interferogram is one in which the effects of orbital baselines and topography have been removed. It is called as DInSAR.

Other components of SAR applications is co-registration that aims to find an optimal transformation model which requires pixel-to-pixel match between common features in SAR image pairs (Li and James, 2008). The precise co-registration rises the coherence of the interferogram, improves the value of the phase unwrapping process and therefore leads to a more accurate phase in the final interferogram (Marinkovic and Ramon, 2004). In this level, a main question comes up "How does InSAR achieve the monitoring

of ground displacement?" The sensitivity of many studies indicate that the accuracy InSAR is~ 0.75 mm in vertical (N-S) and ~ 0.5 mm in horizontal (E-W) direction by using a series of 10-30 images. The difference between the accuracy of N-S and E-W directions depend on many factors like noise in N-S (Samieie-Esfahany et al., 2009). This result has been obtained that in case of a number of high resolution images applied to arid (low vegetation) and structural areas such as buildings, bridges, pipelines, etc., the outcomes are more accurate.

Microwave radiation is emitted as short signals with the help of antennas on the satellite platform. The signals have a specific wavelength, amplitude and polarization. In the properties of signals sent to the target on the earth. There are some changes in the transmission and recovery process throughout the atmosphere. These signals are reversed by the same antenna and recorded in phase, polarization and amplitude. Finally, the image production process, which varies depending on the satellite sensor and which covers the target area, is realized (eg IS2-mode image size for ASAR data of Envisat 100 km x 100 km, ALOS PALSAR data (FBS mode) 70 km x 70 km (including a frame).

Perpendicular sensor-target direction to satellite orbit; the direction of the radar (Line of Sight -LOS) or the oblique length. The coordinates of a radar image consist of the target-sensor distance and the position component shown along the trajectory of the sensor. The second is called azimuth. The geometric description of the SAR system is shown in figure 2 with the geometric elements.

The coordinate system of a SAR image is different from the location coordinate (or geographic) coordinate system. x and y axes are considered as latitude and longitude in geographic system, but in SAR system it is considered as azimuth and slant range (Figure 3).

2.1. Ascending and Descending Pass

Satellite platforms produce images according to two different modes, increasing and decreasing. The geometry of the ascending mode occurs at the South-North transition of the satellite and the target is observed from the west, while in the descending mode the target is observed from the east during the North-South transition.

The basis of the observation of the SAR satellites is that they display the surface as inclined instead of

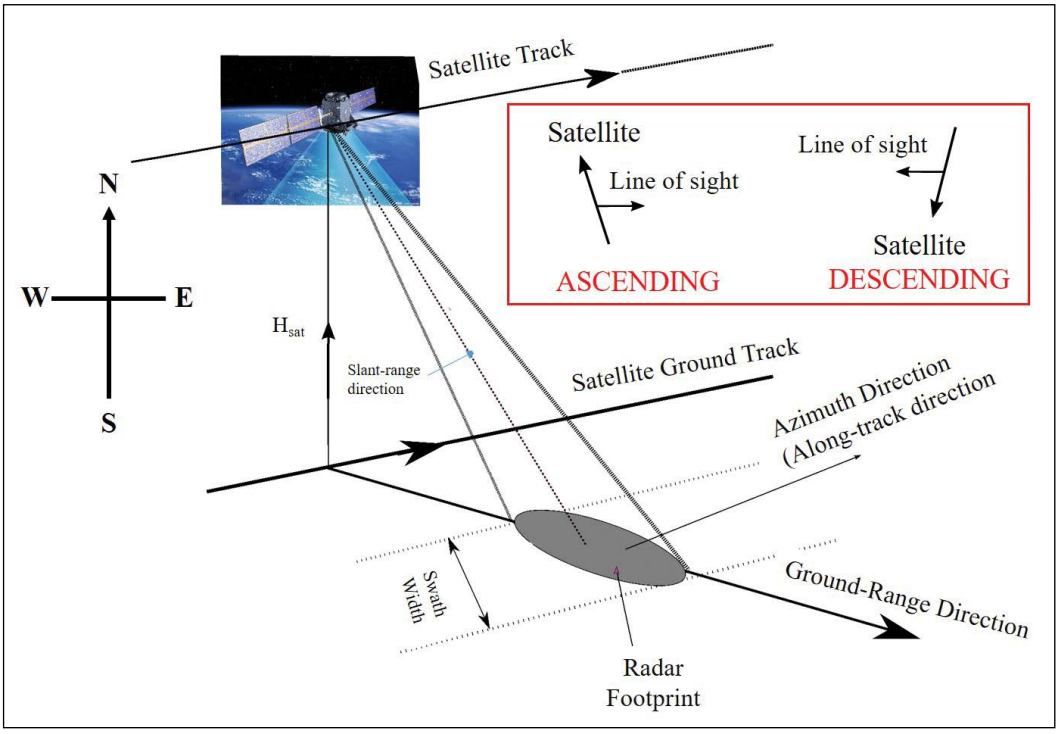

Figure 2- Geometric description of the SAR system.

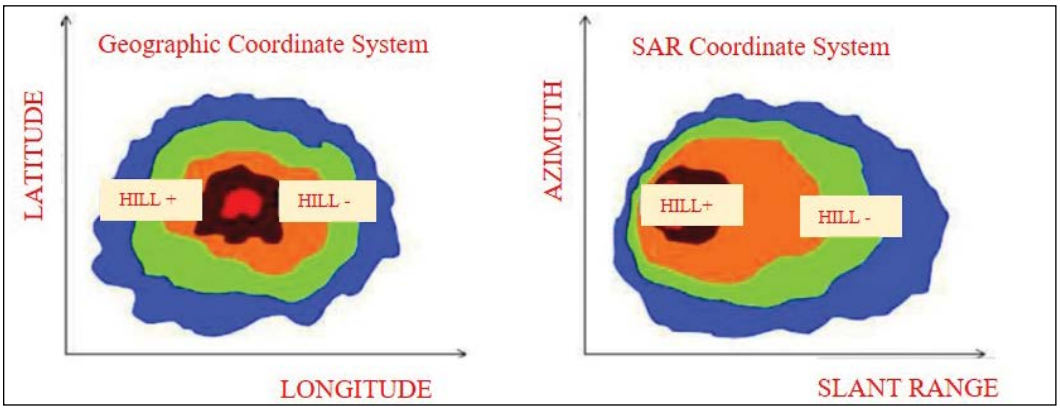

Figure 3- Comparison of Geographic Coordinates with SAR coordinates (by changing from Hooper, 2006).

vertical. When the ground moves west, the ground motion is close to the satellite if the satellite is observing the orbit that is increasing in the north. On the contrary, if the satellite is observing in the descending mode towards the south, ground motion is far from the satellite (Figure 4).

The numbers written under the color chart in figure 4. shows distance between the ground and the satellite from line-of-sight (LOS) of the satellite. Negative values indicate that the distance between the satellite and the ground is reduced. In this study, it has been used both data from ascending and descending orbits to recognize certain displacement and compare the results for clear understanding the fault track between each interferograms.

2.2. DInSAR Processing Steps

All InSAR processing steps except phase unwrapping stage, have been calculated with using SNAP (Sentinel Application Platform) software which is free for remote sensing software users created by ESA (European Space Agency). Processing steps were started with co-registrating master and slave images, interferogram formation, topographic phase removing, phase filtering and phase unwrapping which is the last and one of the most critical step of InSAR processing made using by SNAPHU (Statistical-Cost, Network-Flow Algorithm for Phase Unwrapping). 'Unwrapping' is the process of converting the cyclical (modulo 2π) phase signal of an interferogram into a continuous phase signal. It is usually preferable to use unwrapped phase for deformation or topography estimation. After all steps completed successfully, geocoding step (conversion of phase values from Line

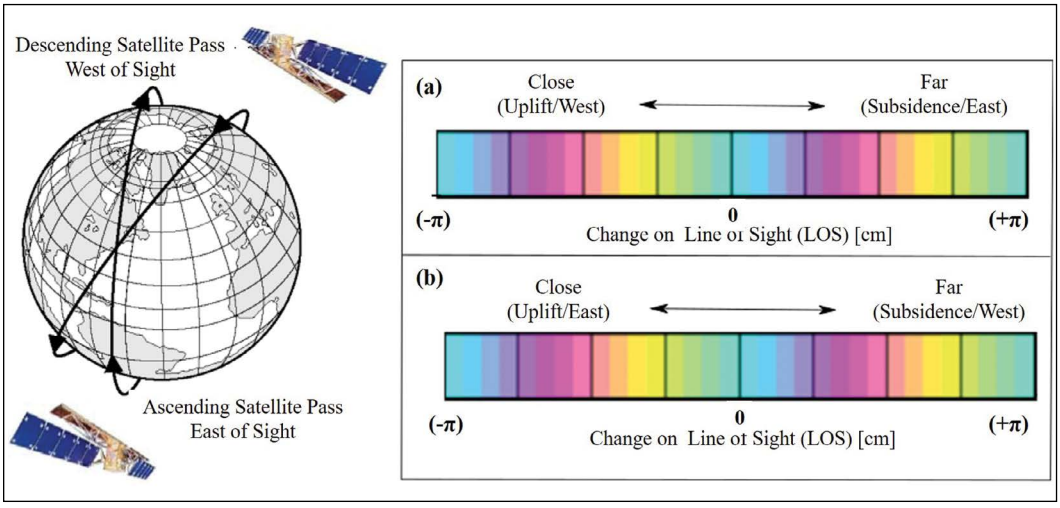

Figure 4- Schematic representation of the polar orbital satellites with an east and west view perspective, (Left panel). a) observations from ascending and b) descending orbits (right panel) (by from Çomut, 2016).

of Sight to Ellipsoidal Height) done for geo-location.

Briefly; a typical DInSAR processing chain in practice will have multiple steps, usually in this order:

1) Matching (co-registering) the SLCs
2) Forming the interferogram by differencing phases
3) Removing the effects of orbit position and Earth curvature
4) Registering the interferogram to a DEM; removing the effects of topography
5) Filtering and unwrapping

The detailed explanation of DInSAR processing flow chart is shown in figure 5.

3. Study Area

The Zagros fold-and-thrust belt is the world's most seismically active mountain ranges, and is influential in our understanding of continental collisions. It is almost 1500 km in length and ~300 km wide around the south-western Iran and a major structural element of the Alpine–Himalayan belt (Nissen et al., 2007, 2010 and 2011). This belt extends towards northwest up to Taurides in Turkey. Because of the continuation in mountainious topography, the suture zone represents the geological units related to collision of Eurasian and Arabian plates, it is called as Bitlis-Zagros suture zone in literature. Zagros fold belt is an important structure due to the accumulation of hydrocarbons that provides 2/3 oil and 1/3 gas-resources of the world. The accumulation is directly related to the stratigraphy and structural evolution of the belt (Alavi,

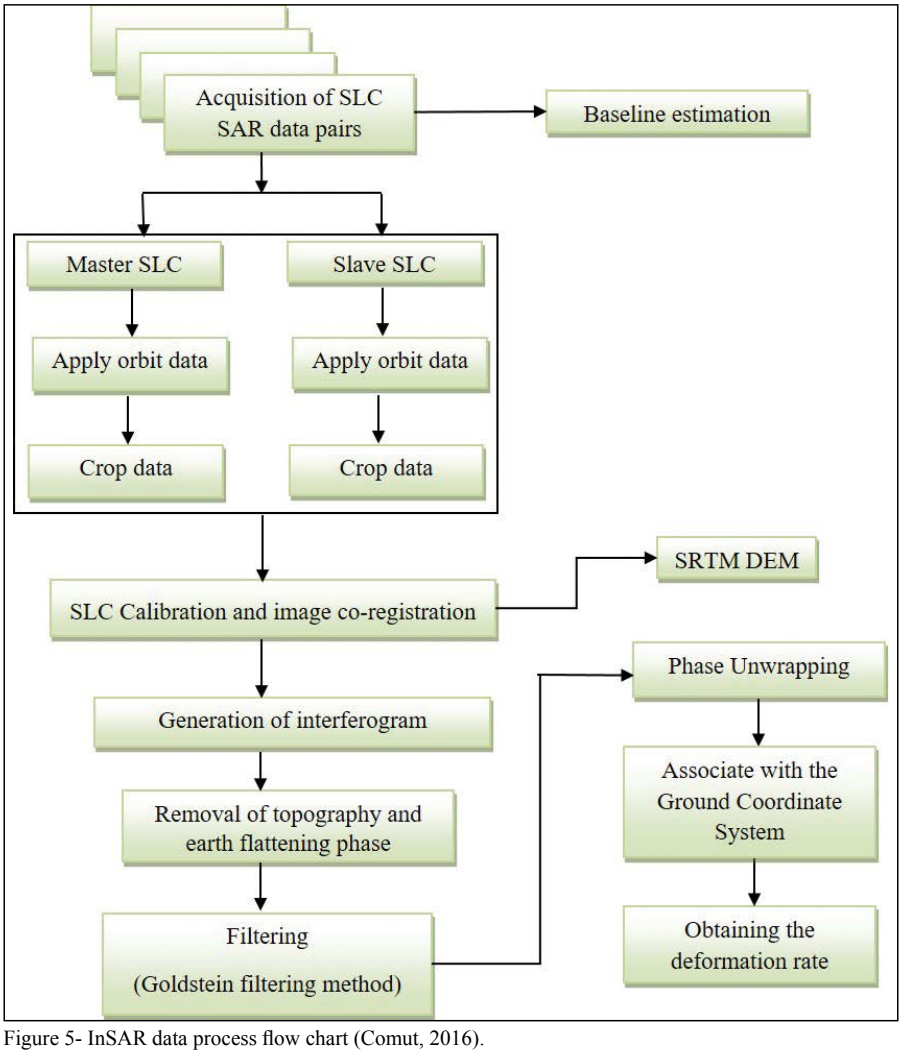

Figure 5- InSAR data process flow chart (Comut, 2016).

2007). This situation results a number of studies based on stratigraphy and geophysical exploration of SW verging folds and NW-SE trending thrust-reverse fault system (Colman-Sadd, 1978; McQuarrie, 2004; Dehbozorgi et al., 2010) (Figure 6). Furthermore, there are several studies related to the earthquakes in the area. Because of the very rare (Walker et al., 2005) and usually absent indications of coseismic ruptures at the surface, these earlier studies concluded that the larger earthquakes in the Zagros involve faulting mostly within the basement. However, more recent geodetic studies, which use radar interferometry (InSAR) to determine the depth extents of coseismic faulting, have revealed that moderate-sized earthquakes (up to Mw ~6) also occur within the sedimentary cover, rupturing between depths of ~4 and ~9 km (Nissen et al., 2007, 2010; Roustaei et al., 2010).

Zagros fault system which is the boundary between Arabian plate in the SW and Eurasian plate in the NE is a seismically active area experiencing a number of huge earthquakes. The events are the main reason for the deformation of the area by means of convergent plate motions. According to the fault mechanism solutions of different observartory centers (Figure 7), the strike of source fault is approximately NNW-SSE and dipping towards NE. The configuration of the hangingwall and footwall blocks indicate that NE block (hanging block) of the fault is uplifted. The key point what is the amount of uplift or vertical displacement near epicentral area. In November 12th 2017, a devastating earthquake with M=7.3 happened around Sarpol-e Zahab town. The epicenter location is determined near the border of Iraq-Iran according to USGS (34.905°N 45.956°E, 22.0 km depth).

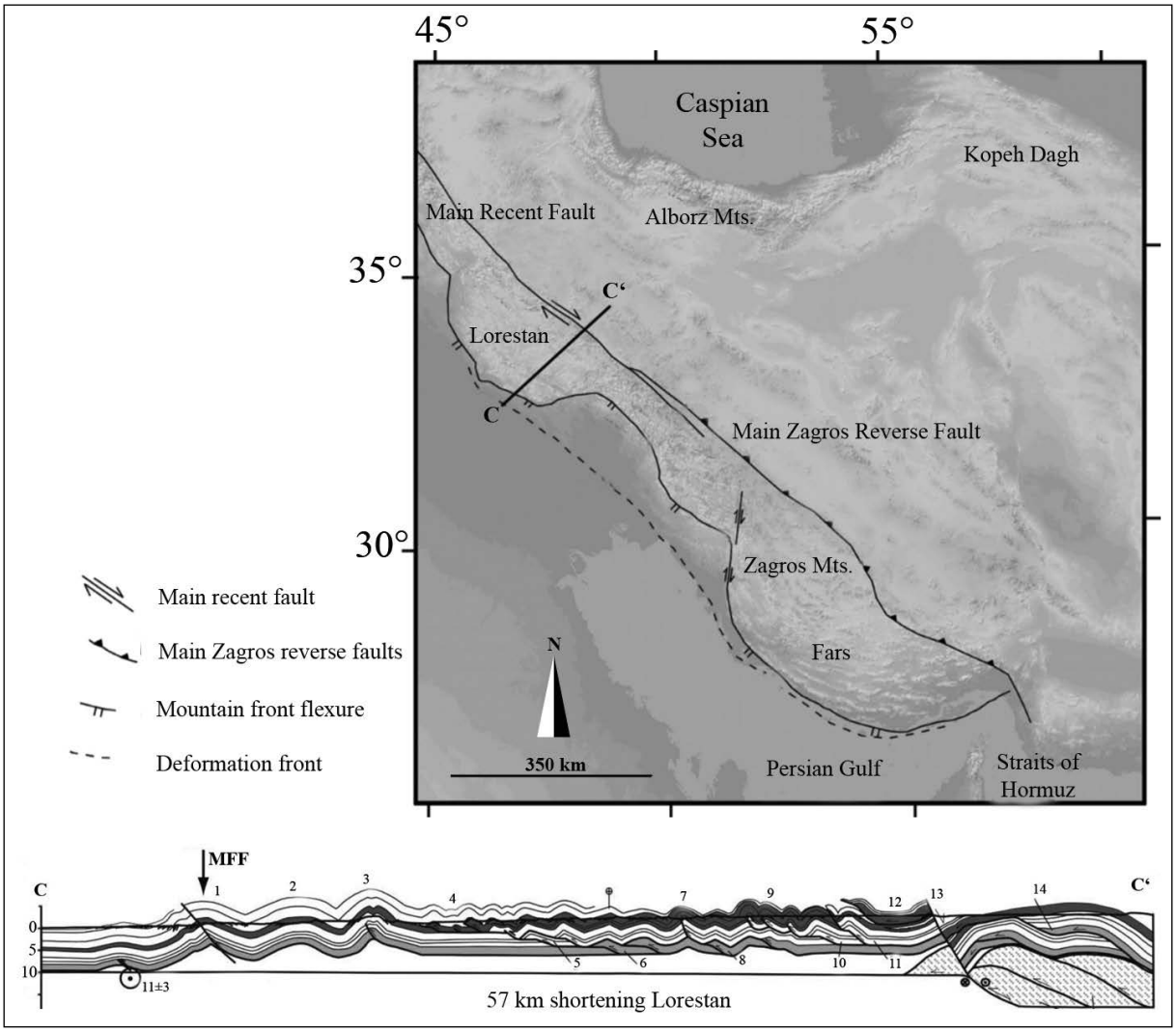

Figure 6- Location of the Zagros fault system and cross-section of epicentral area C-C' (McQuarrie, 2004).

Eigth different observatory centers figured out focal mechanism solutions of the earthquake and they are mostly the same attitude thrust faulting with minor strike slip component (Figure 7). The convergent plate boundary between Arabian and Eurasian creates such strong seismic activities and a significant infrastructure damages had caused, over 530 people were killed and 8000 were injured.

Even though there are a number of geological studies in literature related to the area that is a huge laboratory for the plate motions, we focused on the surface deformation because of the earthquake by means of SAR analyses. A series of SAR images have been obtained from Sentinel-1. The intensity of the SAR image directly corresponds to terrain slope and surface roughness, the AOI (Area of Interest) have rough topography with rugged terrain, mountains and rivers (Figure 8). Selecting ascending or descending paths is very important step to determine the deformation from different angles. If the selection has not been done properly, InSAR does not give the best results.

4. Data

Four scenes of Sentinel-1 C-band were used for InSAR processing that areas represented in table 1. All scenes are vertical-transmit and vertical-receive

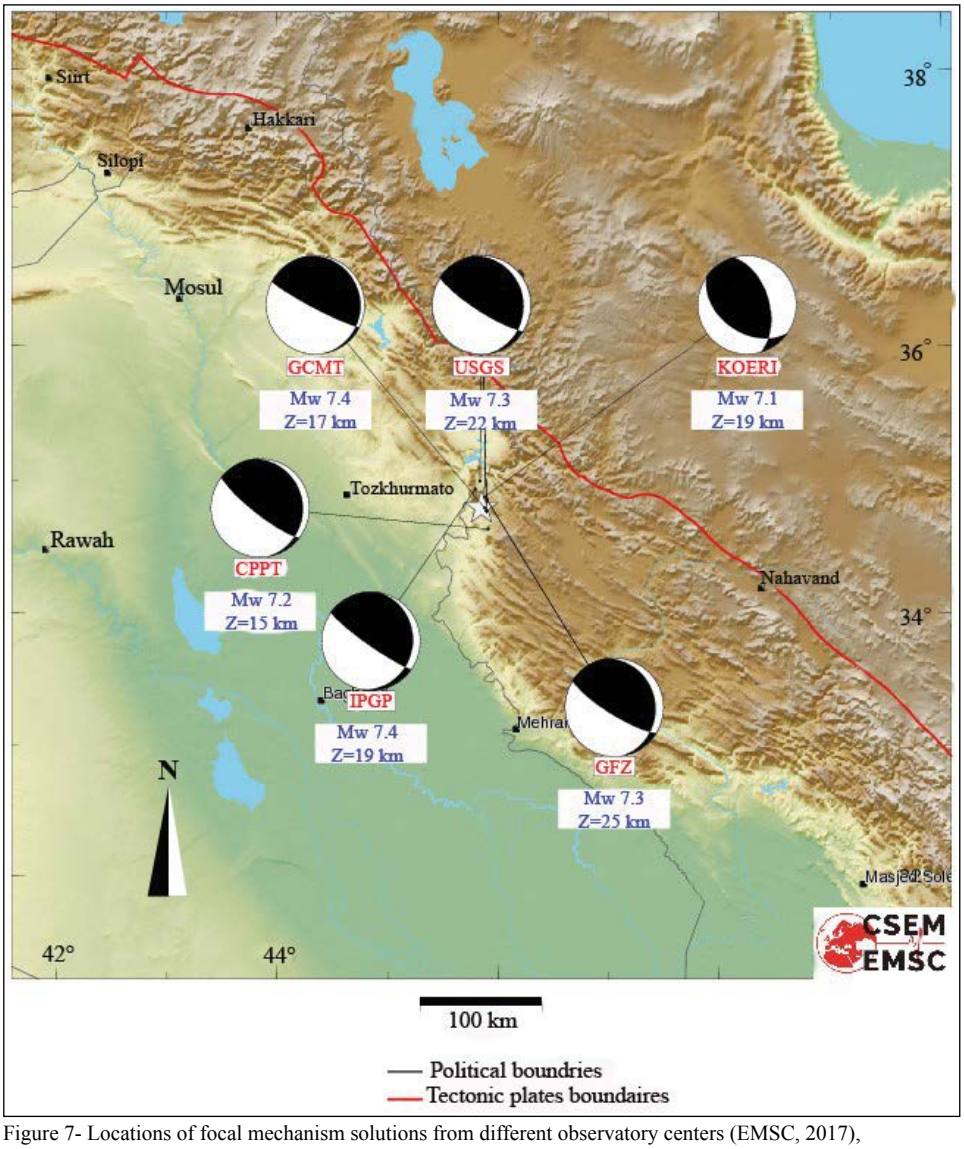

Figure 7- Locations of focal mechanism solutions from different observatory centers (EMSC, 2017), https://earthquake.usgs.gov/earthquakes/eventpage/us2000bmcg#region-info.

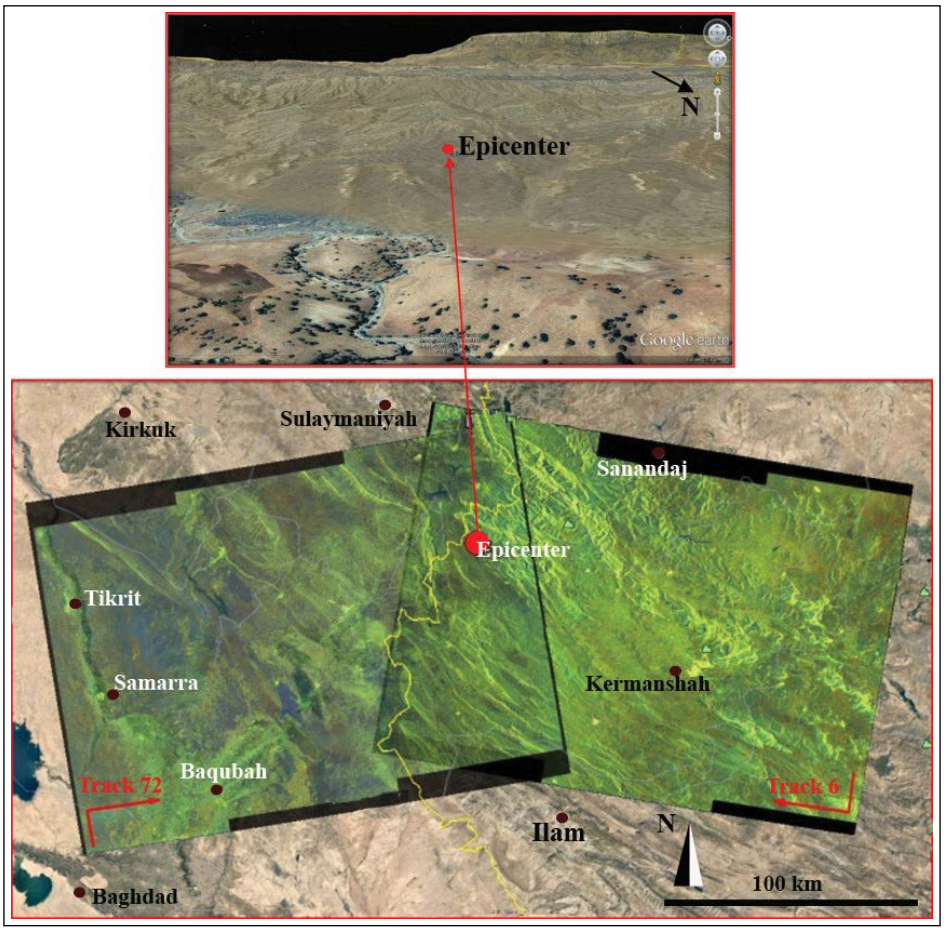

Figure 8- AOI Relief map, Iran and the frames of the ascending (left) and descending (right) configuration of Sentinel-1 image used for the study (base maps are from Google earth).

Table 1- Characteristics of Sentinel-1 InSAR pairs for the 72 and 6 Tracks (B_{tem}: temporal baseline, B_{per}: perpendicular baseline).

Track	**72 VV**		**6 VV**	
Pass	ASCENDING		DESCENDING	
Date	11/11/2017	11/17/2017	11/07/2017	11/19/2017
B_{per} (m)	62.22		14.44	
B_{temp} (m)	6		12	
Height Ambiguity (m)	252.47		1087.6	
Orbit	19219	8323	19328	19153
SENTINEL	1A	1B	1A	1A

(VV) polarized. The SAR images cover southern Halabja (30 km). The incidence angles of Sentinel-1 are approximately 20° to 46°, and have wavelength of 5.546 cm.

5. SAR Interferometric Analyses

To infer co-seismic land uplift and subsidence, we had used Sentinel-1 data, and Differential InSAR method (DInSAR). This technique allows investigating where and how the crust deform near of the epicenter. DInSAR processing is monitoring surface movement by computing a differential interferogram of the same SAR data from two repeat pass acquisitions. Figure 9 presents the differential phase interferograms from the ascending and descending orbits of the AOI.

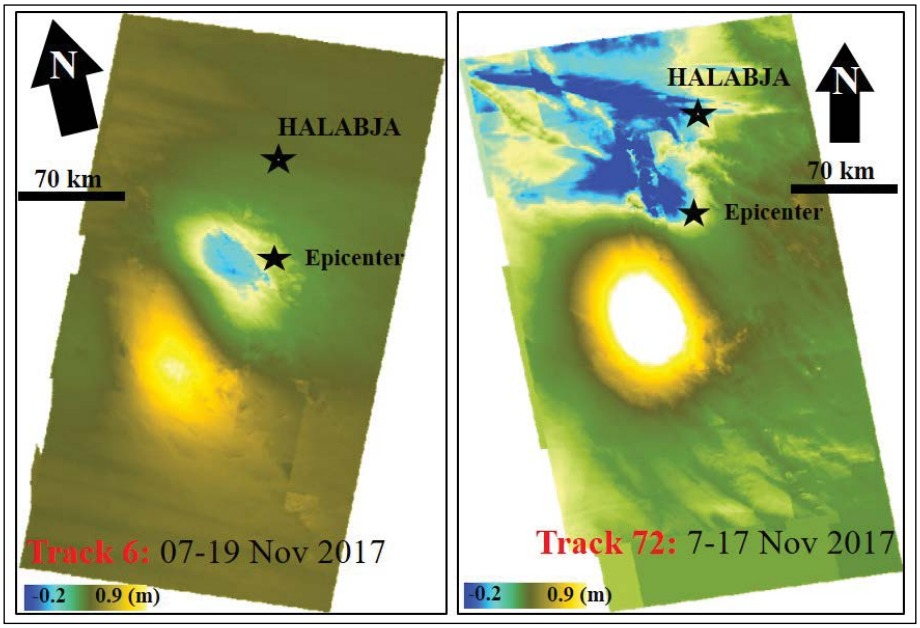

Figure 10- Deformation map along the LOS. After phase unwrapping and phase to displacement conversion.

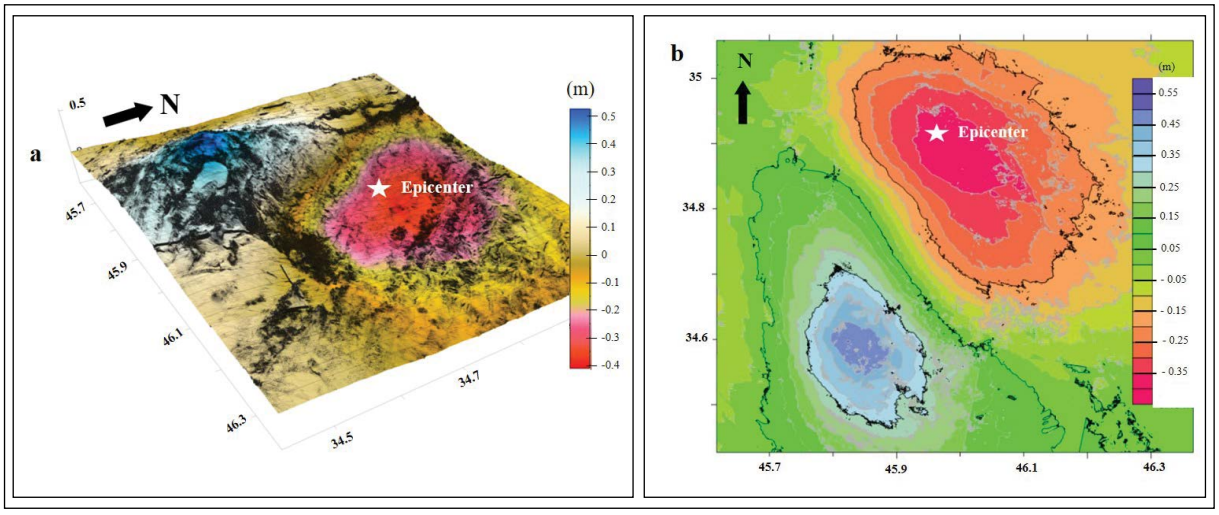

Figure 11- a) 3D view deformation map of the track6 (07-19 November 2017) and b) contour map along LOS displacement.

are reported in Appendix A, including noise and atmospheric phase effects for the analysed cases.

6. Damages in the Infrastructures

The buildings in the cities and villages are suspected to be submitted for deformation. In both cases subsidence or uplift, the infrastructures may experience heavy damages. Figure 12 represents 3D view deformation map of the track 6 (07-19 November 2017). The black line is approximate strike of fault at the surface and ~ N35°W striking direction inferred from InSAR. The greatest damage is considered to be on the fault line shown in figure 1 and in its vicinity.

During field observation by AFAD committee it is seen that many infrastructures get damaged. Due to seismic reports from Zare et. al., (2017); "8.000 injured, 70.000 displaced, and over 12.000 buildings have been damaged". Associated with this earthquake

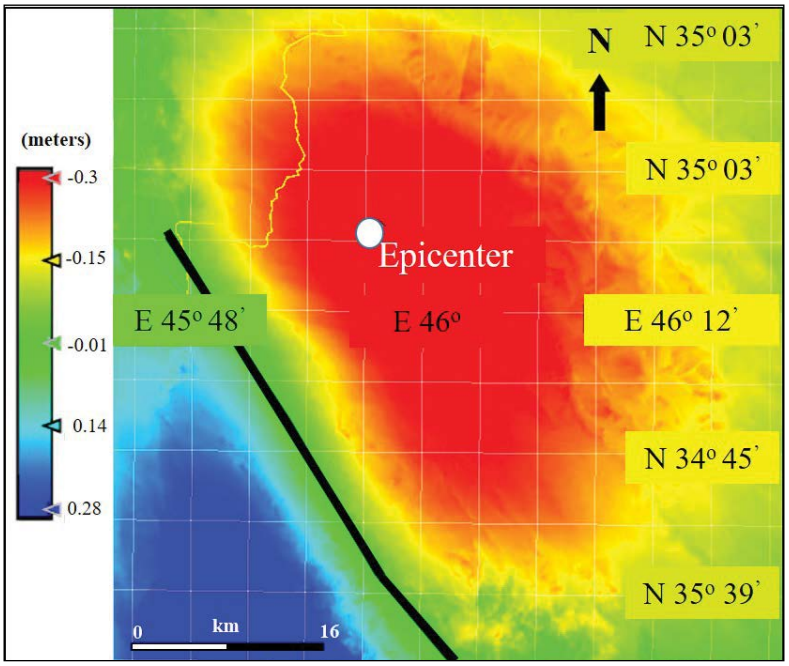

Figure 12- 3D view deformation map of the track 6 (07-19 November 2017), the black line is suspected fault location and direction inferred from InSAR and the location of villages.

and its aftershocks, approximately 5,000 buildings in the disaster impact area were heavily damaged beyond repair (Figure 13).

7. Conclusions

Zagros Mountains is the result of mountain range between two plates (Şengör and Kidd, 1979; Dewey et al., 1986; Dilek et al., 2009; Ghalamghash et al., 2016; Fahim Guilany et al., 2019). The plates' motions create high earthquake activitiy and remarkable surface topography. After Iran earthquake, we would like to test the ability of DInSAR method to detect the surface motion in vertical scale. The present paper has two main objectives; one of them is to reveal the surface deformation caused by Mw 7.3 2017 Iran Earthquake in (12 November 2017), and second is to determine the strike of fault line at the surface by using InSAR method without visiting the study area. Before testing the results without ground truth data,

Figure 13- Photos from study area, a) photo from one damaged house, b) AFAD President's investigation over damaged dam (taken by AFAD) and c) general scene from destroyed houses (Google search).

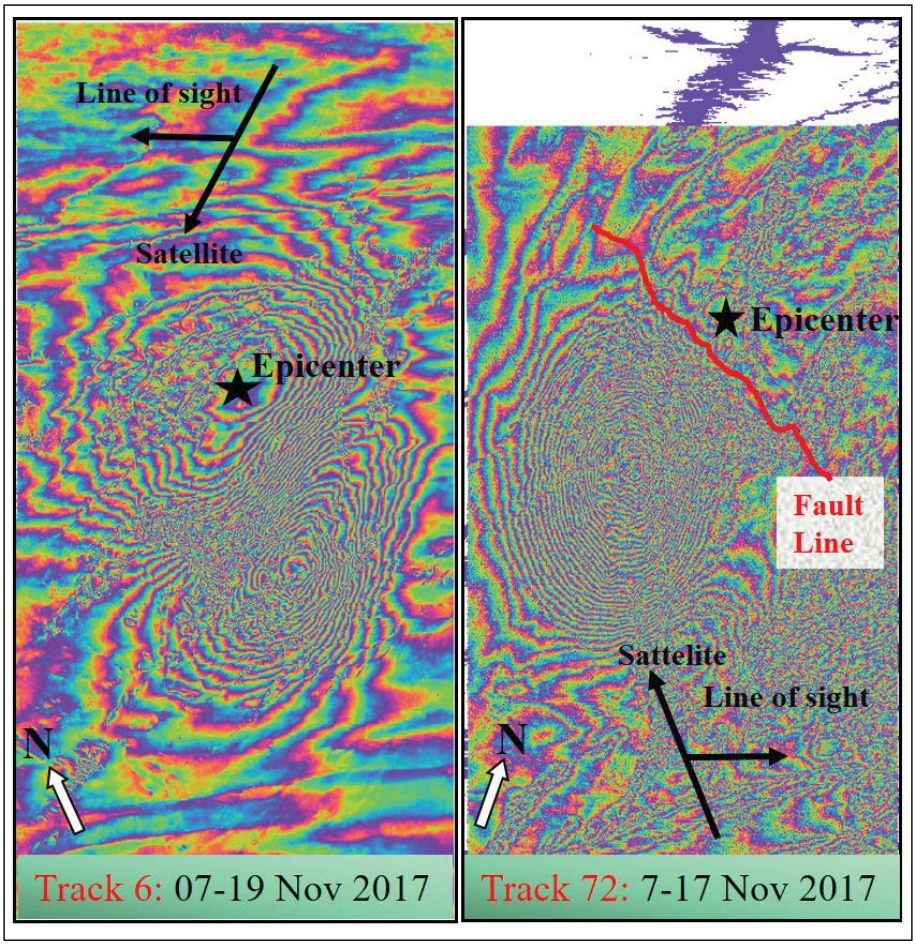

Figure 9- Interferograms from Sentinel-1 InSAR pairs, each fringe is colored by the cycle of $-\pi$ to π.

The interferograms generated confirmed the existence of deformation surrounding the epicenter. The amount of displacements and its directions calculated after the phase unwrapping reveals a huge deformation area reach 90 cm and -41 cm, and it extend to 80 km from the location of epicenter. Yellow spot indicates the uplifted and the blue spot represent subsided areas in figure 10.

The maximum and minimum displacement values from the ascending and descending orbit of the scene are calculated as:

Track 06 = 07-19 November 2017 Min: -0.411, Max: 0.526m

Track 72 = 11-17 November 2017 Min: -0.191, Max: 0.898m

The track 72 in figure 10; due to 'blue spots' indicates some differences from the track 6. At first look; ever if the "blue colour change" demonstrates displacement in track 72, when the area with blue interpret with topography (Figure 8) and the wrapped interferogram phase (Figure 9), it is clear that this colour changes result is only because of unwrapping errors or no Data representation. Therefore, unwrapping error and less data; low coherent zone represents the 'blue spot' area. After re-masking the interferogram, the unwrapping result cannot be fully improved to get better result without scattered blue zone. More examples of InSAR measurements for aftershocks of the earthquake are reported in Appendix A to show similar results.

Figure 11(a) represents surface deformation of the AOI on the digital elevation model and (b) contour map of the same area along the LOS. It can be said from the deformation shape that two blocks of the fault moved significantly in vertical direction. More examples of fitted monitored displacements for the study area affected by the earthquake of aftershocks

the amount of displacement could be obtained by processing two different acqusition mode which are ascending (from S to N) and descending (from N to S). To determine the surface deformation, one of the phases could be used in case of a landslide but in an earthquake, descending and ascending track modes of the satellite should be used. The difference between descending and ascending interferograms is that SAR interferogram shows the displacement only in the direction where the ground moves close to or away from the satellite. As a result, in spite of detecting the same deformation, an interferogram from ascending orbits different to one from descending orbits. As such, it is difficult to determine the direction of displacement using a single SAR interferogram, but determination of the direction can be made by comparison of InSAR data with GPS measurement data, or by combining the several data from different directions (i.e. ascending and descending).

In our study, two modes were used to find out the uplift and subsidence in both blocks of the fault. As conclusions, the potential of SAR image was investigated for assessment of vertical displacement caused by the earthquake in the field of Halabja. The summaries are given below:

1. The deformation is observed straight up and surrounding the Epicenter.
2. Approximate fault strike is detected in the direction of ~ N35°W.
3. The analysis of the deformation has revealed that the ground reach more than – 40 cm subsidence in the footwall (in the SW of fault line) and + 90 cm uplift in the hangingwall block (in the NE of fault line).
4. Fault detection is possible to track with DInSAR. The estimation of its horizontal displacement is a challenge to be inferred.

Acknowledgements

Authors are grateful to have provided freely the Sentinel-1A/B data by European Space Agency (ESA) through Copernicus Programme. Sentinel-1 precise orbit ephemerides were acquired from ESA Sentinel-1 Quality Control group. Authors also acknowledge the use of Google Earth to display the result.

References

Alavi, M.A. 2007. Structures of the Zagros Fold-Thrust Belt in Iran. American Journal of Science 307, 1064-1095.

Ambraseys, N.N., Melville, C.P. 1982. A History of Persian Earthquakes, Cambridge University Press, Cambridge.

Colman-Sadd, S.P. 1978. Fold development in Zagros simply folded belt, Southwest Iran. Am Assoc Petrol Geol Bull 62, 984–1003.

Çomut, F.C. 2016. Farklı yeryüzü özelliklerinde ileri InSAR teknikleri kullanılarak yüzey deformasyonlarının belirlenmesi (Doctoral dissertation, Selçuk Üniversitesi Fen Bilimleri Enstitüsü).

Dehbozorgi, M., Pourkermani, M., Arian, M., Matkan, A.A., Motamedi, H. Hosseiniasl, A. 2010. Quantitative analysis of relative tectonic activity in the Sarvestan area, central Zagros , Iran. Geomorphology 121, 329-341.

Dewey, J. F., Hempton, M.R, Kidd, W.S.F., Şaroğlu, F., Şengör, A.M.C. 1986. Shortening of continental lithosphere: The neotectonics of eastern Anatolia-a young collision zone, in Collosion Tectonics (Coward, M.P., and Ries, A.C., edts.), Geological Society Special Publications 19, 3-36.

Dilek, Y., Imamverdiyev, N., Atunkaynak, S. 2009. Geochemistry and tectonics of Cenozoic volcanism in the Lesser Caucasus (Azerbaijan) and the peri-Arabian region: collision-induced mantle dynamics and its magmatic fingerprint. International Geology Review 1-42, DOI:10.1080/00206810933604422.

Emami, H., Vergés, J., Nalpas, T., Gillespie, P., Sharp, I., Karpuz, R., Blanc, E. P., Goodarzi, M.G.H. 2010. Structure of the Mountain Front Flexure along the Anaran anticline in the Pusht-e Kuh Arc (NW Zagros, Iran): insights from sand box models. Geological Society, London, Special Publications 330, 155-178.

EMSC, 2017. https://www.emsc-csem.org/Earthquake/260/M7-3-Iran-Iraq-Border-Region-on-November-12th-2017-at-18-18-UTC

Fahim Guilany, R., Darvishzadeh, A., Sheikhzakariaee, S.J., Vosoughi Abedini, M. 2019. Geochemical characteristics of Sabalan volcanic rocks in Northwestern Iran. Bulletin of the Mineral Research and Exploration 158, 217-233.

Falcon, N. L. 1974. Southern Iran: Zagros Mountains. In: SPENCER, A. M. (ed.) Mesozoic–Cenozoic Orogenic Belts. Data for Orogenic Studies. Geological Society, London, Special Publications 4, 199–211.

Ferretti, A., Bianchi, M., Prati, C., Rocca, F. 2005. Higher-Order Permanent Scatterers Analysis. – EURASIP Journal on Applied Signal Processing 20, 3231–3242.

Ghalamghash, J., Mousavi, S.Z., Hassanzadeh, J., Schmitt, A.K. 2016. Geology, zircon geochronology, and petrogenesis of Sabalan volcano (Northwestern Iran). Journal of Volcanology and Geothermal Research 327, 192-207. Doi: 10.1016/j.

Goudarzi, M.A. 2010. Detection and measurement of land deformations caused by seismic events using InSAR, sub-pixel correlation and inversion techniques. University of Twente Faculty of Geo-Information and Earth Observation (ITC). jvolgeores.2016.05.001

Hanssen, R. F. 2001. Radar interferometry: Data interpretation and error analysis. Dordrecht: Kluwer Academic Publishers 328 pp. ISBN 0-7923-6945-9.

Hooper, A. J. 2006. Persistent scatter radar interferometry for crustal deformation studies and modeling of volcanic deformation, AAI3219289; ISBN: 9780542706905, Stanford University, 124 p.

https://earthquake.usgs.gov/earthquakes/eventpage/us2000bmcg#region-info

https://sentinels.copernicus.eu/web/sentinel/technical-guides/sentinel-1-sar/sar-instrument

Intrieri, E., Gigli, G., Casagli, N., Nadim, F. 2013. Brief communication Landslide Early Warning System: Toolbox and general concepts, Natural Hazards and Earth System Science 13(1), 85–90, doi:10.5194/nhess-13-85-90.

Kim, J. W. 2013. Applications of Synthetic Aperture Radar (SAR)/SAR Interferometry (InSAR) for Monitoring of Wetland Water Level and Land Subsidence. The Ohio State University.

Li, Z., James, B. 2008. Image coregistration in SAR interferometry. The International Archives of the Photogrammetry. Remote Sensing and Spatial Information Sciences 37, 433-438.

Marinkovic, P., Ramon, H., 2004. Advanced InSARcoregistration using point clusters. Geoscience and Remote Sensing Symposium, 2004. IGARSS'04. Proceedings. 2004 IEEE International. Vol. 1. IEEE

McQuarrie, N. 2004. Crustal scale geometry of the Zagros fold-thrust belt, Iran. J Struct Geol 26, 519–535.

Netzband, M,, William, L. S., Charles, R. 2007. Applied remote sensing for urban planning, governance and sustainability. Springer Science & Business Media.

Nissen, E., Ghorashi, M., Jackson, J., Parsons, P., Talebian, M. 2007. The 2005 Qeshm Island earthquake (Iran) – a link between buried reverse faulting and surface folding in the Zagros Simply Folded Belt? Geophys J Int 171, 326–338.

Nissen, E., Yamini-Fard, F., Tatar, M., Gholamzadeh, A., Bergman, E., Elliott, J.R., Jackson, J.A., Parsons, B. 2010. The vertical separation of mainshock rupture and microseismicity at Qeshm island in the Zagros Simply Folded Belt, Iran. Earth Planet Sci Lett 296, 181–194.

Nissen, E., Tatar, M., Jackson, J.A., Allen, B. 2011. Geodynamics and tectonics New views on earthquake faulting in the Zagros fold-and-thrust belt of Iran. Geophys J Int doi: 10.1111/j.1365-246X.2011.05119.x.

Pritchard, M, E. 2006. InSAR, a tool for measuring Earth's surface deformation. Physics Today 59, 7, 68.

Samieie-Esfahany, S., Hanssen, R., Karin van Thienen-Visser, Annemarie, M. 2009. On the Effect of Horizontal Deformation on InSAR Subsidence Estimates. In Proceedings of the Fringe 2009 Workshop, ESA SP, 677.

Şengör, A.M.C., Kidd, W.S.F. 1979. Post-collisional tectonics of the TurkishIranian. Plateau and a comparison with Tibet, Tectonophysics 55, 361-376.

Thiebes, B. 2012. Integrative Early Warning. Landslide Analysis and Early Warning Systems. Springer Berlin Heidelberg, 215-219.

Walker, R.T., Andalibi, M.J., Gheitanchi, M.R., Jackson, J.A., Karegar, S., Priestley, K. 2005. Seismological and field observations from the 1990 November 6 Furg (Hormozgan) earthquake: a rare case of surface rupture in the Zagros mountains of Iran. Geophys J Int 163, 567–579.

Zare, M., Kamranzad, F., Parcharidis, I., Tsironi, V. 2017. Preliminary report of Mw7. 3 Sarpol-e Zahab, Iran earthquake on November 12, 2017. EMSC Report 1-10.

Appendix A: Estimation of Co-Seismic Land Deformation Due to Mw 5.5, 11 January 2018 Iran Earthquake by Mean of DInSAR Technique

This section reports the larger-area interferograms of different date combinations. SAR image dates were selected to display the effects of two earthquakes, particularly on 11 January 2018, of 5.5 Mw and 5.4 Mw (Mw 5.5 – 18 km E of Mandali, Iraq 2018-01-11 06:59:31 UTC 33.764°N 45.749°E10.0 km, Mw 5.4 - 14km E of Mandali, Iraq 2018-01-11 08:00:40 UTC 33.774°N 45.710°E10.0 km). From each interferogram it can be seen various errors, due to weather conditions in some of the dates. But some of them also indigates significant information about displacement along the fault zone.

Table A1- Characteristics of Sentinel-1 InSAR pairs for the 72 and 6 Tracks. https://sentinels.copernicus.eu/web/sentinel/technical-guides/sentinel-1-sar/sar-instrument

Track	**6 VV**	
Pass	DESCENDING	
Date	**1/6/2018 2:54**	**1/18/2018 2:54**
Bper	-64.88	
Btem	12	
Height Ambg m	242.16	
Orbit	20028	20203
SENTINEL	1A	1A
Track	**6 VV**	
Pass	DESCENDING	
Date	**12/31/2017 2:53**	**1/18/2018 2:54**
Bper	10.3	
Btem	18	
Height Ambg m	-1515.86	
Orbit	8957	20203
SENTINEL	1B	1A
Track	**6 VV**	
Pass	DESCENDING	
Date	**1/6/2018 2:54**	**1/12/2018 2:53**
Bper	21.25	
Btem	6	
Height Ambg m	734.99	
Orbit	20028	9132
SENTINEL	1A	1B
Track	**6 VV**	
Pass	DESCENDING	
Date	**12/31/2017 2:53**	**1/12/2018 2:53**
Bper	-34.94	
Btem	12	
Height Ambg m	446.88	
Orbit	8957	9132
SENTINEL	1B	1B
Track	**72 VV**	
Pass	ASCENDING	
Date	**1/4/2018 14:59**	**1/16/2018 14:59**
Bper	62.22	
Btem	6	
Height Ambg m	252.47	
Orbit	9023	9198
SENTINEL	1B	1B

($\mathbf{B}_{tem}$: temporal baseline, $\mathbf{B}_{per}$: perpendicular baseline).

06 January 2018 - 18 January 2018 06 VV – DESCENDING

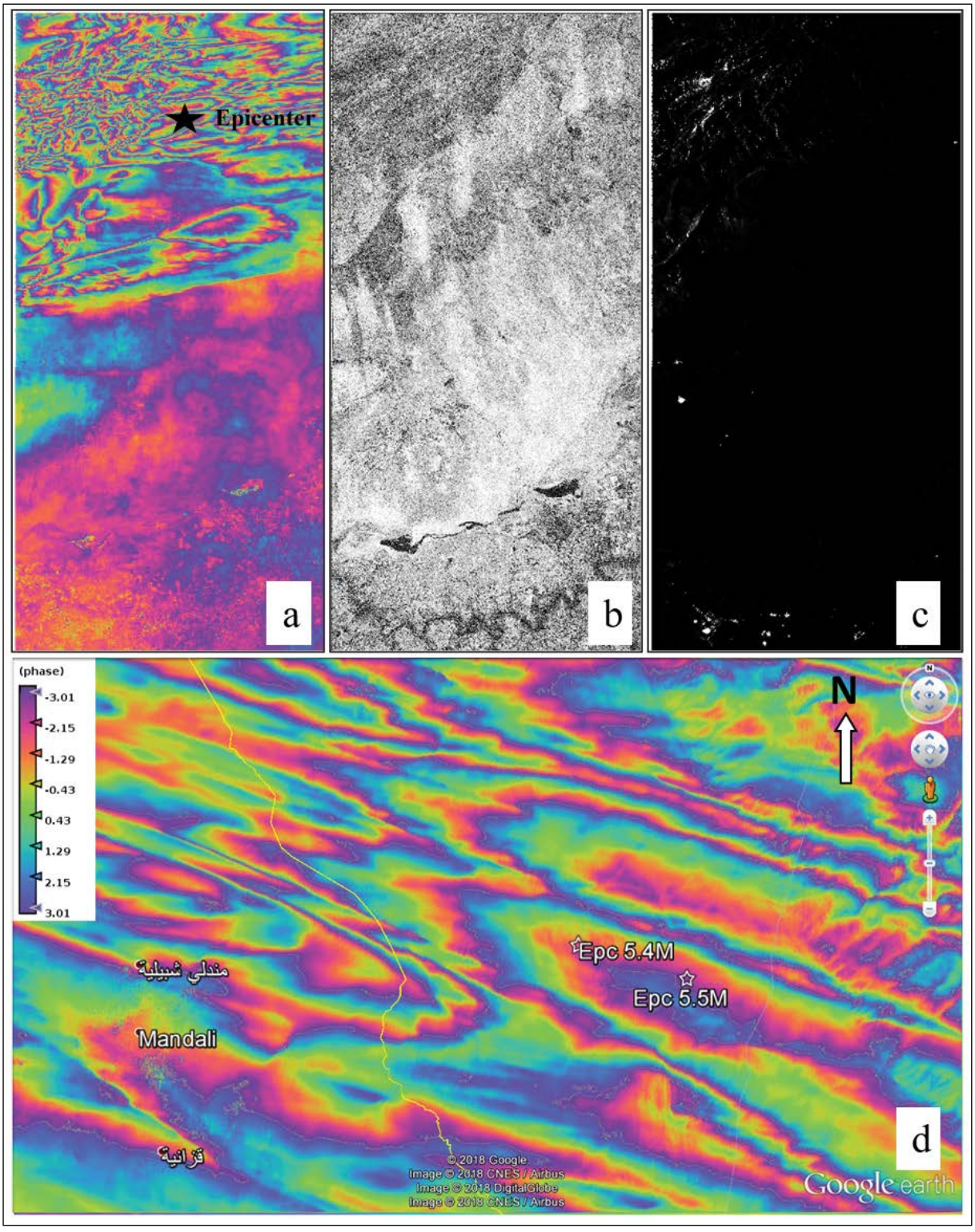

Figure A1- Interferograms from Sentinel-1 InSAR pairs (06 January 2018 - 18 January 2018 06 VV – DESCENDING), a) interferogram, b) intensitiy, c) coherence maps and d) filtered interferogram. There is no information about displacement due to atmospheric errors.

31 December 2017 - 18 January 2018 06 VV – DESCENDING

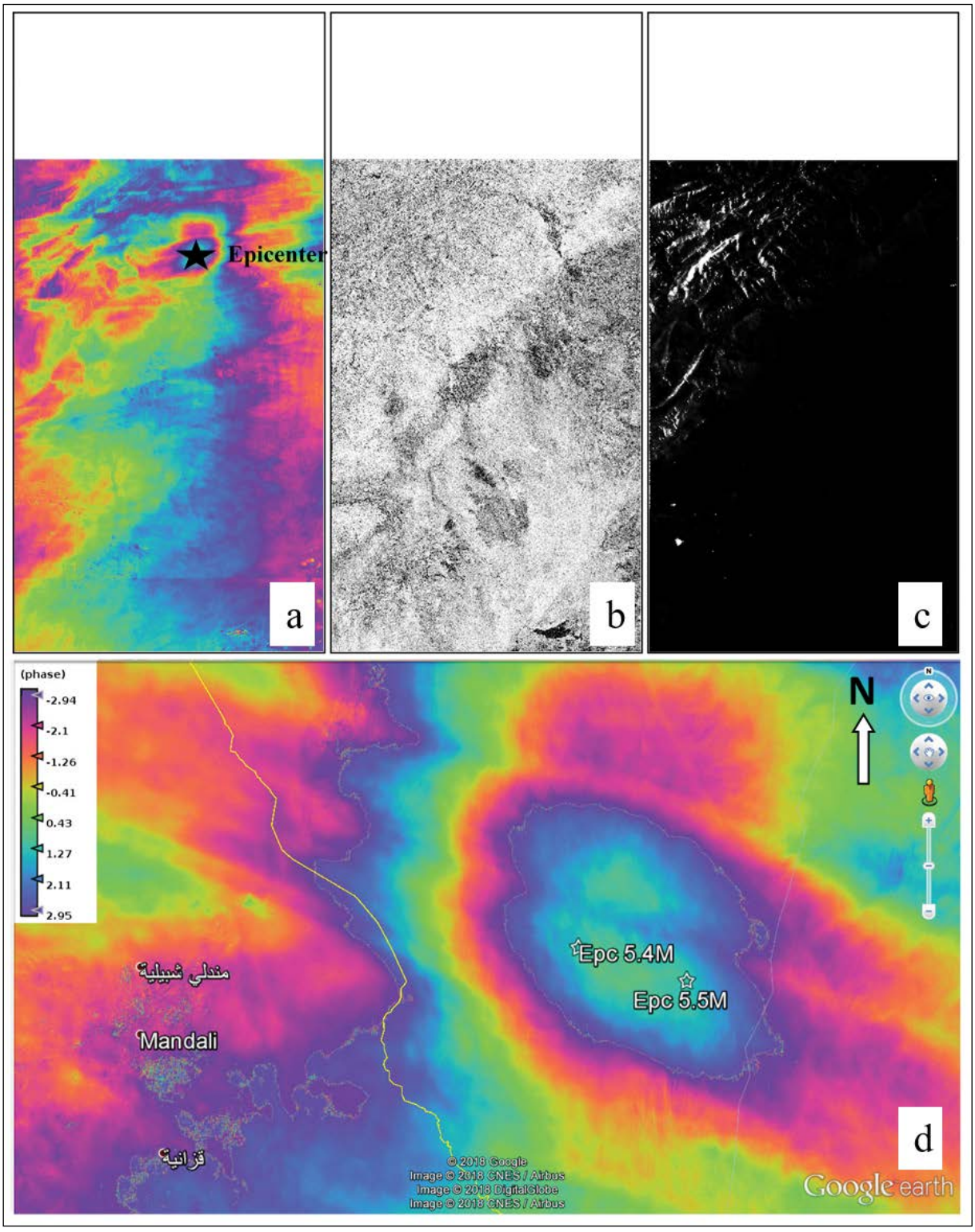

Figure A2- Interferograms from Sentinel-1 InSAR pairs (31 December 2017 - 18 January 2018 06 VV - DESCENDING), a) interferogram, b) intensitiy, c) coherence maps and d) filtered interferogram. Each fringe is colored by the cycle of $-\pi$ to π.

06 January 2018 - 12 January 2018 06 VV – DESCENDING

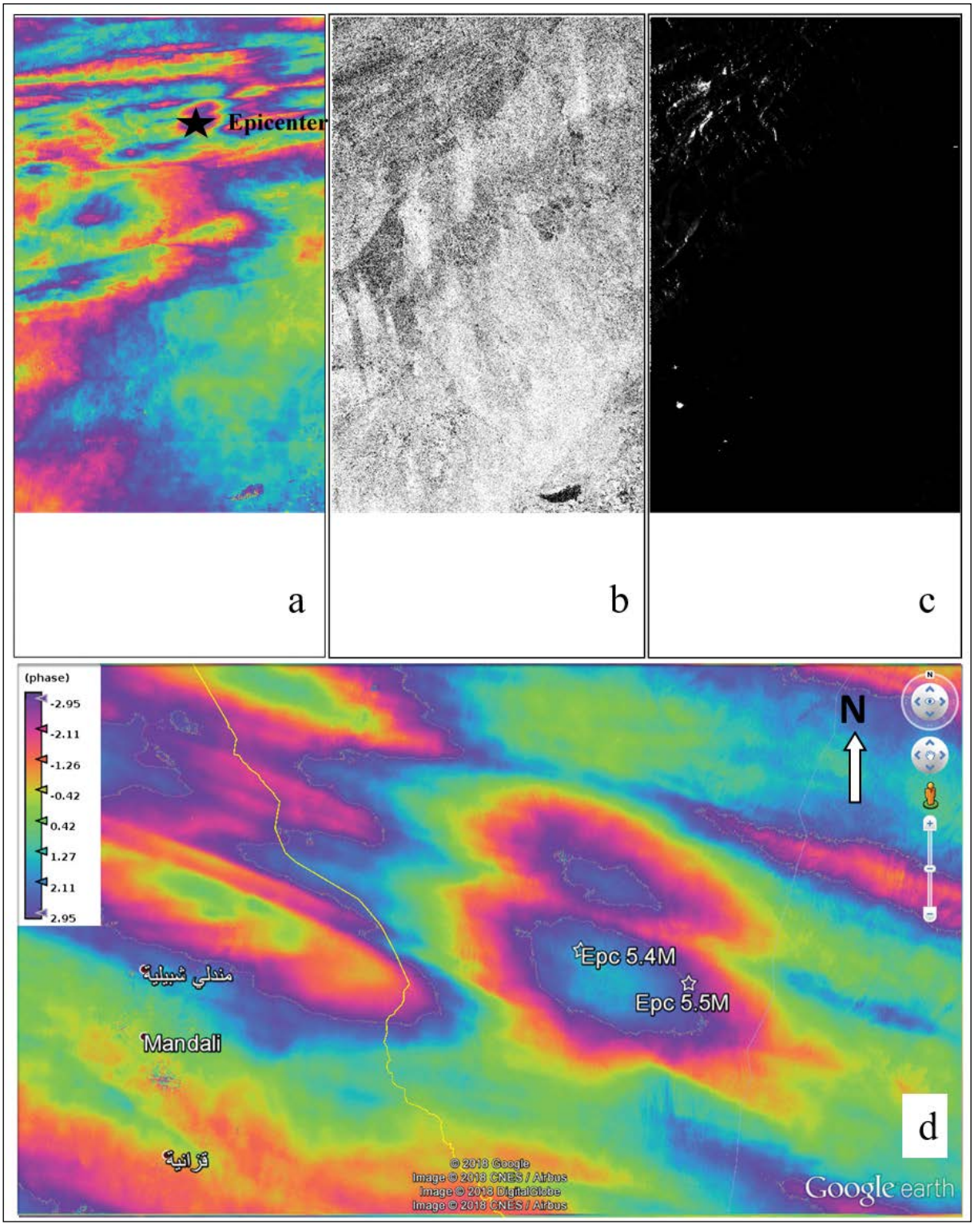

Figure A3- Interferograms from Sentinel-1 InSAR pairs (06 January 2018 - 12 January 2018 06 VV – DESCENDING), a) interferogram, b) intensitiy, c) coherence maps and d) filtered interferogram. Each fringe is colored by the cycle of $-\pi$ to π.

31 December 2017 - 12 January 2018 06 VV – DESCENDING

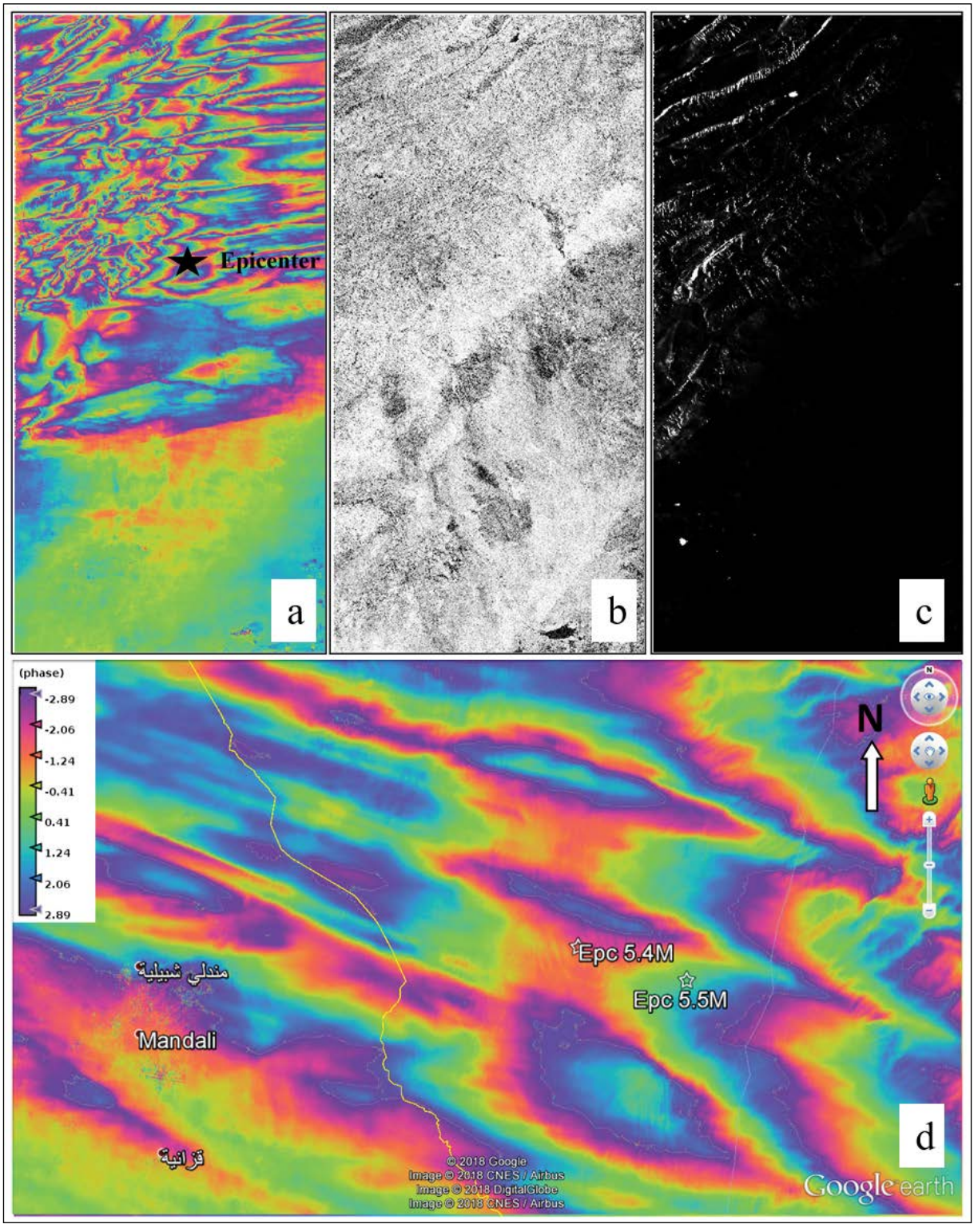

Figure A4- Interferograms from Sentinel-1 InSAR pairs (31 December 2017 - 12 January 2018 06 VV - DESCENDING), a) interferogram, b) intensitiy, c) coherence maps and d) filtered interferogram. There is no information about displacement due to weather conditions.

04 January 2018 - 16 January 2018 72 VV - ASCENDING

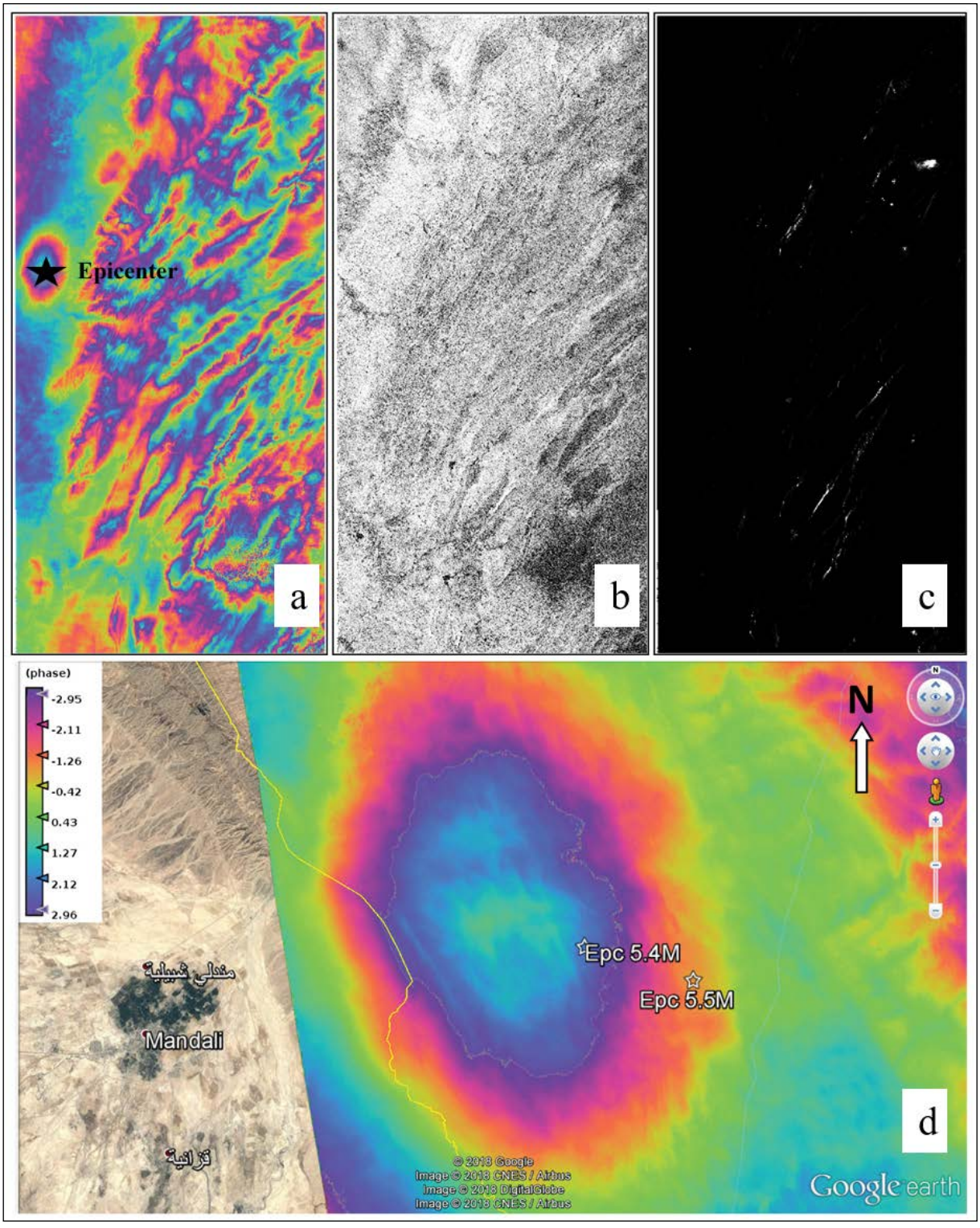

Figure A5- Interferograms from Sentinel-1 InSAR pairs (04 January 2018 - 16 January 2018 72 VV - ASCENDING), a) interferogram, b) intensitiy, c) coherence maps and d) filtered interferogram. Each fringe is colored by the cycle of $-\pi$ to π.

Bulletin of the Mineral Research and Exploration

http://bulletin.mta.gov.tr

Neogene stratigraphy and regional correlation of the Çeşme Peninsula, Western Anatolia, Turkey

Fikret GÖKTAŞ[a*]

[a]*119/8 Sok., 6/5, K.3, D.12, Evka-3, Bornova, İzmir, Turkey*

Research Article

Keywords:
Western Anatolia, Çeşme Peninsula, Neogene stratigraphy, Neogene volcanism.

ABSTRACT

This study aims to investigate the stratigraphy and regional correlation of terrestrial Neogene sediments and volcanics in the Çeşme Peninsula. Neogene deposition is represented by two main sedimentary successions separated from each other by an angular unconformity. The lacustrine dominated Çeşme group characterized the Lower-Middle Miocene deposition is formed by Şifne, Ovacık and Çiftlik formations. The felsic pyroclastics (Alaçatı pyroclastics), which are the early products of the Armağandağı volcanism, laterally associated with the Çeşme group deposition, deposited on the Şifne formation and interrupted the lacustrine sedimentation. The lacustrine sedimentation continued uninterruptedly with Ovacık and Çiftlik formations after the deposition of pyroclastics, which terminated the sedimentation of the Şifne formation. The calc-alkaline Armağandağı volcanism is composed of felsic pyroclastics, andesitic volcaniclastics (Reisdere volcaniclastics) and lavas (Zeytineli lava) respectively from bottom to top. The Late Miocene-Early (?) Pliocene Kaştepe group, which covers all these units with angular unconformity, is represented by a succession, which grades from alluvial fan (Karagöz formation) up to lacustrine deposits (İnlice formation).

Received Date: 19.02.2019
Accepted Date: 06.06.2019

1. Introduction

This study, which was performed in order to map the region on a 1/25000 scale by defining the terrestrial Neogene deposits and volcanics in the Çeşme Peninsula, is the summary of the geological investigation widely reported in Göktaş (2010) (Figure 1). The Neogene geology of the eastern part of the peninsula was presented by Göktaş (2016*b*). To reveal the stratigraphic succession of rock units in the Çeşme Peninsula, which was subject of local studies in previous investigations, and to investigate the possibilities of regional correlation are the main purpose of the study.

The main geological surveys starting with Kalafatçıoğlu (1961) in the Karaburun Peninsula are mainly related to pre-Neogene rock units (Çakmakoğlu and Bilgin, 2006). Few studies on Neogene carried out in the Çeşme Peninsula include magmatism (Innocenti and Mazzuoli, 1972; Borsi et al., 1972; Türkecan et al., 1998; Kaçmaz and Köktürk, 2004; Helvacı et al., 2009), hydrogeology-geothermal energy (Koçak, 1974; Yılmazer and Yakabağı, 1995; Gemici and Filiz, 2001) and Neogene geology (Besenecker, 1973; Göktaş, 2010, 2016*b*). Innocenti and Mazzuoli (1972) put forward that the "Alaçatı massif" (Armağandağı volcanics in this study) is represented by the calc-alkaline character of latite-andesitic volcanics in their pioneering studies in which they examined petrochemical properties of the Neogene volcanics in the Karaburun Peninsula. Borsi et al. (1972), obtained 18.2 Ma age from the andesite outcrop to the southeast

Citation info: Göktaş, F. 2020. Neogene stratigraphy and regional correlation of the Çeşme Peninsula, Western Anatolia, Turkey. Bulletin of the Mineral Research and Exploration 162, 31-54. https://doi.org/10.19111/bulletinofmre.581658

* *Corresponding author: Fikret GÖKTAŞ, fikretgoktas50@gmail.com*

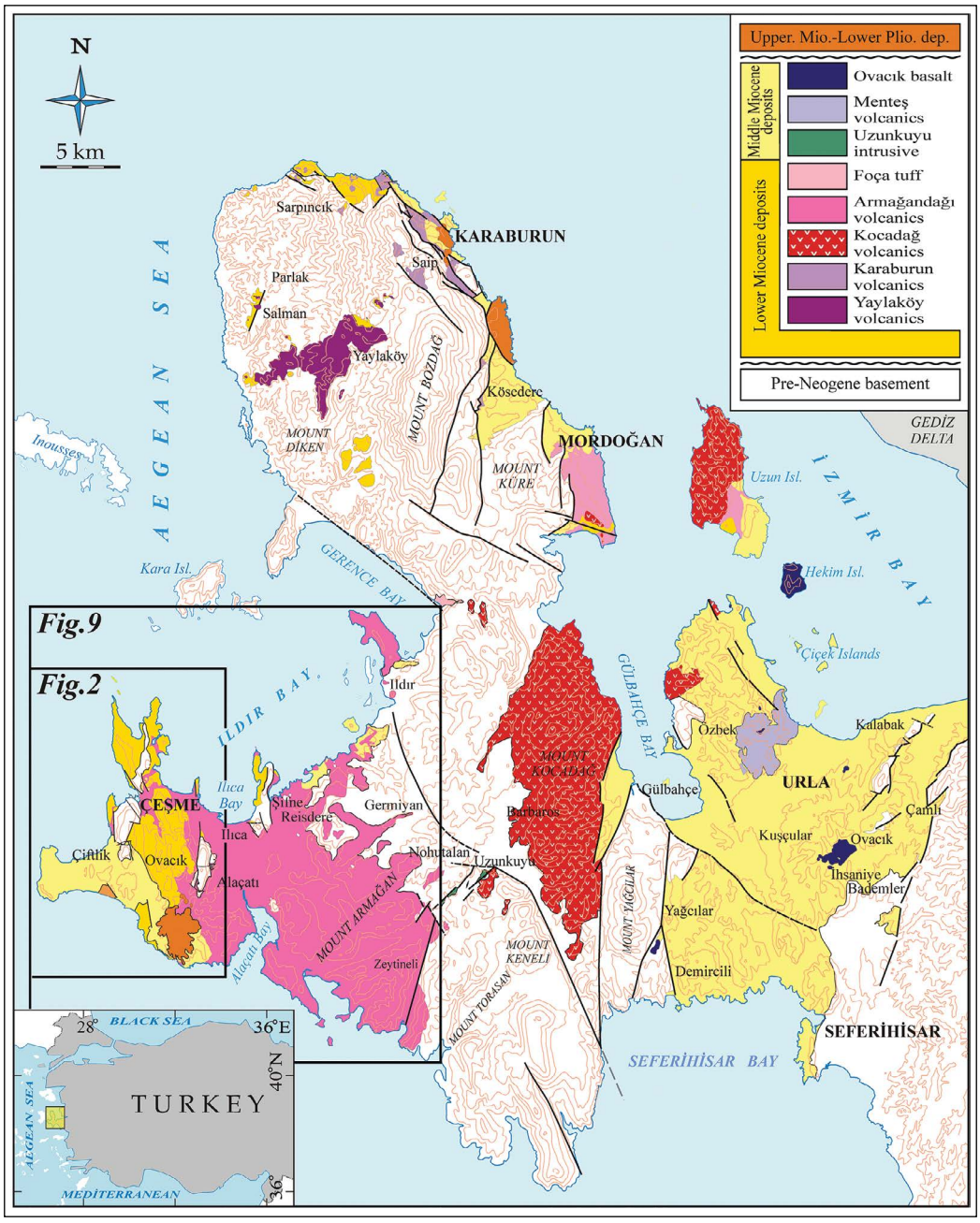

Figure 1- Location of the study area in the Karaburun Peninsula.

of Alaçatı and 17.0 Ma age from dacite cropped out near the Ildır Village by K/Ar method. Besenecker (1973) showed that there were correlating equivalents of Neogene deposits of Chios Island in the Çeşme Peninsula by means of lithostratigraphic correlations and large mammal fossils. Kaçmaz and Köktürk (2004) examined the geochemical and mineralogical properties of "silicic vitric tuffs" (Alaçatı pyroclastics) near Alaçatı and stated that authigenic zeolitizations (mordenite, clinoptilotite-heulandite) developed in the parts subjected to partial alteration. The stratigraphies proposed for Neogene rock units in the Karaburun Peninsula by Türkecan et al. (1998) and Helvacı et al. (2009) were constructed based on the radiometric ages and it was accepted that the Neogene sedimentation and volcanism had developed in a laterally relationship from bottom to top. Göktaş (2010) mapped the region on a 1: 25000 scale revealing the stratigraphy of

the Neogene deposits and volcanics on the Çeşme Peninsula the first time. Additionally, Göktaş (2016*b*) examined the Neogene stratigraphy of the region in southern part of the Gulf of Ildır and correlated it with the western part of the peninsula. The latest study on the general geology of the peninsula was performed by Göktaş and Çakmakoğlu (2018).

2. General Geology

The basement under the Neogene rock units are composed of carbonate rocks of the Late Triassic Güvercinlik formation (Erdoğan et al., 1990), which forms N-S extending structural highlands in the Early Miocene basin in the study area. The lacustrine deposits of the Early-Middle Miocene Çeşme group overlap on these structural uplifts with time-lapse transgressive contacts represented by basal conglomerate levels. The basement rocks cropped out in the eastern part of the peninsula (between Ildır, Ilıca and Germiyan districts) are represented by marine sediments deposited from Silurian to Jurassic. Silurian-Carboniferous turbiditic Dikendağı formation (Çakmakoğlu and Bilgin, 2006) and Bashkirian-Viseen Alandere formation (Erdoğan et al., 1990) consisting of clastic and carbonate rocks represent the Paleozoic marine deposition. The Gerence formation (Erdoğan et al., 1990) at the bottom of the Mesozoic sequence, which overlies the Paleozoic basement with an angular unconformity, begins with the Scythian transgressive deposits in its lower part and continues with the carbonate rock-dominated deep sea sediments during the Anisian. The Camiboğazı formation (Brinkmann et al., 1972), which reflects the neritic carbonate deposition of the Ladinian period, transitionally overlies the Gerence formation. The Mesozoic deposition continued with shallow marine carbonate rocks (Güvercinlik formation) in the Upper Triassic (Carnian-Rhaethian), and neritic carbonates of the Nohutalan formation was deposited in the Jurassic (Brinkmann et al., 1972) (Çakmakoğlu and Bilgin, 2006).

Terresterial Neogene rock units, which have exposures in NW part of the Karaburun Peninsula and partly correlated with the Çeşme Peninsula, are represented by the Early Miocene alluvial fan/delta and lacustrine deposits and overlying calc-alkaline Yaylaköy volcanics in two phases (Innocenti and Mazzuoli, 1972; Borsi et al., 1972; Türkecan et al., 1998; Aras et al., 1999; Helvacı et al., 2009; Çakmakoğlu et al., 2013). The lacustrine-dominant Lower-Middle Miocene deposits are exposed along the northern shores of the peninsula whereas the Middle-Upper Miocene deposits on the northeast part. The calc-alkaline "Karaburun volcanics" exposed in N-NE coastal parts of the peninsula intruded in three phases into the lacustrine dominant succession of the Early-Middle Miocene "Karaburun group" (Göktaş, 2014*a, b*). "Kocadağ" and "Armağan Mount" volcanic complexes consisting of calc-alkaline volcanis in rhyolite, dacite and andesite compositions are located in the southern part of the Karaburun uplift seperating from the Urla depression by Gülbahçe fault (Emre et al., 2005; Innocenti and Mazzuoli, 1972; Borsi et al., 1972; Türkecan et al., 1998; Helvacı et al., 2009; Göktaş, 2010).

3. Neogene Sedimentation

The Neogene rock units exposed in the Çeşme Peninsula consist of terrestrial deposits and calc-alkaline volcanics. The oldest deposits in the study area are represented by lacustrine dominant Çeşme group. Armağandağı volcanics have lateral interfingering contact relationship with the section of the Çeşme group over the Şifne formation [Ovacık formation, Çiftlik formation and Ildır formation (Göktaş, 2016*b*)], which is the equivalent the last unit]**.** The Kaştepe group, which overlies all these units with an angular unconformity, has deposits grades from alluvial fan to lacustrine types (Figure 2).

3.1. Çeşme Group

In the study area, the Çeşme group (Göktaş, 2010), which includes of Şifne formation, Ovacık formation, Alaçatı pyroclastics and Çiftlik formation from bottom to top, is represented by a terrestrial deposit succession of approximate 600 meters thick (Figure 3).

3.1.1. Şifne Formation

The type locality of the Şifne formation (Göktaş, 2010), which forms the first succession of the Neogene sedimentation and grades from conglomerate-sandstone assemblage to algal limestones from bottom to top is the Şifne District nearly 5 km west of the Germiyan Village in L16-b3 sheet (Figure 1).

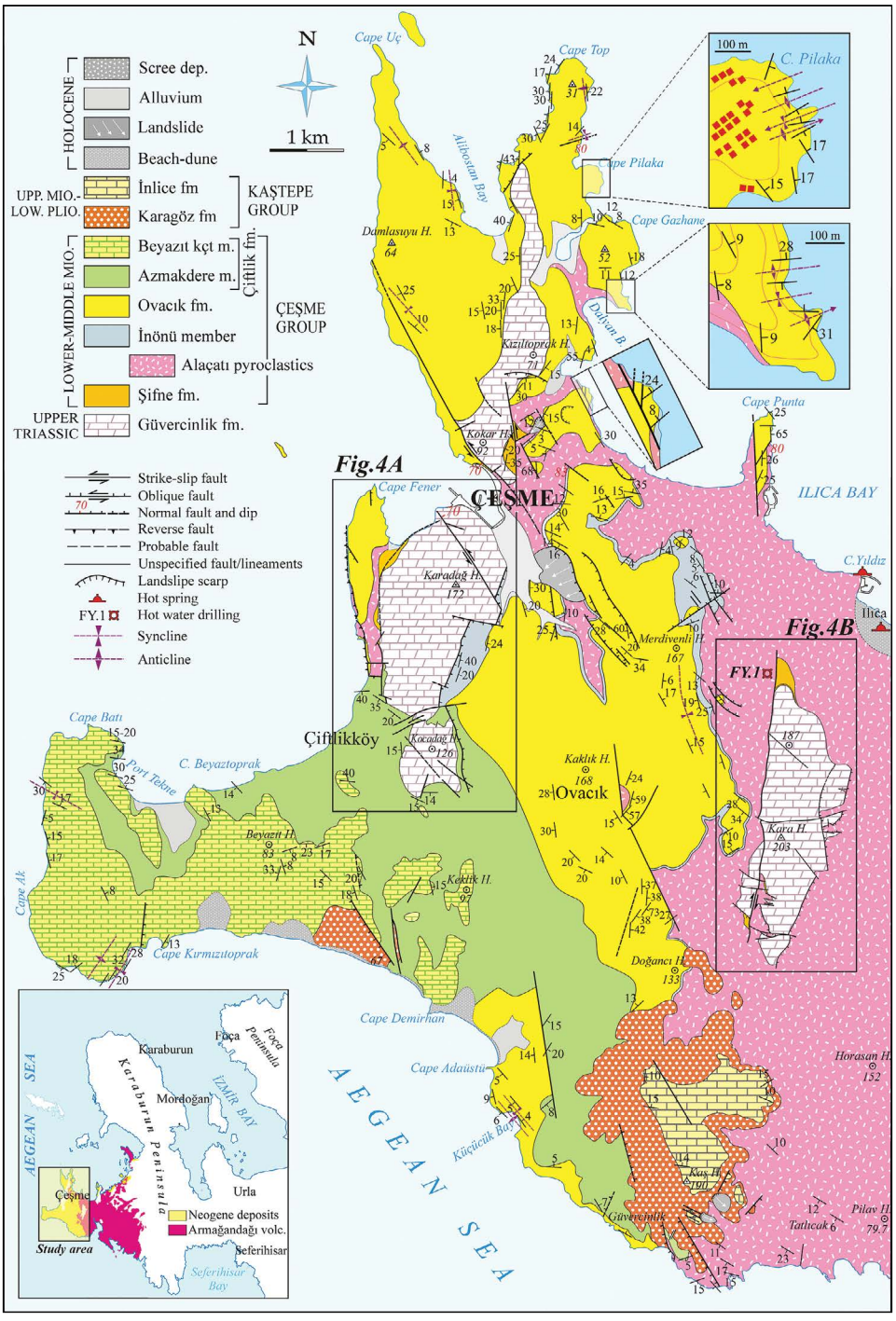

Figure 2- Geological map of the study area (modified after Göktaş, 2010; Göktaş and Çakmakoğlu, 2018).

The Şifne formation, which has few outcrops in the Çeşme Peninsula due to the cover of younger Neogene deposits and Armağandağı volcanics (Türkecan et al., 1998), is represented by limestone. As stated in Göktaş (2016*b*), the main outcrops of the succession, which can be observed at the highest part of 40 meters on the west coast of Şifne Bay, i.e. its type locality, are located in Çeşme district center, on western slopes of the Karadağ Hill and around Kara Hill highs (Figures 2 and 4). The total thickness of the Şifne formation cut from bottom to top in the geothermal drill "FY-1" performed by General Directorate of Mineral Research and Exploration (MTA) is 215 meters (Yılmazer and Yakabağı, 1995) (Figure 3).

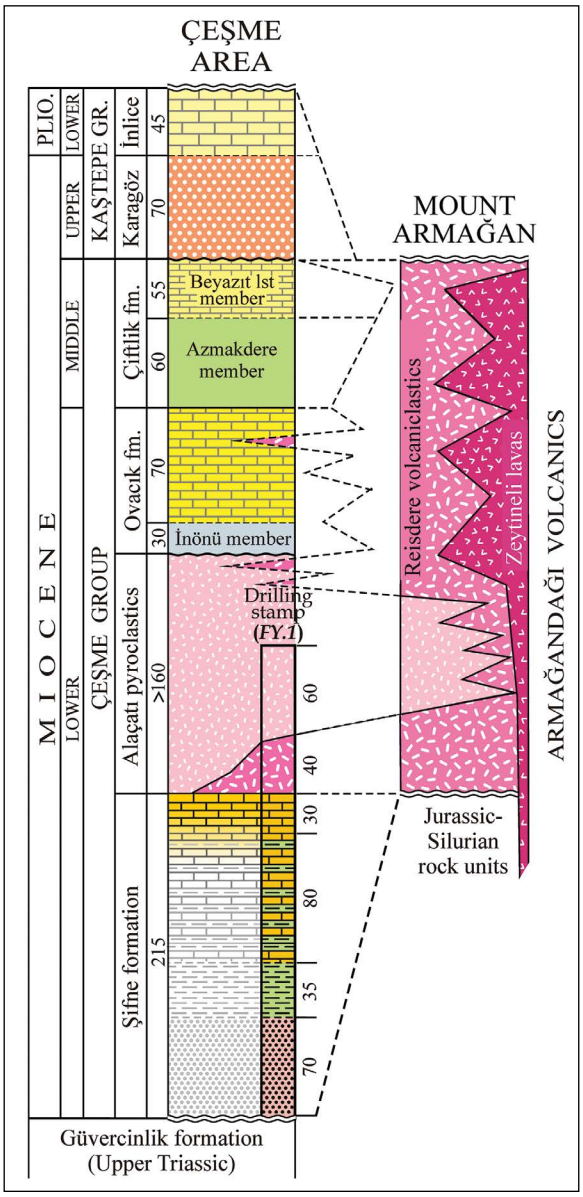

Figure 3- Detailed stratigraphical synthesis of Neogene rock units in the study area.

According to the drilling section data presented by Yılmazer and Yakabağı (1995), the 70 m thick lower part of the sedimentary succession consists of "gray and brown pebbly mudstone, pebbly sandstone and pebblestone, which is interpreted as the alluvial fan/delta deposits. The overlying 145 m thick lacustrine succession starts with gray and green claystones (35 m) containing few marl, clayey limestone and coal-seams and continues with limestone-clayey limestone-marl-claystone alternation (80 m) and then finishes with cream colored algal limestones (30 m) (Figure 3).

The parts of the unit exposed in the study area are lacustrine. In general, it is represented by fresh water algal limestone and thin to medium-bedded clayey limestone in few amounts. The algal limestone at the uppermost part of the succession and underlying sequence of algal limestone, clayey limestone, marl and claystone alternation are exposed on the northern coastline of the Gulf of Şifne to the east of the study area (Göktaş, 2016*b*). Algal limestone is less clear, thick to very thick-bedded and generally has microcrystalline texture. Freshwater algal content is represented by undulating/planar parallel laminated stromatolites. Fenestraes spaces developed parallel to the algal laminae are common. The branched algae in small amounts has been reworked and broken, and formed biosparitic accumulation levels in decimetric thickness within limestone layers. The limestone layers just below the overlying Alaçatı pyroclastics are partly/fully silicified and contain black/brown discoidal chert nodules (Göktaş, 2016*b*).

As mentioned above, biggest part of the Şifne sedimentary succession does not expose in the Çeşme Peninsula and only its uppermost 40 m thick part can be observed. Detritious limestones and carbonated mudstones, which overlap over the basement rocks with time-lapse transgressive contacts, filled karstic cavities and fractures on the unconformity surface along the western slopes of the Karadağ Hill in the SW of Çeşme district center, on the eastern slope of Kokar Hill and in the north of Kızılkaya uplift at the NW of Alaçatı. The Alaçatı pyroclastics were syn-sedimentary deposited on the Şifne formation. According to the well section of Yılmazer and Yakabağı (1995), there is a nearly 40 m thick and possibly laterally discontinuous andesitic agglomerate level between the Alaçatı pyroclastics and Şifne formation which is interpreted as the primary product of the Armağandağı volcanism (Figure 3).

There is not any biochronological data to date the Şifne formation, which constitutes the first sedimentary sequence of the terrestrial Neogene sedimentation in the Çeşme Peninsula. It is known that 18.2 ± 3.5 Ma K/Ar (Borsi et al., 1972) and 17.3 ± 0.1 Ma $^{40}Ar/^{39}Ar$ (Helvacı et al., 2009) ages were taken from Zeytineli lavas within the Armağandağı volcanics which overlie the Şifne formation after the settlement of Alaçatı pyroclastics. Based on these indirect data, it can be proposed that the unit was deposited in Early Miocene sensu lato.

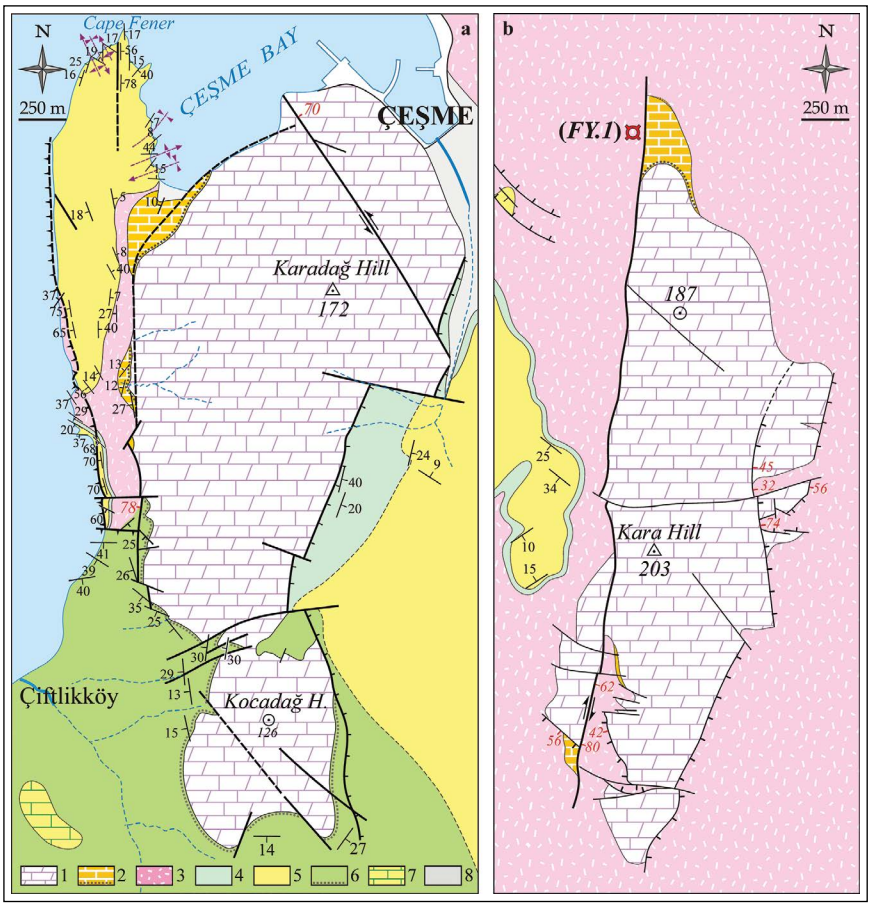

Figure 4- a) Detailed geological map of Karadağ Hill-Kocadağ Hill uplift and its vicinity, 1) Güvercinlik formation, 2) Şifne formation, 3) Alaçatı pyroclastics, 4) İnönü member, 5) Ovacık formation, 6) Azmakdere member, 7) Beyazıt limestone member, 8) alluvium and b) detailed geological map of Kara Hill and its surroundings.

3.1.2. Ovacık Formation

The Ovacık formation consists of a planar, thin-bedded limestone dominant succession. İnönü member signifies the reworked felsic tuff level at the bottom of the sedimentary succession (Göktaş, 2010).

The thickness of the Ovacık formation, which is located between the Alaçatı pyroclastics (Göktaş, 2010) and Çiftlik formation (Göktaş, 2010) in the middle of the Çeşme Peninsula, has an approximate thickness of 100 meters together with the İnönü member (Figure 3).

The succession, which is represented by planar parallel, thin-bedded, laminated limestones, contains claystone and rarely volcanic sandstone interlayers of different thicknesses from bottom to top. The general alteration color of the sequence is whitish/yellowish light gray (Figure 5). The sedimentary succession was broken by NW-SE and N-S trending (reverse, strike-slip and oblique-normal) post-depositional faults and folded in NW-SE, N-S, NE-SW axial directions. The most of these folds, which their axes usually dip to both directions, have several hundreds of meters of axial extension (Figures 2 and 4). The limestone, which is the dominant lithofacies of the sequence, is mostly micritic in texture. Chert bands located in partly or totally silicified limestone layers in cm size and discoidal chert nodules aligned parallel to the bedding are more common in the upper parts of the succession (Figure 5c). Locally, black chert or entirely silicified limestone layers varying in between 40-60 cm in thickness are observed. Brecciated limestone intercalations due to slumping are common (Figure 5c). Limestone layers mostly formed by planar to parallel laminated stromatolites are frequently

Figure 5- a) Angular coarse clasts derived from the Güvercinlik formation observed in carbonaceous mudstones in the transgressive lowermost part of the Ovacık formation, (L16-b4; eastern slopes of the Kızıltoprak Hill), b) yellowish, sandy limestone filled the karstic cavities in the carbonates of Güvercinlik formation in time-lapse transgressive contacts (L16, b4; eastern slopes of the Kızıltoprak Hill), c) chert nodules and brecciated limestone intercalations (black arrow) in distinct thin-bedded limestones of the Ovacık formation, d) parallel, thin-bedded, laminated levels characterizing the lower-middle parts of the Ovacık succession (L16-b1; south of Top Cape), e) claystone interlayers observed within Ovacık succession (L16-b1; south of Top Cape) and f) silicified limestone layers composed of undulating-planar parallel laminated stromatolites in the upper parts of the Ovacık limestone deposit (L16-c1; north of Küçücük Bay).

encountered in the succession. Entirely silicified, thick limestone layers with laminated stromatolites, increase in the upper parts of the succession (approaching the contact with Alaçatı pyroclastics) (Figure 5f). Some of these limestone layers are high-bioturbated. They have low gastropod contents. Claystone in the form of green, yellow, bluish gray colored and massive levels is intercalated as intercalations in limestone dominant parts or alternate with limestones. There are abundant gastropod shell fragments in the levels of blackish-brown claystone, where organic materials are concentrated. The claystone dominant levels,

which have 12 meters of thickness, include siltstone, sandstone or limestone intercalations in decimetric thicknesses. Volcanic sandstone interlayers are bluish dark gray colored, massive and have thicknesses varying between 1-3 meters. The volcanic clasts in reworked coarse tuff matrix consist of pumice and andesite fragments in the form of laterally discontinuous lenses and alignments. Andesite fragments are maximum 3 cm in size and angular. The pumices are up to 15 cm in size and subrounded. The clayey diatomite interlayers rarely found in the sequence are whitish light gray, planar parallel thin-bedded/thick laminated in thicknesses ranging from 5-40 cm.

The succession of the Ovacık formation, conformably overlain by the Azmakdere member (Göktaş, 2010) of the Çiftlik formation at WSW of the Kaş Hill (L16-c1), ends with some sedimentary beds which reflect the drying of the lake. Dark beige colored, 60 cm thick limestone layer, which has desiccation cracs, root marks and iron nodules at its surface, is overlain by 10 cm thick, laterally discontinuous claystone with thin lignite seams. Overlying 80 cm thick, light gray clayey diatomite level is parallel laminated and weakly cemented, and consists of discoidal iron concretions, fresh water algae and coalified flora remnants in cm size.

Thin to medium, distinct bedded and pale yellow colored transgressive limestones observed on the E and W slopes of Kızıltoprak Hill, the north of Çeşme district center laterally overlapped the Alaçatı pyroclastics and rested on the dolomitic limestones of the Güvercinlik formation. In the lowermost part, the massive limestone (Figure 5a) containing angular components derived from the in situ weathering of the Güvercinlik formation carbonates filled the karstic cavities and fractures on the unconformity surface of the Upper Triassic carbonates (Figure 5b).

There is no direct fossil data showing the age of Ovacık formation deposited in the lacustrine environment. It is regarded that the Ovacık lacustrine deposition occurred in the late Early Miocene based on: i) MN4 small mammal fauna (17.2-16.4 Ma, Hilgen et al., 2012) contained by the "Aktepe member" (Göktaş, 2014*b*), the equivalent of the unit in the north of the Karaburun Peninsula, ii) the age of 14,6 Ma (Göktaş, 2016*b*) of the lava flow syn-sedimentary emplaced within the Ildır Formation, the lateral equivalent of the unit in south of Ildır Bay and iii) the stratigraphical relationship with the Çiftlik formation, which conformably overlies the unit and consists of big mammal fossils of the MN5 biozone (16.4-14.2 Ma; Hilgen et al., 2012).

İnönü Member: İnönü member (Göktaş, 2010) defines the reworked felsic tuff level, which forms a lateral continuous reference level at the lowermost part of the Ovacık formation that transgressively overlaps the Alaçatı pyroclastics. The type locality of the subunit is Çeşme İnönü District and it has an average thickness of 30 meters.

The main components of the volcanic sandstone lithofacies, which represent the İnönü member, are derived from the underlying Alaçatı pyroclastics. Coarse-grained transgressive sandstone level at the bottom of the sequence is massive and carbonate-cemented in varying proportions in lateral and vertical directions in decimetric or metric thicknesses (Figure 6a, b, c). Specifically, it includes transported accretionary lapillies. Accretionary lapillies, which form lateral discontinuous deposits, is generally poorly sorted. In addition to the accretionary lapilli levels showing individual and irregular distribution grain-supported, packed lenticular deposits are also observed (Figure 6d). The succession, which was deposited by following the transgressive sandstone level and characterize the İnönü member, is represented by bluish dark gray, specifically planar, parallel and thin to medium-bedded, grain supported and well-sorted volcaniclastic sandstone. It is well stratified and has laterally equal layer thicknesses (Figure 6a).

İnönü member, which reflects the initial phase of Ovacık lacustrine sedimentation, unconformably overlies the Alaçatı pyroclastics. It transitionally underlies the limestone-dominant succession in a narrow range. Levels in the transitional zon are represented by carbonate cemented volcaniclastic sandstone and tuffaceous limestone lithofacies.

3.1.3. Çiftlik Formation

Çiftlik formation (Göktaş, 2010) represents the last sedimentary succession of Early-Middle Miocene lacustrine deposition within Çeşme group. The succession, which conformably overlies the

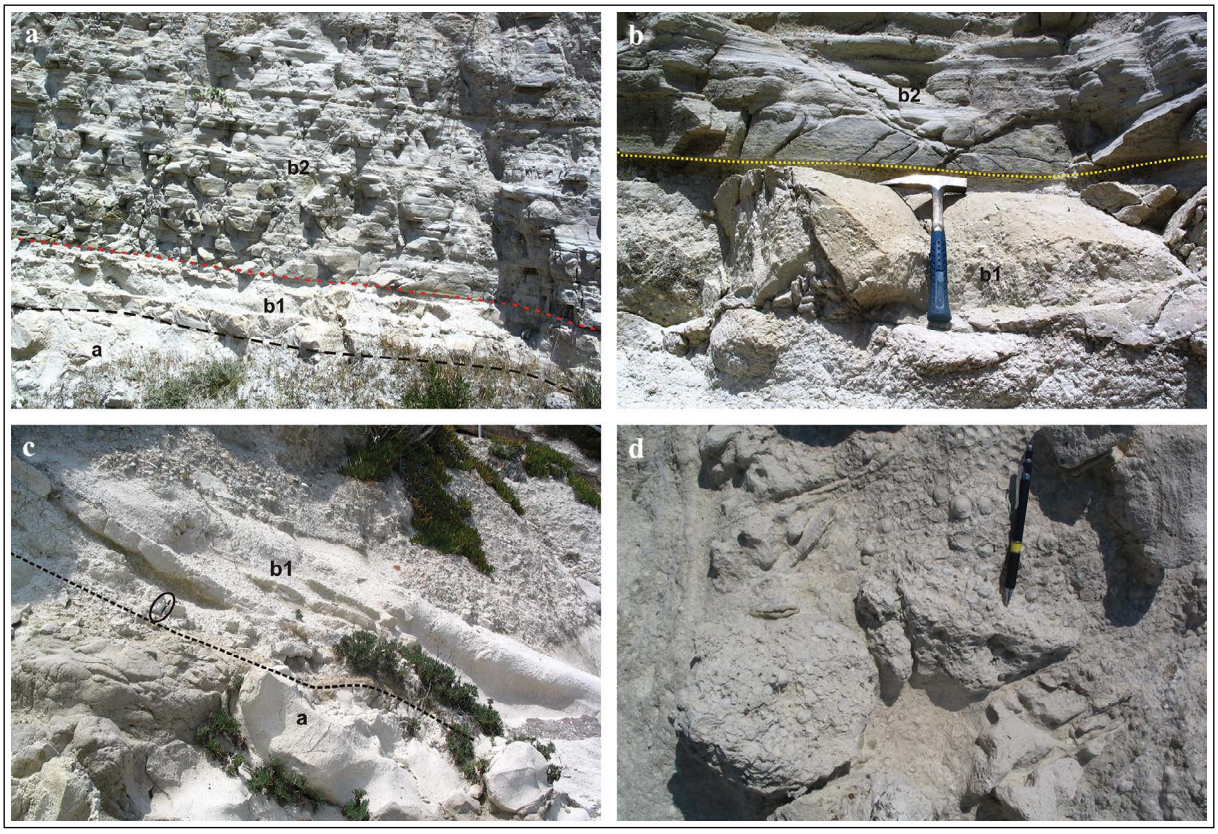

Figure 6- a) A view from the lower section of the sequence (L16-b4; around Kalkandere Hills, north of Çeşme district center). a: Alaçatı pyroclastics, b1: transgressive sandstone level at the bottom of the sequence, b2: planar, parallel thin-bedded volcanic sandstone deposit, characterizing the İnönü member, b) Close-up view of the lowermost part of the sequence, c) Transgressive sandstone level comprises carbonates in varying ratios and includes tuffaceous limestone intercalations (L16-b4; the coastline in east of Kalkandere hills), d) Close-up view of accretionary lapillies.

Ovacık formation, is made up of the Azmakdere member composed of the green claystone-sandstone association, and the Beyazıt limestone member at the top. The type locality of the unit is the Çiftlik District, which is approximately 4 km SW of Çeşme district center. It has a maximum thickness of 115 meters.

Large mammal fossils characterizing the MN5 biozone in the Azmakdere member at the lower part of the sedimentary succession and in the Keramaria unit (Besenecker, 1973), which is the equivalent of the member in Chios Island, indicate the early Middle Miocene (Besenecker, 1973; Bonis et al., 1998). In this study, it is assumed that the Çiftlik formation was deposited in the Middle Miocene sensu lato.

Azmakdere Member: It is located in the lower part of the Çiftlik formation and composed of claystone at the lower part and sandstone-dominant sequences at the upper part. The type locality the subunit shown by Göktaş (2010) is the Azmak stream flowing in N-S direction in southern part of L16-b4 sheet.

The main outcrops of the succession are located in the SW part of the Çeşme Peninsula. Its average thickness is 60 meters.

The sedimentary deposit is generally dark green, partly yellowish or bluish gray colored. Sediments deposited from suspended load are mainly represented by dark green claystone-siltstone assemblage and dominant in the lower part of the sedimentary succession. Rare sandstone and clayey diatomite intercalations are located in the lowermost parts of the massive claystone-siltstone succession. These medium to coarse-grained sandstones are grain supported, generally well sorted, massive or very low-angle climbing rippled. Clayey diatomite consists of laterally continuous intercalations, which their thicknesses vary between 5 and 15 cm and do not

show thickness changes in laterally. Claystone layers consisting of high organic matter are blackish, dark green colored. The sand size extraclast content and the average grain size increase towards the middle and upper parts of the succession, and the sandstone deposition developed over the wave base dominates in the shoreface deposit. Storm sand layers represented by coarse sandstone reach thicknesses in decimeters in the same direction. Some levels in which Fe pigment concentration increases are light/dark yellowish brown and well cemented. Claystone-siltstone intercalations are common. It is rarely observed that 10-15 cm thick wave rippled sandstone layers. Grain supported and well sorted coarse sandstone lithofacies in decimetric thickness are generally planar parallel laminated, locally planar (large scale low-angle) cross laminated. Climbing and sinusoidal rippled levels in similar textural properties have decimetric thickness and are rarely found.

At Batı Cape, the levels close to the overlying Beyazıt limestone member are represented by the claystone-dominant succession containing sandstone intercalations (Figure 7a). Green claystone is generally high-bioturbated, massive and rarely planar parallel laminated. It includes white to beige carbonate nodules and rarely laterally discontinuous, clayey limestone intercalations in thicknesses ranging from 20-40 cm. Sandstones, which have more or less laterally continuous interlayers in thicknesses ranging from 10-300 cm, are yellowish or green, massive or cross-bedded (Figure 7b). These sandstone levels include intraclasts derived from claystones and large mammal remains described by Besenecker (1973).

It has conformable stratigraphic relationship with the underlying lacustrine Ovacık formation. The green claystone-dominant succession of the Azmakdere member was deposited by following the sedimentary levels indicating the almost dry up of the Ovacık Lake. This relationship tells us that the sedimentation conditions changed due to the sudden deepening of the basin or the rise of the water level. The transgressive parts of the Azmakdere member rest unconformably

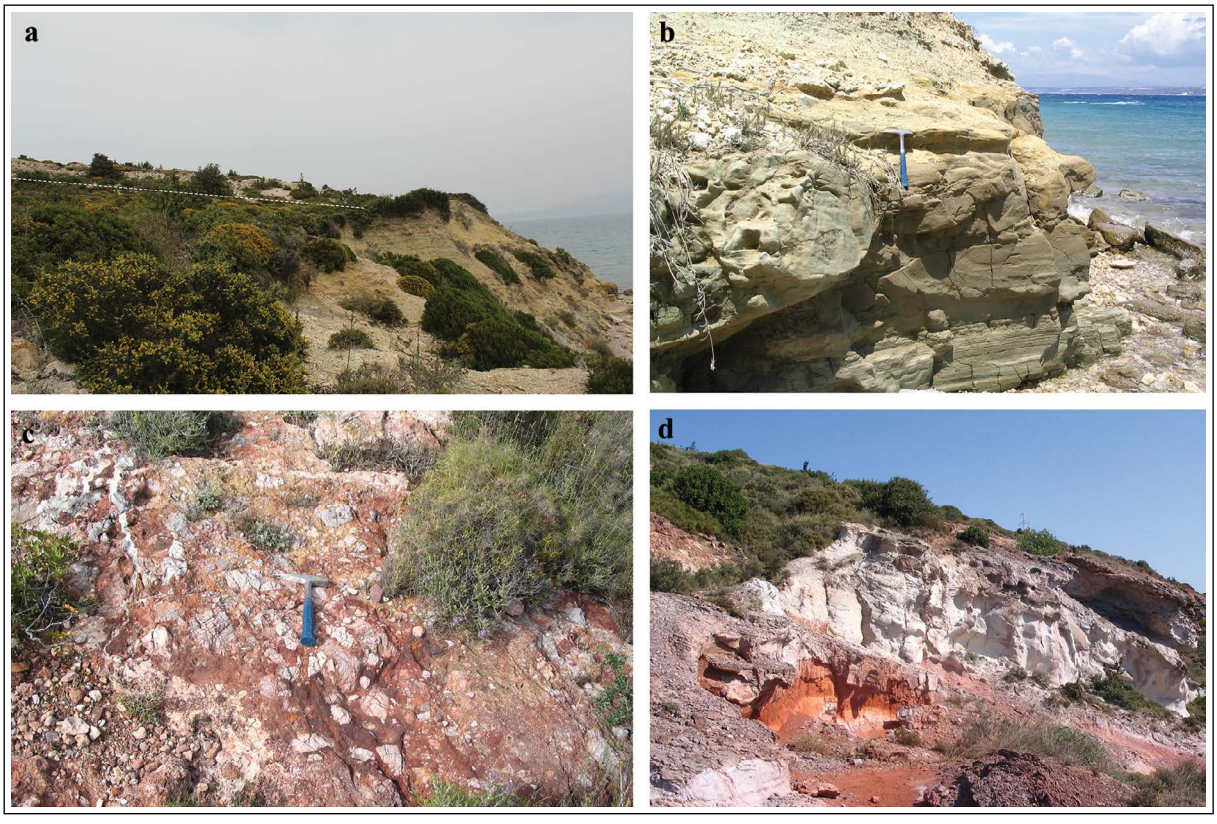

Figure 7- a) A view of the Azmakdere member in the lower part and the Beyazıt limestone member at the top (L16-a3; Batı Cape), b) the sandstone intercalation in the Azmakdere member (L16-a3; Batı Cape), c) transgressive pebbles along the time-lapse unconformable contacts between the carbonates of the Güvercinlik formation and the Azmakdere member deposits (L16-b4; west of Kocadağ Hill) and d) The Azmakdere member deposits rested on the western slopes of the Kocadağ Hill was hydrothermally altered.

on the Karadağ-Kocadağ uplift, which consists of the carbonates of the Güvercinlik formation. At the lowermost parts of these sections, there are basement derived, monolithic, coarse components (Figure 7c). Particularly, on the western slopes of the Kocadağ Hill, the basement carbonate rocks and parts of the formation close to the tectonic contact were affected by effective hydrothermal alteration (Figure 7d). The Azmakdere member is transitionally overlain by the Beyazıt limestone member in general. However, it is unconformably overlain by the alluvial fan deposits of the Karagöz formation in the south of the study area.

The fossil remains of large mammals found by Besenecker (1973) (*Sanitherium leobense, Gomphotherium* sp., *Diplocynodon* sp., *Ruminantia sp.* indet.) in the uppermost part of the Azmakdere deposit outcropping on the Batı Cape on the Çeşme Peninsula is included in MN5 biozone according to Kaya et al. (2003). The "Thymiana mammal fauna" described in the Keramaria unit (Besenecker, 1973), the equivalent of Azmakdere member in Chios, also belongs to MN5 biozone (Bonis et al., 1998) and it is dated approximately as 15.5 Ma according to magnetostratigraphic data of Koufos (2006). MN5 mammalian biozone confined to 14.2-16.4 Ma biochronologically indicates the early Middle Miocene (Hilgen et al., 2012).

This sedimentary succession reflects the lacustrine shoreface deposition. The fine grained clastics which form the lower part of the succession are generally deposited from the suspended material under normal wave base. The upper part of the sequence is dominated by the sandstone deposition developed on the normal wave base.

Azmakdere member is the chrono- and litho-stratigraphic equivalent of the "Karabağları member" defined by Göktaş (2014*b*) in north of the Karaburun Peninsula and also the "Keramaria unit" in Chios (Besenecker, 1973).

Beyazıt Limestone Member: The type locality of the Beyazıt limestone member (Göktaş, 2010), which forms the upper part of the Çiftlik formation, is the Beyazıt Hill in the SW of the Çiftlik District. The apparent thickness of the succession, which its main outcrops are exposed in the south of Çiftlik District, is maximum 55 meters.

The member, which is generally composed of medium to thick-bedded clayey limestone, has rarely distinct thin-bedded and very thick-bedded levels. General alteration color of the unit is whitish light gray. Green claystone, yellowish pale brown and massive mudstone interlayers are common. The limestone is locally dolomitic. Levels bearing algae are common; however gastropod and bivalvia contents are scarce. Beds with polygonal desiccation cracks and levels subjected to synsedimentary deformation are uncommon (Figure 8).

The sub-unit, which transitionally overlies the Azmakdere deposit in a narrow range, is unconformably covered by alluvial fan deposits of the Karagöz formation. The upper boundaries of the

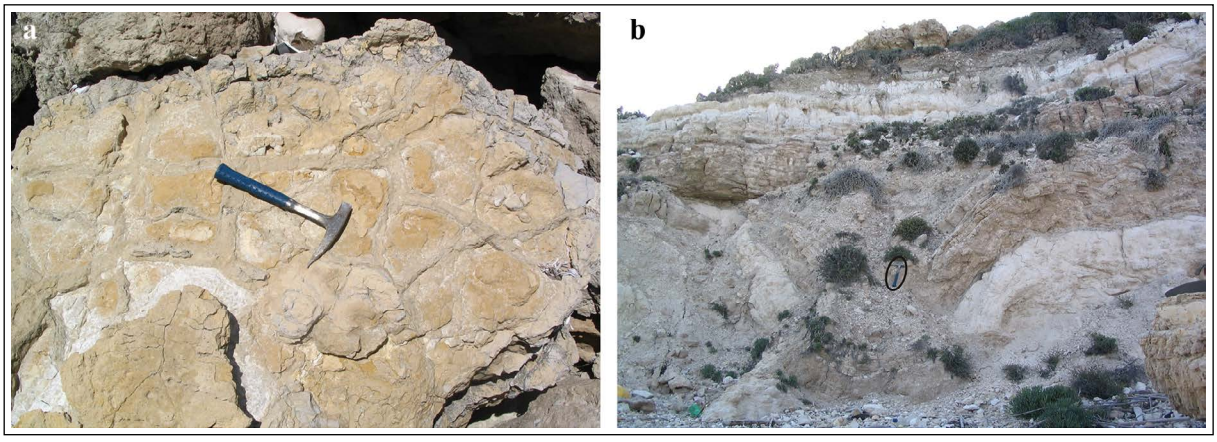

Figure 8- a) Desiccation cracks and b) syn-sedimentary deformations at some levels of the Beyazıt limestone succession exposed on the coast to the SW of Kırmızıtoprak Cape (L16-a3) (Hammer length is 33 cm).

sub-unit are generally determined by the Quaternary erosional surfaces.

3.2. Kaştepe Group

The Kaştepe group (Göktaş, 2010), the last sedimentary sequence of terrestrial Neogene sedimentation in the Çeşme Peninsula (Göktaş, 2010), is bounded by unconformities both at the bottom and the top. The Kaştepe group is constituted by the Karagöz formation in the lower part, which reflects the sedimentation in the alluvial fan environment, and transitionally overlapping lacustrine İnlice formation (Göktaş, 2010). Because of the continuing erosion until today, the apparent thickness of the Kaştepe group is over 100 meters (Figure 3).

There is no age data indicating the depositional period of the sedimentary sequence in the Miocene, which is bounded by the Quaternary erosion surfaces at the top. Kaştepe group, which unconformably overlies the Çiftlik formation, is relatively younger than Middle Miocene. It was proposed that the sedimentation occurred during the Late Miocene-Early Pliocene based on the stratigraphic correlation with the equivalent deposits on the Karaburun Peninsula ("Eşendere group": Göktaş, 2014*a, b*). The Late Miocene-Pliocene "Mytilini" and "Kokkarion" formations (Meissner, 1976; Weidmann et al., 1984) defined on Samos Island can be correlated with the rock units of the Kaştepe group.

3.2.1. Karagöz Formation

Karagöz formation (Göktaş, 2010), which forms the lower part of the Kaştepe sedimentary sequence, is represented by conglomerate, sandstone and mudstone assemblage. The type locality of the unit is the Karagöz Hill in the southern part of the L16-b4 sheet. Most of its outcrops are located in the southern part of the Çeşme Peninsula and the thickness of the succession is 70 meters.

The facies of conglomerate is dominantly channel-fill and associated with pebbly sandstone. Gravels were derived from the pre-Neogene basement rocks and Armağandağı volcanics. The size of gravels shows variation between pebble and cobble and their roundness is generally high. The mudstone consists of pinkish light brown colored, massive and very thick levels and dominates the upper parts of the alluvial deposit. It is poorly sorted and commonly includes sand and granule size clasts with rare pebbles. Due to its carbonate content, it is moderately medium to well cemented and rarely contains caliche nodules. Claystone levels are red colored, massive and moderately consolidated, and accompanies with mudstone.

The formation shows a fining-upward sequence and reflects a braided river dominant alluvial fan deposition. The unit overlies the Alaçatı pyroclastics, Ovacık and Çiftlik formations with an angular unconformity within the territory of Kaş Hill. The İnlice formation, which created the lacustrine part of the Kaştepe group, transitionally overlies the Karagöz formation.

The Saip formation (Göktaş, 2014*b*), defined around the Karaburun district center, is the stratigraphic equivalent of the Karagöz formation. The Karagöz formation can be correlated with the alluvial fan deposits "Mytilini formation" (Meissner, 1976; Weidmann et al., 1984), covering large mammal fossils of Turolian age in Samos Island. In the studies carried out in some Neogene basins such as Urla, Söke-Kuşadası and Aliağa surround, the alluvial fan deposits that could be interpreted as the equivalents of the Karagöz formation were not reported (Kaya, 1979; Eşder et al., 1991; Göktaş, 1998, 2011; Ünay and Göktaş, 1999; Ünay and Göktaş, 1999; Uzelli et al., 2017).

3.2.2. İnlice Formation

İnlice formation (Göktaş, 2010), which constitutes the upper part of the Kaştepe group, is generally characterized by micritic limestones with blue-green algae. The type locality of the unit is İnlice Stream (L16-c1) and its outcrops are mainly located around the Kaş Hill (L16-c1). Here, approximate thickness of the formation is 45 meters.

The deposition, which developed on distal deposits of the Karagöz alluvial succession starts with the lacustrine shore belt deposits composed of massive mudstones and distinct medium-bedded limestone levels. Massive mudstones are dominant in the lower part of the transition horizon. In the upper layers, the mudstone levels of which their frequency and singular

thicknesses gradually decrease in succession alternate with limestones. Bluish/greenish, dark gray mudstone levels are generally very thick or massive due to intense bioturbation. The limestone is fine detritious, intense bioturbated and commonly gastropod bearing. The weathering surface is pale yellow or gray. Some limestone layers contain freshwater algae accumulation levels parallel to the bedding planes. The algal grainstone levels, in which branched, tubular and oncoidal algae are packed in the form of grain-supported are located in the lower parts of the succession.

İnlice formation, which is the last Neogene unit on the Çeşme Peninsula reflecting the deposition in the lacustrine environment, transitionally overlies the Karagöz alluvial succession. Its upper boundary was determined by the Late Pliocene (?) - Recent erosion.

The unit is the chrono- and litho-stratigraphic equivalent of the Çukurcak limestone defined by Göktaş (2014*b*) in the NW of Karaburun Peninsula. The İnlice Formation is the equivalent of the "Kokkarion formation" in Samos Island, (Meissner, 1976; Weidmann et al., 1984).

4. Neogene Volcanism

4.1. Armağandağı Volcanics

The Armağandağı volcanics, which start with an acidic volcanism in phreatomagmatic type and continue with predominantly andesitic volcanism, reflect the late Early Miocene-early Middle Miocene calc-alkaline volcanism in the Çeşme Peninsula. Volcanostratigraphically, the underlying felsic pyroclastics were investigated as the Alaçatı pyroclastics, the upper andesitic-dacitic pyroclastics and epiclastic intercalations as the Reisdere volcaniclastics, and the lava assemblages in andesite and less dacite composition as the Zeytineli lavas (Figure 9). Andesitic-dacitic lavas and their cognate volcaniclastics were described by Türkecan et al. (1998) under the name of "Armağandağı volcanics"; and the felsic pyroclastics were considered as the extensions of Foça tuff (Kaya, 1979).

4.1.1. Alaçatı Pyroclastics

According to its volcanostratigraphic level, the Alaçatı pyroclastics, which are regarded to reflect the acidic type early period of Armağandağı volcanism, are made up of rhyolitic-rhyodacitic pyroclastics predominantly represented by superimposed ignimbrite units. No cognate lava extrusions occur throughout the Çeşme Peninsula. Kalafatçıoğlu (1961) first mentioned the existence of these tuffs spreading in the Çeşme Peninsula. The unit was defined as the "silicic vitric tuffs" by Kaçmaz and Köktürk (2004) and named as the "Alaçatı tuff" by Göktaş (2010).

Typical outcrops of the unit, which has an open and covered spread in the majority of the Çeşme Peninsula, are located in the territory of the Alaçatı district. The approximate thickness of the Alaçatı pyroclastics covering the thickest and most widespread products of the Armağandağı volcanism is over 160 meters.

Pyroclastic succession with a whitish light gray weathering surface consists of levels of poorly welded ignimbrite, base surge, fallout and ash fall facies in the order of majority (Figure 10a, b). It was predicted that the phreatomagmatism had developed in shallow lake where the stromatolytic-algal limestones of Şifne formation had been deposited. It can be proposed that the ignimbrite currents in the Çeşme Peninsula, which are mostly oriented towards the west, do not reach the Chios Island, based on the study of Besenecker (1973). 2-4-meter-thick, laterally discontinuous rare volcanic sandstone intercalations in pyroclastic succession, are the products of inactive phases during the volcanism.

The base surge deposits and distal ignimbrites exposed along the coastline to the southwest of the Karadağ Hill (L16-b4) consist extensively of armored or cored accretionary lapillies. The milimetric cores (up to 5 mm) of lapilli diameters (ranging from 2-4 cm) were derived from non-cognate lava fragments or pumices in ignimbrites (Figure 10c). In tafonized pyroclastics along the shoreline between the Tatlıcak and Güvercinlik locations, secondary diagenetic occurrences such as; "liesegang rings" and carbonate(?) concretions cutting the stratigraphication are observed (Figure 10d). Diagenetic concretions with lenticular geometries of which their long axes each metric sizes, form dark gray or dark beige topographic protrusions within generally whitish light gray pyroclastic levels (Figure 10e).

It is the typical feature of ignimbrites that accidental lithic concentration showing irregular grains size distribution from sand fraction to coarse

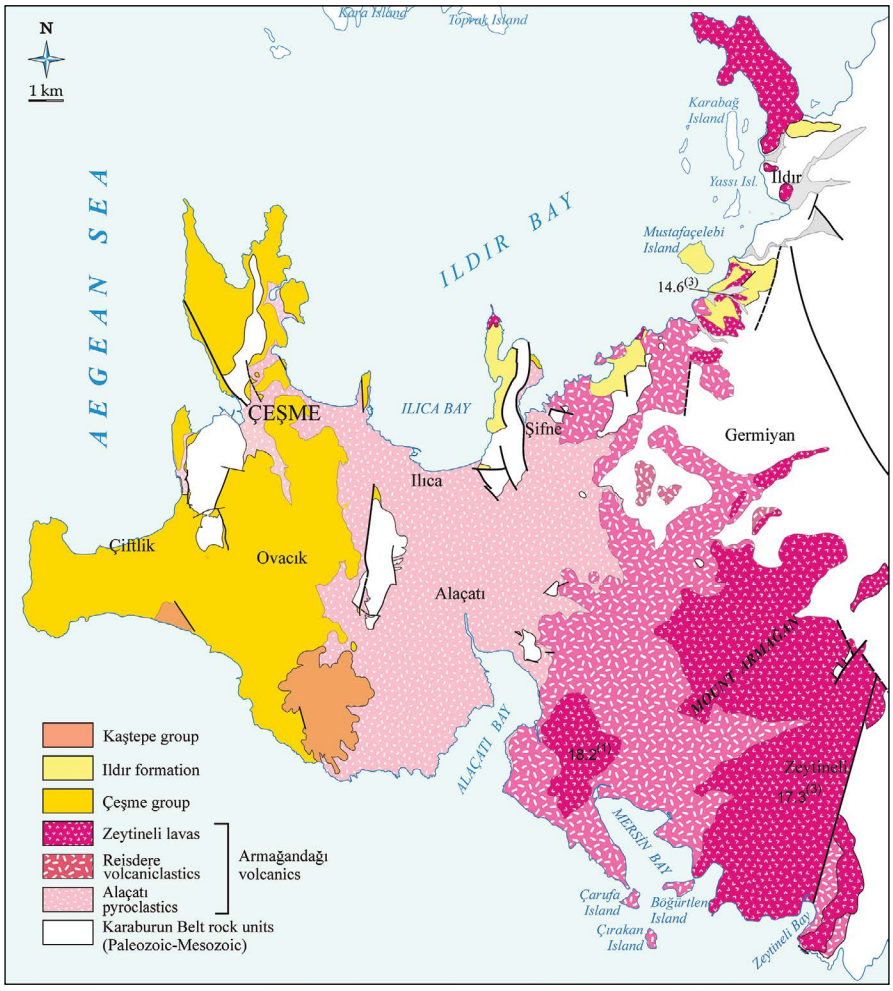

Figure 9- The distribution of the Armağandağı volcanics in the Çeşme Peninsula (Göktaş, 2010).

boulder sizes is high in general. Most of the lithic components are derived from Zeytineli lavas in andesitic and less dacitic composition (Figure 10f). Components carrying from the Reisdere volcaniclastics and the limestones of Şifne formation are more sparse (Figure 10f, g). Lithics transferred from pre-Neogene basement rocks are rare. There was not encountered any cognate lava fragments. The size and concentration of coarse lava fragments mostly in andesitic composition show a significant increasing in the proximal facies of ignimbrite flows. In this facies, decimetric-metric sizes andesitic boulders are encountered. Black andesite boulders over 1 meter size are observed to the east of Alaçatı, (Figure 10h). The concentration of proximal ignimbrites containing coarse andesite fragments in the eastern area of Alaçatı indicates that crater producing the Alaçatı pyroclastics is on the Mount Armağan, and it could not be observed as it covered by the Reisdere volcaniclastics and Zeytineli lavas. Towards the west and especially to the NW of Alaçatı, the transition into distal ignimbrites is observed, the volcanic lithics gradually decrease and the average pumice sizes become smaller as they move away from the probable eruption center.

Black colored, basalt-like andesites with fine crystalline textures are predominant among the lava fragments. The phenocrystalline content of from these lavas, which are defined mostly as pyroxene andesite in porphyritic texture are composed by plagioclase, amphibole and pyroxene. The groundmass is composed of volcanic glass, plagioclase microliths, pyroxene crystallites and opaque minerals. Plagioclase (andesine-labrador) is generally prismatic and polysynthetic twinning. Amphibole (hornblende) is usually subhedral. Orthopyroxene (hyperstene) is in green tones and has abundant cracks. Clinopyroxene (augite) has brown tones, subhedral and zoned. The

Figure 10- a) General view of the Alaçatı pyroclastics (L16-c1; between Tatlıcak and Güvercinlik locations), b) ignimbrite units separated by base turbulence levels (L16-c1; Shoreline between Tatlıcak and Güvercinlik locations), c) close views of ignibrite unit comprising accretionary lapillies in the lower part, and base surge level and cross sections of cored lapillies (L16-b4; shoreline in the sw of Karadağ Hill), d) liesegang rings in the lower part and carbonate(?) concretions (black arrows) and taphonization (L16-c1; Shoreline between Tatlıcak and Güvercinlik locations), e) a lenticular carbonate(?) concretion in massive ignimbrite unit comprising accretionary lapillies (L16-c1; Shoreline between Tatlıcak and Güvercinlik locations), f) some parts of ignimbrites are richer in andesite lava clasts but less in dacite lava fragments. Algal limestone clasts derived from the Şifne formation are rare (black arrows) (L16-b4; east of Alaçatı district, g) a block derived from Reisdere volcaniclastics in ignimbrites (L16-b4; east of Yumru Bay) and h) some of andesitic lava blocks has a size up to 1 meter (L16-b4; east of Alaçatı district).

minor dacite clasts in the volcanic lithic content show red-black color zonation in concordant with the flow structure.

In the region, the Alaçatı pyroclastics overlies the laterally discontinuous andesitic volcaniclastics reflecting the beginning of the Armağandağı volcanism and algal-biostromal limestones of the Şifne formation. The contact relationship with Şifne formation is observed in the center of Çeşme district and around the Kara Hill basement uplift to the west of Alaçatı. As seen on the eastern shores of the Gulf of Alaçatı, the density currents formed the Reisdere volcaniclastics overlie the Alaçatı pyroclastics with laterally interfingering. The alluvial fan deposits of the Karagöz formation extensively exposed in the SW of Alaçatı overlie the Alaçatı pyroclastics with an angular unconformity.

4.1.2. Reisdere Volcaniclastics

The Reisdere volcaniclastics are mainly composed of intermediate pyroclastics and lahar levels of the Armağandağı volcanism. These volcaniclastics are widespread in the west of Mount Armağan (Figure 9).

Andesitic pyroclastics are predominantly in the facies of blocky ash flow. The multilayered pyroclastic flow units together with lahar layers are meters in thickness and have no internal structures. The size andesitic lava fragments are centimeters and decimeters, they are angular and sub-angular. The concentration of coarse lava fragments is variable and they show irregular distribution in the coarse ash matrix. The pyroclastic flow units, inwhich coarse lava fragments are reverse graded, are rarely observed.

The epiclastic levels, which were deposited by reworking previous density flow deposits, are in volcanic mud/debris flow facies known as the "lahar". The andesitic coarse volcaniclastic content is generally high. These mass flow layers, whose matrix is composed of poorly sorted volcanic sandstone, are usually massive and their thickness is generally metric. They form superimposed sedimentation units or alternate with blocky ash flow layers. The stratification, which becomes evident by the vertical change in coarse clast concentration, is mostly less developed (Figure 11).

Based on field data, the Reisdere volcaniclastics widely spreads over the basement rocks of the Karaburun Belt and Alaçatı pyroclastics. According to evaluations on the FY-1 geothermal drilling conducted by MTA, 40 meters thick "andesitic agglomerate" which is considered to reflect the beginning of the Armağandağı volcanism (Yılmazer and Yakabağı, 1995), underlies the Alaçatı pyroclastics and overlies the Şifne formation (Figure 3). Andesitic coarse lava fragments are common in the Alaçatı pyroclastics support the andesitic volcanism that precedes the settlement of felsic ignimbrites. The Reisdere volcaniclastics are accepted as laterally interfingered with the Zeytineli lavas from bottom to top, which constitute the lava assemblage of Armağandağı volcanics (Figure 3). There is no contact relationship between the Reisdere volcaniclastics and the Ovacık

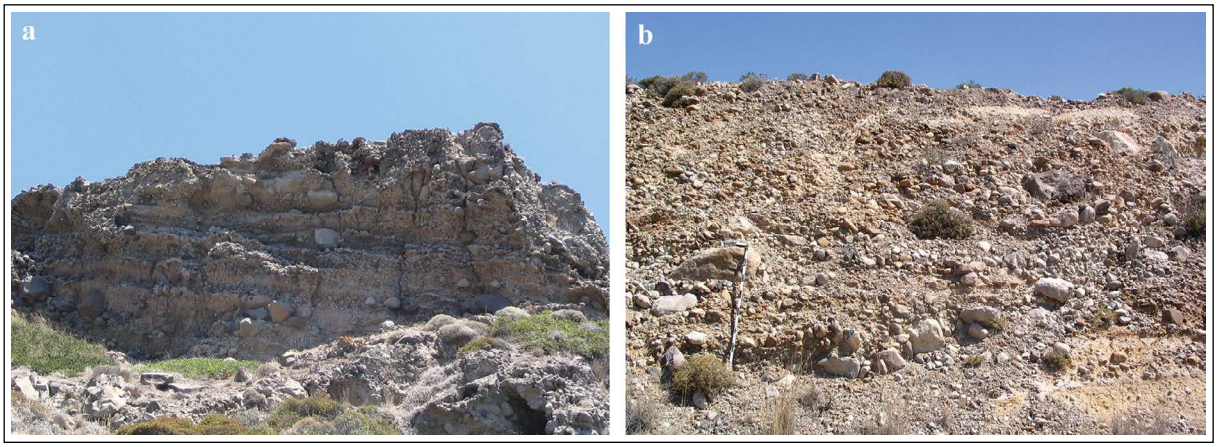

Figure 11- a) General view of the lahar layers and b) a layer having high pebble-block concentration (Jacob's staff is 150 cm) (L16-b4; NE of the Alaçatı district).

and Çiftlik formations, which are considered to have deposited synchronously. This lateral relationship was proposed based on the indirect data. The volcanic sandstone interlayers with andesitic component in the Ovacık formation and Reisdere volcaniclastics deposited with lateral interfingering into the Ildır formation, which is accepted as the equivalent of the Çiftlik formation as defined in Göktaş (2016*b*), are indirect examples.

4.1.3. Zeytineli Lavas

Zeytineli lavas represent mostly andesitic and less dacitic lava assemblage of Armağandağı calc-alkaline volcanism. The first study related to the petrographic and petrochemical properties of lava belongs to Innocenti and Mazzuoli (1972). Türkecan et al. (1998) examined the petrographical and geochemical properties of the lava assemblage within scope of the "Armağandağı Volcanics".

The lava samples examined in previous studies have been described as quartz-latite andesite (Innocenti and Mazzuoli, 1972), 'andesite' and 'pyroxene andesite' (Türkecan et al., 1998). In this study, the phenocrystals of mostly the hyalomicrolitic-porphyritic samples with few flow textured samples, which are defined as "pyroxene-hornblende andesite", are composed of plagioclase, pyroxene, amphibole and biotite. Plagioclase (andesine-labrador) is mostly subhedral, usually polysynthetic twinned, and locally zoned. Clinopyroxene (augite) is euhedral-subhedral, pale brown colored, rarely twinned and glomeroporphyritic textured. Orthopyroxene (hyperstene) is in green tones and usually fractured. Amphibole (hornblende) is usually subhedral and in brown tones, and it forms glomeroporphyritic texture or is found as opacified relicts. Biotite is in the form of large and small lamellae and it is rarely observed. The groundmass is composed of volcanic glass, plagioclase and biotite microliths, pyroxene crystallites and opaque minerals. Biotite microliths are in elongated prismatic form. Opacification is widespread in amphibole and biotites.

The sample taken from black, fine-crystalline and basalt-like lava level which overlies the Alaçatı pyroclastics near Zeytineli, is defined as the "olivine basalt". Plagioclase and pyroxene form the phenocrystals of hypocrystalline-porphyritic (intersertal) textured rock. Plagioclase (labrador) has generally polysynthetic twinning and prismatic shape. The groundmass of the rock is composed of volcanic glass, oriented plagioclase, olivine and pyroxene microliths and opaque minerals.

The Zeytineli lava assemblage, which is considered as laterally interfingered with the Reisdere volcaniclastics, represented the multi-phased lava eruptions synchronously developed with the deposition of lacustrine units on the Şifne formation of the Çeşme group. The lateral relationship was constructed based on the chronostratigraphic relations and limited lithostratigraphic observations. The first order stratigraphic relationship was observed between the Zeytineli lavas and Ildır formation sediments (Göktaş, 2010; 2016*b*).

4.1.4. Major Element Oxide Geochemistry of the Armağandağı Volcanics

The major element oxide compositions of 12 samples collected from the Alaçatı pyroclastics by Kaçmaz and Köktürk (2004) were evaluated on the TAS diagram of Le Bas et al. (1986) and determined that all the samples plotted in the sub-alkaline zone and accumulated mostly in rhyolitic and few in dacitic areas (Figure 12a). Kaçmaz and Köktürk (2004), showed that the samples, which they had plotted on the Zr/TiO_2-Nb/Y diagram based on the stable elements prepared by Winchester and Floyd (1977), were concentrated in rhyodacite/dacite composition area (Figure 12b). The samples Ç.18 in the andesite composition area and Ç.20 in the dacite composition area represent lava clasts commonly found in felsic ignimbrites. All samples are calc-alkaline in character (Figure 12c) and have high potassium content (Figure 12d).

The main element oxide compositions of the samples taken from the previous studies (Innocenti and Mazzuoli, 1972; Türkecan et al., 1998; Helvacı et al., 2009; Göktaş, 2010), which represent the lava assemblage of the Armağandağı volcanics (Table 1), were plotted on the TAS diagram of Le Bas et al. (1986), and it shown that all samples were located in the subalkaline zone and accumulated mainly in the andesitic and less dacitic composition area (Figure 12A). In the AFM diagram of Irvine and Baragar (1971), the samples in calc-alkaline character are located in "high potassium andesite" area in the K_2O-

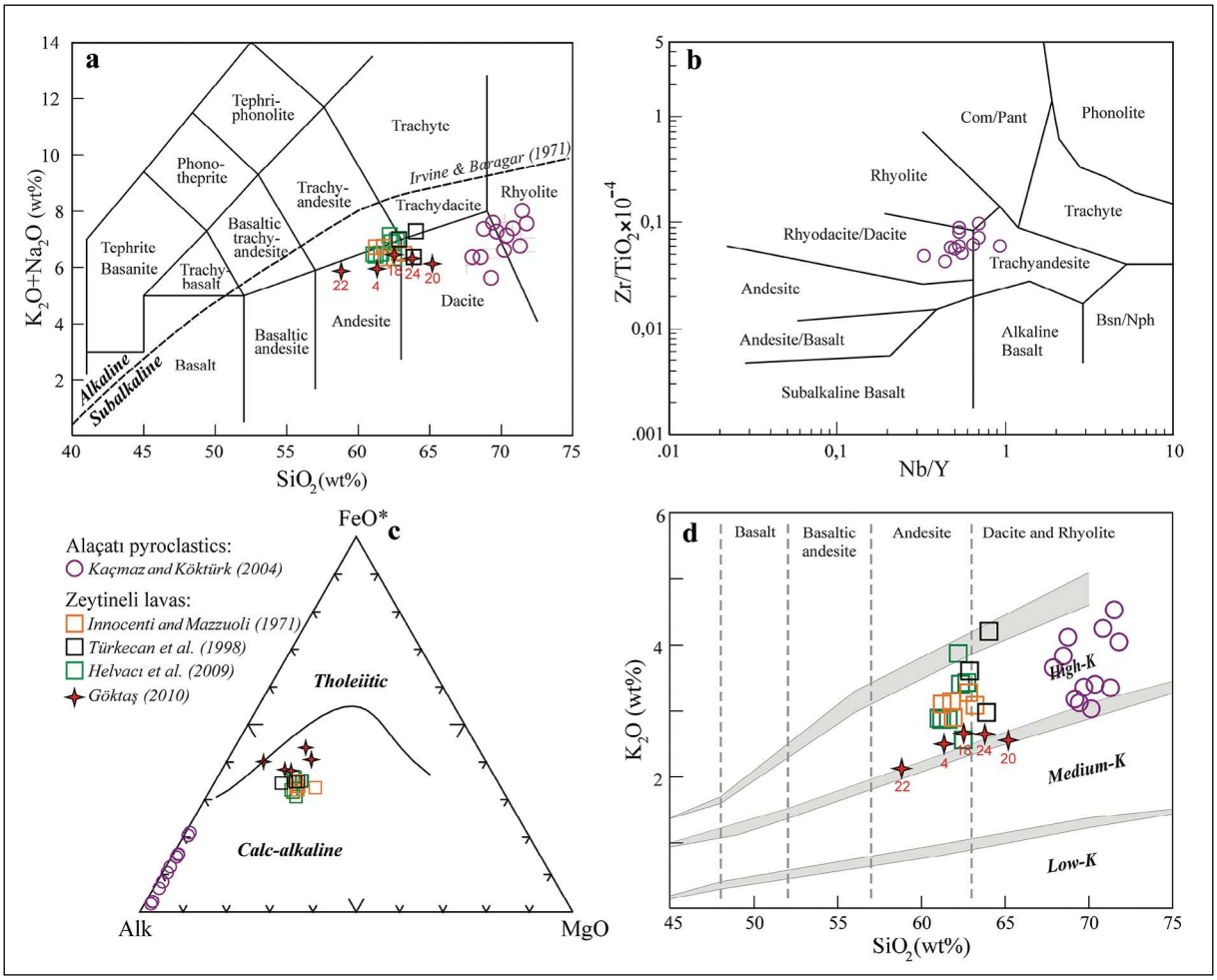

Figure 12-Evaluation of the results of major element analysis of the Armağandağı volcanics taken from previous studies; a) TAS diagram (Le Bas et al., 1986), b) Zr/TiO_2-Nb/Y diagram (Winchester and Floyd, 1977), c) AFM diagram (Irvine and Baragar, 1971) and d) K_2O-SiO_2 diagram (Le Maitre, 1989).

Table 1-Results of the major element oxide analysis of the samples collected by Göktaş (2010) from the Zeytineli lavas.

Sample	*East*	*North*	SiO_2	Al_2O	Fe_2O_3	MgO	CaO	Na_2O	K_2O	TiO_2	P_2O_5	MnO	SrO	BaO	LOI
Ç.18	*47.615*	*38.673*	61.10	16.80	5.70	2.20	5.30	3.70	2.60	0.50	0.30	0.10	0.08	0.14	1.35
Ç.20	*47.615*	*38.673*	63.80	16.00	5.20	1.00	5.60	3.50	2.50	0.50	0.20	0.10	0.08	0.14	1.35
Ç.22	*57.140*	*33.585*	58.10	18.20	7.10	2.40	5.70	3.70	2.10	0.80	0.30	0.10	0.08	0.08	0.25
Ç.24	*52.150*	*36.550*	62.60	16.30	5.50	1.90	5.30	3.60	2.60	0.60	0.20	0.10	0.06	0.07	0.20
Ç.4	*53.275*	*45.380*	59.90	16.70	6.30	0.10	5.90	3.40	2.40	0.60	0.20	0.10	0.07	0.09	1.40

SiO_2 diagram of Le Maitre et al. (1989) (Figures 12c and 12d).

4.1.5. Geochronology of the Armağandağı Volcanics

Borsi et al. (1972), took an age of 18.2 ± 3.5 Ma from quartz-latite andesite (biotite) by the K/Ar method. The age obtained from an andesite sample of Helvacı et al. (2009) is 17.3 ± 0.1 Ma by means of the $^{40}Ar/^{39}Ar$ method. These radiometric data are related to the activity of the Armağandağı intermediate volcanism in the late Early Miocene. The age of 14.6 ± 0.6 Ma by K/Ar method taken by Göktaş (2010) from a lava flow, which is considered as an extension of Zeytineli lavas around Ildır, shows that the calc-alkaline andesitic volcanism in the Çeşme Peninsula continued until the early Middle Miocene.

5. Stratigraphical Correlation and Paleogeographic Evolution

Large part of the Early-Middle Miocene basin, which has deposits on the Çeşme Peninsula and along the eastern shores of Chios Island, has been submerged by the collapse of the Aegean land. Early Miocene deposits defined by Besenecker (1973) in Chios Island and the possible chronostratigraphic equivalents in the Çeşme Peninsula are represented by different sedimentary facies. However, Middle Miocene sedimentation can be correlated in terms of depositional environment, rock composition and mammal faunas. The green lacustrine shoreface succession, representing the early Middle Miocene (Langhian) deposition, is the stratigraphic reference level that enables the first-degree correlation between the Early-Middle Miocene successions in the western (Chios Island) and eastern (Çeşme Peninsula) parts of the basin. The Azmakdere member, which forms the lower part of the Çiftlik formation on the Çeşme Peninsula, and Keramaria unit, its equivalent in Chios Island, was firstly correlated by Besenecker (1973) based on the mammalian fossils belonging to the MN5 biozone. The Early Miocene sedimentary deposits under this datum level are dominantly represented by lacustrine limestones (Şifne and Ovacık formations) in the east of the basin, whereas in the Chios Island representing the west of the basin, the fluvial sediments were filled defined by Besenecker (1973) as "Thymiana" and "Zyfia" units (Figure 13).

In this study, the chrono-lithostratigraphic equivalents of the Early-Middle Miocene lacustrine dominant sediments studied within scope of the Çeşme group in the north of Karaburun Peninsula are included in the Karaburun group (Göktaş, 2014*a, b*) (Figure 14). Şifne formation, which corresponds to the beginning of terrestrial Neogene sedimentation in coastal Aegean regions and ends with algal limestones grading from alluvial deposits to lacustrine sediments, can be correlated with Salman+Yeniliman limestone members of the Haseki formation, the same stratigraphic level with the Karaburun group (Göktaş, 2014*a*). Şifne formation, which its important part does not expose in the Çeşme Peninsula, is represented by laminated stromatolithic limestones that increase in the upper part of the succession.

By the syn-sedimentary deposition of the Alaçatı pyroclastics on the Şifne lacustrine carbonate platform, the Early Miocene lacustrine sedimentation was interrupted (restricted with the settlement time and spread areas of pyroclastics). The Alaçatı pyroclastics, which reflect the acidic early period of the Armağandağı volcanism are the products of phreatomagmatism developed in the shallow lacustrine environment where Şifne formation were deposited. The gradual increase of non-cognate (in composition of andesite and less dacite) coarse lava fragments contained by ignimbrites towards the Mount Armağan indicates that the crater which produce the Alaçatı pyroclastics were located around this mountain. The field data indicate that ignimbrite flows are mostly oriented to the west and south. However, it has been evaluated that these ignimbrite flows did not reach Chios Island. In Chios, the rhyolitic ignimbrite level of 15.5 Ma (Bellon et al., 1979) spreading as a reference level at the bottom of the Keramaria succession, is younger than the ignimbrites in the Alaçatı pyroclastics and has no equivalent in the Çeşme Peninsula (Figure 13).

Early Miocene lacustrine sedimentation maintained its continuity in the regions outside the spreading areas of Alaçatı pyroclastics, as it was in the north of the Karaburun Peninsula. The Early Miocene basin suddenly deepened with the settlement of Yaylaköy volcanics on the stromatolitic-algal limestone platform, blue-green algae with limited photosynthetic possibilities gradually decreased and the lacustrine sedimentation characterized by thin-laminated micritic limestone (Aktepe member: Göktaş, 2014*a*) developed in north of the Karaburun Peninsula. In the Çeşme Peninsula, the Ovacık formation was deposited during the lacustrine transgression process following the settlement of Alaçatı pyroclastics in the Early Miocene basin. Ovacık formation, which unconformably overlies the Alaçatı pyroclastics by its İnönü member, reflects the continuation of the Early Miocene lacustrine sedimentation, which was interrupted by the settlement of the Alaçatı pyroclastics. The rock type assemblage and stratigraphic position of the Ovacık formation suggests a first-degree correlation with the Aktepe member (Figure 14).

Early-Middle Miocene lacustrine sedimentation on the Çeşme Peninsula continued with the Çiftlik formation, which was conformably deposited over the Ovacık formation. In contrast to the conformable relationship between the two successions, the

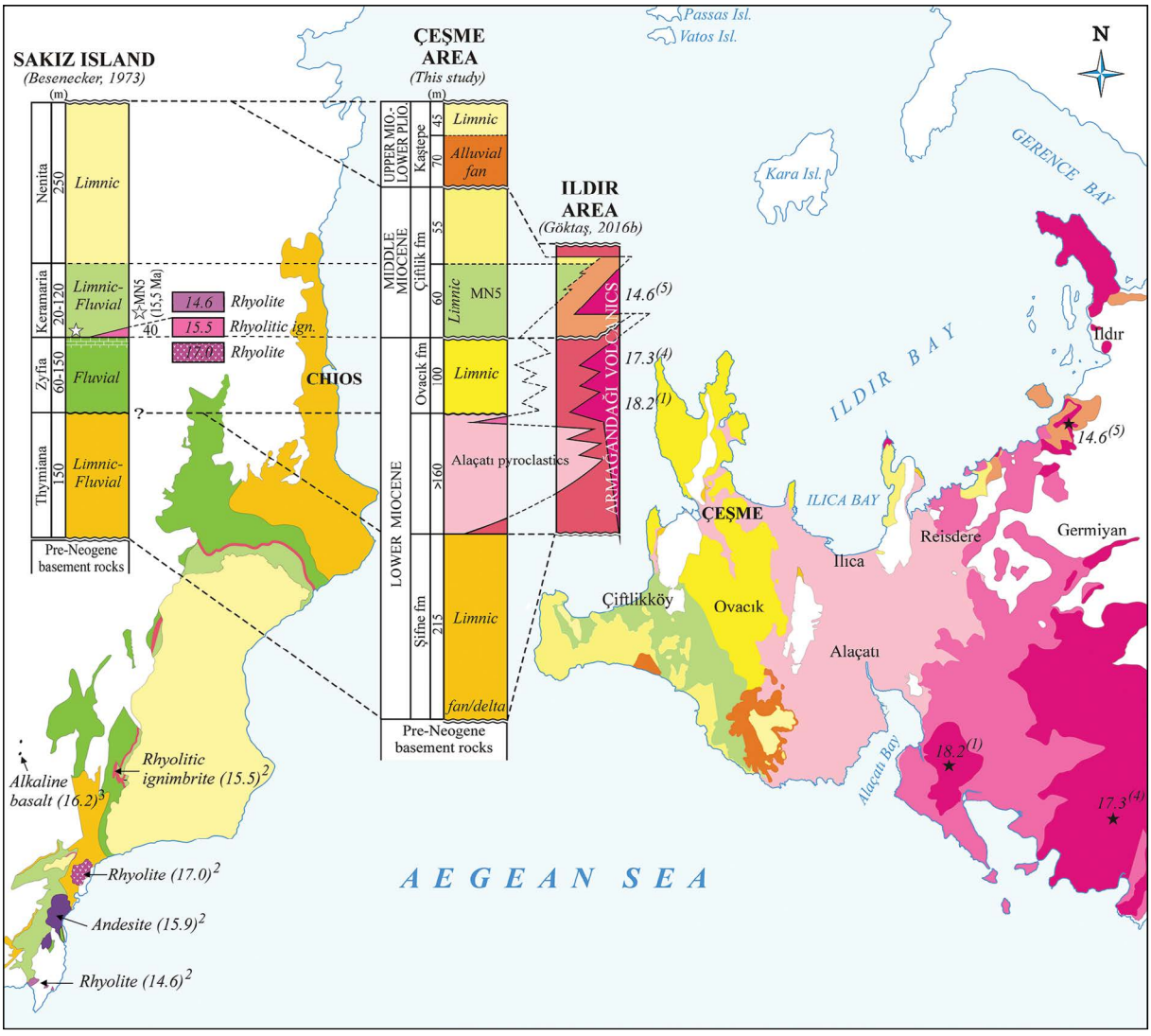

Figure 13-Stratigraphic correlation of Neogene rock units in Chios Island and the Çeşme Peninsula. Radiometric ages: [1]Borsi et al. (1972), [2]Bellon et al. (1979), [3]Pe-Piper et al. (1994), [4]Helvacı et al. (2009), [5]Göktaş (2010).

lithofacies change reflecting the sudden deepening of the basin is evident. The environmental frame where the Ovacık formation was deposited remained unchanged and lacustrine sedimentation continued under the depositional conditions specific to different depths of the same basin. The thin detritious shoreface sedimentation of the Azmakdere member developed on the limestones of the Ovacık formation, show that the basin was suddenly deepened on a regional scale and the fine clastic sediment transportation increased. The sedimentation energy of the Azmakdere deposit increases from bottom to top. The deposition from suspension under normal wave bottom, represented by the dark green claystone-siltstone assemblage, dominates the lower parts of the succession. Intercalations of climbing rippled storm sand rarely found in the deposit are typical. In upward direction, sand-size sediment transportation increased, and a massive, locally cross-bedded and weakly compacted sandstone dominating succession was deposited. The large mammalian bones found by Besenecker (1973) in the Batı Cape are in this sandstone layers. The overlapping of the Azmakdere deposits outcropping around the Kocadağ Hill onto the carbonates of the Güvercinlik formation with diachronous transgressive contacts shows that this elevation is one of the islands that existed in the Early Miocene basin. The N-S trending fault, which restricts the Kocadağ uplift from the west, reactivated after deposition and altered the Azmakdere member deposits by giving way to high Fe

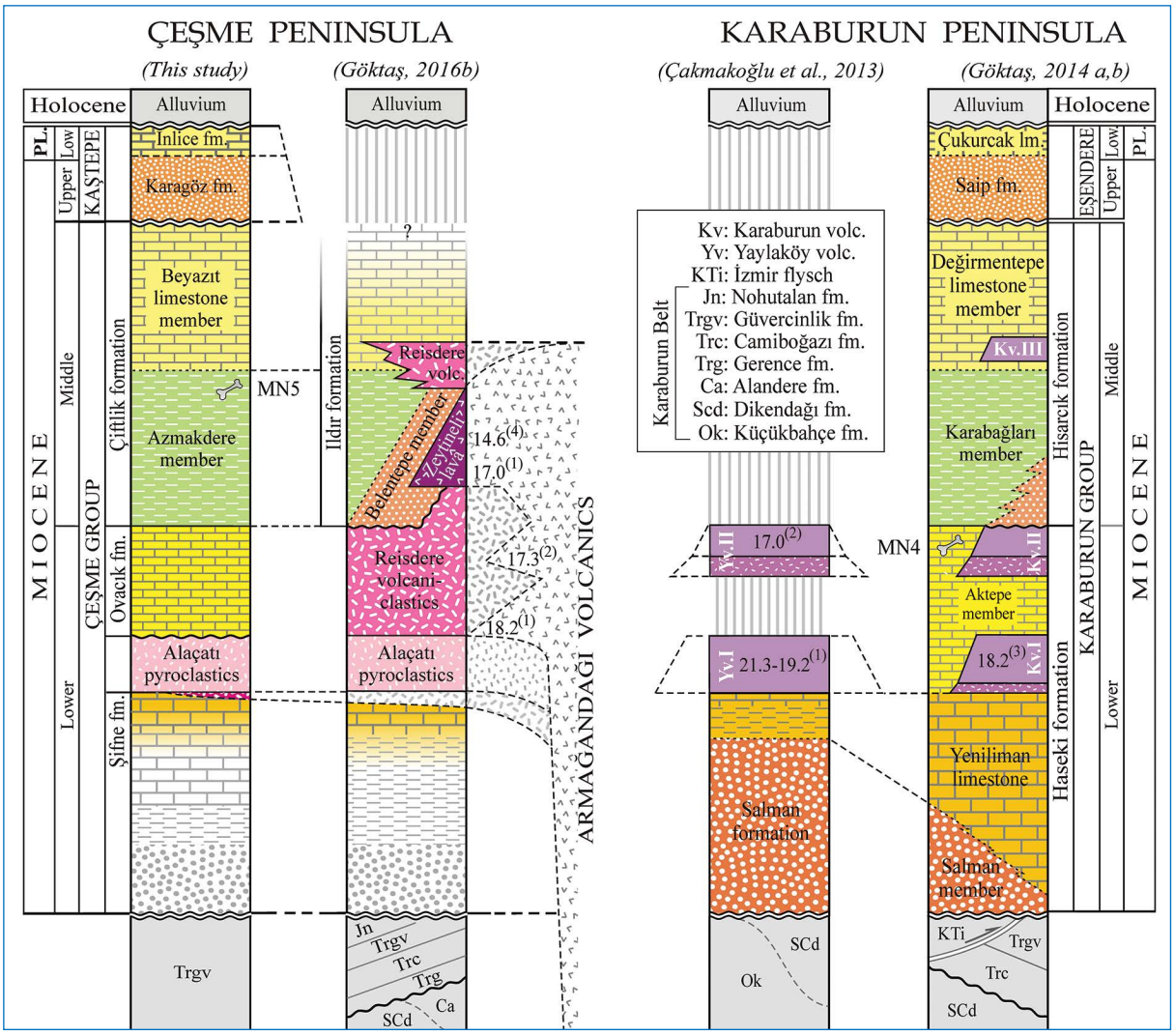

Figure 14- Correlation of Neogene rock units in the Çeşme and Karaburun peninsulas (modified from Göktaş 2016*b*). Radiometric ages: [1]Borsi et al. (1972), [2]Helvacı et al. (2009), [3]Göktaş (2014*a*), [4]Göktaş (2010).

bearing hydrothermal solutions. The Beyazıt limestone member, which forms the upper part of the Çiftlik formation, is the last unit of the Çeşme group. It can be asserted that the Early-Middle Miocene lacustrine sedimentation, which is represented by the Çeşme group, regionally ended with short compressional phase prior to the Late Miocene extension that affects the Western Anatolia (Yılmaz, 2000; Yılmaz et al., 2000). The stratigraphical position, type of deposition and rock type assemblage of the Çiftlik formation suggest the correlation with the Ildır formation defined in south of Ildır Gulf (Göktaş, 2016*b*) and the Hisarcık formation (Göktaş, 2014*b*) in the north of the Karaburun Peninsula (Figure 14). However, the alluvial deposits forming the lower parts of the Ildır and Hisarcık formations (Belentepe member: Göktaş, 2016*b* and Hacıhüseyintepe member: Göktaş, 2014*b*) do not have correspondence in the region where the Çiftlik formation was deposited. According to Göktaş (2016*b*), the Belentepe member was deposited at the margins of the Early Miocene basin around the Ildır Bay, which tectonically deepened early in the Middle Miocene and expanded towards NE of the Çeşme Peninsula. The Azmakdere member, which was deposited synchronously in the west of peninsula, represents the open lake facies. The Azmakdere member can be regarded as the equivalent of the Karabağları member defined by Göktaş (2014*b*) in north of the Karaburun Peninsula. The Beyazıt limestone member is the equivalent of

the Değirmentepe limestone member in the same area (Figure 14). The Middle Miocene Urla group (Göktaş, 2011; 2016*a*), defined in the Urla basin and İzmir Bay islands, includes the sedimentary assemblages that can be correlated with the Çiftlik formation.

The fields observations related to the order of succession of the Armağandağı volcanics formed by the products of Early-Middle Miocene calc-alkaline acidic-intermediate volcanism on the Çeşme Peninsula, suggest that the volcanism developed mainly with the settlement of the Alaçatı pyroclastics. However, i) the "andesitic agglomerate" level situated between the Şifne formation and Alaçatı pyroclastics according to drilling data and ii) andesitic lava fragments largely present especially in proximal sections of the felsic ignimbrites presenting the Alaçatı pyroclastics show that the intermediate volcanism started just before the settlement of the Alaçatı pyroclastics (Figure 3). There is not any data related to the volcanic activity during the depositional period of Şifne formation. Andesitic (-dacitic) volcanics observed on the Alaçatı volcanics start with Reisdere volcaniclastics consisting of pyroclastics and epiclastics in lahar facies and continues with laterally interfingered cognate lava extrusions along the whole succession (Zeytineli lava). The youngest known products of the Zeytineli lavas are laterally associated with the sediments of the Ildır formation (Göktaş, 2016*b*). The 14.6 ± 0.6 Ma K/Ar age obtained from the andesite flow in alluvial deposits of the Belentepe member indicates that the Armağandağı intermediate volcanism has continued at least until the early Middle Miocene (Göktaş, 2016*b*). Based on radiometric data, the bimodal alkaline volcanism started in the Urla depression, which continued its activity until the end of the Middle Miocene, while the Armağandağı calc-alkaline volcanism became extinct in the Early Middle Miocene (Göktaş, 2011, 2016*a, b*).

The Kaştepe group, extending in south of the Çeşme Peninsula, starts with the alluvial deposits (Karagöz formation) and ends with the lacustrine deposits (İnlice formation), and it is the last succession of the Neogene sedimentation. The succession, considered to have deposited during the Late Miocene-Early Pliocene, overlies the Alaçatı pyroclastics and the lacustrine sediments of Ovacık and Çiftlik formations with an angular unconformity. The Eşendere group defined by Göktaş (2014*b*) in NE sections of the Karaburun Peninsula, which represents the western edge of the Foça Depression, is considered as the equivalence of the Kaştepe group in terms of regional stratigraphic position, order of succession and similar rock type assemblages. In the studies carried out in other parts of the Foça Depression (Urla section, İzmir Bay islands and Foça section) and in Söke-Kuşadası basin, no succession that can be compared to those of the Kaştepe group were identified (Kaya, 1979; Eşder et al., 1991; Göktaş, 1998, 2011; Ünay and Göktaş, 1999; Uzelli et al., 2017). The Late Miocene-Early Pliocene "Mytilini"+"Kokkarion" formations (Meissner, 1976; Weidmann et al., 1984) identified in Samos Island can be correlated with the Kaştepe group.

The area where the Çeşme Peninsula is located is fragmented by the average N-trending faults in the Early Miocene and mostly by NW trending (strike-slip, reverse, oblique-normal) faults after the Middle Miocene, and folded in NW-SE, N-S, NE-SW axis extensions as commonly observed in the Ovacık formation (Sözbilir et al., 2007). Most of ones having relatively short-axis plunge dipping in two directions (Figure 2). All lacustrine units within the Çeşme group overlap with transgressive conglomerates on the basement rocks, which are represented by the Güvercinlik formation uplifted by the N trending faults. This relationship reflects that these uplifts constitute the basement islands within the Early-Middle Miocene basin. The majority of these faults reactivated after the deposition of the Çeşme group. In the region uplifted during the short compressional phase before the late Miocene extension (Yılmaz, 2000; Yılmaz et al., 2000), the Early-Middle Miocene lacustrine basin deposited by the Çeşme group became terrestrial and the eroded basin fill has become material for the alluvial fans (Karagöz formation) which reflect the beginning of the Late Miocene deposition.

Acknowledgements

This study consists a part of the MTA project titled as "Çeşme, Urla, Cumaovası, Kemalpaşa-Torbalı Çöküntülerindeki Neojen ve Kuvaterner Havzalarının Stratigrafisi ve Paleocoğrafik Evrimi Projesi (2007-30-14-01.f)" (Stratigraphy and Paleogeographic Evolution Project of Neogene and Quaternary Basins in Çeşme, Urla, Cumaovası, Kemalpaşa-Torbalı Deposits). Murat Yükünç (Geol. Eng. with Ms) helped during field studies. Thanks to Dr. H. Yavuz Hakyemez for corrections in English edition.

References

Aras, A., Göktaş, F., Demirhan, M., Demirhan, H., İçöz, S. 1999. Karaburun kilinin stratigrafisi, mineralojisi ve pişme özellikleri. 1. Batı Anadolu Hammadde Kaynakları Sempozyumu (BAKSEM'99), 8-14 Mart 1999, İzmir, 238-247.

Bellon, H., Jarrige, J.J., Sorel, D. 1979. Les activités magmatiques égéennes de l'Oligocène à nos jours et leurs cadres géodynamiques. Données nouvelles et synthèse. Revue du géologie dynamique et géographie physique 21, 41-55.

Besenecker, H. 1973. Neogen und Quartär der Insel Chios (Ägäis): PhD Thesis, Freien Universität Berlin, 195 p.

Bonis, L. De, Koufos, G.D., Şen, Ş. 1998. Ruminants (Bovidae and Tragulidae) from the Middle Miocene (MN5) of the Island of Chios, Aegean Sea (Greece). Neues Jahrbuch für Geologie ve Paläontolog Abhandlungen 210, 339-420.

Borsi, S., Ferrara,C., Innocenti, F., Mazzuoli, R. 1972. Geochronology and petrology of recent volcanics of Eastern Aegean Sea. Bulletin of Volcanology 36, 473-496.

Brinkmann, R., Flügel, E., Jacopshagen, V., Lechnert, H., Rendel, B., Trick, P. 1972. Trias, Jura und Unterkreide der Halbinsel Karaburun (West Anatolien). Geology and Paleontology 6, 139-150, Marburg.

Çakmakoğlu, A., Bilgin, Z. R. 2006. Pre-Neogene Stratigraphy of The Karaburun Peninsula (West of İzmir, Turkey), Bulletin of the Mineral Research and Exploration 132, 33-62.

Çakmakoğlu, B., Göktaş, F., Demirhan, M., Helvacı, C. 2013. Karaburun Yarımadası'nın kuzey kesimindeki killerin stratigrafisi, sedimantolojisi ve ekonomik kullanım olanaklarının araştırılması. Türkiye Jeoloji Bülteni 56/1, 39-58.

Emre, Ö., Özalp, S., Doğan, A., Özaksoy, V., Yıldırım, C., Göktaş, F. 2005. İzmir yakın çevresinin diri fayları ve deprem potansiyelleri. Maden Tetkik ve Arama Genel Müdürlüğü Rapor No: 10754, 80 s, Ankara (unpublished).

Erdoğan, B., Altıner, D., Güngör, T., Özer, S. 1990. Stratigraphy of Karaburun Peninsula. Bulletin of the Mineral Research and Exploration 111, 1-24.

Eşder, T., Yakabağ, A., Sarıkaya, H., Çiçekli, K. 1991. Aliağa (İzmir) yöresinin jeolojisi ve jeotermal enerji olanakları. Maden Tetkik ve Arama Genel Müdürlüğü Rapor No: 9467, Ankara (unpublished).

Gemici, Ü., Filiz, Ş. 2001. Hydrochemistry of Çeşme geothermal area in western Turkey. Journal of Volcanology and Geothermal Research 110, 171-187.

Göktaş, F. 1998. Söke havzasının Neojen ve Kuvaterner stratigrafisi. Maden Tetkik ve Arama Genel Müdürlüğü Rapor No: 10222, Ankara (unpublished).

Göktaş, F. 2010. Çeşme Yarımadası'ndaki Neojen tortullaşması ve volkanizmasının jeolojik etüdü. Maden Tetkik ve Arama Genel Müdürlüğü Rapor No: 11389, 64 s. Ankara (unpublished).

Göktaş, F. 2011. Urla (İzmir) çöküntüsündeki Neojen tortullaşması ve volkanizmasının jeolojik etüdü. Maden Tetkik ve Arama Genel Müdürlüğü Rapor No: 11568, 112 s. Ankara (unpublished).

Göktaş, F. 2014*a*. Neogene Stratigraphy of the Northern Part of Karaburun Penınsula. Bulletin of the Mineral Research and Exploration 148, 43-61.

Göktaş, F. 2014*b*. Neogene Stratigraphy and Paleogeographic Evolution of the Karaburun Area, İzmir Western Turkey. Bulletin of the Mineral Research and Exploration 149, 63-92.

Göktaş, F. 2016*a*. Neogene Stratigraphy Of The İzmir -Outer- Bay Islands. Bulletin of the Mineral Research and Exploration 152, 1-24.

Göktaş, F. 2016*b*. Ildır Körfezi güneyindeki bölgenin Neojen stratigrafisi, Çeşme Yarımadası (Batı Anadolu). Türkiye Jeoloji Bülteni 59/3, 299-321.

Göktaş, F., Çakmakoğlu, A. 2018. 1:100.000 ölçekli Türkiye Jeoloji Haritaları Serisi, Urla-L16 Paftası, No: 258, Maden Tetkik ve Arama Genel Müdürlüğü, Ankara.

Helvacı, C., Ersoy, Y., Sözbilir, H., Erkül, F., Sümer, Ö., Uzel, B. 2009. Geochemistry and $^{40}Ar/^{39}Ar$ geochronology of Miocene volcanic rocks from the Karaburun Peninsula: Implications for amphibole-bearing lithospheric mantle source, Western Anatolia. Journal of Volcanology and Geothermal Research 185, 181-202.

Hilgen, F., Lourens, L.J., Van Dam, J.A., with contributions by Beu, A.G., Boyes, A.F., Cooper, R.A., Krigsman, W., Ogg, J.G., Piller, W.E., Wilson, D.S. 2012. The Neogene Period. In: Gradstein, F.M., Ogg, J.G., Schmitz, M., Ogg, G. (Eds), The Geological Time Scale 2012. Elsevier Publications, 923-978.

Innocenti, F., Mazzuoli, R. 1972. Petrology of İzmir-Karaburun volcanic area (West Turkey). Bulletin of Volcanology 36, 83-104.

Irvine, T.N., Baragar, W.R.A. 1971. A guide to the chemical classification of the common volcanic rocks: Canadian Journal of Earth Sciences 8, 523-548.

Kaçmaz, H., Köktürk, U. 2004. Geochemistry and mineralogy of zeolitic tuffs from the Alaçatı (Çeşme) Area, Turkey. Clays and Clay Minerals 52/6, 705-713

Kalafatçıoğlu, A. 1961. A Geological Study in the Karaburun Peninsula. Bulletin of the Mineral Research and Exploration 56, 53-63.

Kaya, O. 1979. Orta Doğu Ege çöküntüsünün (Neojen) stratigrafisi ve tektoniği. Türkiye Jeoloji Kurumu Bülteni 22, 35-58.

Kaya, T., Geraads, D. P., Tuna, V. 2003. A new Middle Miocene mammalian fauna from Mordoğan (Western Turkey). Paläontologische Zeitschrift 77/2, 293-302.

Koçak, A. 1974. Çeşme ılıcası hidrojeolojik etüt raporu. Maden Tetkik ve Arama Genel Müdürlüğü Rapor No: 5321, Ankara (unpublished).

Koufos, G.D. 2006. The Neogene mammal localities of Greece: Faunas, chronology and biostratigraphy. Hellenic Journal of Geosciences 41, 183-214.

Le Maitre, R.W. 1989. A Classification of Igneous Rocks and Glossary of Terms: Blackwell Scientific Publications, Oxford, 208 p.

Le Bas, M. J., Le Maitre, R. W., Streckeisen, A., Zanettin, B. 1986. A chemical classification of volcanic rocks based on total alkali-silica diagram. Journal of Petrology 27, 745-750.

Meissner, B. 1976. Das Neogene von Ost-Samos Sedimentationsgeschichte und Korrelation. Neues Jahrbuch für Geologie und Paläontologie, Abhandlung 152, 161–176.

Pe-Piper, G., Piper, D.J.V., Kotopouli, C.N., Panagos, A.G. 1994. Neogene volcanoes of Chios, Greece: the relative importance of subduction and back-arc extension. Geological Society, London 81, 213-231.

Sözbilir, H., Helvacı, C., Sümer, Ö., Uzel, B., Ersoy, Y., Erkül, F., Tatar, S., Oskay, M. 2007. Batı Anadolu'da Tortullaşmayla Yaşıt ve Tortullaşma Sonrası Doğrultu Atım Tektoniğine Ait Arazi Verileri: Miyosen Yaşlı Volkanosedimanter İstifinden Örnekler, Çeşme Yarımadası, İzmir. Ç. Ü. Jeoloji Mühendisliği Bölümü 30. Yıl Jeoloji Sempozyumu, 25 - 27 Ekim 2007, Adana, 177-178.

Türkecan, A., Ercan, T., Sevin, D. 1998. Karaburun Yarımadası'nın Neojen volkanizması. Maden Tetkik ve Arama Genel Müdürlüğü Rapor No: 10185

Ünay, E., Göktaş, F. 1999. Söke Çevresi (Aydın) Geç-Erken Miyosen ve Kuvaterner yaşlı küçük memelileri: Ön sonuçlar. Türkiye Jeoloji Bülteni 42, 99–113.

Uzelli, T., Baba, A., Mungan, G.G., Dirik, R.K., Sözbilir, H. 2017. Conceptual model of the Gülbahce geothermal system, Western Anatolia, Turkey: Based on structural and hydrogeochemical data. Geothermics 68, 67-85.

Weidmann, M., Solounias, N., Drake, R.E., Curtis, J. 1984. Neogene stratigraphy of the Mytilini Basin, Samos Island, Greece. Geobios 17(4), 477–490.

Winchester, J.A., Floyd, P.A. 1977. Geochemical discrimination of different magma series and their differentiation products using immobile elements. Chemical Geology 20, 325-343.

Yılmaz, Y. 2000. Ege bölgesinin aktif tektoniği. Batı Anadolu'nun depremselliği Sempozyumu (BADSEM-2000), 24-27 Mayıs 2000, İzmir, Bildiriler, 3-14.

Yılmaz, Y., Genç, Ş.C., Gürer, O.F., Bozcu, M., Yılmaz, K., Karacık, Z., Altunkaynak, Ş, Elmas, A. 2000. When did the western Anatolian grabens begin to develop?, Bozkurt, E., Winchester, J.A., Piper, J.A.D. (eds), Tectonics and Magmatism in Turkey and the Surrounding Area. Geological Society of London, Special Publication 173, 353–384.

Yılmazer, S., Yakabağı, A. 1995. Çeşme Fevzi Yıldız jeotermal kuyusunun kuyu bitirme raporu. Maden Tetkik ve Arama Genel Müdürlüğü Rapor No: 9955, Ankara (unpublished).

Bulletin of the Mineral Research and Exploration

http://bulletin.mta.gov.tr

Geochemical characteristics of the Eocene Karataş volcanics (Northeast Sivas, Turkey) in the İzmir-Ankara-Erzincan Suture Zone

Oktay CANBAZ[a*], Ahmet GÖKCE[a], Taner EKİCİ[a] and Hüseyin YILMAZ[b]

[a]*Sivas Cumhuriyet University, Department of Geological Engineering, 58140, Sivas, Turkey*
[b]*Sivas Cumhuriyet University, Department of Geophysical Engineering, 58140, Sivas, Turkey*

Research Article

Keywords:
Karataş volcanics, Sivas-Zara, Eocene, Geochemistry.

ABSTRACT

Karataş volcanics, is the product of Eocene volcanics crop out in the form of two belts along the northern and southern boundaries of the İzmir-Ankara-Erzincan Suture Zone. According to geochemical data, these volcanics have alkaline basic-intermediate character and consist of basaltic trachyandesite, trachyandesite and trachyte. This volcanic activity has been controlled by fractional crystallization and crustal contamination from basaltic trachyandesite to trachyte. Orientation of the samples towards amphibole area on the Rb/Sr - Ba/Rb ratio diagrams, dispersion of the Zr/Ba ratios (0.08 - 0.33) in the lithospheric mantle range, increase in the Ba/Rb ratio, decreases in the MgO, Ni and Cr contents point out that this volcanism originated from enriched lithospheric mantle rather than asthenospheric mantle. Geochemical data show that this enriched lithospheric mantle material is upper continental crustal material, main part of enrichment resulted by the subduction related fluids and also the contribution of the sedimentary materials. This situation may be explained that; the melts, derived from N-MORB or OIB bearing material ascended into the continental crust in a pre-collisional period and were reactivated by extensional tectonic and/or delamination processes during the post-collisional period, possibly caused the partial melting within the upper continental crust and produced the Karataş volcanics.

Received Date: 07.03.2019
Accepted Date: 25.12.2019

1. Introduction

İzmir-Ankara-Erzincan Suture Zone (IAESZ) which is one of the most important tectonic units of Turkey, separates the Sakarya continent from the Kırşehir block in the northern part of central Anatolia. Products of Eocene volcanism cover large areas along the northern and southern border of this suture zone. (Figure 1). These volcanics have been studied by a number of researchers (Yılmaz and Tüysüz, 1984; Büyükönal, 1985; Tüysüz and Dellaloğlu,1992; Yılmaz et al., 1994, 1997; Alpaslan and Terzioğlu, 1998; Alpaslan, 2000; Koçbulut et al., 2001; Keskin et al., 2008; Akçay et al., 2008; Dalkılıç et al., 2008; Atakay Gündoğdu, 2009; Görür vd., 2010; Tiryaki and Ekici, 2012; Akçay and Beyazpirinç, 2017; Göçmengil et al., 2018). And, various models have been proposed for the origin of these volcanics which outcrops from west of Sivas to Çankırı and Çorum; development in the compressional regime (Bozkurt and Koçyiğit, 1995; Tüysüz et al., 1995; Görür and Tüysüz, 1997; Görür et al., 1998; Kaymakçı et al., 2003; Okay and Satır, 2006), slab break off oceanic lithosphere in the North plunging subduction environment (Keskin et al., 2008), development in the post-collisional regime (Genç and Yılmaz, 1997; Keskin et al., 2004;

Citation info: Canbaz, O., Gökce, A., Ekici, T., Yılmaz, H. 2020. Geochemical characteristics of the Eocene Karataş volcanics (Northeast Sivas, Turkey) in the İzmir-Ankara-Erzincan Suture Zone. Bulletin of the Mineral Research and Exploration 162, 55-74. https://doi.org/10.19111/bulletinofmre.669717

* *Corresponding author: Oktay CANBAZ, ocanbaz@cumhuriyet.edu.tr*

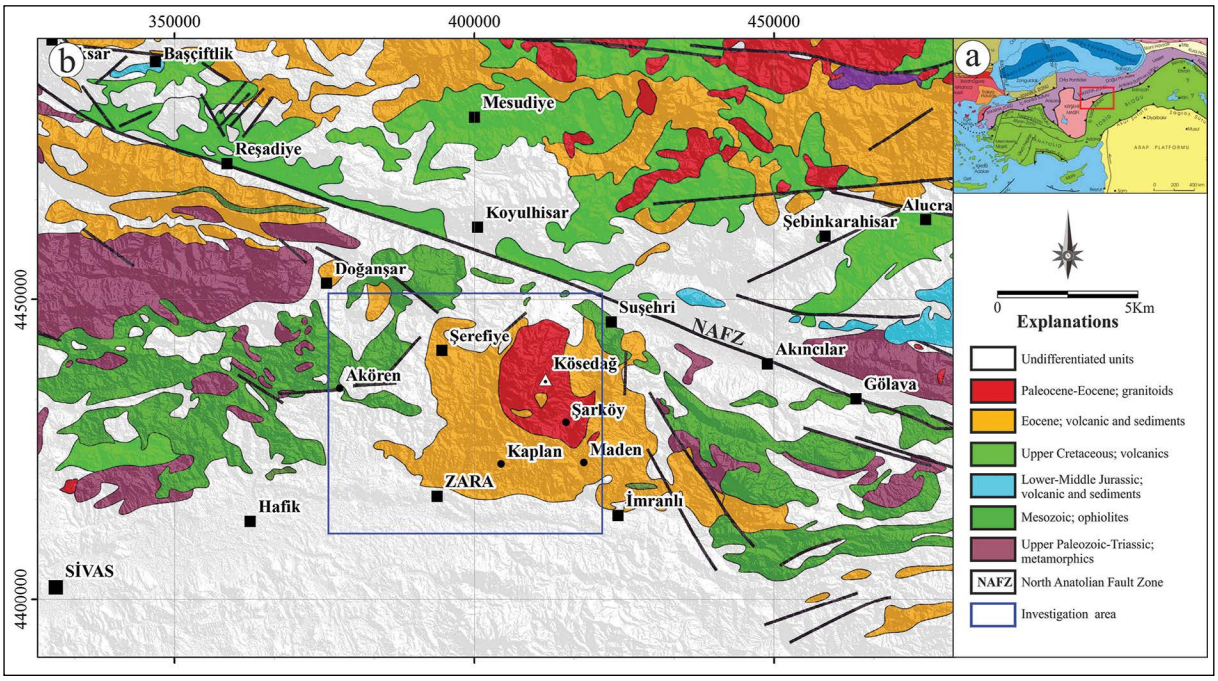

Figure 1- a) Tectonic map showing main sutures and continental blocks (Okay and Tüysüz, 1999) and b) regional geological map (Revised from MTA, 2002).

Altunkaynak and Dilek, 2006; Altunkaynak, 2007), crustal thickening (Topuz, 2005), crustal delamination and lithospheric subduction (Temizel et al., 2016; Yücel et al., 2017; Göçmengil et al., 2018).

Karataş volcanics are located in the area between Zara, İmranlı and Suşehri towns at the east of Sivas, on the IAESZ. In this study, petrographic and geochemical characteristics of Karataş volcanics have been investigated to be able to determine their source and formation environment, comparing the obtained results with those of rocks from different sources and volcanic rocks occurred in different tectonic environments, and give help to understanding geodynamic evolution of the region during Eocene.

2. Geology of the Study Area

Paleozoic metamorphic rocks (Tokat massif in the north and Akdağmadeni metamorphics in the south) and tectonically overlaying ophiolitic rocks with Upper Cretaceous emplacement age (Refahiye ophiolite melange) form the basement of the study area. Eocene Akıncılar Formation consists of alternations of sandstones and volcanic materials-siltstone interlayers discordantly overlie these units (Yılmaz et al., 1985). Eocene Karataş volcanics (Yılmaz et al., 1985) cut and overlie this formation and the basement rocks. Lutetian Kösedağ syenite (Kalkancı, 1974; Yılmaz et al., 1985; Başıbüyük, 2006; Boztuğ, 2008; Eyüboğlu et al., 2017) intruded all these units. In places younger volcanics and sedimentary units discordantly overlay Karataş volcanics and Kösedağ syenite (Figure 2-3).

Karataş volcanics with basaltic-andesitic lavas and pyroclastics (agglomerates and tuffs) cover large areas in and around the study area. Andesitic rocks in general have greenish-black, altered parts have yellowish-brown colour. Depending upon cooling and regional tectonics they are heavily fractured. Quartz and calcite filled gas cavities (vesicular texture) are seen macroscopically in various parts of the study area. Rocks with basaltic composition are greyish-black in generally, altered parts have yellowish colours, massive structure are dominated and flow structures are developed in some places. The base levels of the pyroclastic rocks consist of light green colored, hard and compact agglomerates, while the upper and middle levels are loose and easily disintegrable tuffs.

3. Age of the Volcanism

Karataş volcanics cut the Akıncılar formation which contains Eocene fossil at the outcrops in the Aluçlubel area at the north of Zara (Yılmaz et al.,

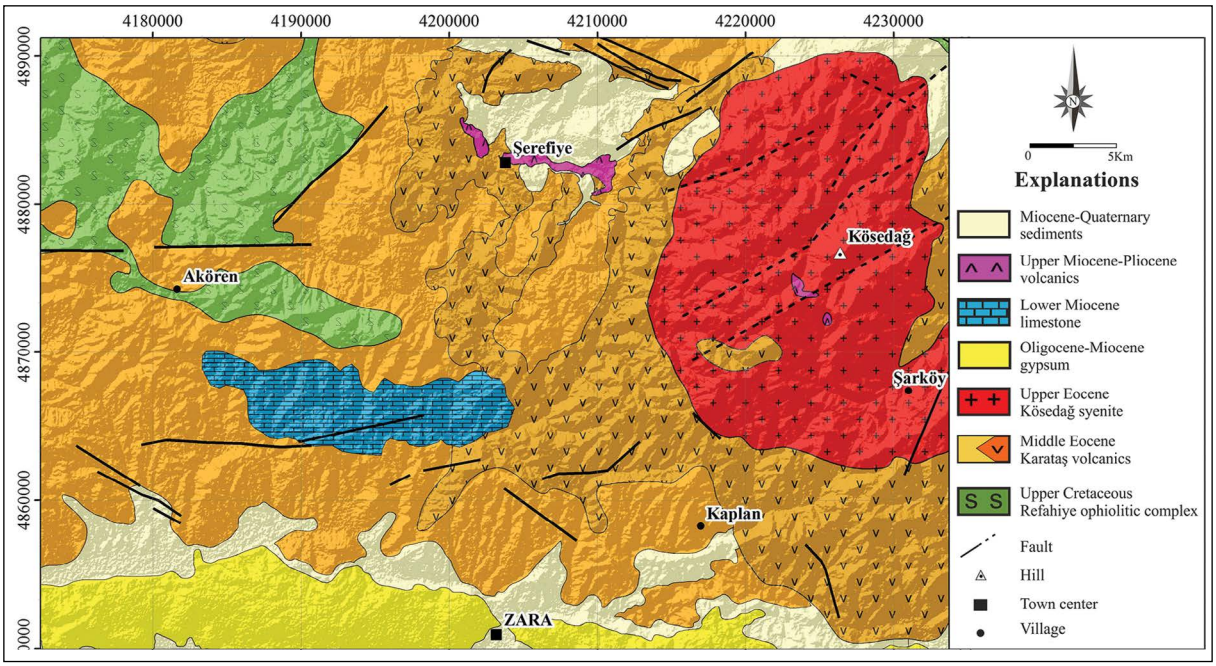

Figure 2- Geological map of the study area (Revised from Kalkancı, 1974; Yılmaz et al., 1985; MTA, 2002; Başıbüyük, 2006; Özdemir, 2016; Canbaz et al., 2018).

1985). These units have been intruded by Kösedağ syenite. Kalkancı (1974) estimated the age of syenite as Upper Eocene with Rb-Sr method; Boztuğ et al. (1994) estimated the age as Ypresian with Zircon $^{207}Pb/^{206}Pb$ method; Başıbüyük (2006) estimated Lutetian age with K-Ar method on alunites and Eyüboğlu et al. (2017) estimated same age with zircon U-Pb method. All these data indicate that the age of volcanism was younger than Lutetian and not older than Lower Eocene. In this study, the age of Karataş volcanics has been considered to be Middle Eocene.

4. Analytichal Methods

Representative rock samples were collected during the field study for petrographic and geochemical investigations. In addition, representative core samples were taken from the drillings carried out by MTA (General Directorate of Mineral Research and Exploration). Thin sections of these samples have been studied (with the criteria's described by Moorhouse, 1969; Erkan, 1972, 1994; MacKenzie and Guilford, 1980; Yardley et al., 1990) using polarizing microscope. Following thin section studies, representative 24 unaltered samples were selected for geochemical analyses. These samples were crushed and powdered in the laboratory to prepare for the analyses. Major element analyses of the samples were carried out in the ACME laboratory in Canada by using ICP-ES (inductively coupled plasma emission spectrometer) and ICP-MS (inductively coupled plasma mass spectrometer) spectrometers. ICP-ES spectrometer was used for major and trace element analyses. 0.2 gr powdered samples were mixed with 1.5 gr $LiBO_2$, then heated to 1050 °C to have the dissolved mixture. The mixtures were dissolved in a 100 ml %5 HNO_3 liquid, then were evaporated and then were analysed with ICP-ES spectrometer. The samples prepared for the above mentioned analyses were also used for the Rare Earth Element analyses by using ICP-MS spectrometer. For the major oxides, lower determination limit was 0.01%, for the trace elements it varied between 0.01-1.0 ppm. During the analyses in the ACME analytical laboratory GS311-1, GS910-4, SO-19, DS-11, OREAS45EA and SY-4(D) standards were used and analyses of 8 samples were repeated. For the evaluation of the diagrams, GCDkit 3.0 program was used.

5. Results

5.1. Mineralogy and Petrography

Mineralogical and petrographical studies show that Karataş volcanics have basaltic, andesitic and trachytic mineralogical compositions. Rocks with

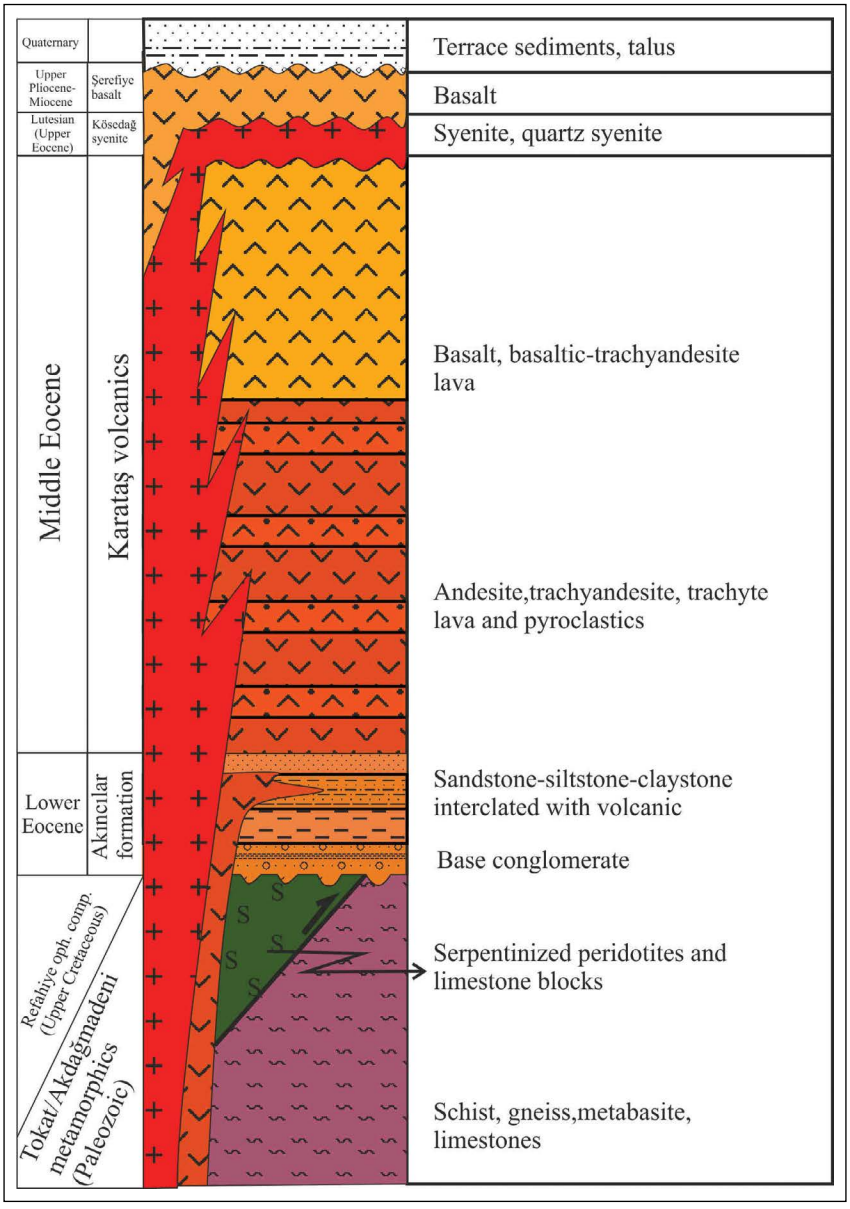

Figure 3- Stratigraphic section of the study area.

basaltic composition have generally hypocristalline porphyritic texture, and contain olivine, plagioclase, pyroxene (augite) phenocrysts. Plagioclase microlites and volcanic glass are also found in the matrix (Figure 4a-b).

Andesitic rocks consist of larger plagioclase phenocrystals (1-3 cm) and finer grained mafic minerals such as augites and hornblends comparing with the basaltic rocks levels, (Figure 4c-d). Trachytic rocks show holocrystalline and hypocrystaline porphyritic textures and contain plagioclase and sanidine phenocrysts (Figure 4e-f). Besides plagioclase and sanidine microlites, pyroxene and amphibole microlites are also present in the matrix of the trachytes.

Some sieve textures developed around some large plagioclase phenocrysts and the presence of small plagioclase crystals with different extinction angle within some thin sections of basaltic and andesitic rocks of Karataş volcanics (Figure 4g-h) were accepted as prints of magma-solid interaction and mixtures of magmatic melts with different compositions (e.g. Hibbard, 1991; Boztuğ et al., 1994).

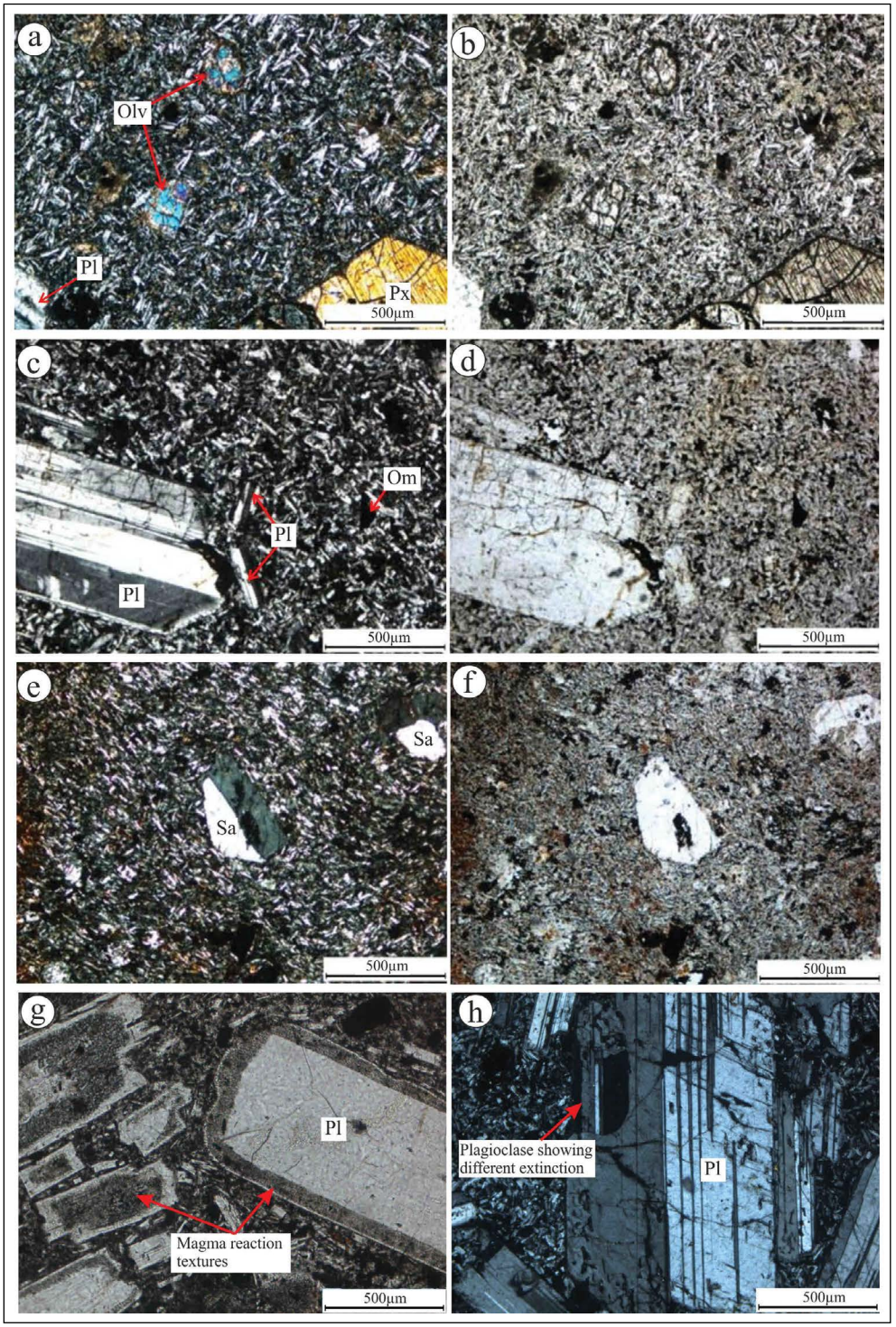

Figure 4- Microscopic characters of samples collected from various levels of Karataş volcanics. a-b) In basaltic samples olivine and pyroxene phenocrysts matrix made of plagioclase microliths (sample no: OK-108, cross/plane polarised light, c-d); plagioclase phenocrysts and microlites (sample no: OK-35, cross/plane polarised light), e-f) in a trachyte sample sanidine phenocrysts and matrix made of sanidine and plagioclase microlites (sample no: Ok-7, cross/plane polarised light), g) view of magma reaction textures on plagioclase phenocrysts, h) view of plagioclases with different extinctions in plagioclase phenocrysts (sample no: Ok-7, cross/plane polarised light). (Pl= Plagioclase, Px=Pyroxene, Olv=Olivine, Sa=Sanidine, Om=Opaque Mineral).

5.2. Geochemistry

Major, trace and rare earth elements contents of Karataş volcanics are given in tables 1, 2, 3. The samples fall in the basaltic trachyandesites, trachyandesite and trachyte fields of the TAS diagram (LeMaitre et al., 1989) (Figure 5). Most of the samples, excluding 5 of them, of the rock groups fall above the alkaline-sub alkaline (tholeiitic) separating line and have strong alkaline character.

We have tried to compare and discuss the geochemical characteristics of Karataş volcanics with the results of the earlier works carried out on the Eocene volcanics by Akçay and Beyazpirinç (2017) and Göçmengil et al. (2018) in the west of the study area, between Yozgat and Sivas provinces.

5.2.1. Major Elements Geochemistry

SiO_2 contents of Karataş volcanics show variation in the range of 50.30-61.80% (basaltic trachyandesites 51.20-54.60%; trachyandesites 54.00-58.10%; trachyte 61.80%).

Some selected major oxides versus SiO_2 diagrams; while CaO, Fe_2O_3, MgO and TiO_2 contents show negative trend from basaltic andesites to trachytes, Na_2O, K_2O, Al_2O_3 and P_2O_5 contents show positive trends (Figure 6). Those indicate that negative trend showing major oxides were used by the olivine, pyroxene, calcic plagioclases and titanomagnetites crystallized in earlier stage of crystallization and separated from the melt, and these earlier crystallized minerals did not use much Na and K, so the melt became enriched with Na and K showing positive correlation

Table 1- Major elements results of Karataş volcanics (weight %).

Rock types	Sample No	SiO_2	Al_2O_3	Fe_2O_3	CaO	MgO	Na_2O	K_2O	MnO	TiO_2	P_2O_5	Loss of ignition	Total
Basaltic trachyandesite	Ok-109	52.40	15.90	7.96	7.47	5.17	3.18	3.28	0.15	0.80	0.39	3.27	99.48
	Ok-114	51.20	17.20	8.57	7.82	4.26	3.20	2.72	0.10	0.97	0.38	3.06	99.70
	Ok-120	53.70	19.30	6.73	6.97	2.71	3.55	2.84	0.10	0.77	0.47	2.56	100.41
	Ok-124	52.60	17.60	8.79	9.06	4.62	3.32	2.08	0.15	0.82	0.29	1.08	99.93
	Ok-193	52.80	17.70	8.90	7.59	3.45	3.51	3.02	0.17	0.89	0.41	1.49	99.98
	Ok-205A	54.60	18.90	6.06	7.82	2.83	3.40	2.96	0.11	0.78	0.47	2.05	100.16
	Ok-206A	52.50	17.30	9.50	7.43	4.97	3.17	2.40	0.16	0.84	0.30	1.59	99.76
	Ok-210	54.30	19.00	7.59	6.21	2.66	3.78	2.99	0.23	0.77	0.47	1.76	100.53
	Ok-215B	52.30	17.80	9.18	6.47	4.79	4.36	2.29	0.12	0.85	0.31	2.06	100.28
	Ok-247	51.80	18.10	8.87	7.97	4.39	3.30	2.06	0.15	0.80	0.25	2.59	100.30
	Ok-248	53.00	16.90	8.55	6.10	4.31	4.13	2.99	0.10	0.84	0.33	3.05	99.91
	Ok-255C	54.60	19.00	6.96	7.70	3.06	3.80	3.09	0.11	0.81	0.46	0.32	99.33
Trachyandesite	Ok-35	54.00	19.30	5.34	6.82	1.59	4.02	3.81	0.13	0.72	0.45	3.15	99.55
	Ok-57	58.10	18.60	6.96	2.96	0.64	4.01	5.60	0.26	0.80	0.45	1.17	99.47
	Ok-58	57.30	20.60	5.79	4.49	0.19	4.29	4.26	0.13	0.78	0.50	1.14	99.74
	Ok-84	54.50	18.70	9.95	6.01	1.16	3.91	3.72	0.07	0.73	0.46	0.53	98.61
	Ok-99	55.50	17.70	5.59	5.05	2.09	3.92	4.54	0.09	0.76	0.45	2.92	99.86
	Ok-131A	54.20	19.50	6.46	7.38	1.54	3.95	3.71	0.12	0.71	0.45	1.84	99.68
	Ok-141	55.50	19.40	8.05	5.64	1.10	4.01	3.85	0.08	0.73	0.46	0.86	99.80
	Ok-222	54.60	19.90	6.72	6.43	2.46	4.03	3.62	0.06	0.75	0.49	0.74	100.08
	Ok-223	54.70	18.90	6.64	5.79	3.08	3.68	3.34	0.20	0.71	0.46	2.58	99.73
	Ok-244	54.70	19.50	5.78	5.62	1.34	4.07	4.67	0.08	0.67	0.47	2.83	100.42
	Ok-253	56.60	20.40	6.08	4.57	1.17	4.39	4.81	0.05	0.77	0.50	1.08	99.67
Trachyte	Ok-7	61.80	16.60	6.31	1.38	0.20	4.13	7.04	0.28	0.72	0.29	0.92	100.34

Table 2- Trace elements results of Karataş volcanics (ppm, *=ppb).

Rock type	Sample No	Ba	Co	Cs	Ga	Hf	Nb	Rb	Sr	Th	U	V	Zr	Cu	Pb	Zn	Mo	Ni	As	Sb	Hg	Au*
Basaltic trachyandesite	Ok-109	510	26.1	1.4	12.3	4.3	10.3	83.2	529.2	10.4	3.4	203	172.7	129.0	3.3	92	2.2	58.8	35.6	0.1	0.05	1.2
	Ok-114	558	24.3	0.7	14.2	3.6	8.5	55.3	591.8	6.5	2.4	256	133.2	205.4	9.0	85	1.7	16.3	5.7	0.1	0.03	2.7
	Ok-120	766	15.5	0.5	15.5	3.9	10.0	54.3	742.2	8.7	3.2	158	154.3	238.9	5.3	73	1.9	11.1	3.5	0.2	0.04	1.9
	Ok-124	516	23.8	0.6	14.0	2.8	5.5	46.8	645.7	5.0	1.7	255	98.8	66.3	2.7	52	1.7	15.4	1.4	0.2	0.04	<0.5
	Ok-193	608	21.4	0.6	15.7	3.7	9.2	74.0	708.8	7.7	3.2	236	143.5	140.0	8.6	50	4.7	10.6	8.7	0.4	0.02	7.4
	Ok-205A	765	18.1	0.3	15.7	3.7	9.9	53.9	775.6	8.8	3.3	167	156.4	22.7	3.3	58	1.7	12.5	14.2	0.3	0.02	2.9
	Ok-206A	1377	27.1	0.8	14.8	2.7	5.8	45.6	635.8	5.4	2.2	260	105.7	122.9	1.6	20	1.5	12.5	5.5	1.2	0.02	1.2
	Ok-210	691	36.6	0.9	16.0	3.8	9.6	76.5	752.2	9.2	3.2	171	157.5	19.3	2.8	38	2.2	17.0	4.3	<0.1	0.01	0.8
	Ok-215B	627	27.9	4.4	15.1	2.8	6.7	49.7	565.7	6.4	2.5	251	110.7	177.1	5.3	39	1.9	12.0	33.9	1.2	0.02	2.2
	Ok-247	526	26.4	0.8	14.4	2.4	4.8	42.0	627.4	4.5	1.9	277	87.7	228.0	4.4	30	1.7	10.7	5.6	0.1	0.02	1.4
	Ok-248	609	24.3	2.1	15.7	3.3	7.2	66.9	556.5	6.7	2.3	235	127.7	235.8	2.1	19	1.6	14.2	18.2	0.3	0.01	1.5
	Ok-255C	715	18.2	0.8	17.6	3.5	9.9	81.5	767.6	8.3	3.0	194	146.4	262.9	2.0	54	2.3	9.7	6.3	0.6	0.03	2.6
Trachyandesite	Ok-35	705	12.8	0.9	15.3	4.0	10.3	99.3	762.3	9.3	3.7	169	162.9	11.1	4.1	34	2.2	8.9	4.0	0.3	0.01	3.9
	Ok-57	826	13.2	1.5	14.9	5.8	14.9	138.3	390.7	13.8	5.3	137	234.1	11.3	5.0	67	1.8	8.7	7.6	1.1	0.06	0.7
	Ok-58	911	9.1	1.2	15.9	4.3	10.2	113.3	648.5	9.4	3.6	177	171.0	123.8	5.6	69	1.8	7.4	15.2	0.3	0.01	1.6
	Ok-84	666	9.2	0.6	14.4	3.9	9.8	96.7	733.7	9.3	3.3	172	160.1	52.5	7.6	59	3.6	5.5	29.1	0.9	0.04	2.6
	Ok-99	704	12.2	1.2	13.9	5.6	13.2	127.0	523.2	13.1	5.2	146	217.4	19.2	5.2	150	3.1	6.4	9.0	1.8	0.04	2.8
	Ok-131A	692	10.1	0.8	15.9	3.9	9.6	97.5	784.5	9.1	3.7	160	158.3	25.5	4.8	56	3.8	7.5	8.6	0.3	0.02	5.8
	Ok-141	793	10.0	1.2	15.1	4.0	9.9	102.7	743.9	9.3	3.7	173	162.3	14.0	9.6	55	2.2	6.7	18.0	0.2	0.03	5.8
	Ok-222	734	15.1	1.7	15.9	3.6	8.3	91.3	859.3	7.6	3.0	218	140.2	43.2	7.2	104	2.3	14.6	7.1	0.2	<0.01	2.0
	Ok-223	1013	16.1	1.7	15.4	3.4	8.2	82.4	774.9	7.5	4.0	242	134.9	733.8	4.2	38	1.9	9.9	6.0	0.3	0.04	1.1
	Ok-244	600	12.0	2.0	15.4	4.1	11.1	112.9	673.5	9.0	2.7	104	174.3	55.8	2.9	64	1.3	4.8	6.4	0.8	0.03	<0.5
	Ok-253	780	8.5	3.2	18.7	4.7	12.7	131.0	742.9	10.3	3.3	173	197.8	224.0	4.3	44	1.8	3.8	6.1	0.1	0.03	5.2
Trachyte	Ok-7	977	12.5	2.6	17.3	7.9	21.4	203.3	156.0	20.0	7.7	109	331.9	62.5	11.4	74	4.9	4.5	11.8	0.1	0.01	3.6

Table 3- Rare Earth Elements results of Karataş volcanics (ppm).

Rock type	Sample No	La	Ce	Pr	Nd	Sm	Eu	Gd	Tb	Dy	Ho	Er	Tm	Yb	Lu
Basaltic trachyandesite	Ok-109	25.0	47.4	5.57	22.5	4.71	1.18	4.48	0.66	3.76	0.84	2.54	0.37	2.46	0.37
	Ok-114	23.0	45.1	5.19	21.4	4.69	1.22	4.28	0.63	3.69	0.76	2.36	0.32	2.24	0.34
	Ok-120	27.3	52.8	5.83	23.3	4.47	1.27	4.24	0.63	3.49	0.77	2.33	0.33	2.14	0.36
	Ok-124	18.1	35.0	4.08	17.6	3.57	1.07	3.72	0.58	3.38	0.72	2.08	0.30	1.81	0.31
	Ok-193	24.6	48.9	5.56	21.5	4.69	1.31	4.72	0.69	3.91	0.84	2.45	0.35	2.42	0.37
	Ok-205A	27.2	52.9	5.96	24.2	4.58	1.29	4.50	0.68	3.87	0.79	2.33	0.32	2.19	0.34
	Ok-206A	19.9	36.2	4.47	18.7	4.21	1.18	4.20	0.61	3.58	0.74	2.17	0.31	2.06	0.31
	Ok-210	28.1	53.3	6.08	25.4	4.94	1.30	4.59	0.67	3.77	0.71	2.41	0.33	2.21	0.35
	Ok-215B	21.1	39.3	4.62	19.4	4.00	1.14	3.90	0.59	3.48	0.73	2.11	0.29	1.96	0.28
	Ok-247	16.4	31.4	3.62	15.0	3.22	1.03	3.41	0.51	2.95	0.62	1.80	0.24	1.74	0.28
	Ok-248	20.9	41.0	4.69	19.3	3.97	1.15	4.18	0.63	3.84	0.77	2.30	0.32	2.14	0.34
	Ok-255C	26.8	53.1	5.89	23.6	4.58	1.31	4.38	0.65	3.65	0.77	2.34	0.36	2.32	0.35
Trachyandesite	Ok-35	27.2	52.7	5.90	23.0	4.72	1.26	4.33	0.63	3.73	0.76	2.32	0.35	2.24	0.35
	Ok-57	37.6	67.9	7.76	31.0	6.10	1.47	5.60	0.82	4.89	1.07	3.01	0.46	3.01	0.46
	Ok-58	29.8	53.2	6.41	26.1	4.90	1.40	4.65	0.70	3.98	0.77	2.59	0.33	2.30	0.37
	Ok-84	26.3	50.7	5.73	21.7	4.49	1.22	4.19	0.65	3.77	0.77	2.41	0.34	2.40	0.36
	Ok-99	33.4	62.6	7.03	28.0	5.56	1.27	4.85	0.72	4.22	0.89	2.73	0.42	2.63	0.46
	Ok-131A	26.9	50.9	5.84	23.9	4.49	1.23	4.22	0.64	3.49	0.76	2.32	0.32	2.20	0.36
	Ok-141	27.3	52.8	6.03	23.5	4.79	1.30	4.30	0.65	3.81	0.79	2.27	0.34	2.26	0.35
	Ok-222	27.4	49.4	5.76	22.9	4.74	1.35	4.36	0.64	4.00	0.74	2.29	0.32	2.20	0.34
	Ok-223	25.2	47.6	5.50	22.0	4.46	1.27	4.18	0.61	3.65	0.67	2.18	0.30	1.98	0.32
	Ok-244	28.6	55.0	6.07	24.5	4.37	1.21	4.19	0.63	3.69	0.77	2.29	0.35	2.35	0.37
	Ok-253	36.0	63.6	7.28	27.8	5.22	1.40	5.00	0.74	4.40	0.94	2.82	0.41	2.64	0.44
Trachyte	Ok-7	40.9	75.6	8.18	30.6	5.97	1.17	5.45	0.84	5.05	1.09	3.40	0.52	3.53	0.56

with SiO_2 trough the later stage of crystallization and they formed the sodium plagioclases and mica minerals.

MgO contents of Karataş volcanics show wide variation range (0.19%-6.09). Basaltic trachyandesites 3.06-5.17%; trachyandesites 0.19-3.08%; trachyte 0.20%.

In the Harker correlations diagrams, trends of major oxides plotted against SiO_2, especially the negative correlation of the MgO indicate the importance of fractional crystallization process during the formation of Karataş volcanics. CaO/Al_2O_3 vs. MgO, Al_2O_3 vs. CaO and Zr/Nb vs. MgO variation diagrams prepared by various workers which indicate the fractionations of olivine, clinopyroxene, amphibole and plagioclase fractionations from basic trough intermediate composition also support the effectiveness of fractional crystallization idea for the formation of Karataş volcanics (Figure 7).

Akçay and Beyazpirinç (2017) and Göçmengil et al. (2018) also indicated that fractional crystallization processes were effective in the development of Eocene volcanics, crop out in Almus, Yıldızeli, Kiremitli and Pazarcık area, at the west of the study area.

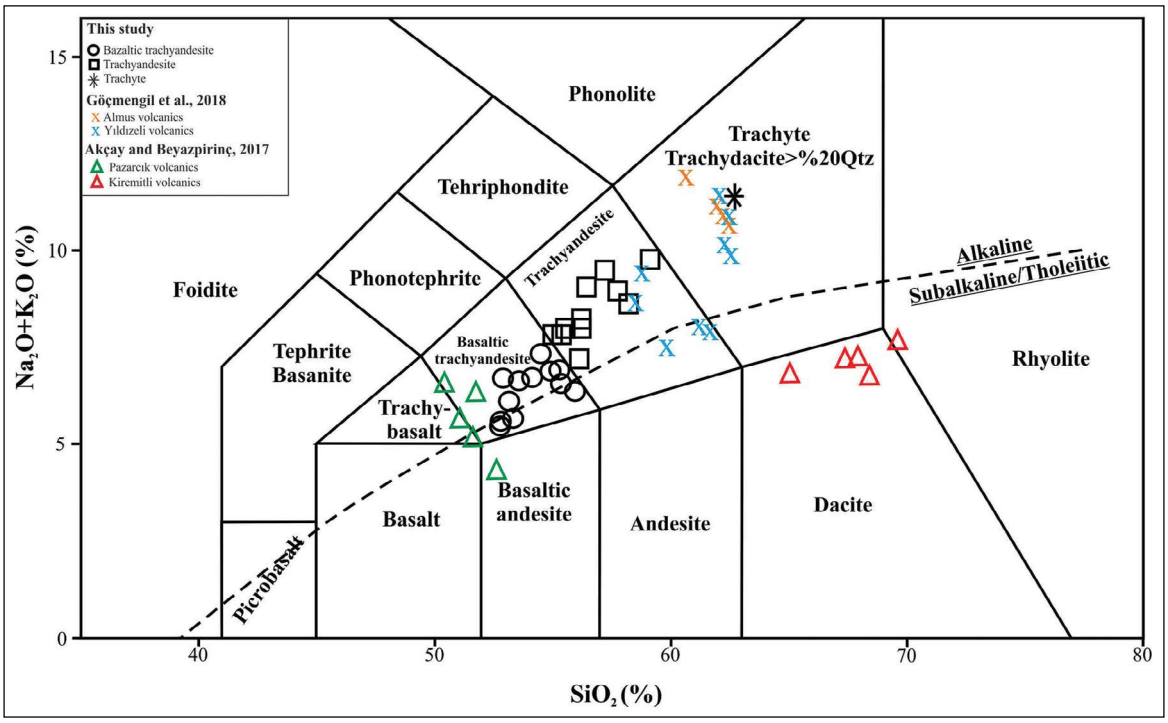

Figure 5-Total Alkali-Silica classification for Karataş volcanics (LeMaitre et al., 1989), Alkali/Sub alkali line (Irvine and Baragar, 1971).

5.2.2. Trace and Rare Earth Elements Geochemistry

Ba, Rb, Nb, Zr, Th, La and Ce values are increased but Sr values are decreased in accordance with SiO_2 values on the trace elements versus SiO_2 diagrams (Figure 8). Ba, Rb, Th, and Hf show positive correlation with SiO_2 because they are taken place within the feldspars and hornblendes which occur in later stage of crystallization. Positive correlation of Zr is related magnetite differentiation. In addition, positive correlation of Y with SiO_2 may be related with apatite crystallizations. Depletion in the Sr values may be explained as the entrance of Sr in place of Ca in the earlier formed calcic plagioclases.

Trace elements spider diagrams were prepared to make some approaches to the origin of the material and tectonic environments of Karataş volcanics occurred (Figure 9a). Samples of Karataş volcanics show enrichments in some lithophile elements with large-ion lithophile elements (LILE) like Ba, Sr, K, Rb, Cs and also high field strength elements (HFSE) like Zr, U, Th, Y, while they show decreases in Nb, Ce, Ti values. Noticeable enrichment of the elements with large ion radius and negative Nb anomalies present similarity to the magmatism developed in active continental edge or in arc environment and point out to the subduction component (Gill, 1981; Pearce, 1983; Fitton et al., 1988; Hall, 1989; Hawkesworth et al., 1997). In addition, Göçmengil et al. (2018) indicated that similar characteristics may also reflect assimilated continental crust. The lack of deep negative Eu anomalies in those samples indicates that the effect of plagioclase fractionation was not very important during the formation of these volcanics. Negative Ti anomaly is thought to be related to the early crystallization and abandonment from melt of Ti-bearing oxide minerals like Ti-magnetite (Kerrich and Wyman, 1997). On the other hand, negative Nb and Ti anomalies are quite common in the magmas associated with subduction developed in post collisional environment (Ekici, 2016).

All REEs, especially the lighter ones, show noticeable enrichments comparing to the Primitive Mantle normalized REEs dispersion diagram (Figure 9b). This distribution trend indicates the effect of differentiation of amphiboles and pyroxenes during crystallization. The presence of hydrous minerals like amphiboles in trachyandesite and trachyte samples point out the continental crust origin and/or contamination. The similarity of the dispersion patterns of the samples with upper continental crust pattern on the spider diagrams support this approach.

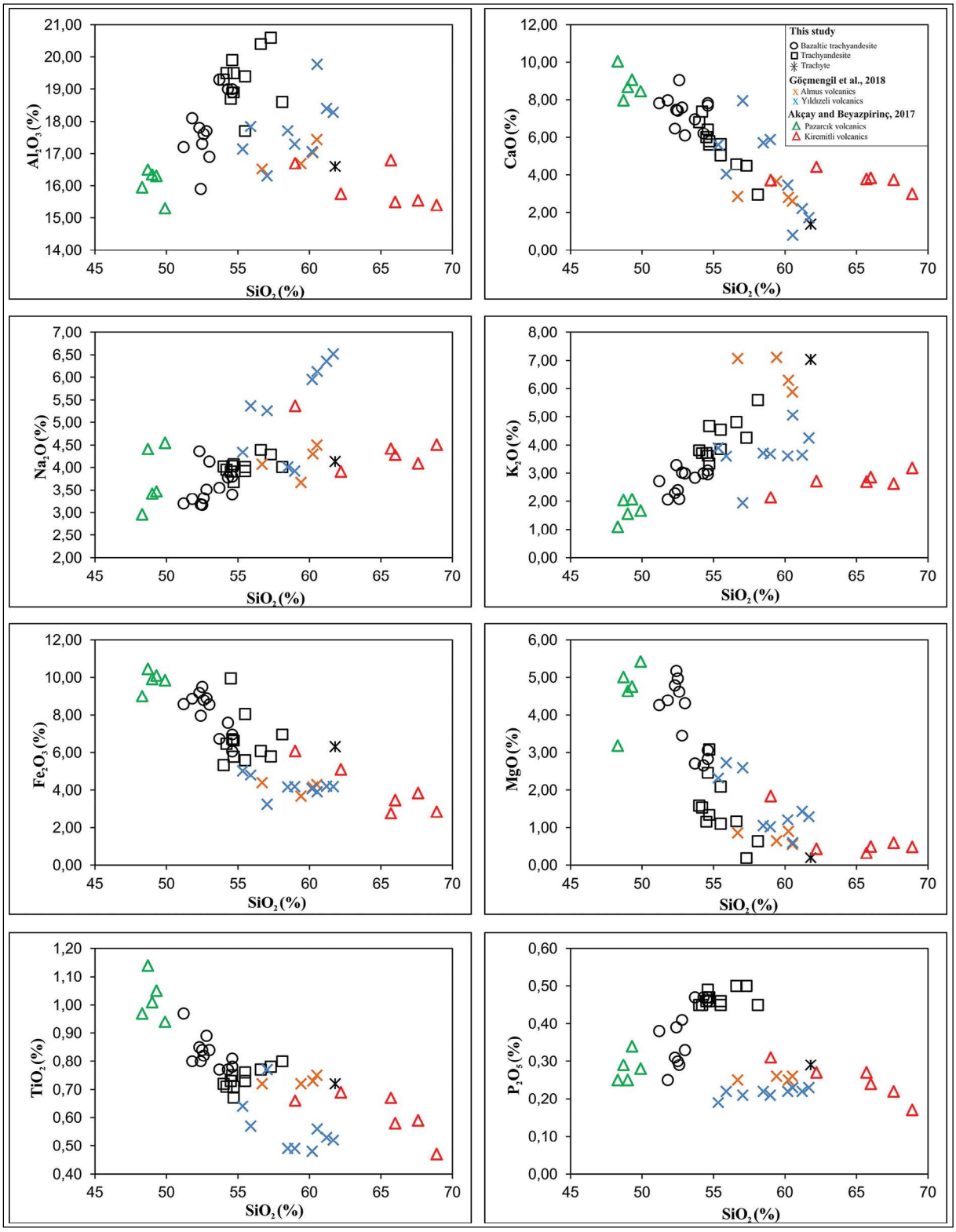

Figure 6- Variation of selected major elements vs. SiO_2 in Karataş volcanics.

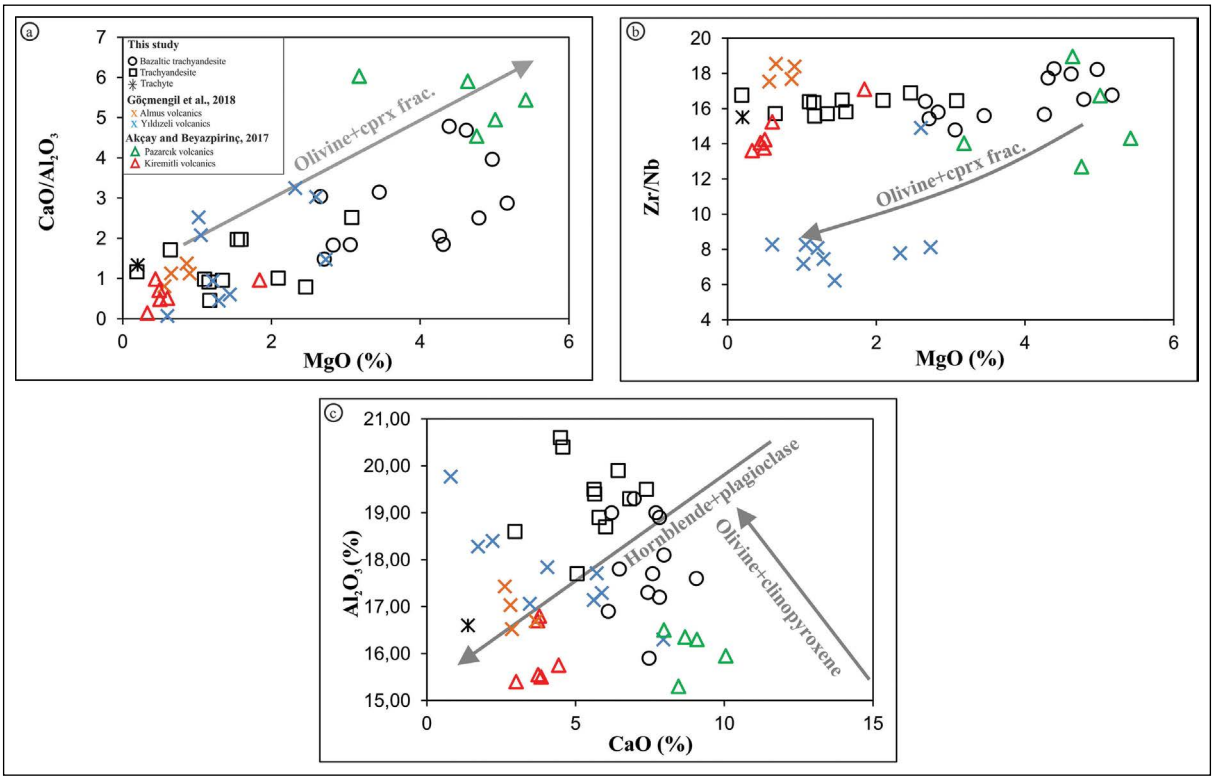

Figure 7- In Karataş volcanics, distribution of a) CaO/Al_2O_3-MgO ratio diagram, b) distribution in the Al_2O_3-CaO ratio diagram, c) distribution in the Zr/Nb-MgO ratio diagram.

Karataş, Pazarcık, Almus and Yıldızeli volcanics, which have similar SiO_2 content, show parallel pattern on the Harker and spider diagrams, Kiremitli volcanics with higher SiO_2 contents differ from the others.

6. Discussion

6.1. Crustal Contamination

Karataş volcanics Nb/U ratios vary between 2.53-3.54 in the basaltic trachyandesites and 2.05-4.11 in the trachyandesites. Nb/La ratios show variations between 0.29-0.41 and 0.30-0.40, K_2O/P_2O_5 ratios between 6.04-9.06 and 7.26-12.44 in basaltic trachyandesites and trachyandesites respectively.

Haase et al. (2000) suggest that Nb/U ratios close to MORB values (average 47.00, Hofmann et al., 1986) in the rocks which have not been subjected to sedimentary assimilation, and this value will considerably get lower with the sedimentary assimilation. On the other hand, Hoffman et al. (1986) claims that Nb/La ratios higher than 1.00 would be indicative for typical mantle derived and uncontaminated magmas. Since these ratio values in Karataş volcanics are low (Nb/U; 2.05-4.11, Nb/La; 0.29-0.41), it may be said that the source magma was subjected to crustal/sedimentary contamination (Figure 10a). Carlson and Hart (1988) say that basalts generated from mantle have K_2O/P_2O_5 ratio values ≤2 value, with the crustal assimilation or apatite fractionation, this ratio would increase. The quite high K_2O/P_2O ratio values (6.04-12.44) of Karataş volcanics indicate that the magma produced Karataş volcanics was either subjected to crustal assimilation or to apatite fractionation. The plots of these values on the SiO_2 versus K_2O/P_2O_5 diagram show that the effects of crustal contaminations increase from basaltic trachyandesites towards trachyte (Figure 10b).

Akçay and Beyazpirinç (2017), indicated that subduction zone enrichment and/or crustal contribution had important part in magmas generated Pazarcık and Kiremitli volcanics, and these more significant in Kiremitli volcanics. Göçmengil et al. (2018) indicated that Almus volcanics had negligible amounts of crustal contamination comparing with Yıldızeli volcanics.

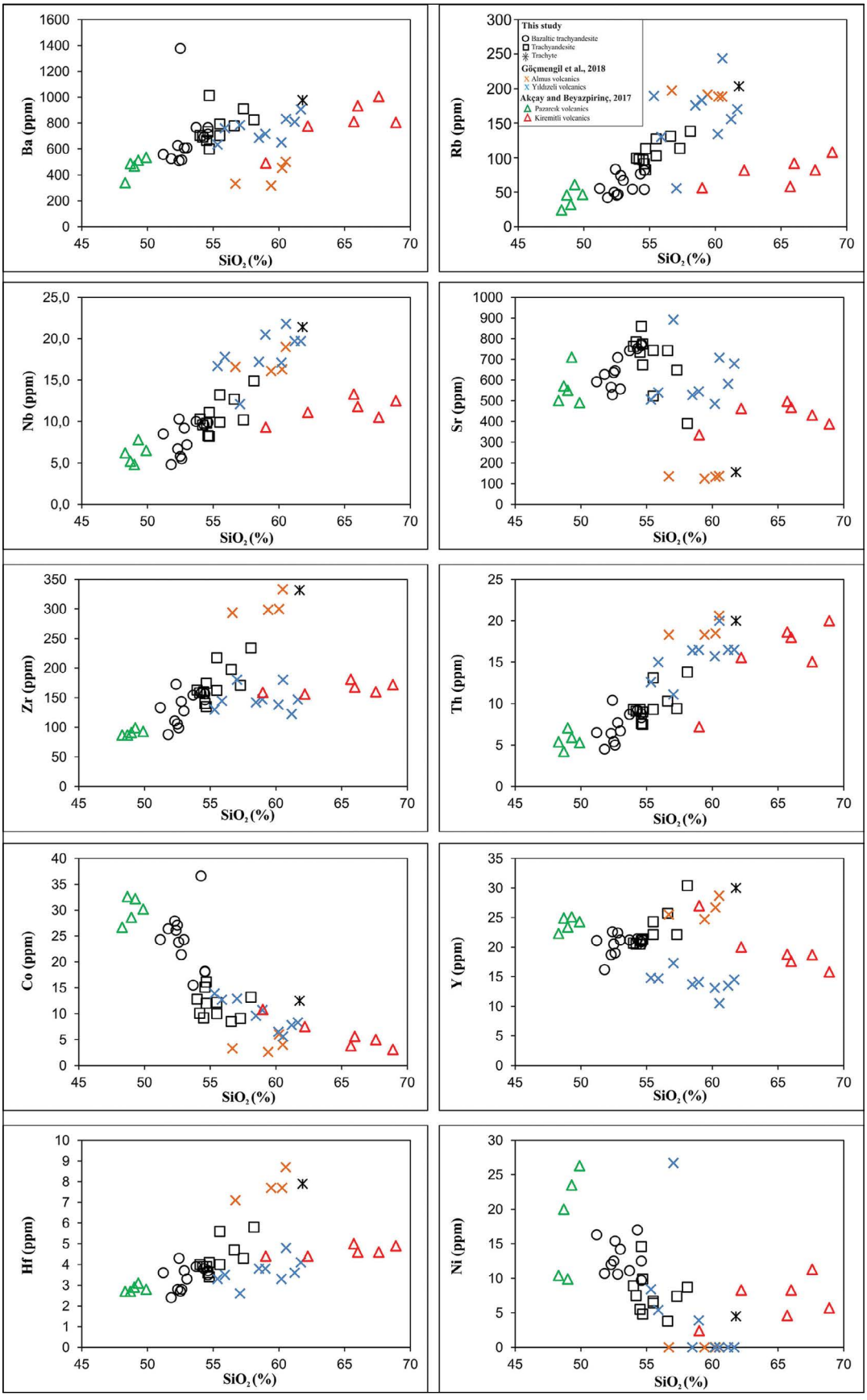

Figure 8- Variation of selected trace elements vs. SiO_2 in Karataş volcanics.

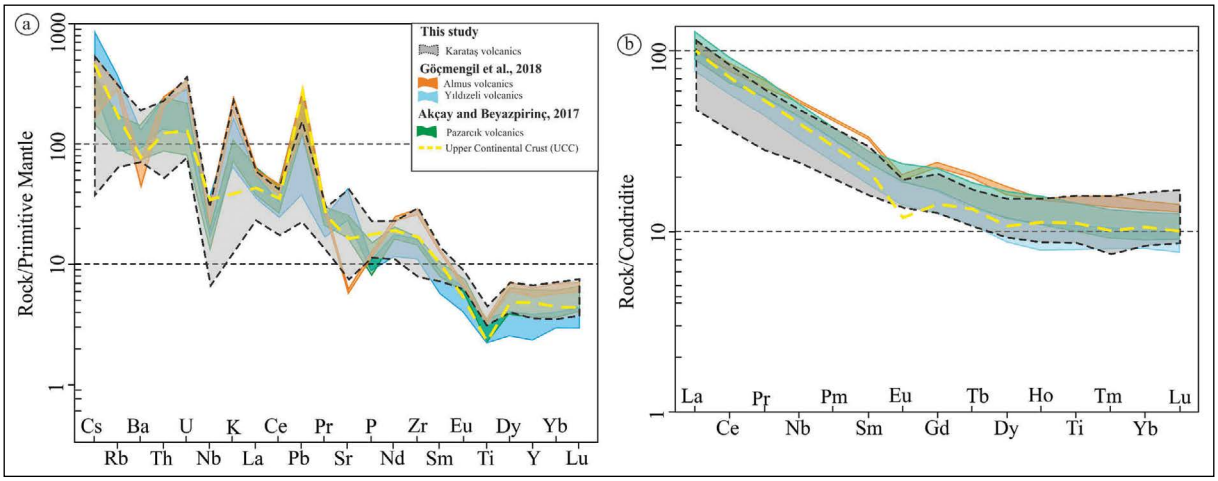

Figure 9- Multiple element variation diagram of Karataş volcanis, analyses normalized based on primary mantle Normalized based on primary mantle. a) Trace element (Primary mantle values from Sun and McDonough, 1989), b) Rare Earth Elements (REE values is normalized based on Boynton, 1984). Upper continental crust values are taken from Taylor and McLennan (1985), as Kiremitli volcanics have much higher SiO_2 contents than Karataş volcanics so they were not included in the evaluations.

6.2. Partial Melting

No mantle xenoliths were determined in Karataş volcanics and in their equivalents along IAESZ during this and previous studies. Because of the lack of isotope data, the partial melting degree was tried to be explained with only geochemical data.

In the samples of Karataş volcanics, MgO contents show following ranges; 5.17-2.66% in basaltic trachyandesites, 3.08- 0.19% in trachyandesites. The La/Yb(N) ratios are 6.76 - 9.15 and 7.86-9.78, Zr/Nb ratios are 14.78-18.27 and 15.5-16.89, in the same order. These values may suggest a low degree partial melting (normalized values have been calculated according to Sun and McDonough, 1989). In addition, Zr vs. La, La/Yb vs. Tb/Yb, La/Yb vs. La and La/Sm vs. La diagrams have been prepared. Again, to be able to evaluate partial melting degrees. it is observed that the samples fall in compatibility with each other on these diagrams (Figure 11). When this compatibility in the samples and the enrichments in the LILE/HFSE ratio diagrams evaluated together, it was concluded that even it was low degree; still some partial melting might have developed.

Karataş volcanics fall in the same fields on these diagrams with Pazarcık, Kiremitli and Yıldızeli volcanics. Alpaslan (2000) suggested that Pazarcık volcanics developed from partial melting of mantle under extensional tectonic regime, following collision. Akçay and Beyazpirinç (2017) interpreted

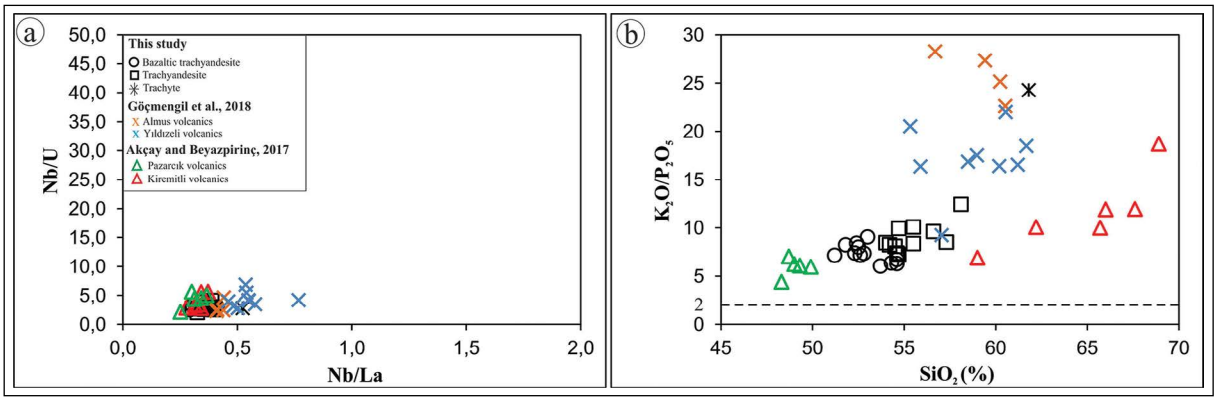

Figure 10- a) Nb/U vs. Nb/La, b) SiO_2 vs. K_2O/P_2O_5 diagrams for Karataş volcanics ($K_2O/P_2O_5 \leq 2$, from Carlson and Hart 1988).

that Pazarcık and Kiremitli volcanics derived from the partial melting of the continental lithosphere basement material which was metasomatized by subduction events. Göçmengil et al. (2018) concluded that basaltic trachyandesites with basic-intermediate (neutral) compositions of Yıldızeli volcanics were developed from the partial melting of their metasomatic source area.

The plots of the data of Karataş volcanics close to Pazarcık volcanics in all geochemical diagrams suggest that Karataş volcanics were formed in a similar environment with Pazarcık volcanics; partial melting of upper mantle in the extensional tectonic regime in post collisional period suggested by Alpaslan (2000). But the composition of magma occurred Karataş volcanics was significantly changed by crustal contamination/sedimentary addition.

6.3. Origin of Magma

Karataş volcanics show mostly shift towards amphibole field and very weakly to the phlogopite field on the Rb/Sr vs. Ba/Rb diagram (Figure 12a). Kürkçüoğlu et al. (2015) suggest that high Ba/Rb ratios indicate enriched lithosphere with high amphibole contents. But the shift towards phlogopite field, even if it is weakly, suggest that the source was probably enriched from asthenospheric mantle. But the similarity of the Zr/Ba ratio values of Karataş volcanics (for basaltic trachyandesite; 0.08-0.33 and for trachyandesites; 0.13-0.30) to those of lithospheric mantle (0.12-0.34) rather than those of asthenospheric mantle suggest the lithospheric mantle source (lithospheric and asthenospheric mantle values; after Menzies et al., 1991). Low Nb/U, Nb/La and Tb/Yb ratios also suggest that the origin of this magma is not asthenospheric. Again, low MgO, as well as low Ni, Cr values and enrichments in trace and rare earth elements also suggest that the source of the magma might have been evolved and differentiated lithospheric rather than asthenospheric mantle. Göçmengil et al. (2018) also suggested similar conclusions for Almus and Yıldızeli volcanics.

The samples fall above the mantle metasomatic array on the Th/Yb vs. Ta/Yb binary diagrams developed by Pearce (1983) (Figure 12b). This may be explained that the products of Karataş volcanics occured from a source enriched either during subduction or contamination by sedimentary materials.

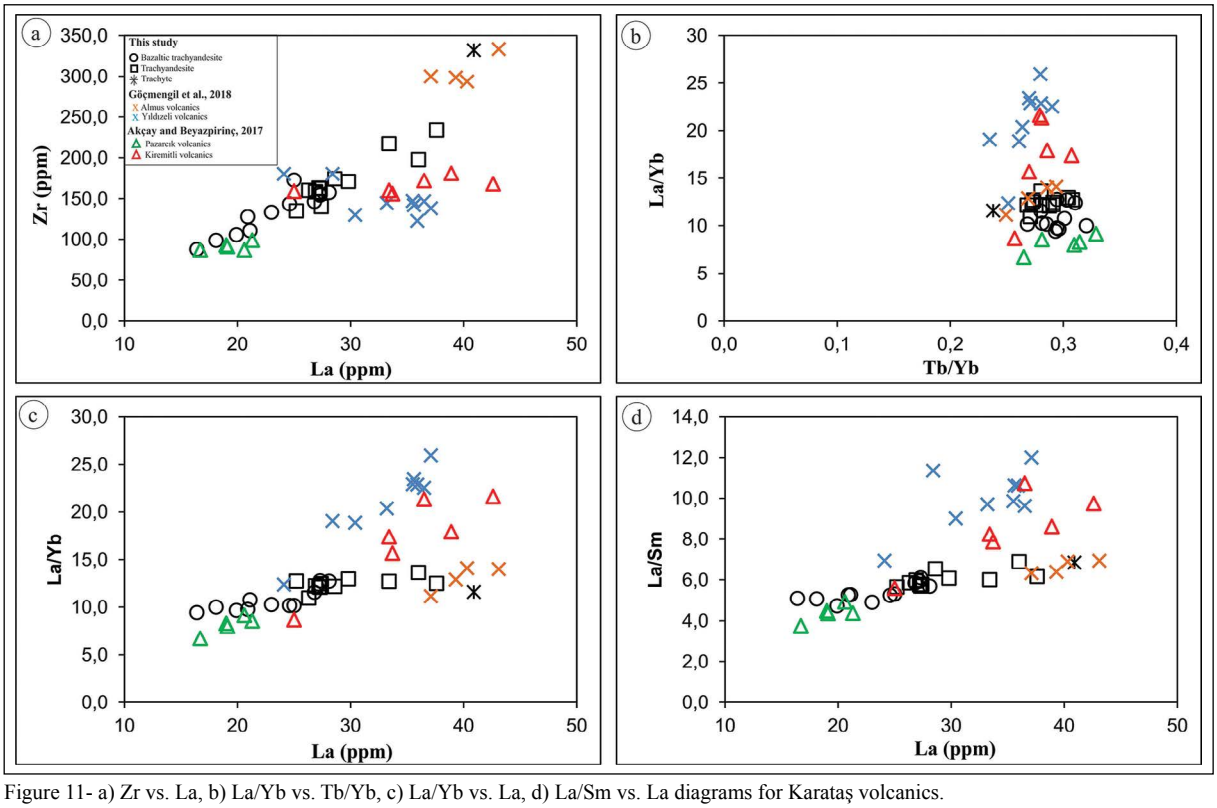

Figure 11- a) Zr vs. La, b) La/Yb vs. Tb/Yb, c) La/Yb vs. La, d) La/Sm vs. La diagrams for Karataş volcanics.

Various element ratio diagrams proposed by different researchers have been prepared to be able to determine whether this source, which forms volcanics has been enriched during subduction or by contamination with sedimentary materials. Hawkesworth et al. (1997) suggest that high Ba/Th ratio values in the arc magmatism products indicate enrichment resulted from subduction related aqueous solutions / or melt enrichment. Th and LILE contents significantly contributed to the enrichment of subduction related sediments. The results of Karataş volcanics mostly shift towards subduction related enrichment field on the Th/Yb vs. Ba/La and Ba/Th vs. Th binary diagrams indicate the significant subduction related enrichment. The weak shift toward the melt sourced from sedimentary material suggest also the possibility of presence sedimentary materials in the source area and sedimentary contamination (Figure 12c-d). It may be said that sedimentary related materials contributed to the development of Yıldızeli and Kiremitli volcanics

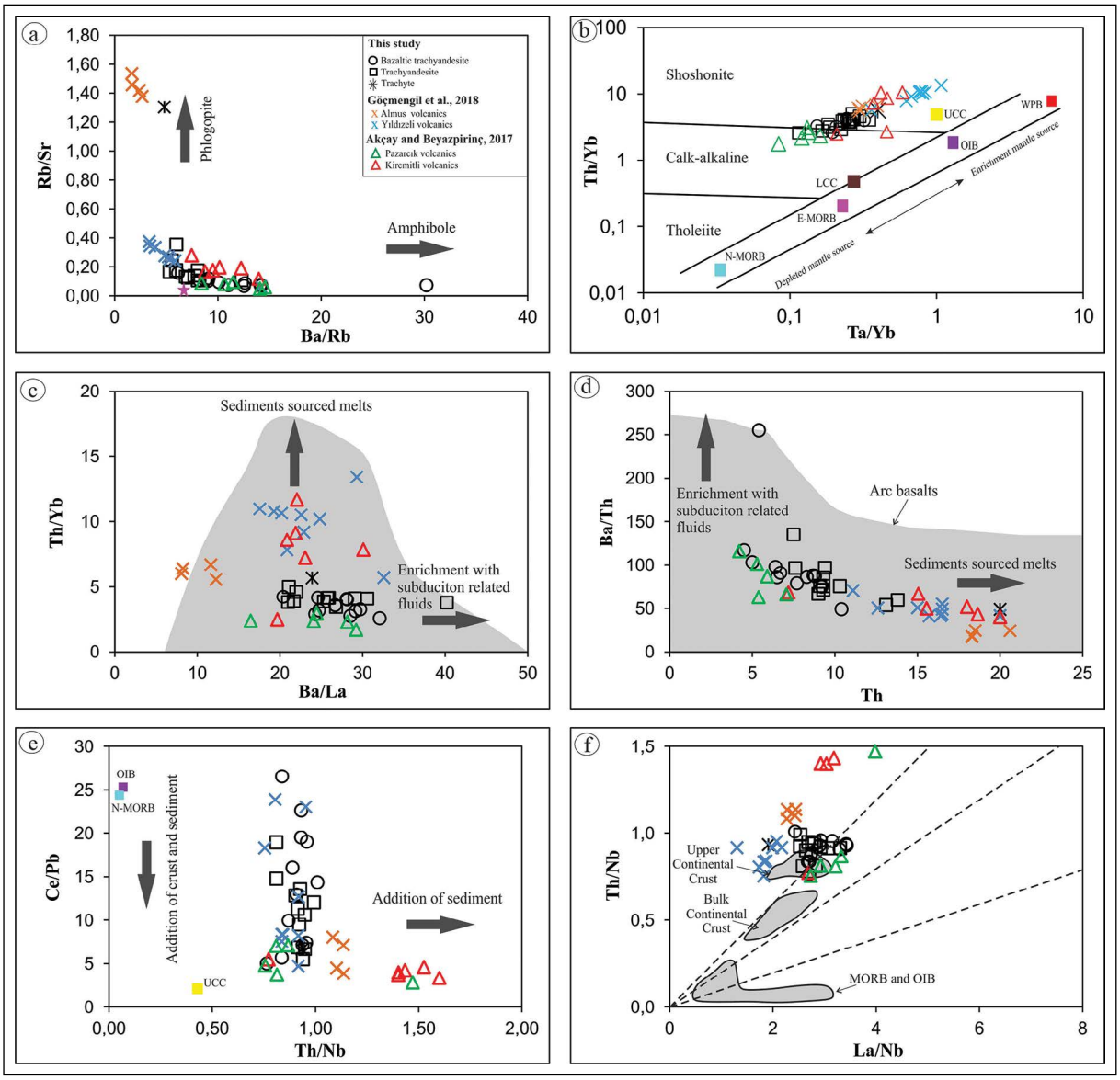

Figure 12- a) Rb/Sr vs. Ba/Rb (Ionov et al., 1997; Tommasini et al., 2011), b) Th/Yb vs. Ta/Yb (Pearce, 1983), c) Th/Yb vs. Ba/La (Kirchenbaur et al., 2012), d) Ba/Th vs. Th (Hawkesworth et al., 1997), e) Ce/Pb vs. Th/Nb (Hofmann et al., 1986), f) Th/Nb vs. La/Nb (Plank, 2005; Kürkçüoğlu et al., 2015). Upper continental crust (UCC) and Lower continental crust (LCC) values from Taylor and McLennan (1985), Ocean Island Basalt (OIB), Normalized Middle Ocean Ridge Basalt (N-MORB) and Enriched Middle Ocean Ridge Basalt (E-MORB) (values from Hofmann (1988) and Sun and McDonough (1989), Within Plate Basalt (WPB) (values from Pearce, 1982).

more than Karataş volcanics. Distribution pattern of the samples on the Ce/Pb vs. Th/Nb binary diagram show that crust and sedimentary materials were both effective in the source area (Hoffmann et al., 1986; Kürkçüoğlu et al., 2015) (Figure 12 e). Similarities of the distribution patterns to the upper continental crust on the spider diagrams, and plots of the samples in the upper continental crust field on the Th/Nb vs. La/Nb binary diagrams suggest the involvement of the crust material (Figure 12f). The basic product of Karataş volcanics fall close to normalized mid ocean ridge basalts (N-MORB) and Ocean Island Basalt (OIB) locations and acidic and intermediate products fall close to the Upper Continental Crust (UCC) area on the Ce/Pb vs. Th/Nb diagrams. These locations of the samples on this diagram suggest the presence of crust of the Tethys Ocean before the collision, the basic products of these volcanics were derived from N-MORB or OIB and acidic and intermediate products were formed by possible partial melting of the Upper Continental Crust material.

Keskin et al., (2008) studied Eocene volcanics in the Amasya and Çorum areas which have similar tectono-stratigraphic features with Karataş volcanics. They indicated that Eocene volcanics were the products of asthenospheric mantle giving rise as a result of the slab breakoff and concurrent uplift that occurred following the collision of the Sakarya continent and the Kırşehir block. But, Karataş volcanics shows data that is the enriched lithospheric mantle rather than the asthenospheric mantle, it was interpreted that the volcanics were not interacted with the asthenospheric mantle.

Göçmengil et al. (2016), interpreting the distribution of the samples on the Ce/Pb vs. Th/Nb diagram, also suggested the possibility of melt source derived from N-MORB or OIB material and enrichment continental crust and/or sedimentary material in the formation model of Almus and Yıldızeli volcanics. But, Göçmengil et al. (2018) suggested that the basic trachytic volcanism was possibly developed with trench tectonics controlled mainly by delamination and/or lithospheric removal processes at the first step, basic-intermediate (basaltic trachyandesite) rocks developed from the partial melting of metasomatic source area and trachytic lavas of latest period developed following reactivation of these basic-intermediate rocks by processes of extensional tectonic and decompression of the magma chamber.

Since the magma forming Karataş volcanics is geochemically lithospheric mantle characteristic, it is interpreted as the lithospheric removal either not developed or slightly developed during the formation of Karataş volcanics. Although Karataş volcanics were post collisional products, they show signs of subduction related enrichment. This complexity was interpreted as the lithospheric mantle material enriched in the crust during subduction developed in a pre-collisional episodes was reactivated by post collisional extensional tectonic and/or delamination processes (Topuz et al., 2011; Temizel et al., 2016; Göçmengil et al., 2018) the reactivated melt gave rise into the aggregated / accumulated material and produced Karataş volcanics causing to melt and assimilation of this material.

7. Conclusions

Karataş volcanics outcropping at the NE Sivas have alkaline character and represent last stages of Eocene volcanism. They consist of basaltic trachyandesites, trachyandesites and trachytes which are the products of basic and intermediate magma. In generally, this volcanism was controlled by fractional crystallization and the effects of crustal contamination increased from basaltic trachyandesites to trachytes.

According to geochemical data, the samples shift towards the amphibole area on the Rb/Sr vs. Ba/Rb ratio diagrams, variation of Zr/Ba ratios in the range of 0.08-0.33, high Ba/Rb ratio, low MgO, Ni, Cr contents indicate that the magma which produced these volcanics started being enriched from lithospheric rather than asthenospheric mantle. It could be suggested that enrichments were associated to subduction related fluids and probably to small amount of sedimentary materials.

In this study, when petrological and geochemical characteristics of Karataş volcanics evaluated with together, it is considered that these volcanics occurred as follows; oceanic crust situated between the Kırşehir block and the Sakarya continent subducted toward north, beneath the Sakarya continent during the pre-collision period, developed subduction related melt derived from N-MORB or OIB gave rise into the continental crust, following collision these melts

were reactivated by extensional tectonics and/or delamination processes during post collisional period and Karataş volcanics were occurred.

Acknowledgement

This study was supported as M-613 project by the Scientific Research Projects Unit in Sivas Cumhuriyet University. We thank Dr. M. Emrah Ayaz (previous Director of Sivas Regional Directorate of MTA) and Zara field camp personnel for supplaying MTA facilities during field studies and giving MTA's drilling data. Dr. Biltan Kürkçüoğlu (Hacettepe Univ.) and two other anonymous referees are thanked for helpful comments improved the text.

References

Akçay, A. E., Beyazpirinç, M. 2017. The Geological Evolution of Sorgun (Yozgat)-Yıldızeli (Sivas) Foreland Basin, Petrographic, Geochemical Aspects and Geochronology of Volcanism Affecting The Basin. Bulletin of the Mineral Research and Exploration 155, 1-32.

Akçay, A. E., Dönmez, M., Kara, H., Yergök, A. F., Esentürk, K. 2008. 1/100.000 Ölçekli Türkiye jeoloji haritaları, Kırşehir İ-34 paftası, No: 81. Maden Tetkik ve Arama Genel Müdürlüğü, Ankara.

Alpaslan, M. 2000. Pazarcık Volkanitinin (Yıldızeli-Sivas) Mineralojik Petrografik ve Jeokimyasal Özellikleri. Türkiye Jeoloji Bülteni 43(2), 49-60.

Alpaslan, M., Terzioğlu, N. 1998. Pontidlerde çarpışma sonrası volkanizmaya bir örnek: Sürmeli Volkaniti (Taşova-Amasya). Cumhuriyet Üniversitesi Yerbilimleri Dergisi 15(1), 13-20.

Altunkaynak, Ş. 2007. Collision Driven Slab Breakoff Magmatism in Northwestern Anatolia, Turkey. The Journal of Geology. https://doi.org/10.1086/509268.

Altunkaynak, Ş., Dilek, Y. 2006. Timing and nature of postcollisional volcanism in western Anatolia and geodynamic implications. Geological Society of America Special Paper. https://doi.org/10.1130/2006.2409(17).

Atakay Gündoğdu, E. 2009. Çorum güneybatısındaki volkanik kayaçların jeolojik ve petrolojik özellikleri ve Alaca Höyük kazısında jeoarkeolojik çalışmalar. Ankara Üniversitesi, Fen Bilimleri Enstitüsü Doktora Tezi. 212s.

Başıbüyük, Z. 2006. Hydrothermal alteration mineralogy-petrography and geochemistry of Eocene volcanics: an example from quadrangle of Zara-Imranli-Susehri-Serefiye (Northeast of Sivas, Central Eastern Anatolia, Turkey). Doktora Tezi. Sivas Cumhuriyet University Science Institute.

Boynton, W. V. 1984. Geochemistry of the rare earth elements: meteorite studies. In Handerson P. (Ed.). Rare Earth Element Geochemistry. 1st ed. Amsterdam, the Netherlands: Elsevier, 63-114.

Bozkurt, E., Koçyiğit, A. 1995. Stratigraphy and geologic evolution of the Almus fault zone in Almus-Tokat region. Turkish Association Petroleum Geologists Bulletin 7(1), 1-16.

Boztuğ, D. 2008. Petrogenesis of the Kösedag Pluton , Suşehri-NE Sivas. Turkish Journal of Earth Sciences 17, 241-262.

Boztuğ, D., Yılmaz, S., Keskin, Y. 1994. İç -Doğu Anadolu alkalin provelisindeki Kösedağ plütonu (Suşehri-KD Sivas) doğu kesiminin petrografisi, petrokimyası ve petrojenezi. Türkiye Jeoloji Bülteni 2, 1-14.

Büyükönal, G. 1985. Distribution of he Major and Trace Elements in The Volcanic Rocks of Yozgat Area, Turkey. Bulletin of the Mineral Research and Exploration 105(106), 97-111.

Canbaz, O., Gürsoy, Ö., Gökçe, A. 2018. Detecting Clay Minerals in Hydrothermal Alteration Areas with Integration of ASTER Image and Spectral Data in Kösedag-Zara (Sivas), Turkey. Journal of Geological Society of India 91(4), 389-516.

Carlson, R. W., Hart, W. K. 1988. Flood basalt volcanism in the northwestern United States. Continental Flood Basalts. https://doi.org/10.1007/978-94-015-7805-9_2.

Dalkılıç, H., Dönmez, M., Akçay, A. E. 2008. 1/100.000 Ölçekli açınsama nitelikli Türkiye Jeoloji Haritaları Serisi, Yozgat-Sheet İ35, No: 82. General Directorate Mineral Research and Exploration, Ankara.

Ekici, T. 2016. Petrology and Ar/Ar chronology of Erdembaba and Kuyucak volcanics exposed along the North Anatolian Fault Zone (Eastern Pontides, NE Turkey): Implications for the late Cenozoic geodynamic evolution of Eastern Mediterranean region. Journal of the Geological Society of India. https://doi.org/10.1007/s12594-016-0409-6.

Erkan, Y. 1972. Petrografi ders notları. Hacettepe Yerbilimleri Enstitüsü, 118 (unpublished).

Erkan, Y. 1994. Kayaç Oluşturan Önemli Minerallerin Mikroskopta İncelenmesi. TMMOB Jeoloji Mühendisleri Odası Yayın No: 42.

Eyüboğlu, Y., Dudas, F. O., Thorkelson, D., Zhu, D. C., Liu, Z., Chatterjee, N., Keewook, Y., Santosh, M. 2017. Eocene granitoids of northern Turkey:

Polybaric magmatism in an evolving arc-slab window system. Gondwana Research. https://doi.org/10.1016/j.gr.2017.05.008.

Fitton, J. G., James, D., Kempton, P. D., Ormerod, D. S., Leeman, W. P. 1988. The role of lithospheric mantle in the generation of late cenozoic basic magmas in the western united states. Journal of Petrology. https://doi.org/10.1093/petrology/Special_Volume.1.331.

Genç, Ş., Yilmaz, Y. 1997. An example of the post-collisional magmatism in northwestern Anatolia: the Kızderbent volcanics (Armutlu Peninsula, Turkey). Turkish Journal of Earth Sciences 6, 33-62

Gill, J. B. 1981. Orogenic Andesites and Plate Tectonics. Springer, Berlin. 390p.

Göçmengil, G., Karacık, Z., Genç, Ş. C. 2016. Çarpışma Sonrası Ortamda Kalk-alkali/Alkali Volkanizmadan- Şoşonitik Volkanizmaya Geçişe Bir Örnek: Almus(Tokat) ve Yıldızeli (Sivas) Orta Eosen Volkanikleri. 3-5 Ekim 2016, 1. Volkanoloji Kurultayı. Maden Tetkik ve Arama Genel Müdürlüğü, Ankara / Türkiye.

Göçmengil, G., Karacık, Z., Genç, C., Billor, M. Z. 2018. 40Ar-39Ar geochronology and petrogenesis of postcollisional trachytic volcanism along the İzmir-Ankara-Erzincan Suture Zone (NE, Turkey). Turkish Journal of Earth Sciences 27(1), 1-31. https://doi.org/10.3906/yer-1708-4.

Görür, N., Tüysüz, O. 1997. Petroleum geology of the southern Continental Margin of the Black Sea. In Regional and Petroleum Geology of the Black Sea and Surrounding Region. AAPG memoir no. 68.

Görür, N., Tüysüz, O., Celal Şengör, A. M. 1998. Tectonic Evolution of the Central Anatolian Basins. International Geology Review. https://doi.org/10.1080/00206819809465241

Görür, N., Tüysüz, O., Şengör, A. M. C. 2010. Tectonic Evolution of the Central Anatolian Basins Tectonic Evolution of the Central Anatolian Basins. 6814(1998). https://doi.org/10.1080/00206819809465241

Haase, K. M., Mühe, R., Stoffers, P. 2000. Magmatism during extension of the lithosphere: Geochemical constraints from lavas of the Shaban Deep, northern Red Sea. Chemical Geology. https://doi.org/10.1016/S0009-2541(99)00221-1.

Hall, A. 1989. M. Wilson. Igneous Petrogenesis: a Global Tectonic Approach. London (Unwin Hyman), 1989, xx + 466 pp. Mineralogical Magazine. https://doi.org/10.1180/minmag.1989.053.372.15.

Hawkesworth, C. J., Turner, S. P., McDermott, F., Peate, D. W., Van Calsteren, P. 1997. U-Th isotopes in arc magmas: Implications for element transfer from the subducted crust. Science 276(5312) 551-555. https://doi.org/10.1126/science.276.5312.551.

Hibbard, M. J. 1991. Textural anatomy of twelve magma mixed granitoid systems. In: Didier, J. ve Barbarin, B. (eds), Enclaves and Granite Petrology. Development in Petrology 13. Elseiver, 431-444.

Hofmann, Albrecht W. 1988. Chemical differentiation of the Earth: the relationship between mantle, continental crust, and oceanic crust. Earth and Planetary Science Letters. https://doi.org/10.1016/0012-821X(88)90132-X.

Hofmann, A. W., Jochum, K. P., Seufert, M., White, W. M. 1986. Nb and Pb in oceanic basalts: new constraints on mantle evolution. Earth and Planetary Science Letters. https://doi.org/10.1016/0012-821X(86)90038-5.

Ionov, D. A., Griffin, W. L., O'Reilly, S. Y. 1997. Volatile-bearing minerals and lithophile trace elements in the upper mantle. Chemical Geology. https://doi.org/10.1016/S0009-2541(97)00061-2.

Irvine, T. N., Baragar, W. R. A. 1971. A Guide to the Chemical Classification of the Common Volcanic Rocks. Canadian Journal of Earth Sciences, 8(5), 523-548. https://doi.org/10.1139/e71-055.

Kalkancı, Ş. 1974. Etüde geologique et petrochimique du sud de la region de Suşehri. Geochronologie du massif syenitique de Kösedağ (Sivas Turquie). These de doctoral de 3 e cycle, L'universite de Grenoble,135p.

Kaymakçı, N., Duermeijer, C. E., Langereis, C., White, S. H., Van Dijk, P. M. 2003. Palaeomagnetic evolution of the Çankiri Basin (central Anatolia, Turkey): Implications for oroclinal bending due to indentation. Geological Magazine. https://doi.org/10.1017/S001675680300757X.

Kerrich, R., Wyman, D. A. 1997. Review of developments in trace-element fingerprinting of geodynamic settings and their implications for mineral exploration. Australian Journal of Earth Sciences 44(4), 465-487. https://doi.org/10.1080/08120099708728327.

Keskin, M., Genç, Ş. C., Tüysüz, O. 2004. Tectonic setting and petrology of collision-related Eocene volcanism around the Çankırı basin, north central Turkey. 32nd International Geological Congress, Florence, Italy, August 20-28, Abstracts, Part 2, p. 1299.

Keskin, M., Genç, Ş. C., Tüysüz, O. 2008. Petrology and geochemistry of post-collisional Middle Eocene volcanic units in North-Central Turkey: Evidence for magma generation by slab breakoff following the closure of the Northern Neotethys

Ocean. Lithos 104(1-4), 267-305. https://doi.org/10.1016/j.lithos.2007.12.011.

Kirchenbaur, M., Münker, C., Schuth, S., Garbe-schönberg, D., Marchev, P. 2012. Tectonomagmatic constraints on the sources of Eastern Mediterranean K-rich lavas. Journal of Petrology 53(1), 27-65. https://doi.org/10.1093/petrology/egr055.

Koçbulut, F., Yılmaz Şahin, S., Tatar, O. 2001. Akdağmadeni (Yozgat)- Yıldızeli (Sivas) Arasındaki Kaletepe Volkanitinin Mineralojik-Petrografik ve Jeokimyasal İncelenmesi. İstanbul Üniversitesi Yerbilimleri Dergisi, 14(1-2), 77-91.

Kürkçüoğlu, B., Pickard, M., Şen, P., Hanan, B. B., Sayit, K., Plummer, C., Şen, E., Yürür, T., Furman, T. 2015. Geochemistry of mafic lavas from Sivas, Turkey and the evolution of Anatolian lithosphere. Lithos. https://doi.org/10.1016/j.lithos.2015.07.006.

LeMaitre, R. W., Streckeisen, A., Zanettin, B., LeBas, M. J., Bonin, B., Bateman, P., Bellieni, G., Dudek, A., Efremova, S., Keller, J., Lameyre, J., Sabine, P.A. Schimid, R., Sorensen, H., Woolley, A. R. 1989. Igneous Rocks: A classification and glossary of terms. International Union of Geological Sciences Subcommission on the Systematics of Igneous Rocks, 32-39. https://doi.org/10.1017/S0016756803388028.

MacKenzie, W. S., Guilford, C. 1980. Atlas of rock forming minerals in thin section. John Wiley and Soons, Inc, New York.

Menzies, M. A., Kyle, P. R., Jones, M., Ingram, G. 1991. Enriched and Depleted Source Components for Tholeiitic and Alkaline Lavas from Zuni-Bandera, New Mexico: Inferences About Intraplate Processes and Stratified Lithosphere. Journal of Geophysical Research. 96(B8), 13645-13671p.

Moorhouse, W. W. 1969. The study of rocks in thin section. Harper and Row, New York, 514.

MTA. 2002. 1/500.000 ölçekli Türkiye Jeoloji Haritası, Sivas Paftası. Maden Tetkik ve Arama Genel Müdürlüğü, Ankara.

Okay, A. I., Tüysüz, O. 1999. Tethyan sutures of northern Turkey. Geological Society, London, Special Publications 156(1), 475-515. https://doi.org/10.1144/GSL.SP.1999.156.01.22.

Okay, A., Satır, M. 2006. Geochronology of Eocene plutonism and metamorphism in northest Turkey: evidence for a possible magmatic arc. Geodinamica Acta. https://doi.org/10.3166/ga.19.251-266.

Özdemir, K. F. 2016. Sivas'ın Doğusundaki Eosen Yaşlı Karataş ve Neojen Yaşlı Şerefiye Volkanitlerinin Petrolojisi. Sivas Cumhuriyet Üniversitesi Fen Bilimleri Enstitüsü, Yüksek Lisans Tezi. 83 s.

Pearce, J. A. 1982. Trace element characteristics of lavas from destructive plate boundaries. In Orogenic Andesites and Related Rocks, 525-548.

Pearce, J. A. 1983. Role of the sub-continental lithosphere in magma genesis at active continental margins. In: Hawkesworth, C.J. and Norry, M.J. eds. Continental basalts and mantle xenoliths, Nantwich, Cheshire: Shiva Publications, pp. 230-249.

Plank, T. 2005. Constraints from Thorium/Lanthanum on sediment recycling at subduction zones and the evolution of the continents. Journal of Petrology. https://doi.org/10.1093/petrology/egi005.

Sun, S. S., McDonough, W. F. 1989. Chemical and isotopic systematics of oceanic basalts: implications for mantle composition and processes. Geological Society, London, Special Publications 42(1), 313-345. https://doi.org/10.1144/GSL.SP.1989.042.01.19.

Taylor, S. R., McLennan, S. M. 1985. The Continental Crust: Its Composition and Evolution. Geological Magazine 122(06), 673. https://doi.org/10.1017/S0016756800032167.

Temizel, I., Arslan, M., Yücel, C., Abdioğlu, E., Ruffet, G. 2016. Geochronology and geochemistry of Eocene-aged volcanic rocks around the Bafra (Samsun, N Turkey) area: Constraints for the interaction of lithospheric mantle and crustal melts. Lithos. https://doi.org/10.1016/j.lithos.2016.04.023.

Tiryaki, C., Ekici, T. 2012. Çarpışma Sonrası Kalk-Alkalin Yozgat Volkaniklerinin Petrolojisi. Türkiye Jeoloji Bülteni 55(1), 19-42.

Tommasini, S., Avanzinelli, R., Conticelli, S. 2011. The Th/La and Sm/La conundrum of the Tethyan realm lamproites. Earth and Planetary Science Letters. https://doi.org/10.1016/j.epsl.2010.11.023.

Topuz, G., Altherr, R., Schwarz, W. H., Siebel, W., Satir, M., Dokuz, A. 2005. Post-collisional plutonism with adakite-like signatures: The Eocene Saraycık granodiorite (Eastern Pontides, Turkey). Contributions to Mineralogy and Petrology. https://doi.org/10.1007/s00410-005-0022-y.

Topuz, G., Okay, A.I., Altherr, R., Schwarz, W.H., Siebel, W. Zack, T., Satır, M., Şen, C. 2011. Post-collisional adakite-like magmatism in the Ağvanis Massif and implications for the evolution of the Eocene magmatism in the Eastern Pontides (NE Turkey). Lithos 125, 131-150.

Tüysüz, O., Dellaloğlu, A. A. 1992. Çankırı havzasının tektonik birlikleri ve havzanın tektonik evrimi. In: Proceedings of 9th Turkish Petroleum Congress Turkey, Ankara. Turkish Association of Petroleum Geologists 333-349.

Tüysüz, O., Dellaloğlu, A. A., Terzioğlu, N. 1995. A magmatic belt within the Neo-Tethyan suture zone and its role in the tectonic evolution of northern Turkey. Tectonophysics. https://doi.org/10.1016/0040-1951(94)00197-H.

Yardley, B. W. D., MacKenzie, W. S., Guilford, C. 1990. Atlas of metamorphic rocks and their textures. John Wiley and Sons, Inc, NewYork. 120p.

Yılmaz, A., Okay, A., Bilgiç, T. 1985. Yukarı Kelkit Çayı yöresi ve güneyinin temel jeoloji özellikleri ve sonuçları. Maden Tetkik ve Arama Genel Müdürlüğü Rapor No: 7777. 124 s, (unpublished).

Yılmaz, A., Uysal, Ş., Yusufoğlu, H., Ağan, A., İnal, A., Aydın, N., Bedi, Y., Havzoğlu, T., Göç, D., İnal, E., Erkan, E.N. 1994. Akdağmasifi (Sivas) dolayının jeolojik incelemesi. Maden Tetkik ve Arama Genel Müdürlüğü Rapor No:9721, Ankara (unpublished).

Yılmaz, A., Uysal, S., Bedi, Y., Atabey, E., YusufoğIu, H., Havzoğlu, T., Aydın, N. 1997. 1/100.000 Ölçekli Türkiye jeoloji haritaları, Sivas-F22 paftası, No: 46. Maden Tetkik ve Arama Genel Müdürlügü, Ankara.

Yılmaz, Y., Tüysüz, O. 1984. Kastamonu-Boyabat-Vezirköprü-Tosya arasındaki bölgenin jeolojisi (Ilgaz-Kargı masiflerinin etüdü). Maden Tetkik ve Arama Genel Müdürlüğü Rapor No: 275, 275 s, (unpublished).

Yücel, C., Arslan, M., Temizel, İ., Abdioğlu Yazar, E., Ruffet, G. 2017. Evolution of K-rich magmas derived from a net veined lithospheric mantle in an ongoing extensional setting: Geochronology and geochemistry of Eocene and Miocene volcanic rocks from Eastern Pontides (Turkey). Gondwana Research. https://doi.org/10.1016/j.gr.2016.12.016.

Bulletin of the Mineral Research and Exploration

http://bulletin.mta.gov.tr

Estimation of the compaction characteristics of soils using the static compaction method

Kamil KAYABALI[a], Ramin ASADİ[a], Mustafa FENER[a], Orhan DİKMEN[a], Farhad HABİBZADEH[a] and Özgür AKTÜRK[b*]

[a]*Department of Geological Engineering, Faculty of Engineering, Ankara University, Ankara, Turkey*
[b]*Department of Geological Engineering, Faculty of Engineering, Akdeniz University, Antalya, Turkey*

Research Article

Keywords:
Static compaction, Standard Proctor, Unconfined compressive strength, Permeability, Compaction energy.

ABSTRACT

Ground improvement using mechanical stabilization is commonly applied by performing the standard Proctor compaction test, which requires a significant quantity of soil, usually obtained from open pits. A static compaction test is an alternative laboratory compaction test. Although researchers have shown that the results of miniature size static compaction tests are comparable with that of standard Proctor tests in terms of the maximum dry density and the optimum water content, no attempt has been made to compare the two fundamental properties of the compacted soil: undrained shear strength and hydraulic conductivity. The scope of this investigation was to estimate the level of static compaction energy required to (1) obtain a compaction curve similar to that of the standard Proctor test; (2) reconstruct compacted soils using the standard Proctor and static compaction tests at the optimum water content; and (3) compare the undrained shear strength and hydraulic conductivity of compacted soils. The compacted soils at the predetermined energy level were subjected to hydraulic conductivity tests using the rigid-wall falling-head permeability method. Undrained shear strength tests were performed by employing a high-capacity laboratory vane shear apparatus on compacted samples of both the standard Proctor and static compaction tests. The present investigation revealed that the static compaction test, requiring about only 10% of the soil necessary to perform the standard Proctor method, provides comparable results in regard to hydraulic conductivity and undrained shear strength.

Received Date: 29.04.2019
Accepted Date: 05.08.2019

1. Introduction

Soils play two major roles: as a construction material and as a foundation for buildings. Their engineering properties such as strength, compressibility and permeability are usually unsatisfactory for the planned use in both cases. The common practice is to stabilize or improve the engineering properties of such soils. Stabilization is accomplished by a variety of means. Amongst these, mechanical stabilization, or compaction is the most common method of soil improvement because it is a cost-effective alternative to many other stabilization techniques.

The benefits of compaction include the increase in soil density and strength, and the reduction of permeability and compressibility. This modification yields a significant reduction in potential settlement; an increase in bearing capacity and slope stability and a decrease in detrimental effects such as swelling and shrinkage and seepage potential in earthen structures (Basheer, 2001).

Citation info: Kayabalı, K., Asadi, R., Fener, M., Dikmen, O., Habibzadeh, F., Aktürk, Ö. 2020. Estimation of the compaction characteristics of soils using the static compaction method. Bulletin of the Mineral Research and Exploration 162, 75-82. https://doi.org/10.19111/bulletinofmre.603873

* *Corresponding author: Özgür AKTÜRK, akturko@akdeniz.edu.tr*

The common procedure for compacting soils for engineering works in the field is small-scale physical modeling in a laboratory. Typical tests on this include vibration, impact, kneading, and static compaction methods. Proctor tests (standard and modified) have been extensively used in physical modeling of soils in a laboratory to determine the maximum dry density in which a soil gains its highest strength and lowest compressibility state. This way, soils are compacted under a certain level of energy per unit volume and the final product of the process is a dry density versus water content graph.

Although the theoretical energy to be delivered onto soil in the compaction mold is about 600 kJ/m^3 for the standard Proctor method, the rammer diameter is smaller than the compaction mold and a significant portion of energy is wasted due to the bulging of compressed soil around the rammer during impacts. Day and Daniel (1985) reported that the maximum dry unit weights produced with the reduced compactive effort, by using only 10 blows of the compaction ram per lift rather than the usual 25 blows per lift, were approximately 90% of the values obtained with full compactive effort. Bell (1977) investigated the compaction energy relationships for cohesive soils using the impact, kneading, and static compaction methods and concluded that static compaction was the most efficient method for all moisture conditions. Hadas (1987) compared the fast (i.e. the impact) compaction with the slow (i.e. static) compaction in regard to compaction energy and concluded that the energy ratio of slow to fast method ranged from 0.10 to 0.43 to give the same bulk density. On average, this ratio was 0.2, meaning that the static compaction method needs only one fifth of the compactive effort required for the impact (Proctor) method. The energy loss associated with the impact method is attributed to the smaller diameter of the falling rammer (64 mm) than that of the soil specimen (102 mm) (Venkatarama Reddy and Jagadish, 1993). The kinetic energy losses involved in the impact method include the energy dissipated into heat, sound, and high-frequency elastic vibrations (Sridharan and Sivapullaiah, 2005).

The preceding review points out that the impact method is not an energy-efficient method. More importantly, the most common impact method (i.e. the standard Proctor method) requires a significant amount of soil to sample. The requirement of the American Society of Testing Materials (ASTM) D698 standard is 16 kg (ASTM, 2003). Such a huge amount of soil can only be obtained from open pits. When the earthwork involves construction of a large dam, for instance, hundreds of thousands of cubic meters of soil are needed. Even though there exists a nearby geological formation capable of providing such an enormous volume of material, the open pit sampling does not permit a geotechnical engineer to characterize the geological materials at greater depths. In this case, the geotechnical engineer should rely on soil samples from boreholes, which would not meet the quantity requirement of the standard Proctor test. Therefore, it is inevitable to work with a compaction method that can characterize the restricted amount of soil samples obtained from a borehole.

Sridharan and Sivapullaiah (2005) devised a mini compaction test apparatus for fine-grained soils. Their equipment consisted of a mold 3.81 cm in diameter and 10 cm in height, the volume of which was only one tenth of standard Proctor. They employed two types of hammers, i.e. 1 kg and 2.5 kg in mass, to simulate the standard Proctor and modified Proctor tests, respectively. Tien et al. (2004) used a mold 30 cm in height and 7 cm in diameter to examine the compaction characteristics of bentonite-sand mixtures. They employed the static compaction method and concluded that their model greatly reduced the amount of soil for compaction tests on composite mixtures.

This investigation aimed to determine the proper level of the compactive effort for the static compaction test and compare the compaction characteristics from standard Proctor and static compaction tests. The next step involves comparing the undrained shear strength and hydraulic conductivity obtained from both tests.

2. Materials

The present investigation included the use of ten soil samples of different gradational and plasticity characteristics, as presented in table 1 and figure 1. The tools employed for the research consisted of an automated standard Proctor unit, a loading frame for static compaction along with a recording unit for the work done during static compaction, and standard and miniature sized molds. Undrained shear strengths were measured using a miniature vane shear test (VST) device equipped with an electronic transducer for

Table 1- Basic properties of soils used in the investigation.

No	LL (%)	PL (%)	PI (%)	USCS	FC (%)	Sand (%)
01	44.9	23.1	21.8	SC	24	76
02	43.8	21.3	22.5	SC	19	81
03	45.2	23.1	22.1	SC	13	87
04	40.1	21.9	18.2	SC	21	79
05	40.5	21.4	19.1	SC	13	87
06	41.1	21.7	19.4	SC	22	78
07	36.4	19.2	17.2	SC	22	78
08	34.4	20.8	13.6	SC	15	85
09	33.7	16.3	17.4	SC	19	81
10	31.8	15.3	16.5	SC	17	83

measuring the applied torque. The maximum capacity of torque is 3 N.m, which is equivalent to shear stress of about 700 kPa when the smallest size blade (12.7 x 12.7 mm) is used. For the hydraulic conductivity tests, a rigid-wall type of apparatus was employed along with the falling-head permeability test method.

3. Methods

Standard Proctor and static compaction tests were the compaction methods employed for this investigation. For the standard Proctor, the ASTM D668 standard was employed (ASTM, 2003). The theoretical energy delivered to compacted soil in this test was 592.7 kN-m/m^3. As for the static compaction test, the following procedure was employed. The compaction mold was 5 cm in both diameter and height, with a volume of 98.17 cm^3, which is about 1/10 th of that of the standard Proctor mold (V=944 cm^3). The compaction apparatus includes a mold, a collar, and a rammer. Approximately 200 g of soil was used to generate a single point on the graph of the dry density versus water content. As in the case of the standard Proctor test, the static compaction procedure included three compacted layers, each of which was constructed under a predetermined amount of work. The amount of work to be applied onto each of three soil layers was computed as follows. First, the compactive effort for the standard Proctor had to be expressed:

$$\text{Compactive effort}=\frac{2{,}495\ \text{kg}\ (9{,}81\text{m/s}^2)(0.3048\text{m})(3\ \text{layers})(25\ \text{drops/layer})}{0{,}944\ \text{x}\ 10^{-3}\ \text{m}^3}=592{,}7\ \text{kN.m/m}^3$$

where 2.495 kg is the mass of the rammer and 0.3048 m is the drop height. The amount of work to be delivered to each layer had to be calculated using the area under the force-displacement curve in figure 2:

$$\text{Compactive effort}=\int_0^h F\Delta h$$

To obtain the compaction energy per layer:

$$592{,}7\ \text{kN.m/m}^3=\frac{\int_0^h F\Delta h\ (3\ \text{layers})}{98{,}17\ \text{x}\ 10^{-6}\ \text{m}^3}$$

which eventually becomes:

$$\int_0^h F\Delta h = 19{,}4\ \text{N.m}\ \text{(per layer)}$$

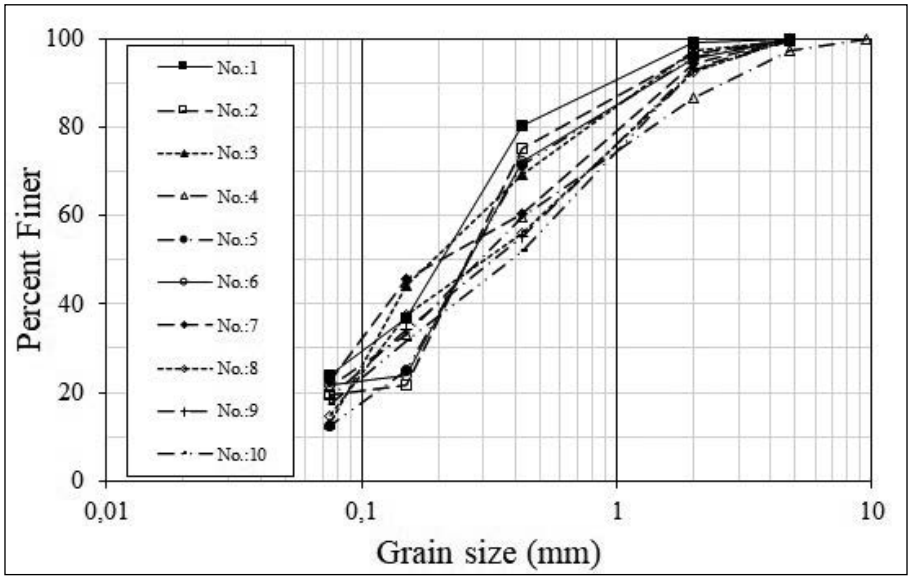

Figure 1- Gradation curves for soil samples.

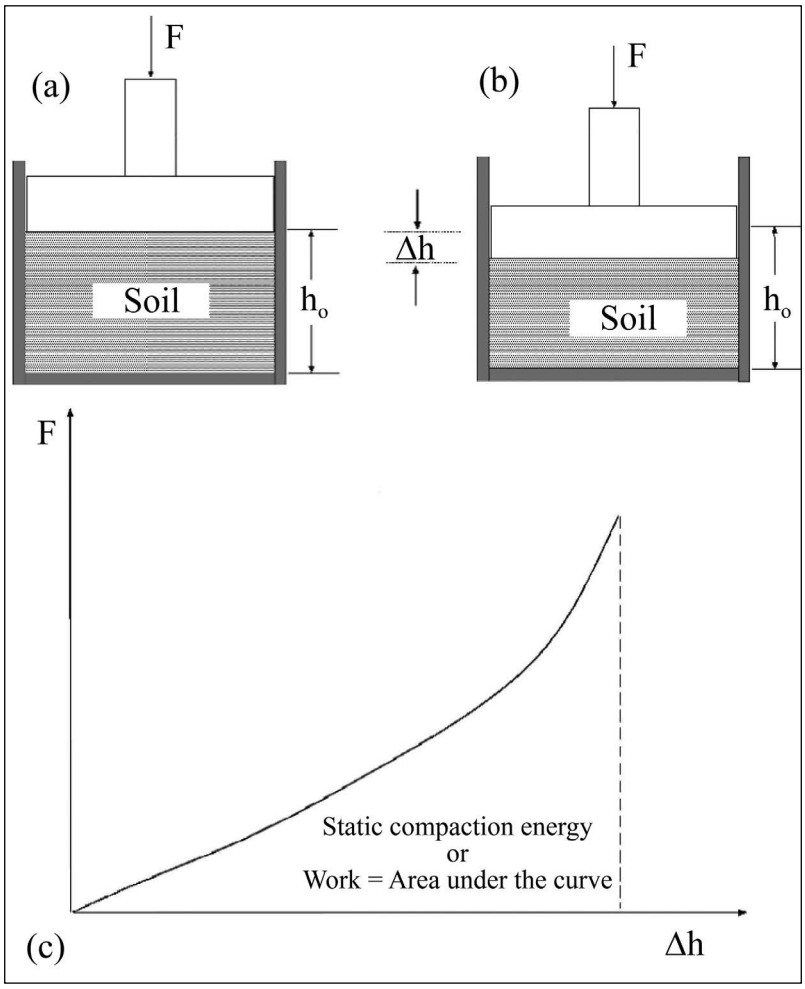

Figure 2- The principle of static compaction and the definition of work done by it.

The soil was compacted in a brass mold by compression from one end only. After compaction, the sample was extruded from the mold and weighed, then a moisture sample was taken and the water content and dry density were computed. Each of these compaction tests was repeated 5-7 times for all soil samples to construct dry density versus water content plots.

Unconfined compression tests were performed on compacted soils at optimum water contents. A miniature vane shear was employed to conduct shear strength tests on compacted specimens of both the standard Proctor and the static compaction. The VST apparatus recorded the torque by an electronic transducer, which eliminated the use of springs of different stiffness. The tests were performed in accordance with the ASTM D4648 standard (ASTM, 2000). The rate of shear strain was 75°/min, matching a median value for the suggested range of 60-90°/min in the ASTM standard.

A series of falling-head permeability tests were performed on ten soil samples, which were compacted at optimum water contents. As shown in figure 3, molds containing compacted soil specimens were placed in a permeability testing apparatus and a hydraulic gradient of 20-25 was applied. The test duration ranged from one to two weeks to ensure that at least one pore volume of water permeated through the compacted specimen. Three specimens were tested for each of the soil samples for each compaction procedure. Daily readings were taken and the permeabilities were computed by the following equation:

$$k = (aL/A\Delta t)\ln(h_1/h_2)$$

where k is permeability (cm/s), a is the cross sectional area of standpipe (cm^2), L is the height of specimen (cm), A is the cross sectional area of specimen (cm^2), and Δt is time (s) for standpipe head to decrease from the height h_1 to height h_2. The average permeability was

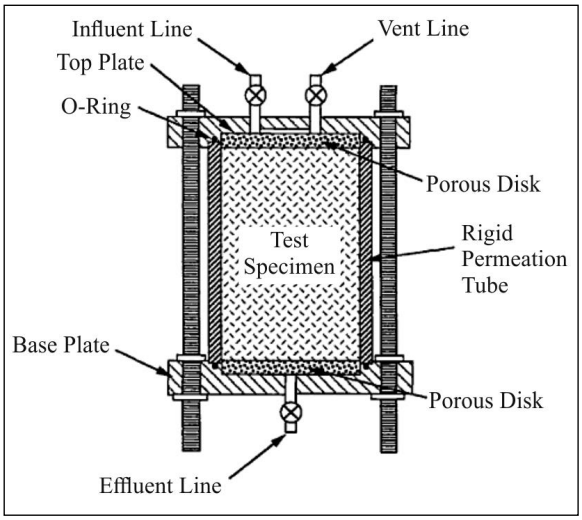

Figure 3- Schematic illustration of the permeameter used to conduct hydraulic conductivity tests.

computed using the overall results per specimen, and the representative permeability for each compaction method per soil sample was taken as the average of three specimens.

4. Results of Experiments

The mechanics of standard Proctor and static compaction tests are totally different. The rate of loading for the static compaction tests is considered to affect the test results. To observe whether or not this is the case, different loading rates were applied on static compaction specimens under constant compaction energy conditions. The selected strain rates were 2.5 mm/min, 5.0 mm/min, and 10 mm/min. Figure 4 shows a comparison between the standard Proctor curve and the curves of static compaction for different strain rates. The level of energy applied on soil 1 was 40% of the standard Proctor compactive effort. A close look at figure 4 reveals that the effect of strain rate on the shape of the compaction is insignificant. The strain rate of 10 mm/min was subsequently selected as the loading rate for the proceeding static compaction tests.

Another series of static compaction tests was performed on soil sample 7 to observe the effect of the compaction energy on the test results. In essence, the goal of such a procedure is to set the appropriate level of the compaction energy for the static compaction test, whose experimental curve matches the compaction curve of the standard Proctor. Figure 5 shows the experimental curves of the static compaction for the energy levels of 15%, 20%, 30%, 35%, 40%, and 50% for soil number 7 in comparison with the compaction curve of standard Proctor. Figure 5 reveals that the level of energy for static compaction curve matching the curve of standard Proctor should lie somewhere between 30% and 50%.

To set the appropriate level of compaction energy for the static compaction method, another series of static compaction tests was performed on all soils at the energy levels of 30%, 40%, and 50%. The strain rate was 10 mm/min in each case. Figure 6 shows the curves of static compaction for the energy levels of 30%, 40%, and 50% in comparison with the standard

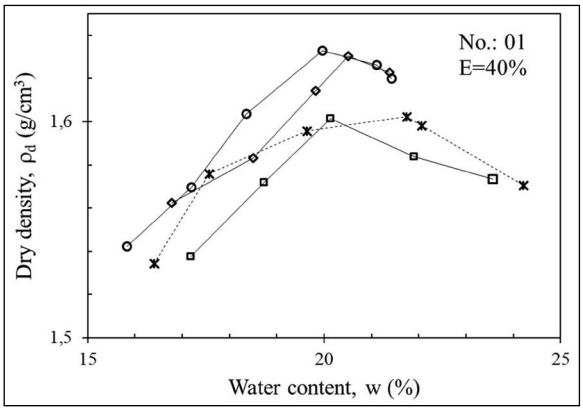

Figure 4- Static compaction curves obtained using the loading rate of 2.5 mm/min (circles), 5.0 mm/min (diamonds), and 10 mm/min (squares) along with the compaction curve of the standard Proctor (asterisks) for soil No. 1.

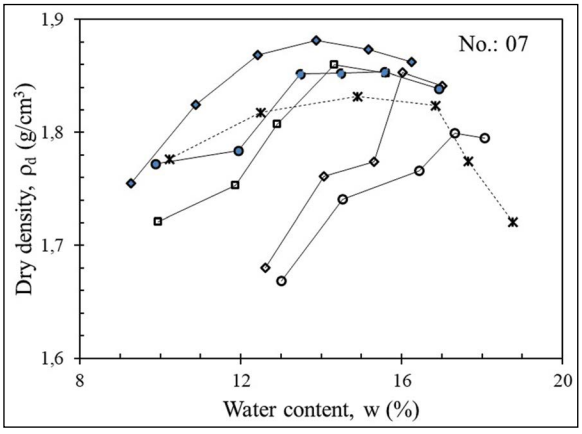

Figure 5- Static compaction curves obtained using different compactive efforts: 15% of standard Proctor energy (SPE, open circles), 20% of SPE (open diamonds), 25% of SPE (squares), 30% of SPE solid circles), and 40% of SPE (solid diamonds) along with the standard Proctor compaction curve (asterisks) for soil No. 7.

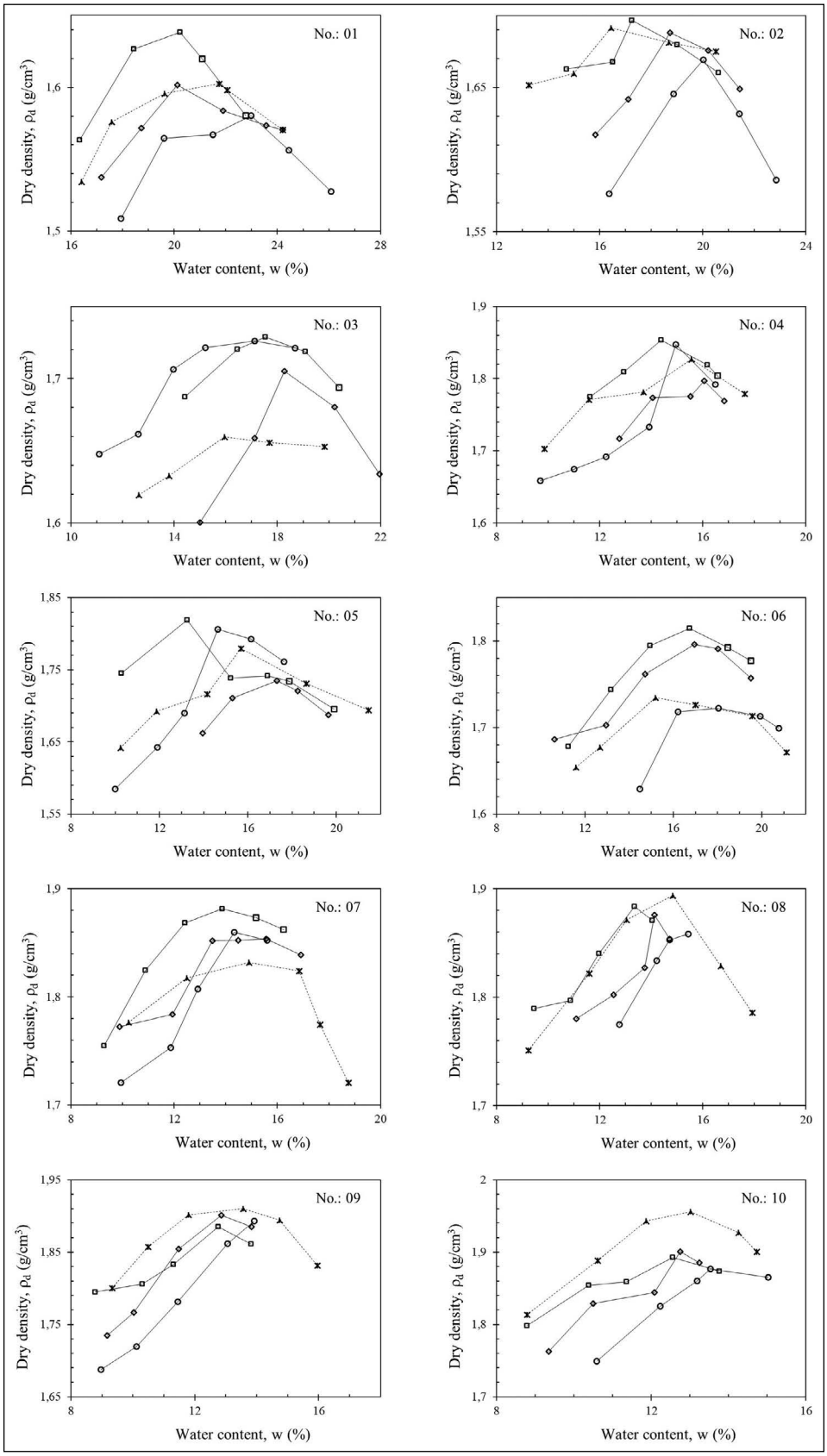

Figure 6- Static compaction curves obtained using 30% of SPE (circles), 40% of SPE (diamonds), and 50% of SPE (squares) along with the standard Proctor compaction curve for all soils.

Proctor curve for all soil samples. The evaluation of figure 6 suggests that the energy level of the static compaction test should be around 40% to match the standard Proctor curve. The difficulty of making a perfect match should be appreciated. The differences between the optimum water contents and the maximum dry densities are not large and considered to be within acceptable ranges.

Permeability tests were performed on three specimens of each soil. Compaction molds were used as the rigid-wall permeameters. Tests were conducted on the compacted soils at the optimum water contents. For the static compaction specimens, the samples were prepared at the 40% energy level along with the optimum water content. Table 2 shows the results of permeability tests along with their mean values. A plot for a comparison between the results of two different techniques would better serve the purpose. However, there is not a systematic relationship between the two sets of hydraulic conductivity values. Table 2 illustrates the comparison of the ratio of the hydraulic conductivity of one method to that of the other method. A quick glimpse at table 2 reveals that, generally, the difference between the permeabilities of the soil samples compacted using the two different techniques is less than one order and that the permeabilities of soils using the Proctor method are a few times higher than those of the soils of the static compaction method.

Undrained shear strength tests involved the use of a laboratory vane shear with a high torque capacity. The compacted specimens at the optimum water content for the standard Proctor test were subjected to the undrained shear strength test from both ends. As expected, the top end of the specimen yielded a slightly higher strength value for almost all samples and the average of the two was assigned as the undrained shear strength of the tested specimen. Because the static compaction mold was not as high as that of the standard Proctor test, the undrained shear strength tests using the VST apparatus were performed only once at the mid-level of the specimen. Two specimens for each soil sample compacted using both the static and standard Proctor compaction tests were subjected to undrained shear strength tests. Table 3 shows the results along with their mean values. Like the comparison of the permeability test results, the undrained shear strength values obtained for the compacted specimens using the standard Proctor technique were compared with those of the static compaction method in the form of a ratio for the very same reasons at the last column of table 3. The undrained shear strength values obtained over the soil samples compacted using the standard Proctor method were higher than those determined over the compacted

Table 3- The results of the undrained shear strength tests (kPa).

No.	Standart Proctor			Static Compaction			$s_{u(Pro)}/s_{u(sta)}$
	Test 1	Test 2	Mean	Test 1	Test 2	Mean	
01	442	407	424	259	432	346	1.2
02	526	515	520	355	453	404	1.3
03	584	520	552	203	484	343	1.6
04	481	328	405	554	514	534	0.8
05	467	453	460	505	381	443	1.0
06	553	553	553	264	481	373	1.5
07	342	451	396	364	362	363	1.1
08	404	411	407	194	418	306	1.3
09	525	492	508	269	208	238	2.1
10	269	518	393	161	206	183	2.1

Table 2- The results of the falling-head permeability tests (cm/s).

No.	Standart Proctor				Static Compaction				k_{Pro}/k_{sta}
	Test 1	Test 2	Test 3	Mean	Test 1	Test 2	Test 3	Mean	
01	9.23E-08	4.91E-08	2.15E-08	5.43E-08	1.37E-08	1.72E-08	2.51E-09	1.11E-08	4.9
02	1.52E-07	1.74E-07	1.01E-07	1.42E-07	4.73E-08	8.21E-08	8.74E-09	4.60E-08	3.1
03	3.3E-07	2.34E-07	1.52E-07	2.39E-07	1.51E-08	3.4E-08	7.89E-09	1.90E-08	13
04	3.13E-08	2.34E-08	2.57E-08	2.68E-08	2.09E-08	3.12E-08	2.12E-08	2.44E-08	1.1
05	1.82E-07	8.24E-08	3.57E-08	1.00E-07	2.5E-08	2.7E-08	2.47E-08	2.56E-08	3.9
06	4.83E-07	1.62E-07	1.12E-07	2.52E-07	3.38E-08	3.14E-08	1.12E-08	2.55E-08	9.9
07	6.57E-08	6.04E-08	3.19E-08	5.27E-08	2.75E-08	5.09E-08	4.5E-08	4.11E-08	1.3
08	6.48E-08	6.17E-08	4.77E-08	5.81E-08	3.26E-08	2.85E-08	3.3E-08	3.14E-08	1.9
09	8.14E-08	5.31E-08	4.57E-08	6.01E-08	7.39E-08	3.22E-08	5.16E-08	5.26E-08	1.1
10	9.05E-08	8.02E-08	5.43E-08	7.50E-08	1.04E-07	4.17E-08	2.18E-07	1.21E-07	0.6

samples using the method of static compaction. The range of variation could be up to 100%.

5. Conclusions

A great portion of the compaction energy is wasted during a standard Proctor test. The compaction curve for a soil could be constructed with 60% less energy when the static compaction method is employed. In the static compaction test, the entire soil mass is subject to displacement, no energy is wasted, and almost all of the energy is used to densify the soil. The level of the compaction energy applied to ten soil samples showed that the required energy level for the static compaction test is about 40% of the standard Proctor method or 237 kJ/m^3.

The compacted specimens were tested for as-compacted undrained strength; the undrained shear strengths obtained using the static compaction test were slightly lower than those obtained using the standard Proctor method. The variations are considered to be within the acceptable ranges.

Likewise, the hydraulic conductivities determined using the static compaction test were slightly lower than those determined using the compacted samples of the standard Proctor method. Considering the large variations of typical permeability tests performed either in the field or in the laboratory, the variations of hydraulic conductivity between the results of the two compaction methods were negligibly small.

The results of this study are based solely on ten soil samples within a rather narrow range of gradation. Further research using a wider range of particle gradation is recommended to validate the findings of the present investigation.

The quantity of soil required for the static compaction test, the volume of whose mold is only 10% of that of the standard Proctor, is less than half a kilogram; the test could be performed on a limited quantity of soils obtained from boreholes. The use of the apparatus is restricted to soils containing particles smaller than 2 mm.

Depending on the skills of the operator, the time duration for the standard compaction test ranges from 1-2 hours to obtain a sufficient number of points to construct a compaction curve, thereby significantly shortening the duration spent for the standard Proctor test.

The static compaction test is environmentally friendly and totally eliminates the noise encountered during the performance of the standard Proctor test, particularly by the automated test. Almost all of the energy is used to densify the soil and no energy is wasted as in the standard Proctor test.

References

American Society for Testing Materials. 2000. Standard test method for laboratory miniature vane shear test for saturated fine-grained soil. ASTM Standard D4648-00, West Conshohocken, PA.

American Society for Testing Materials. 2003. Standard Test Methods for Laboratory Compaction Characteristics of Soil Using Standard Effort. ASTM D668-00, West Conshohocken, PA.

Basheer, I. A. 2001. Empirical modeling of the compaction curve of cohesive soils: Canadian Geotechnical Journal 38, 29-45.

Bell, J. R. 1977. Compaction energy relationships of cohesive soils: Transportation Research Record No. 641, Stabilization of Soils 29-34.

Day, S. R., Daniel, D. E. 1985. Hydraulic conductivity of two prototype clay liners: ASCE Journal of Geotechnical Engineering 111(8), 957-970.

Hadas, A.1987. Soil compaction under quasi-static and impact stress loading: Soil and Tillage Research 9, 181-186.

Sridharan, A., Sivapullaiah, P. V. 2005. Mini compaction test apparatus for fine grained soils: Geotechnical Testing Journal 28(3), 1-7.

Tien, Y. M., Wu, P. L., Chuang, W. S., Wu, L. H. 2004. Micromechanical model for compaction characteristics of bentonite-sand mixtures: Applied Clay Science 26, 489-498.

Venkatarama Reddy, B., Jagadish, K. S. 1993. The static compaction of soils: Geotechnique 43(2), 337-341.

Bulletin of the Mineral Research and Exploration

http://bulletin.mta.gov.tr

Petrographic- mineralogical examination and diagenetic history of the Paleogene evaporites in Bulanık (Muş), Turkey

Pelin GÜNGÖR YEŞİLOVA[a*]

[a]*Department of Geological Engineering, Faculty of Engineering, Van Yüzüncü Yıl University, Van, Turkey*

Research Article

Keywords:
Muş, Evaporite, Diagenesis, Petrography, Minerology

ABSTRACT

Oligocene aged evaporite formations are observed in shallow sea-sabkha environments that develop in highly restricted conditions from sea in northeastern of the Muş basin. Evaporites are observed as alternated and intercalated with clastics and carbonates that developed under the control of factors such as climate, tectonism, volcanism and diagenesis. Evaporites consist of primary and secondary gypsum and minor anhydrite. In petrographic and minerologic examinations, secondary gypsum textures such as alabastrin, porphyroblastic and satin spar with anhydrite relicts, late diagenetic calcite, bitumen and bioturbation traces were detected. In SEM-EDS studies; celestine crstals, autogenic and detritic clay and quartz grains and euhedral dolomite mineral were observed. As a result of all these studies, the conditions and phases of the evaporites from the sedimentation stage to early diagenesis and late diagenesis processes of the evaporites were illuminated. Secondary gypsum consists of the origin of primary anhydrite and gypsum. From the diagenetic fluids released during the gypsum-anhydrite transformation, the late diagenetic calcite and by the interaction of the ions carried by the hydrothermal solutions to the basin with the groundwater were formed the celestite. Stream activity in the basin was determined by the presence of detritic minerals in gypsum minerals.

Received Date: 10.05.2019
Accepted Date: 22.05.2019

1. Introduction

The Muş Basin is an intermontane basin, which remains among ancient massives and contains the marine and terrestrial Paleogene sediments, in eastern Turkey. During the Oligocene period, the northeastern parts of the basin started to become shallow and the lagoons, lakes and sabkhas occasionally replaced with the sea in these restricted marine conditions (Şen et al., 2011). The best known of these basins are marine coastal sabkhas (Warren and Kendall, 1985) and shallow hypersaline environments (salt or lagoon: Orti Cabo et al., 1984; Rosell et al., 1998). In restricted basins in the study area, due to arid climatic conditions and high evaporation, the carbonate, clastic and evaporitic deposits were formed. These deposits were spread over the areas until mud flats. The evaporite formation in coastal sabkhas can be affected from factors such as; marine activities, groundwater, the position of groundwater table; sediments formed in the environment, climate and topography. The solution entry, which will release evaporite in the coastal sabkha can be provided both from the sea and groundwater (Kendall, 1978). The current similar formations to coastal sabkhas in the region are the shores of Abu Dhabi, Egypt, South Australia and North Africa in the Arabian Gulf (Perthuisot, 1980; Warren, 1982). In shallow water evaporitic environments (such as lagoons), the paleo-temperature, microbial activity and the salinity effect

Citation info: Güngör Yeşilova, P. 2020. Petrographic- mineralogical examination and diagenetic history of the Paleogene evaporites in the Bulanık (Muş). Bulletin of the Mineral Research and Exploration 162, 83-92. https://doi.org/10.19111/bulletinofmre.569619

* *Corresponding author: Pelin GÜNGÖR YEŞİLOVA, yesilovapelin@gmail.com*

affect the diagenetic processes (especially mineral substitutions). One example to the lagoon where these conditions occur can be given in Brazil (Vasconcelos and Mckenzie, 1997). In addition, the lagoon-sabkha environment in which similar conditions were formed was developed in the southwestern Sivas basin Tuzhisar Formation (Yeniköy and Küllü Members) and Erzurum-Aşkale sub-basins (Gündoğan et al., 2005; Abdioğlu et al., 2015). The evaporite-containing section reflecting these environments is located near Sıradere Village of Bulanık district of Muş (Figure 1). The Upper Cretaceous granitoid unit consists of the basement of the evaporitic unit. The evaporitic units are successively overlain by; Lower Miocene reefal limestones, Upper Miocene clastics, Upper Pliocene volcanoclastic and clastics and Quaternary alluvials (Figure 1). Since these evaporitic rocks are highly affected by the Miocene compressional tectonics, diagenesis and volcanism in the region, it will be quite interesting to define and solve the sedimentary structures, textures, lithofacies and diagenetic stages (dissolution, recrystallization, volumetric shrinkage, substitution, cementation and volatilization) of the sedimentary structures and textures developed on those rocks. So far, stratigraphic, oil and mapping studies have heavily been carried out in the study area and its surroundings (Birgili, 1968; Dinçer, 1969; Ünal, 1970; Soytürk, 1973; Sakınç, 1982; Göncüoğlu and Turhan, 1983; Şaroğlu, 1986; Akay et al., 1989; Sancay et al., 2006; Hüsing et al., 2009). Therefore, this study aims to determine the diagenetic processes and stages of these by field observations and to have an idea about the environmental conditions (pH, temperature, salinity, solution input and type, amount of detritic material) by means of petrographic and mineralogical studies.

2. Material and Method

This study was conducted in the form of field and laboratory studies. In field studies, the measured stratigraphic section, facies analysis and systematic sampling studies were carried out within field observations. For petrographic and mineralogical studies, more than 50 samples were collected from sections in horizontal and vertical directions where the facies are best observed in the measured stratigraphic sections. Evaporite samples were prepared in Thin

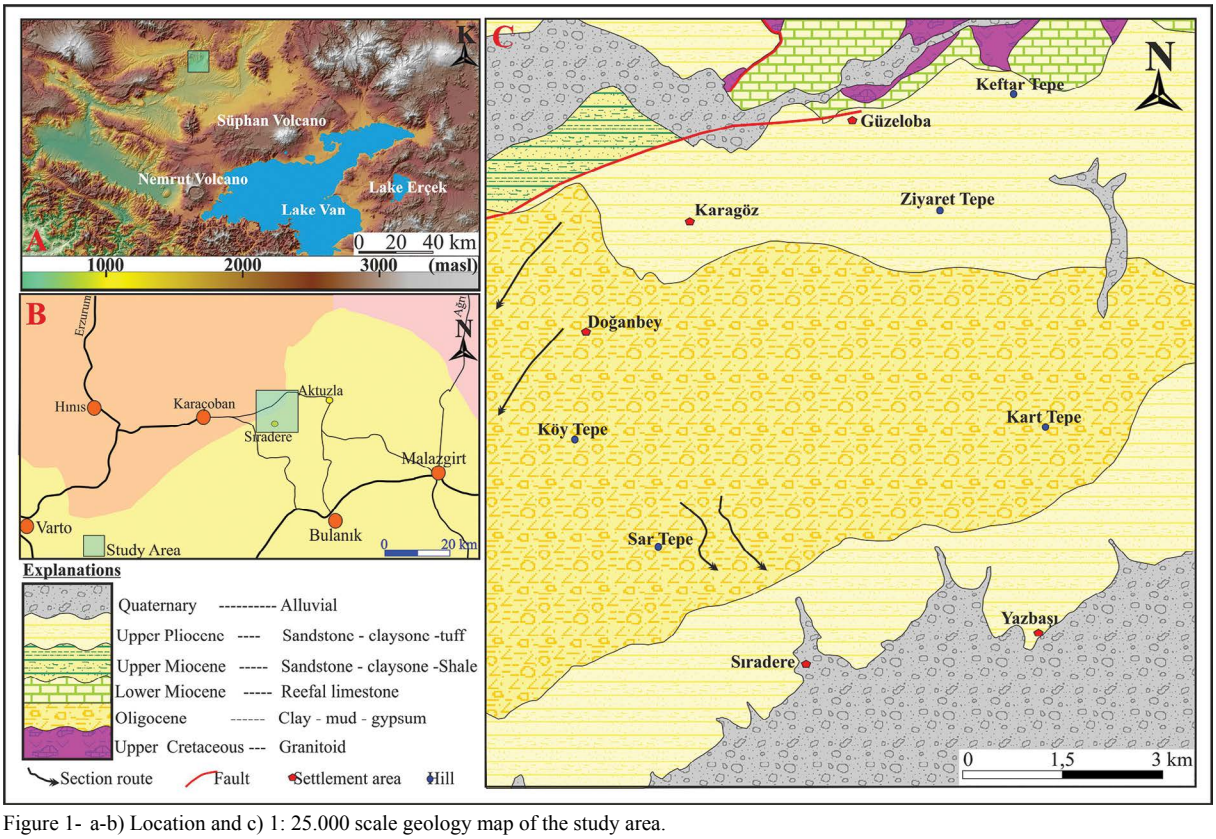

Figure 1- a-b) Location and c) 1: 25.000 scale geology map of the study area.

Section Laboratory of the Dokuz Eylül University for petrographic thin sections. Cutting, polishing and thinning processes were performed respectively in optical microscopic studies. The cutting process was performed on oil-based machine. As evaporite (gypsum, anhydrite) samples are quickly affected from temperature change when they are heated, the bonding process was carried out without heating. After the samples were left to dry, the method of cold bonding was used by hardening them 10-15 sec. under ultraviolet light utilizing the Loctite 358 adhesive. In order to see the evaporite samples more clearly, the thinning process was performed using emeries ranging between 400-800 microns then they were examined under polarized microscope. Scanning Electron Microscopy (SEM-EDS) study on 20 evaporite samples was carried out at İzmir Katip Çelebi University for the determination of some mineralogical and micro textural properties. Within the scope of the study, natural-graded crush type and polished section samples prepared for research were coated with Au-Pd, and examined and photographed on Zeiss 6060 model SEM microscope.

3. Findings and Discussion

3.1. Sedimantological and Petrographical Studies

For the sedimentological investigations in the study area, different lithofacies and sedimentary structures (folds, undulations, ripple structures) ranging from bottom to top was determined by taking measured stratigraphic sections from different areas where evaporite sequences are well observed (Figure 2). Then, petrographic thin section studies were carried out on these systematically collected samples. The measured stratigraphic sections show the depositional environments developing from lagoon-sabkha to mud flats formed by fluctuations in water levels and multiple transgression-regression processes. This evaporitic section is approximately 250 m and is composed of primary and secondary gypsum and minor anhydrites. These evaporites are occasionally interlayered and intercalated with clastic rocks such as carbonate, marl, clay, mudstone and sandstone (Figures 2 and 3a-b). All these are evidences of shallow water environmental conditions (Schreiber et al., 1976).

Secondary gypsums encountered in all sections are observed as laminated, banded, nodular, nodular

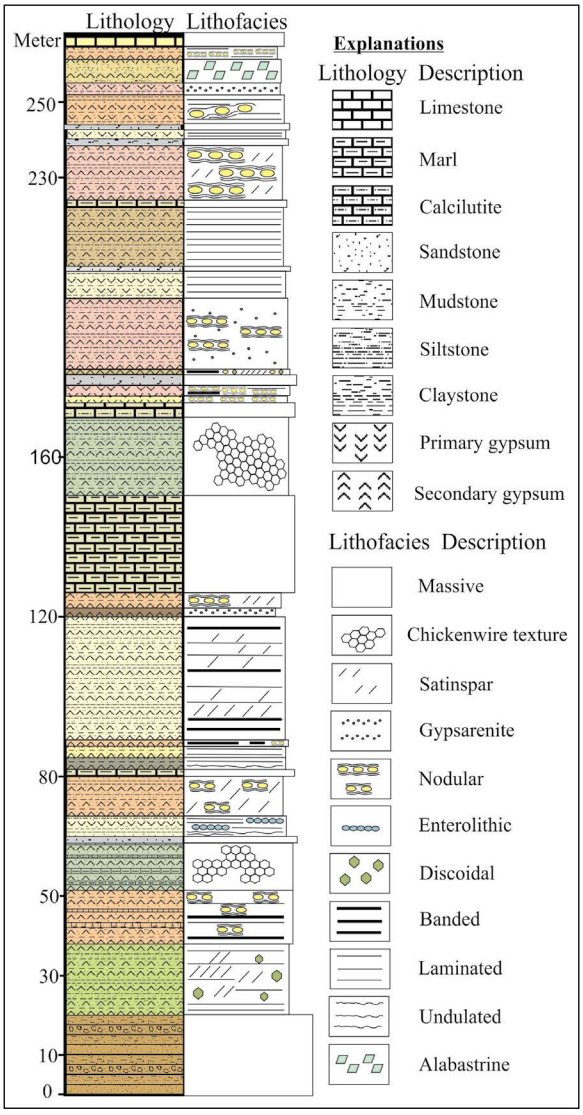

Figure 2- Generalized measured stratigraphic section of the evaporite sequence.

banded, massive and gypsum facies formed first by anhydration then transformation into secondary gypsum (gyps-arenite, selenitic, discoidal) or by the hydration of primary anhydrite (Figure 2). The selenitic primary gypsums are transparent, bright and have excellent cleavages (Figure 3c). It is observed in mudstones and are euhedral to semi-euhedral, with clear twinnings in petrographic thin sections (Figure 3d). The primarily formed gyps-arenites are dark gray, massive, sand-sized gypsums formed by dissolution and recrystallization of selenitic gypsums (Figure 3e). The ripple mark and cross-bedding morphology are evident in these gypsums. Arenitic gypsum texture in petrographic thin sections manifests itself as floating clastic grains in clay matrix (Figure 3f).

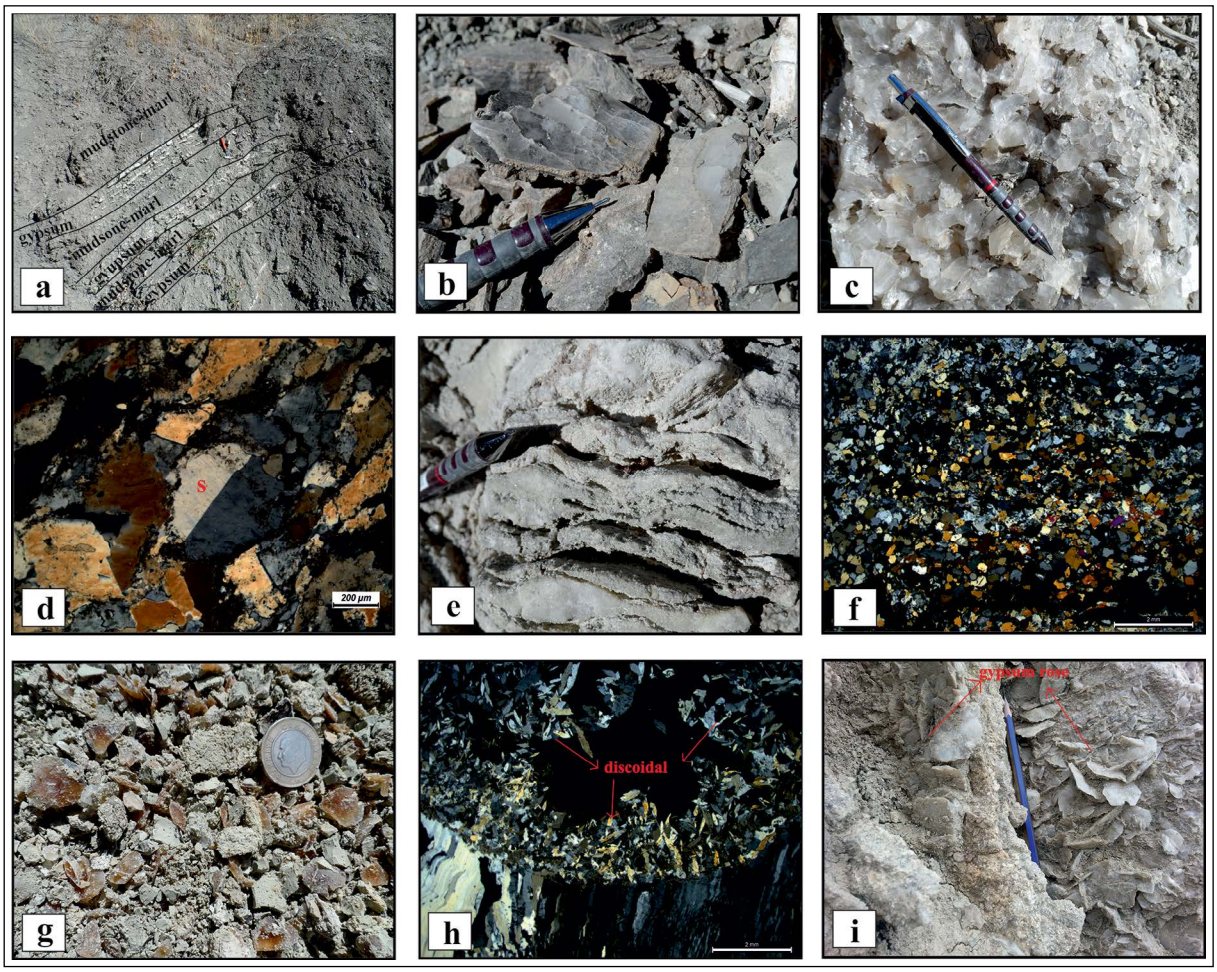

Figure 3- Sedimentological and petrographical images of primary evaporitic lithofacies. a) Mudstone-marl level alternating with gypsum, b) selenitic gypsum with claystone intercalations, c) cleavage of perfectly transparent selenitic gypsum, d) simple twinning in primary gypsum (S), e) clastic gypsum arenite, f) gypsum arenite texture (cross nicol polarizing microscope), g) brown discoidal gypsum with in mudstones, h) discoidal gypsum replaced to mudstones (cross nicol polarizing microscope) and i) cream colored gypsum rosettes.

Discoidal primary gypsums are observed as crack fill or spear head in mudstone, which range between 0.5 mm and 5 cm in size and vary from white to brown depending on the organic matter content (Figure 3g). These gypsums are observed as substituting gypsum formations replacing the carbonate matrix in petrographic studies (Figure 3h). Gypsums occur in the regression process due to the humic acid-rich groundwater within mud flats. Humic acid is a type of acid, which the bacteria produce microbially under reducing environmental conditions. Then, depending on the increase in temperature and salinity, they form gray gypsum rosettes. These roses vary in size from 0.5 cm to 4 cm.

Massive secondary gypsums have white-cream colored, occasionally gray anhydrite interbands (Figure 4a). In nodular and micro-nodular secondary lithofacies, the diameters of nodules vary between 1-20 cm and sometimes contain chicken wire, enterolithic structures and exhibit diagenetic characteristics that show replacing growth feature within the clay-carbonate matrix (Figure 4b-c-d). In petrographic thin sections the rod-like prismatic anhydrite lats, which replace with micritic matrix in early diagenetic phase in and around the nodules, are observed (Figure 4e). In addition, the areas of bituminization reflecting the reducing environment conditions are observed around the nodules (Figure 4f). The anhydrite lats growing in unconsolidated sediment combine by the effect of temperature and salinity to form anhydrite nodules. These nodules then turn into secondary gypsum in late diagenesis. This lithofacies was generally deposited with laminated secondary gypsums consisting of

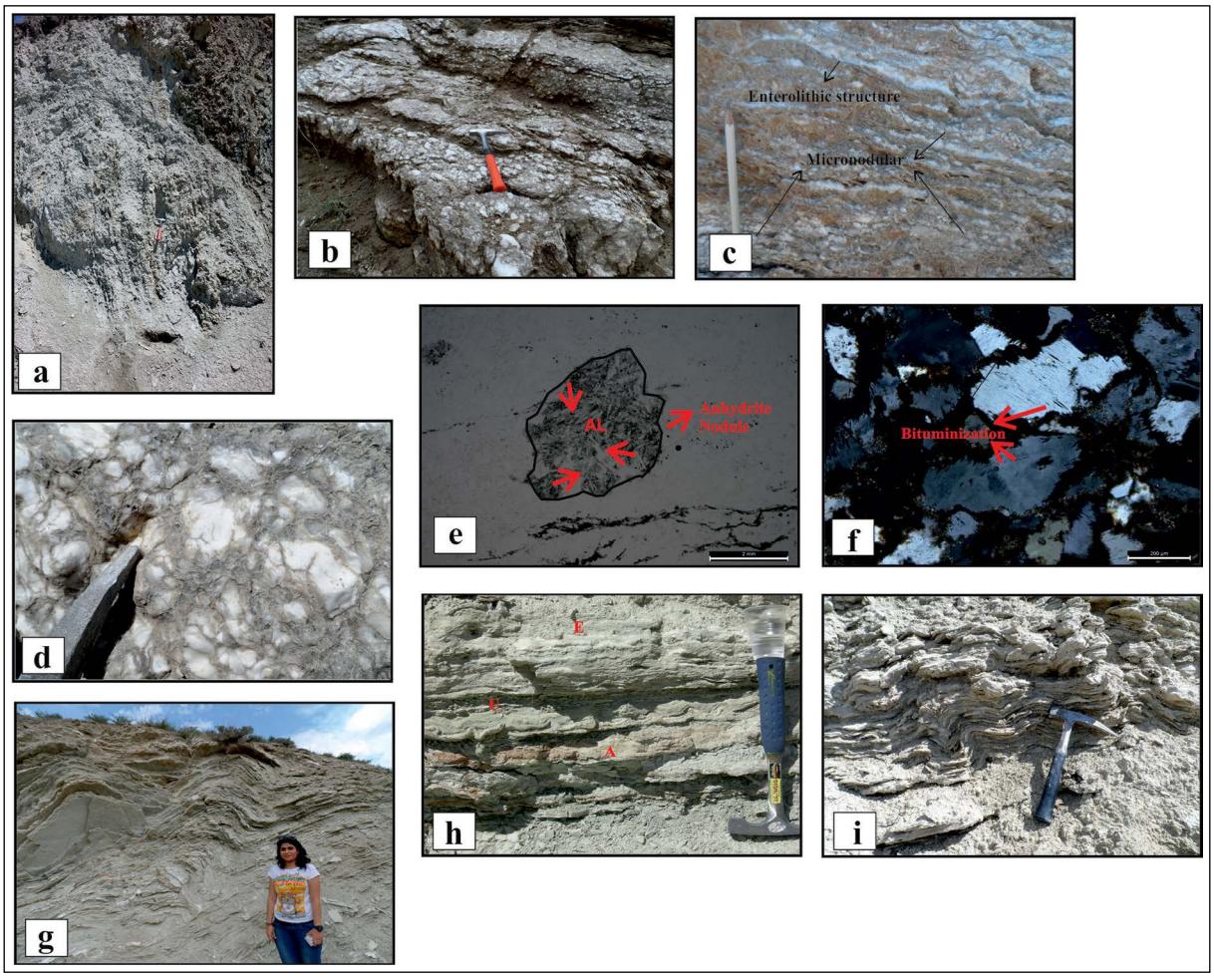

Figure 4-Sedimentological and petrographical images of secondary evaporitic lithofacies. a) Massive gypsum, b) nodular gypsum, c) gypsum containing micronodular and enterolithic structures, d) sedimentary structure showing chicken-wire texture, e) primary prismatic anhydrite lats (AL) within the micritic host sediment, these lats merge into anhydrite nodules in early-to-late diagenesis. f) bituminous areas around nodular gypsum, g) folds to the deformed version due to tectonism within these secondary gypsum, h) enterolithic (E) undulated (U) and alteration levels (A) in laminated gypsum and i) microfolds levels in laminated gypsum.

clayey, carbonated laminated between 0.1 cm and 10 cm. In laminated gypsums, the enterolithic folds, microfolds, creep structures, undulations and alteration interbands are observed (Figure 4g-h). These units to be observed together can be shown as an evidence of transition from lagoon to the coastal sabkha (Hardie and Eugster, 1971). Laminated gypsums are observed in petrographic thin sections as folded and undulated microcrystalline gypsum laminations (Figure 4i). Massive, nodular and laminated lithofacies consists of alabastrine, porphyroblastic, sutured restricted porphyroblastic gypsum textures, and anhydrite relicts (Figure 5a). This is a proof that the previous mineral is anhydrite. Alabastrine texture is seen as a fine-grained texture, which has indefinite, interlocking and undulating extinction in grain boundaries (Figure 5b). Porphyroblastic texture is generally observed with medium to coarse grained, alabastrine texture and the effect of dissolution and recrystallization processes in thin sections is easily observed (Figure 5b). The sutured boundaries in porphyroblastic, secondary gypsums (Figure 5c) indicate that they were formed earlier than alabastrine gypsums (Abdioğlu et al., 2015). Satin spar gypsums observed in both the field observations and thin sections were formed due to the effect of sediment load, hydraulic pressure and dissolution during the transformation of minerals to each other and placed in the form of cutting layers between the cracks or in vertical position (Figure 5d). The hydration channels in petrography are observed in such a way that it has been filled by these gypsums and sometimes as folded along their long axes (Figure

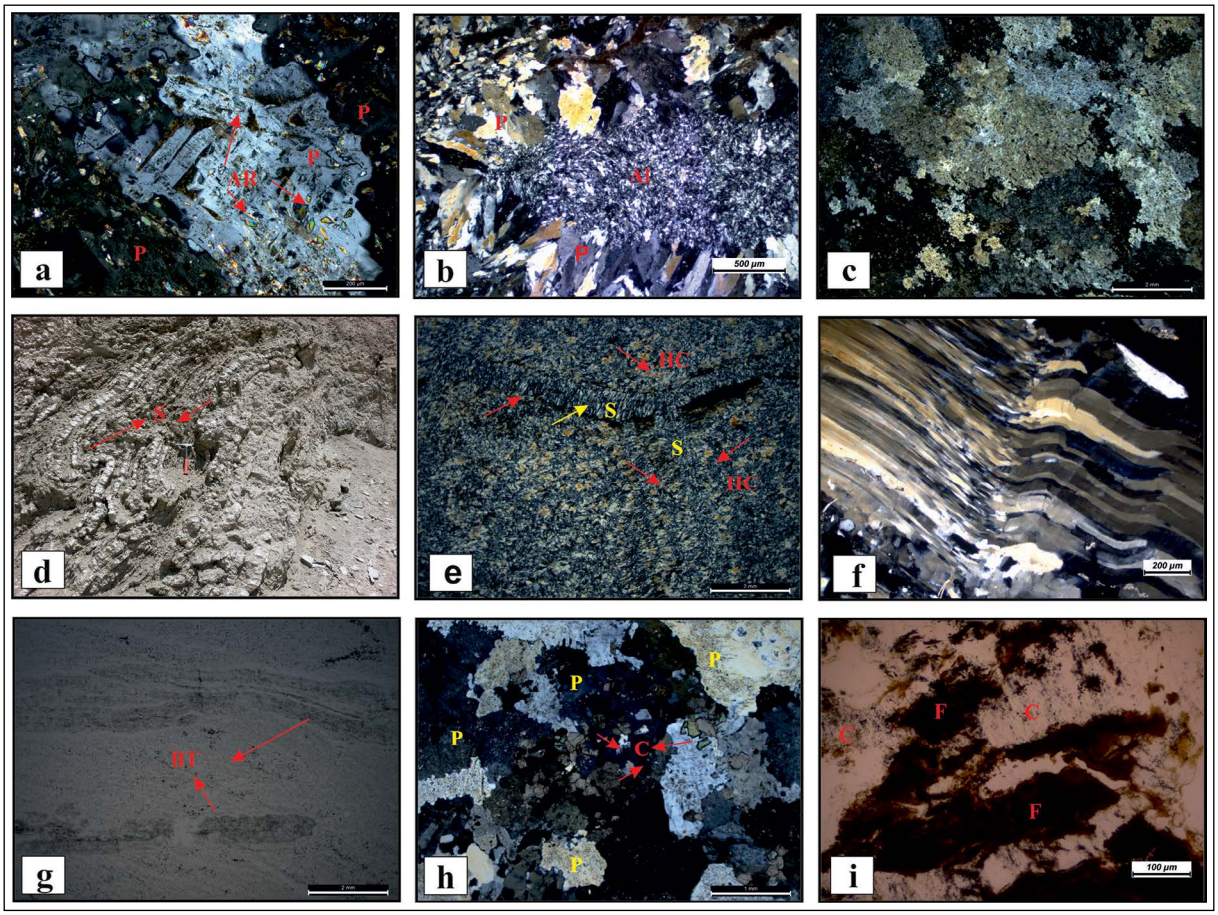

Figure 5- Petrographic images of evaporitic lithofacies. a) Primary anhydrite relicts (AR) in porphyroblastic gypsum (P), (b) alabastrin (Al) and porphyroblastic gypsum (P) textures, c) sutured-bounded porphyroblastic gypsum, d) satin-spar gypsum (S) that fill mud cracks in gypsum, e) fibrous satin-spar gypsum (S) filling the hydration channels (HC), f) curved satin spar gypsum along longaxes. g) traces of bioturbation in laminated microcrystalline gypsum (BT), h) late diagenetic calcite (C) formations in late diagenesis replacing the surface with porphyroblastic (P) secondary gypsum and i) Fe-oxidation (F) and carbonation zones (C) in gypsum.

5e-f). In addition, the bioturbition structures were encountered reflecting some foreshore environments in laminated gypsums showing micro crystalline, alabastrine texture (Figure 5g). In addition, the euhedral, semi-euhedral and anhedral calcite grains and dolomites are frequently observed and calcites are observed as replaced secondary gypsums in the late diagenetic phase (Figure 5h-i).

3.2. Mineralogical Studies

In order to identify some unidentified minerals and textures in petrographic studies, the Scanning Electron Microscope (SEM-EDS) analyses from mineralogical examinations were carried out from different evaporitic lithofacies. As a result of these studies, it was determined that minerals accompanying gypsum and anhydrites were calcite, dolomite, celestine, some clay and siliciclastic grains. Euhedral, hexagonal crystalline dolomite and clay grains are scattered in primary gypsums (Figure 6a). Gypsums are accompanied by some smectite, clay minerals and quartz grains in the syn-sedimentary process. Smectite minerals break away in spaces among nodules and exhibit corn-grain texture and curly appearances (Figure 6b). The euhedral, primary calcite mineral occasionally spreads in these clays (Figure 6b). Parallel laminated, banded and folded gypsum laminations are often observed with the effect of tectonism (Figure 6c). In addition, the siliciclastic authigenic quartz grains are planar surface and are observed in the form of scattered butterfly wings among gypsum crystals (Figure 6d). In addition, white, subhedral to euhedral tabular celestine show

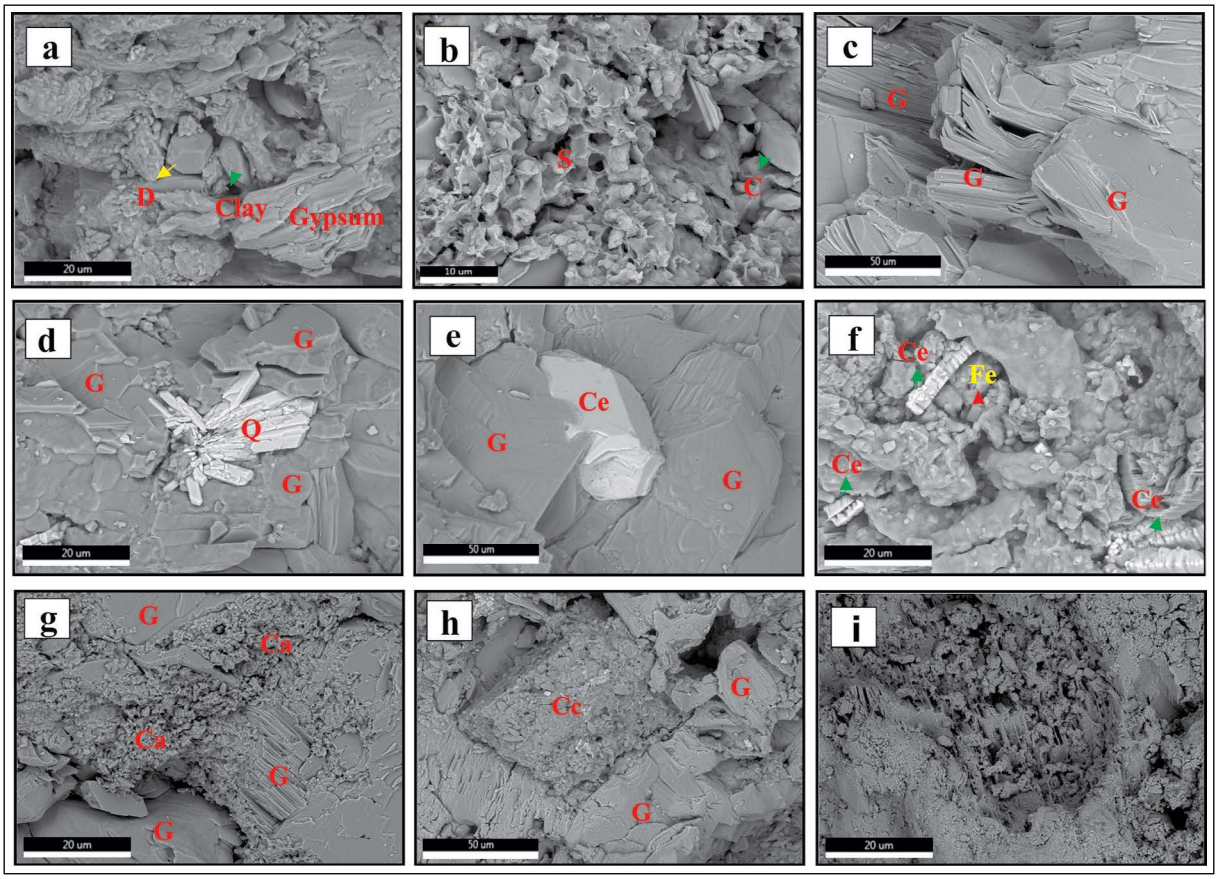

Figure 6- SEM images of evaporitic rocks. a) Euhedral hexagonal dolomite crystal (D) and clay grains during sedimentation with gypsum, b) curly textured smectite group clays (S) and euhedral calcite (C) in gypsum, c) folds and bends in laminated gypsum (G), d) scattered grains of autogenic quartz (Q) in the gypsum (G), e) celestine (Ce) grains replacing gypsum (G) in late diagenesis, f) semi-euhedral-euhedral celestines (Ce) andeuhedral feldspar (Fe) dispersed with in gypsums, g) late diagenetic carbonation (Ca) in gypsum (G), h) calcite coatings (Cc) on gypsum (G) and i) bacterial texture in gypsum.

itself as distributed in secondary gypsums (Figure 6e-f). These grains were replaced by secondary gypsums in late diagenesis. In addition, the late diagenetic carbonations, traces of alteration, calcite coatings and detritic clasts accompany gypsums (Figure 6f-g-h). In some gypsums, the textures showing the bacterial activity were determined (Figure 6i).

3.3. Diagenetic History of the Evaporites

As a result of sedimentological, petrographic and mineralogical studies, the diagenetic history of evaporites in the study area was enlightened (Figure 7). According to this, the calcite is the first mineral that was formed during sedimentation in the basin. Later, it turned into dolomite in very early diagenesis with the circulation of Mg rich waters and increasing salinity and temperature (Önalgil et al., 2015). The primary gypsum crystals (such as; discoidal and gyps-arenite) are formed in displaced character in dolomitic sediment and then turn into anhydrite with increasing salinity in syn-sedimentary to very early diagenetic stage by being dehydrated (Figure 7). These gypsums, which are buried due to sedimentation and lose water in them, were subjected to volumetric shrinkage, compressed and cemented. At this time, the prismatic anhydrite lats growing in the unconsolidated dolomitic sediment during the early diagenesis phase prior to compression were grown and formed anhydrite nodules. As the sedimentation is continuous and pressure increases, these nodules were combined to form chicken-wire and enterolithic structures. These compressed anhydrite nodules at depths were rehydrated in late diagenesis by interacting with groundwater and/or meteoric waters as they exhume under the influence of pressure or tectonism and were transformed into secondary gypsums (alabastrine, porphyroblastic textures) (Figure 7). The primary anhydrite lats in

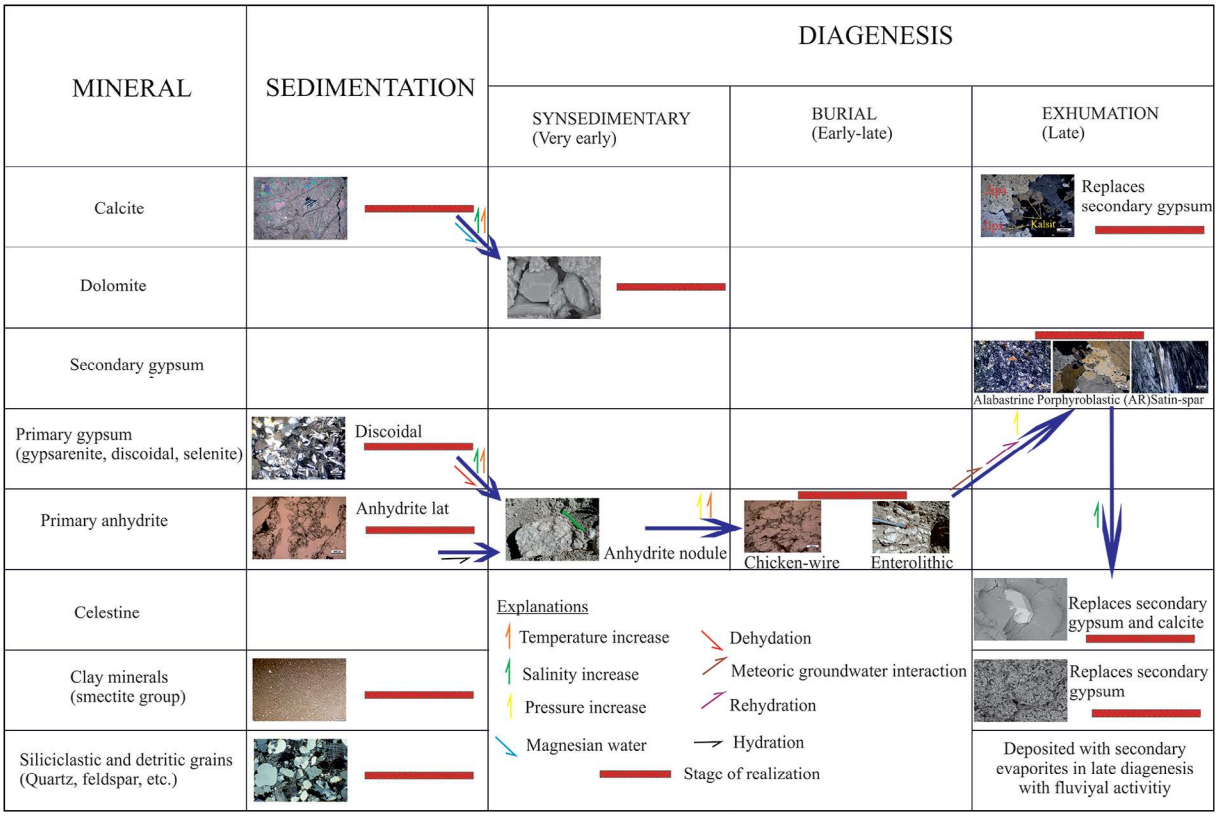

Figure 7-Diagram showing the diagenetic history of evaporites.

micritic carbonate with the presence of anhydrite relicts in secondary gypsums indicate that gypsums were originated from the primary anhydrite (Kinsman, 1966). The satin spar gypsum filling the hydration channels as an indicator of volumetric increase during the gypsum-anhydrite transformation were formed on the surface in late diagenesis (Shearman et al., 1972) (Figure 7). In addition, celestines may have formed during epigenetic hydration events (released diagenetic fluids) that occurred during anhydrite-gypsum transformation (Shearman, 1964; Rosell et al., 1998; Gündoğan et al., 2005; Orti et al., 2014). The dissolved Sr^{2+} in the evaporitic units may have been obtained by the circulation of meteoric or groundwaters, which mixed with Sr-rich fluids like seawater and hydrothermal solutions related to volcanic activity in the region. Sr ions obtained in this way settle in the crystal lattices of gypsums, they replace Ca^{2+}, and lead to the formation of celestine (Ceyhan, 1996). In addition, the diagenetic calcite was replaced by the secondary gypsum lithofacies from the waters released during mineral transformation in the last diagenetic phase. The stream activity in syn-sedimentary and late diagenetic phase caused a large amount of detritic material to be transported into the basin and precipitated with evaporites (Figure 7).

4. Conclusion

Massive, laminated, nodular, discoidal, gyps-arenite and selenitic lithofacies defined by sedimentological and petrographical studies and chicken-wire, enterolithic structures, ripple formations, folds and undulations including the sedimentary structures show that this basin is an isolated shallow water environment extending to the lagoon-sabkha and mud flats. This basin is under the influence of seasonal water level changes (repeating lithofacies in measured stratigraphic sections), tectonism (formation of sedimentary structures), arid climate (presence of smectite mineral) and reducing conditions (bituminization and bacterial activity).

Some of the secondary gypsums were formed by the hydration of anhydrite and the others were formed by the dehydration of primary gypsum and rehydration. Mineralogical studies showed that the minerals accompanying these evaporites were carbonate,

celestine, authigenic clay and siliciclastic grains and the deformation structures were formed on evaporites by the effect of carbonations in the evaporites in late diagenesis, tectonism and diagenesis.

High pH (>7.5), salinity, temperature, organic matter and long arid climatic conditions led to the formation of various and smooth gypsum crystals. In addition, it was noticed that the most important factors in the transformation of minerals in diagenetic processes (early-late) were temperature, pressure, salinity, the interaction with surface and groundwater, diagenetic and hydrothermal solutions. Under these circumstances, the texture, sedimentary structure and mineralogical compositions of the evaporites determined as a result of all these studies showed that they underwent diagenetic stages such as volumetric shrinkage, cementation, replacement, substitution, dissolution and recrystallization.

As a result of these studies, the diagenetic development of the gypsums in the study area was formed as follows; the calcite, dolomite, primary gypsum and anhydrite were transformed to each other in the syn-sedimentary-early diagenetic phase respectively. Later on; the porphyroblastic secondary gypsum, alabastrine secondary gypsum, satin spar gypsum, celestine and calcite minerals were formed in the late diagenetic phase at or near the surface.

Acknowledgements

This study was carried out within the scope of Van Yüzüncü Yıl University Scientific Research Project (No: 2014-MİM-B082). I would like to thank Çetin Yeşilova and Mustafa Açlan for their contributions during field studies. I would also like to thank İbrahim Gündoğan for his assistance in petrographic and mineralogical studies.

References

Abdioğlu, E., Arslan, M., Aydınçakır, D., Gündoğan, İ., Helvacı, C. 2015. Stratigraphy, mineralogy and depositional environment of the evaporite unit in the Aşkale (Erzurum) sub-basin, Eastern Anatolia (Turkey). Journal of African Earth Sciences 111, 100–112.

Akay, E., Bıkan, E., Ünay, E. 1989. Stratigraphy of The Muş Tertiary Basin. Bulletin of The Mineral Research and Exploration 109, 59–76.

Birgili, Ş. 1968. Muş bölgesi 1/25000 ölçekli J48 d3, d4 ve Muş K47 b2 paftalarının detay petrol etüdü hakkında rapor. Maden Tetkik ve Arama Genel Müdürlüğü Rapor No: 1707, Ankara (unpublished)

Ceyhan, F. 1996. Occurence and Origin of Celestite Mineralization Around Sivas. PhD, Cumhuriyet University, Sivas (unpublished).

Dinçer, A. 1969. Muş K47-b3 paftasının jeolojisi. Maden Tetkik ve Arama Genel Müdürlüğü Rapor No: 1997, Ankara (unpublished)

Gündoğan, İ., Önal, M., Depçi, T. 2005. Sedimentology, petrography and diagenesis of Eocene-Oligocene evaporites: the Tuzhisar formation, SW Sivas Basin. Turkish. Journal Asian Earth Science 25, 791–803.

Göncüoğlu, C.M, Turhan, N. 1983. Geology of the Bitlis Metamorphics Belt. Geology of Taurus Belt, International Symposium, 26–29 September 1983, Ankara.

Hardie, L.A., Eugster, H.P. 1971. The depositional environment of marine evaporites: A case for shallow, clastic accumulation. Sedimentology 16, 187–220.

Hüsing, S.K., Zachariasse, W.J., Van Hinsbergen, D.J., Krijgsman, W., İnceöz, M., Harzhauser, M., Mandic, O., Kroh, A. 2009. Oligocene Miocene basin evolution in SE Anatolia, Turkey: constraints on the closure of the eastern Tethys gateway. Geology Sociecty London Special Publication 311, 107–132.

Kendall, A.C. 1978. Facies Models 12: Subaqueous Evaporites. Geoscience 5, 124–138.

Kinsman, D.J.J. 1966. Gypsum andanhydrite of recentage, Trucial Coast, Persian Gulf. Proceedings of the 2nd International Salt Symposium, Cleveland, Ohio, 302–326.

Önalgil, N., Kadir, S., Külah, T., Eren, M., Gürel, A. 2015. Mineralogy, geochemistry and genesis of the modern sediments of Seyfe Lake, Kırşehir, Central Anatolia, Turkey. Journal Afican Earth Science 102, 116–130.

Ortí, F., Pueyo, J.J., Geisler-Cussey, D., Dulau, N. 1984. Evaporitic sedimentation in the coastal salinas of SantaPola (Alicante, Spain). Revista del Instituto de Investigaciones Geologicas 38/39, 169–220.

Orti, F., Perez-Lopez, A., Garcia-Veigas, F., PerezValera, F. 2014. Sulfate isotope compositions ($\delta^{34}S$, $\delta^{18}O$) and strontium isotopic ratios ($^{87}Sr/^{86}Sr$) of Triassic evaporites in the Betic Cordillera (SE Spain). Revista de la Sociedad Geológica de España 27, 79–89.

Perthuisot, J.P. 1980. Sites et processes delaformationd' evaporites dans la natureactuelle. Bull. Cent. Rech.Explor. Elf-Aquitaine 4, 207–233.

Rosell, L., Orti, F., Kasprzyk, A., Playa, E., Peryt, T.M. 1998. Strontium geochemistry of primary gypsum: Messinian of southeastern Spain and Sicily and Badenian of Poland. Journal Sediment. Res. 68, 63–79.

Sakınç, M. 1982. Mollababa-Uruman (Muş ili) yöresinin jeolojisi biostratigrafisi ve paleontolojisi. İstanbul Yerbilimleri 3, 1-2.

Sancay, R.H., Batı, Z., Işık, U., Kırıcı, S., Akça, N. 2006. Palynomorph, foraminifera, and calcareous nanoplankton biostratigraphy of Oligo-Miocene sediments in the Muş Basin, Eastern Anatolia, Turkey. Turkish Journal Earth Science 15, 259–319.

Schreiber, B.C, Freidman, G.M, Decima, A., Schreiber, E. 1976. Depositional environments of upper Miocene (Messinian) evaporite deposits of the Sicilian Basin. Sedimentology 23, 729–760.

Shearman, D.J. 1964. Recent celestine from the sediments of theTrucial Coast of the Persian Gulf. Nature 202 (4930), 385 – 386.

Shearman, D.J., Mossop, G.D., Dunsmore, H., Martin, M. 1972. Origin of gypsum veins by hydraulic fracture. Trans. Inst. Min. Metall. 81, 149–155.

Soytürk, N. 1973. Murat Havzası jeolojisi ve hidrokarbon imkânları. TPAO, Arama Grubu Rap. No. 791, Ankara (unpublished).

Şaroğlu, F. 1986. Doğu Anadolu'nun neotektonik dönemde jeolojik ve yapısal evrimi. Maden Tetkik ve Arama Genel Müdürlüğü Rapor No: 244, Ankara (unpublished).

Şen, S., Antoine, P.O., Varol, B., Ayyıldız, T., Sözeri, K. 2011. Giant rhinoceros Paraceratherium and other vertebrates from Oligocene and Middle Miocene deposits of the Kağızman-Tuzluca Basin Eastern Turkey. Naturwissenschaften 98, 407–423.

Ünal, A. 1970. Muş bölgesi 1/25 000 ölçekli Erzurum J47-C4 Muş K47-b4-cl-e2 paftalarının detay petrol etüdü. Maden Tetkik ve Arama Genel Müdürlüğü Rapor No: 4754, Ankara (unpublished).

Vasconcelos, C., McKenzie, J.A. 1997. Microbialmediation of modern dolomite precipitation and diagenesis under anoxic conditions (LagoaVermelha, Rio De Janeiro, Brazil). Journal of Sedimentary Petrology 67, 378–390.

Warren, J.K. 1982. The hydrological setting, occurrence and significance of gypsum in late Quaternary salt lakes in South Australia. Sedimentology 29, 609–637.

Warren, J.K., Kendall, C.G.S.C. 1985. Comparison of sequnces formed in marine sabkha (subaerial) and salina (subaqueas) settings-modern and ancient. American Association of Geology Bulletin 69, 1013–1023.

Bulletin of the Mineral Research and Exploration

http://bulletin.mta.gov.tr

Rare earth element contents, geochemistry of soil samples between Burdur and Isparta region and assessment of their origin

Ebru TAT[a]* and Mustafa Gürhan YALÇIN[b]

[a]*Kahramanmaraş Provincial Directorate of Disaster and Emergency, Kahramanmaraş*
[b]*Akdeniz University, Faculty of Engineering, Department of Geological Engineering, Antalya*

Research Article

Keywords:
Rare earth element, Geochemistry, Origin, Gölcük Volcanism, Burdur, Isparta.

ABSTRACT

This study was carried out in 5 locations between Burdur and Isparta in the inner southern part of Isparta Bend. The study aims to determine the rare earth element (REE) concentrations in the soil samples collected from the field and to interpret the origin of the high concentrations detected. In this context, a total of 104 samples were collected from Canakli Village (19 samples), Cobanisa Village (34 samples), Kuyubasi Village (17 samples), Kuzca Village (17 samples), and Yilanli Village (17 samples) in the study field. The average ∑REE (La, Ce, Pr, Nd, Sm, Eu, Gd, Tb, Dy, Ho, Er, Tm, Yb, Lu) concentration values of the samples by their locations were determined to be Çobanisa (821.88 ppm) > Yılanlı (723.39 ppm) > Kuzca (692.54 ppm) > Çanaklı (583.46 ppm) > Kuyubaşı (484.04 ppm). The average light rare earth element (LREEs) concentration (such as La 229 ppm, Ce 378 ppm) of the samples collected from all locations is higher than the average rare earth element concentration in the Earth's crust. According to the Chondrite-normalized Rare Earth Elements diagram, the distributions of the rare earth elements in these 5 locations were determined to be very similar and the high concentrations were considered to occur under similar conditions or originated from similar sources. In this context, based on the idea that Gölcük Volcanism may be the source of high concentrations, the rare earth element concentrations of Gölcük Volcanism in the northwest of the zone were compared to those taken from the study area and the values were found to be consistent with each other.

Received Date: 15.05.2019
Accepted Date: 11.02.2020

1. Introduction

Actually, the rare earth elements are not as scarce as they are expressed. They have been named in this way because they were defined between 18th and 19th centuries and they were rare compared to other earth elements such as calcium oxide and magnesium oxide (US Geological Survey, 2002). Rare earth elements (RREs) with atomic numbers between 57 (Lanthanum) and 71 (Lutetium) in the Periodic Table show similar physical and chemical properties. This similarity is particularly related to their +3 atomic charge and electron configuration (Verplanck et al., 1999). Rare earth elements are commonly classified as Light Rare Earth Elements (LREE) and Heavy Rare Earth Elements (HREE) according to their atomic weights (Sen et al., 2012). The light rare earth elements (LREEs) have relatively enriched the Earth's crust (Alfaro et al., 2018).

The great interest in rare earth elements in geochemical studies is due to the chemical properties

Citation info: Tat, E., Yalçın, M. G. 2020. Rare earth element contents, geochemistry of soil samples between Burdur and Isparta region and assessment of their origin. Bulletin of the Mineral Research and Exploration 162, 93-102. https://doi.org/10.19111/bulletinofmre.687929

* *Corresponding author: Ebru TAT, ebrupaksu@gmail.com*

of these elements. Because the rare earth elements have been enriched in certain areas due to their chemical properties (Budakoğlu et al., 2015). Therefore, these elements, which can provide precise analyses at very low concentrations of single or a few elements, can also provide hints about the origin of the rock (Henderson, 1984).

Usually, the rare earth elements are associated primarily with alkali rock complexes, carbonatites, and placers, and secondarily pegmatites and various metamorphic rocks. Therefore, these geological rock groups are usually taken into account when researching rare earth elements. However, limited scientific studies have been carried out on volcanic lands (Price and Taylor, 1973; Joron et al., 1991; Fulignati et al., 1999; Moller et al., 2003; Roy et al., 2010; Sen et al., 2012; Kaçmaz, 2016; Rahimi et al., 2016; Bragin et al., 2017; Inguaggiato et al., 2017; Carvalho et al., 2019). In the literature of various disciplines, there are scientific studies related to the study area and Taurus region (Blumenthal, 1963; Dumont, 1976; Gutnic, 1977; Poisson, 1977; Koçyiğit, 1981; 1983; Poisson et al., 1984; Şenel et al., 1992; Karaman, 1994; Görmüş and Özkul, 1995; Yağmurlu et al., 1997; Savasçın and Oyman, 1999; Francalanci et al., 2000; Piper et al., 2002; Poisson et al., 2003; Elitok and Görmüş, 2011; Platevoet et al., 2014; Budakoğlu et al., 2015). Only a scientific study conducted by Simandl (2014) on the "market of rare earth elements" provides information about the rare earth elements in Çanaklı Village. A table in this study reveals that the rare earth elements concentration in Çanaklı Village ranges between 100-1000 tons and 10-100 wt%, however, there is no more detail in this study.

Considering their usage as raw materials (in electronic devices, green energy, medical technology, telecommunication and defense industry, production of high-technology products, etc.), the studies on rare earth elements are of great importance. In this context, the study aims to examine REE contents and enrichment conditions in samples collected from 5 locations determined between Burdur and Isparta, which have not been scientifically studied before. Furthermore, interpretations of the origins of these REEs have been also provided. The results of the analysis of the samples collected from these five locations were compared to each other, as well as, the data of Gölcük Volcanism, which has been considered to be the source of high concentrations and the relationship between them evaluated statistically.

2. Typical Geological Features

Extensive geological studies have been carried out in the study area located between the provinces of Isparta and Burdur (Blumenthal, 1963; Dumont, 1976; Gutnic, 1977; Koçyiğit, 1981, 1983; Poisson et al., 1984; Karaman, 1994). The area between Burdur Fault on the west and Aksu Thrust on the east in the northern part of the Gulf of Antalya was defined as Isparta Bend by Blumenthal (1963). The origin of this bend was a controversial issue for a long time. But later, it has been suggested that it represents a part separated by the break of the northeastern part of Gondwana at the beginning of the Permian-Triassic period, and it is a part of the Gondwana Supercraton (Piper et al., 2002; Poisson, 2003).

The study area and its vicinity have been evaluated in four main units in general. The oldest of these major four units that represent the study area is the unit consisting of limestones, neritic limestones, basalt, tuff, tuffite, gabbro, diabase, harzburgite blocks containing carbonate formation of Permian age and radiolarite and chert deposited in the Triassic-Cretaceous period (Şenel, 1997; Cox et al., 2013). The largest spread area in the region belongs to the Beydaglari Carbonate Platform from Mesozoic age. The youngest unit in the region is the unit with molasses character belonging to Aksu formation (Poisson, 1977) from Tortonian age (Dumont, 1976; Şenel et al., 1992, 1996). The alluviums in most of the quaternary deposits are represented by unconsolidated tuffs (Cox et al., 2013) (Figure 1). It has been determined that the sample materials are not tuff, but are partly alluvium or ground cover derived from tuffs. In general, it can be stated that the samples are alluviums containing tuff fragments.

One of the important factors affecting the geomorphology and geochemical structure of the region is Gölcük Volcanism. This wide area, which covers Isparta and its vicinity, was under the influence of compression tectonics until the Upper Miocene period and the pulling tectonics in the later periods (Karaman, 1994). In this context, Gölcük Volcanism, which was affected by the post-Miocene stress regime, is volcanism related to tectonism (Elitok and

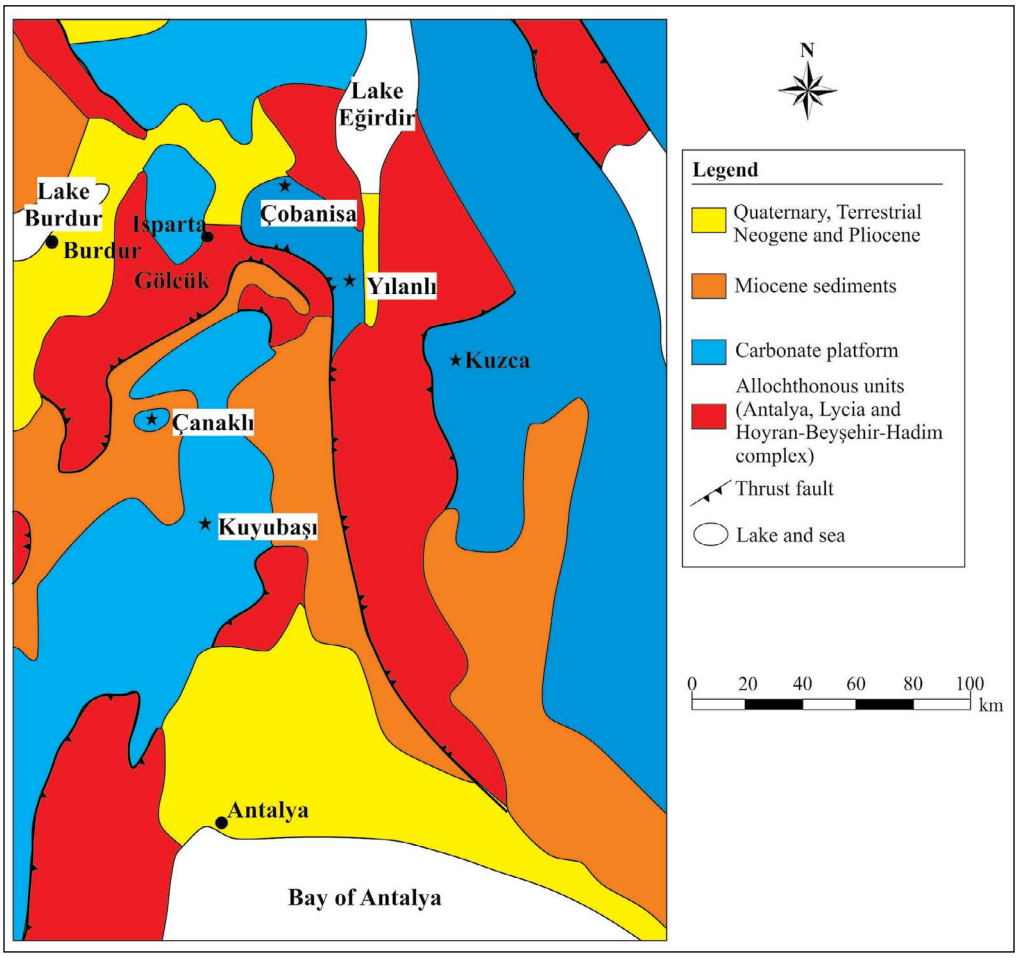

Figure 1- Geological map of the study area (see Cox et al., 2013).

Görmüş, 2011). The products of Gölcük Volcanism from Pliocene age (Savasçın and Oyman, 1998) are in traki-andesitic composition (Görmüş and Özkul, 1995; Yağmurlu et al., 1997; Nemec and Kazancı, 1999; Francalanci et al., 2000) and they are observed in Isparta province and its vicinity.

3. Material and Method

The study area covers 5 locations within the boundaries of the Isparta and Burdur provinces. These locations Çanaklı, Çobanisa, Kuyubaşı, Kuzca, and Yılanlı. A total of 104 samples (i.e. 17 samples from Kuyubaşı, 17 samples from Kuzca 17, 17 samples from Yılanlı, 19 samples from Çanaklı, and 34 samples from Çobanisa) were collected from these locations. The samples were taken from a depth of approximately 10-15 cm, similar to each other. The samples were screened using a 0.125 mm sieve, thus, the coarse grain contents were removed. The samples collected from the field were brought to Mine Deposits and Geochemistry Laboratory at Akdeniz University Faculty of Engineering and prepared for the chemical analysis. The samples were divided into groups of 17 samples and kept in an oven at 105°C for 24 hours.

The samples were weighed before and after the drying process and as a result, the loss on ignition (LOI) value was calculated for each sample. The samples were taken from the oven and ground; the mortar was washed with distilled water before sample grinding each sample against artificial contamination. The samples taken from the grinder were filtered through a 0.063-micron filter and filled in packages of about 25 g; then, the samples were sent to be analyzed in ACME Analytical Laboratories. Inductive Conjugate Plasma - Mass Spectrometry (ICP-MS) method was used in the geochemical analysis of the ground and packaged samples.

4. Findings

4.1. Geochemical Analysis

In this study, the geochemical structure of the rare earth elements of the samples collected from five locations in the Burdur and Isparta zone were examined. The samples were taken from the upper horizon. The average rare earth element contents of the samples are shown in table 1. The concentration values of the locations are close to each other. The following average total rare earth element concentration values were determined in the order: Çobanisa (822.82 ppm) > Yılanlı (736.45 ppm) > Kuzca (692.14 ppm) > Çanaklı (584.21 ppm) > Kuyubaşı (483.82 ppm). The location with the highest ∑LREE concentration is Çobanisa whereas the location with the lowest value is Kuyubaşı. Kuzca and Yılanlı locations have been relatively enriched by HREEs.

The average concentration values in the study area are quite higher than the rare earth element concentration values in the earth's crust. The rare earth element enrichments can be observed in these locations in the study area. The rare earth element concentration of the products of Gölcük Volcanism (GV), which is the possible source of this enrichment in the vicinity (Platevoet et al., 2014), and the same element concentrations in the region between Burdur and Isparta are quite close to each other.

REE values of the samples from earth crust, Burdur – Isparta zone, and Gölcük Volcanism were normalized according to the chondrite values determined by Anders and Grevesse (1989) (Figure 2). The samples collected from Burdur and Isparta show almost the same trend as the samples from Gölcük Volcanism. However, samples collected from Burdur and Isparta were determined to be enriched in terms of heavy rare earth elements (HREE) compared to samples from Gölcük Volcanism. On the other hand, it can be suggested that the samples from Burdur-Isparta and Gölcük Volcanism were determined to be enriched in terms of light rare earth elements (LREE) compared to the earth crust.

Figure 3 shows the bar charts in which the REE contents of the samples collected from Burdur and Isparta are compared to the samples from the earth's crust and Gölcük Volcanism. The REE concentration values of the samples from the Burdur-Isparta zone are higher than the concentration values of the

Table 1- Average rare earth element concentrations (ppm) of samples taken from the study area, and the samples from earth crust, and Gölcük Volcanism (GV).

	Çanaklı	Çobanisa	Kuyubaşı	Kuzca	Yılanlı	Ortalama	Earth Crust (USGS 2014)	Gölcük Volcanism (GV) (Platevoet et al.. 2014)
La	161	229	123	176	181	174	39	192.78
Ce	270	378	210	312	340	302	66.5	341.82
Pr	25.8	38.1	23.3	33.2	33.6	30.8	9.2	33.9
Nd	86.4	128	82.2	115	117	105.72	41.5	117.67
Sm	12.4	17.6	12.9	17.4	17.2	15.5	7.05	16.45
Eu	3.05	4.24	3.01	4.02	4.04	3.672	2	4.25
Gd	9.07	11.4	10	12.5	11.9	10.974	6.2	9.16
Tb	1.17	1.3	1.38	1.6	1.5	1.39	1.2	1.09
Dy	6.27	6.62	7.56	8.79	7.81	7.41	5.2	4.98
Ho	1.18	1.13	1.4	1.54	1.41	1.332	1.3	0.75
Er	3.46	3.24	4.01	4.42	4	3.826	3.5	2.09
Tm	0.51	0.48	0.6	0.66	0.6	0.57	0.52	0.29
Yb	3.38	3.22	3.86	4.35	3.89	3.74	3.2	1.95
Lu	0.52	0.49	0.6	0.66	0.6	0.574	0.8	0.3
∑HNYE	558.65	794.94	454.41	657.62	704.74	631.69	165.25	706.87
∑ANYE	25.56	27.88	29.41	34.52	31.71	29.82	21.92	20.61
∑NYE	584.21	822.82	483.82	692.14	736.45	661.51	187.17	727.48

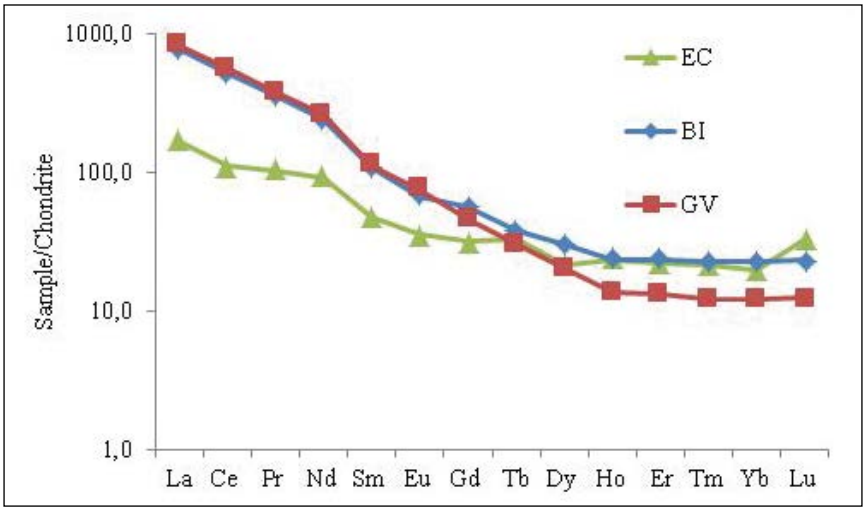

Figure 2- Chondrite-normalized REE diagram (Anders and Grevesse 1989) of the samples from Earth's Crust (EC), Burdur-Isparta (BI), and Gölcük Volcanism (GV).

samples from the earth's crust in terms of all elements except for Lu and Ho. The concentration values of La, Ce, Pr, Nd, Sm, Eu are significantly higher than the concentration values of the samples from the earth's crust and other examples. It can be suggested that these samples had an enrichment in terms of the light rare earth elements. Also, these graphics are consistent with the diagram comparing chondrite-normalized values.

Figure 4 shows the chondrite-normalized REE diagram of the locations between Burdur and Isparta zone where the samples were collected from. The REE distributions of the locations in the zone are quite similar. It can be suggested that these soils developed on the same bedrock underwent similar conditions. The concentration values of light rare earth elements (LREE) are higher than those of heavy rare earth elements (HREE) at all locations.

The trace element values of the samples from Çanaklı, Çobanisa, Kuyubaşı, Kuzca and Yılanlı were normalized according to the chondrite values determined by McDonough and Sun (1995) (Figure 5). The rare earth elements tend to be LREE > HREE. It is a typical trend for the soil samples (Aide and Aide, 2012). In this chondrite-normalized diagram, it was observed that the light rare earth elements were remarkably enriched in the samples from all of the locations. Also, this diagram shows a sharp positive anomalies of Rb, Nb, Sr, Zr, and Y elements in all samples likewise.

5. Discussion

There are unconsolidated tuffs in the zone between Burdur and Isparta (Cox et al., 2013). The covered units in the studied five locations are alluviums on the carbonated rocks. However, these alluviums are not the result of the decomposition of the carbonate rocks. They are considered to form by the tuffs, their fragments, and decomposition or weathering of them carried from another place. In general terms, they can be defined as alluvium placers containing tuff fragments. In the study area, it was observed that the study locations which are far from each other are quite similar in terms of the properties of basement rocks, geographical structure, and their location in the basin. The similarity of these properties indicates that the conditions enriching the REEs, which were placed secondarily, reflect the similar environmental conditions.

However, it has been observed that there is a regional difference in the distribution of REE concentration values. When the concentration values of these elements are compared, it can be seen that the northern part of the study area contains higher values of concentrations, whereas, the southern parts contain lower values. This indicates that the source causing REE enrichment is in the northern parts of the study area. The fact that the element contents of the samples from the study area show a decreasing trend from north to south suggests that the source of this enrichment is the Gölcük Volcanism, which is located in the northwest of the study area.

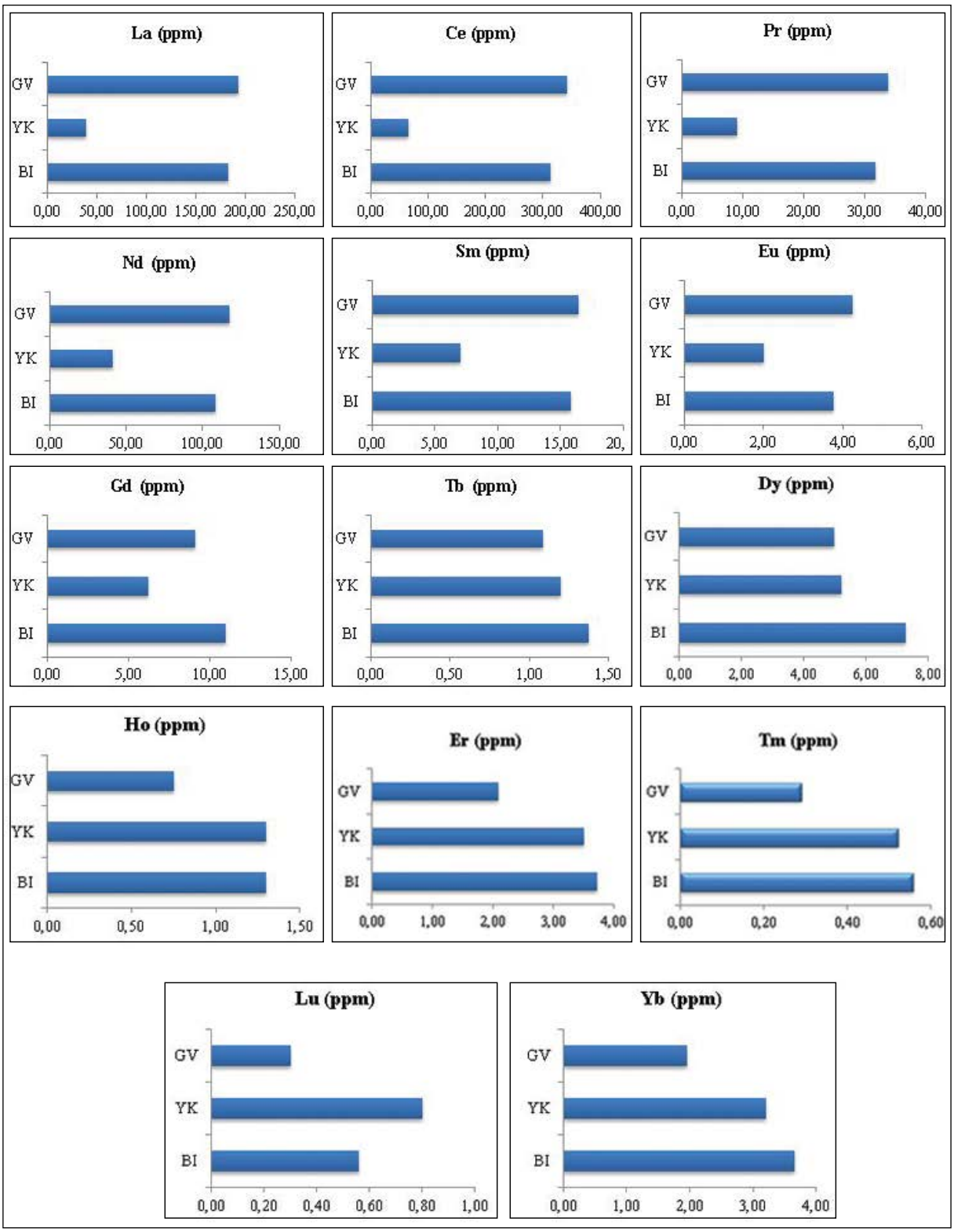

Figure 3- Rare earth element concentration values of the samples from Earth's Crust (EC), Burdur-Isparta (BI), and Gölcük Volcanism (GV).

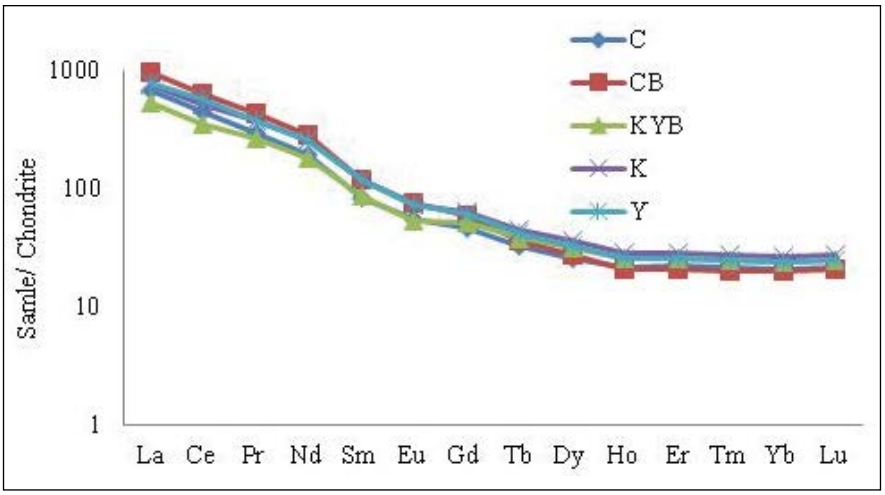

Figure 4- Chondrite-normalized Rear Earth Element Diagram of the samples from Çanaklı (C), Çobanisa (CB), Kuyubaşı (KYB), Kuzca (K) and Yılanlı (Y).

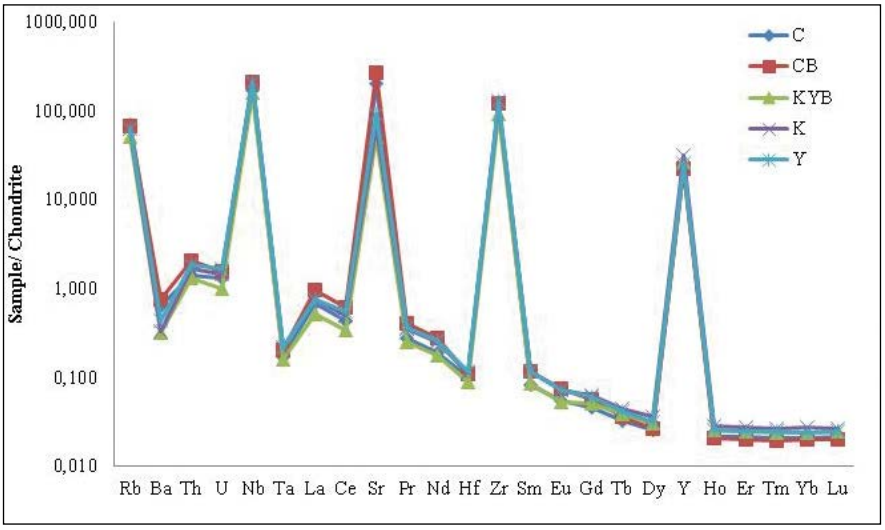

Figure 5- Chondrite-normalized trace and REE diagram (McDonough and Sun, 1995) of the samples from Çanaklı (C), Çobanisa (CB), Kuyubaşı (KYB), Kuzca (K) and Yılanlı (Y).

It has been stated that the origin of rare earth elements in placers in the Çanaklı (Burdur) location is the Pliocene Gölcük alkaline volcanism which is located approximately 8 km west of this area (http://www.eurare.eu/countries/turkey.html).

6. Conclusion

The REE contents of Kuyubaşı and Çanaklı locations in the boundary of Burdur province and Çobanisa, Kuzca, and Yılanlı locations in the boundary of Isparta province have gained importance for the first time with this study. Considering the concentration values of REEs, it is understood that Çanaklı, Çobanisa, Kuyubaşı, Kuzca, and Yılanlı locations have anomaly values. Among these 5 locations, for which element contents and anomaly conditions were determined, the highest concentration value was observed in the samples collected from Çobanisa. However, the samples collected from Kuyubaşı location showed the lowest concentration values. In these samples, the light rare earth elements (LREE) showed higher concentration values than the heavy rare earth elements (HREE), which is a typical

characteristic. This is a typical characteristic of the soil samples.

In the chondrite-normalized trace element diagram, Rb, Nb, Sr, Zr, and Y elements show sharp positive anomalies. The positive correlation of the same elements in all samples from the study area shows similar anomalies. The positive correlation of the samples collected from the carbonated rocks and the similar anomalies presented by the discordant elements may have occurred as a result of their reaction with hydroxide minerals such as Fe and Mn and after the weathering of the minerals. The thermodynamic conditions related to the solubility of these elements weathered from the minerals may have revealed the anomaly and positive correlation of the elements.

It has been determined that the REE values of the samples collected from the study area and Gölcük Volcanism are consistent with each other. The tuff fragments and some of the weathered materials observed in the alluviums where the samples were collected are thought to be the products of the Gölcük Volcanism. Therefore, it can be suggested that the origin of REE observed in the study area is not of the primary bed type but they occurred secondarily in alluvial placers.

References

Aide, M.T., Aide, C. 2012. Rare earth elements: their importance in understanding soil genesis. ISRN Soil Science 2012.

Alfaro, M.R., do Nascimento, C.W.A., Biondi, C.M., da Silva, Y.J.A.B., da Silva, Y.J.A.B., de Aguiar Accioly, A.M., Montero, A., Ugerto, O. M., Estevez, J. 2018. Rare-earth-element geochemistry in soils developed in different geological settings of Cuba. Catena 162, 317-324.

Anders, E., Grevesse, N. 1989. Abundances of the elements: Meteoritic and solar. Geochimica et Cosmochimica acta 53(1), 197-214.

Blumenthal, M. 1963. Le systeme structural du Taurus sud-anatolien, In Livre a'memoire du Professeur P. Fallot. Mem Soc Geol Fr 2, 611-662.

Bragin, I.V., Chelnokov, G.A., Chudaev, O.V., Kharitonova, N.A. 2017. Fractionation of rare-earth elements in surface streams of Baransky volcano (Etorofu, Southern Kuriles). Procedia Earth and Planetary Science 17, 45-48.

Budakoğlu, M., Abdelnasser, A., Karaman, M., Kumral, M. 2015. The rare earth element geochemistry on surface sediments, shallow cores and lithological units of Lake Acıgöl basin, Denizli, Turkey. Journal of Asian Earth Sciences 111, 632-662.

Carvalho, L., Monteiro, R., Figueira, P., Mieiro, C., Pereira, E., Magalhães, V., Pinheiro, L., Vale, C. 2019. Rare earth elements in mud volcano sediments from the Gulf of Cadiz, South Iberian Peninsula. Science of The Total Environment 652, 869-879.

Cox, J.J., Masun, K.M., Fayram, T. 2013. Technical report on the Aksu Diamas rare earth element and minor metals, Isparta district, Southwest Turkey. AMR Technical Report No: 43-101, Canada

Dumont, J.F. 1976. La Courbure D'Isparta Et L'origine Des Nappes D'Antalya; Hypothese D'un Decrochement Majeur, L'accıdent Trans-Taurique, Qui A Dedouble Le Dispositif Structural Taurique Etabli Par La Tectogenese Du Cretace Superieur. Bulletin of the Mineral Research and Exploration 86, 56-67.

Elitok, Ö., Görmüş, M. 2011. Isparta ve Jeoloji; Gölcük volkanizması (Isparta) ve çevresel sorunlar. SDUGEO Dergi 2 (1), 32-43.

Francalanci, L., Innocenti, F., Manetti, P., Savasçin, M.Y. 2000. Neogene alkaline volcanism of the Afyon-Isparta area, Turkey: petrogenesis and geodynamic implications. Mineralogy and Petrology 70(3-4), 285-312.

Fulignati, P., Gioncada, A., Sbrana, A. 1999. Rare-earth element (REE) behaviour in the alteration facies of the active magmatic–hydrothermal system of Vulcano (Aeolian Islands, Italy). Journal of Volcanology and Geothermal Research 88(4), 325-342.

Görmüş, M., Özkul, M. 1995. Gönen-Atabey (Isparta) ve Ağlasun (Burdur) Arasındaki Bölgenin Stratigrafisi. Süleyman Demirel Üniversitesi Fen Bilimleri Enstitüsü Dergisi 1, 43-64.

Gutnic, M. 1977. Géologie du Taurus Pisidien au nord d'Isparta (Turquie).(Principaux résultats extraits des notes de M. Gutnic entre 1964 et 1971 par O. Monod.). Univ. Paris-Sud, Faculté des Sciences Centre d'Orsay.

Henderson, P.A.U.L. 1984. General geochemical properties and abundances of the rare earth elements. In Developments in Geochemistry 2, 1-32.

http://www.eurare.eu/countries/turkey.html, REE Mineralisation in Turkey. (n.d.). Retrieved January 22, 2020, from http://www.eurare.eu/countries/turkey.html

Inguaggiato, C., Burbano, V., Rouwet, D., Garzón, G. 2017. Geochemical processes assessed by Rare Earth Elements fractionation at "Laguna Verde" acidic-sulphate crater lake (Azufral volcano, Colombia). Applied Geochemistry 79, 65-74.

Joron, J.L., Schiano, P., Turpin, L., Treuil, M., Gisbert, T., Leotot, C., Brousse, R. 1991. Exceptional rare earth element enrichments in Tahaa volcano (French Polynesia). Comptes Rendus Académie des Sciences 523-530.

Kaçmaz, H. 2016. Major, trace and rare earth element (REE) characteristics of tuffs in the Yenice-Saraycık area (Demirci, Manisa), Western Anatolia, Turkey. Journal of Geochemical Exploration 168, 169-176.

Karaman, M.E. 1994. Isparta-Burdur arasının jeolojisi ve tektonik özellikleri. Türkiye Jeoloji Kurumu Bülteni 37(2), 119-134.

Koçyiğit, A. 1981. Isparta Büklümü'nde (Batı Toroslar) Toros Karbonat Platformunun Evrimi. Türkiye Jeoloji Kurumu Bülteni 24, 15-23.

Koçyiğit, A. 1983. Hoyran gölü (Isparta Büklümü) dolayının tektoniği. Türkiye Jeoloji Kurumu Bülteni 26, 1-10.

McDonough, W.F., Sun, S.S. 1995. The composition of the Earth. Chemical Geology 120(3-4), 223-253.

Möller, P., Dulski, P., Morteani, G. 2003. Partitioning of rare earth elements, yttrium, and some major elements among source rocks, liquid and vapor of Larderello-Travale Geothermal Field, Tuscany (Central Italy). Geochimica et Cosmochimica Acta 67(2), 171-183.

Nemec, W., Kazancı, N. 1999. Quaternary colluvium in west-central Anatolia: sedimentary facies and palaeoclimatic significance. Sedimentology 46(1), 139-170.

Piper, J.D., Gürsoy, H., Tatar, O., İşseven, T., Koçyiğit, A. 2002. Palaeomagnetic evidence for the Gondwanian origin of the Taurides and rotation of the Isparta Angle, southern Turkey. Geological Journal 37(4), 317-336.

Platevoet, B., Elitok, Ö., Guillou, H., Bardintzeff, J.M., Yağmurlu, F., Nomade, S., Poisson, A., Deniel,C., Özgür, N. 2014. Petrology of Quaternary volcanic rocks and related plutonic xenoliths from Gölcük volcano, Isparta Angle, Turkey: Origin and evolution of the high-K alkaline series. Journal of Asian Earth Sciences 92, 53-76.

Poisson, A. 1977. Recherches géologiques dans les Taurides occidentales (Turquie). Universite de Paris-Sud (Centre D'orsay).795 p.

Poisson, A., Akay, E., Dumont, J. F., Uysal, Ş. 1984. The Isparta Angle (western Taurides-Turkey): a Mesozoic paleorift. Geology of Taurus Belt: Proceedings Int. Sym. 26-29.

Poisson, A., Yağmurlu, F., Bozcu, M., Şentürk, M. 2003. New insights on the tectonic setting and evolution around the apex of the Isparta Angle (SW Turkey). Geological Journal 38(3-4), 257-282.

Price, R.C., Taylor, S.R. 1973. The geochemistry of the Dunedin volcano, east Otago, New Zealand: Rare earth elements. Contributions to Mineralogy and Petrology 40(3), 195-205.

Rahimi, E., Maghsoudi, A., Hezarkhani, A. 2016. Geochemical investigation and statistical analysis on rare earth elements in Lakehsiyah deposit, Bafq district. Journal of African Earth Sciences 124, 139-150.

Roy, P.D., Morton-Bermea, O., Hernández-Álvarez, E., Pi, T., Lozano, R. 2010. Rare earth element geochemistry of the Late Quaternary tephra and volcano-clastic sediments from the Pachuca sub-basin, north-eastern Basin of Mexico. Geofísica Internacional 49(1), 3-15.

Savaşcın, M.Y., Oyman, T. 1998. Tectono-magmatic evolution of alkaline volcanics at the Kırka-Afyon-Isparta structural trend, SW Turkey. Turkish Journal of Earth Sciences 7(3), 201-214.

Simandl, G.J. 2014. Geology and market-dependent significance of rare earth element resources. Mineralium Deposita 49(8), 889-904.

Şen, P., Kuşcu, E., Ak, S. 2012. Nadir toprak elementler, özellikleri, cevherleşmeleri ve Türkiye nadir toprak element potansiyeli. Maden Tetkik ve Arama Genel Müdürlüğü Doğal Kaynaklar ve Ekonomi Bülteni 13: 1-9.

Şenel, M. 1997. Türkiye Jeoloji Haritaları Isparta K12 Paftası, Maden Tetkik ve Arama Genel Müdürlüğü No: 2, Ankara.

Şenel, M., Dalkılıç, H., Gedik, İ., Serdaroğlu, M., Bölükbaşı, A.S., Metin, S., Esentürk, K., Bilgin, A.Z., Uğuz, F., Korucu, M., Özgül, N. 1992. Eğirdir Yenişarbademli-Gebiz ve Geriş-Köprülü (Isparta/Antalya) Arasında Kalan Alanların Jeolojisi: Maden Tetkik ve Arama Genel Müdürlüğü Rapor No: 9390, 559 s., Ankara (unpublished).

Şenel, M., Gedik, İ., Dalkılıç, H., Serdaroğlu, M., Bilgin, A. Z., Uğuz, M. F., Bölükbaşı, A.S., Korucu, M., Özgül, N. 1996. Isparta büklümü doğusunda, otokton ve allokton birimlerin stratigrafisi (Batı Toroslar). Bulletin of the Mineral Research and Exploration 118, 111-160.

US Geological Survey, 2002. Rare Earth Elements: Critical Resources for High Technology. USGS Fact Sheet 087-02.

US Geological Survey, 2014. Rare Earth Elements – Vital to Modern Technologies and Lifestyles USGS Fact Sheet 3078.

Verplanck, P.L., Nordstrom, D.K., Taylor, H.E. 1999. Overview of rare earth element investigations in acid waters of US Geological Survey abandoned mine lands watersheds. US Geol. Surv. Wat. Resourc. Invest. Rep. 83-92.

Yağmurlu, F., Savaçcın, Y., Ergün, M. 1997. Relation of alkaline volcanism and active tectonism within the evolution of the Isparta Angle, SW Turkey. The Journal of Geology 105(6), 717-728.

Bulletin of the Mineral Research and Exploration

http://bulletin.mta.gov.tr

Mineralogical characteristics of metamorphic massif units outcropping in Göksun, Afşin and Ekinözü (Kahramanmaraş) region

Deniz HOZATLIOĞLU[a*], Ömer BOZKAYA[b], Hüseyin YALÇIN[a] and Hüseyin YILMAZ[c]

[a]*Department of Geological Engineering, Faculty of Engineering, Sivas Cumhuriyet University, Sivas, Turkey*
[b]*Department of Geological Engineering, Faculty of Engineering, Pamukkale University, Denizli, Turkey*
[c]*Department of Geological Engineering, Faculty of Engineering, Sivas Cumhuriyet University, Sivas, Turkey*

Research Article

Keywords:
Southeast Anatolian Metamorphic Massifs, Phyllosilicate mineralogy, Metamorphism, XRD.

ABSTRACT

This study aims to investigate and correlate the mineralogical-petrographic characteristics of Metamorphites in Göksun, Afşin and Ekinözü in the Southeast Anatolian Metamorphic Massifs. In this context, the optical microscopy and XRD investigations were performed on several samples. Göksun Metamorphites are constituted by phyllite, calcphyllite, marble and they contain mainly calcite, dolomite, quartz, feldspar, phyllosilicate. KI and b-cell dimension data reflect high anchizone-epizone and medium pressure conditions. Afşin Metamorphites are represented by phyllite, calcphyllite, calcschist, micaschist, amphiboleschist, marble. Phyllosilicates have consisted of illite/mica, IIb chlorite, mixed-layers, smectite. KI and b-cell dimension data correspond to the subgreenschist-greenschist facies conditions. Ekinözü Metamorphites are made of chloriteschist, amphiboleschist, micaschist, micagneiss in lower parts, while calcitic and/or dolomitic marbles are present in the upper parts. Mica is dioctahedral and trioctahedral, whereas chlorite tends to be trioctahedral. Based on mineral associations, Ekinözü Metamorphites belong to amphibolite facies in the lower parts, but the greenschist facies conditions at the upper parts. The coarse-grained biotite, muscovite and chlorite are accompanied by mixed-layers. According to mineral composition and degrees of metamorphism, Göksun and Afşin Metamorphites are similar to the Keban and Malatya Metamorphites; however, Ekinözü Metamorphites to Pütürge Metamorphites. The data show that metamorphics in the western extension of the Southeast Anatolian Metamorphic Massifs have different origin and/or lithologies according to the regions, increasing temperature-pressure conditions from Göksun to Ekinözü and have groups of rock with different geological evolutions.

Received Date: 21.05.2019
Accepted Date: 19.08.2019

1. Introduction

The Taurus Mountain or the Tauride Belt belongs to the Tauride-Anatolian Platform or the Tauride-Anatolian Tectonic Unit and bear traces of the pre-Alpine geological history as inferred from the diagenetic-very low grade metamorphic Paleozoic sequences (Göncüoğlu et al., 1997). The tectono-stratigraphic units forming the Taurides are distinguished by their paleogeographical settings, stratigraphic and structural characteristics as well as their depositional environments and metamorphism characteristics (Özgül, 1976; 1984). It is reported that the Early Paleozoic part of these was deposited in an environment associated with rifting at the northwestern border of Gondwana, and turned into

Citation info: Hozatlıoğlu, D., Bozkaya, Ö., Yalçın, H., Yılmaz, H. 2020. Mineralogical characteristics of metamorphic massif units outcropping in Göksun, Afşin and Ekinözü (Kahramanmaraş) region. Bulletin of the Mineral Research and Exploration 162, 103-143. https://doi.org/10.19111/bulletinofmre.610884

* *Corresponding author: Deniz HOZATLIOĞLU, denizhozatlioglu@gmail.com*

the bi-directional nappe system with the closure of the northern and southern branches of Neotethys in the Late Cretaceous (Göncüoğlu, 2010).

Metamorphic massives associated with the Alpine orogeny of the Tauride Belt were referred to under different names in the studies that have been carried out in the last 50 years (Alanya, Malatya, Göksun, Binboğa, Engizek and Keban Metamorphites) and different units (Antalya, Alanya, Geyikdağı, Bozkır, Aladağ, Bolkardağı, Pütürge and Bitlis) (Özgül, 1976, 1984; Yılmaz et al., 1987, 1992, 1993; Yılmaz and Yiğitbaş, 1990; Yılmaz, 1993; Göncüoğlu, 2010). These complexities make their correlation very difficult, especially linking different metamorphic units found within the belt. The same holds true for the understanding of their geological evolution. However, the previous studies related to the Upper Paleozoic-Lower Mesozoic metamorphic units in the Tauride Belt (Bozkaya, 1999, 2001; Bozkaya and Yalçın, 2004; Bozkaya et al., 2007*a*, *b*) were compared with the non-metamorphic units and made significant contributions to the interpretation of the evolution of Tauride tectono-stratigraphic units.

This study aims to investigate the mineralogical-petrographic features of the Upper Paleozoic-Lower Mesozoic metamorphic units defined as the Göksun, Binboğa and Engizek metamorphites. Their geographic positions outline the wide and typical outcrops around Göksun, Afşin and Ekinözü districts in the north of Kahramanmaraş province in the western part of the Eastern Taurus Mountains. In accordance with this goal, equivalent levels of Keban, Malatya and Pütürge metamorphites and in the eastern extension of the same metamorphic belt were compared lithologically, mineralogically and petrographically by determining the degrees of diagenesis/metamorphism and characteristics of the related units. In this context, it is considered that the data obtained from the detailed phyllosilicate mineralogy (associations, illite crystallinity, illite/mica *b*-cell distance, polytype), which is applied first time to the Upper Paleozoic metamorphic units in the study area, will provide additional contributions to the interpretation of the geological evolution of the region.

2. Geological Setting

2.1. Regional Geology

The Taurides cover the units which were deposited in Cambrian-Paleogene period, reflecting different basin conditions, and stratigraphy and metamorphism characteristics and separated from their present structural settings (Özgül, 1976). It was reported that the units commonly referred to as the Bozkır Unit, Bolkardağı Unit, Aladağ Unit, Geyikdağı Unit, Antalya Unit and Alanya Unit from the north to south showed lateral continuities for hundreds of kilometers and mainly were allochthonous with each others (Özgül, 1976). Of these, it is known that Bolkardağı, Aladağ, Geyikdağı and Alanya units contain shelf type carbonate and clastic rocks, whereas Bozkır and Antalya units include the deep sea sediments, ophiolites and submarine volcanics with basic composition (Özgül, 1976). These units were imbricated as a result of the closure of the northern and southern branches of Neotethys in the Late Cretaceous and the collision of the continental micro plates (Şengör and Yılmaz, 1981). Thus, the units (Bozkır, Bolkardağı and Aladağ) in north of the platform thrusted southward and the units (Antalya and Alanya) representing the south of the platform thrusted on the Geyikdağı Unit towards north (Özgül, 1976; 1984) (Figure 1).

In the Southeastern Anatolian Orogenic Belt, where the Metamorphic Massives are located, three tectonic belts were distinguished as the Arabian Platform, the Accretionary Zone and the Nappe Region from south to north by Yılmaz and Yiğitbaş (1990) and Yılmaz (1993) (Figure 2). Of these, the Arabian Platform and Nappe Region are represented by autochthonous sedimentary rocks of the Cambrian-Paleogene range (Southeast Anatolian Autochthonous) and ophiolitic, metamorphic and volcanic-volcanoclastic sedimentary rocks and the study area is located within second zone. The accretionary zone is composed of reverse fault and thrust slices that delimit the northern extension of the Arabian Platform. The relations of these tectonic units with each other are presented in figure 3. The Cambrian-Paleogene sedimentary units of the Eastern Taurus Autochthonous (Geyikdağı Autochthonous) are exposed in northwest of the Nappe Region. These units in the region are unconformably overlain by Neogene-Quaternary sedimentary and volcanic rocks.

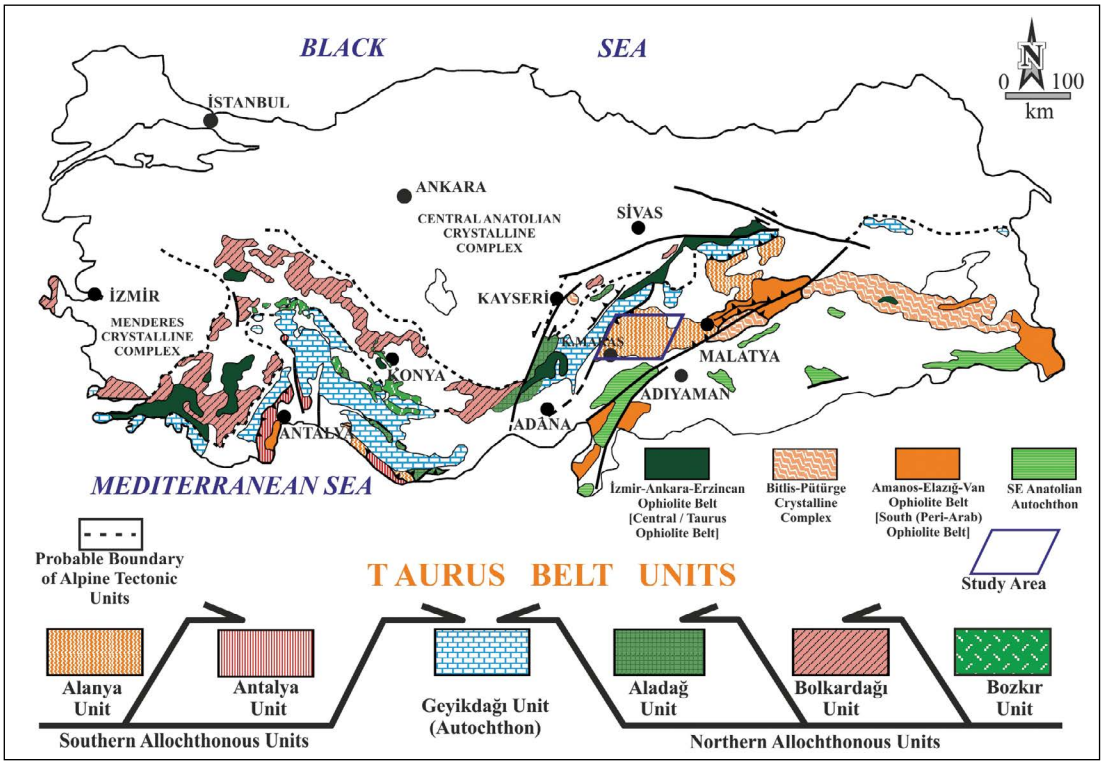

Figure 1- Geographical distribution and tectonic setting of autochthonous and allochthonous units in the Tauride Belt (the nomenclature of tectonic units: Özgül, 1976, 1984; Göncüoğlu et al., 1997; the nomenclature of Ophiolite Belts: Juteau, 1980; the probable boundary of Alpine Tectonic Units: organized from Göncüoğlu et al., 1997; Göncüoğlu, 2010; Bozkaya and Yalçın, 2014).

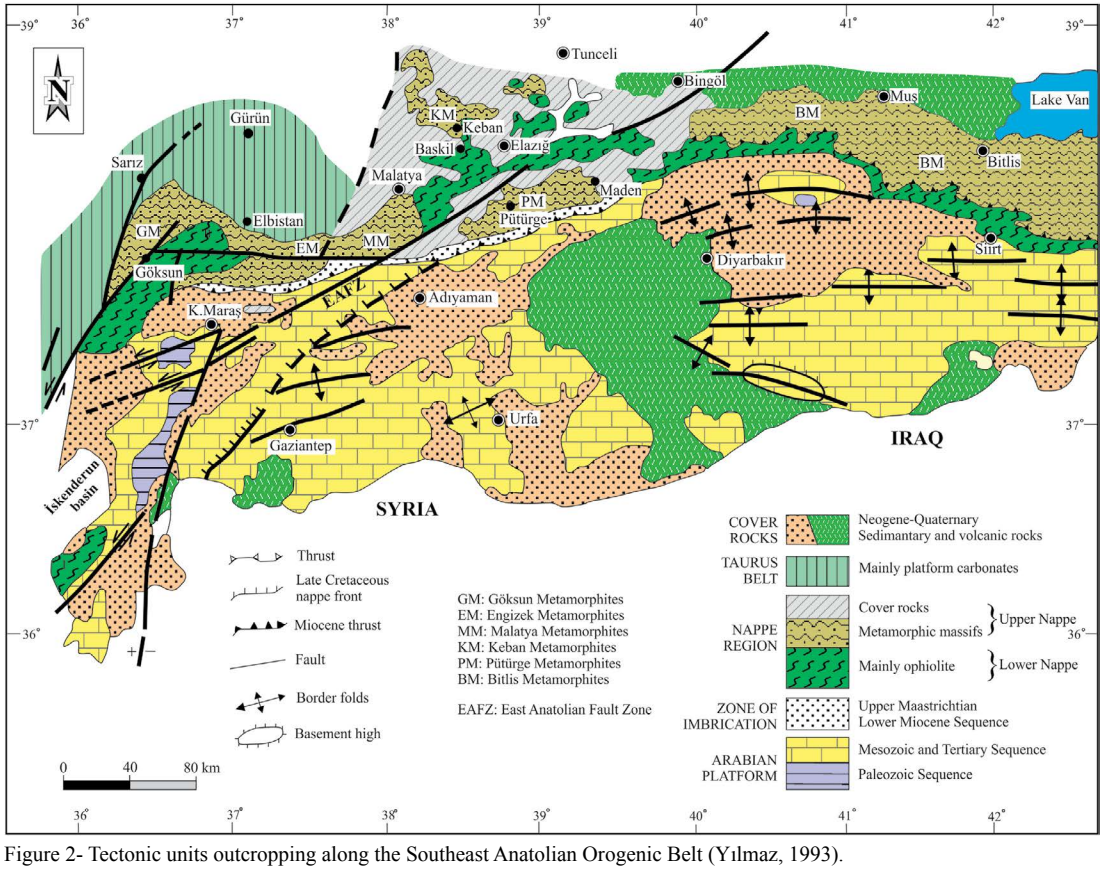

Figure 2- Tectonic units outcropping along the Southeast Anatolian Orogenic Belt (Yılmaz, 1993).

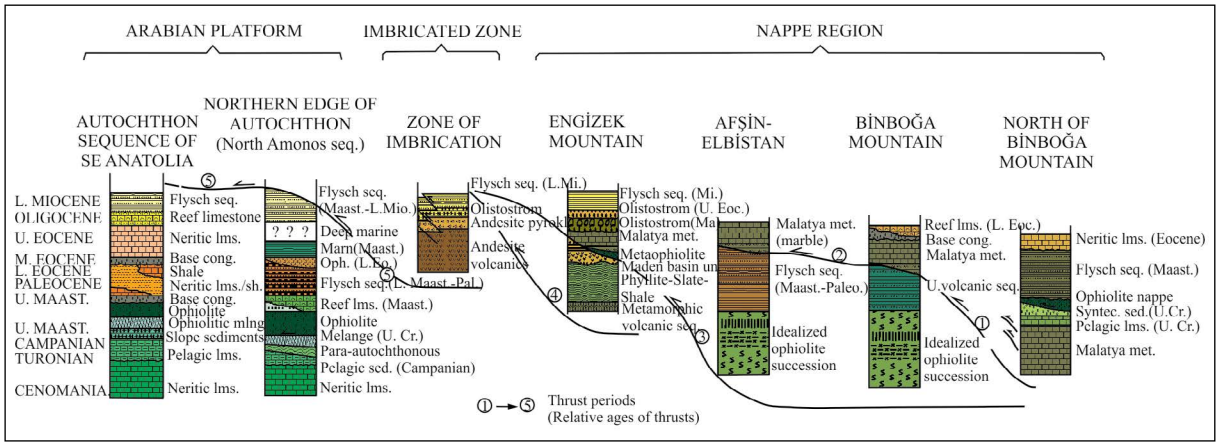

Figure 3- Generalized stratigraphic sections showing different tectonic units of the Southeast Anatolian Orogeny (prepared from Yılmaz and Yiğitbaş, 1990).

2.2. Geology of the Study Area

In the study area, there are east-west trending tectonic units, which are pre-Maastrichtian in age and show different environmental characteristics. These are made up of allochthonous rock assemblages in the northern, central and southern parts of the Eastern Taurus Mountains, respectively (Figure 4, Yılmaz et al., 1993, 1997).

The basement of the study area is constituted by metamorphic rocks of the Upper Paleozoic-Triassic greenschist facies that is the oldest unit in the region (Yılmaz et al., 1993) and the granitic intrusions cutting

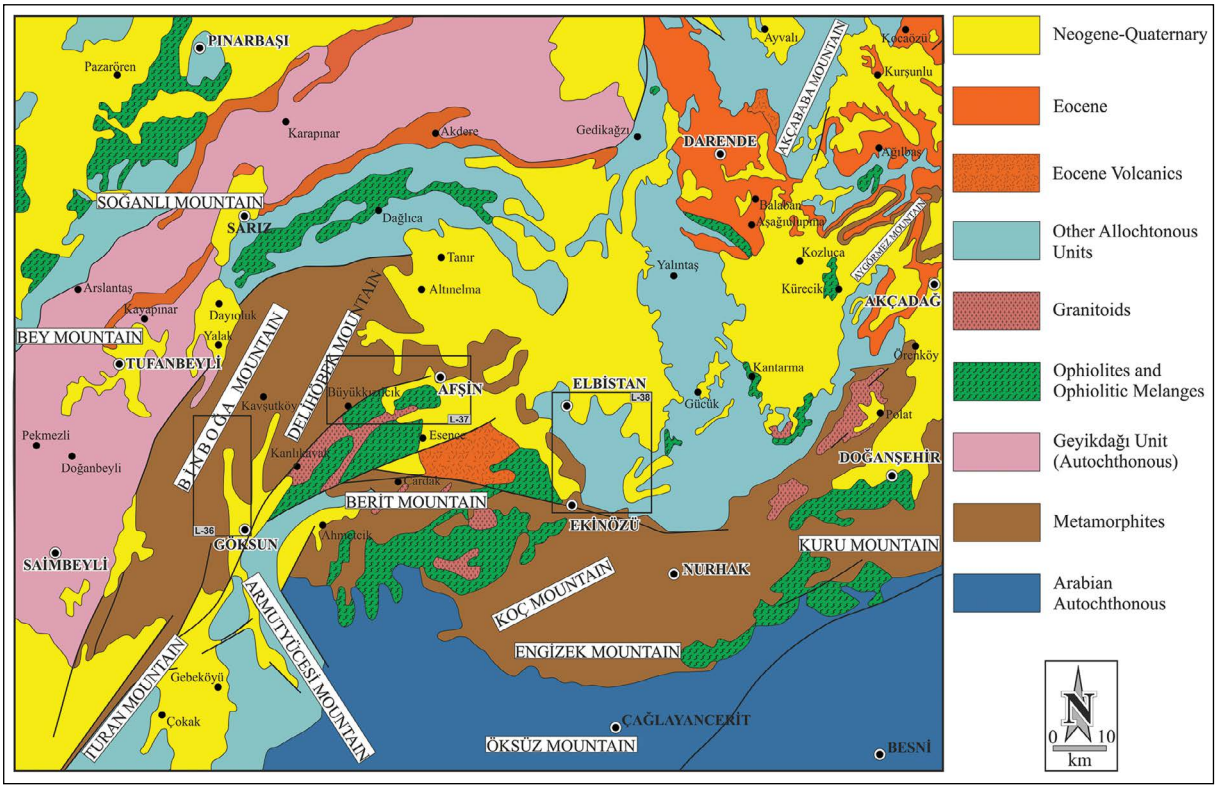

Figure 4- A simplified regional geology map of the study areas and their near surroundings covering three different subareas in the Eastern Taurus Mountains (prepared from Bedi et al., 2005, 2009 and 1/500.000 scale geology map from MTA, 2002).

them. This rock group tectonically passes upwards into the Jurassic-Lower Cretaceous carbonate rocks which are not affected by the metamorphism. The lower parts of metamorphic rocks, which are rich in metapelites, are named as the Yoncayolu formation, however; the upper parts rich in metacarbonates are named as the Çayderesi formation that is located conformably (Figure 5, Özgül and Turşucu, 1984; Yılmaz et al.,

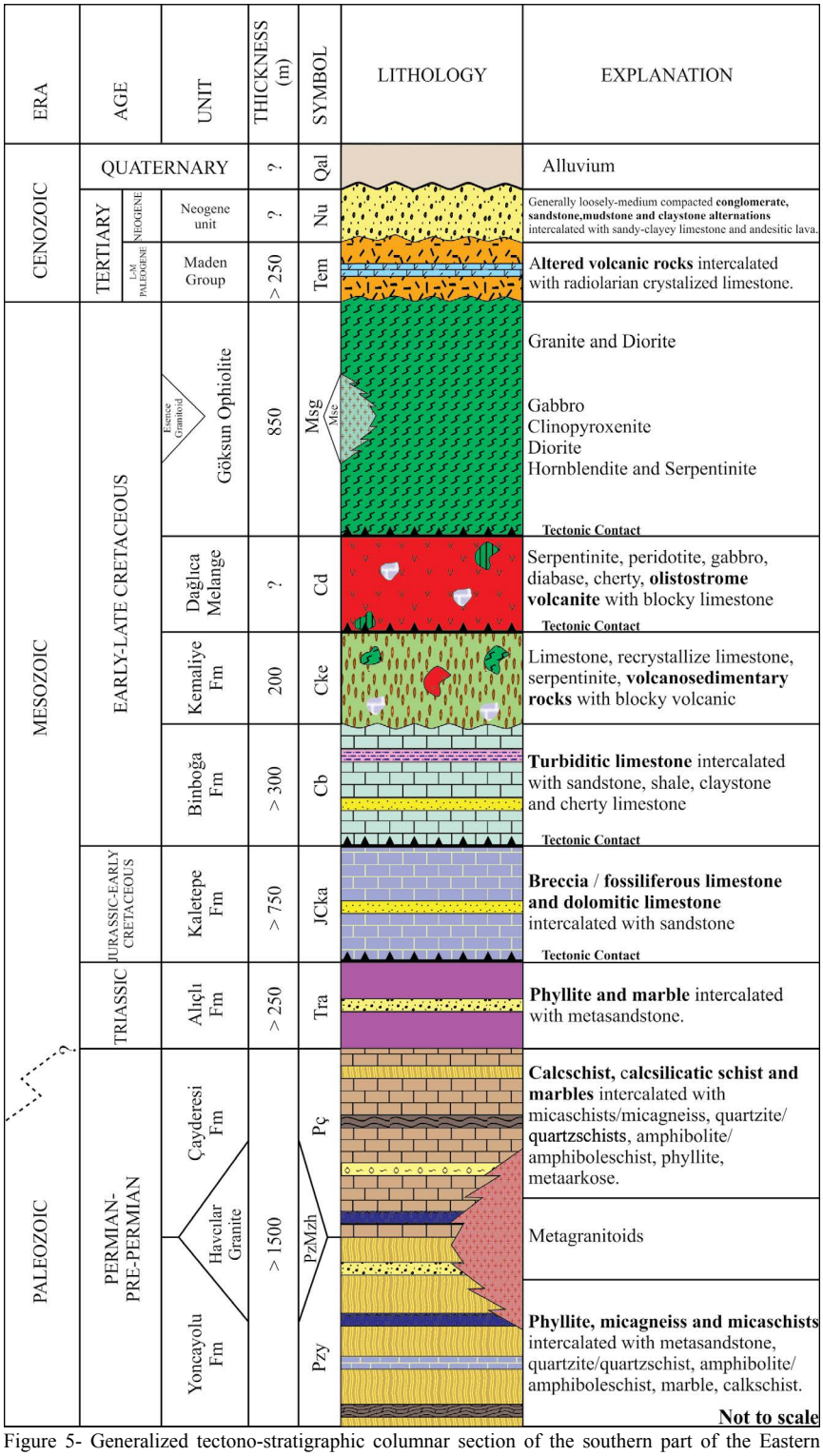

Figure 5- Generalized tectono-stratigraphic columnar section of the southern part of the Eastern Taurus (modified from Yılmaz et al., 1993).

1993). These units are overlain by Triassic and Jurassic-Lower Cretaceous sedimentary units. The ophiolitic rocks (Göksun Ophiolite), one of the oceanic and arc sections of the allochthonous rock group, tectonically overlie the metamorphics. The Upper Cretaceous allochthonous units, which are located in the south of Gürün Relative Autochthone, which is the local equivalent of the Geyikdağı Unit, and whose positions in the study area are controversial, unconformably overlie the other units. The Maden Group (Yılmaz et al., 1993) and the Neogene-Quaternary sedimentary-volcanic sediments of the Middle Eocene volcano-sedimentary rocks represent the cover units (Figure 5).

3. Stratigraphy and Lithology

Metamorphic successions outcropping along the Tauride Belt are ordered as Paleozoic-Mesozoic Alanya Metamorphics (Işık and Tekeli, 1995), Alanya Massif (Blumenthal, 1951), Alanya Nappe (Öztürk et al., 1996), Alanya Tectonic Window (Özgül, 1984) in the Central Taurides, and as Göksun Metamorphites (Metin et al., 1982, 1986), Devonian Kabaktepe and Çağılhan Metamorphics (Tarhan, 1982, 1984), Jurassic-Lower Cretaceous Engizek formation, Engizek Metamorphites, Engizek Unit (Baydar, 1989; Yılmaz et al., 1992), Pre-Carboniferous(?) Nergile formation (Yıldırım, 1989; Yiğitbaş, 1989), Upper Devonian-Lower Cretaceous Binboğa Metamorphite (Yılmaz et al., 1987; Bedi et al., 2004, 2005), Permo-Carboniferous Malatya Metamorphites (Perinçek and Kozlu, 1984; Yıldırım, 1989; Yiğitbaş, 1989; Karaman et al., 1993), Carboniferous-Permian Keban and Malatya Nappes (Yazgan, 1983), Keban-Malatya Unit (Yılmaz et al., 1993, 1997), Keban Metamorphites (Özgül, 1976; Perinçek, 1979*b*, *c*), Keban Union (Özgül, 1981; Özgül and Turşucu, 1984), Cambrian-Permian Pütürge Metamorphites (Perinçek, 1979*a*; Ricou, 1980) and Devonian-Triassic Mutki Group (Göncüoğlu and Turhan, 1984) from west to east in the Eastern Taurus (Figure 6).

Among these, the Alanya, Göksun, Engizek and Malatya metamorphites were defined as the Alanya Unit by Özgül (1976) and were evaluated within the Taurus orogenic belt. Pütürge and Bitlis metamorphites were excluded from the Tauride Units and were defined as the Misis Unit (Özgül, 1976) or Bitlis Zone (Göncüoğlu et al., 1997).

In order to find an answer to different nomenclature and correlation problems for the same units, one measured stratigraphic section was carried out from each region to determine both the stratigraphic-lithostratigraphic and mineralogical-petrographic changes of metamorphic units in the study area. The relationship of these stratigraphic sequences and their positions from west to east are presented in figure 7.

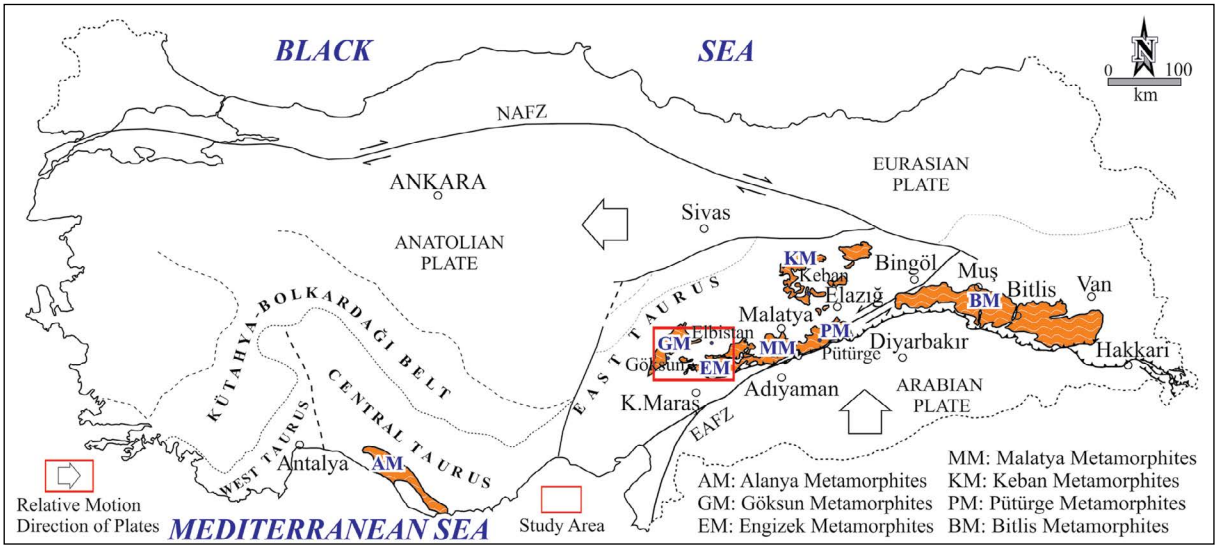

Figure 6- The metamorphic successions outcropping along the Tauride Belt and the location of the study area (modified from Özgül, 1984 and Göncüoğlu et al., 1997; main tectonic boundaries: Schildgen et al., 2014; relative movement direction of the plates: Reilinger et al., 1997; McClusky et al., 2000).

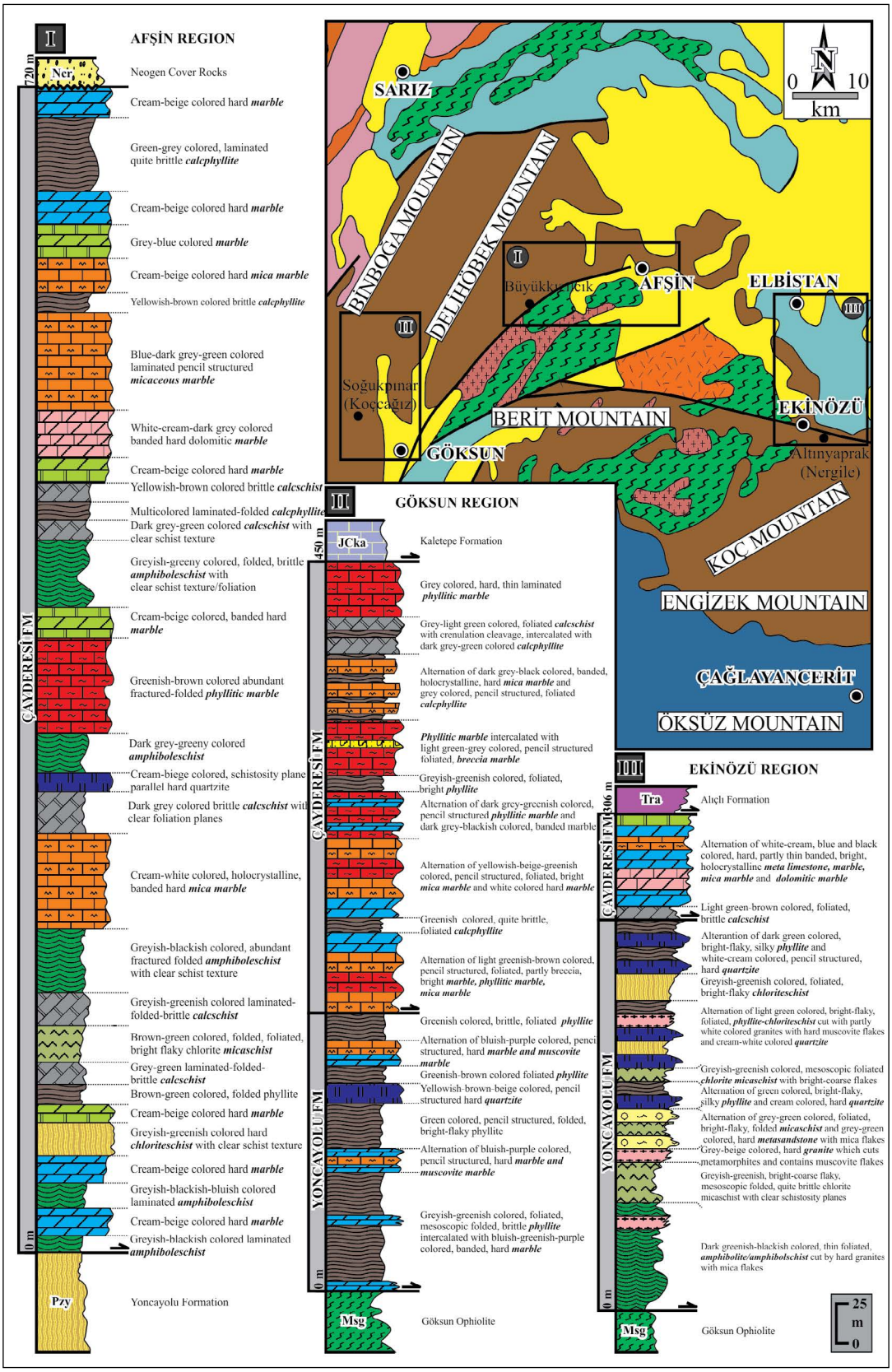

Figure 7- Stratigraphic distribution of the metamorphic sequences from west to east in the study area (The positions of the sequences are II-I-III from west to east; regional geology map: Bedi et al., 2005, 2009 and 1/500.000 scale geology map prepared from MTA, 2002).

3.1. Göksun Region

The unit shows very large outcrops mostly in north-northwestern parts of Göksun and in its immediate vicinity, (in an area of approximately 300 km^2) in the study area (Figure 8). The type section measurement of this region was taken in the northeastern part of Koçcağız/Soğukpınar village in the northwest of Göksun and approximately 450 m thickness was measured (Figure 9a).

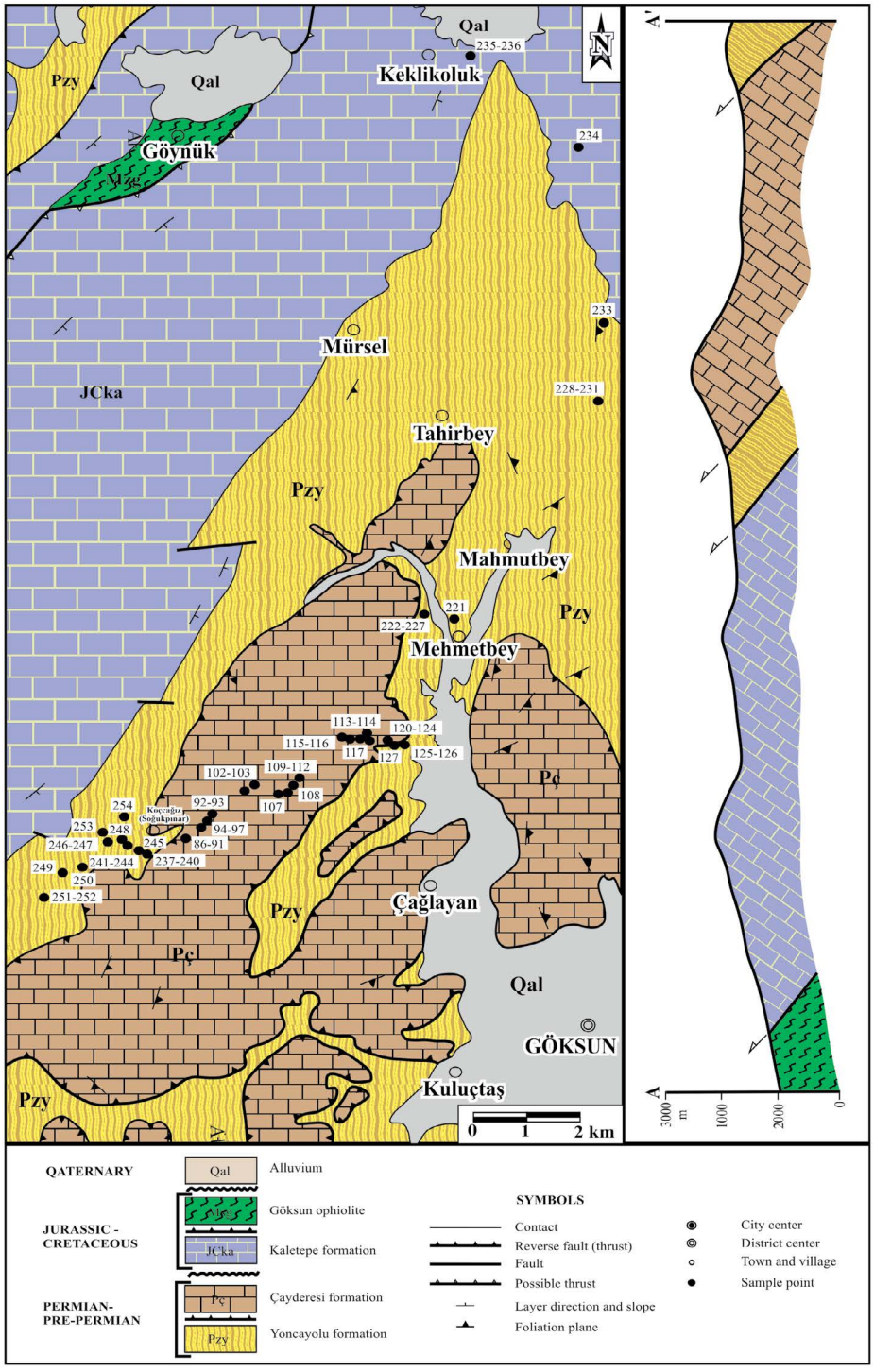

Figure 8- Geological map of the Göksun region (modified from 1/100.000 scale geological map of Turkey, series Elbistan-I22/L-36 sheets, Metin et al., 1989).

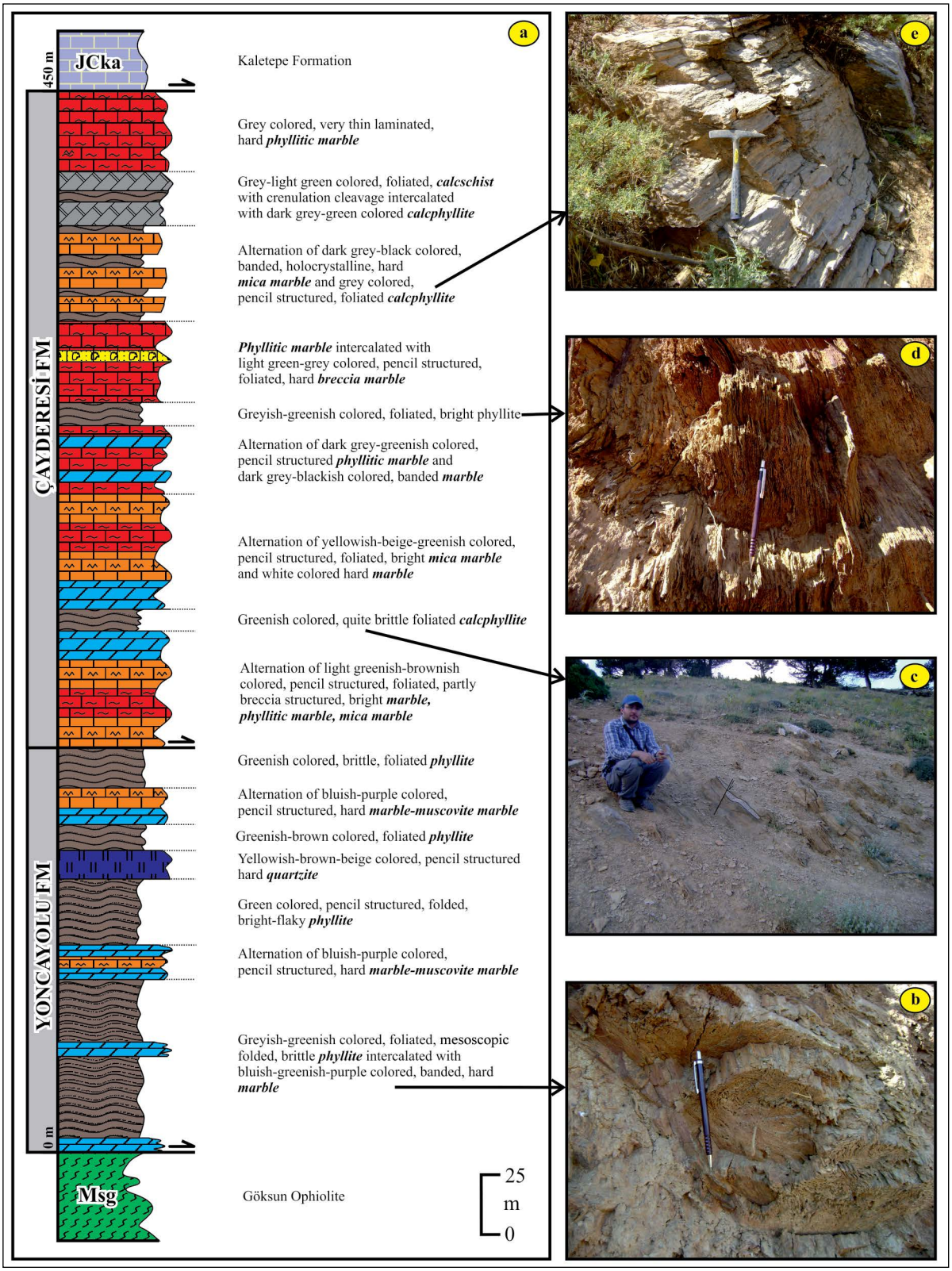

Figure 9- a) Columnar section of the Göksun region (the north of Göksun-Koçcağız/Soğukpınar village). Field views of rock groups b) grayish-greenish colored, pencil structured and banded marbles, c) yellowish-brown colored and foliated phyllites, d) normal faults developed in light brown-green colored calcphyllites and e) yellowish-greenish colored, mesoscopically folded and foliated phyllites.

The dominant lithology of the unit consists of the rock assemblages that are Upper Paleozoic (Özgül and Turşucu, 1984) Yoncayolu formation at the bottom and Çayderesi formation of the same age with a tectonic contact. From these units, Yoncayolu formation tectonically overlies the Middle-Upper Cretaceous Göksun Ophiolite, and as for the Jurassic-Lower Cretaceous Kaletepe formation, it tectonically overlies the Çayderesi formation.

At the bottom of the Yoncayolu formation, which is approximately 163 m thick and located in lower parts of the unit, the phyllites with banded marble intercalations are present. They have bluish/purple-greenish, hard, grayish-greenish-yellowish, foliated/cleavaged, mesoscopically folded, very fragile and bright in appearance (Figure 9b). Towards the upper parts of the unit, the yellowish-brown-beige colored, hard, pencil-structured quartzites with a thickness of about 1 m are followed. At the top of the formation, the bluish-purple colored, pencil structured, hard, marble-muscovite marble intercalated and/or alternated greenish colored, brittle, foliated phyllites transit into the tectonically overlying Çayderesi formation.

The basement of the Çayderesi formation, which has a thickness of approximately 287 m in the unit, consists of the alternation of light greenish-brown, pencil structured, bright marble, phyllitic marble and mica marble containing distinctive foliation planes with brecciated appearance in places. Towards the upper parts of the unit, there is observed a grayish-greenish phyllite-calcphyllite alternation, with distinct schistosity planes in the form of stratifications of 10-30 cm in thickness that have very fragile, foliated and bright colored crenulation folds and show small scale normal faulting (Figure 9c-d). Metacarbonates, which form the common lithology of the formation, are composed of pencil structured, foliated, banded, coarse-crystalline, bright-looking, hard marble (Figure 9e), phyllite marble, mica marble and calc-schist intercalations offering yellowish-beige-greenish and grayish-blackish colors.

3.2. Afşin Region

The unit outcrops in an area of approximately 250 km^2 in western-southwestern and eastern parts of Afşin within the study area (Figure 10). Type section measurements in the region were taken in the southwestern parts of the Büyükkızılcık village in the southwest of Afşin and a thickness of approximately 720 m was measured (Figure 11a).

The dominant rock group of the unit belongs to Upper Paleozoic Çayderesi formation (Özgül and Turşucu, 1984). While this unit tectonically overlies the same aged Yoncayolu formation, the Neogene units unconformably overlie the Çayderesi formation.

In lower parts of the unit, there are observed amphiboleschist levels with a thickness of approximately 0.5-1 m, exhibiting a grayish-blackish-purplish color and prominent schistosity plane alternating with cream-beige, hard marbles (Figure 11b). The foliated and shiny-flaked chloriteschists, which contain grayish-green, distinct schistosity planes, are another metapelitic rocks in lower parts of the unit.

Towards the intermediate levels of the formation, the cream-beige colored hard marbles, and greyish-greenish, laminated, foliated and brittle calcschists, and brown-green colored micaschists with distinct schistosity planes and foliated and shiny-flaked appearance (Figure 11c), and grayish blackish colored, heavily jointed, foliated amphiboleschists with distinct schistosity planes show an alternated structure. The metacarbonate levels, which increase markedly towards the upper levels of the unit, begin with creamy-white, coarse crystalline, banded, thick layered and hard micaceous marbles and continue with brittle calc-schists showing dark gray colored distinct foliation planes. Dark grayish-greenish, foliated and brittle amphiboleschist levels with distinct schist-texture/cleavage are regularly observed which continue until upper levels from the middle parts of the formation within these metacarbonate levels. In some places, cream-beige, thin-bedded, hard quartzite levels parallel to the schistosity plane are also observed. Towards the upper levels of the unit, the dark gray-greenish and schist textured calcschists alternate with pied colored, thin-bedded and foliated calcphyllites.

In the upper levels of the formation, the dark gray-cream-beige, sporadically banded, hard, pencil-structured and very thick-layered marble (Figure 11d), dolomitic marble and marble with mica intercalate with light green-gray colored, very brittle, thin layered calcphyllites containing distinct schistosity planes (Figure 11e), and the succession is completed.

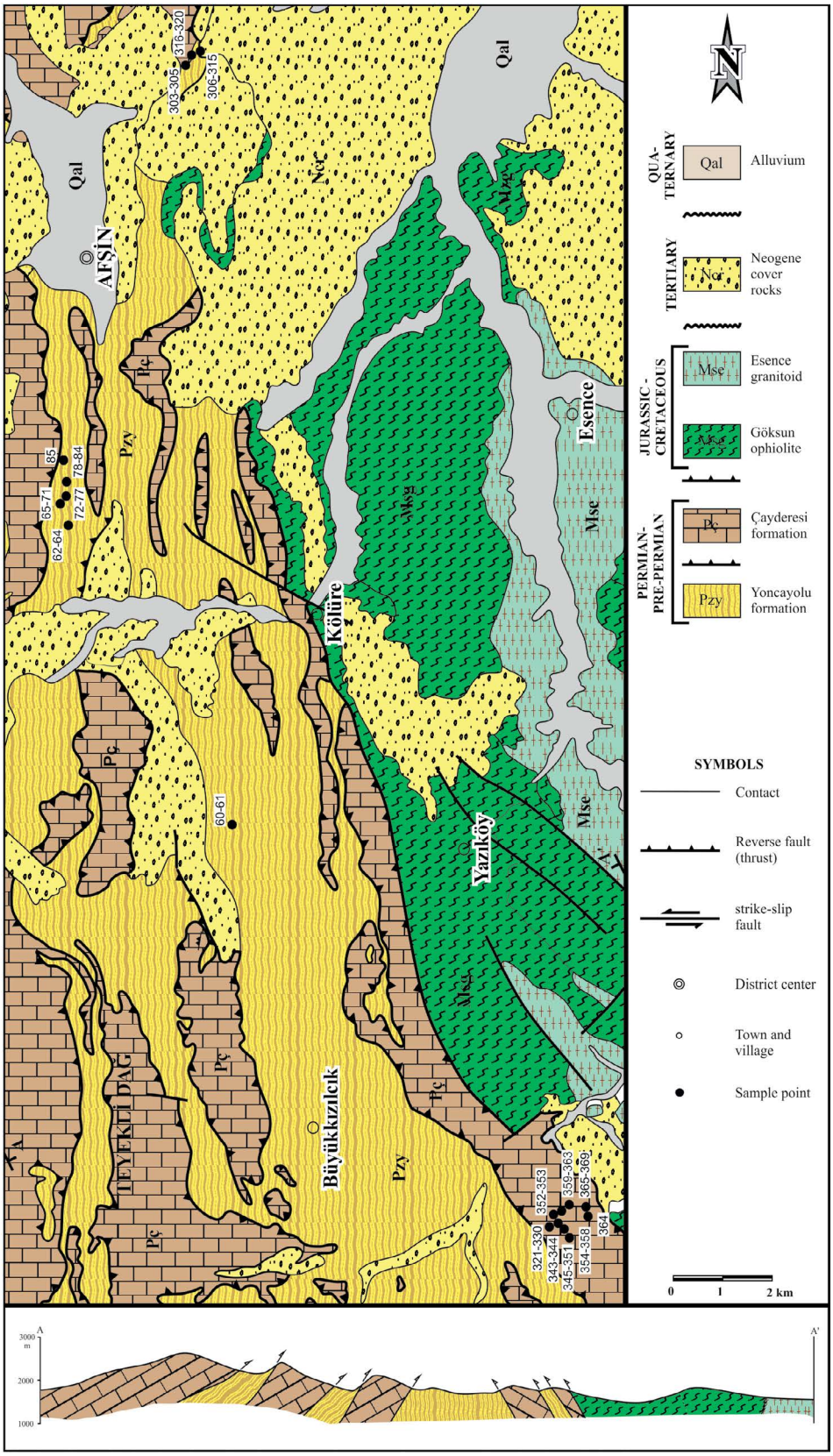

Figure 10- Geological map of the Afşin region (prepared from 1/100.000 scale geological map of Turkey, series Elbistan-I23/L-37 sheet, Yılmaz et al., 1997; age data of Paleozoic rocks taken from Özgül and Turşucu, 1984).

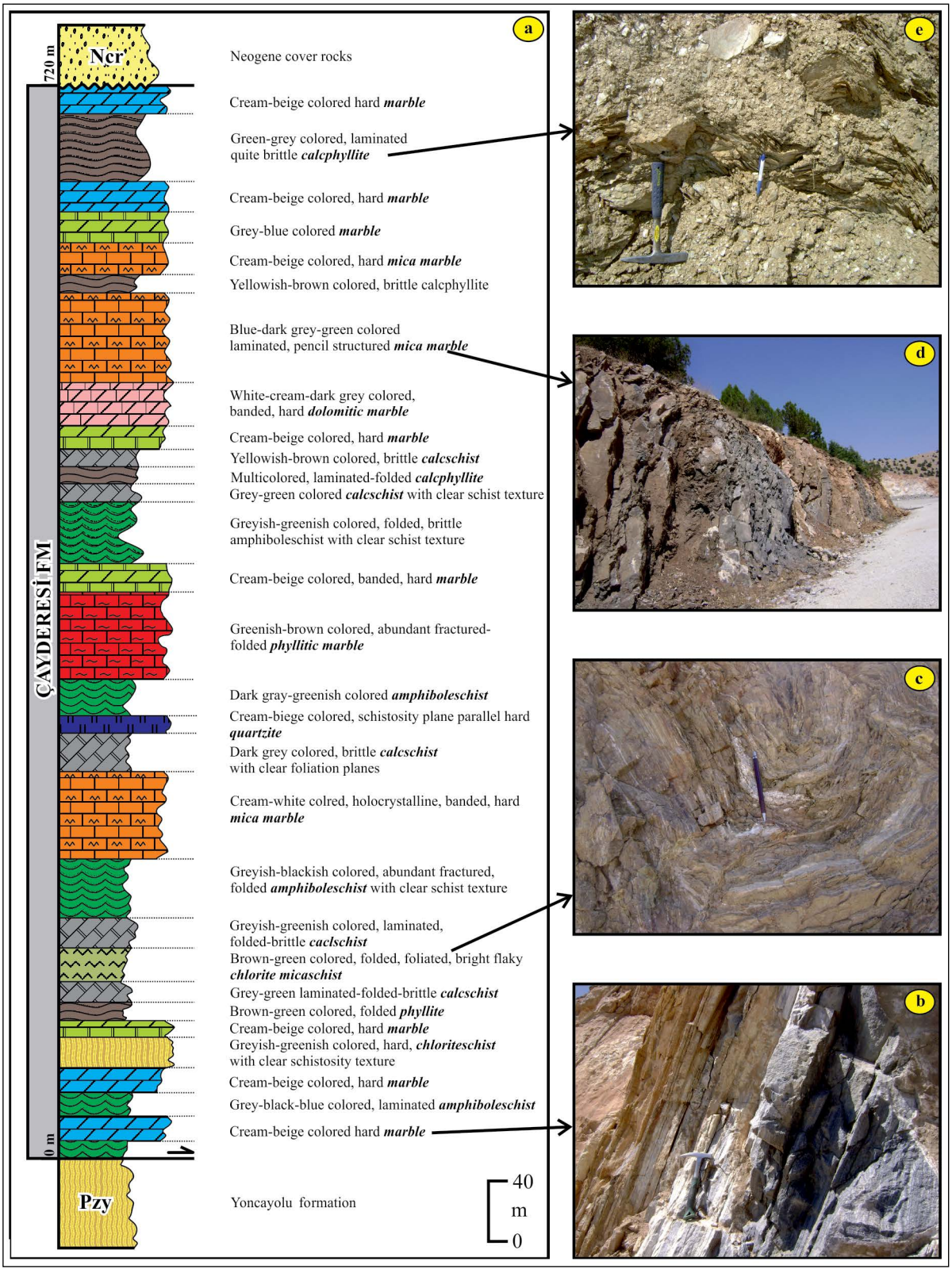

Figure 11- a) Columnar section of the Afşin region (the south of Afşin-Büyükkızılcık Village). Field views of rock groups, b) whitish-cream and purple colored, hard, medium-thick layered and banded marbles, c) folded structures in gray-green colored mica schists, d) grayish-purplish-greenish colored and thick-layered marbles, e) mesoscopic foliations in grayish-greenish colored phyllites/ calcphyllites.

3.3. Ekinözü Region

The unit within the study area has very large outcrops in an area of approximately 250 km^2 in south-southeast of Elbistan and north, south-southeast of Ekinözü and in its close vicinity (Figure 12). The type section measurement of the units was taken in the northwestern parts of Altınyaprak/Nergile village in the southeast of Ekinözü and a thickness of more than 300 m was measured (Figure 13a).

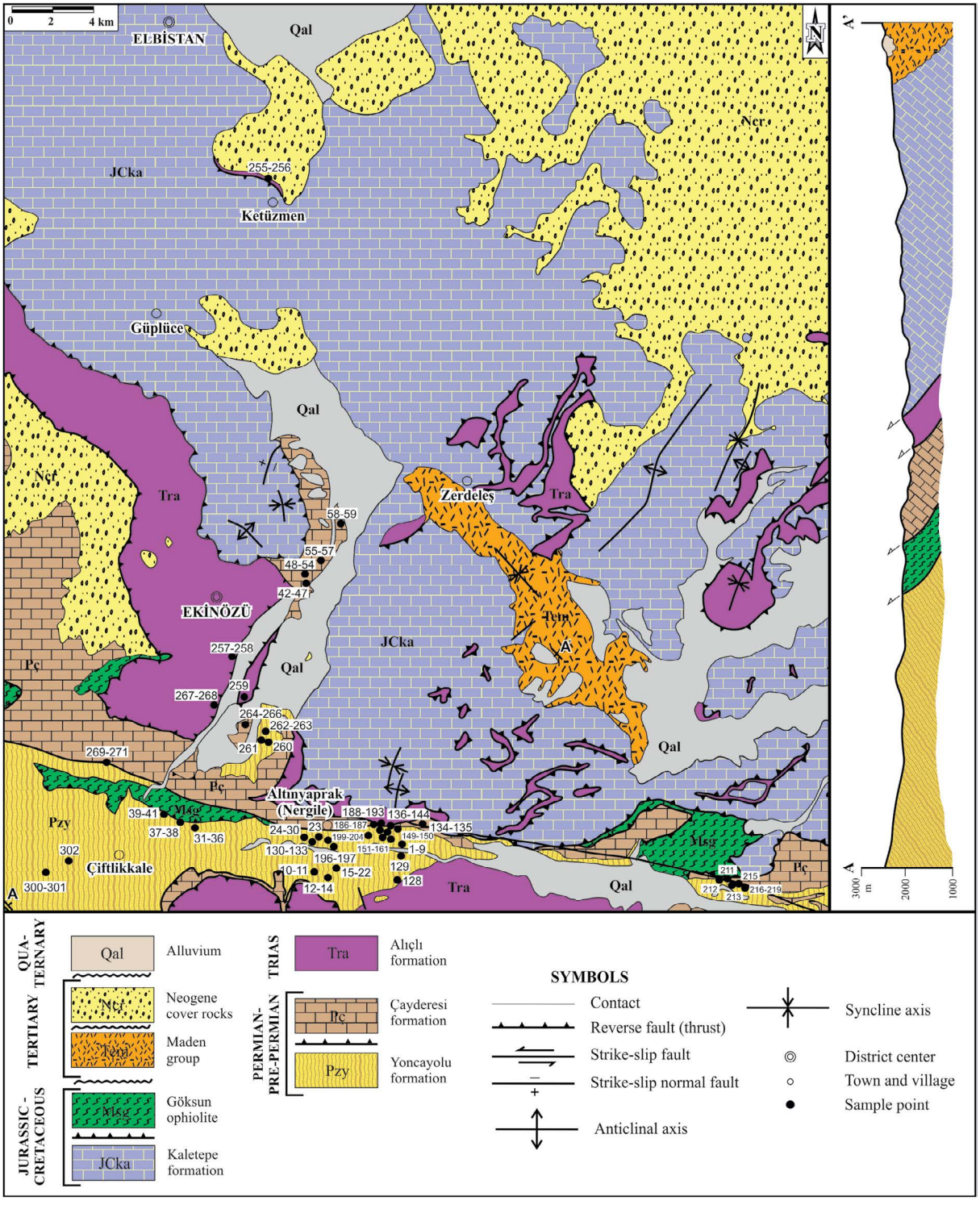

Figure 12- Geological map of the Ekinözü region (prepared from 1/200.000 scale of Kahramanmaraş province geology map, MTA, 2008).

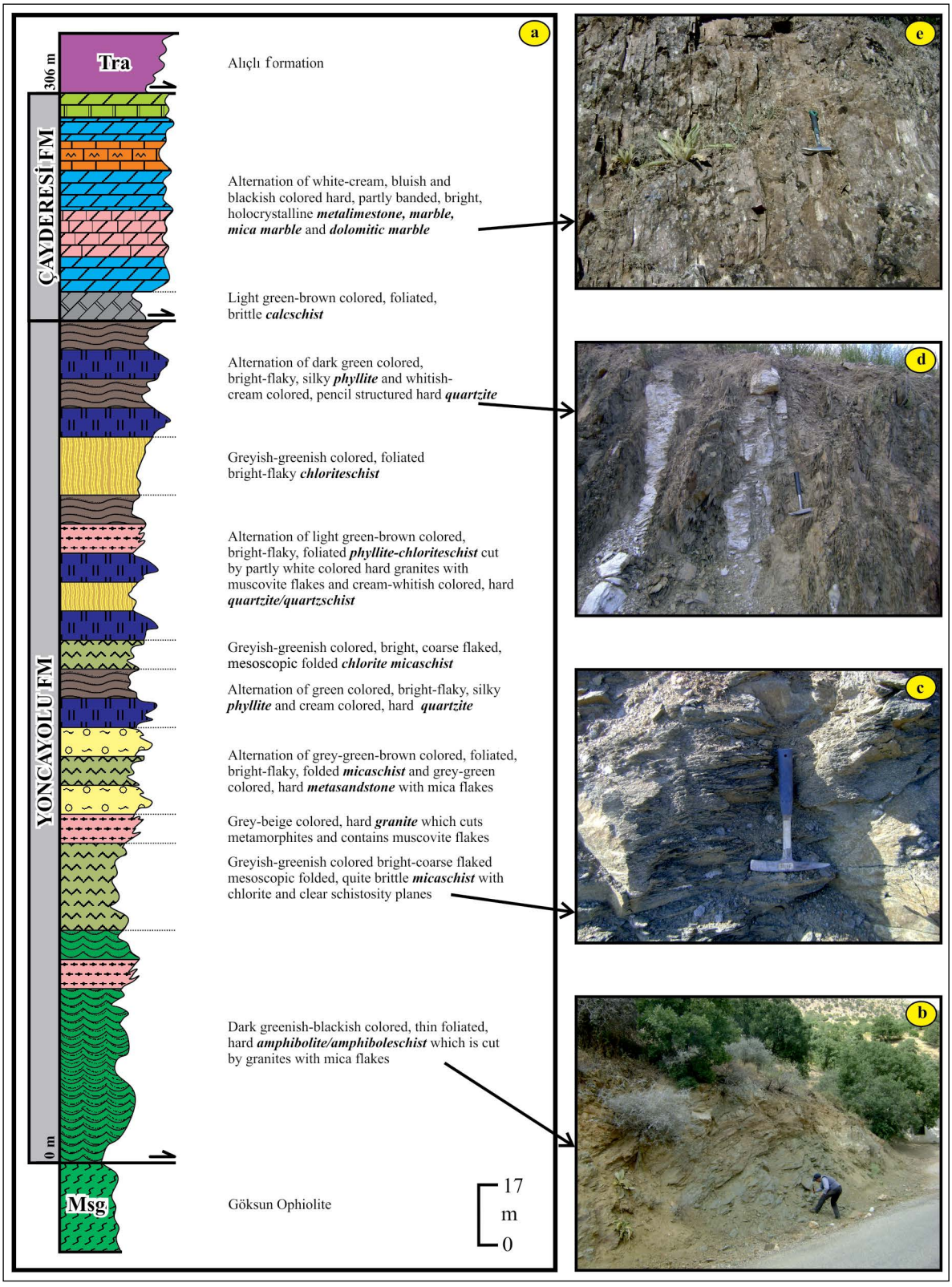

Figure 13- a) Columnar section of the Ekinözü region (the north of Ekinözü-Altınyaprak/Nergile village). Field views of the rock groups, b) greenish-blackish colored and thin-medium bedded amphiboleschists), c) grayish-greenish colored and micaschists with coarse flakes, d) perpendicularly developed phyllite-quartzite alternation and e) gray-white colored and thin-medium bedded marbles.

The Upper Paleozoic (Özgül and Turşucu, 1984) Yoncayolu formation at the bottom and tectonically overlying same aged Çayderesi formation consist of mainly dominant units of the region. Of these, the Yoncayolu formation and the Triassic Alıçlı formation tectonically overlie the Middle-Upper Cretaceous Göksun Ophiolite and the Çayderesi formation, respectively.

The bottom of Yoncayolu formation with totally 240 m thickness consists of bright-looking, greenish-black decomposition colored, thinly foliated amphibolite/amphiboleschists (Figure 13b) with 25-30 cm thick quartz bands and partly with mica flakes. These rocks are cut by hard granites. In the middle levels of the formation, there are grayish-greenish, bright-coarse flaked, mesoscopically folded, highly brittle chlorite micaschists with distinct schistosity planes (Figure 13c). Inside of this unit, gray to beige colored granitic intrusions with muscovite flakes are observed. Above these levels, the gray-green-brown distinctively foliated and flaky micaschists alternate with purplish-gray-green, 25-40 cm thick, medium-bedded, hard metaclastic sandstones containing moderately thick muscovite flakes. In the formation, partly whitish, thin-bedded phyllite-quartzite alternations with muscovite flakes are observed towards the upper layers (Figure 13d). In this alternated structure, the grayish-greenish, bright-coarse flaked chloritic micaschists and chlorite schists, which show distinct wrinkle folds and cut by hard granitic intrusions, intercalate with each others. Phyllites are generally light greenish-grayish, bright-flaked and silky-like in appearance, however; the quartzites are hard, cream-colored and developed parallel to the foliation plane.

At the bottom of the Çayderesi formation, which tectonically overlies the Yoncayolu formation and presents a thickness of approximately 70 m in the region, there are light green-brown calcschists exhibiting cleavage and brittle structure. The sequence ends with the intercalation of whitish cream, bluish, blackish, hard, exhibiting occasionally thin banded structure, bright, coarse crystalline metalimestone, marble, mica marble and dolomitic marble (Figure 13e).

4. Material and Method

Totally 369 rock and mineral samples with each weighing approximately 1 kg were collected from points and measured sections in the field study. In addition, the mesoscopic structures developed in the units and their relations with each others were observed and photographed in detail. The samples were washed with distilled water, cleaned from surface dusts, dried and then made ready for analyses.

The optical microscopy (OM), X-ray diffraction (XRD)-whole rock (WR) and clay fraction (CF) investigations were performed by using binocular polarizing microscope on thin sections and X-ray diffractometer devices. These analyses were carried out in Crushing-Grinding-Sieving, Clay Separation and Mineralogy-Petrography and Geochemistry Research Laboratories (MIPJAL) in Geological Engineering Department of Sivas Cumhuriyet University.

The optical microscope studies were carried out on a LEICA brand binocular polarizing microscope. Thin sections were prepared especially by cutting cleavage planes perpendicularly in low-medium grade metamorphic (slate, phyllite and schist) rock samples, and thus the petrographical properties developed depending on metamorphism by determing the textural relationships within mineral and matrix were interpreted. With this method, both the components and textural properties were defined. In addition to the nomenclature of the rocks, the weathering and alteration products, indirectly the origin of the minerals and textural and mineralogical properties developed by the effect of metamorphism were clarified.

XRD has been the most widely used method to determine the whole rock and clay size mineralogical compositions of the rocks with very small (submicroscopic) grain size and also to detect polymorphic changes in minerals. Hard specimens to be used in XRD studies were first crushed in 3-5 cm pieces with hammer, crushed in FRITISCH jaw crusher as granules smaller than 5 mm, and then the rocks were milled for 0.5-3.0 min. using an ÜNAL brand tungsten bowl ring mill. XRD analyses were carried out in Rigaku brand DMAX IIIC model X-ray diffractometer (Anode = Cu (CuK_a = 1.541871 Å), Filter = Ni, Voltage = 35 kV, Current = 15 mA, Goniometer speed = 2°/min., Paper speed = 2 cm/min., Time constant = 1 sec., Slits = 1° 0.15 mm 1° 0.30 mm, Paper range = 2q = 5-35°). The whole rock and clay fraction components (< 2 mm) were defined (J.C.P.D.S., 1990) and semi-quantitative percentages were calculated based on the external standard method

(Brindley, 1980) in rocks collected from units in the study area. The mineral intensity factors were used in whole rock and clay fraction calculations and the reflections were measured in mm. In this method, the dolomite for the whole rock and the kaolinite for the clay fraction were taken as the reference from glycol preparations (Yalçın and Bozkaya, 2002). Quartz was used as an internal standard for measuring d-spacings. The definition of clay minerals was made based on their (001) basal reflections.

The necessary clay separation process for XRD-CF analyses generally are; chemical dissolution (removal of non-clay fraction), centrifugation - decantation/ resting and washing, suspension - sedimentation in the first step and siphon - centrifugation and bottling in the second stage. 10 % HCl in dolomite and 10 % CH_3COOH in calcite bearing samples were used to dissolve carbonate minerals. In the absence or long duration of the suspension process, a small amount of calgon (sodium hexametaphosphate) was added to accelerate this process. The centrifugation process was performed in HERAEUS SEPATECH brand VARIFUGE 3.2 S centrifuge with 5600 rpm and 200 cc metal codes. Three oriented slide preparations were prepared in suspension from each of the separated clay mud by plastering, and they were dried at room temperature. The clay fraction diffractograms were obtained by normal-N (air-dried), glycolation-EG (retention in ethylene glycol vapor at 60° C for 16 hours in desiccator) and heating-H (heating at 490° C for 4 hours in oven). The goniometer speed as 1°/min and the recording interval was set as 2q = 2-30° (error amount ± 0.04°).

The width of the 10-Å illite and 7-Å chlorite peaks at half-height in D°2q (Kübler index - KI: Kübler, 1968, Arkai index - AI: Árkai, 1991 and Guggenheim et al., 2002) was used in the crystallinity measurements of illite and chlorite. As a result of peak analysis by means of WINFIT (Krumm, 1996) software (http://xray.geol.uni-erlangen.de/html/software/soft.html), the calibration was made based on (Full Width Half Maximum - FWHM) Kisch (1980) and Warr and Rice (1994) standards from peak widths determined sensitively. Since the measurements taken at different universities were performed on different brand XRD devices, the separate calibration equations were used for the patterns at each university. The obtained CIS-calibration values were re-converted to the original KI_{Basel} values by means of the equation proposed by Warr and Ferreiro-Mählmann (2015) (KI_{CIS} = 1.1523 x KI_{Basel} + 0.036, R^2 = 0.986).

Polytype studies were made on illite, chlorite, biotite and muscovite. Recording range applied from non-oriented preparations is between 2q = 5-65°, 16-36° and 31-52°, respectively. The diagnostic peaks suggested by Bailey (1988) were used to determine the polytypes. $2M_1$, $1M$ and $1M_d$ ratios were determined according to the peak area (A) ratios proposed by Grathoff and Moore (1996) and listed below. WINFIT software was used to determine peak areas (Bozkaya and Yalçın, 2007). The b_0 parameter (Sassi and Scolari, 1974) was measured by taking the quartz (211) peak (2q=59.97°, d=1.541 Å) as an internal standard from the reflection of $d_{(060)}$.

The analysis of peaks of d_{002} and d_{003} reflections in order to measure the d_{001} values of paragonite, and the crystalline sizes (*N* nm) of illite/mica were determined by applying the WINFIT software.

5. Mineralogy-Petrography

5.1. Optical Microscope Studies

The metamorphic rocks in the Göksun area consist mostly of metacarbonates (muscovite, biotite, chlorite and/or tremolite-bearing marble) and less metapelitics (phyllite, tourmaline-garnet phyllite, calcphyllite) and rarely metapsammitic rocks (metasandstone, phyllitic quartzite). The main texture of metamorphites is consisted by the rock assemblages that have grano-lepido-nemato-fibroblastic and blastopsammitic texture with respect to the ratio of granular, platy, rod and fibrous minerals. The main mineralogical compositions of the rocks are represented by quartz, feldspar (plagioclase, orthoclase), mica (muscovite, biotite, and sericite), chlorite, calcite, dolomite, and tremolite and hematite minerals. These are accompanied by index minerals such as garnet and tourmaline and secondary minerals such as hematite and zircon.

Calcite or rarely observed dolomite in metacarbonates are bright pearly gray in color and very fine grained (0.063-0.25 mm) and there are polysynthetic twinnings with single or double directions in some coarse grained parts (0.5-2 mm) (Figure 14a). In some sections of these marbles, the

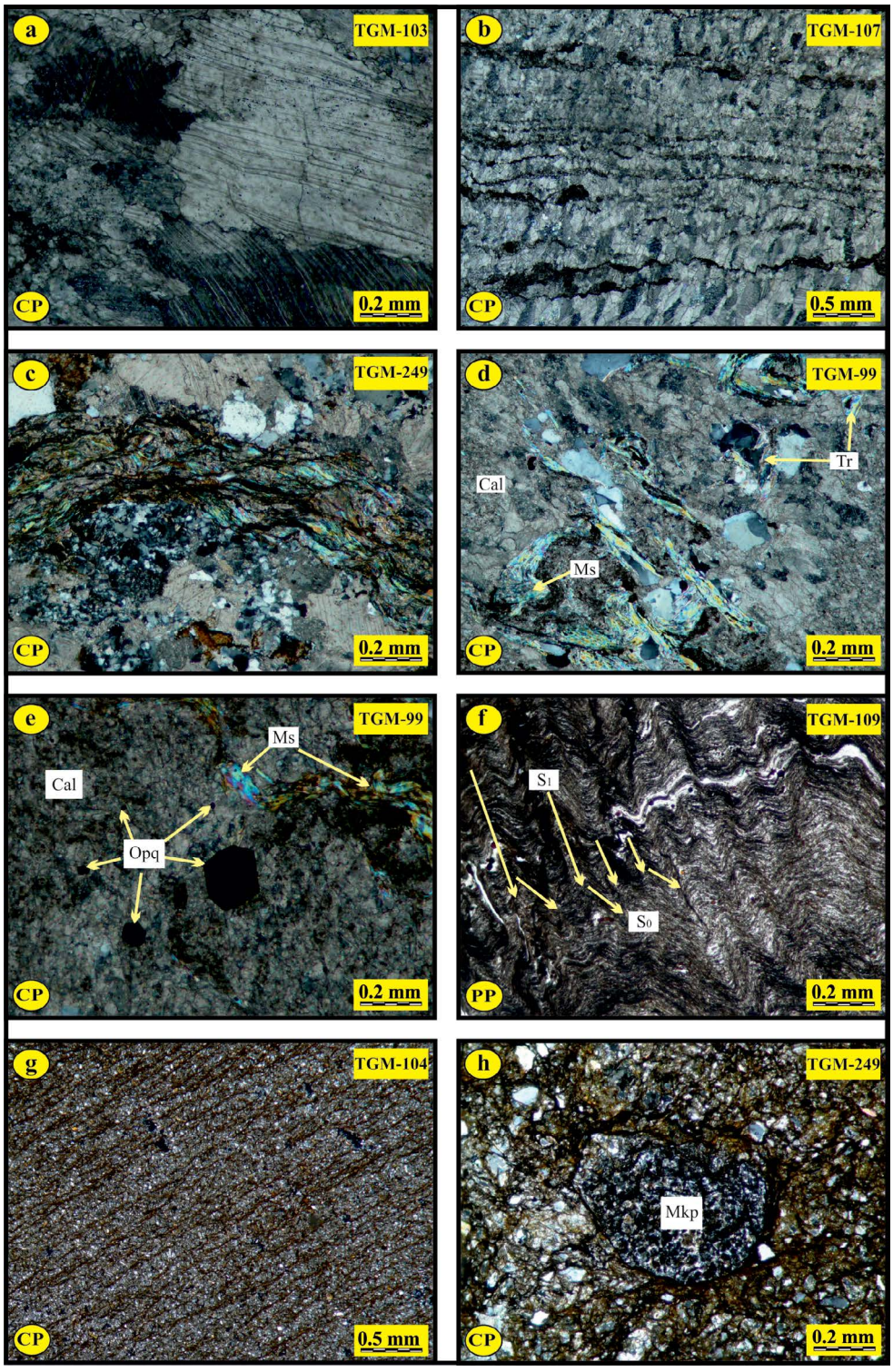

Figure 14- The optical microscopic views of metamorphic rocks in the Göksun region (CP: Cross polarised, PP: Plane polarised, Cal: Calcite, Ms: Muskovite, Tr: Tremolite, Opq: Opaque mineral, Mrf: Magmatic rock fragment, S0: Primary bedding plane, S1: Slate cleavage), a) coarse calcites with single and double polysynthetic twinning, b) remarkable banding in marbles, c) microfolded and oriented opacifications developed from phyllosilicates, d) folds and orientations in the minerals of tremolite-muscovite marbles, e) euhedral opaque minerals and folded muscovites in the marbles, f) clear slate type of crenulation cleavage and planes developed in the phyllites, g) weak folding and orientations in the phyllites and h) Magmatic rock fragment observed in the metasandstones.

coarse grained (0.5-2 mm) secondary crack fillings are observed in addition to significant banding (Figure 14b). The most common and prominent feature observed in metacarbonates is crenulaton cleavage (Figure 14c) and banding (Figure 14d). The euhedral Fe-oxide (hematite) rich levels are also observed in these rocks (Figure 14e).

The most distinctive feature of phyllitic rocks is the observation of the crenulation-type slaty cleavage and the microfoliation/banding and the angle between the primary bedding or primary cleavage plane (S_0) and the later developed cleavage planes (S_1) vary between 90-135° (Figure 14f). In these rocks, where Fe-oxide rich levels are commonly observed, porphyroblastic textures composed of coarse grained (0.5-2 mm) quartz in places are also found. While some phyllites do not show crenulation cleavage, they often contain continuous or smooth with intermittent (Powell, 1979), and sometimes partly weak and discontinuous slaty cleavages (Figure 14g). In these, (S_0) and (S_1) are approximately parallel to each others or intersect at an angle of less than 10-40°.

Metasandstones have fine to medium grained (0.063-0.25 and 0.25-0.5 mm) and they have the mineral orientation and crenulation cleavages as well as primary sedimentary foliation. In addition, the metamorphic, magmatic (Figure 14h) and sedimentary rock fragments were occasionally distinguished in these rocks.

In phyllitic quartzite rocks, the pale greenish chlorite appears in the fan form and phyllitic lamination and folding and orientations are typical for mica. There are opaque mineral laminations in these rocks, where large mica pods/stacks are occasionally observed.

The metamorphic rocks located in Afşin area are mostly; metacarbonate (marble, tremolite/actinolite marble, mica marble, dolomitic marble, tremolite/ actinolite-muscovite marble, phyllitic marble and chlorite epidote marble), schist (calcschist, garnet calcschist, calcsilicatic schist, chlorite micaschist, biotite chloriteschist), less metapelite (phyllite, calcphyllite), metabasite (amphiboleschist, epidote amphiboleschist, garnet epidote amphiboleschist, epidote clinopyroxene amphiboleschist) and metapsammite (feldspar quartzite).

The main texture of metamorphites are consisted by the rock assemblages that have granoblastic, lepido-granoblastic, nemato-granoblastic, lepido-nemato-granoblastic, nemato-lepido-granoblastic, and nematoblastic textures according to the ratio of granular/platy/rod/ fibrous minerals.

The major mineralogical compositions of the rocks that form the metamorphites in the region are mainly; quartz, feldspar (plagioclase, orthoclase), mica (muscovite and/or sericite, biotite), chlorite, calcite, dolomite, amphibole (tremolite/actinolite, antophyllite), clinopyroxene (diopside), epidote and hematite minerals. In addition to these minerals, the index minerals such as scapolite and garnet are also present. All these mineral assemblages are accompanied by accessory minerals such as apatite, titanite and/or xenotime and zircon.

Calcite and dolomite, which are commonly observed in granoblastic textured metacarbonates, exhibit a bright pearly grayish color and generally have evidently relief, single or double directed polysynthetic twinnings with medium to coarse grains (0.25-0.5 mm) (Figure 15a). The orientation, banding/ lamination, zig-zag/kink and band structures are clearly observed in these rocks (Figure 15b). While quartz is observed as polycrystalline and thick veins in places, the orthoclases present a euhedral structure and show intense argillizations. In rocks rich in mica minerals, which are widely observed in metacarbonates, clear micro folds and orientations (Figure 15c), schistosity plane and phyllitic laminations, mica pods (Figure 15d) and chloritizations developed from mica minerals. Amphibole in the form of tremolite/actinolite and anthophyllite generally shows a needle-rod like form (Figure 15e-f), but are also occasionally observed as rhombus clevage. In calcsilicatic schists, which are rarely observed in metacarbonates, there are viable interference colored scapolites and clinopyroxene containing typical parallel lines (Figure 15g).

In metapelites; the microlamination, microfracture and orientations are typical. In these rocks, where distinct schistosity planes are observed, in addition to opaque mineral laminations, alterations such as epidotization and in occasion porphyroblastic textures are observed (Figure 15h-i-j). Another feature observed in this rock group is the stack structures in different paragenesis such as biotite-muscovite (BMS), chlorite-muscovite (CMS) and/or chlorite-

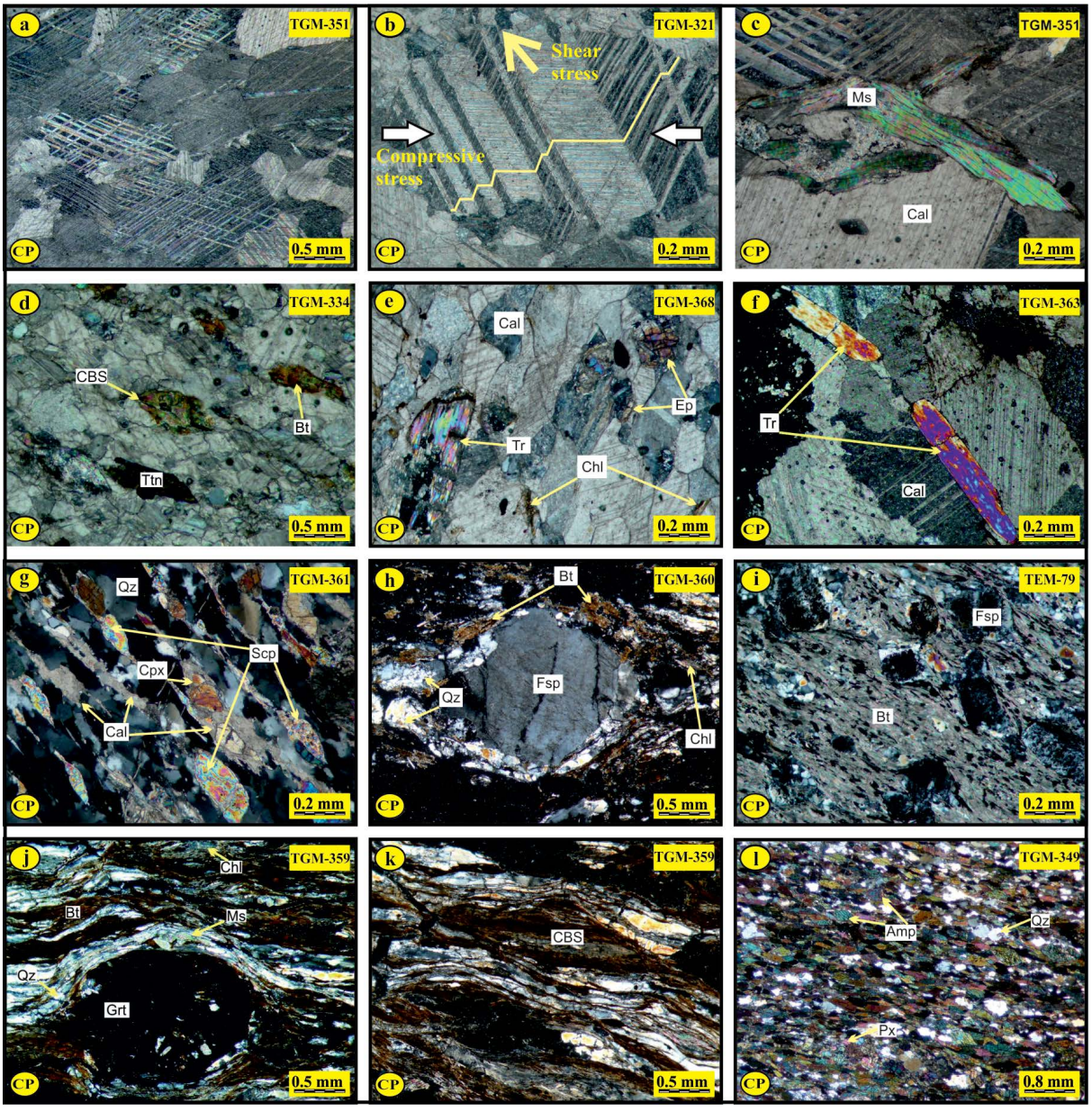

Figure 15- Optical microscopic wiews of metamorphic rocks in Afşin region (CP: Cross polarised, PP: Plane polarised, Cal: Calcite, Ms: Muscovite, Bt: Biotite, Chl: Chlorite, Qz: Quartz, Fsp: Feldspar, Ep: Epidote, Amp: Amphibole, Cpx: Clinopyroxene, Scp: Scapolite, Grt: Garnet, Tr: Tremolite, Ttn: Titanite, Opq: Opaque mineral, Mrf: Magmatic rock fragment, CBS: Chlorite-biotite stack), a) single and double directional polysynthetic twinning in the calcites forming marbles, b) high shear stresses in asymmetric monoclinal kinking folds in marbles (arrows indicate the direction of stress), c) significant orientation and weakly folded structure in the mica marbles, d) biotite-chlorite stack in the mica marbles, e) platy chlorites, rod-needle tremolites and epidote with crack and high optical relief in the chlorite-tremolite-epidote marbles, f) tremolite orientations in the tremolite/actinolite marbles, g) distinct diallag type divisions in the clinopyroxenes in the calcsilicate schists, h) polycrystalline quartzs developed around highly argillized and seriticized feldspar porphyroblasts in the micaschists, i) lepidoporphyroblastic texture formed by greenish colored biotites in the micaschists, j) garnet porphyroblast in the garnet-chlorite micaschists, k) chlorite-biotite stack in the garnet-chlorite micaschists and l) significant schistosity planes and orientations in the amphiboleschists.

biotite (CBS) formed by mica and chlorite (Figure 15k).

In metabasics, distinct schistosity planes developed from amphibolites are one of the most typical features (Figure 15l). Opaque mineral orientations, titanites exhibit a semi-rounded to rounded appearance and porphyroblastic texture in some places reflect other features of these rocks.

The metamorphic rock assemblages in the Ekinözü region based on the amount of abundance are; metapelitic and quartz-feldspar bearing rocks (granitic augen gneiss/mica gneiss, phyllite, micaschist, chlorite micaschist, garnet micaschist, tourmaline micaschist, tourmaline sillimanite micaschist, sillimanite kyanite micaschist, tourmaline staurolite garnet micachist, staurolite garnet micaschist, chlorite schist, actinolite chloriteschist, kyanite actinolite chlorite schist), metacarbonates (marble, mica marble, epidote mica marble, biotite marble, chlorite marble, tremolite chlorite marble), metabasics (amphibolite/amphiboleschist, hornblendeschist, garnet hornblende schist, chlorite actinolite schist), metapsammites (quartzschist/quartzite, tremolite quartzschist, biotite chlorite quartzschist, chlorite quartzschist, tourmaline garnet mica quartzschist, epidote muscovite quartzschist, chlorite quartzschist, metasandstone).

The main texture of metamorphics are nematoblastic (lepido-nematoblastic), lepidoblastic (nemato-lepidoblastic and fibro-nemato-lepidoblastic), granoblastic (lepido-granoblastic, nemato-granoblastic and nemato-lepido-granoblastic), rarely blastopisamitic texture, morter and mylonitic in occasion.

The main mineralogical compositions of the metamorphic rocks are; quartz, feldspar (plagioclase, orthoclase), mica (muscovite, biotite, sericite), chlorite, calcite, dolomite, amphibole (hornblende, tremolite/actinolite and antophyllite/gedrite), pyroxene, epidote and hematite. In addition to these major minerals, the index minerals such as sillimanite, kyanite, staurolite, garnet and tourmaline, which can reflect the type and intensity of metamorphism, are also present. All these mineral assemblages are accompanied by accessory minerals such as apatite, titanite/xenotime, beryl, rutile and zircon. Sillimanite and kyanite minerals were observed together in the same rock in some samples, indicating that the temperature and pressure conditions during the metamorphism of the rock exceeded 500°C and 4 kbar conditions (Deer et al., 1992; Pattison, 1992).

In addition to chloritic alteration in mica minerals, where distinct schistosity planes, microfolds, orientations (Figure 16a) and also the porphyroclastic textures (Figure 16b) are typically observed in metapelitics, the muscovite cuts biotite in occasion and biotite is sometimes at a perpendicular to schistosity plane as a result of granitic intrusion. The quartz has generally undulatory and microfractured phyllosilicate fillings were perpendicular to the schistosity plane. In the feldspar, while excessive argillization and partly sericitization developed, the pleochroic zircon grains and garnet with poikiloblastic texture (Figure 16c) were partially rounded.

The staurolite porphyroblasts (Figure 16d), containing poikiloblastic quartz inclusions, were formed under regional metamorphism conditions from pelitic rocks and reflect the intermediate grade metamorphism conditions corresponding the upper parts of amphibolite facies. The kyanite formed by the medium-high pressure metamorphism of Al rich pelitic rocks have been transformed into sericite by retrograde metamorphism (Figure 16e). In metapelitic rocks where sillimanite is observed in the form of fibrous-needle and perpendicular to the c-axis (Figure 16f), the tourmaline has also sections with perpendicular to the c-axis. Opaque oxide minerals are abundant occasionally, mostly euhedral, partly anhedral/semihedral and sometimes microfolded and oriented. According to petrographic observations, the accessory mineral defined as beryl is in trace amount and rarely observed as coarse porphyroblasts. Rutile, which offers a color ranging from reddish to brownish due to the increased iron content, has a very high optical relief.

In metabasics, there are observed hornblends (Figure 16g), which are considered as chermakitic with distinct schistosity planes and occasionally rod-prismatic (Figure 16h), both single and double directed cleavages and/or separations (Figure 16i). The traces of cataclasm in feldspar and quartz were rarely seen, as well as common argillization and sericitization in the feldspar. In pyroxene, where single and double directional cleavages are typically being followed and the alterations such as uralitization are present.

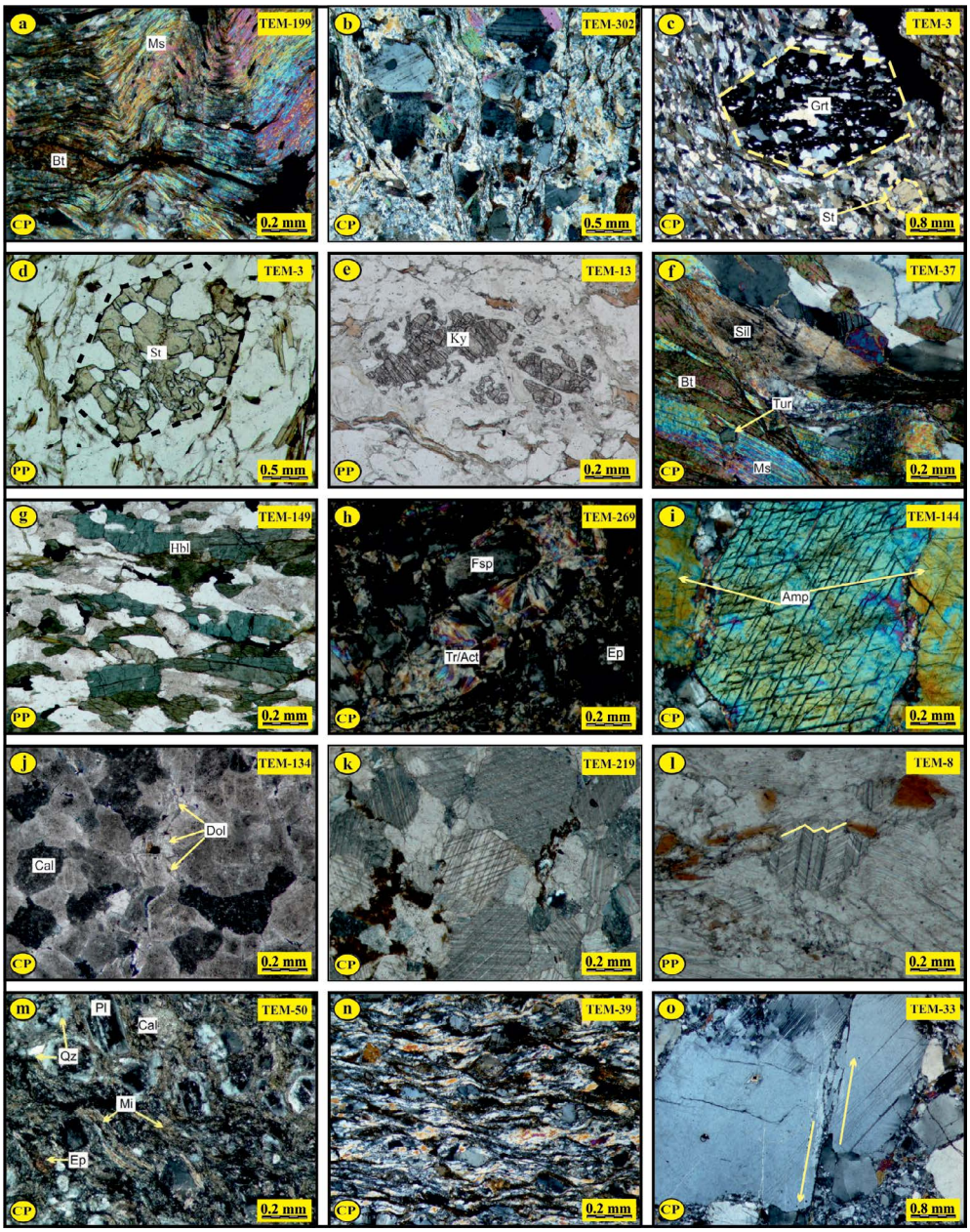

Figure 16- Optical microscopic views of the metamorphic rocks in the Ekinözü region (CP: Cross polarised, PP: Plane polarised, Cal: Calcite, Dol: Dolomite, Mi: Mica, Ms: Muscovite, Bt: Biotite, Qz: Quartz, Fsp: Feldspar. , Pl: Plagioclase, Ep: Epidote, Amp: Amphibole, Hbl: Hornblende, Tr: Tremolite, Act: Actinolite, Sil: Sillimanite, Ky: Kyanite, St: Staurolite, Grt: Garnet, Tour: Tourmaline, a) significant schistosity planes, folds and orientations in the micaschists, b) porphyroclastic texture in the granitic augen gneisses, c) poikiloblastic texture developed in the euhedral garnets and staurolites, d) euhedral staurolite porphyroblast containing poikiloblastic quartz inclusions in the micaschists, e) kyanite porphyroblasts surrounded by sericites in the kyanite micaschists, f) fibrous sillimanite and associated minerals developed in the micaschists, g) chermakitic hornblends observed in the amphiboleschists, h) fan-shaped tremolite/actinolites and associated minerals in the tremolite/actinolite epidotefels, i) double directional cleavages developed in the perpendicular section to the c-axis of the amphiboles in the amphibolites, j) euhedral dolomite crystals developed in the dolomitic marbles, k) distinct single and double directional polysynthetic twinning in the calcites from marbles, l) kinking band structures developed from calcite minerals in the biotite marbles, m) argillization and sericitizations in the metaarcoses, n) lenticular feldspar and quartz porphyroclasts in the mylonite/protomylonites and o) shear traces caused by cataclasm effect in the morter textured amphibolites.

In addition to distinct polysynthetic twinnings (Figure 16j), mostly in fine grained (0.063-0.25 mm) calcite or occasionally euhedral dolomite in metacarbonates, there are cracks that developed perpendicular to the microlaminations (Figure 16k). They are partly mesh/porous in texture, micro-faulted and kinking band structures are remarked (Figure 16l). The chloritization type of alterations is observed in occassion in the mica minerals. Biotite and epidote minerals are rarely found as the crack filling. Chlorite is fan-shaped and occasionally opacitized; as to tremolite, they have been fibreous and needle forms. Rare quartz and opaque minerals are generally found as in cavities or crack fillings.

The quartz in metapsammites, whose origin is mostly the quartz sandstones are partly fine grained (0.063-0.25 mm), generally with undulatory and polycrystalline (Figure 16m). In feldspar, the intense argillization and partly sericitization are seen. Chloritizations in phyllosilicate minerals in some places and slate and/or phyllite foldings are observed, while in some parts muscovite cuts biotite. While the folds are occasionally observed in rod, needle-like tremolite, the zircon is generally rounded and opacities are in the form of cavities and crack fillings.

Mylonite and/or protomylonites, which are among the products of the cataclastic metamorphism, rarely observed in the region, exhibit a lenticular appearance with porphyroclast grains (Figure 16n). In addition, there are traces of slip formed by the cataclasm effect in these rocks (Figure 16o).

5.2. X-Ray Mineralogy

5.2.1. XRD-WR and XRD-CF Analyses

The metamorphic rocks located in the Göksun region are represented mostly by metacarbonate, less metapelitic and partly by metapsammitic rock groups (Figure 17). In metacarbonates (TGM-98), which constitute the dominant lithology in the region, the calcite and dolomite are the dominant minerals, whereas the metapelitic rocks (TGM-254) mainly contain phyllosilicate, feldspar, quartz and hematite. Metapsammitic rocks on the other hand are represented by quartz, feldspar and phyllosilicate minerals.

The clay minerals in metacarbonates are mainly formed of illite, chlorite and partly smectite and kaolinite. However, in metapelitic rocks (TGM-122, 124, 230) illite, less chlorite, paragonite, smectite, kaolinite and mixed layers (C-V and I-C) are observed (Figure 18-19).

The metamorphic rocks located in the Afşin region according to abundance order are; metacarbonate, metapelite and metabasics (Figure 20). Calcite and dolomite are the most abundant minerals in metacarbonate rocks (TGM-358, 365), followed by less quartz, feldspar, phyllosilicate and rare epidote. Metapelitic rocks (TEM-60, 84, 303); are consisted by phyllosilicate, quartz, feldspar, partly hematite and rare paragonite, epidote, scapolite and pyroxene minerals. Metabasic rocks according to abundance are; mainly amphibole, feldspar, and less calcite and phyllosilicate. The clay mineral components of the metacarbonate rocks (TEM-84, 85) in the region are composed by illite, chlorite, smectite and mixed layers (C-V, C-S and I-C). The clay minerals of the metapelitic rocks (TEM-71) are formed mainly by illite, then chlorite, smectite, paragonite, kaolinite and mixed layers (C-V, C-S and I-C). Clay minerals of the metabasic rocks in the abundance order are represented by chlorite, smectite and mixed layers (C-V and C-S) (Figure 21-22).

The metamorphic rocks in the Ekinözü region are mainly metapelitic and metabasic, less metacarbonates and rare metapsammitic rock groups (Figure 23). The rock assemblages forming the metapelitics (TEM-136, 159) in abundance order are represented by phyllosilicate, feldspar, quartz, amphibole, calcite, dolomite and hematite, and index minerals such as pyroxene, epidote and tremolite. Calcite, quartz, feldspar, phyllosilicate, amphibole, hematite, pyroxene and epidote constitute the whole rock association of metabasic rocks (TEM-171, 270). Whole rock compositions of the marble and calcschist rocks in the unit are either completely pure or close to pure calcite and/or dolomite, or in each sample, calcite + quartz + feldspar + mica + chlorite in different amounts and numbers. This paragenesis is accompanied by very few specimens and a small amount of amphibole and hematite. Quartz + feldspar + phyllosilicate in trace amount accompanied by hematite forms the whole rock association of the metapsammitic rocks which are the least available in the unit.

When clay mineral associations of rocks in the region are examined, of the phyllosilicate association

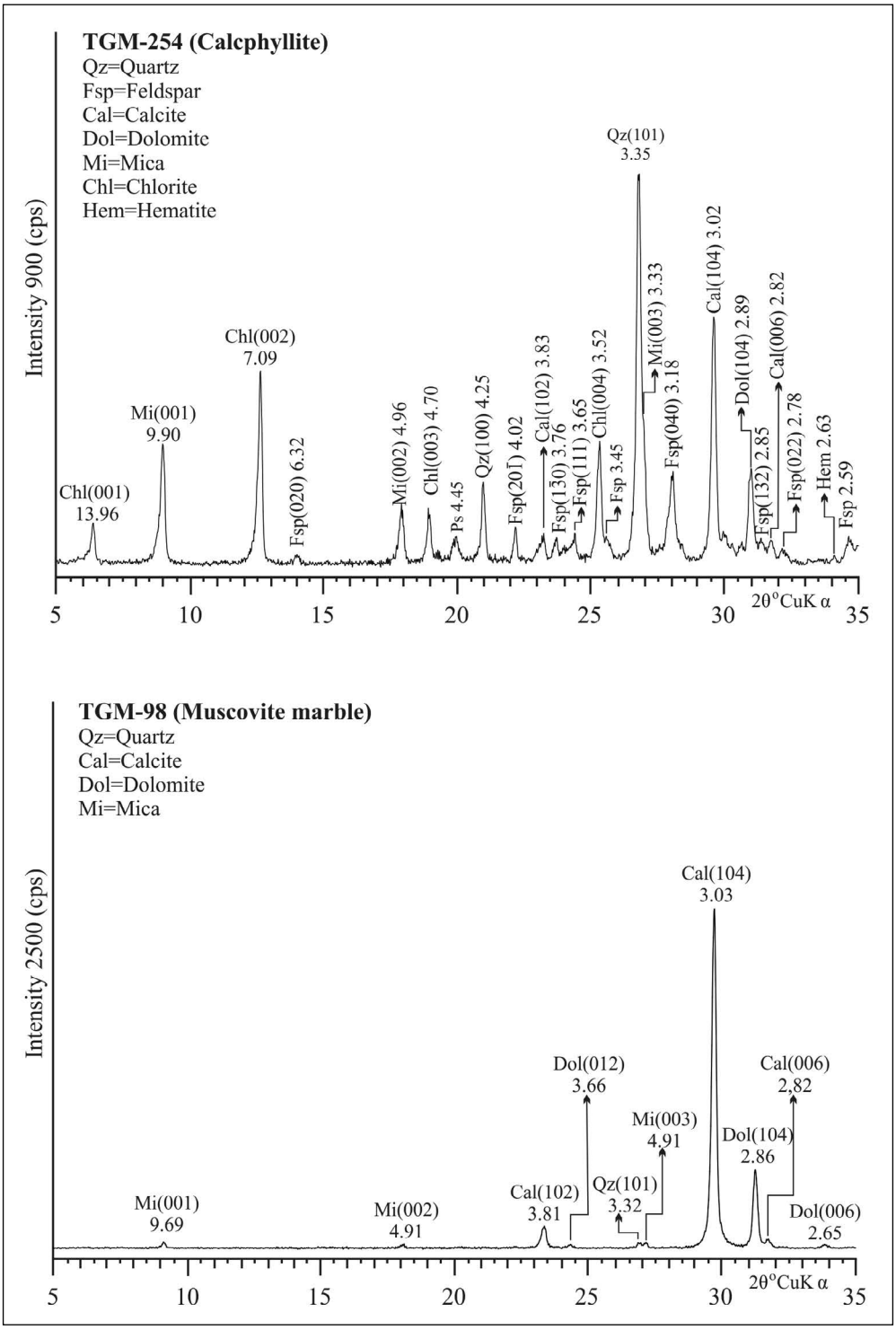

Figure 17- XRD-WR diffractograms of the metamorphites from Göksun region.

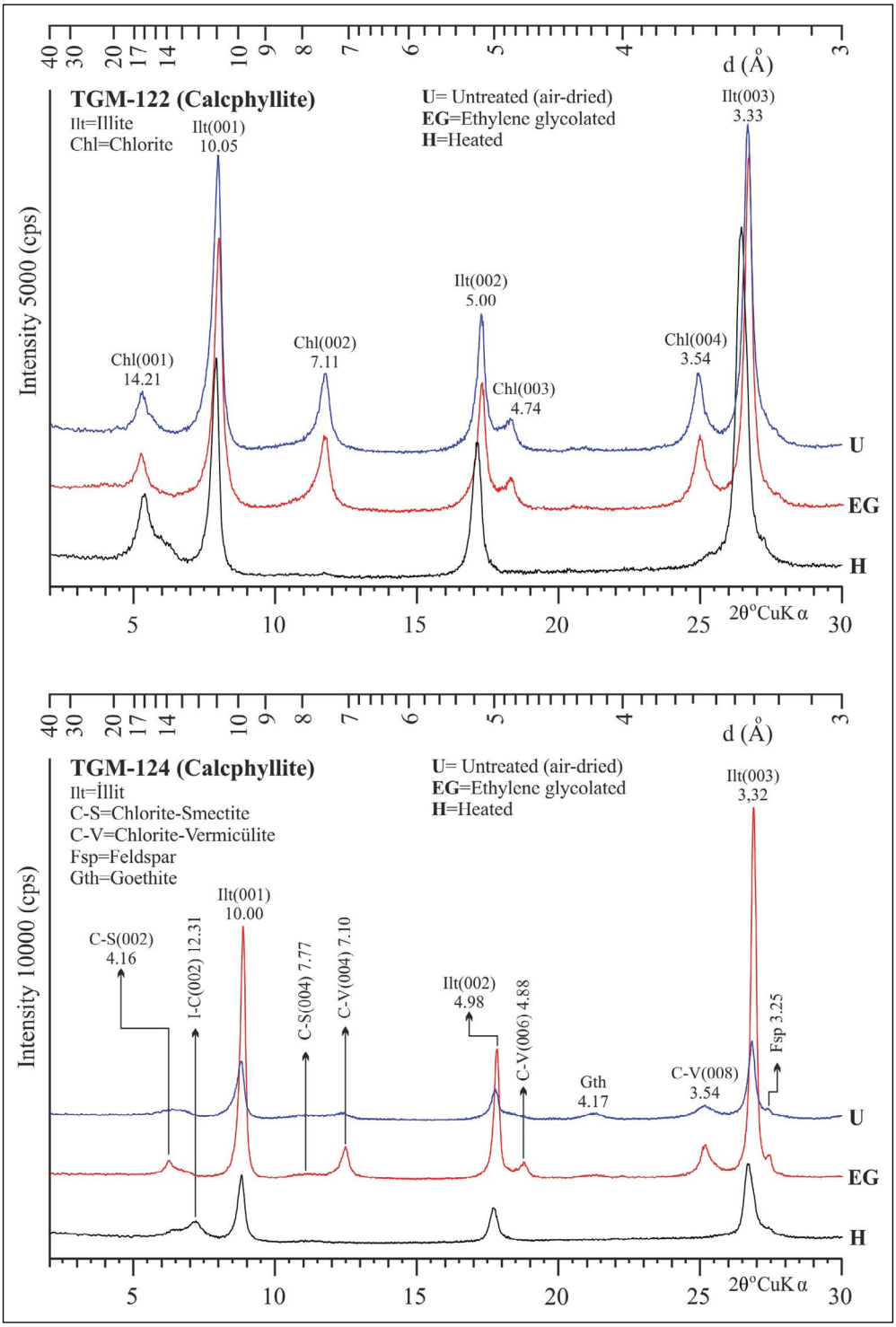

Figure 18- XRD-CF diffractograms of the metamorphites from Göksun region.

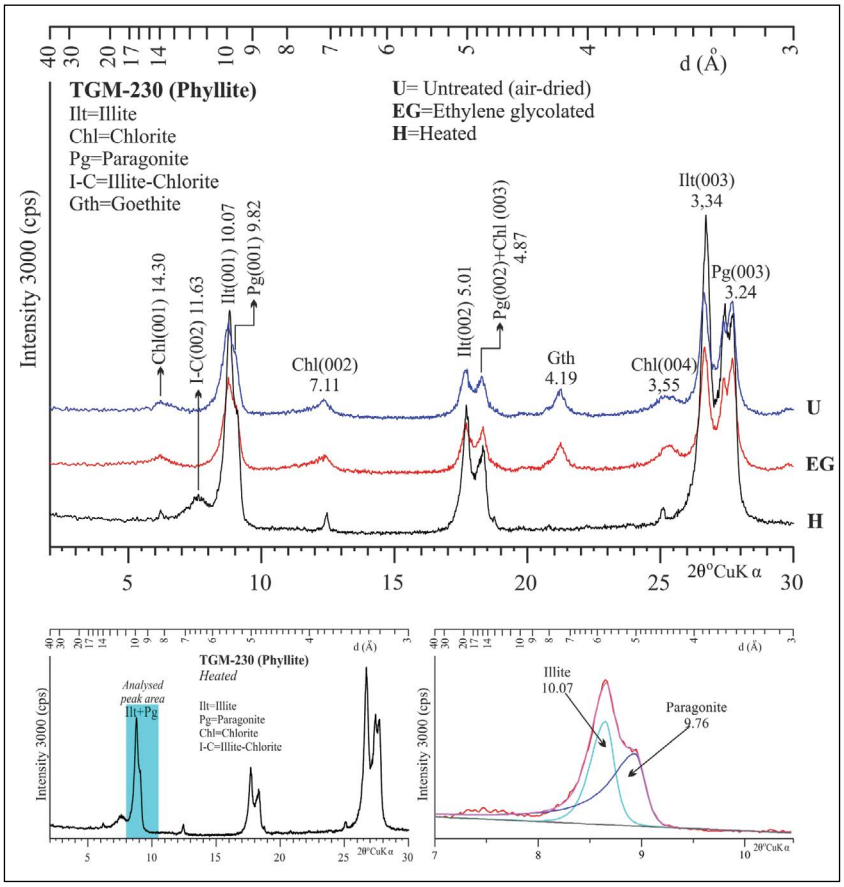

Figure 19- The analysis of complex peaks belonging to illite + paragonite association in XRD-CF diffractograms using WINFIT software from the metamorphites in the Göksun region.

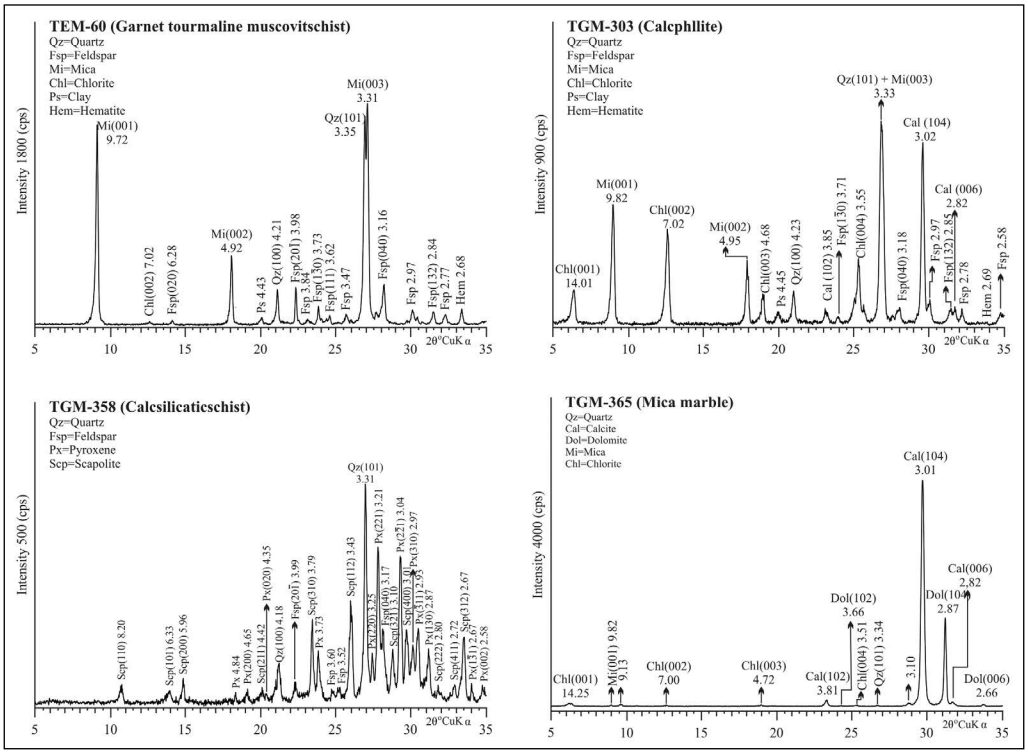

Figure 20- XRD-CF diffractograms of the metamorphites from Afşin region.

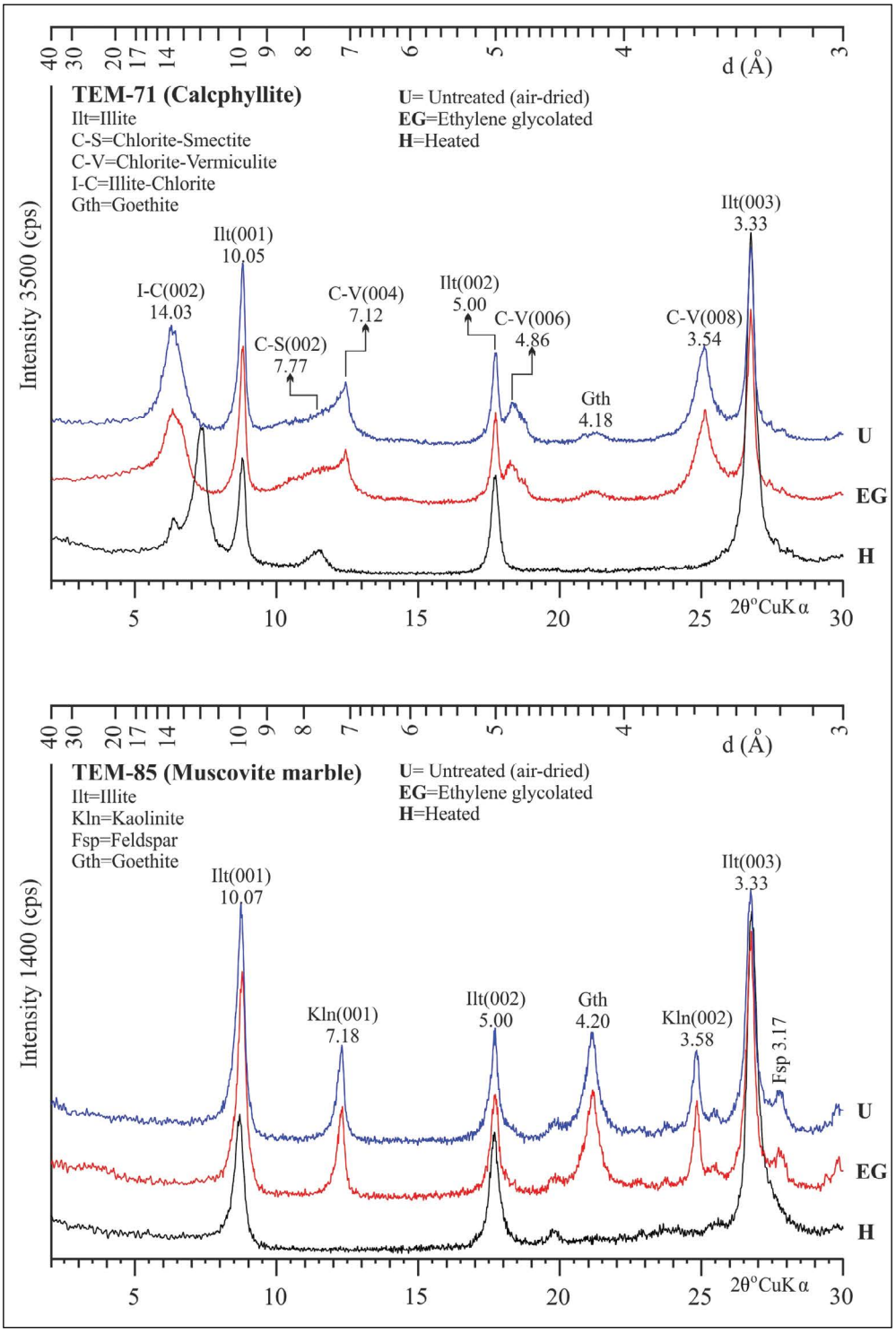

Figure 21- XRD-CF diffractograms of the metamorphites from Afşin region.

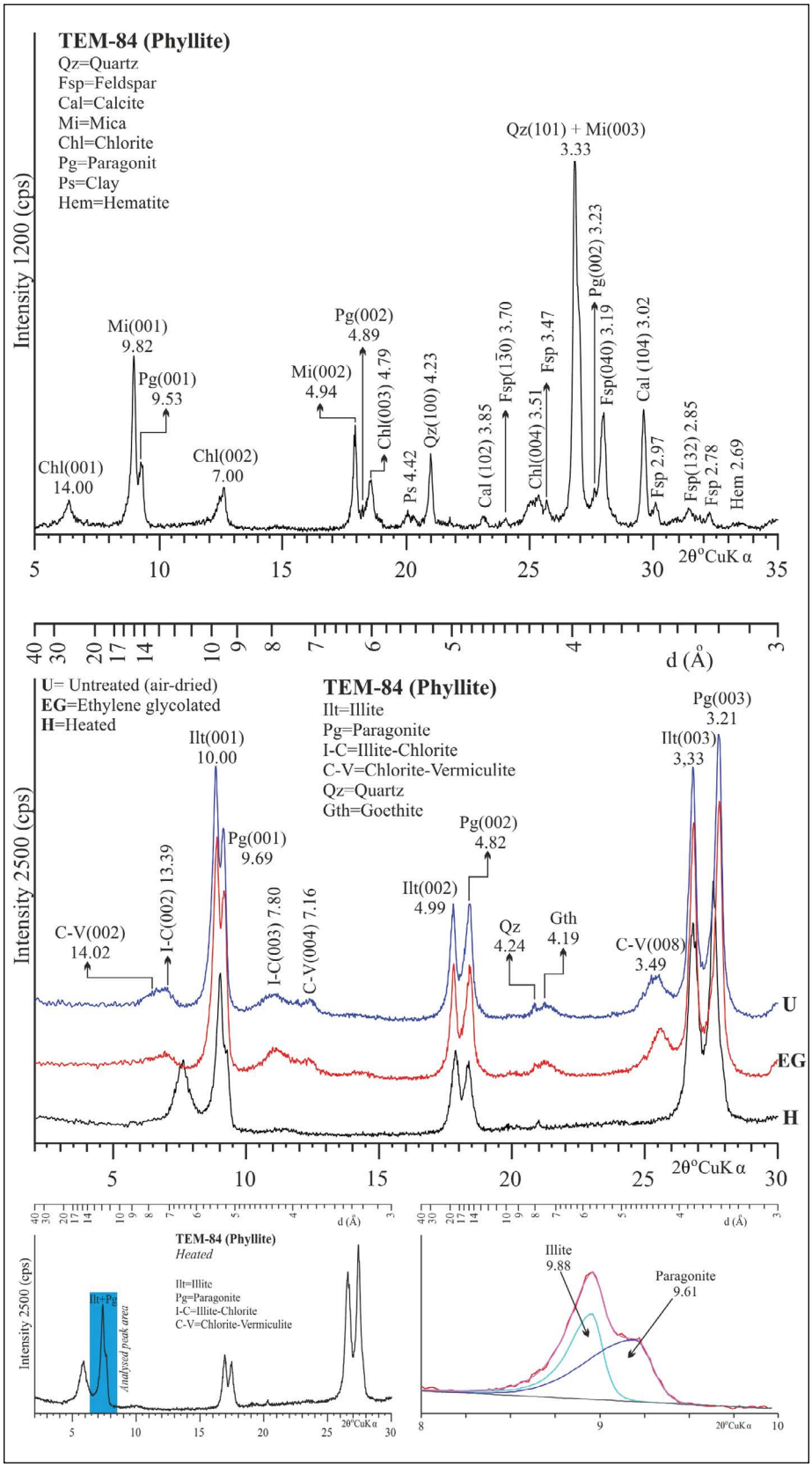

Figure 22- XRD-WR-CF diffractograms and WINFIT analysis of complex peaks of the metamorphites from Afşin region.

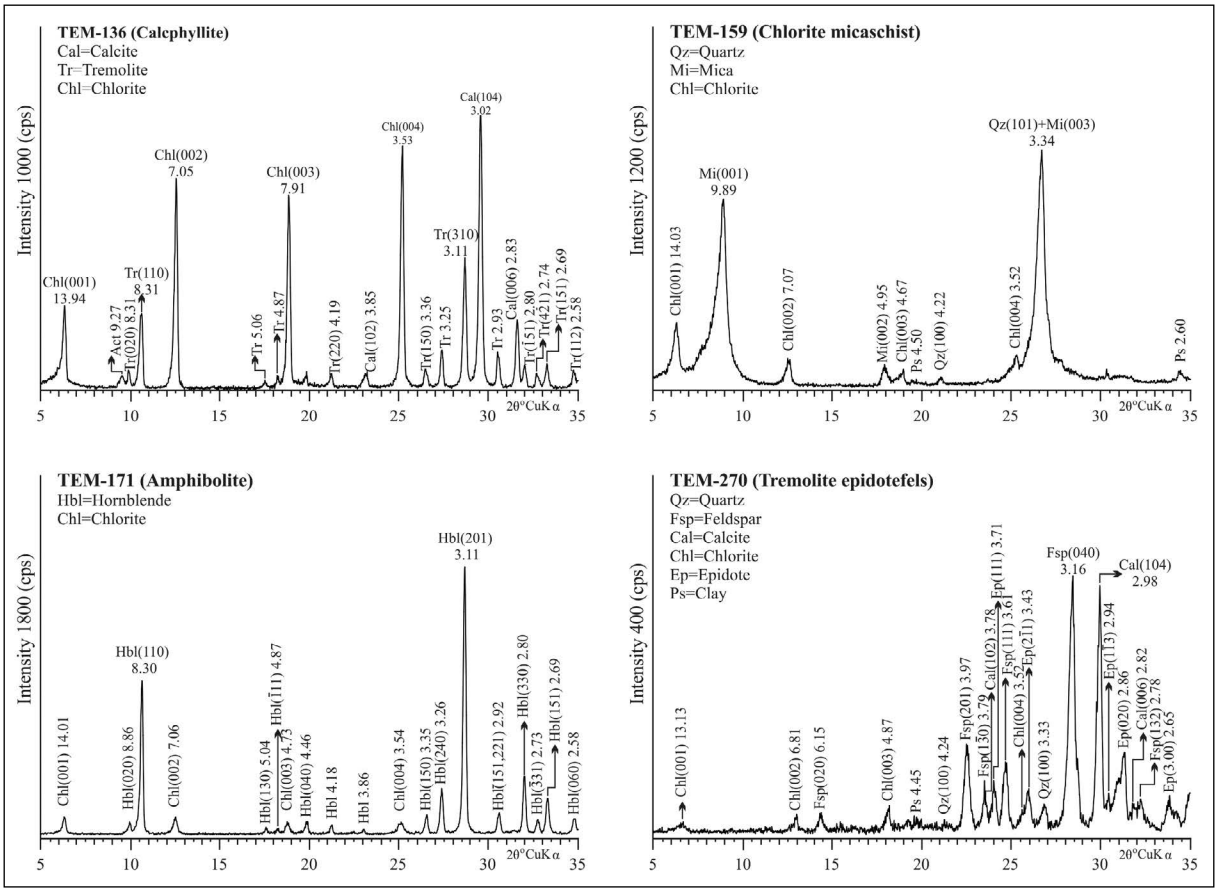

Figure 23- XRD-WR diffractograms of the metamorphites from Ekinözü region.

of metapelites (TEM-203, 209, 218, 265, 299) are composed of C-V, I-C, I-V and C-S types of mixed-layered clay minerals, in addition to smectite, illite, chlorite, vermiculite, kaolinite. The phyllosilicate association of metabasics is represented by smectite, illite, chlorite and mixed layers (C-V, I-C, I-V and C-S). In the phyllosilicate association of metacarbonates, the illite, chlorite and C-S mixed layered clay minerals were determined. The phyllosilicate compositions of metapsammitics are consisted of illite + chlorite + C-V + I-C association (Figure 24-25). Illite peak intensity of 5 Å in TEM-203 sample indicates that they are biotite.

5.2.2. Crystalo-Chemical Analyses of the Phyllosilicates

The results of polytype analysis of pure K-mica fractions belonging to the rocks in Göksun, Afşin and Ekinözü regions are given in table 1, and the polytype and d_{060} measurements are given in figure 26. Illite has mainly $2M_1$ white K-mica (muscovite) and 1*M* biotite polytypes, however; chlorite minerals are entirely composed of IIb polytype. According to d_{060} values octahedral (Mg + Fe) compositions in all three regions (Göksun d_{060} 1.4972-1.5093 Å, average 1.5032 Å and (Mg + Fe) 0.18-0.77 and average 0.47, Afşin d_{060} 1.5007-1.5106 Å, average 1.5051 Å and (Mg + Fe) 0.35-0.84 and average 0.56, Ekinözü d_{060} 1.4977-1.5088 Å, average 1.5040 Å and (Mg + Fe) 0.20-0.75 and avergae 0.51), illite is completely dioctahedral in composition.

Crystallinity values obtained by calibrating the half-height peak width (FWHM) values of illite and chlorite minerals of the Göksun, Afşin and Ekinözü regions by WINFIT software (Kübler Index-KI: Kübler, 1968, and Arkai Index-Al: Árkai, 1991; Guggenheim et al., 2002 for illite and chlorite, respectively), the peak intensity ratios and the calculation results of the crystalline sizes of illite determined by two different methods (Merriman et al., 1990 and WINFIT software) are given in table

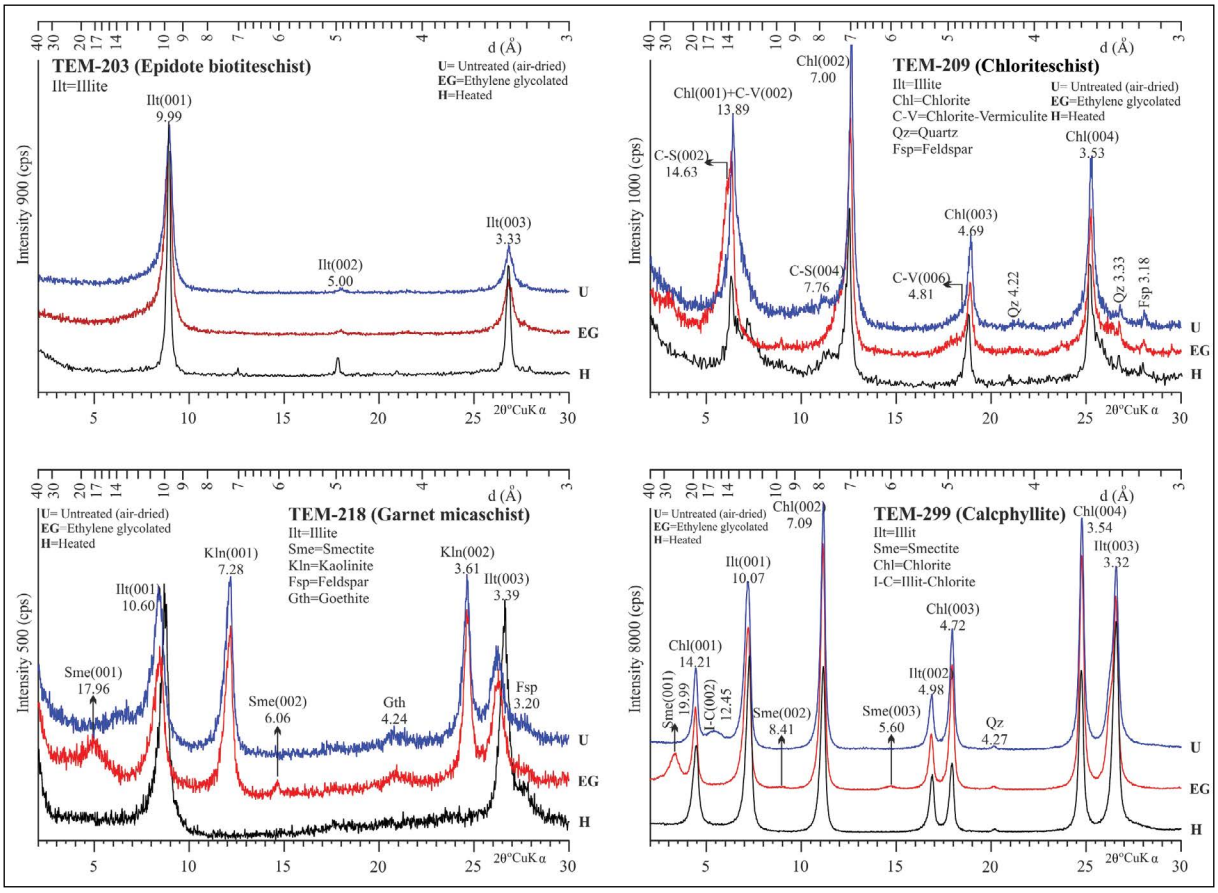

Figure 24- XRD-WR diffractograms of the metamorphites from Ekinözü region.

2. The sizes of illite crystallites range between 15-96 nm (average 53 nm) in the Göksun region, 13-128 nm (average 57 nm) in the Afşin region and 11-96 nm (average 29 nm) in the Ekinözü region based on the formula suggested by Merriman et al. (1990) (N001 = 8.059 / β; β = 1.038949) x KI-0.08250323).

The crystallinity measurement values for each region are evaluated in KI-I (002)/(001) diagrams (Figure 27). According to these, it is seen that the Göksun region has 0.16-0.58 Δ˚2θ and with the average value of 0.26 Δ˚2θ corresponding mostly to epizone, partially anchizone and rarely diagenesis, the Afşin region has 0.14-0.67 Δ˚2θ with the average value of 0.24 Δ˚2θ mainly corresponding to epizone, rarely anchizone and diagenesis, and the Ekinözü region has 0.07-0.77 Δ˚2θ and with the average value of 0.40 Δ˚2θ corresponding mostly anchizone, partially epizone and diagenesis values.

The b_0 results together with average values and standard deviations of illite/K-mica of the Göksun, Afşin and Ekinözü regions are presented in table 3. All three regions were evaluated as a whole and the b_0 vs cumulative frequency (%) distribution of illite/K-mica minerals were given in figure 28. Thus, it is seen that the *b* cell parameters of illite/K-mica varies between 8.9912-9.0574 Å and their average values with 9.0271 Å, represent mostly the medium pressure, and low and high pressure facies series in less ratios. On the other hand, it was seen that b_0 values of illite/K-mica were reached to typical low pressure and high pressure and glaucophanitic greenschist facies conditions for Barrovian type of regional metamorphism conditions given for Wales (Sassi and Scolari, 1974) and Sanbagawa (Robinson and Bevins, 1986).

6. Conclusions

Lithological, mineralogical and petrographical investigations of the Upper Paleozoic-Lower Mesozoic metamorphic units outcropping around the Göksun, Afşin and Ekinözü districts in the north

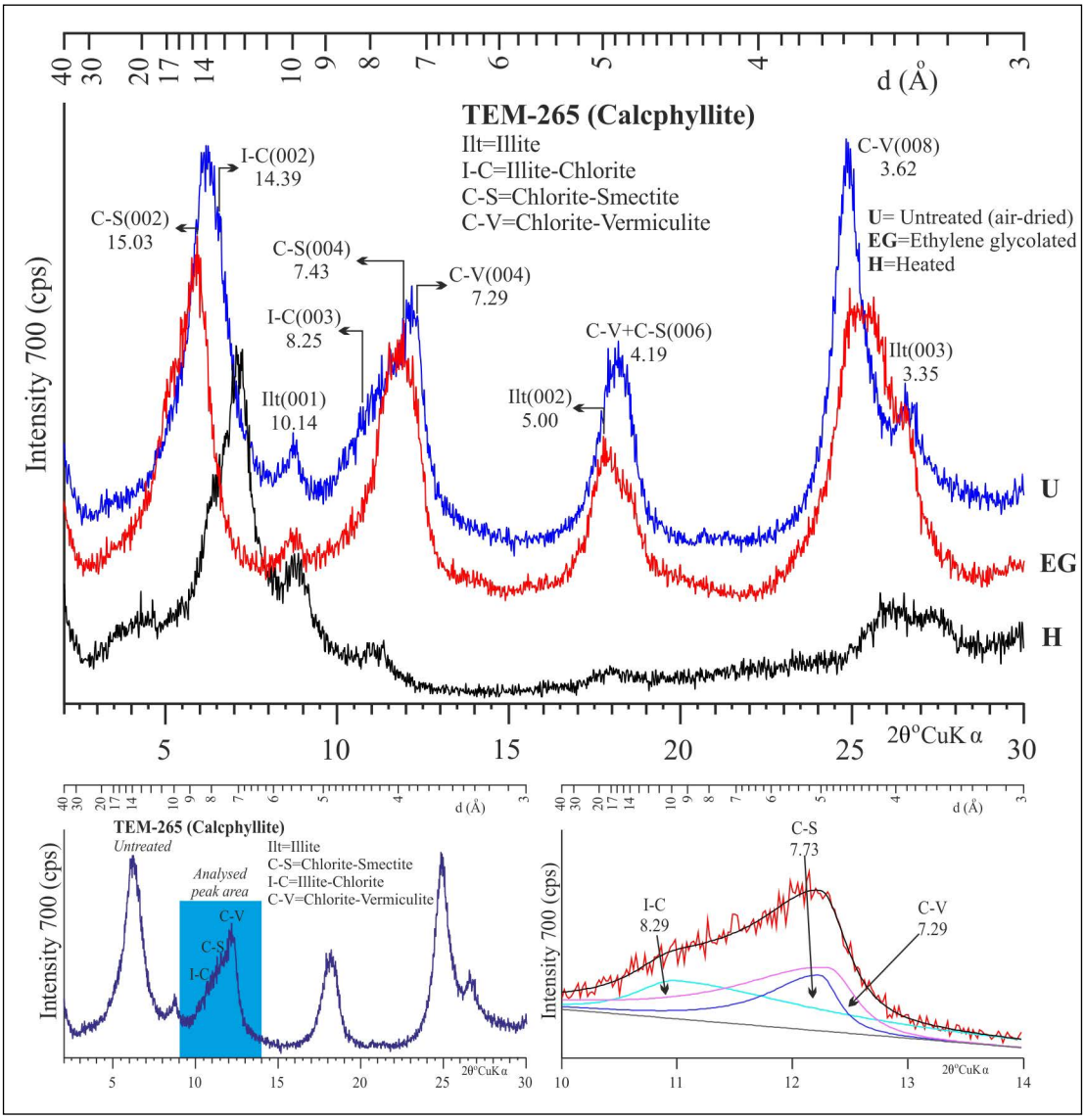

Figure 25- XRD-WR-CF diffractograms and WINFIT analysis of complex peaks of the metamorphites from Ekinözü region.

Table 1- Results of polytype analysis of illite/K-mica and biotite minerals in Göksun, Afşin and Ekinözü regions.

GÖKSUN		AFŞİN		EKİNÖZÜ			
Sample No	Illite/K-mica	Sample No	Illite/K-mica	Sample No	Illite/K-mica	Biotite	Chlorite
TGM-100	$2M_1$	TEM-60	$2M_1$	TEM-24			*II*b
TGM-112	$2M_1$	TEM-75	$2M_1$	TEM-28			*II*b
TGM-121	$2M_1$	TEM-79	$2M_1$	TEM-37	$2M_1$	1*M*	
TGM-125	$2M_1$	TEM-81	$2M_1$	TEM-40		1*M*	
TGM-222	$2M_1$	TEM-304	$2M_1$	TEM-42		1*M*	
		TEM-312	$2M_1$	TEM-43		1*M*	
				TEM-48		1*M*	
				TEM-57	$2M_1$	1*M*	
				TEM-59	$2M_1$	1*M*	
				TEM-299			*II*b
				TEM-302	$2M_1$		

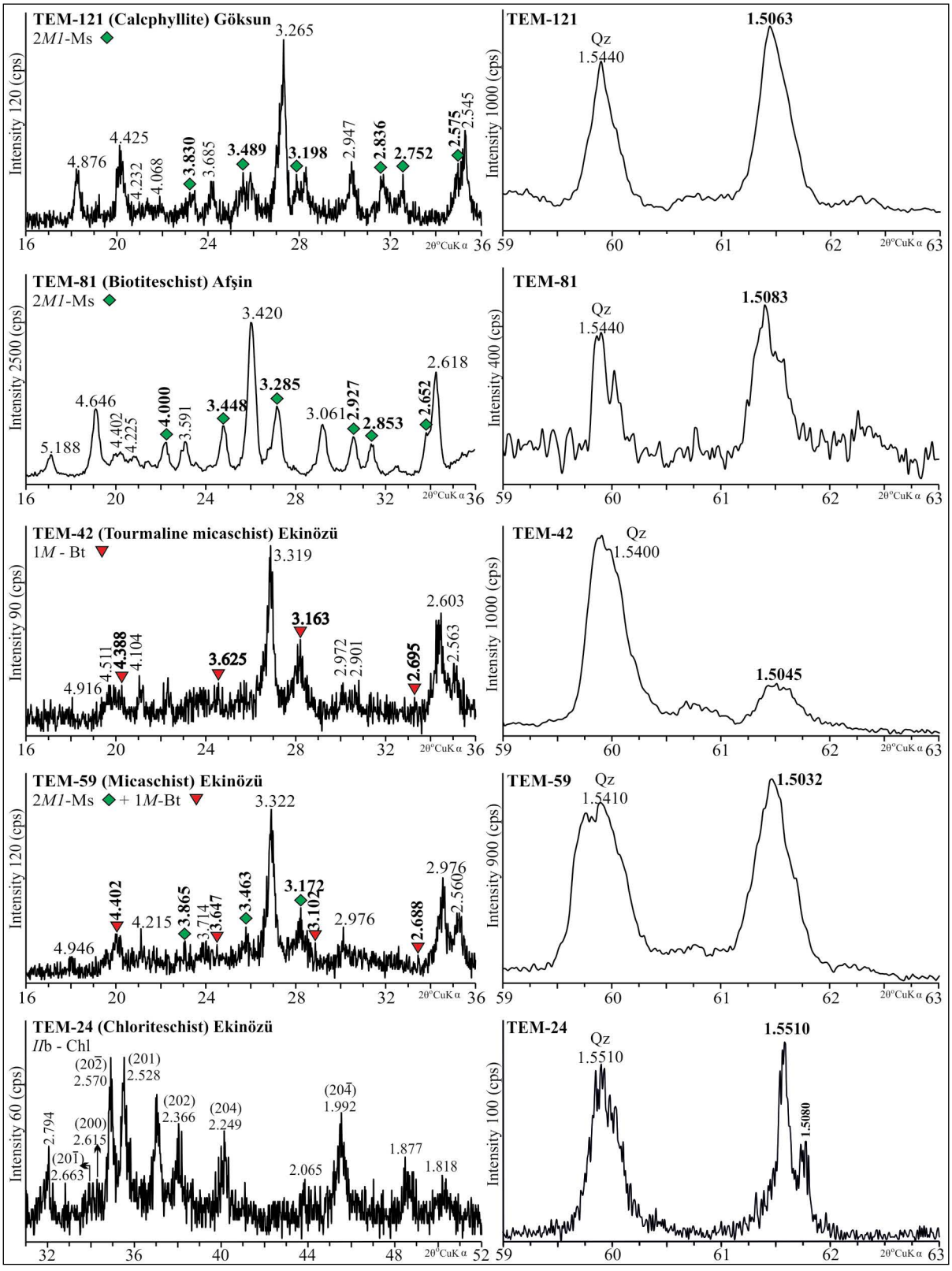

Figure 26- Polytypes and d_{060} XRD diffractograms of illites and chlorites in the Göksun, Afşin and Ekinözü regions.

Table 2- Results of crystallinity analysis of K-mica and chlorite minerals in Göksun, Afşin and Ekinözü regions and crystallite sizes (*N*, nm) determined by Merriman et al. (1990) and WINFIT methods (KI:Kubler Index, AI:Arkai Index).

GÖKSUN						AFŞİN					
Sample No	KI	AI	I(002)/I(001)	N(*)	N(**)	Sample No	KI	AI	I(002)/I(001)	N(*)	N(**)
TGM-86	0.23	0.24	0.54	52	11	TEM-60	0.19		0.29	70	19
-87	0.23	0.29	0.52	52	16	-63	0.24		0.67	48	20
-90	0.21	0.28	0.57	59	18	-66	0.25		0.67	45	15
-91	0.24	0.30	0.52	48	19	-68	0.21		0.55	59	22
-93	0.20	0.35	0.53	64	19	-69	0.19		055	70	22
-100	0.17		0.61	86	24	-70	0.23		0.48	52	16
-102	0.21		0.60	59	19	-71	0.20		0.53	64	21
-109	0.21		0.62	59	21	-72	0.22		0.48	55	19
-112	0.16		0.70	96	24	-74	0.17		0.61	86	19
-117	0.34	0.48	0.56	30	13	-75	0.18	0.28	0.57	77	20
-119	0.20	0.18	0.59	64	17	-79	0.20		0.29	64	20
-120	0.18		0.50	77	21	-81	0.20		0.32	64	19
-121	0.16		0.51	96	24	-82	0.23		0.55	52	17
-122	0.29	0.36	0.46	37	15	-83	0.25		0.45	45	19
-124	0.27		0.53	41	16	-84	0.21		0.47	59	15
-125	0.16		0.54	96	25	-85	0.29		0.49	37	14
-126	0.25		0.49	45	16	TGM-303	0.30	0.46	0.54	35	21
-127	0.20		0.60	64	21	-304	0.14		0.64	128	23
-222	0.24		0.46	48	18	-305	0.26		0.73	43	18
-223	0.38	0.71	0.64	26	13	-306	0.21		0.65	59	20
-224	0.16	0.38	0.63	96	15	-310	0.23		0.66	52	19
-229	0.58		0.25	15	11	-312	0.21		0.42	59	27
-230	0.50		0.54	18	11	-314	0.24	0.41	0.79	48	18
-231	0.48		0.45	19	14	-316	0.17	0.31	0.56	86	22
-237	0.30	0.73	0.51	35	15	-322	0.67	0.48	0.33	13	8
-238	0.20		0.86	64	16	-359	0.45		0.30	21	9
-241	0.23	0.42	0.60	52	16						
-242	0.23	0.30	0.42	52	23						
-243	0.22	0.35	0.86	55	16						
-245	0.30		0.54	35	21						
-246	0.27		0.57	41	16						
-247	0.26		0.80	43	17						
-248	0.25		0.91	45	16						
-254	0.25	0.24	0.60	45	16						

Table 2- Continue.

EKİNÖZÜ											
Sample No	KI	AI	I(002)/I(001)	N(*)	N(**)	Sample No	KI	AI	I(002)/I(001)	N(*)	N(**)
TEM-3	0.34	0.28	0.10	30	11	TEM-154	0.42		0.25	23	4
-4	0.53	0.37	0.21	17	10	-155	0.38		0.13	26	8
-5	0.37	0.28	0.12	27	12	-157	0.35		0.05	29	8
-10	0.16	0.29	0.69	96	27	-159	0.77	0.28	0.33	11	8
-12		0.25				-161	0.68		0.41	13	8
-13	0.30	0.18	0.45	35	13	-162	0.38		0.44	26	13
-17		0.18				-163	0.18		0.16	77	8
-18		0.24				-164	0.46		0.53	20	11
-20		0.15				-165	0.22		0.83	55	22
-21		0.21				-175		0.33			
-24		0.22				-176		0,21			
-27	0.41	0.21	0.23	23	11	-177		0.35			
-28		0.25				-194	0.44		0.11	22	13
-29	0.45	0.22	0.33	21	11	-195	0.52		0.48	18	11
-31		0.21				-197	0.32	0.21	0.20	32	15
-37	0.30		0.15	35	14	-198	0.39	0.08	0.57	25	13
-40	0.56		0.05	16	7	-199	0.51	0.12	0.31	18	11
-42	0.38		0.10	26	11	-200	0.56	0.38	0.39	16	9
-43	0.43		0.21	22	10	-201	0.16		0.16	96	12
-44	0.28		0.10	39	14	-202	0.49		0.21	19	10
-46	0.33		0.41	31	14	-203	0.30		0.04	35	12
-48	0.32		0.09	32	11	-209		0.32			
-49	0.27		0.07	41	14	-210		0.55			
-50	0.07	0.20	0.17	24	11	-215		0.24			
-52	0.42	0.23	0.24	23	11	-218	0.57		0.12	16	8
-53	0.38		0.22	26	13	-220	0.51		0.08	18	13
-54	0.37		0.34	27	12	-277	0.32	0.36	0.08	32	17
-56	0.30		0.23	35	16	-279	0.39	0.44	0.20	25	11
-57	0.51		0.15	18	10	-280	0.59	0.35	0.20	15	16
-59	0.37		0.13	27	12	-281	0.33	0.36	0.46	31	12
-133	0.35		0.36	29	13	-283	0.51		0.39	18	11
-139		0.40				-284	0.47	0.51	0.50	20	11
-140		0.36				-286	0.45		0.23	21	13
-142		0.28				-299	0.24	0.16	0.35	48	18
-148		0.41				-300	0.39		0.09	25	14
-150	0.55		0.35	16	4	-301	0.51		0.20	18	9
-151	0.31		0.27	34	10	-302	0.57		0.16	16	7
-153	0.52		0.15	18	8						

N*= Merriman et al. (1990) N (nm), N**= WINFIT N (nm), N_{001}=8.059/β; β=1.038949) x KI-0.08250323

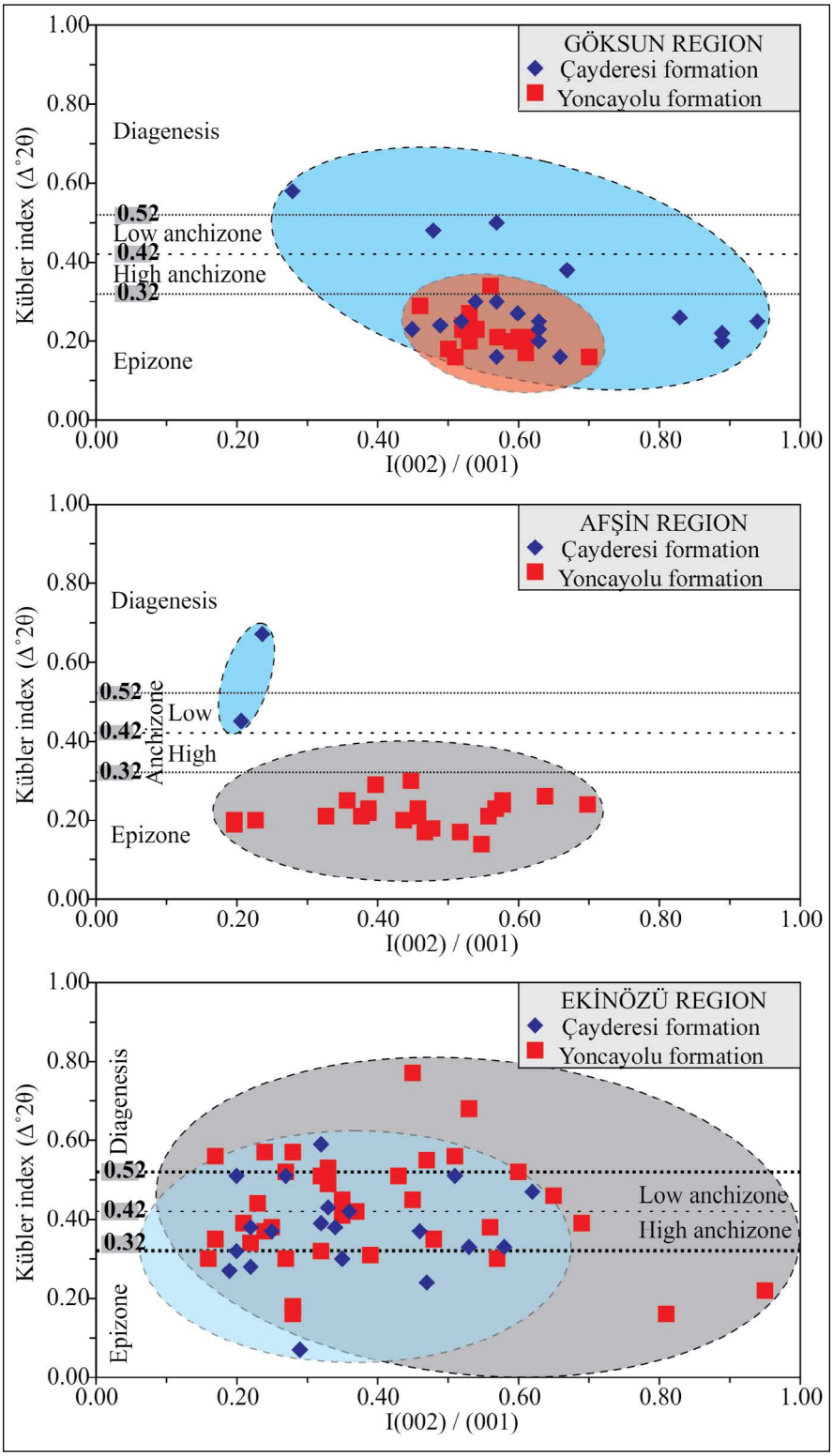

Figure 27- Distribution of illite/K-mikas in Göksun, Afşin and Ekinözü regions according to KI-I(002)/I(001) peak intensity ratios.

of Kahramanmaraş province, the western part of the Eastern Taurus Mountains, are presented below.

The Upper Paleozoic - Triassic metamorphites and crosscutting granitic intrusions constitute the oldest rock units outcropping in these regions. These rock assemblages are tectonically overlain in upward direction by non-metamorphosed allochthonous units, while the cover units are unconformably located on all units.

In the upper levels of the Göksun region, the very thick layered phyllitic or mica marbles bearing distinct foliation planes with pencil structure exhibit an alternating appearance, however; in lower levels mainly the banded marble with pencil structure, mesoscopically folded phyllites/calcphyllites, foliated and intercalated with metasandstone and quartzite are observed. In upper levels of the Afşin region, the medium-thick bedded, hard marbles intercalate with calcphyllite and phyllitic schists, whereas in lower-middle levels, the phyllite/calcphyllites with distinct schistosity planes and highly brittle structures present an alternation with marbles. In upper levels of the Ekinözü area, the foliated calcschists form an alternating structure with thin banded metalimestone, marble, mica marble and dolomitic marbles in places. The lower levels consist of quartzite and metasandstone intercalating with marble, gneiss, phyllite/phyllitic schist, micaschist, chloriteschist, amphibolite/amphiboleschist and calcschist lithologies that are occassionally cut by granitoid intrusions.

Metamorphic rocks around Göksun mainly contain calcite, dolomite, quartz, feldspar and phyllosilicate minerals ($2M_1$ illite / K-mica, IIb chlorite, paragonite, kaolinite, C-V and I-C). The metamorphic rocks around Afşin are mainly represented by calcite, dolomite, quartz, feldspar, garnet, chlorite, epidote, and amphibole and tremolite association. The phyllosilicates on the other hand numerate illite/mica (1*M* biotite; $2M_1$ muscovite, paragonite), IIb chlorite, mixed layers (C-V, I-C and I-S) and smectite. The metamorphic rocks around Ekinözü are composed of feldspar, quartz, amphibole, chlorite, garnet, sillimanite, staurolite and kyanite in the lower levels; and by calcite, dolomite, tremolite, actinolite, biotite, muscovite and chlorite associations in the upper levels. The phyllosilicate minerals of the region are accompanied by smectite, illite/mica (1*M* biotite, $2M_1$ muscovite), IIb chlorite, vermiculite and kaolinite as well as C-V, C-S, I-C and I-V indicating very low-grade retrograding metamorphism. Of these, especially the index minerals such as sillimanite ($T > 500 \pm 50$ °C), kyanite ($P > 4 \pm 0.5$ kbar), staurolite ($P > 1.5$ kbar and T 500-700 °C), garnet ($T < 785$°C) correspond to high-grade metamorphism (Deer et al., 1992). The association of Al_2SiO_5 polymorphs was also observed in metamorphic rocks of the Sivrihisar (Eskişehir) region and it was reported that this paragenesis was caused by the effect of successive metamorphism factors (counter clockwise P-T evolution) (Whitney, 2002). In authors' opinion, transformations of the andalusite-kyanite as a result of burial during subduction causing an increase of pressure in the first stage occurred and the kyanite-sillimanite with post collisional heating.

Illite, chlorite, paragonite, mixed layers (C-V, I-C, C-S, C-V and I-V), smectite, kaolinite and vermiculite types of phyllosilicates are identified in the abundance order. The mixed layers indicate advanced diagenesis conditions of vertical diagenesis/metamorphism transition (e.g., Frey, 1987). Smectite, kaolinite and vermiculite represent the weathering and/or hydrothermal alteration products.

K-mica has $2M_1$ muscovite polytype in Göksun and Afşin regions, and 2 M_1 muscovite, 1 *M* biotite or 2 M_1 muscovite + 1 *M* biotite polytypes in the Ekinözü region. Chlorite is represented by IIb polytype in all regions.

In the Göksun region, the KI values of illite and AI values of chlorite vary between 0.16-0.58 Δ°2θ (mean 0.26 Δ°2θ) and 0.18-0.73 Δ°2θ (mean 0.37 Δ°2θ), respectively. The specimens mostly point out epimetamorphic, less anchimetamorphic, and rarely diagenetic grades. The KI values in the Afşin region were detected as 0.14-0.67 Δ°2θ (mean 0.24 Δ°2θ) and AI values as 0.28-0.48 Δ°2θ (mean 0.40 Δ°2θ). Almost all of the samples are located in the epizone, partly in the low anchizone and diagenesis zones. The KI values in the Ekinözü region were estimated as 0.07-0.77 Δ°2θ (mean 0.40 Δ°2θ) and AI values as 0.08-0.55 Δ°2θ (mean 0.28 Δ°2θ). Illite/K-mica in the Ekinözü region, where the metamorphism degree is the highest, to have KI data indicating lower degrees of metamorphism according to the petrographic studies is because they contain biotite (Frey, 1987).

Table 3- Results of b_0 analysis of illite/K-mica minerals in Göksun, Afşin and Ekinözü regions (N.S.: Number of samples, S.D.: Standard deviation).

GÖKSUN		AFŞİN		EKİNÖZÜ	
Sample No	*b0 (Å)*	Sample No	*b0 (Å)*	Sample No	*b0 (Å)*
TGM-86	9.0324	TEM-60	9.0618	TEM-1	9.0306
-87	9.0294	-63	9.0084	-3	8.9862
-90	9.0306	-65	9.0084	-5	9.0528
-91	9.0312	-66	9.0054	-8	9.0192
-95	9.0366	-67	9.0342	-9	9.0246
-96	9.0540	-68	9.0210	-12	9.0438
-99	9.0222	-69	9.0300	-13	9.0408
-105	9.0156	-70	9.0042	-18	9.0264
-106	9.0012	-72	9.0300	-21	9.0048
-109	9.0360	-74	9.0492	-29	9.0450
-110	9.0390	-75	9.0486	-38	9.0048
-111	9.0246	-76	9.0252	-42	9.0270
-112	9.0348	-78	9.0504	-43	9.0486
-113	9.0558	-79	9.0636	-44	9.0276
-114	9.0426	-80	9.0360	-46	9.0120
-115	9.0474	-81	9.0498	-48	9.0024
-117	9.0300	-82	9.0180	-49	9.0150
-119	9.0180	-83	9.0480	-50	9.0414
-120	9.0360	-85	9.0204	-51	9.0186
-121	9.0378	TGM-303	9.0102	-52	9.0312
-122	9.0378	-304	9.0198	-53	9.0324
-123	9.0462	-306	9.0312	-54	9.0108
-124	9.0456	-310	9.0084	-56	9.0066
-125	9.0042	-312	9.0324	-59	9.0192
-126	9.0246	-313	9.0468	-277	9.0198
-127	9.0174			-280	9.0252
-222	9.0462			-281	9.0270
-229	8.9952			-283	9.0186
-231	9.0096			-284	9.0180
-238	9.0204			-299	9.0342
-242	9.0150			-300	9.0156
-247	8.9832				
-248	9.0222				
-254	9.0174				
N.S.	34	N.S.	25	N.S.	31
Smallest b0 (Å)	8.9832	Smallest b0 (Å)	9.0042	Smallest b0 (Å)	8.9862
Biggest b0 (Å)	9.0558	Biggest b0 (Å)	9.0636	Biggest b0 (Å)	9.0528
Average b0 (Å)	9.0272	Average b0 (Å)	9.0307	Average b0 (Å)	9.0233
S.D.	0.0161	S.D.	0.0184	S.D.	0.0150

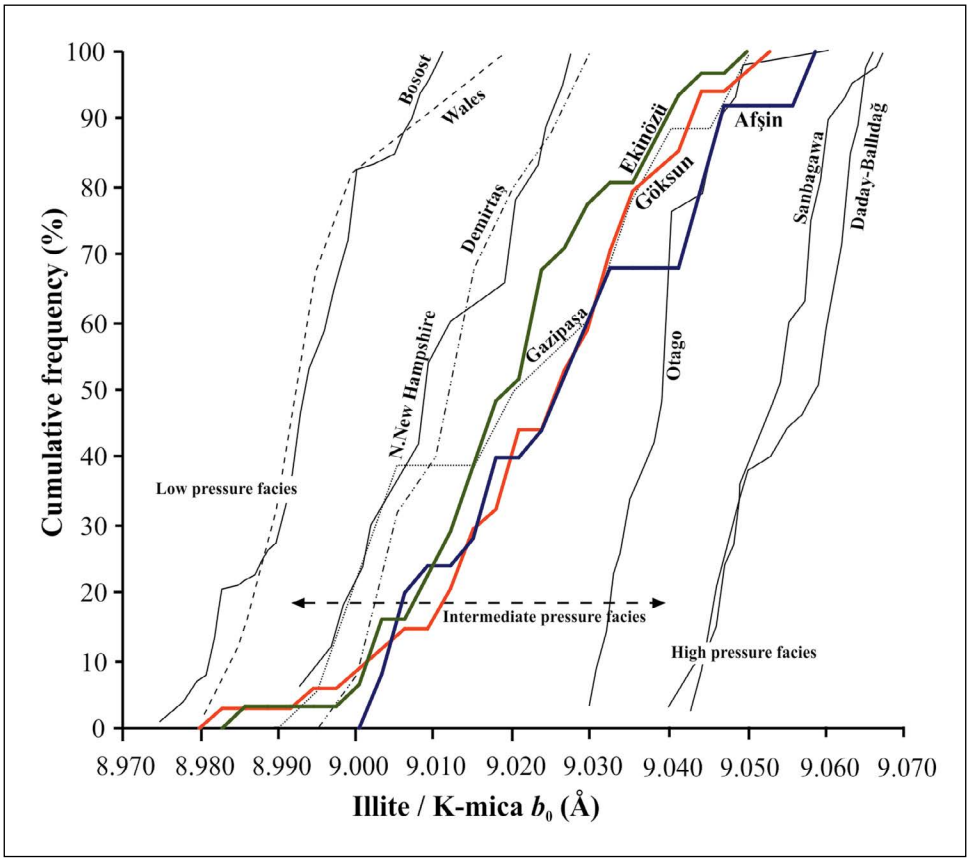

Figure 28- The relationship between the cumulative frequency and b_0 values in Göksun, Afşin and Ekinözü regions (Demirtaş, Gazipaşa b_0 values: Bozkaya and Yalçın, 2005; Wales: Robinson and Bevins, 1986; others: Sassi and Scolari, 1974).

In the Göksun region, the b_0 values of dioctahedral illite range from 8.9832 to 9.0558 Å (mean 9.0272), mostly indicating the medium-pressure (lower greenschist facies). These obtained values reflect the series of pressure facies less than 4 kbar (Buchan type; Turner, 1981) and Barrovian type regional metamorphism conditions between the borders represented by Wales (Sassi and Scolari, 1974) and Otago (Robinson and Bevins, 1986). The b_0 values of dioctahedral illite in the Afşin region, vary between 9.0042-9.0636 Å (average 9.0307 Å), corresponding to the medium-high pressure (lower greenschist-greenchist facies) and represent the glaucophanitic greenschist facies conditions mostly between the boundaries of Wales and Sanbagawa (Sassi and Scolari, 1974). The b_0 values of dioctahedral illite in the Ekinözü region are between 8.9862-9.0528 Å (mean 9.0238 Å) and have medium-high pressure (amphibolite facies in lower levels rich in metabasic and metapelites, and greenschist facies in upper levels rich in metacarbonates). Most of the rocks in the region show typical Barrovian metamorphism between the border lines of Wales and Otago (Sassi and Scolari, 1974). Furthermore, according to the cumulative frequency curves of b_0 values for illite/K-mica formed for three regions, it can be stated that Afşin region has higher b cell parameters than those of Göksun and Ekinözü regions.

Metamorphites in the Göksun, Afşin, Keban and Malatya regions are of Carboniferous-Triassic; however, the metamorphites in the Ekinözü and Pütürge Metamorphites are of Permian and pre-Permian. The metamorphic rocks in the Göksun and Afşin regions contain the characteristic paragonite mineral for Malatya Metamorphites, however; the rocks in the Ekinözü region contain 1*M* biotite, sillimanite and kyanite minerals characteristic for the Pütürge metamorphics. These differences are related to the fact that these metamorphic sequences have

different histories of metamorphism (Bozkaya et al., 2007*a*) and also show that the metamorphites of Göksun and Afşin regions developed in the opposite direction of P-T, however the metamorphites in the Ekinözü region developed in the direction of P-T. The similar evaluations were made for Keban, Malatya, Pütürge metamorphites (Bozkaya et al., 2007*a*) in the Eastern Taurus Belt, and Alanya Nappes (Bozkaya and Yalçın, 2004) in the Central Taurus Belt, and the clockwise P-T and anti-clockwise P-T represent the environments related with continental collision (Alpine collision) and extensional basins in passive continental margins, respectively (e.g., Robinson, 1987; Merriman and Frey, 1999).

When textural and mineralogical data are evaluated together, the metamorphic units in the Afşin and Göksun regions are similar to the Malatya Metamorphites and the ones in the Ekinözü region show similarity to the Pütürge Metamorphites (Bozkaya et al., 2007*a*, *b*). The Pınarbaşı and Kalecik formations of the Malatya Metamorphites (Karaman et al., 1993) correspond to those of Göksun and Afşin regions, however, the metapelitic and metacarbonate units named as without rule of the Pütürge Metamorphites (Yazgan et al., 1986, 1987) are the equivalent of the Yoncayolu and Çayderesi formations in the Ekinözü and Afşin regions. In the light of the findings obtained from this study, it was detected that the metamorphic rocks representing the western extension of the Southeast Anatolian Metamorphic Massifs had different origin rocks and/or lithologies depending on the regions and exhibited increasing temperature and pressure conditions from the west (Göksun) to the east (Ekinözü) and each of them were rock assemblages having different geological evolution.

Acknowledgements

This study has been supported by the project number M510 by the Head of Scientific Research Projects of the Sivas Cumhuriyet University. We thank technical staff in the laboratories of Geological Engineering Department for their helps during the preparation of thin section and XRD analyses, to Assoc. Prof. Dr. Sema Tetiker for her supports during XRD studies, to Assoc. Prof. Dr. Taner Ekici and to Prof. Dr. Musa Alparslan for their contributions during the petrographic examinations, to Assoc. Prof. Dr. B. Levent Mesci and Dr. Derya Toksöz for map drawings and trainee students for their assistance during field and laboratory studies. We also thank Dr. Branimir Segvic who edited and reviewed the manuscript.

References

Árkai, P. 1991. Chlorite crystallinity: an empirical approach and correlation with illite crystallinity, coal rank and mineral facies as exemplified by Palaeozoic and Mesozoic rocks of northeast Hungary. Journal of Metamorphic Geology 9, 723-734.

Bailey, E.B. 1988. X-ray diffraction identification of the polytypes of mica, serpentine and chlorite. Clays and Clay Minerals 36, 193-213.

Baydar, O. 1989. Berit-Kandil dağları (Kahramanmaraş) ve civarının jeolojisi. Doktora Tezi, İstanbul Üniversitesi, Fen Bilimleri Enstitüsü, 248 s. İstanbul (unpublished).

Bedi, Y., Şenel, M., Usta, D., Özkan, M. K., Beyazpirinç, M. 2004. Binboğa Dağları'nın jeolojik özellikleri ve batı-orta Toroslar'daki benzer birimler ile deneştirilmesi. 57. Türkiye Jeoloji Kurultayı, 8-12 Mart 2004, Ankara, 271-272.

Bedi, Y., Usta, D., Özkan, M.K., Beyazpirinç, M., Yıldız, H., Yusufoğlu, H. 2005. Doğu Toroslar'da (Göksun-Sarız-Elbistan) allokton istiflerin tektono-stratigrafik özellikleri. 58. Türkiye Jeoloji Kurultayı, 11-17 Nisan 2005, Ankara, 262-263.

Bedi, Y., Yusufoğlu, H., Beyazpirinç, M., Özkan, M.K., Usta, D., Yıldız, H. 2009. Doğu Toroslar'ın Jeodinamik Evrimi (Afşin-Elbistan-Göksun)-Sarız Dolayı). Maden Tetkik ve Arama Genel Müdürlüğü Rapor No: 11150, 388 s. Ankara (unpublished).

Blumenthal, M.M. 1951. Batı Toroslar'da Alanya ard ülkesinde jeolojik araştırmalar. Maden Tetkik ve Arama Genel Müdürlüğü Rapor No: 5, 194 s. Ankara (unpublished).

Bozkaya, Ö. 1999. Alanya Metamorfitleri doğu kesiminin (Anamur Kuzeyi) mineralojisi: Kristalinite, b_0 ve politipi. 11. Mühendislik Haftası, Yerbilimleri Sempozyumu, 20-23 Ekim 1999, Isparta, 183-192.

Bozkaya, Ö. 2001. Demirtaş-Alanya yöresinde Alanya naplarının metamorfizmasına ilişkin yeni mineralojik bulgular, Orta Toroslar, Türkiye. Yerbilimleri 23, 71-86.

Bozkaya, Ö., Yalçın, H. 2004. New mineralogical data and implications for the tectono-metamorphic evolution of the Alanya Nappes, Central Tauride Belt, Turkey. International Geology Review 46, 347-365.

Bozkaya, Ö., Yalçın, H. 2005. Diagenesis and very low-grade metamorphism of the Antalya Unit: mineralogical evidence of Triassic rifting, Alanya-Gazipaşa, Central Taurus Belt, Turkey. Journal of Asian Earth Sciences 25, 109-119.

Bozkaya, Ö., Yalçın, H. 2007. X-ışını difraktogramlarında kil minerallerinin karmaşık piklerinin çözümlenmesi: Türkiye'den örnekler. 13. Ulusal Kil Sempozyumu, 12-14 Eylül 2007, Isparta, 16-31.

Bozkaya, Ö., Yalçın, H. 2014. Mineral jeokimyası ile fillosilikatların kökeni, diyajenez/metamorfizma derecesi ve basınç/sıcaklık evrimi arasındaki ilişkilerin belirlenmesi: Torid, Pontid ve Güneydoğu Anadolu Otoktonu birliklerinde yüzeylenen Paleozoyik-Alt Mesozoyik yaşlı birimlerden örnekler. Cumhuriyet Üniversitesi Bilimsel Araştırma Proje No: M-469, 191 s. Sivas (unpublished).

Bozkaya, Ö., Yalçın, H., Başıbüyük, Z., Özfırat, O., Yılmaz, H. 2007*a*. Origin and evolution of the Southeast Anatolian Metamorphic Complex (Turkey). Geologica Carpathica 58, 197-210.

Bozkaya, Ö., Yalçın, H., Başıbüyük, Z., Bozkaya., G. 2007*b*. Metamorphic-hosted pyrophyllite and dickite occurrences from the hydrous al-silicate deposits of the Malatya-Pütürge region, Central Eastern Anatolia, Turkey. Clays and Clay Minerals 55, 4, 423-442.

Brindley, G.W. 1980. Quantitative X-ray mineral analysis of clays. In: Cristal Structures of Clay Minerals and Their X-ray Identification, Brindley, G.W. and Brown, G. (Eds.), Mineralogical Society London, 411-438.

Deer, W. A., Howie, R. A., Zussman, J. 1992. Rock-forming Minerals. Longmans, 2nd edition, London, 270 p.

Frey, M. 1987. Very low-grade metamorphism of clastic sedimentary rocks. In: Low Temperature Metamorphism, M. Frey (Ed.). Blackie, Glasgow and London, 9-58.

Göncüoğlu, M.C. 2010. Türkiye Jeolojisine Giriş: Alpin ve Alpin Öncesi Tektonik Birliklerin Jeodinamik Evrimi. Maden Tetkik ve Arama Genel Müdürlüğü Monografi Serisi 5, 69 s.

Göncüoğlu, M.C., Turhan, N. 1984. Geology of the Bitlis metamorphic belt. Tekeli, O. ve Göncüoglu, M.C. (Eds.), In: International Symposium on the Geology of the Taurus Belt, 26-29 September 1983, Ankara, 237–244.

Göncüoğlu, M.C., Dirik, K., Kozlu, H. 1997. Pre-Alpine and Alpine Terranes in Turkey: Explanatory notes to the terrane map of Turkey. Annales Géologique Pays Hellénique 37, 515-536.

Grathoff, G.H., Moore, D.M. 1996. Illite polytype quantification using Wildfire© calculated X-ray diffraction patterns. Clays and Clay Minerals 44, 835-842.

Guggenheim, S. Bain, D.C. Bergaya, F. Brigatty, M.F. Drits, A. Eberl, D.D. Formoso M.L.L. Galan, E. Merriman, R.J. Peacor, D.R. Stanjek, H., Watanabe T. 2002. Report of the AIPEA nomenclature committee for 2001: order, disorder and crystallinity in phyllosilicates and the use of the "Crystallinity Index". Clay Minerals 37, 389-393.

Işık V., Tekeli, O. 1995. New petrographical data at the eastern part of Alanya Metamorphites (Anamur, S. Turkey). Bulletin of the Mineral Research and Exploration 117, 49-57.

J.C.P.D.S. 1990. Powder Difraction File. Alphabetical Indexes Inorganic Phases, Swarthamore, U.S.A. 871 p.

Juteau, T. 1980. Ophiolites of Turkey. Ofioliti 2, 199-238.

Karaman, T., Poyraz, N., Bakırhan, B., Alan, İ., Kadınkız,G, Yılmaz, H., Kılınç, F. 1993. Malatya-Doğanşehir-Çelikhan Dolayının Jeolojisi. Maden Tetkik ve Arama Genel Müdürlüğü Rapor No: 9587, 57 s. Ankara (unpublished).

Kisch, H.J. 1980. Illite crystallinity and coal rank associated with lowest-grade metamorphism of the Taveyanne greywacke in the Helvetic zone of the Swiss Alps. Eclogae Geologicae Helvetiae 73, 753-777.

Krumm, S. 1996. WINFIT 1.2: version of November 1996 (The Erlangen geological and mineralogical software collection) of WINFIT 1.0: a public domain program for interactive profile-analysis under WINDOWS. XIII Conference on Clay Mineralogy and Petrology, Praha, 1994, Acta Universitatis Carolinae Geologica 38, 253-261.

Kübler, B. 1968. Evaluation quantitative du métamorphisme par la cristallinitéde l'illite. Bulletin du Centre de Recherches de Pau, Société Nationale des Pétroles d'Aquitaine 2, 385–397.

McClusky, S., Balassanian, S., Barka, A., Demir, C., Ergintav, S., Georgiev, I., Gurkan, O., Hamburger, M., Hurst, K., Kahle, H., Kastens, K., Kekelidze, G., King, R., Kotzev, V., Lenk, O., Mahmoud, S., Mishin, A., Nadariya, M., Ouzounis, A., Paradissis, D., Peter, Y., Prilepin, M., Reilinger, R., Sanli, I., Seeger, H., Tealeb, A., Toksoz, M.N., Veis, G. 2000. Global Positioning System constraints on plate kinematics and dynamics in the eastern Mediterranean and Caucasus. Journal of Geophysical Research-Solid Earth 105, 5695-5719.

Merriman, R.J., Frey, M. 1999. Patterns of very low-grade metamorphism in metapelitic rocks. In: Low Grade Metamorphism, Frey, M. and Robinson, D. (Eds.), Blackwell, Oxford, 61-107.

Merriman, R.J., Roberts, B., Peacor, D.R. 1990. A transmission electron microscopy study of white mica crystallite size distribution in a mudstone to slate transitional sequence, North Wales, UK. Contributions to Mineralogy and Petrology 106, 27-44.

Metin, S., Papak, İ., Keskin, H., Özsoy, İ., Polat, N., Altun, İ., İnanç, A., Hazinadar, H., Konuk, O., Karabalık, M.N. 1982. Tufanbeyli-Sarız-Göksun ve Saimbeyli Arasının Jeolojisi (Doğu Toroslar). Maden Tetkik ve Arama Genel Müdürlüğü Rapor No: 7129, 123 s. Ankara (unpublished).

Metin, S., Ayhan, A., Papak, İ. 1986. Geology of the western part of the Eastern Taurus Belt (SSE of Turkey). Bulletin of the Mineral Research and Exploration 107, 1-12.

Metin, S., Ayhan, A., Papak, İ. 1989. 1/100.000 ölçekli Türkiye Jeoloji Haritası, Elbistan-İ22 paftası. Maden Tetkik ve Arama Genel Müdürlüğü 15 s. Ankara.

MTA. 2002. 1/500 000 ölçekli Türkiye Jeoloji Haritaları, Sivas ve Hatay Paftaları. Maden Tetkik ve Arama Genel Müdürlüğü, Ankara.

MTA. 2008. 1/200 000 ölçekli Kahramanmaraş İlinin Jeoloji Haritası. Maden Tetkik ve Arama Genel Müdürlüğü, Ankara.

Özgül, N. 1976. Toroslar'ın bazı temel jeoloji özellikleri. Türkiye Jeoloji Bülteni 19, 65-78.

Özgül, N. 1981. Munzur Dağlarının jeolojisi. Maden Tetkik ve Arama Genel Müdürlüğü Rapor No: 6995, 136 s. Ankara (unpublished).

Özgül, N. 1984. Stratigraphy and tectonic evolution of the Central Taurides. In: International Symposium on the Geology of Taurus Belt, Tekeli, O. and Göncüoğlu, M.C. (Eds.), September 26-29, 1983, Ankara, 77-90.

Özgül, N., Turşucu, A. 1984. Stratigraphy of the Mesozoic carbonate sequence of the Munzur Mountains (Eastern Taurides). In: International Symposium on the Geology of the Taurus Belt, Tekeli, O. and Göncüoglu, M. C. (Eds.), September 26-29, 1983, Ankara, 173-180.

Öztürk, A., Boztuğ, D., Yalçın, H., İnan, S., Gürsoy, H., Bozkaya, Ö., Yılmaz, S., Uçurum, A. 1996. Hekimhan (KB Malatya) ve Kangal (GD Sivas) Yörelerinde Mevcut Maden Yataklarının Jeolojik ve Madencilik Açısından Değerlendirilmesi Çalışmaları. Cilt I: Jeolojik Etüdler. DPT Proje No: 89 K 120450, 186 s. Sivas (unpublished).

Pattison, D.R.M. 1992. Stability of andalusite and sillimanite and the Al_2O_5 triple point: constraints from the Ballachulish aureole, Scotland. Journal of Geology 100, 423-446.

Perinçek, D. 1979*a*. Çelikhan-Sincik-Koçali (Adıyaman) alanının jeolojik incelemesi. Türkiye Petrolleri Anonim Ortaklığı, Arama Grubu Başkanlığı Rapor No: 1395.

Perinçek, D. 1979*b*. Geological investigation of the Çelikhan-Sincik-Koçali area (Adıyaman province). İstabul Üniversitesi, Fen Fakültesi Mecmuası Seri B, 44, 127-147.

Perinçek, D. 1979*c*. Interrelations of the Arabian and Anatolian plates. First Geological Congress on Middle East, Geological Society of Turkey, Ankara, Guide book for excursion B., 17 p.

Perinçek, D., Kozlu, H. 1984. Stratigraphy and structural relation of the units in the Afşin-Elbistan-Doğanşehir region. In: International Symposium on the Geology of the Taurus Belt, Tekeli, O. and Göncüoglu, M.C. (Eds.), September 26-29, 1983, Ankara, 181-198.

Powell, C. McA. 1979. A morphological classification of rock cleavage. Tectonophysics 58, 21-34.

Reilinger, R.E., McClusky, S.C., Oral, M.B., King, R.W., Toksoz, M.N., Barka, A.A., Kinik, I., Lenk, O., Sanli, I. 1997. Global Positioning System measurements of present-daycrustal movements in the Arabia-Africa Eurasia plate collision zone. Journal of Geophysical Research-Solid Earth 102, 9983-9999.

Ricou, L.E. 1980. La tectonique de coin et la genèse de l'arc égéen. Revue de Géologie Dynamique et de Géographie Physique. 13, 147-155.

Robinson, D. 1987. Transition from diagenesis to metamorphism in extensional and collision settings. Geology 15, 866–869.

Robinson, D., Bevins, R.E. 1986. Incipient metamorphism in the Lower Palaeozoic marginal basin of Wales. Journal of Metamorphic Geology 4, 101-113.

Sassi, F.P., Scolari, A. 1974. The b_0 value of the potassic white micas as a barometric indicator in low-grade metamorphism of pelitic schists. Contributions to Mineralogy and Petrology 45, 143–152.

Schildgen, T.F., Yildirim, C., Cosentino, D., Strecker, M.R. 2014. Linking slab break-off, Hellenictrench retreat, and uplift of the central and Eastern Anatolian plateaus. Earth-Science Reviews 128, 147–168.

Şengör, A.M.C., Yılmaz, Y. 1981. Tethyan evolution of Turkey, a plate tectonic approach. Tectonophysics 75, 181-241.

Tarhan, N. 1982. Göksun-Afşin-Elbistan jeolojisi. Maden Tetkik ve Arama Genel Müdürlüğü Rapor No: 7296, 63 s. Ankara (unpublished).

Tarhan, N. 1984. Göksun-Afsin-Elbistan Dolayının Jeolojisi. Jeoloji Mühendisliği Dergisi 19, 3-9.

Turner, F.J. 1981. Metamorphic petrology. New York, McGraw-Hill, 524 p.

Warr, L.N., Rice, A.H.N. 1994. Interlabratory standartization and calibration of clay mineral crystallinity and crystallite size data. Journal of Metamorphic Geology 12, 141-152.

Warr L.N., Ferreiro-Mählmann, R. 2015. Recommendations for Kübler Index standardization. Clay Minerals 50, 283-286.

Whitney, D.L. 2002. Coexisting andalusite, kyanite, and sillimanite: Sequential formation of three Al_2SiO_5 polymorphs during progressive metamorphism near the triple point, Sivrihisar, Turkey. American Mineralogist 87, 405-416.

Yalçın, H., Bozkaya, Ö. 2002. Hekimhan (Malatya) çevresindeki Üst Kretase yaşlı volkaniklerin alterasyon mineralojisi ve jeokimyası: Denizsuyu-kayaç etkileşimine bir örnek. Cumhuriyet Üniversitesi Mühendislik Fakültesi Dergisi Seri A-Yerbilimleri 19, 81-98.

Yazgan, E. 1983. A geotraverse between the Arabian Platform and the Munzur Nappes. International Symposium on the Geology of the Taurus Belt, September 26-29, 1983, Ankara, Guide book for excursion V., 17p.

Yazgan, E., Asutay, J., Gültekin, M.C., Poyraz, N., Yıldırım, H. 1986. 1/100.000 ölçekli Türkiye Jeoloji Haritası, Malatya- İ27 Paftası. Maden Tetkik ve Arama Genel Müdürlüğü, Ankara.

Yazgan, E., Asutay, J., Gültekin, M.C., Poyraz, N., Sirel, E., Yıldırım, H. 1987. Malatya güneydoğusunun jeolojisi ve Doğu Toroslar'ın jeodinamik evrimi. Maden Tetkik ve Arama Genel Müdürlüğü Rapor No: 2268, 178 s. Ankara (unpublished).

Yıldırım, M. 1989. K.Maraş Kuzeyindeki (Engizek-Nurhak Dağları) Tektonik Birliklerin Jeolojik, Petrografik İncelenmesi. Doktora Tezi, İstanbul Üniversitesi, 306 s. İstanbul (unpublished).

Yılmaz, A., Bedi, Y., Uysal, Ş., Yusufoğlu, H., Aydın, N. 1993. Doğu Toroslar'da Uzunyayla ile Beritdağı arasının jeolojik yapısı. Türkiye Petrol Jeologları Derneği Bülteni 5, 69-87.

Yılmaz, A., Bedi, Y., Uysal, Ş., Aydın, N. 1997. 1/100.000 ölçekli Türkiye Jeoloji Haritası. Elbistan-İ23 Paftası. Maden Tetkik ve Arama Genel Müdürlüğü, 18 s. Ankara.

Yılmaz, Y. 1993. New evidence and model on the evolution of the southeast Anatolian orogen. Geological Society of American Bulletin 105, 251-271.

Yılmaz, Y., Yiğitbaş, E. 1990. SE Anadolu'nun farklı ofiyolitik-metamorfik birlikleri ve bunların jeolojik evrimdeki rolü. Türkiye 8. Petrol Kongresi Bildirileri, 16-20 Nisan 1990, Ankara, 128-140.

Yılmaz, Y., Gürpınar, O., Kozlu, H., Gül, M. A., Yiğitbaş, E., Yıldırım, M., Genç, Ş. C., Keskin, M. 1987. Maraş kuzeyinin jeolojisi (Andırın-Berit-Engizek-Nurhak-Binboğa Dağları). Türkiye Petrolleri Anonim Ortaklığı Rapor No: 2028, Cilt (II-III), 218 s. Ankara (unpublished).

Yılmaz, Y., Yiğitbaş, E., Yıldırım, M., Genç, Ş.C. 1992. Güneydoğu Anadolu metamorfik masiflerinin kökeni. Türkiye 9. Petrol Kongresi Bildirileri, 17-21 Şubat 1992, Ankara, 296-306.

Yılmaz, Y., Yiğilbaş, E., Genç, Ş.C. 1993. GD Anadolu Orojenik Kuşağı'nın batı kesimlerinin jeolojik evrimi. Ozan Sungurlu Sempozyumu Bildirileri, Kasım 1991, Ankara, 356-385.

Yılmaz, Y., Yiğitbaş, E., Genç, S.C., Şengör, A.M.C. 1997. Geology and tectonic evolution of the Pontides. In: A.G.Robinson (Ed.), Regional and petroleum geology of the Black Sea and surrounding region. American Association of Petroleum Geologists Bulletin, Memoir 68, 183-226.

Yiğitbaş, E. 1989. Engizek Dağı (K.Maraş) Dolayındaki Tektonik Birliklerin Petrolojik İncelenmesi. Doktora Tezi, İstanbul Üniversitesi, 347 s. İstanbul (unpublished).

Bulletin of the Mineral Research and Exploration

http://bulletin.mta.gov.tr

Determination of structural characteristics of Tuzgölü Fault Zone using gravity and magnetic methods, Central Anatolia

Bahar DİNÇER[a*] and Veysel IŞIK[b]

[a]*Turkish Petroleum Corporation, TR-06530, Ankara, Turkey*
[b]*Ankara University, Department of Geological Engineering, Tectonics Research Group, TR-06830, Ankara, Turkey*

Research Article

Keywords:
Geophysical method, Downward continuation, Tuzgölü Basin, Fault Zone, Central Turkey.

ABSTRACT

The anomaly maps and amplitude and wavelength changes of the anomalies obtained from gravity and magnetic methods can provide to identify fault traces in the underground. The Tuzgölü Fault Zone (TFZ), the NW-SE striking active fault zone in central Anatolia, includes fault strands that cut the basement and basin deposits. Our magnetic and gravity analysis suggests that Tuzgölü Basin and its surroundings are characterized by distinct depression and ridge areas. Gravity anomaly data show the presence of faults at depths of sea level (0 m), -1000 m, -2000 m, -3000 m, and -4000 m. These faults are mostly normal and reverse faults, as well as the lesser amount of vertical faults (high-angle normal/reverse faults) with NW-SE, N-S, and NE-SW-striking. The normal faults are of the structural development and the deposition of the Tuzgölü Basin units, which occurred late Cretaceous-Middle Eocene and Early Miocene-Quaternary Periods. The reverse faults originated from the result of the regional-scale compressional regime during Middle Eocene-Late Oligocene/ Early Miocene based on the fault dating data from the literature. The active TFZ, including several fault strands, are relatively younger faults in the region that have initiated to develop during faulting events from after Middle Miocene or Early Pliocene.

Received Date: 30.05.2019
Accepted Date: 18.12.2019

1. Introduction

Gravity and magnetic methods are natural potential methods that have been performed for many years in the subsurface surveys. They have been used extensively, especially in oil and gas researches, since the beginning of the 20th century (Reynolds, 2011). Among the critical problems encountered in the studies related to subsurface geology, determination of buried faults, determination of the locations, characteristics (e.g., geometry, type, amount of throw) of buried and surfaced faults, as well as the determination of geological contacts are prominent. Natural potential methods are among the geophysical methods used to understand these discontinuities. Accordingly, gravity and magnetic measurements and anomalies obtained to enable the determination of faults in shallow sections of the continental crust, mapping these structures and determining their characteristics.

Horizontal and vertical changes in density and magnetization show the transition between different geological units, and this situation appears as an anomaly in the maps (Wilcox, 1974). In this context, there are studies in the literature that use derivative-based algorithms to identify anomaly exchange lines (Boschetti, 2005; Cooper and Cowan, 2008; Hosseini et al., 2013), such as the total horizontal derivative

Citation info: Dinçer, B., Işık, V. 2020. Determination of structural characteristics of Tuzgölü Fault Zone using gravity and magnetic methods, Central Anatolia. Bulletin of the Mineral Research and Exploration 162, 145-174. https://doi.org/10.19111/bulletinofmre.661245

* *Corresponding author: Bahar DİNÇER, badincer@tpao.gov.tr*

(Cordell and Grauch, 1982; 1985; Lyatsky and Dietrich, 1998), boundary determination (Blakely and Simpson, 1986), analytical signal (Roest et al., 1992), tilting signal derivative (Miller and Singh, 1994; Salem et al., 2008) and total horizontal tilting angle derivative method (Verduzco et al., 2004). Images created with the total horizontal derivative technique are important in determining the linearities representing discontinuities, understanding lateral changes in lithologies and interpreting some other structural formations (Saad, 2006; Cooper and Cowan, 2008; Aydoğan, 2011; Zhang et al., 2011; Hosseini et al., 2013).

The Central Anatolian Region, which also includes the study area, is among the areas where gravity and magnetic methods are successfully applied to understand the underground lithology and structural features (Uğurtaş, 1975; İlkışık et al., 1997; Aydemir and Ateş, 2006*a*; 2006*b*; 2008; Aydoğan, 2011; Oruç, 2011). Tuzgölü Basin and its surroundings in the region are home to many fault zones (Dirik and Göncüoğlu, 1996; Koçyiğit, 2003; Özsayın and Dirik, 2007; Özsayın et al., 2013; Işık et al., 2014). Although the morphological features of TFZ and the contact relationship between Quaternary-Holocene sediments and old units are evident, the character and age of the fault zone is a subject of discussion in the literature.

This study aims to reveal the deep characteristics of the TFZ, which is located in the northeastern part of the Tuzgölü basin and has an active fault zone, with the help of gravity and magnetic methods. In this context, the TFZ study area includes Kırşehir, Aksaray, Karaman, Adana sections of Active Fault Map of Turkey prepared and printed by the MTA (Emre et al., 2011). The northwest-southeast trending fault zone consists of several fault strands with different orientations and spread. To reach the aim of the study, firstly gravity and magnetic properties of a vast region including TFZ were determined, then the fault trace of the TFZ and its immediate surroundings at sea level (0 km), -1000 m, -2000 m, -3000 m and -4000 m depths were interpreted. With this study these are aimed; (1) determination of fault traces up to 4 km depth in TFZ and its near surroundings, (2) preparation of the map showing fault traces in 6 areas where faulting is typical along the zone, and determination of fault characteristics from individual sections of the areas, (3) demonstration of the descriptive/interpretive geometries of the faults on the vertical plane, and (4) evaluation of the TFZ in the light of the obtained findings and data from the literature.

2. Tuzgölü Basin

Central Anatolia region is characterized by paleotectonic units that are Sakarya Zone, Kırşehir Block/Menderes-Taurus Platform, and İzmir-Ankara-Erzincan Suture Zone. Although controversial, the Inner-Taurus Suture Zone is another paleotectonic unit in the region. (Şengör and Yılmaz, 1981; Okay and Tüysüz, 1999) (Figure 1). The region consists of different lithologies, both continental and oceanic crust affinity. Metamorphics, ophiolitic rocks, granitoids and volcanic rocks, and sedimentary rocks are the occuring type of lithologies (Göncüoğlu et al., 1992; Tüysüz et al., 1995; Poisson et al., 1996; Görür et al., 1998; Seyitoğlu et al., 2000; Yalınız et al., 2000; Whitney et al., 2001; Kaymakçı et al., 2003; Işık et al., 2008; 2014; Keskin et al., 2008; Lefebvre et al., 2011; Özsayın et al., 2013; Gülyüz et al., 2013).

The Tuzgölü Basin is one of the Central Anatolian Basins that is formed in Anatolides in the paleotectonic classification of Turkey by Ketin (1966) or the Anatolide-Tauride platform classified by Şengör and Yılmaz (1981) and Okay and Tüysüz (1999). The basin might be a fault-controlled basin developed in the Kırşehir Block of the paleotectonic period and the Anatolian Plate of the neotectonic period of Turkey (Figure 1). Görür et al. (1984) define Tuzgölü Basin as the forearc basin that develops between Kırşehir arc and Inner-Taurus Suture Zone. The Central Anatolian Basins, including the Tuzgölü Basin, are divided into three groups (magmatic arc-related basins, collision-related peripheral arc-front basins, and sedimentary cover basins) according to their tectonic location, structural and stratigraphic features by Görür et al. (1998); the Tuzgölü Basin is defined as the magmatic arc associated basin.

Stratigraphical and sedimentological features of the Tuzgölü Basin are well-known with the evidence of paleontological findings (Rigo de Righi and Cortesini, 1960; Arıkan 1975; Ünalan and Yüksel, 1978; Görür et al., 1984; Derman et al., 2003; Dirik and Erol, 2003). The basin is northwest-southeast trending in terms of its present geometry. The Haymana Basin is located in the northwest extension of the Tuzgölü basin, and the Ulukuşla Basin is located in the southeast

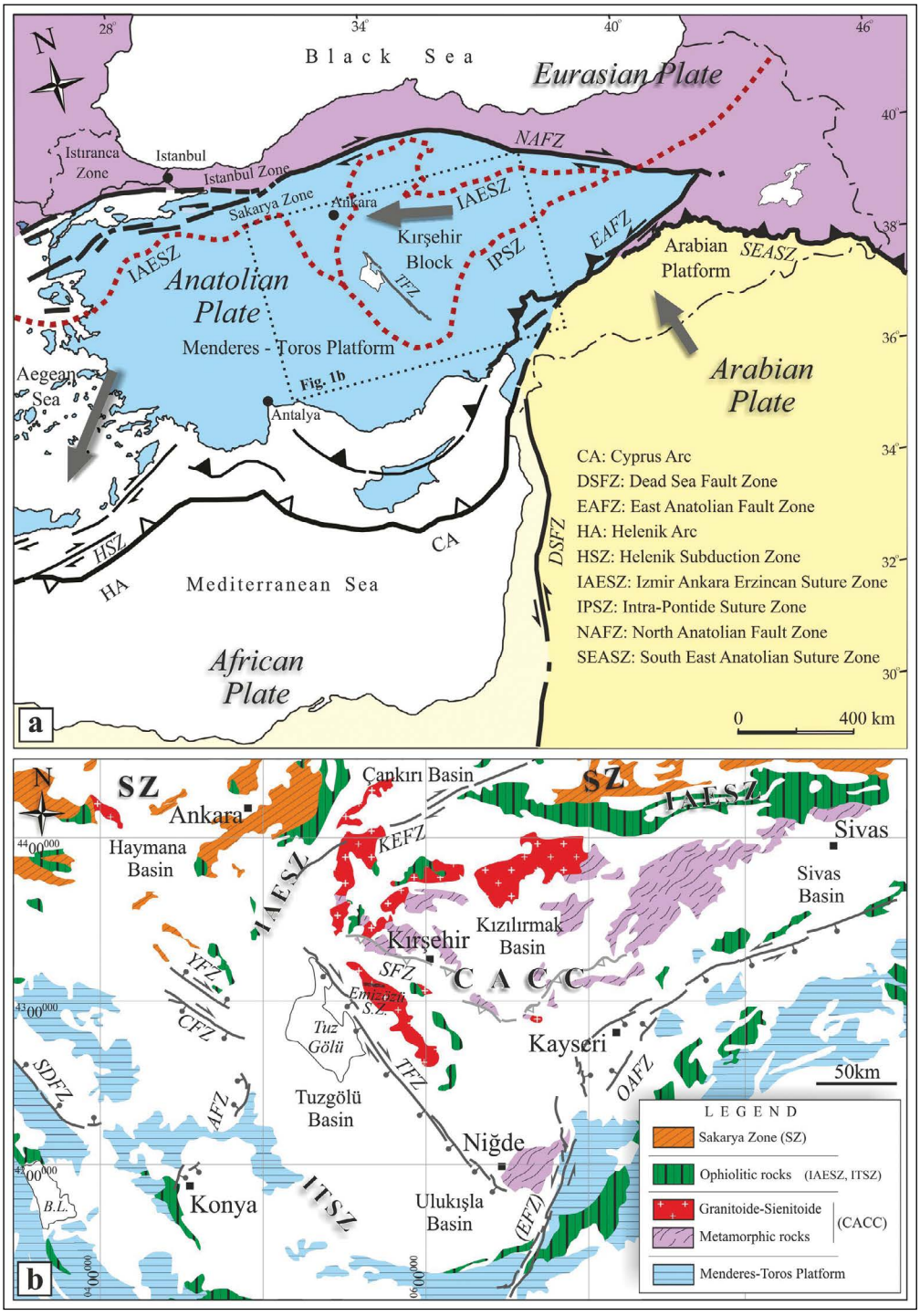

Figure 1- a) Map showing the main tectonic features of Turkey and surrounding area and regional plate boundaries of the Alpine-Himalayan orogeny (Redrawn from Işık et al., 2014) and b) simplified geological map of the Central Anatolia (Modified from Işık et al., 2008; 2014). Some of the faults are drawn from the Emre et al., 2011 Active Fault Map of Turkey. *Abbreviations:* AFZ: Altınekin Fault Zone, BG: Beyşehir Lake, CFZ: Cihanbeyli Fault Zone, EFZ: Ecemiş Fault Zone, IAEKZ: Izmir-Ankara-Erzincan Suture Zone, ITKZ: Intra-Tauride Suture Zone, KEFZ: Kırıkkale-Erbaa Fault Zone, OAFZ: Orta Anadolu Fault Zone, OAKK: Central Anatolian Crystalline Complex, SZ: Sakarya Zone, SFZ: Savcılı Fault Zone, SDFZ: Sultandağ Fault Zone, TFZ: Tuzgölü Fault Zone, YFZ: Yeniceoba Fault Zone.

extension of it (Figure 1b). Görür et al. (1984) divided the Tuzgölü Basin into two sub-basins and called Tuzgölü and Haymana sub-basins, although known the Tuzgölü and Haymana Basins in present literature, respectively. The eastern part of the Tuzgölü Basin is bordered by the Kırşehir Massif / Central Anatolian Crystalline Complex rocks, while the western part is bordered by the Bolkar unit / Inner-Taurus Ocean / Kütahya-Bolkardağ metamorphics / Afyon Zone rocks (Menderes-Tauride Platform) (Figure 1b).

Basin stratigraphy consists of two main lithology groups. These are basement rocks and basin units. The Central Anatolian Crystalline Complex commonly exposed, especially in Kırşehir and its surroundings, occurs in the eastern part of the basin. It includes metamorphites, granitoid rocks, and ophiolitic melange rocks (Seymen, 1984; Göncüoğlu and Türeli, 1993; Köksal et al., 2004; Işık, 2009; Işık et al., 2014) (Figure 2). The western part of the basin is represented by the metamorphic rocks of the Bolkar Unite and the ophiolitic rocks remnant of the Izmir-Ankara ocean (Karaman, 1986; Göncüoğlu et al., 1996; Eren, 2003*b*). These lithologies are considerably overlain by young units. Ophiolitic rocks characterize the basement rocks in the northern part of the basin. The ophiolitic rocks also separate the Tuzgölü Basin and Haymana Basin and constitute the primary lithology of the basement of both basins (Görür et al., 1984; Rojay, 2013). Göncüoğlu et al. (1996) interpreted that all these ophiolitic rocks constitute the Central Anatolian Ophiolites, and are a product of accretionary prism that occurred during the closure process of the Izmir-Ankara Ocean.

Stratigraphy of the Tuzgölü Basin is well-known, although there is a controversy (Turgut, 1978; Dellaloğlu and Aksu, 1984; Görür et al., 1984; Ulu et al., 1994; Göncüoğlu et al., 1996; Derman et al., 2003; Dirik and Erol, 2003). The basin units are divided into three rock groups based on sediment characteristics and the main unconformity surface of the basin units. These are Late Cretaceous-Cenozoyic units, Oligo-Miocene units, and Plio-Quaternary units (Figure 3). Late Cretaceous-Cenozoyic units of Tuzgölü Basin are mostly overlain by young units. Widespread outcrops of the Late Cretaceous-Cenozoyic units are seen in the eastern part of the basin. Data from some deep drilling wells in different parts of the basin contributed to the forming of basin stratigraphy. The western and eastern parts of the basin show distinctive differences in terms of the spread of lithologies and facies characteristics (Görür et al., 1984; Derman et al., 2003; Dirik and Erol, 2003; Özsayın and Dirik, 2007; Gürbüz, 2012; Kürçer, 2012; Göksu, 2015) (Figure 3).

The southeastern part of the basin is covered by Miocene-Quaternary/Holocene volcanic rocks, which the area in literature is defined as Cappadocia Volcanic Region (Beekman, 1966; Ercan et al., 1992; Aydar et al., 1994; Deniel et al., 1998; Toprak, 2003; Schmitt et al., 2014). Volcanoes such as Karacadağ, Kötüdağ, Keçikalesi, Hasandağ, Keçiboyduran, and Melendiz are volcanoes that have had activity at different intervals in this period. Keçikalesi caldera is the oldest volcanic complex with 12.4-13.7 Ma (K-Ar method: Besang et al., 1977). Hasandağ caldera is a multi-caldera complex (Beekman, 1966; Aydar and Gourgaud, 2002). U-Th zircon dating method reveals that Hasandağı volcano was active during the Holocene period (6960 ± 640 BC: Schmitt et al., 2014). The Keçiboyduran and Melendiz volcanoes in the east have similar features and are interpreted as Early Pliocene (Toprak, 2003).

All these basin units reveal that Tuzgölü Basin has a thick sedimentary and volcanic sequence. Data from deep drilling wells show more than 4 km of a structural thickness of basin units in some areas (e.g., Bezirci-1 Well). Aydemir and Ateş (2006*b*) determined the deepest part of the Haymana and Tuzgölü Basins using the basin modeling of the gravity and magnetic data with some assumptions. The density of the metamorphic rocks forming the basement rocks of the basins and the basin units are conceded 2.65 gr/cm^3 and 2.40 gr/cm^3, respectively. According to these researchers, different parts of Tuzgölü Basin have varying depths and can reach a depth of 12-13 km.

3. Tuzgölü Fault Zone (TFZ)

The geological structures in the Central Anatolia to be differentiated as paleotectonic and neotectonic periods are widely accepted. The faults that occurred during the paleotectonic period are related mainly to the obduction of ophiolitic rocks. Ophiolitic rocks with different sizes and geometries overlie Mesozoic and Lower Cenozoic units with tectonic contact. These faults can be seen in limited areas uncovered by young rock units in the region. Emizözü shear zone, defined

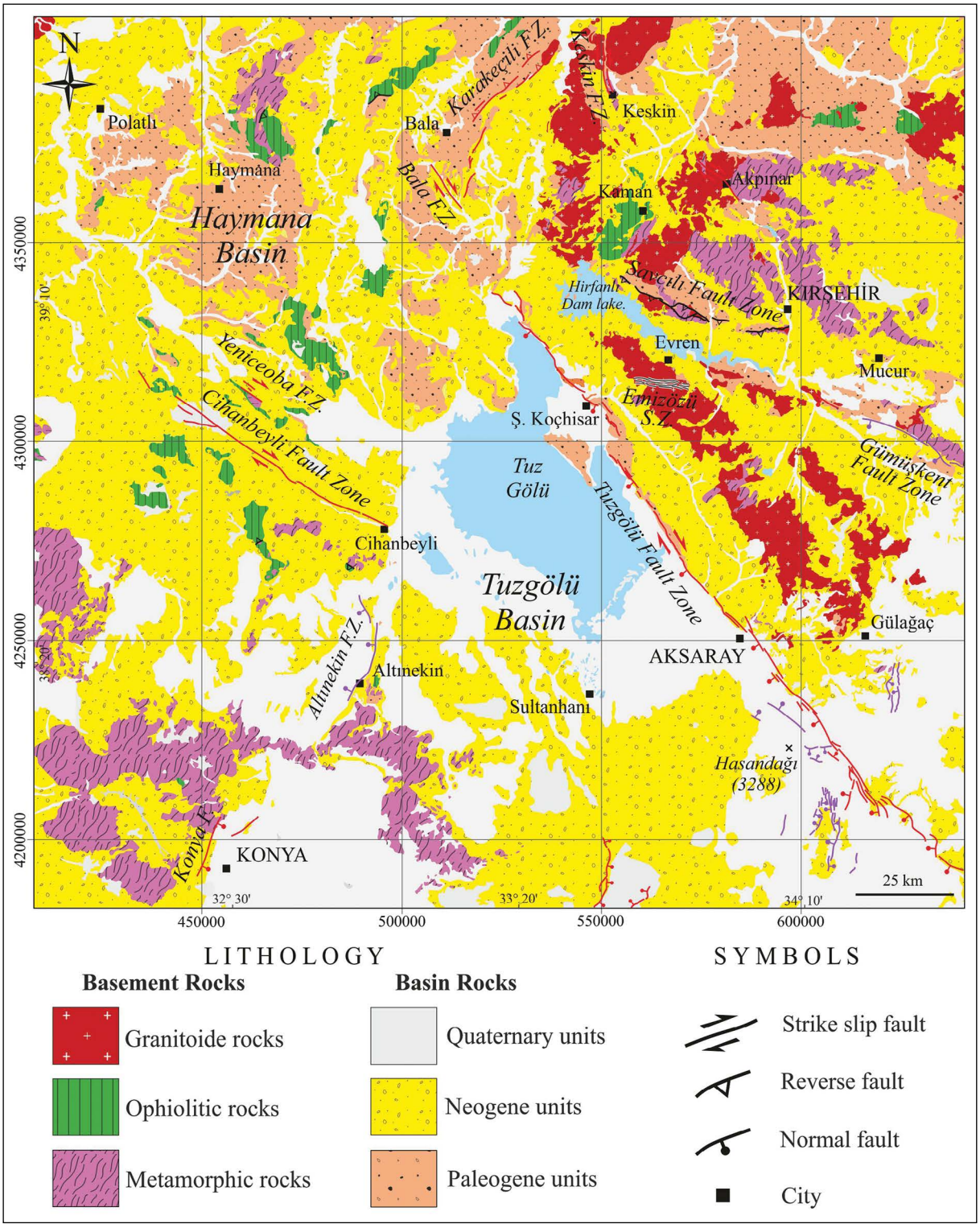

Figure 2- Simplified geological map of the Tuzgölü basin and surrounding area (Modified from MTA-2002 1:500.000 scale Geological Map of Turkey - Ankara, Kayseri). Active faults with red and violet-colored adopted from MTA-2011 Active Faults Maps of Turkey. Emizözü Shear Zone and Savcılı Fault Zone adopted from Işık, (2009) and Işık et al. (2014), respectively.

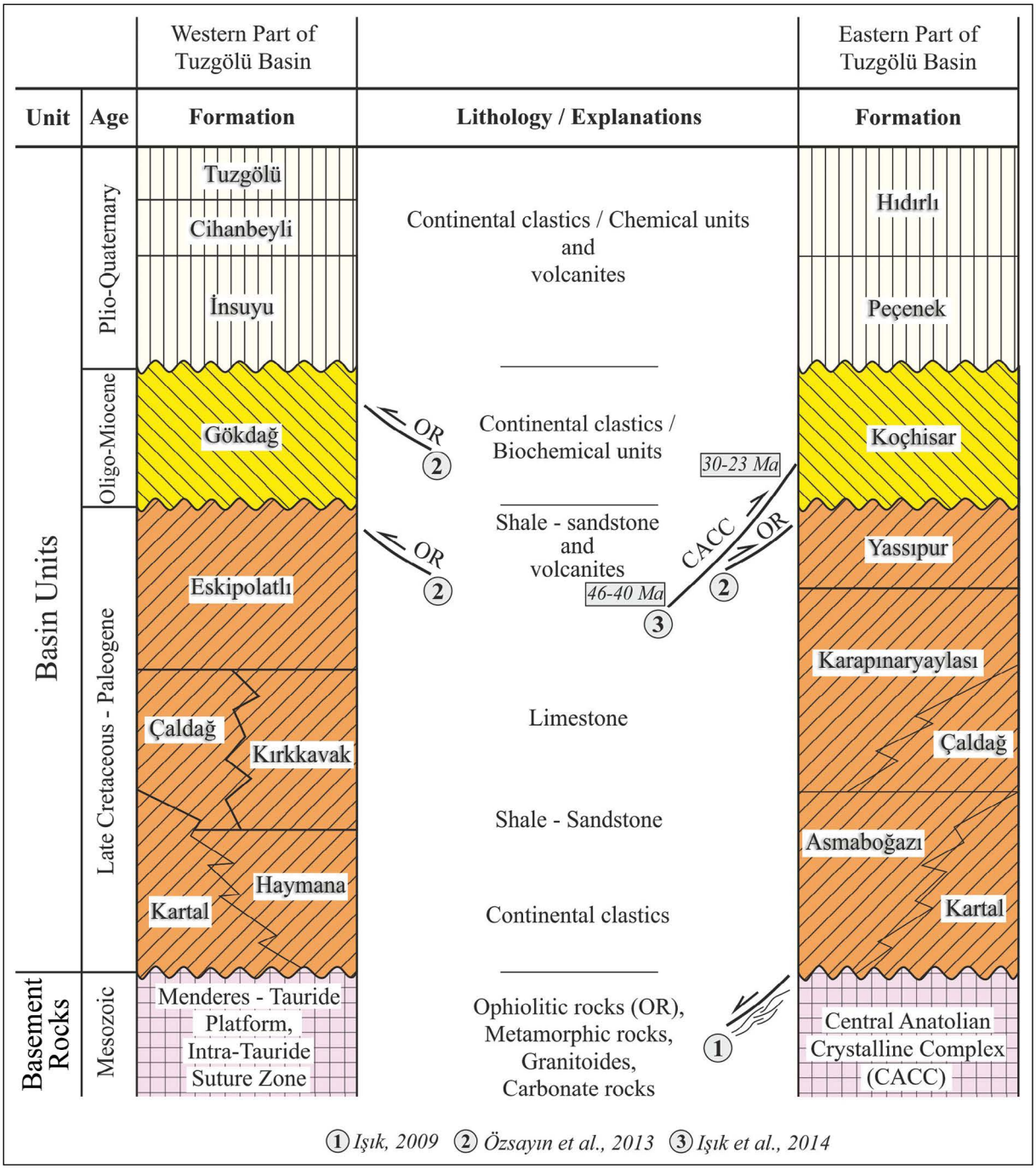

Figure 3- Correlation of the simplified stratigraphic columns of the western and eastern parts of the Tuzgölü Basin. (Modified from Dirik and Erol, 2003).

by Işık (2009), occurred during the Upper Cretaceous extensional regime, represent the structure of the paleotectonic period in the region. The Savcılı Fault Zone with well-constrained age is a regional-scale fault zone formed between middle Eocene and late Oligocene, which is another essential paleotectonic structure (Çağlayan, 2010; Işık et al., 2014). According to Çağlayan (2010) and Işık et al. (2014), the Savcılı Fault Zone is characterized by reverse/thrust faults due to compression regime. There are also studies suggesting that the zone might be occurred tectonic regime either extensional regime (Yürür and Genç, 2006) or lateral compressional regime (Lefebvre et al., 2013; Gürer and van Hinsbergen, 2019).

Central Anatolian Fault Zone, Niğde Fault Zone, Konya-Blok Fault Zone/Altekin Fault Zone, Tuzgölü Fault Zone (TFZ), İnönü-Eskişehir Fault Zone (System) and Akşehir Fault Zone are NW and NE trending, which are important fault zones of the neotectonic period (Dirik and Erol, 2003; Eren, 2003*a*; Koçyiğit, 2003; Özsayın and Dirik, 2007; Işık, 2009; Kürçer, 2012; Fernandez-Blanco et al., 2013; Özsayın el al., 2013).

The Tuzgölü Fault Zone (TFZ) is an NW-SE trending intra-continental fault zone. The TFZ is first shown as a lineament in the tectonic map by Edmund Naumann (1896). In geology based-studies, the zone is described in not only different names but also its fault characteristics. For example, According to Koçyiğit (2003), the TFZ extend between Paşadağı (Ankara) and Bor (Niğde) and has approximately 220 km in length and range between 15 and 25 km in width. Furthermore, the same zone is 190-200 km long and 5-25 km wide, as suggested by Dirik and Erol (2003). The length of the TFZ is about 195 km if we consider fault traces in MTA-Active Fault Map. The width of the zone displays significant local differences because of the distribution of the fault traces along the TFZ. Changing the width of the TFZ is related to fault geometries such as bending, step-over, or networks of fault splays. The southwest extension of the zone, especially from Aksaray, is approximately 25 km in width, while other parts of it vary between 1 km and 5 km.

Although the present structure of the TFZ appears to be geological fault contact between Plio-Quaternary deposits and older basin rocks and/or cutting them, fault characteristic and age of faulting is a matter of debate. Şaroğlu et al. (1987) suggest that the TFZ is a high-angle reverse fault component right-lateral strike-slip faulting. According to Dirik and Erol (2003), the fault zone is represented by steps, sub-parallel faults with half-graben, or horst-graben morphology. Dirik and Göncüoğlu (1996) paid attention to the presence of deformed alluvial fans, fault scarps in downthrown western block, and clockwise rotation of stream beds on the eastern block of the main fault. Toprak and Göncüoğlu (1993), and Toprak (2003) suggest that southern part of the TFZ display parasitic cone arrays and volcanic activity, hot springs and travertines, fault-controlled terrace developments and some markers (e.g., displaced lava flows) representing right-lateral faulting. Koçyiğit (2003) mentioned that the TFZ is conjugate of the Central Anatolian Fault Zone, and shows the right lateral fault zone with a significant amount of a normal component. Kürçer (2012) and Kürçer and Gökten (2014) divided the TFZ into 11 fault segments with ranging from 9 km to 30 km longs. In these studies, the amount of normal displacement of the zone from the Pliocene to the present was calculated as 230-290 m. These researchers also suggest that the TFZ is an oblique normal fault zone. Derman et al. (2003) suggested that the zone initially acts as a normal fault character and later left-lateral strike-slip fault character during Eocene; in the following period again, it was acted like a normal fault.

Some of the researchers consider the starting age of the TFZ as Late Cretaceous (Uygun et al., 1982; Görür et al., 1984; Çemen et al., 1999; Fernandez-Blanco et al., 2013). Ages of the post-Maastrichtian (Derman et al., 2003), Eocene (Arıkan, 1975) and Miocene (Dellaloğlu and Aksu, 1984) are also recommended for the occurrence of the TFZ. Işık (2009) documented that the Tuzgölü Basin developed during extensional tectonics coexisting with a ductile shear zone and related with normal faulting in the late Cretaceous, which present morphology of the TFZ is characterized by post-Miocene faulting. Koçyiğit (2003) and Kürçer (2012) argue that the TFZ is at a post-Early Pliocene age, which some segments of the zone is also seismically active. The relative activity of the TFZ during Quaternary was documented by Yıldırım (2014) using morphometric index data.

4. Method and Findings

4.1. Method

Gravity and magnetic methods are fundamental geophysical methods. In use, it is necessary to obtain a large number of measurements in a short period of time and be relatively low cost. That is why both methods are widely used for economic purposes (e.g., petroleum-natural gas, mineral, geothermal fields) as well as exposing underground geology (e.g., crust thickness, basin or basement elevation areas, sediment thickness, volcanic propagation, salt domes, other geological structures) (Telford et al., 1990; Soengkono, 1999; Reynolds, 2011). These methods also are frequently used in the detection of ancient

objects buried underground and in areas performed seismic studies where the image quality is not good enough.

Density in the gravity method and magnetization in the magnetic method creates potential field anomalies in measurements (Wilcox, 1974). The maximum and minimum values of the primary or secondary derivatives of the potential area are used to determine the source causing the anomaly that occurred during sudden changes in density or magnetization and to find the boundaries of the structure (Cordell, 1979; Pınar, 1984). To identify the geological formations causing this anomaly, horizontal and vertical derivatives of the potential area is preferred by many researchers (Cordell, 1979; Cordell and Grauch, 1985; Miller and Singh, 1994; Aydın, 1997; Verduzco et al., 2004; Cooper and Cowan, 2008; Aydoğan, 2011). The potential field method provides the ability to take derivatives in horizontal (x, y) and vertical (z) directions using the available data (Saad, 2006). Derivatives taken in the horizontal direction reveal the discontinuities, while the derivative taken in the vertical direction reveals the depth and spread of the source. Isostatic gravity maps, which are balanced by removing their continental effects, also include the total effect of deep and shallow structures like Bouguer gravity maps. Regional anomalies refer to deep structures, and residual anomalies refer to shallow structures. Regional and local anomalies should be separated from each other to make the interpretation more accurate. In this study, firstly, isostatic gravity values are divided into local and regional anomalies. Low pass filter is applied to isostatic gravity anomalies up to 4 km depth for each kilometer depth from sea level. Horizontal derivative grids in x-direction were calculated for each depth on the maps obtained. Fault traces were determined on these grid maps with the help of positive and negative anomalies. Separate color is used in drawing the fault traces determined for each depth.

Gravity values can generally be measured on the ground or in the air, reduced to sea level, and interpreted at this level; however, in some cases, it can be moved to different planes for interpretation purposes (Oruç, 2013). In this methodical study called up and down extension, both temporal and spatial environment can be preferred (Pick et al., 1973; Huestis and Parker, 1979). Thus, it is possible to differentiate the anomalies caused by the geological structures and the sources that constitute the anomalies (Blakely, 1995). The amplitude and wavelength variations of the gravity and magnetic anomalies, and the depth with the lithology, respectively, can be estimated. A similar situation is applied in determining the faults affecting these lithologies. Maximum and minimum changes of gravity anomalies help us in determining the types of faults (e.g, Telford et al., 1990; Yüksel, 2011; Lowrie, 2007). The locations of the blocks formed as a result of faulting and the slope angles of the fault plane provide the opportunity to make inferences from the changes in gravity fault anomalies. Accordingly, it is possible to understand whether faulting from gravity fault anomalies is close to vertical or less than 90° inclined. More importantly, it is possible to determine whether the inclined plane faulting is of normal or reverse fault character. Mathematical relations about these are given by Telford et al. (1990).

Air magnetic data obtained from MTA General Directorate was used for total magnetic (air magnetic) field data of the region, especially the TFZ, which is the subject of the study. These data were obtained between 1978-1989 at the height of 600 m in the region and with a profiled interval of approximately 1-5 km; data were re-grided with 5x5 km intervals and then 1x1 km. Magnetic anomaly map was created by applying the correction of - the International Geomagnetic Reference Area (IGRF-1985) - with an algorithm developed by Baldwin and Langel (1993) (Ateş, 1999). After the IGRF corrections have been made taking into account the measurement dates, the data has been reduced to the magnetic pole in order to eliminate magnetic deviations, to facilitate the interpretation and to eliminate the complexity of the process and to ensure that the anomaly is located on its actual location (Blakely, 1995). Then 600 m down extension was applied.

Gravity data were obtained from Turkish Petroleum (TPAO). In the region, including the study area, measurements were made at approximately 120,000 station points with the gravimeter device, and these data were recorded. Within the scope of this study, tool drift, latitude, free air, Bouguer plate, topographic correction, sea surface reduction, and isostasy corrections were applied to the obtained raw data. In the Bouguer calculation, the reduction density is 2.20 gr/cm^3 in the topographic correction, the density values of 2.20 gr/cm^3 are used. Oasis Montaj 2007 software was used for all corrections, and afterward,

since it is necessary to work in a wide area, isostatic gravity values balanced by removing deep continental effects were mapped, and subsequent operations were performed using these values.

4.2. Findings

Figure 4a displays the air magnetic anomaly map that is formed for the broad region, including the TFZ. The map shows the total effect of anomalies from

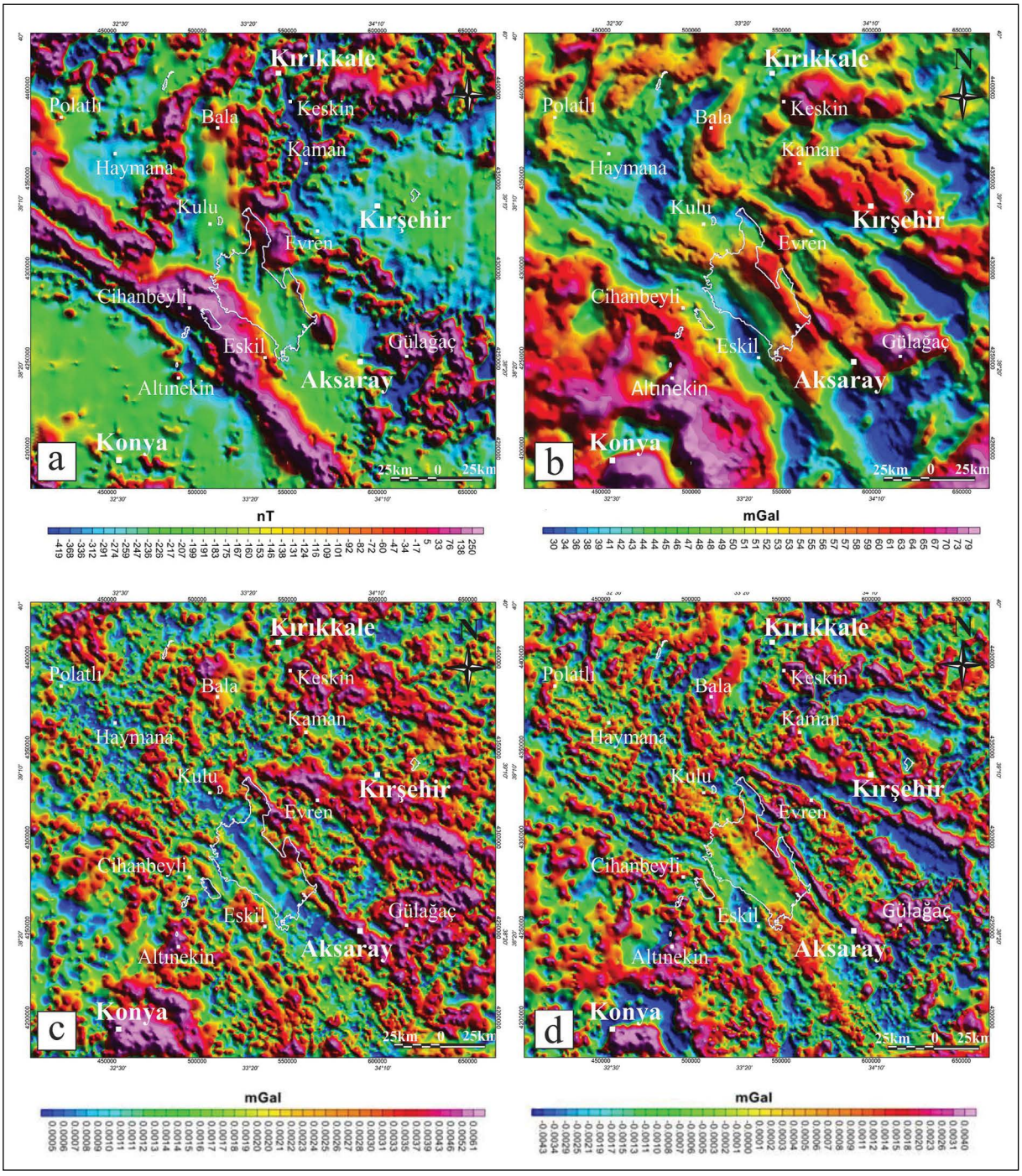

Figure 4- a) Aeromagnetic anomaly map (Contour interval was taken as 50 nT), b) isostatic gravity map (Contour interval was taken as 5 mGal), c) analytic signal map of the isostatic gravity data, and d) vertical derivative map of the isostatic gravity data.

lithologies of different depths. In the map where the contour interval is taken as 50 nT, especially the areas formed by positive anomalies of 85 nT and above are quite remarkable. These areas are represented by red and pink colors or their shades (Figure 4a). The areas with high anomaly values indicate the presence of magnetic susceptibility and/or lithologies with density. Therefore, the areas seen in the pink-red color range on the map have high magnetic susceptibility values. The areas where colors from yellow to green indicate that these parts have low magnetic susceptibility values. The areas colored in blue on the map refer to the areas where the magnetic susceptibility value is little or no according to the surrounding rocks. The isostatic gravity map for the region is given in figure 4b. The map shows the total effect of lithologies of different depths and distinct densities. In the map, the areas pink-purple in colors indicate the lithologies with high-density and blue-colored sections of the map show the lowest density lithologies.

Gravity and magnetic maps reveal where and how negative and positive anomalies are located in the region (Figures 4a, 4b). Correlation of simplified gravity and magnetic maps allow the depths of the rock units forming the anomaly in the map area (Figure 5). This comparison enables us to deduce the location and geometry of basins (e.g., Tuzgölü,

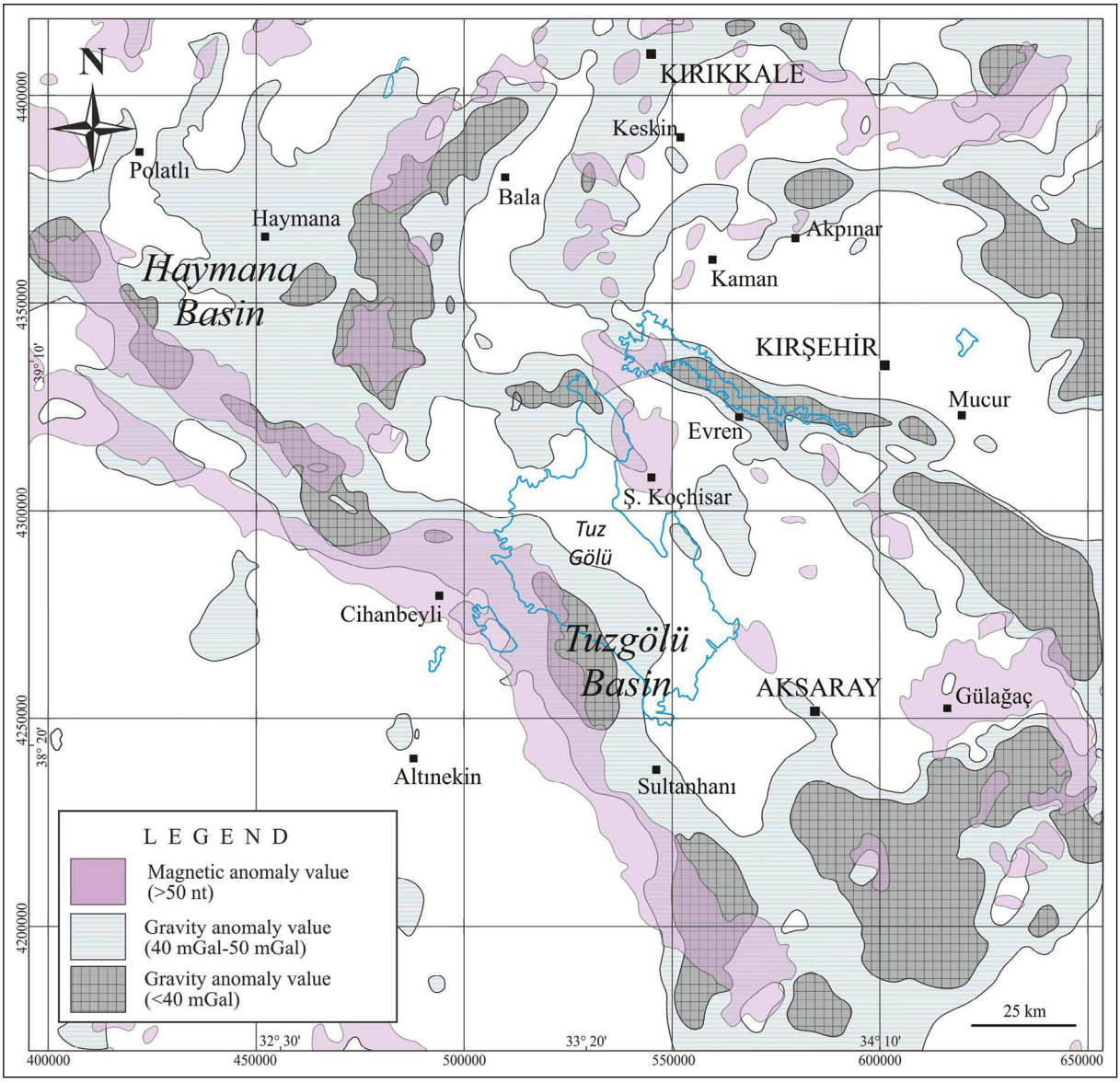

Figure 5- Map showing comparative magnetic and gravity anomalies data of the Tuzgölü Basin and its surroundings.

Haymana) and the extension of the basement units. Correlation of these data with surface geology reveals some compatibility and differences. The anomalies in gravity and magnetic maps indicate that the faultings in the region are mostly NW-SE-trending, but in the limited areas, it shows N-S orientation. The long-wavelength positive anomaly in the magnetic map with the NW-SE orientation is of deep origin and possibly represents the suture belt.

Figures 4c and 4d display maps of analytical signal and vertical derivative generated from gravity data. These maps allow us to interpret the anomalies in the map of isostatic gravity in detail. From both maps (analytical signal, vertical derivative), it can be interpreted whether the basin units in the region are too thick or how shallow the basin depths are (Figure 4c, 4d). It is essential to evaluate the positive/negative anomaly areas on the analytical signal map together with the anomaly areas on the gravity map. Areas with positive anomalies in the analytical signal map and areas with similar anomalies in the isostatic gravity map show that the units that make up this anomaly are located close to the surface or on the surface. Again, the positive/negative anomaly areas in the vertical derivative maps allow the understanding of how deep or shallow the units are. This fact is as possible as for faults.

In determining the basement rock depth for the Tuzgölü Basin and its surroundings, a graph (Figure 6) prepared with the depth estimation technique (Yüksel,

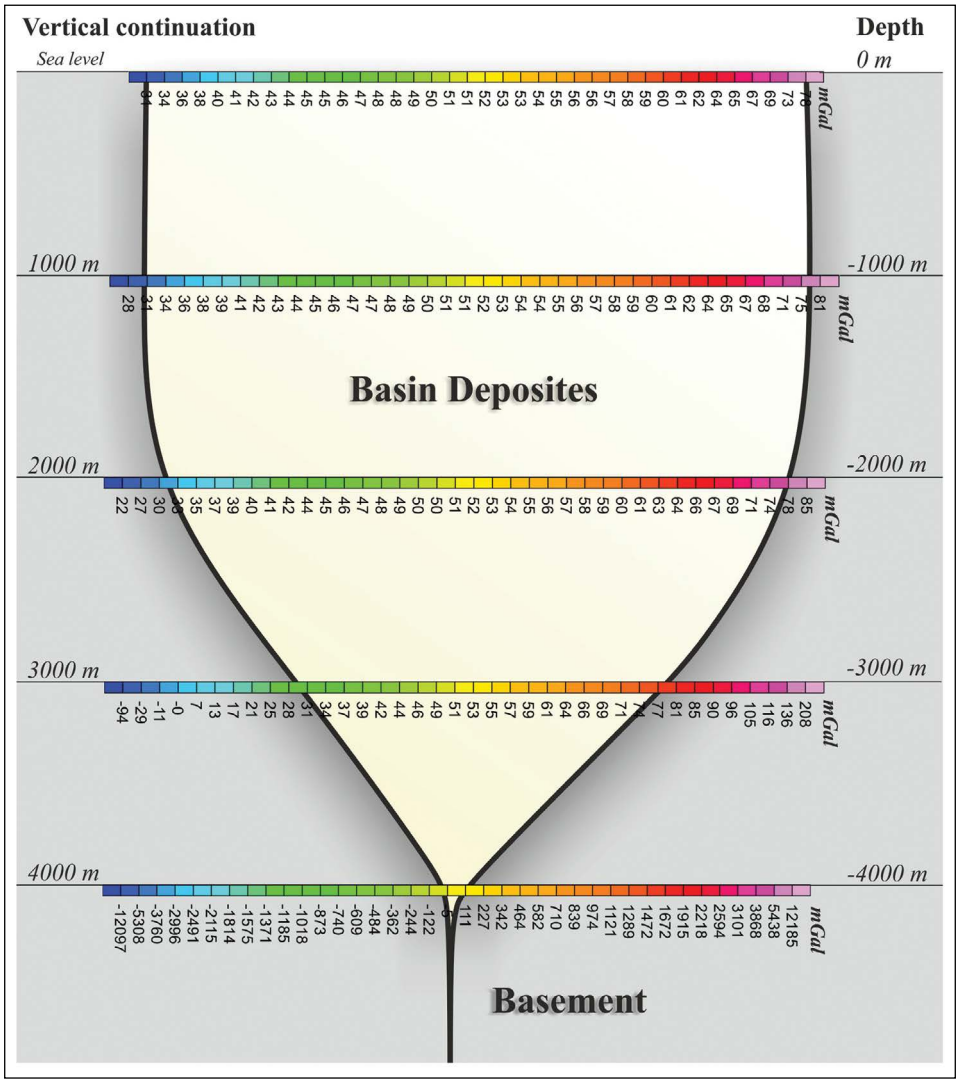

Figure 6- Estimation graphic showing regional depths of basement rocks using the downward continuation maps of the Tuzgölü Basin and its surroundings.

2011) and power spectrum graphics (Figure 7) were made. In this context, downward continuation maps (Sea level, -1000 m, -2000 m, -3000 m, and -4000 m) have been prepared to determine how deep the basement rock buried in the region is located from the sea level.

The estimation graph from the downward continuation map values created for every -1000 m from the sea level up to -4000 m is given as figure 6; The estimation graph shows the average rock depths entered in the base rocks in the region. The downward continuation map created for sea level reveals that the border between low-density units and high-density units is in the range of 31 mGal to 78 mGal values (Figure 6). If this value range is taken into account as a template, there are no remarkable changes in the values representing low and high-density units in the downward continuation maps representing depths of -1000 and -2000 meters from sea level. However, in the downward continuation map created for a depth of -3000 m, there is a significant change in values; at these depths, basic units are entered in places, and anomalies respond to inversion, reflections with deviations in the high and low-value ranges, and the values representing this response between low-density units and high-density units are between 208 mGal and -94 mGal (Figure 6). At -4000 m depths from the sea level, the noises reach the maximum size, the template value range disappears completely, and base units are entered in the whole area. In response, these values appear to be between 12185 mGal and -12097 mGal, which is unlikely to be on Earth or on similar planets.

Findings obtained with downward continuation maps reveal that density changes are not observed in units of about -4000 meters from sea level; in other words, base rocks are reached at these depths. Considering approximately 1000 m topography, it means talking about 5000 m depth from the surface.

The power spectrum graph consists of two different graphs as the total power-wave number and depth-wave number (Figure 7). It contains three

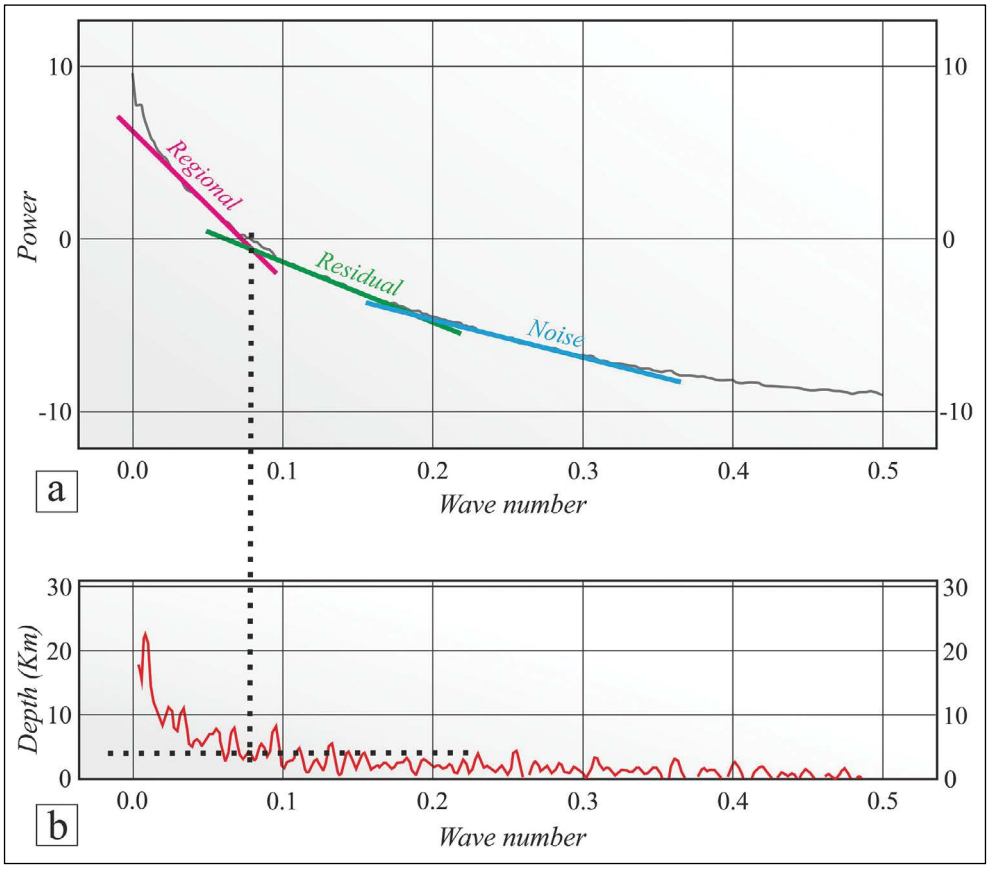

Figure 7- Graphs showing a) the average power spectrum and b) estimated depth obtained from isostatic gravity data.

lines with different inclined, which refers to the high power-wave number, the low power-wave number, and the very low power-wave number, respectively (Figure 7a). While the highly inclined line represents deep structures (regional), the line with low inclined indicates shallow structures (residual); the line with very low inclined corresponds to the undesired signals, which are called noise. By evaluating with the depth-wave graph and the power-wave number graph together allow us to determine the approximate depths of the basement rocks in the region and checking the values obtained from the estimation graph. The shallow and deep impact separation from the graph was determined as -4000 m to -5000 m depth. This depth is also consistent with the amount of depth obtained from the regional estimation graph.

4.3. Faults Obtained From Gravity Anomaly Values

Our gravity anomaly analysis in the area covering the TFZ and its surroundings indicate the presence of fault traces at levels of sea level (0 m) and -1000 m, -2000 m, -3000 m, and -4000 m depths (Figure 8). Fault traces limited by gravity anomaly analyzes in the region show mostly NW-SE orientation. Also,

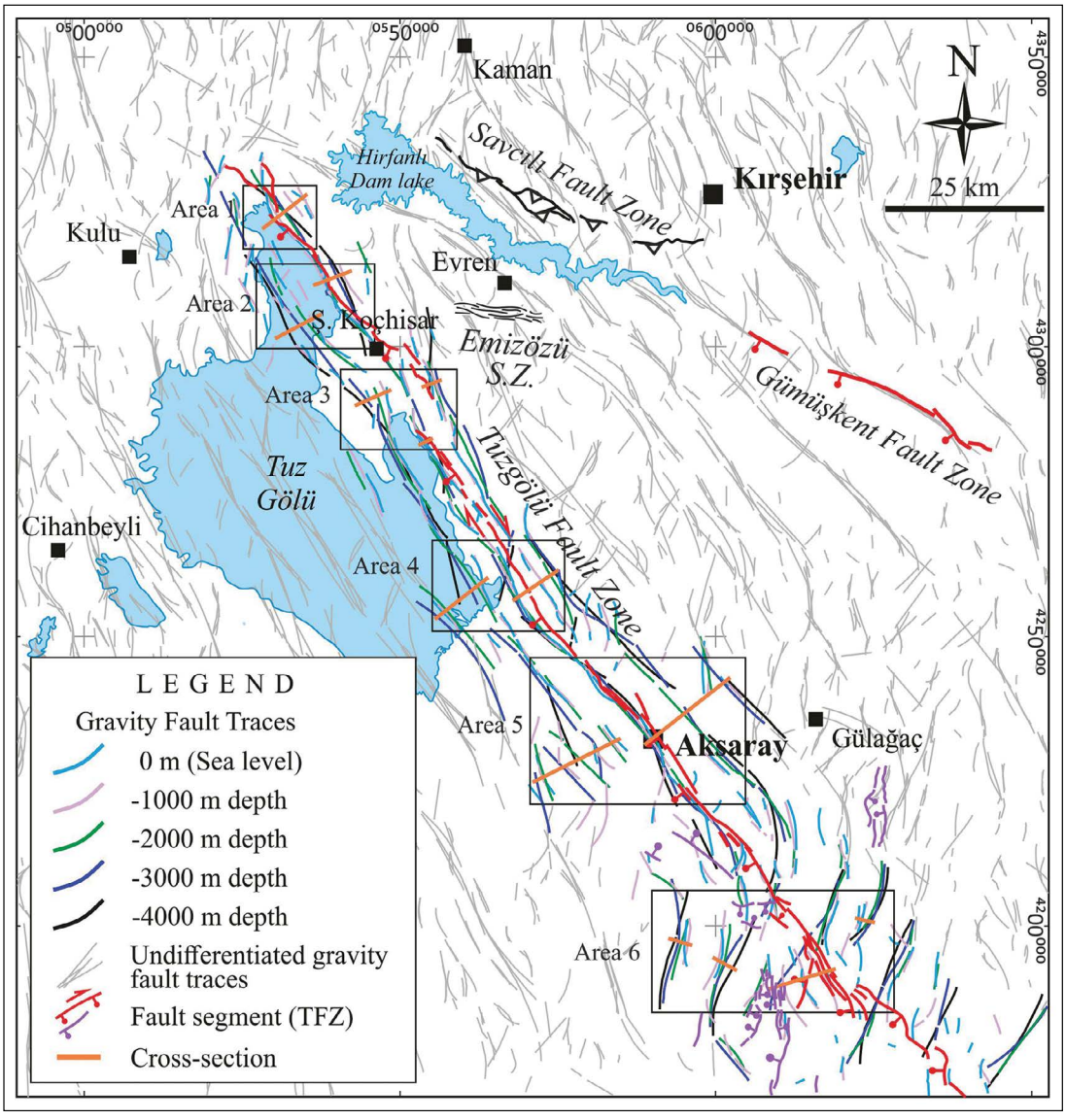

Figure 8- Map showing fault traces in-depth obtained from gravity anomalies along the TFZ and its surroundings. Fault strands of the Tuzgölü Fault Zone have adopted from MTA Active Fault Maps of Turkey (Emre et al., 2011). The Savcılı Fault Zone adopted from Çağlayan, 2010 and Işık et al., 2014.

there are fault traces with NE-SW and E-W trendings (Figure 8).

Within the scope of the study, gravity anomalies in six areas were studied in detail to determine the extending of the faults toward depth and their characteristics along the TFZ. The fault traces determined from gravity anomalies in each area were drawn on a map of the digital elevation model (DEM). The fault traces in these maps made for six areas are shown in different colors so that one could distinguish which faults appear in which levels. According to this; it is shown that faults at a depth of -4000 m from the sea level are black, faults at a depth of -3000 m are dark blue, faults at a depth of -2000 m are green in color, faults at a depth of -1000 m are lilac in color, and faults at a depth of 0 m referring to sea level light blue.

Amplitude and wavelength changes in gravity and magnetic anomalies provide lithology and depth estimation, respectively. Maximum and minimum changes of gravity anomalies of faults provide to determine the types of faults (Lowrie, 2007). It could be only possible that the faults at depths are mainly qualified as normal, reverse, and vertical faults using a method (Telford et al., 1990). In vertical faults, the ratio of maximum and minimum anomaly values is equal to 1. Anomaly defining the normal fault differs significantly from the anomaly of the vertical fault, and the ratio between the maximum and minimum anomaly values is less than 1. Similarly, the difference between these anomalies indicates the reverse faults, in which the ratio between the maximum and minimum anomaly values is greater than 1 (Telford et al., 1990). The type of all these faults is displayed using the appropriate symbol in the fault maps.

In order to better visualize the faults in the areas, the cross-sections were made up of every map. The type of faults is also marked on cross-sections considering their depths. In addition, the rose diagrams showing the orientation of fault traces in map areas were developed in case of understanding the main fault orientations at any level.

4.3.1. Area 1

Area 1 is located in the northwest extension of the TFZ. The TFZ is characterized by various structural segments (fault strands). The segments are commonly NW-SE-oriented; some of them strike to approximately N-S (Figures 9a, 9c). The segments along this part of the zone have a right-lateral strike-slip fault with a normal component. The gravity anomaly data in the region suggest evidence the faults at any level starting from sea level and towards 4000 m in depth. The rose diagram analysis indicates that the fault traces have NW-SE orientation, although the angle of strikes shows differences (Figures 9a, 9c). A lesser amount of these fault traces has an NNE-SSW orientation (Figure 9c). The type of most of these faults in area 1 is a normal fault. A limited number of fault traces show reverse and vertical fault characteristics (Figures 9a, 9b).

4.3.2. Area 2

Within Area 2, the fault segments representing the TFZ have an NW-SE trending and curved geometry. The fault type of segments comprises normal component strike-slip faults (Figure 10a). The gravity anomaly data indicate that these faults are of normal, reverse, and vertical fault character (Figures 10A, 10b, 10c). The rose diagram data show that the faults at depths of -4000 m and -3000 m are mostly similar to orientations (Figure 10d). A similar correlation could be made for faults at depths of -2000 m and -1000 m. These faults display NW-SE directions (Figure 10d). Our anomaly data suggest that the faults at depths along the TFZ have a normal fault with southwest dipping. While most of the faults occurred within the Tuz Gölü area and in the southwestern part of the map area are normal faults with northeast dipping, some of these faults show reverse fault character (Figures 10a, 10c). The fault traces identified at depths of -1000 m and sea level (0 m) are reverse faults. Both dip direction and hanging-wall and footwall relations suggest that sense of movement of the reverse faults is from the southwest to the northeast.

4.3.3. Area 3

The TFZ with fault segments in Area 3 step over to the northeast, and have an NW-SE trending with curved geometry (Figure 11a). The fault type of these segments is strike-slip faults with a normal component. The faults deduced from the gravity anomaly data in the area are mostly normal faults; a lesser amount of these faults display reverse fault characters (Figures 11a, 11b, 11c, 11d).

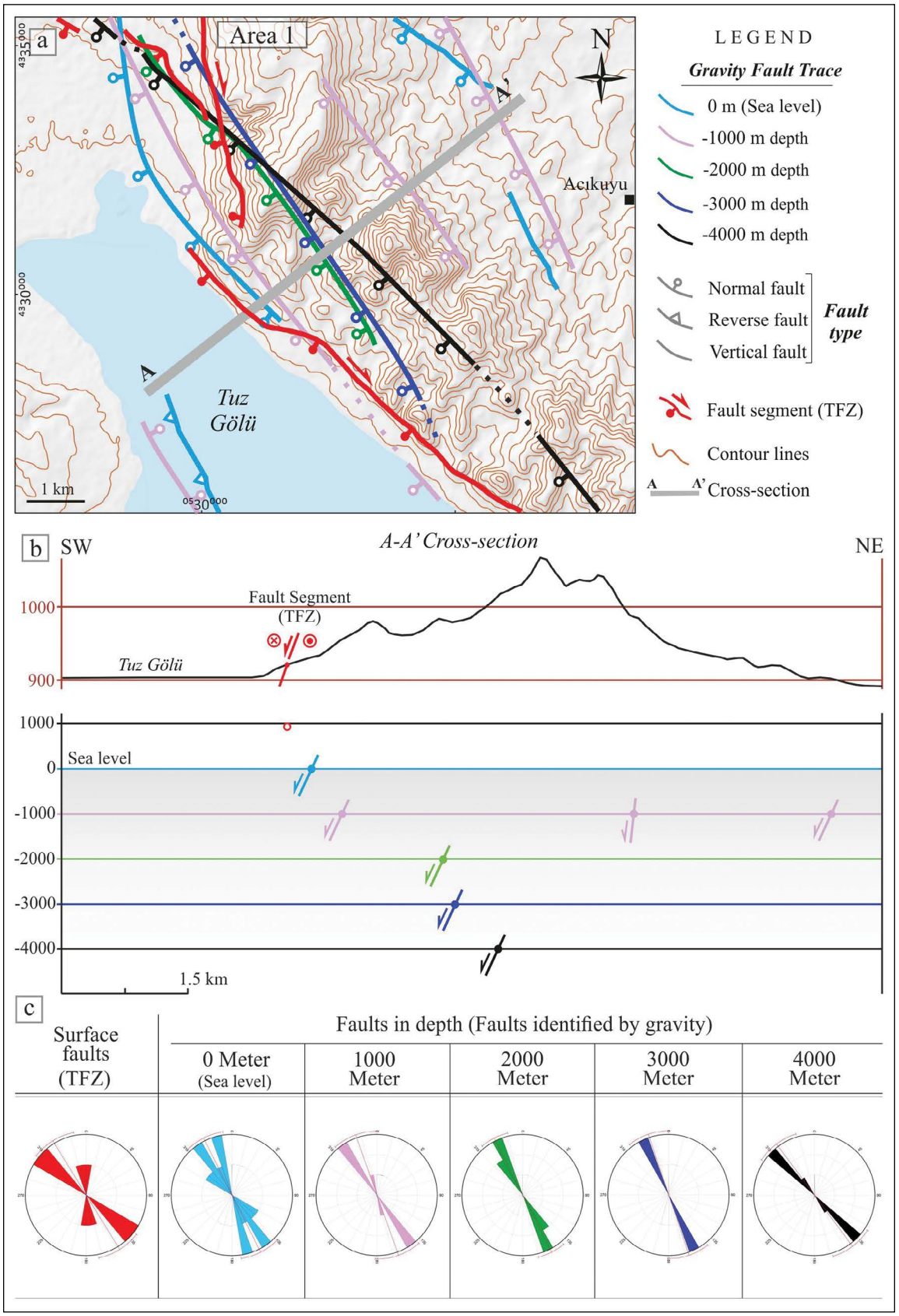

Figure 9- a) Map, b) cross-section and c) rose diagram view of the TFZ segments and fault traces in-depth obtained from gravity anomalies in Area 1.

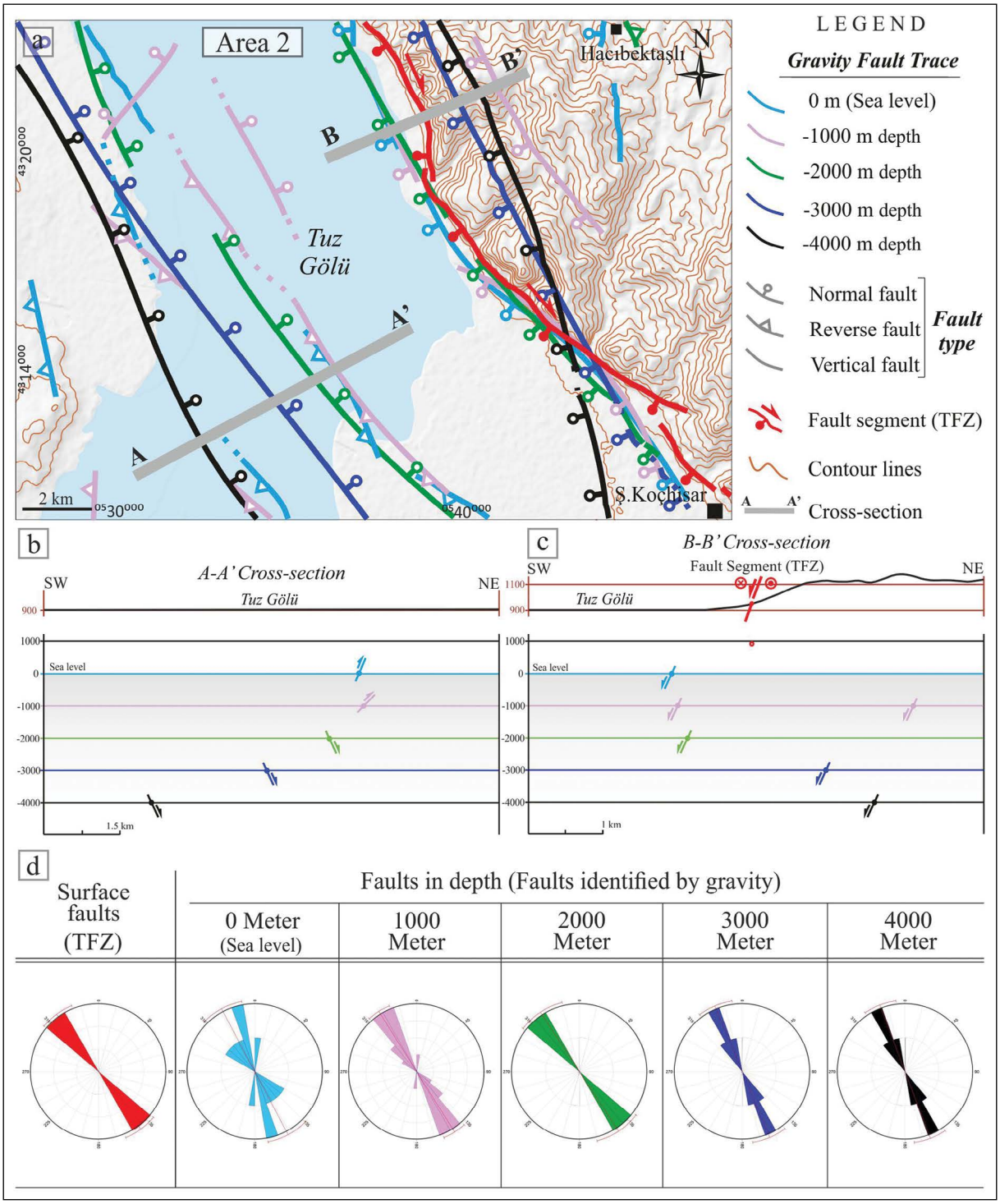

Figure 10- a) Map, b-c) cross-section and d) rose diagram view of the TFZ segments and fault traces in-depth obtained from gravity anomalies in Area 2.

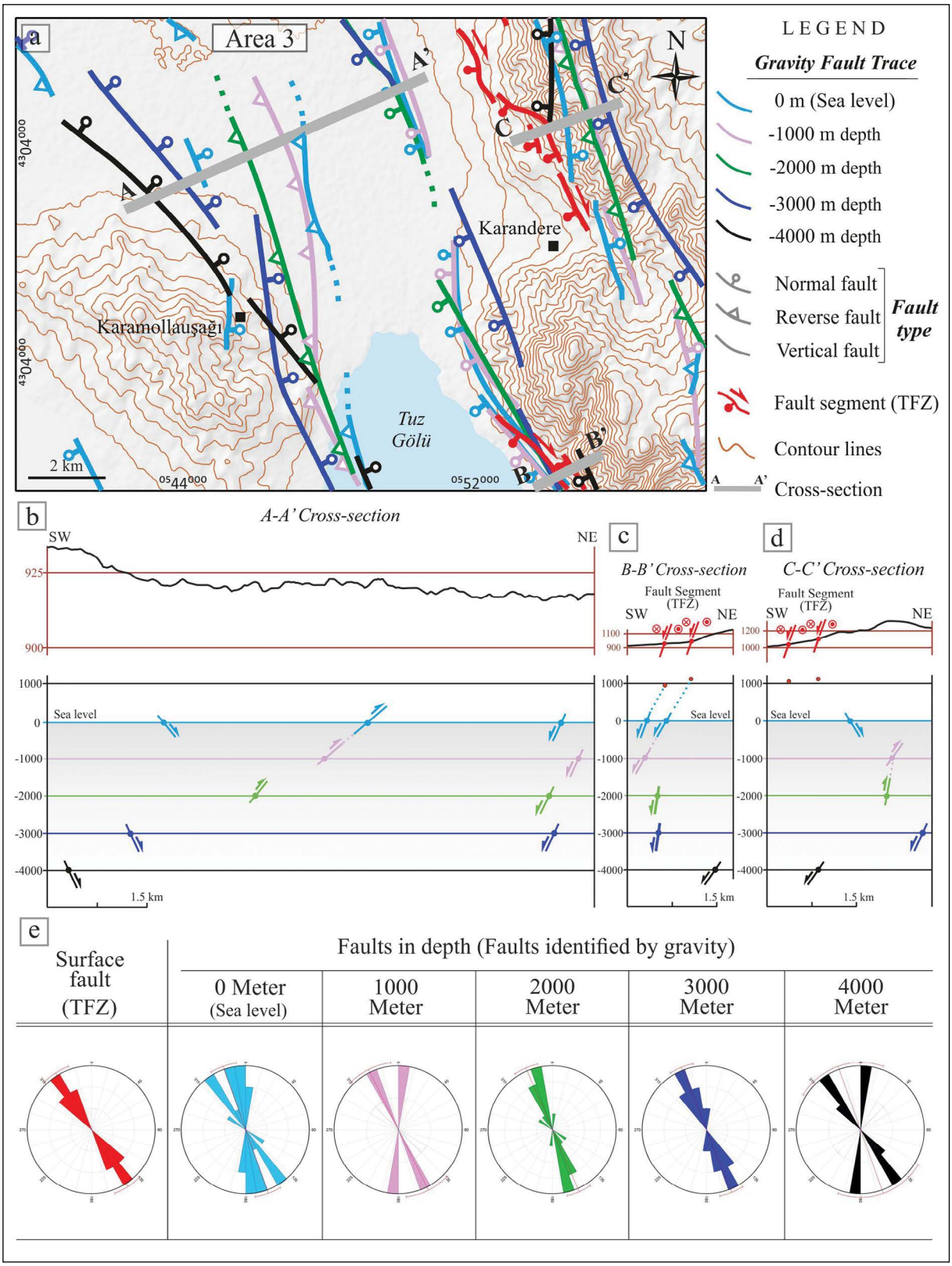

Figure 11- a) Map, b-c-d) cross-section and e) rose diagram view of the TFZ segments and fault traces in-depth obtained from gravity anomalies in Area 3.

Fault traces at depths of -4000 and -3000 m are normal fault characteristics; ₌2000 m, -1000 m, and some sea level faults have normal fault character, also (Figure 11b, 11c, 11d). The normal faults in an area dip to SW or NE. Some of the fault traces at -2000 m, and -1000 m depth is the reverse fault character. Dip directions and hanging-wall and footwall relations indicate that the reverse faulting originated in a movement from the southwest toward the northeast. The rose diagram data of the faults covering Area 3 reveal that the fault traces are mostly NW-SE trending; some of these fault traces have approximately N-S trending (Figure 11e).

4.3.4. Area 4

Area 4 covers an area located in the central part of the TFZ. The TFZ in this area includes a single fault segment. The segment strikes NW-SE and shows a strike-slip fault with a normal component. This active fault dip to the southwest (Figure 12a). The fault traces inferred from the gravity anomaly data is approximately NW-SE trending. Some of the faults at-4000 m depth have NNE-SSW striking (Figures 12a, 12d). These faults in Area 4 are of a normal and reverse faulting; some of these faults within a limited part of the areas are characterized by vertical faults. Fault traces at a depth of -4000 m are of a normal fault. Some of the faults at depths of -3000 and -2000 m and 0 m (sea level) are characterized by both a normal and reverse faulting (Figures 12a, 12b, 12c). Faults identified at depths of -1000 m in this area show reverse faulting with NE or SW dipping. The rose diagram pattern in Area 4 reveals that the fault traces are mainly in NW-SE orientation, but few fault traces have approximately N-W, NW-SSW, and NE-SW trends (Figure 12d).

4.3.5. Area 5

Area 5 is a region that includes the Aksaray settlement. The length of fault strands of the TFZ is between 4 km and 14 km in their lateral lengths. These faults have strike slip fault with a normal component. Fault traces inferred from gravity anomaly data form a typical fault zone geometry in the area. Most of the fault traces are NW-SE trending and dip to the southwest or northeast (Figure 13a). Most of these faults are characterized by a normal or reverse faulting. A limited number of faults have been identified as vertical faults (Figures 13b, 13c). As can be seen in the B-B' cross-section, the fault traces at -4000 m, -3000 m, and -2000 m depths are reverse faults with northeast dipping, unlike the fault strands of the TFZ. On the other hand, fault traces identified at -1000 m, and sea level depths are of a normal fault and are relatively compatible with the fault strands of the TFZ (Figures 13a, 13c). In the northeastern continuation of the same cross-section, the faults at-4000 m and -3000 m depths show normal faulting and dip to the southwest. Along the A-A' cross-section, The fault types in the Tuzgölü Basin differ. In this part, the fault traces at a depth of -2000 m are in reverse fault character. But the fault trace at a depth of -4000 m shows normal fault type. The faults identified at depths of -2000 m, -1000 m, and sea level along with the northeastern extension of the A-A' cross-section have noteworthy reverse faults feature (Figure 5b). The rose diagrams in Area 5 reveal that the fault traces are mostly in NW-SE trending (Figure 13d).

4.3.6. Area 6

Area 6 is located in the southeast extension of the TFZ. This part of the fault zone is characterized by dispersed geometry within a broad area. Due to such branching of fault strands suggest different fault orientations showing NW-SE, N-W, and NE-SW trending. In this area, the length of segments of the TFZ is between 1 km and 20 km in their lateral lengths. They show strike slip fault with a normal component (Figure 14a).

The orientation of the fault traces inferred from the magnetic anomaly data in the area is partially different from the other areas containing fault traces showing NNE-SSW and NE-SW orientation. The faults are mainly a normal or reverse faults. Some of these faults are also vertical fault (Figures 14a, 14b, 14c, 14d, 14e). Most of these faults have SE- or NW-dipping. All these orientations suggest that there might be relative rotation comparing the faults of the other areas. Most of the faults at a depth of -4000 m are in reverse fault character. Similar fault types are seen at depths of -3000 m and -2000 m. In this area, the fault traces inferred from the gravity data differ significantly with the fault segments of the TFZ (Figure 14). This difference is also seen in the rose diagrams for Area 6 (Figure 14f).

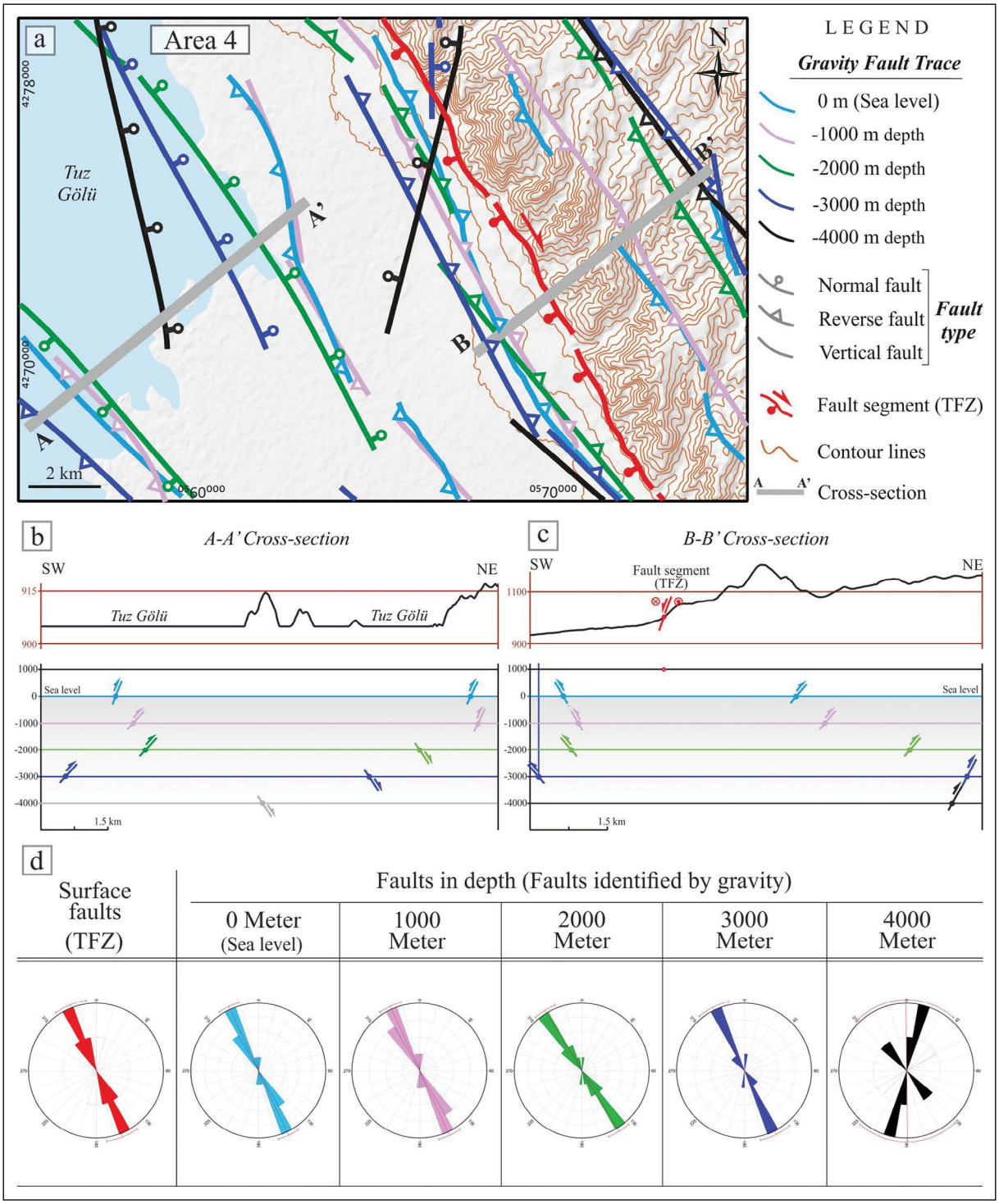

Figure 12- a) Map, b-c) cross-section and d) rose diagram view of the TFZ segments and fault traces in-depth obtained from gravity anomalies in Area 4.

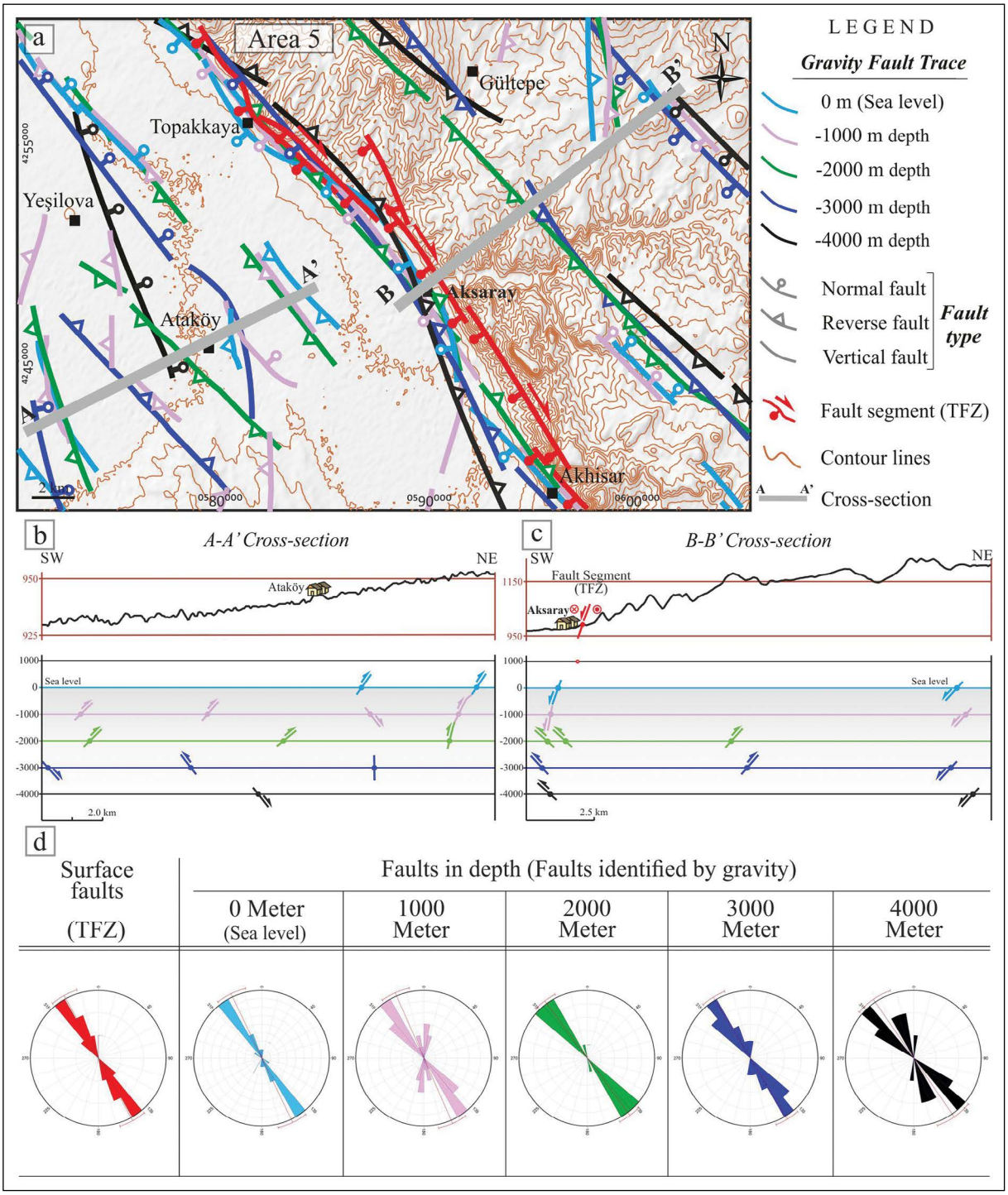

Figure 13- a) Map, b-c) cross-section and d) rose diagram view of the TFZ segments and fault traces in-depth obtained from gravity anomalies in Area 5.

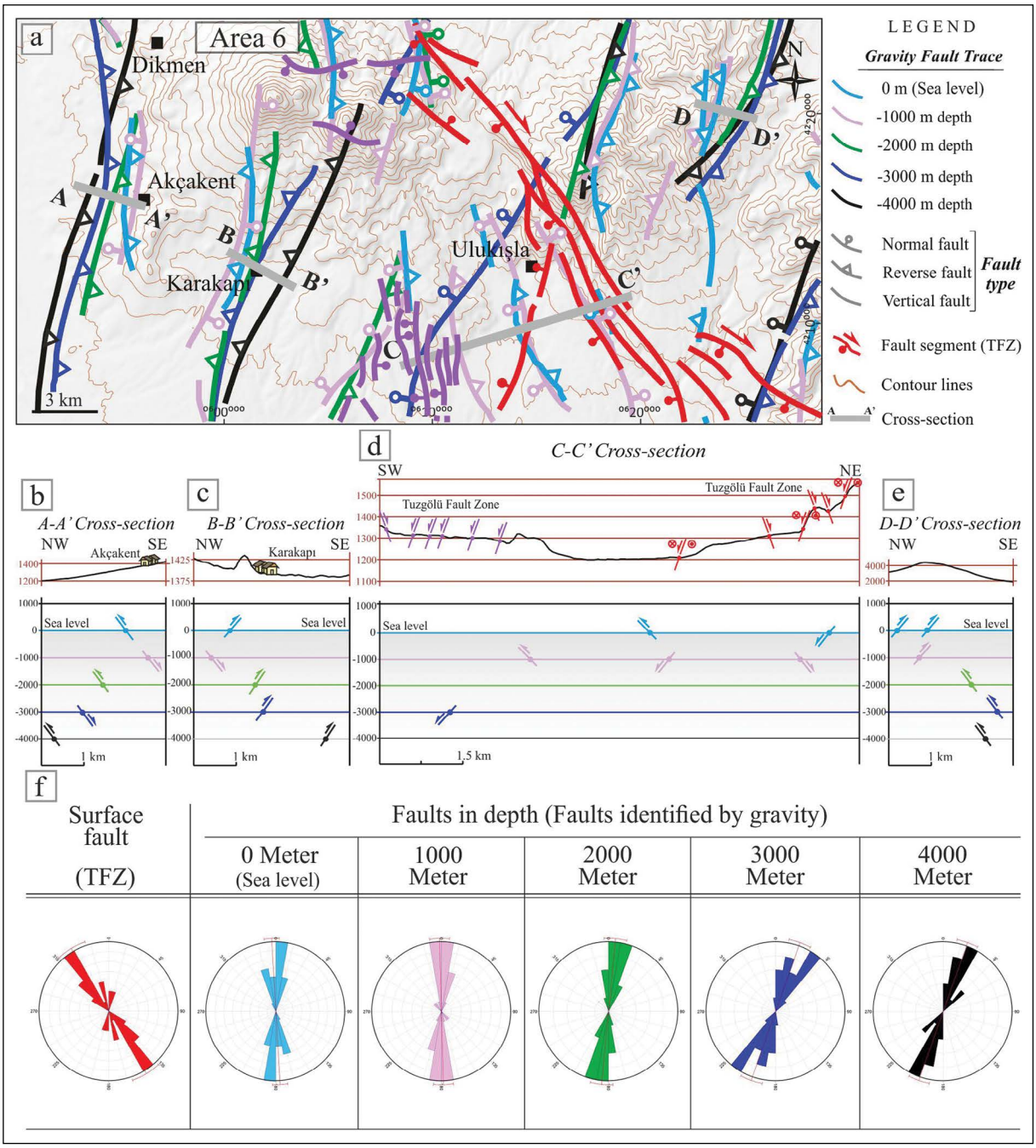

Figure 14- a) Map, b-c-d-e) cross-section and f) rose diagram view of the TFZ segments and fault traces in-depth obtained from gravity anomalies in Area 6.

5. Discussion

Central Anatolia includes many basin developments during the paleotectonic and neotectonic periods. These basins display a complex evaluation of the Neotethys Ocean in the late Cretaceous-Cenozoic period. Although it seems that these basins are different basins from each other based on recent positions in the region, it is known that some of them have the same or mutual geodynamic developments.

Geological-based detail studies state that units of the Central Anatolian Basins overlie both rocks of oceanic crust that represent the Neo-Tethyan Ocean and some rocks of continental crust (e.g., Sakarya Zone, Kırşehir Block) lithologies (Şengör and

Yılmaz, 1981; Görür et al., 1984; 1998; Koçyiğit et al., 1988; Koçyiğit, 1991; Göncüoğlu et al., 1996; Rojay, 2013). According to Görür et al. (1998), most of these basins are either arc-related or molasse basins. However, different evaluation mechanisms are suggested to these basins. (Çemen et al., 1999; Gürer and Aldanmaz, 2002; Derman et al., 2003; Alpaslan et al., 2006; Işık et al., 2008; 2014; Işık, 2009; Lefebvre et al., 2011; Advokaat et al., 2014; Seyitoğlu et al., 2017).

Tuzgölü Basin is one of the important basins in central Anatolia, which has kilometers of sediment thickness with broad distribution. The thickness of the basin deposits is estimated to be 9 km in the light of geological evidence (Görür et al., 1998). It is also interpreted based on geophysical methods (seismic, gravity, magnetic) that the average depth of the Tuzgölü Basin is 8 km, and even its some parts reach 12-13 km depth (Aydemir and Ateş, 2006*b*). Such thicknesses of deposits prove explicitly that the Tuzgölü Basin developed under fault control.

According to Görür et al. (1998), the Tuzgölü Basin is subduction-related arc basin with NE-SW trending that formed on the western side of boomerang-shaped Kırşehir Block and in the İzmir-Ankara Ocean. The researchers agree that the Tuzgölü Basin should be associated initially with the Çankırı, Kırıkkale and Ulukışla Basins and developed in same geodynamic conditions. Nairn et al. (2013) have been positioned the Tuzgölü Basin in the west of the Niğde-Kırşehir microcontinent in the Upper Cretaceous period, and they agree that the basin is associated with west-dipping subduction in the Neotethys Ocean. Yet these researchers, agree that the position of the Çankırı and Ulukışla Basins are different from that it is positioned by Görür et al. (1998). Çemen et al. (1999), Derman et al. (2003) and Dirik and Erol (2003) state that the Tuzgölü Basin continues in the Late Cretaceous-Early Paleocene stretched basin formation and continued in the Paleocene-Middle Eocene, and in the Late Eocene-Oligocene, the basin was affected by the compression regime, and during the Oligo-Miocene period basin also affected by the compressional regime. In Miocene-Early Pliocene, it represents basin development dominated by normal faulting.

Işık (2009) have mapped an extensional ductile shear zone to the northeast of the Tuzgölü Basin, Emizözü Shear Zone, which is responsible for the initiation of the Tuzgölü Basin. He pointed out that active TFZ should not be defined as the fault controlling the sedimentation of the Tuzgölü Basin since Cretaceous, and that the segments of the TFZ most probably occurred after Miocene. The age data from the faults forming the Savcılı Fault Zone using isotopic methods (Işık et al., 2014) present a significant contribution to the understanding of the geodynamic evaluation of the region. According to Işık et al. (2014), the Tuzgölü Basin started to form in Maastrichtian with the extensional regime accompanied by a ductile shear zone. The extensional regime has been replaced by the compression regime, represented by reverse faulting, from the middle Eocene (~ 46-40 Ma). The occurrence of these faults characterized by reverse faults continued until the Late Oligocene-Early Miocene (~ 30-23).

Seyitoğlu et al. (2017) have put forward the development of the basins in central Anatolia, especially the Ulukışla Basin, with the detachment fault in a regional model.

Fernandez-Blanco et al. (2013) suggest two independent basin development phases based on three-dimensional modeling with the help of some seismic reflection profiles for the Tuzgölü Basin. The first one is the Cenozoyic phase, and the other is the Late Miocene-Recent period phases. According to the researchers, the Cenozoyic phase represents the subduction of oceanic crust of the Sakarya Continent beneath the Kırşehir Massif, and thickening of the crust. These comments while supporting the view proposed by Görür et al. (1984); do not match the opinions suggested by Işık et al., 2008; 2014; Işık (2009) and Lefebre et al. (2011). According to Fernandez-Blanco et al. (2013), regional compression continued until the Late Miocene-Pliocene period. Then the extensional regime initiated in Tortonian and continued until recently, which is characterized by approximately 800 meters sediment deposition. However, the researchers also stated that the Late Miocene-Pliocene period could not be associated entirely with the extensional regime, but the basin might be affected by the main compression event for a short period (at the latest Miocene-Pliocene: 7-5 My). In the same study, the insufficiency of the evidence of this short-term compression regime in the Tuzgölü Basin is explained because of the extensional regime that obscures these structures. Unlike Fernandez-Blanco et al. (2013),

Özsayın et al. (2013), copartner of the same project, suggest a slightly different tectonic evaluation of the Tuzgölü Basin. In regard to Özsayın et al. (2013), the Tuzgölü Basin evaluated under two different tectonic regimes, which is before and after the upper Miocene. Accordingly, the compression regime in the basin, constrained by the Ar-Ar aging method (6.81 ± 0.24 Ma), continues until the upper Miocene, and then the basin is under the influence of the N-S and NE-SW extensional tectonic regime.

Understanding the faulting that occurred in the region helps the clarifying the tectonic evaluation of the region, where different views are asserted. The TFZ, the subject of this study, is one of the significant structural discontinuity because of its origin relationship with the Tuzgölü Basin mentioned (Figure 2). The surface geology studies show that the TFZ is an active fault zone with a length of approximately 195 km and a width between 1 km and 25 km. The zone is set mostly as Holocene faults in the Active Fault Map of Turkey produced by MTA 2011; some of these faults located in the southeastern part of the zone are also drawn as Quaternary faults. The majority of these faults in this map are characterized by normal faults and a lesser amount of them in local areas as strike-slip faults with normal components. Koçyiğit (2003) argues that TFZ is a dextral fault zone with normal components. Kürçer (2012) and Kürçer and Gökten (2014) suggest that the zone consists of different segments represented by oblique faulting with normal components.

Due to the possible oil potential of the Tuzgölü Basin, deep drilling and seismic profile studies were carried out in different parts of the basin. Numerous seismic profile sections in the basin covering the TFZ were extrapolated and suggested various structure occurrences for the region.

Uğurtaş (1975) propounded that the subsurface of the Tuz Gölü area includes salt structures based on seismic reflection profiles, gravity, and surface topography data. Çemen et al. (1999) point out based on the interpretation of the seismic profile perpendicular to the TFZ in the northwest of Aksaray that the basin is bordered by, a normal fault with high-angle in the near-surface of the Tuzgölü Basin and, by a low-angle detachment fault, its downward continuation and the basin deposits display folding with anticline geometry to this fault. Similar seismic profiles of the Tuzgölü Basin were also used by Aydemir and Ateş (2006*b*), and their seismic profile interpretations suggest the development of normal faultings with different displacements. Examination of these seismic profiles has also been subjected to the study of Fernandez-Blanco et al. (2013). From the seismic profiles with a depth of approximately 7 km and traverse the TFZ, the evidence of the normal fault with extending kilometers toward depth is interpreted, which is called Tuzgölü Fault. The interpretation of the profile sections in the same study, the presence of the post-Pliocene thrust fault (Şereflikoçhisar-Aksaray Thrust) which extends to the depths in the hanging wall is also remarked.

Işık (2009) records ductile (mylonitic) shear zone (Emizözü Shear Zone) with N70°-80°W trending and southwest dipping that cut the Ağaçören Granitoid in the Central Anatolian Crystalline Complex between Evren and Şereflikoçhisar (Figure 2). The microstructural features of the Emizözü Shear Zone reveal that the zone has occurred with the regional extensional regime; the age of the zone is reported as 78-71 Ma (Işık, 2009). Lefebvre et al. (2011) define the detachment zone, 84-74 Ma age, in the vicinity of Kaman, which advocates the Late Cretaceous extensional tectonic regime proposed by Işık (2009). Another similar extensional ductile shear zone was described in the northern part of the Central Anatolian Crystalline Complex (Işık et al., 2008). Seyitoğlu et al. (2017) present a geological model for the extensional regime of the region covering all these ductile shear zones and the Ivriz Detachment Fault that is responsible for controlling part of deposits in the Ulukışla Basin located in the southern part of Central Anatolia.

Işık et al. (2014) indicate the following tectonic development based on field findings and observations and isotopic age data for Central Anatolia: Central Anatolia is exposed to the extensional regime in the latest Cretaceous during the closure of the Neo-Tethyan Ocean associated with the regional compressional regime. The extensional regime in Central Anatolia is characterized by the emplacement of granitoid intrusion, the development of ductile shear zones, the rising and exhumation of metamorphites and granitoids, and the opening of major basins associated with normal faultings. Then, from the Middle Eocene, the extensional regime gave way to the compressional regime, which causes the development of reverse and

thrust faults in the region commonly. The Savcılı Fault Zone, well-known its age of faulting, is the typical example of the compressional regime. Isotopic age data indicate that this compressional regime lasted until the end of Oligocene or earliest Miocene (Işık et al., 2014). The next period is explicated either extensional or lateral tectonic regime or both. Geological cross-sections in the Tuzgölü Basin set by Dellaloğlu and Aksu (1984) also have the reverse and thrust faults developed in the pre-Miocene period. Borehole data obtained from drilling for hydrocarbon exploration verified the existence of these faults. Remarkably, some of these faults that present in the depth of the basin have similar tectonic movement of the Savcılı Fault Zone. However, there are different views and interpretations about Savcılı Fault Zone (Yürür and Genç, 2006; Lefebvre et al., 2013; Gürer and van Hinsbergen, 2019).

Palaeomagnetic studies have been carried out for a better understanding of structural discontinuities and the spatial and temporal development of lithology in the geology of Turkey. In this context, sense and amount of rotation in local and regional areas have been estimated by using paleomagnetic data obtained from lithologies formed in different ages (Tatar et al., 1996; Gürsoy et al., 1997; 1998; Platzman et al., 1998; Kaymakçı et al., 2003; Kissel et al., 2003; Lefebvre et al., 2013; Çinku et al., 2016; Gürer et al., 2018). Interpretation of the paleomagnetic data obtained from Central Anatolia would be different. Differences in interpretations can vary depending on the type of lithology, the number of samples, and the quality of data. According to Platzman et al. (1998), Central Anatolia has shown a 50° counterclockwise rotation from 12 Ma until recently. Kissel et al. (2003) suggest that Kırşehir Block might be rotated ~ 25° counterclockwise in the Neogene period.

Recently, paleomagnetic measurements performed by Çinku et al. (2016) Mesozoic and Cenozoic units of the Kırşehir Block and Central Taurides show that Central Anatolia record quite complex rotational movements. Accordingly, the upper Cretaceous ophiolitic rocks in west of Kırıkkale and southwest of Yozgat have a clockwise rotation of 26.2° and counterclockwise rotation of 15.5°, respectively. In the same study, counterclockwise rotations of 39.5°±9.9° and 51.5°±13.1° have been estimated in the Tuzgölü Basin, where the place in the northwest extension of the TFZ, and the Ulukışla Basin located in the south-southwest part of the zone and Tuzgölü Basin, respectively. The counterclockwise rotation of 85.5°±19.3° have been suggested in the Tuz Gölü area for the Middle Eocene (Çinku et al., 2016). Also, rotations, mostly counterclockwise and clockwise, have been recorded in widely distributed Niğde and Kırşehir massive areas containing units of the Late Cretaceous-Middle Eocene, Late Cretaceous-Paleocene and Middle Eocene. The range of rotation amounts in the massive areas is distinctly high (Çinku et al., 2016). The researchers have explained that different sense and amount of rotations of paleomagnetic data obtained from regions in Central Anatolia result from the regional faultings. (Lefebvre et al., 2013; Lucifora et al., 2013; Çinku et al., 2016; Gürer et al., 2018). Fault traces (from sea level to -4000 m depth) obtained from the analysis of gravity and magnetic measurements have mainly NW-SE orientation. The initial position of these faults at depth along the TFZ were most probably NNW-SSE and/or N-S orientation if it is considered that Central Anatolia experienced counterclockwise rotations between 25° and 50° for the Neogene (Platzman et al., 1998; Kissel et al., 2003),

6. Conclusions

In this study, we have identified faulting mechanisms in TFZ and its surroundings based on the analysis of gravity and magnetic measurements. Obtained data suggest the following results:

(1) The faults located at sea level (0 m), -1000 m, -2000 m, -3000 m, and -4000 m depths along the Tuzgölü Fault Zone and in its surroundings were determined using the gravity anomaly data.

(2) The lateral extent of the fault traces in these depths ranges from a few kilometers to several tens of kilometers. This NW-SE, N-S, and NE-SW oriented faults show mostly normal and reverse fault characteristics and few numbers of vertical faults. Considering rotational amounts specified for the Paleogene period based on paleomagnetic data in Central Anatolia, it appears that these faults will have slightly different orientations from their present location, many of which are probably represented by NNW-SSE and N-S directions.

(3) Area 1 and Area 2, located in the northwestern extension of Tuzgölü Fault Zone, are mostly dominated by normal faulting. These faults at sea level (0 m), -1000 m, -2000 m, -3000 m and -4000 m depths are dipping to the NE and SW according to the fault trace, and control the sedimentation processes in the Tuzgölü Basin.

(4) Some of the faults identified in depths, from Şereflikoçhisar to the southeastern extension of the Tuzgölü Fault Zone (Area 3, Area 4, Area 5 and Area 6), exhibit reverse fault characteristics. In particular, reverse faults are noteworthy in areas close to the fault strands of active Tuzgölü Fault Zone in Area 4 and Area 5. Compared to other regions, the faults determined along Area 6 are mostly NE-SW oriented.

(5) In the studied areas, among the faults determined from sea level up to -4000 m, those with normal fault characteristics were interpreted as faults controlling the development of the Tuzgölü Basin and the deposition of the basin sediments. The reverse faults, which can be correlated with the faulting ages obtained by Işık et al. (2014) (Middle Eocene: ~ 46-40 My and Late Oligocene-Early Miocene: ~ 30-23), were interpreted as a result of the compression regime that occurred during this period.

(6) The faulting characteristics along the zone reveals that Tuzgölü Basin has not been under the same tectonic regime from the Late Cretaceous to the present day. Moreover, our findings contradict some literature data about the geology of the region, suggesting that the eastern part of the Tuzgölü basin has limited by a single fault trace and that this trace is associated with a single normal fault that continues to depth for kilometers. In particular, reverse faulting revealed in this study, contracts with previous studies based on the seismic profiles in the region, which only highlight the role of normal faulting in the evolution of the basin. It contracts with the faulting models which propose high angle normal faults near the surface that their dips decrease in depths, also. These indicate that seismic profile interpretations should be reviewed. Some of the reverse faulting presented in this study seems to be compatible with the Şereflikoçhisar-Aksaray Thrust revealed by Fernandez-Blanco et al. (2013).

(7) The normal faults identified along the Tuzgölü Fault Zone and its nearby surroundings mainly represent the Late Cretaceous-Middle Eocene and early Miocene-Quaternary periods. The reverse faults also represent the Middle Eocene-Late Oligocene / Early Miocene time interval. The fault segments representing the Tuzgölü Fault Zone and indicated on the MTA Active Fault Map are relatively younger structures in comparison to these faults, which should be formed after Middle Miocene or Early Pliocene.

Acknowledgements

Dr. Ayşe Çağlayan and Reza Saber are thanked for scientific discussion, useful suggestions, and their substantial advice during manuscript preparation. The authors also sincerely thank Prof. Dr. Bora Rojay, Sait Yüksel, Prof. Dr. Nurettin Kaymakçı, and the anonymous reviewers for their constructive and critical comments on an earlier version of this manuscript.

References

Advokaat, E.L., Van Hinsbergen, D.J.J., Kaymakçı, N., Vissers, R.L.M., Hendriks, B.W.H. 2014. Late Cretaceous extension and Palaeogene rotation-related contraction in Central Anatolia recorded in the Ayhan-Büyükkışla basin. International Geology Review 56, 1813-1836.

Alpaslan, M., Boztuğ, D., Frei, R., Temel, A., Kurt, M.A. 2006. Geochemical and Pb-Sr-Nd isotopic composition of the ultrapotassic volcanic rocks from the extension - related Çamardı-Ulukışla basin, Niğde province, central Anatolia, Turkey. Journal of Asian Earth Sciences 27, 613-627.

Arıkan, Y. 1975. The Geology and Petroleum Prospects of The Tuz Gölü Basin. Bulletin of the Mineral Research and Exploration 85, 17-37.

Ateş, A. 1999. Possibility of deep gabbroic rocks, east of Tuz Lake, central Turkey, interpreted from aeromagnetic data. Journal of the Balkan Geophysical Society 2(1), 15-29.

Aydar, E., Gourgaud, A. 2002. Garnet-bearing basalts: an example from Mt. Hasan, Central Anatolia, Turkey. Mineralogy and Petrology 75, 185-201.

Aydar, E., Gündoğdu, M., Bayhan, H., Gourgaud, A. 1994. Kapadokya bölgesi, Kuvaterner yaşlı volkanizmasının volkanik-yapısal ve petrolojik incelemesi. Doğa - Yerbilimleri 3, 25-42.

Aydemir, A., Ateş, A. 2006*a*. Interpretation of Suluklu-Cihanbeyli- Goloren Magnetic Anomaly, Central Anatolia, Turkey: An integration of geophysical data. Physics of the Earth and Planetary Interiors 159, 167-182.

Aydemir, A., Ateş, A. 2006*b*. Structural interpretation of the Tuzgolu and Haymana Basins, Central Anatolia, Turkey, using seismic, gravity and aeromagnetic data. Earth Planets Space 58, 951-961.

Aydemir , A., Ateş, A. 2008. Determination of hydrocarbon prospective areas in the Tuzgolu (Saltlake) Basin, Central Anatolia, by using geophysical data Journal of Petroleum Science and Engineering 62, 36-44.

Aydın, A. 1997. Gravite verilerinin Normalize Edilmiş Tam Gradyan,Varyasyon ve İstatistik ile Hidrokarbon Açısından Değerlendirilmesi, Model Çalışmalar ve Hasankale-Horasan (Erzurum) Havzasının Uygulanması. Doktora Tezi, Karadeniz Teknik Üniversitesi, 151s. Trabzon (unpublished).

Aydoğan, D. 2011. Extraction of lineaments from gravity anomaly maps using the gradient calculation: Application to Central Anatolia. Earth Planets and Space 63(8), 903-913.

Baldwin, R., Langel, R. 1993. Tables and Maps of the DGRF 1985 and IGRF 1990. International Union of Geodesy and Geophysics Association of Geomagnetism and Aeronomy (IAGA Bulletin) 54, 158s.

Beekman, P. 1966. The Pliocene and Quaternary volcanism in the Hasan Dag- Melendiz Dag region. Bulletin of the Mineral Research and Exploration 66, 90-105.

Besang, C., Eckhart, F., Harre, W., Kreuzer, H., Müller, P. 1977. Radiometrische altersbestimmungen an neogenen eruptigesteinen der Tukei. Geol. Jahrb. B25, 3-36.Blakely, R. 1995. Potential Theory In Gravity and Magnetic Applications. Cambridge University Press 441 p.

Blakely, R. 1995. Potential Theory In Gravity and Magnetic Applications. Cambridge University Press, 441 p.

Blakely, R., Simpson, R. 1986. Approximating edges of source bodies from magnetic or gravity anomalies. Geophysics 51(7), 1494-1498.

Boschetti, F. 2005. Improved edge detection and noise removal in gravity maps via the use of gravity gradients. Journal of Applied Geophysics 7(3) 213-225.

Cooper, G., Cowan, D. 2008. Edge enhancement of potential-field data using normalized statistics. Geophysics 73(3), 1MJ-Z46.

Cordell, L. 1979. Gravimetric Expression of Graben Faulting In Santa Fe Contry and The Espanola Basin, New Mexico. In: Ingersoll, R.V., Woodward, L.A., James, H.L. (Ed.), New Mexico Geological Society 30 th Annual Fall Field Conference Guidebook to Santa Fe Country, Socorro 59-64.

Cordell, L.E., Grauch, V.J.S. 1982. Reconciliation of the discrete and integral Fourier transform. Geophysics, 47, 237-243.

Cordell, L.E., Grauch, V.J.S. 1985. Mapping basement magnetization zones from aeromagnetic data in the San Juan Basin, New Mexico. In The utility of regional and magnetic anomaly maps. Edited W.J. Hinze. Society of Exploration Geophysicists 181-197.

Çağlayan, A. 2010. Savcılı Fay Zonunun Yapısal Analizi. Yüksek Lisans Tezi, Ankara Üniversitesi, 82s. Ankara (unpublished).

Çemen, İ., Göncüoğlu, M., Dirik, K. 1999. Structural evolution of the Tuzgölü basin in Central Anatolia Turkey. Journal of Geology 107(6), 693-706.

Çinku, M. C., Hisarli, Z. M., Yılmaz, Y., Ülker, B., Kaya, N., Öksüm, E., Orbay, N., Özbey, Z. Ü. 2016. The tectonic history of the Niğde-Kırşehir Massif and the Taurides since the Late Mesozoic: Paleomagnetic evidence for two-phase orogenic curvature in Central Anatolia. Tectonics 35, 772-811.

Dellaloğlu, A., Aksu, R. 1984. Kulu-Şereflikoçhisar-Aksaray dolayının jeolojisi ve petrol olanakları. TPAO Rapor No: 2020, Ankara (unpublished).

Deniel, C., Aydar, E., Gourgaud, A. 1998. The Hasan Dağı stratovolcano (Central Anatolia, Turkey): evolution from calc-alkaline to alkaline magmatism in a collision zone. Journal Volcanology And Geothermal Research 87, 275-302.

Derman, A., Rojay, B., Güney, H., Yıldız, M. 2003. Şereflikoçhisar-Aksaray fay zonu'nun evrimi hakkında yeni veriler. Türkiye Petrol Jeologları Derneği Özel sayı 5, 47-70.

Dirik, K., Göncüoğlu, M. 1996. Neotectonic characteristics of Central Anatolia. International Geology Review 38, 807-817.

Dirik, K., Erol, O. 2003. Tuzgölü ve çevresinin tektonomorfolojik evrimi, Orta Anadolu-Türkiye. Türkiye Petrol Jeologları Derneği Özel sayı 5, 27-46.

Emre Ö., Duman, T.Y., Özalp, S., Elmacı, H., Olgun, Ş. 2011. 1:250.000 ölçekli Türkiye Diri Fay Haritası Serisi, Aksaray (NJ 36-7) Paftası, Seri No: 26, Kırşehir (NJ 36-3) Paftası, Seri No: 25, Karaman (NJ 35-11) Paftası, Seri No: 27, Maden Tetkik ve Arama Genel Müdürlüğü, Ankara.

Ercan, T., Tokel, S., Matsuda, J., UI, T., Notsu, K., Fujitani, T. 1992. Hasandağı-Karacadağ (Orta Anadolu) Kuvaterner volkanizmasına ilişkin yeni jeokimyasal, izotopik ve radyometrik veriler. Türkiye Jeoloji Bülteni 7, 8-21.

Eren, Y. 2003*a*. Konya bölgesinin depremselliği. Türkiye Petrol Jeologları Derneği Özel sayı 5, 85-98.

Eren, Y. 2003*b*. Tuzgölü Havzası güneybastısındaki (Altınekin-Konya) temel kayaçlarının jeolo0jisi. Türkiye Petrol Jeologları Derneği Özel Sayı 5, 113-116.

Fernandez-Blanco, D., Bertotti, G., Çiner, A. 2013. Cenozoic tectonics of the Tuz Gölü Basin (Central Anatolian Plateau, Turkey). Turkish Journal of Earth Sciences 22, 715-738.

Göksu, B. 2015. Cihanbeyli-Yeniceoba (Konya Kuzeyi) Civarındaki Miyo-Pliyosen Birimlerin Sedimantolojisi. Yüksek Lisans Tezi, Ankara Üniversitesi, 188s. Ankara (unpublished).

Göncüoğlu, M.C., Erler, A., Toprak, V., Yalınız, K., Olgun, E., Rojay, B. 1992. Orta Anadolu Masifinin Batı Bölümünün Jeolojisi. Bölüm 2: Orta Kesim TPAO Rapor No: 3535, Ankara (unpublished).

Göncüoğlu, M., Türeli, T. 1993. Petrology and geodynamic interpretation of plagiogranites from central Anatolian ophiolites (Aksaray-Turkey). Turkish Journal of Earth Sciences 2, 195-203.

Göncüoğlu, M., Dirik, K., Erler, A., Yalınız, K., Özgül, L., Çemen, İ. 1996. Tuzgölü havzası batı kısmının temel jeolojik sorunları. TPAO Rapor No: 3753, Ankara (unpublished).

Görür, N., Oktay, F., Seymen, İ., Şengör, A. M. C. 1984. Paleotectonic evolution of the Tuzgölü Basin Complex, Central Turkey: Sedimentary record of a Neo-Tethyan closure, in Dixion, J.E. and Robertson A.H.F. eds., The Geological Evolution of the Eastern Mediterranean. Geological Society of London Special Publications 17, 455-466.

Görür, N., Tüysüz, O., Şengör, A.M.C. 1998. Tectonic evolution of the Central Anatolian basins. International Geology Review 40, 831-850.

Gülyüz, E., Kaymakçı, N., Meijers, M.J.M., Van Hinsbergen, D.J.J., Lefebvre, C., Vissers, R.L.M., Hendriks, B.W.H., Peynircioğlu, A.A. 2013. Late Eocene evolution of the Çiçekdağı Basin (central Turkey): syn-sedimentary compression during microcontinent - continent collision in central Anatolia. Tectonophysics 602, 286–299.

Gürbüz, A. 2012. Tuz Gölü Havzası'nın Pliyo-Kuvaterner'deki Tektono- sedimanter evrimi. Doktora Tezi, Ankara Üniversitesi, 130 s Ankara (unpublished).

Gürer, Ö.F., Aldanmaz, E. 2002. Origin of the Cretaceous-Tertiary sedimentary basins within the Tauride-Anatolide platform in Turkey. Geological Magazine 139, 191-197.

Gürer, D., van Hinsbergen, D.J.J. 2019. Diachronous demise of the Neotethys Ocean as a driver for non-cylindrical orogenesis in Anatolia. Tectonophysics 760, 191-211.

Gürer, D., van Hinsbergen, D.J.J., Özkaptan, M., Creton, I., Koymans, M.R., Cascella, A., Langereis, C.G. 2018. Paleomagnetic constraints on the timing and distribution of Cenozoic rotations in Central and Eastern Anatolia. Solid Earth 9, 295-322.

Gürsoy, H., Piper, J.D.A., Tatar, O., Temiz, H. 1997. A palaeomagnetic study of the Sivas Basin, Central Turkey: Crustal deformation during lateral escape of the Anatolian Block. Tectonophysics 271, 89-106.

Gürsoy, H., Piper, J.D.A., Tatar, O., Mesci, L. 1998. Paleomagnetic study of the Karaman and Karapinar volcanic complexes, central Turkey: Neotectonic rotation in the south-central sector of the Anatolian block. Tectonophysics 299, 191-211.

Hosseini, S., Ardejani, F., Tabatabaie, S., Hezarkhani, A. 2013. Edge Detection in Gravity Field of the Gheshm Sedimentary Basin. International Journal of Mining and Geo-Engineering Article 4 47(1), 41-50.

Huestis, S. P., Parker, R. L. 1979. Upward and Downward Continuation as Inverse Problems. Geophysical Journal of the Royal Astronomical Society 57, 171-188.

Işık, V., C., Göncüoğlu, C., Demirel, S. 2008. $^{39}Ar/^{40}Ar$ ages from the Yozgat Batholith: Preliminary data on the timing of Late Cretaceous extension in the Central Anatolian Crystalline Complex, Turkey. Journal of Geology 116(5), 510-526.

Işık, V. 2009. Ductile shear zone in granitoid of Central Anatolian Crystalline Complex, Turkey: Implications for Late Cretaceous extensional deformation. Journal of Asian Earth Science 34, 507-521.

Işık, V., Uysal, T., Çağlayan, A., Seyitoğlu, G. 2014. The evolution of intra-plate fault system in central Turkey: structural evidence and Ar-Ar and Rb-Sr age constrains for the savcılı Fault Zone. Tectonics 33(10), 1875-1899.

İlkışık, O., Gürer, A., Tokgöz, T., Kaya, C. 1997. Geoelectromagnetic and geothermic investigations in the Ihlara Valley geothermal field. Journal of Volcanology and Geothermal Research 78, 297-308.

Karaman, E. M. 1986. Altınekin (Konya) çevresinin jeolojik ve tektonik evrimi. Türkiye Jeoloji Bülteni 29(1), 157-171.

Kaymakçı, N., Duermeijer, C.E., Langereis, C.G., White, S.H., Van Dijk, P.M. 2003. Palaeomagnetic evolution of the Çankırı Basin (central Anatolia, Turkey): implications for oroclinal bending due to indentation. Geological Magazine 140 (3), 343-355.

Keskin, M., Genç, S.C., Tüysüz, O. 2008. Petrology and geochemistry of post-collisional Middle Eocene volcanic units in North-Central Turkey: evidence for magma generation by slab breakoff following the closure of the Northern Neotethys Ocean. Lithos 104, 267-305.

Ketin, İ. 1966. Tectonic Units of Anatolia (Asia Mınor). Bulletin of the Mineral Research and Exploration 66, 20-35.

Kissel, C., Laj, C., Poisson, A., Görür, N. 2003. Paleomagnetic Reconstruction of the Cenozoic Evolution of the Eastern Mediterranean. Tectonophysics 362, 199-217.

Koçyiğit, A. 1991. An example of an accretionary forarc basin from northern Central Anatolia and its implications for the history of subduction of Neo-Tethys in Turkey. Geological Society of America Bulletin 103, 22–36.

Koçyiğit, A. 2003. Orta Anadolu'nun genel neotektonik özellikleri ve depremselliği. Türkiye Petrol Jeologları Derneği Özel Sayı 5, 1-26.

Koçyiğit, A., Özkan, S., Rojay, B.F. 1988. Examples from the fore-arc basin remnants at the active margin of northern Neotethys; Development and emplacement age of the Anatolian Nappe, Turkey. METU Journal of Pure and Applied Sciences 21(1-3), 183-210.

Köksal, S., Romer, R.L., Göncüoğlu, M.C., Toksoy-Köksal, F. 2004. Timing of post-collision H-type to A-type granitic magmatism: U-Pb titanite ages from the Alpine central Anatolian granitoids Turkey. International Journal of Earth Sciences 93, 974-989.

Kürçer, A. 2012. Tuz Gölü Fay Zonu'nun Neotektonik Özellikleri ve Paleosismolojisi, Orta Anadolu, Türkiye. Doktora Tezi, Ankara Üniversitesi, 318 sayfa, Ankara (unpublished).

Kürçer, A., Gökten, Y. 2014. Neotectonic-Period Characteristics, Seismicity, Geometry And Segmentation Of The Tuz Gölü Fault Zone. Bulletin of the Mineral Research and Exploration 149, 19-69.

Lefebvre, C., Barnhoorn, A., Van Hinsbergen, D.J.J., Kaymakçı, N., Vissers, R.L.M. 2011. Late Cretaceous extensional denudation along a marble detachment fault zone in the Kırşehir massif near Kaman, central Turkey. Journal Structural Geology 33, 1220-1236.

Lefebvre, C., Meijers, M.J.M., Kaymakçı, N., Peynircioğlu, A., Langereis, C. G., Van Hinsbergen, D.J.J. 2013. Reconstructing the geometry of central Anatolia during the late Cretaceous: Large-scale Cenozoic rotations and deformation between the Pontides and Taurides. Earth and Planetary Science Letters 366, 83-98.

Lowrie, W. 2007. Fundamentals of Geophysics. Second Edition Published in the United States of America by Cambridge University Press, New York 381 p.

Lucifora, S., Cifelli, F., Rojay, B., Mattei, M. 2013. Paleomagnetic rotations in the Late Miocene sequence from the Çankırı Basin (Central Anatolia, Turkey): The role of strike–slip tectonics, Turkey. Journal of Earth Science 22, 778-792.

Lyatsky, H., Dietrich, J. 1998. Mapping Precambrien Basement Structure Beneath The Williston Basin in Canada: Insights From Horizontal-Gradient Vector Processing of Gravity and Magnetic Data. Canadian Journal of Exploration Geophysics 34 (1&2), 40-48.

Miller, H., Singh, V. 1994. Potential field tilt-a new concept for location of potential field sources. Journal of Applied Geophysics 32, 213-217.

MTA. 2002. 1/500.000 ölçekli Türkiye Jeoloji Haritası, Kayseri Paftası. Maden Tetkik ve Arama Genel Müdürlüğü, Ankara.

Nairn, S.P., Robertson, A.H.F., Ünlügenç, U.C., Taşlı, K, İnan, N. 2013. Tectonostratigraphic evolution of the Upper Cretaceous-Cenozoic central Anatolian basins: an integrated study of diachronous ocean basin closure and continental collision. Geological Development of Anatolia and the Easternmost Mediterranean Region. Geological Society, London Special Publication 372, 343-384.

Naumann, E. 1896. Die Grundlinien Anatoliens und Centralasiens. Geographische Zeitschrift 2(1), 7-25.

Okay, A., Tüysüz, O. 1999. Tethyan sutures of northern Turkey. Geological Society, London, Special Publication 156, 475-515.

Oruç, B. 2011. Edge Detection and depth estimation using a tilt angle map from gravity gradient data of the Kozaklı-Central Anatolia region, Turkey. Pure and Applied Geophysics 168, 1769-1780.

Oruç, B. 2013. Yeraltı Kaynak Aramalarında Gravite Yöntemi. Umuttepe Yayınları 270, Kocaeli.

Özsayın, E., Dirik, K. 2007. Quaternary activity of the Cihanbeyli and Yeniceoba Fault Zones: İnönü-

Eskişehir Fault System, central Anatolia. Turkish Journal of Earth Sciences 16, 471-492.

Özsayın, E., Çiner, A., Rojay, B., Dirik, K., Melnick, D., Fernando-Blanco, D., Sudo, M. 2013. Plio-Quaternary extensional tectonics of the Central Anatolian Plateau: A case study from the Tuz Gölü Basin, Turkey. Turkish Journal of Earth Science 22,5, 691-714.

Pınar, R. 1984. Potansiyel Alanlarda Yukarı ve Aşağı Analitik Uzanımlar. Bilimsel Madencilik Dergisi 23(2), 5-18.

Pick, M., Picha, J., Vyskocil, V. 1973. Theory of the Earth's Gravity Field. Elsevier, Amsterdam 538 p.

Platzman, E. S., Tapırdamaz, C., Sanver, M. 1998. Neogene anticlockwise rotation of central Anatolia (Turkey): Preliminary paleomagnetic and geochronological results. Tectonophysics 299, 175–189.

Poisson, A., Guezou, J.C., Öztürk, A., Inan, S., Temiz, H., Gürsoy, H., Kavak, K.S., Özden, S. 1996. Tectonic setting and evolution of the Sivas basin. International Geology Review 38, 833-853.

Reynolds, J.M. 2011. An Introduction to Applied and Environmental Geophysics, 2nd Edition. Wiley&Blackwell 710 p.

Rigo de Righi, M., Cortesini, A. 1960. Regional studies, Central Anatolian Basins progress report. Turkish Gulf Oil Co Rapor No II/11-12 (unpublished).

Roest, W., Verhoef, J., Pilkington, M. 1992. Magnetic Interpretation Using The 3-D analytic signal. Geophysics 57(1), 116-125.

Rojay, B. 2013. Tectonic evolution of the Cretaceous Ankara Ophiolitic Mélange during the Late Cretaceous to pre-Miocene interval in Central Anatolia, Turkey. Journal of Geodynamics 65, 66-81.

Saad, A. 2006. Understanding gravity gradients a tutorial. The Leading Edge 25(8), 942-949.

Salem, A., Williams, S., Fairhead, D., Smith, R., Ravat, D. 2008. Interpretation of magnetic data using tilt-angle derivatives. Geophysics 73(1), 14JF-Z11.

Schmitt, A.K., Danışık, M., Aydar, E., Şen, E., Ulusoy, İ., Lovera, O.M. 2014. Identifying the Volcanic Eruption Depicted in a Neolithic Painting at Çatalhöyük, Central Anatolia, Turkey. PLOS ONE 9(1): e84711.

Seyitoğlu, G., Kazancı, N., Karadenizli, L., Şen, Ş., Varol, B., Karabıyıkoğlu, T. 2000. Rockfall avalanche deposits associated with normal faulting in the NW of Çankırı basin: implication for the post-collisional tectonic evolution of the Neo-Tethyan suture zone. Terra Nova 12, 245-251.

Seyitoğlu, G., Işık, V., Gürbüz, E., Gürbüz, A. 2017. The discovery of a low-angle normal fault in the Taurus Mountains the İvriz detachment and implications concerning the Cenozoic geology of southern Turkey. Turkish Journal of Earth Sciences 26, 189-205.

Seymen, İ. 1984. Kırşehir masifi metamorfitlerinin jeoloji evrimi. Ketin Sempozyumu, Türkiye Jeoloji Kurumu Yayını 133-48.

Soengkono, S. 1999. Te Kopia geothermal system (New Zeland)-the relationship between its structure and extent. Geothermics 28(6), 767-784.

Şaroğlu, F., Emre, Ö., Boray, A. 1987. Türkiye'nin diri fayları ve depremsellikleri. Maden Tetkik ve Arama Genel Müdürlüğü Rapor No: 8174, 394 s. Ankara (unpublished).

Şengör, A., Yılmaz, Y. 1981. Tethyan evolution of Turkey: A plate tectonic approach. Tectonophysics 75, 181-241.

Tatar, O., Piper, J.D.A., Gürsoy, H., Temiz, H. 1996. Regional significance of neotectonic counterclockwise rotation in central Turkey. International Geology Review 38, 692-700.

Telford, W.M., Geldart, L. P., Sheriff, R.E., Keys, D.A. 1990. Applied Geophysics, 2nd Edition. Cambridge University Press, Cambridge 770 p.

Toprak, V. 2003. Tuzgölü Fay kuşağı Hasandağ kesiminin özellikleri. Türkiye Petrol Jeologları Derneği Özel Sayı 5, 71-84.

Toprak, V., Göncüoğlu, M.C. 1993. Tectonic control on the development of the Neogene-Quaternary Central Anatolian Volcanic Province, Turkey. Geological Journal 28, 357-369.

Turgut, S. 1978. Tuz Gölü havzasının stratigrafik ve çökelsel gelişimi: Türkiye IV. Petrol Kongresi Bildirileri 115-126 p.

Tüysüz, O., Dellaloğlu, A.A., Terzioğlu, N. 1995. A magmatic belt within the Neo-Tethyan suture zone and its role in the tectonic evolution of northern Turkey. Tectonophysics 243, 173–191.

Uğurtaş, G. 1975. Geophysical Interpretation of Part of The Tuz Gölü Basin. Bulletin of the Mineral Research and Exploration 85, 38-45.

Ulu, Ü., Öcal, H., Bulduk, A., Karakaş, M., Arbas, A., Saçlı, L., Karabıyıkoğlu, M. 1994. Cihanbeyli-Karapınar yöresi geç Senozoyik çökelme sistemi: Tektonik ve iklimsel önemi. Türkiye Jeoloji Kurumu Bülteni 9, 149-163.

Uygun, A., Yaşar, M., Erkan, M., Baş, H., Çelik, E., Aygün, M., Ayok, F. 1982. Tuzgölü havzası projesi, Cilt 2. Maden Tetkik ve Arama Genel Müdürlüğü Rapor No:6859, Ankara, (unpublished).

Ünalan, G., Yüksel, V. 1978. Eski Bir Graben Örneği: Haymana-Polatlı Havzası. Türkiye Jeoloji Bülteni 21, 165-169.

Verduzco, B., Fairhead, J.D., Green, C.M., Mackenzie, C. 2004. New insights into magnetic derivatives for structural mapping. The Leading Edge 23(2), 116-119.

Whitney, D.L., Teyssier, C., Dilek, Y., Fayon, A.K. 2001. Metamorphism of the Central Anatolian Crystalline Complex, Turkey: influence of orogen-normal collision vs wrench-dominated tectonics on P-T-t paths. Journal of Metamorphic Geology 19, 411-432.

Wilcox, L. 1974. An analysis of Gravity Prediction Methods For Continental Areas. Defense Mapping Agency Aerospace Center, Publication No. 74-001.

Yalınız, M.K., Floyd, P.A., Göncüoğlu, M.C. 2000. Petrology and geotectonic significance of plagiogranite from the Sarikaraman ophiolite (Central Anatolia, Turkey). Ofioliti 25, 31-37.

Yıldırım, C. 2014. Relative tectonic activity assessment of the Tuz Gölü Fault Zone; Central Anatolia, Turkey. Tectonophysics 630, 183-192.

Yüksel, S. 2011. Petrol Aramacılığında Doğal Potansiyel Yöntemler Gravite ve Manyetik. TPAO Kurum İçi Eğitim Notları 231 s.

Yürür, M.T., Genç, Y. 2006. The Savcili thrust fault (Kirsehir region, central Anatolia): a backthrust fault, a suture zone or a secondary fracture in an extensional regime? Geological Carpathica 57, 47-56.

Zhang, H., Tian-You, L., Yu-Shan, Y. 2011. Calculation of gravity and magnetic source boundaries based on anisotropy normalized variance. Chinese Journal of Geophysics 54(4), 560-567.

Bulletin of the Mineral Research and Exploration

http://bulletin.mta.gov.tr

Emplacement conditions of magma(s) forming Jurassic plutonic rocks in Gümüşhane (Eastern Pontides, Turkey)

Emre AYDINÇAKIR[a*], Ramazan GÜNDÜZ[b] and Cem YÜCEL[c]

[a]*Department of Geological Engineering, Faculty of Engineering and Natural Sciences, Gümüşhane University, Gümüşhane, Turkey*
[b]*Department of Geological Engineering, Faculty of Engineering and Natural Sciences, Gümüşhane University, Gümüşhane, Turkey*
[c]*Department of Mining Engineering, Faculty of Engineering and Natural Sciences, Gümüşhane University, Gümüşhane, Turkey*

Research Article

Keywords:
Mineral chemistry, Geothermobarometer, Jurassic magmatism, Eastern Pontides, Gümüşhane, Turkey.

Received Date: 31.05.2019
Accepted Date: 19.11.2019

ABSTRACT

In this study, the petrography, mineral chemistry and crystallization conditions were reported for the Alemdar and Işıkdere plutons located in limited areas in the south of the Eastern Pontides. These plutons, which trend mostly in NE-SW directions, were emplaced by cutting the Early-Middle Carboniferous-aged Gümüşhane Granitoid and Early-Middle Jurassic Şenköy formation. Petrographically, the studied plutons are compositionally fine to medium grained quartz-diorite, quartz monzodiorite and tonalite. The rocks in the plutons have granular, poikilitic, monzonitic, graphic and rare porphyritic textures with consist of plagioclase, (An_{05-92}), hornblende (Mg# = 0.52-0.81), biotite (Mg# = 0.32-0.67), orthoclase, quartz and Fe-Ti oxide. According to thermobarometric calculations, plutons have crystallization temperatures, pressures and oxygen fugacity values ranging from 541°C to 938°C, 0.1 to 4.4 kbar, and -23 to-12, respectively. The estimated water content calculated from amphibole is between 4.4 to 7.8%. It can be concluded that the studied plutons were emplaced at mid to shallow crustal depths (~4-15 km).

1. Introduction

The Eastern Pontide Orogenic Belt (NE Turkey), where the study area is located, comprises volcanic and plutonic rock assemblages (Karslı et al., 2007, 2012; Kaygusuz et al., 2008, 2018; Dokuz, 2011; Temizel et al., 2012, 2018, 2019*a*, 2019*b*; Aydınçakır and Şen, 2013; Arslan et al., 2013; Aydın, 2014; Yücel et al., 2017). The region dominantly hosts plutonic and volcanic rocks formed over long periods of time from the Permo-Carboniferous to the end of the Eocene (Figure 1). Carboniferous-aged plutonic rocks (Yılmaz, 1972; Çoğulu, 1975; Topuz et al., 2010; Dokuz, 2011; Kaygusuz et al., 2012, 2016; Karslı et al., 2016; Dokuz et al., 2017*a*) were emplaced by cutting across the metamorphic rocks. The basement rocks in the region are unconformably overlain by Jurassic volcano-sedimentary sequences (Şenköy formation, Kandemir, 2004) (Kandemir, 2004; Dokuz and Tanyolu, 2006; Eyüboğlu et al., 2006; Şen, 2007; Kandemir and Yılmaz, 2009; Genç and Tüysüz, 2010; Dokuz et al., 2017*b*). Cretaceous-aged plutonic rocks known to be subduction related (Şahin et al., 2004; Kaygusuz and Aydınçakır, 2009, 2011; Karslı et al., 2010; Kaygusuz et al., 2013; Sipahi et al., 2017; Eyüboğlu et al., 2019; Temizel and Kurt, 2019; Temizel et al., 2019*a*) have contact relations with volcanic and/or volcanoclastic rocks. Eocene-aged plutons (Yılmaz and Boztuğ, 1996; Arslan and Aslan,

Citation info: Aydınçakır, E., Gündüz, R., Yücel, C. 2020. Emplacement conditions of magma(s) forming Jurassic plutonic rocks in Gümüşhane (Eastern Pontides, Turkey). Bulletin of the Mineral Research and Exploration 162, 175-196. https://doi.org/10.19111/bulletinofmre.649808

* *Corresponding author: Emre AYDINÇAKIR, aydincakir61@gmail.com*

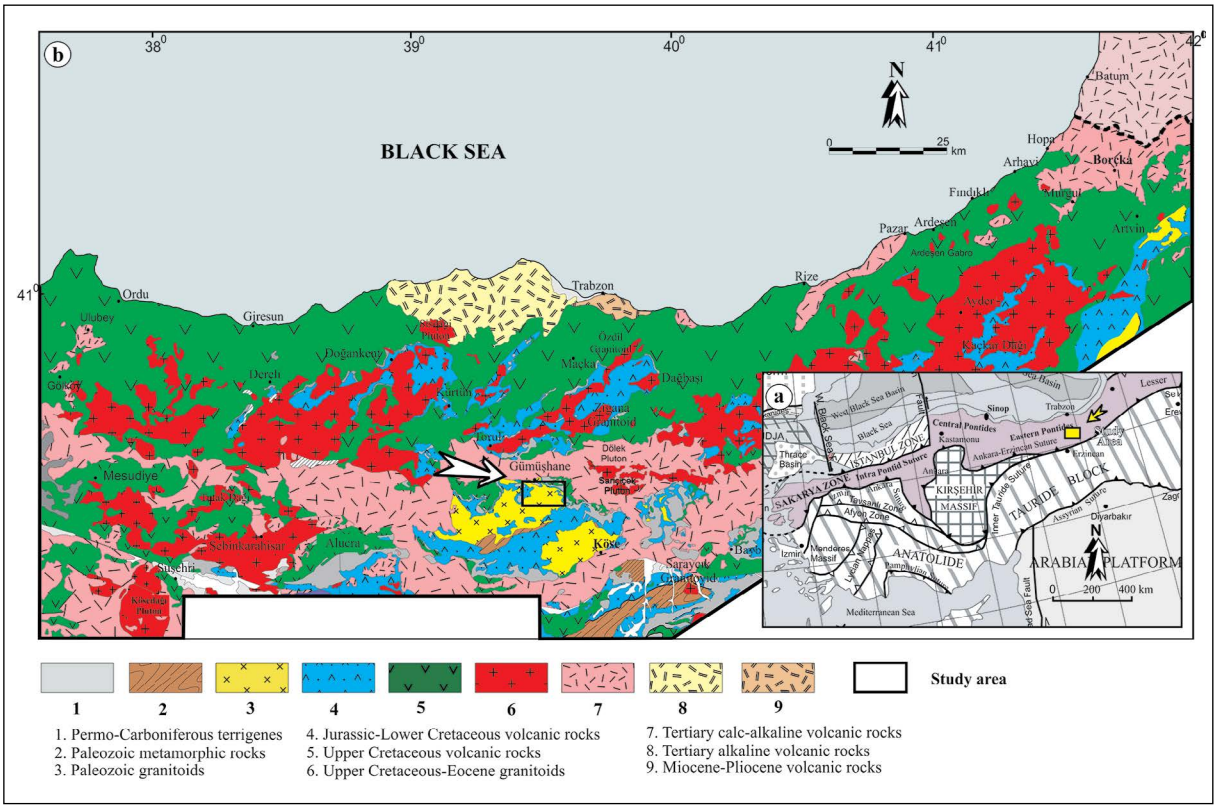

Figure 1- a) Tectonic branches of Turkey (after Okay and Tüysüz, 1999) and b) geologic map showing volcanic and magmatic rocks outcropping in the Eastern Pontides (after Güven, 1993; Aydınçakır and Şen, 2013; Yücel et al., 2017)

2006; Karslı et al., 2007, 2011; 2012; Kaygusuz and Öztürk, 2015; Eyüboğlu et al., 2017; Kaygusuz et al., 2018; Temizel et al., 2018, 2019*b*) were emplaced by cutting the whole series.

In recent years a limited number of studies were completed in the Eastern and Central Pontides about the geodynamic source of mafic and acidic rocks emplaced in the Early-Middle-Late Jurassic period (Dokuz et al., 2010; Karslı et al., 2014, 2017; Eyüboğlu et al., 2016; Çimen et al., 2017, 2018). However, the direction and the time of subduction and the geochemical features of associated magmatic activity are still controversial. Since the emplacement conditions of the plutons have not been studied previously, this is the first study to reveal the emplacement conditions of plutons.

This study focuses mainly on the petrography and mineral chemistry of the Jurassic-aged Alemdar and Işıkdere Plutons observed in a narrow area in the Gümüşhane (Eastern Pontides) region with the aim of 1) determining physicochemical properties such as temperature, pressure and oxygen fugacity effective during crystallisation of magma(s), and 2) combining physicochemical data with geologic data to determine the evolution of magma(s) in the crust.

2. Regional Geology

The oldest units in the Eastern Pontide Orogenic Belt comprise metamorphic basement of Early-Middle Carboniferous gneiss, schist, amphibolite, marble and minor metaperidotites (Topuz et al., 2004, 2007; Okay et al., 2006; Dokuz, 2011) (Figure 1). These rocks were intruded by Middle Carboniferous-Early Permian plutonic rocks (Çoğulu, 1975; Topuz et al., 2010; Dokuz, 2011; Kaygusuz et al., 2012, 2016; Karslı et al., 2016; Dokuz et al., 2017*a*). Late Carboniferous shallow marine-terrestrial sedimentary rocks, unconformably overlying the basement metamorphic rocks, are observed only in the Pulur region (Okay and Leven, 1996; Kandemir and Lerosey-Aubril, 2011). Jurassic rocks in the Eastern Pontides comprise pyroclastic and sedimentary rocks containing clastic and limestone blocks (Ağar, 1977; Saydam Eker et al., 2012). The Şenköy formation

consists of andesite, basalt, agglomerate and diabase displaying lateral transitions, and different thicknesses over short distance, with volcanics, pebblestone, marl, claystone, sandstone and Ammonitico rosso-type limestones (Dokuz and Tanyolu, 2006; Şen, 2007). Recent studies have shown that plutonic equivalents of pillow basalts were formed during the time interval ranging from Middle Triassic to Early Jurassic (Dokuz and Tanyolu., 2006; Eyüboğlu et al., 2010, 2016; Ustaömer and Robertson, 2010; Karslı et al., 2014). In the region, the Late Jurassic-Early Cretaceous period is very barren in terms of tectonic movements and magmatic activity. In this period, carbonate deposition is the common rock lithology.

The Late Cretaceous period present that a lithology dominated by plutonic and volcanic rocks of the north-south direction in the Eastern Pontides (Okay and Şahintürk, 1997; Kaygusuz et al., 2008; Kaygusuz and Aydınçakır, 2009; Karslı et al., 2012; Aydın, 2014; Yücel, 2017; Demir, 2019). High potassium magmatism is also widespread in the region (Altherr et al., 2008; Eyüboğlu et al., 2010; Gülmez et al., 2016; Aydınçakır, 2016, 2017; Özdamar et al., 2017). The collision of the Eastern Pontides magmatic arc and the Anatolide-Tauride continental block occurred in the Late Paleocene-Early Eocene (Okay and Şahintürk, 1997; Dilek, 2006). The Early Eocene (54-48 Ma) adakitic and non-adakitic magmatism in the Eastern Pontides (Eyüboğlu et al., 2010, 2013; Topuz et al., 2011; Karslı et al., 2011; 2013; Dokuz et al., 2013; Aydınçakır, 2014; Temizel et al., 2019*b*) is thought to the last stage of arc to continent collision. As for the Eocene period is represented by the post-collisional calc-alkaline volcanic rocks and high-K calc-alkaline and shoshonitic plutons (Karslı et al., 2007, 2012; Aslan, 2010; Temizel et al., 2012, 2018; Aydınçakır and Şen, 2013; Arslan et al., 2013; Aslan, et al., 2014; Yücel et al., 2017; Eyüboğlu et al., 2017). The clastic rocks are widespread in the region in the post-Eocene (Okay and Şahintürk, 1997) and are generally accompanied by Neogene alkaline volcanic rocks (Aydın et al., 2008; Arslan et al., 2013; Yücel et al., 2014; 2017).

3. Material and Method

During field studies, geological maps of Güven (1993) and MTA (2002) were used to prepare 1/25.000 scale geological map and rock samples were taken from the Alemdar and Işıkdere plutons to perform petrographic and mineral chemistry studies. Thin sections were prepared in Gümüşhane University Department of Geological Engineering Thin Section Laboratory. The thin sections were investigated with polarising microscope and mineral content and textural features were determined. For modal analysis, a Swift brand point counter was used. Counts were generally completed according to grain size at 0.02 to 0.04 mm intervals and nearly 600-800 points were counted in each section.

Mineral chemistry analyses were performed at Bretagne Occidentale University Geoscience Marines (IFREMER) Electron Microprobe Laboratory located in Brest (France). Samples for mineral chemistry analysis with a CAMECA-SX-100 WDS brand device were prepared as carbon-coated polished sections. The device setting was 15 kV electron bombardment and 20 nA bombardment flow. The count time for Si, Al, Ti, Fe, Mn, Mg, Ca, Na and K elements was set to 10 s. Analyses of hornblende and Fe-Ti oxides used 1 μm point ray while feldspar and mica mineral analyses used slightly defocused (10 μm) rays to prevent losses due to sodium evaporation. Analyses used natural mineral standards of forsterite, diopside, orthoclase, albite, anorthite, biotite, apatite, wollastonite and magnetite. Analyses were carried out with analytic error less than 1% for major elements and less than 200 ppm for trace elements.

4. Results

4.1. Geological Setting of Plutons

The basement of the study area where the Alemdar and Işıkdere plutons are located comprises the Early-Middle Carboniferous Gümüşhane Granitoid (Çoğulu, 1975; Topuz et al., 2010) (Figure 2). The Gümüşhane Granitoid is unconformably overlain by the Early-Middle Jurassic pebblestone, marl, sandstone, siltstone, tuff, and Ammonitic Rosso-type limestone and acidic-basic lava, dikes and sills of the Şenköy formation (Kandemir, 2004) (Figure 2). The Şenköy formation is conformably overlain by the Upper Jurassic-Lower Cretaceous carbonate limestones of the Berdiga formation (Pelin, 1977). The youngest unit is Quaternary alluvium (Figure 2).

The Alemdar Pluton covers an area of 7-8 km^2 around Bağlarbaşı town, Alemdar locale and

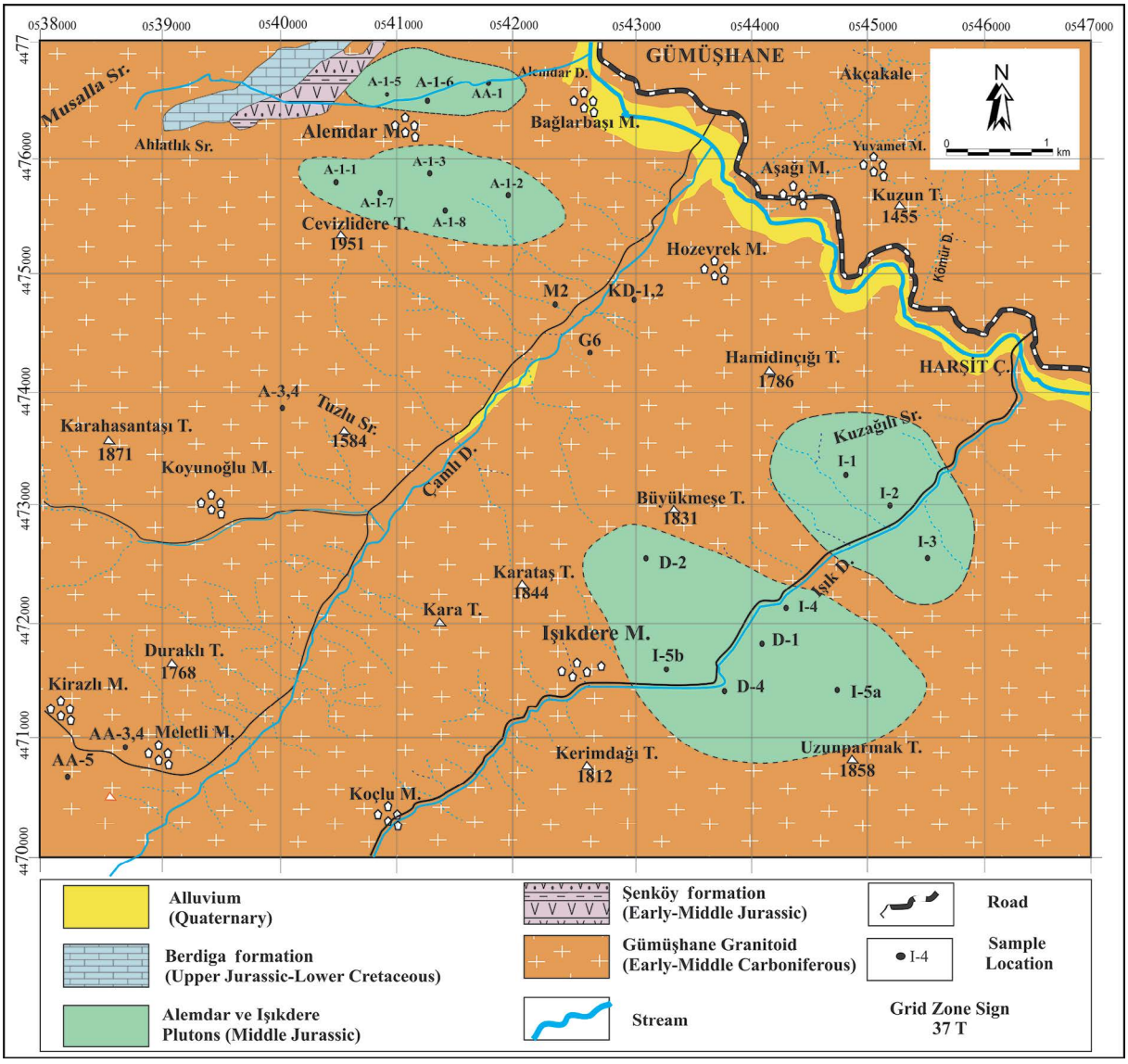

Figure 2- Geologic map of the study area.

Cevizlidere Hill in the south of Gümüşhane province (Figure 2). Alemdar Pluton was intruded into the Early-Middle Carboniferous Gümüşhane Granitoid and volcanic and volcano-sedimentary rocks of the Early-Middle Jurassic Şenköy formation (Figure 3a). According to contact and crosscutting relations of the pluton in the field, the age of the pluton was accepted as Jurassic in this study for the first time. The Alemdar Pluton has elliptical shape (Figure 2) and very hard, fractured and jointed structure. It also outcrops as small blocks (Figure 3a, b). Epidotization and silicification are observed in contact zones between the pluton and country rock (Figure 3c). Outcrops of the Alemdar pluton generally has rounded form. Due to the abundance of ferromagnesian minerals such as hornblende and biotite, it is generally gray-dark gray colored and is moderate-fine grained (Figure 3d, e). The Işıkdere Pluton forms two stocks outcropping in Işıkdere locale and surroundings toward the southwest along the Işık Dere (stream) valley. The Işıkdere Pluton has NW-SE trend with nearly elliptical shape (Figure 2). The Işıkdere Pluton intruded into the Gümüşhane Granitoid (Figure 2). The pluton is clearly distinguished from the Gümüşhane Granitoid by its dark gray and/or greenish-gray colour (Figure 3d). The rocks forming the Işıkdere Pluton appear to be very fresh and are recognized by remarkable mafic mineral content (Figure 3e).

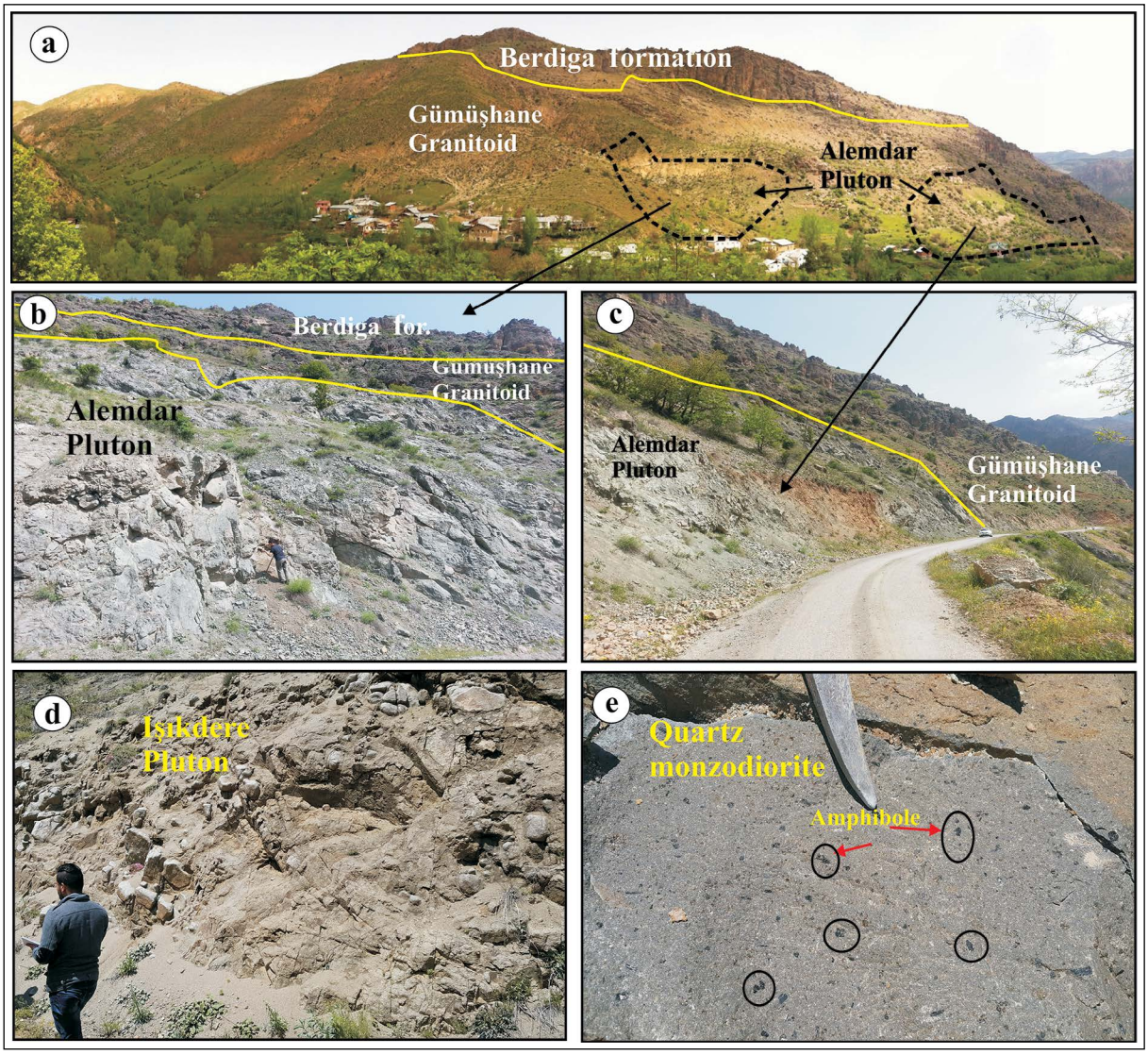

Figure 3- a) Contact relations between the Alemdar Pluton and surrounding rocks (photo taken toward the north in Alemdar locale), b, c) Contact relations between Alemdar Pluton and Gümüşhane Granitoid (Alemdar), d) Field view of Işıkdere Pluton (taken toward the north, Işıkdere neighborhood) and e) close-up view of Işıkdere Pluton.

4.2. Petrography

The petrographic charecteristics of the rocks from the Alemdar and Işıkdere Plutons were investigated and are given in table 1. On the QAP diagram (Streckeisen, 1976) based on modal mineralogical analysis (Figure 4), the Alemdar Pluton is represented by quartz-monzodiorite and quartz diorite, while the Işıkdere Pluton is characterized by tonalite (Figure 4).

Petrographic studied of the Alemdar and Işıkdere Plutons demonstrates that they have fine-medium granular, porphyritic, monzonitic and poikilitic texture (Figure 5a-h). The main minerals are dominated by plagioclase, quartz, K-feldspar, hornblende, biotite and magnetite. Apatite and zircon comprise accessory minerals.

The plagioclase from the Alemdar and Işıkdere Plutons is represented by euhedral and subhedral crystals, mostly coarser grained phenocrysts (57-69%) with finer-grained crystals in the groundmass (Figure 5). Some plagioclase crystals display albite twinning (Figure 5a, d and e), oscillatory zoning (Figure 5b, f) and occasional sieve texture (Figure 5a, b). Inverse zoning in some plagioclase minerals

Table 1- The general petrographical characteristics and modal composition of the rocks from the Alemdar and Işıkdere Plutons.

Pluton	**ALEMDAR (n= 13)**			**IŞIKDERE (n= 15)**		
Rock units	Quartz diorite, quartz monzodiorite			Tonalite		
Texture	Granular, porphyric, poikilitic, monzonitic, myrmekitic			Granular, porphyric, poikilitic, monzonitic, myrmekitic		
Grain size	Fine-medium prophryic			Fine-medium porphryic		
Modal min (%)	Max	Min	Mean	Max	Min	Mean
Plagioclase	66.5	58.0	62.4	68.7	57.1	63.1
Quartz	15.8	12.0	13.8	16.2	11.0	13.8
Orthoclase	9.0	2.0	5.8	13.2	1.6	5.9
Hornblende	17.3	5.2	11.4	11.8	2.0	7.3
Biotite	7.8	2.9	5.2	9.7	6.1	8.2
Opaque minerals	2.6	0.7	1.5	1.7	1.2	1.5
Secondary minerals	4.1	2.2	3.2	5.2	1.1	3.4
Accessory minerals	3.1	1.3	2.4	2.5	1.0	1.5

n= sample number

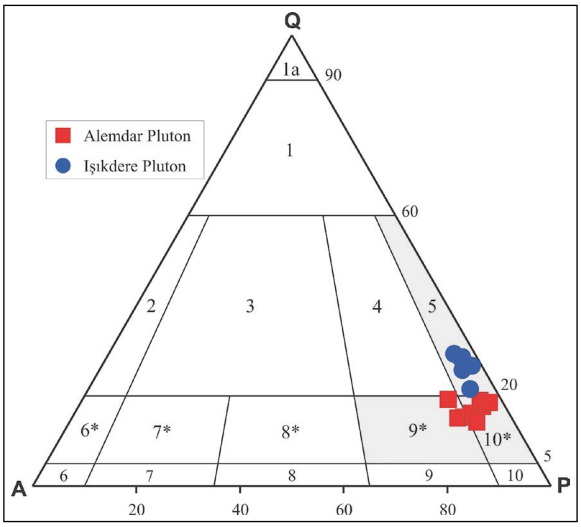

Figure 4- The QAP plot of the rock samples from Alemdar and Işıkdere Plutons (Streckeisen, 1976). The fields; (1a) quarzolite, (1a) quartz rich granitoid, (2) alkaline feldspar granite, (3) granite, (4) granodiorite, (5) tonalite, (6*) quartz alkaline feldspar granite, (7*) quartz syenite, (8*) quartz monzonite, (9*) quartz monzodiorite/quartz monzogabbro, (10*) quartz diorite/quartz gabbro/quartz anorthosite, (6) alkali feldspar syenite, (7) syenite, (8) monzonite, (9) monzodiorite/monzogabbro, (10) diorite/gabbro/anorthosite.

especially indicates disequilibrium crystallization (Figure 5a). Some plagioclases are partially sericitized and kaolinized (Figure 5). The K-feldspars (2-13%) are generally anhedral and common (Figure 5a, g and h). They have carlsbad twin and poikilitic grains tend to contain hornblende, plagioclase and opaque minerals (Figure 5a, e). The poikilitic texture shown by K-feldspar may represent disequilibrium crystallization, forming monzonitic texture surrounding plagioclase in some samples (Figure 5a). Some samples are fractured and partially kaolinized (Figure 5e). Quartz (11-16%) is anhedral, small crystals with generally undulose extinction (Figure 5d). Hornblendes (2-17%) are dark brown and dark green pleochroism, and two directional hornblende cleavage (Figure 5c, f). Poikilitic hornblendes contain inclusions of plagioclase and opaque minerals and may indicate disequilibrium crystallization (Figure 5c). Biotites (3-8%) appears rod-like or leaf-like crystals (Figure 5e, g and h). Biotites have one direction well defined cleavage (001) and light-dark brown pleochroism. Opaque minerals (1-3%) are generally located around, or as inclusions within, mafic minerals such as hornblende and biotite (Figure 5a, c, d and e).

4.3 Mineral Chemistry

4.3.1. Plagioclase

Plagioclase is found in almost all rock types from the Alemdar and Işıkdere Plutons. Plagioclases are observed as euhedral crystals with size varying from 0.1-1 mm. Plagioclases occur as both fine to moderate-large crystals (Figure 6a). The plagioclase crystals display occasional oscillatory (Figure 6a), normal and inverse zoning (Figure 6b). Plagioclases are generally phenocrysts, microlites and laths. The An content of

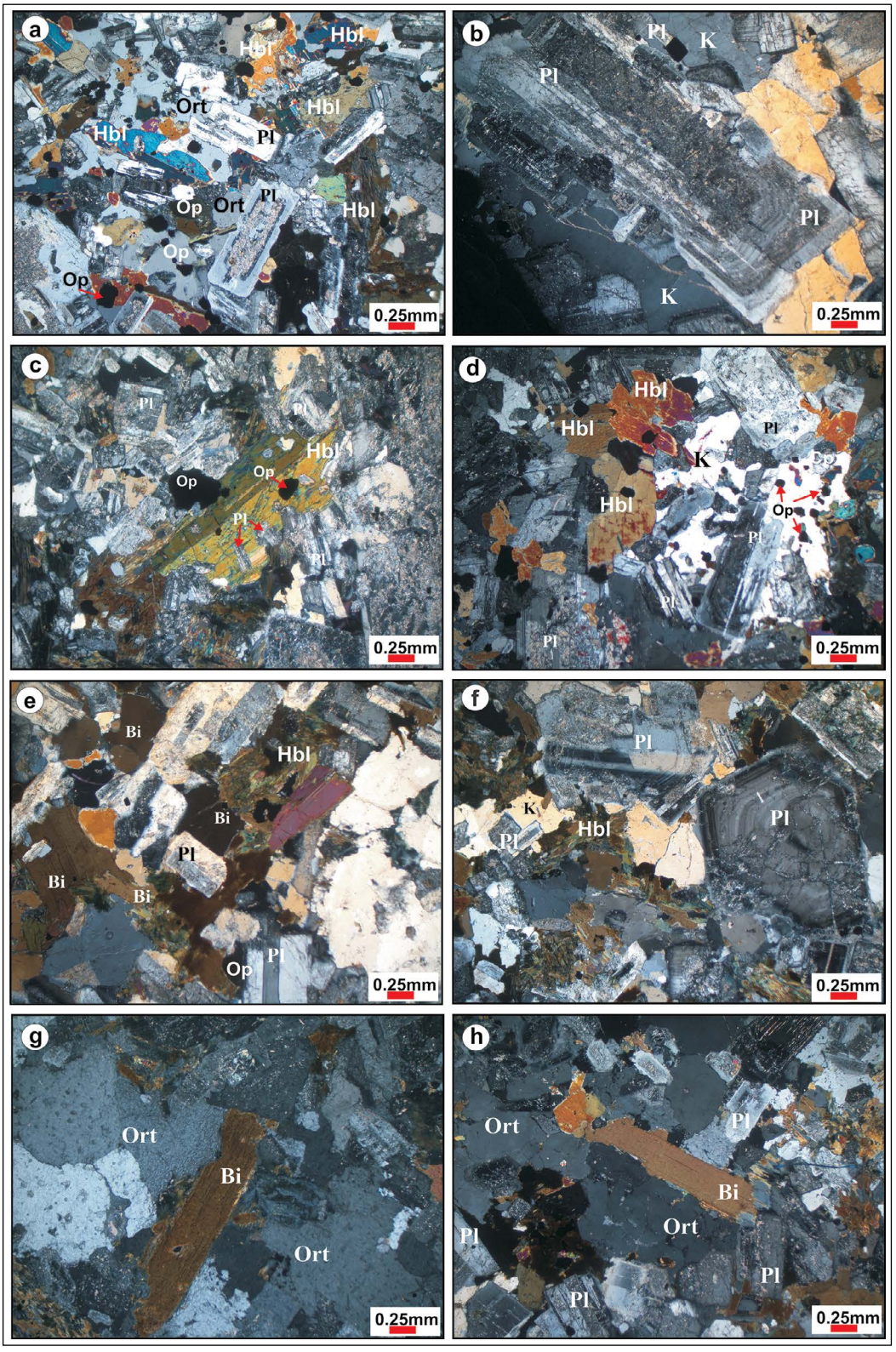

Figure 5- The Alemdar Pluton a) monzonitic texture formed of orthoclase crystal containing plagioclase, b) large-zoned plagioclase crystal surrounded by quartz and containing plagioclase inclusions, c) opaque mineral and hornblende crystal with poikilitic texture containing plagioclase inclusions, d) euhedral plagioclase crystal showing albite twinning, e) euhedral biotite and hornblende crystals. From the Işıkdere Pluton f) plagioclase crystals showing zoned texture and quartz crystal with poikilitic texture and g, h) euhedral biotite crystals (Sample No: A-1-1, I-4; Ç.N.; Pl: Plagioclase, Hbl: Hornblende, Ort: Orthoclase, Bi: Biotite, K: Quartz, Op: Opaque mineral).

plagioclases is from 92 to 05, compositions ranging andesine to anorthite (Figure 7). Andesine composition is $An_{42}Ab_{43}Or_{15}$ in the core and $An_{33-49}Ab_{49-65}Or_{1-4}$, in the rim, labradorite composition is $An_{52-68}Ab_{30-47}Or_{0-4}$ in the core and $An_{51-57}Ab_{42-49}Or_{0-2,}$ at the rim, while bytownite composition is $An_{70-79}Ab_{21-30}Or_{0-1}$ in the core and $An_{71}Ab_{29}Or_{1}$ at the rim. One sample was anorthite $An_{92}Ab_{8}Or_{0}$ composition (Supplementary Table 1, Figure 7).

The plagioclase compositions in the Işıkdere Pluton are oligoclase to bytownite (An_{13-77}) (Figure 7). Oligoclase have composition of $An_{30}Ab_{71}Or_{2}$ in the core and $An_{13-29}Ab_{76-86}Or_{2-3}$ in the rim, andesine has composition of $An_{32-50}Ab_{49-61}Or_{1-2}$ in the core and $An_{36-49}Ab_{49-61}Or_{1-2}$ in the rim, labradorite composition is $An_{50-69}Ab_{29-49}Or_{1-2}$ in the core and $An_{51-58}Ab_{41-48}Or_{1-2}$ in the rim, while bytownite composition is $An_{70-77}Ab_{23-29}Or_{1-2}$ in the core and $An_{77}Ab_{23}Or_{1}$ in the rim.

4.3.2. Hornblende

Hornblendes in the Alemdar and Işıkdere Plutons are calcic (Figure 8a) and are classified as magnesiohornblende according to Leake et al. (1997) (Figure 8b). Fe^{+2} and Fe^{+3} calculations from FeO were based on stoichiometric methods. The Mg numbers ($Mg/(Mg+Fe^{+2})$) of hornblendes from the Alemdar and Işıkdere Plutons vary from 0.52-0.81 and 0.52-0.80, respectively (Supplementary Table 2).

4.3.3. Biotite

The dark-colored micas from the Alemdar Pluton plot on the biotite field of the $Fe^{top}/(Fe^{top}+Mg)$ versus Al^{iv}(apfu) diagram and their $Mg/(Mg+Fe^{top})$ values ranging from 0.47-0.50 (Figure 9, Supplementary Table 3). Micas from the Işıkdere Pluton plot in the biotite (Mg number 0.32-0.67) field of the same classification diagram, with only one sample plot on the Mg-enriched biotite (Figure 9, Supplementary Table 3).

4.3.4. Fe-Ti oxides

Fe-Ti oxides in the Alemdar and Işıkdere plutons are generally anhedral in groundmass and inclusions in ferromagnesian minerals (Figure 10). Fe-Ti oxides in the plutons are classified as magnetite (Supplementary Table 4, Figure 11).

5. Discussion

The variations in temperature (T), pressure (P) and fugacity (partial pressure of oxygen) of magma are the most important factors controlling minerals that will form and the equilibrium status of these minerals. Determination of these factors (T, P, *f*O, etc.) provides significant information about the crystallization process in magma. Thermodynamic features allow the possibility to estimate which minerals will

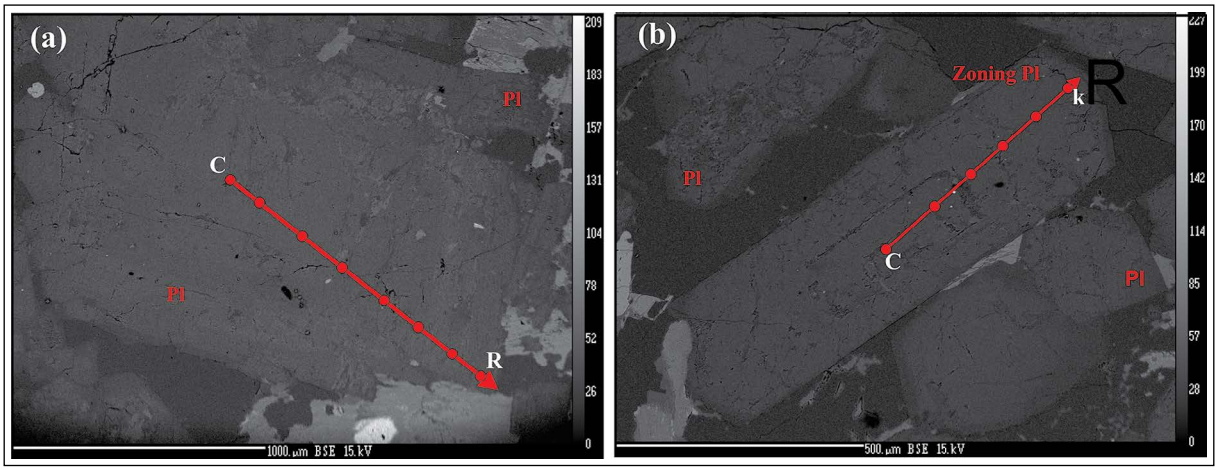

Figure 6- Back scatter electron (BSE) images for euhedral and zoned plagioclases from Alemdar and Işıkdere plutons (Pl: plagioclase, c: core, r: rim).

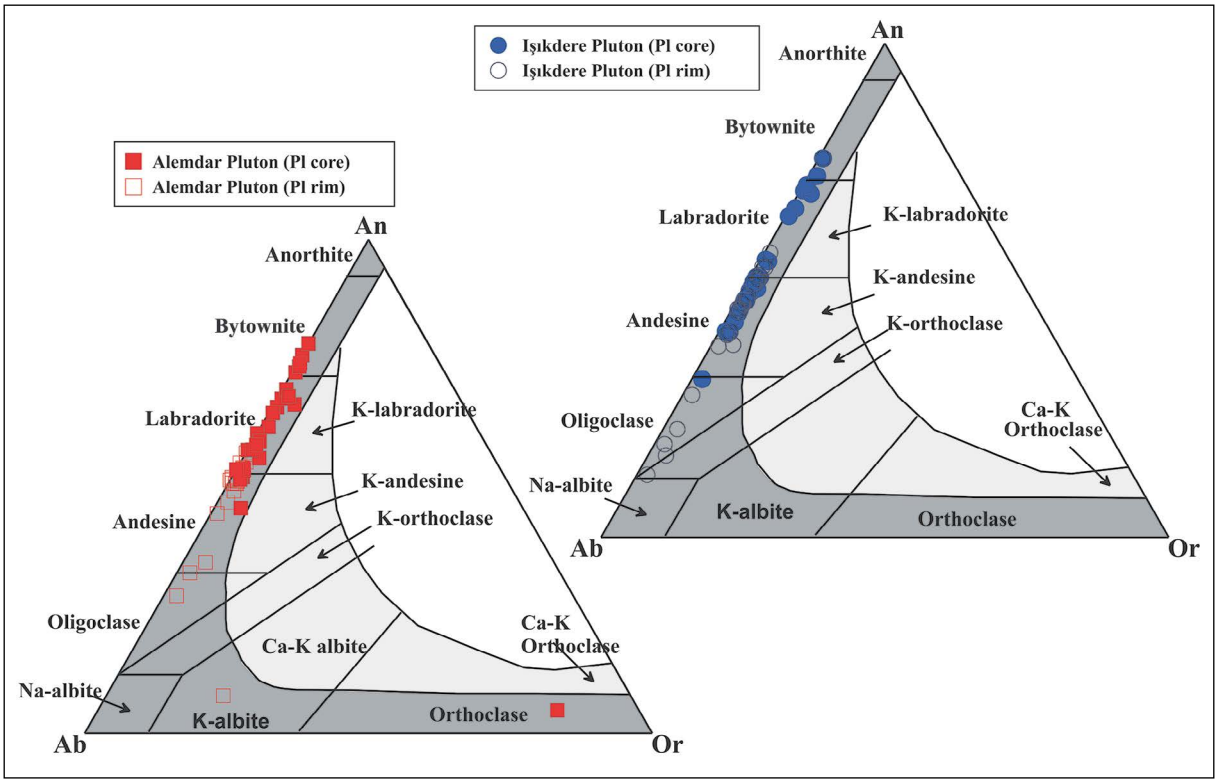

Figure 7- Ab-An-Or ternary diagram showing feldspar compositions of the Alemdar and Işıkdere plutons (Smith and Brown, 1988).

form under different conditions and simultaneously the opportunity to use mineral assemblages and compositions to determine conditions in the setting in which the rock formed (thermobarometry). The error margins in thermodynamic calculations may be determined by revealing the errors in all stages of P-T estimations; these errors may be made in the stages of analyzing mineral compositions, determining and using thermodynamic data and in selecting calibration methods. The error margins for thermodynamic calculations generally vary from ± 30-50°C for temperature and ± 1-0.5 kbar for pressure. In plutonic rocks, limited mineral assemblages that can be used for thermobarometric calculations make determination

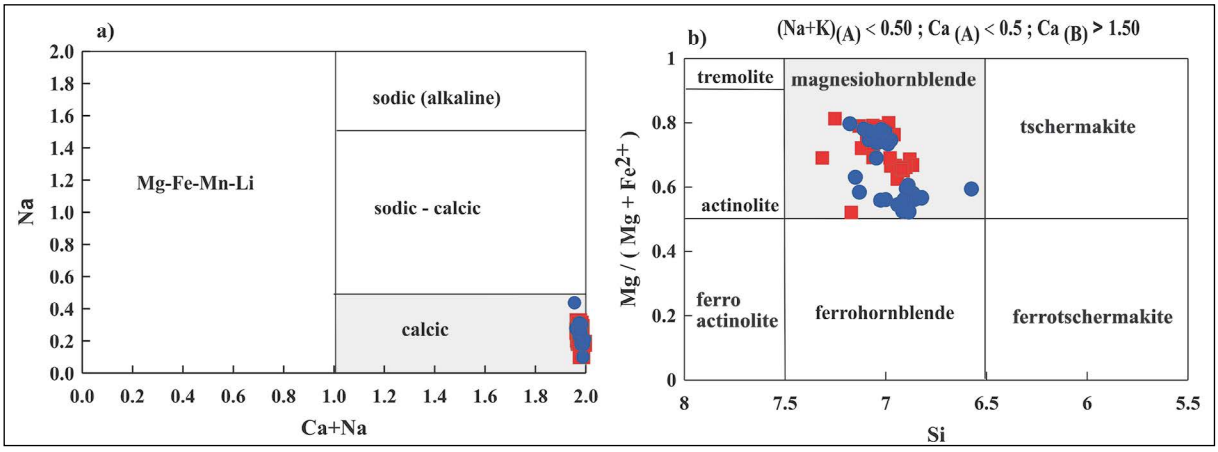

Figure 8- Hornblendes from Alemdar and Işıkdere plutons on classification diagrams (Leake et al., 1997) (symbols as in figure 7).

of pressure and temperature conditions more difficult.

A variety of thermobarometric calculations were made using the minerals and mineral assemblages (hornblende, plagioclase, biotite, K-feldspar, quartz, Fe-Ti oxides) found in these plutonic rocks. Hornblende-plagioclase (Holland and Blundy, 1994), hornblende (Ridolfi et al., 2010; Ridolfi and Renzulli, 2012) and biotite (Luhr et al., 1984) thermometers and hornblende-Al$^{(t)}$ (Hammarstrom and Zen, 1986; Hollister et al., 1987; Johnson and Rutherford, 1989; Schmidt, 1992), amphibole (Ridolfi et al., 2010; Ridolfi and Renzulli, 2012) and biotite (Uchida et al., 2007) barometers were used for the studied rocks. The pressures obtained from the hornblende-Al barometer are compatible with the pressures obtained from geological features and coeval metamorphics (Ague, 1997; Toksoy-Köksal, 2016). The oxidation of magma may be found with these mineral assemblages and mineral chemistry (Wones, 1989; Ridolfi et al., 2010; Ridolfi and Renzulli, 2012). The original oxygen fugacity of the granitic magmas cannot be determined

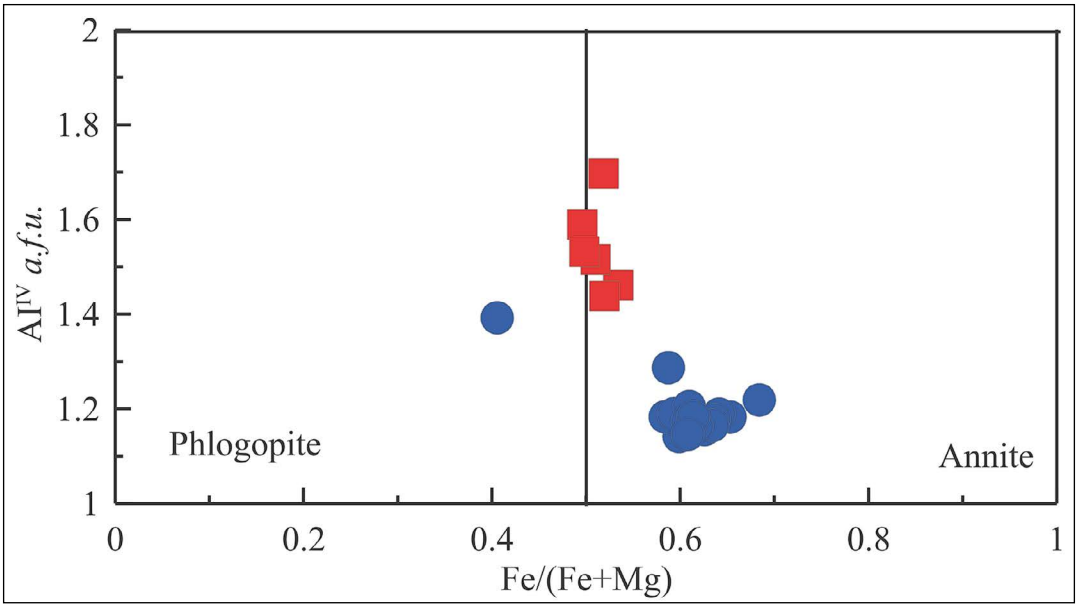

Figure 9- Biotites from the studied plutonic rocks on classification diagram (Speer, 1984) (symbols as in Figure 7).

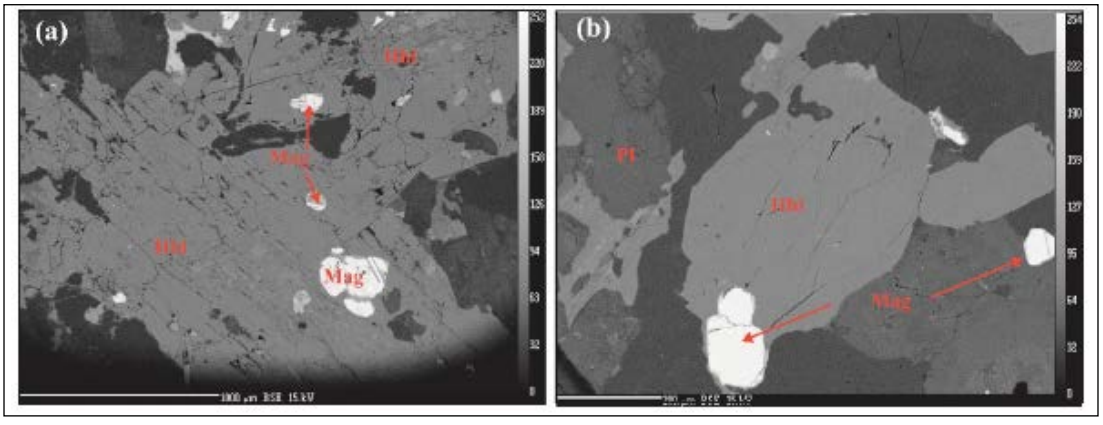

Figure 10- BSE images of Fe-Ti oxides in the Alemdar and Işıkdere plutonic rocks (a and b) euhedral and subhedral magnetite as inclusion in groundmass and hornblende (Sample no: A-1-5 and B-1; Hbl: hornblende, Pl: plagioclase, Mag: magnetite).

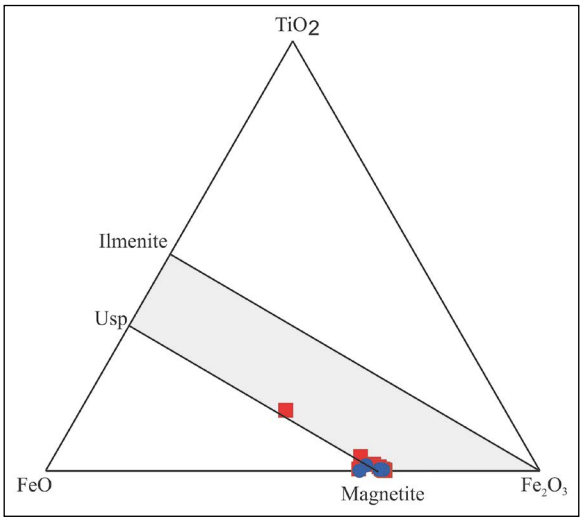

Figure 11- Fe-Ti oxides from the studied plutons on the FeO-TiO_2-Fe_2O_3 ternary diagram (Bacon and Hirschmann, 1988) (symbols as in figure 7).

due to slow cooling, so only relative approaches and calculations can be used (Kemp, 2004).

5.1. Crystallization Conditions of Magmas Forming the Plutons

5.1.1. Geothermobarometer

Since hornblende and plagioclase are mineral pairs commonly found in calcalkaline magmatic rocks, they are used for thermobarometery calculations by many researchers (Hammarstrom and Zen, 1986; Hollister et al., 1987; Johnson and Rutherford, 1989; Blundy and Holland, 1990; Schmidt, 1992; Holland and Blundy, 1994). Mineral composition of the studied plutons is suitable for thermobarometry calculations since they include these two minerals. However, as transformation to actinolite in the system, chloritization, and formation of opaque minerals is common after formation of hornblende, components with alteration should be excluded from the calculations (Hammarstrom and Zen, 1986). Besides, chemical compositions of minerals such as hornblende and plagioclase display variations according to increasing temperature and pressure conditions (Laird and Albee, 1981; Hammarstrom and Zen, 1986).

With the aim of determining temperature (T) conditions, the net-transfer variation reactions (edenite–tremolite (edenite+4 quartz = tremolite+albite) and edenite–richterite (edenite+albite = richterite+anorthite)) recommended for the geothermometer developed for hornblende-plagioclase pairs in calcalkaline granitoids were used (Holland and Blundy, 1994). According to Anderson (1996), the edenite-richterite-based thermometer is more useful compared to other magmatic thermometers and should be chosen. Using the hornblende-plagioclase thermometer recommended by Holland and Blundy (1994), at <5 kbar pressure the temperature calculated for the Alemdar Pluton is between 754 and 931˚C (mean = 829˚C), and varies from 610 to 938˚C (mean = 811±16˚C) for the Işıkdere Pluton varies (Table 2). Additionally, pressures calculated according to Ridolfi et al. (2010) were between 0.6 and 1.1 kbar (mean = 0.9±0.2) for the Alemdar Pluton, 0.7-1.1 kbar (mean = 0.9±0.2) for the Işıkdere Pluton (Table 3), with the temperatures of 741-814°C (mean = 785±16) for the Alemdar Pluton and 764-816°C (mean = 785±16) for the Işıkdere Pluton (Table 2). According to Ridolfi and Renzulli (2012), the estimated crystallization pressures are 0.7-1.2 kbar (mean = 0.9±0.3) and 0.6-1.0 kbar (mean = 0.9±0.2) for the Alemdar and Işıkdere Plutons, respectively (Table 3). The temperature values calculated for the Alemdar and Işıkdere Plutons varied from 662-791°C (mean = 757±38˚C) and 690-786°C (mean = 756±28˚C), respectively (Table 2).

The temperatures and pressures estimated according to biotite minerals (Luhr et al., 1984) in the Alemdar and Işıkdere Plutons (Uchida et al., 2007) vary from 541-741°C (mean. = 645±81˚C) (Table 2) and 2.2-3.8 kbar (mean = 2.8±0.6 kbar) for the Alemdar Pluton and 619-695°C (mean = 674±18°C) and 0.4-1.9 kbar (mean = 0.8±0.4 kbar) for the Işıkdere Pluton (Table 3).

In hornblende minerals from plutonic rocks, total aluminium $Al^{(t)}$ is used as a marker of pressure in pressure calculations. The estimated pressures reflect the crystallization depths of the hornblendes. The pressure (P) estimates based on the $Al^{(t)}$ content of hornblende in the Alemdar Pluton vary between 0.4 and 2.3 kbar (mean = 1.5±0.4 kbar) according to Hammarstrom and Zen (1986), 0.1-2.2 kbar (mean = 1.4±0.5 kbar) according to Johnson and Rutherford (1989), 0.2-1.7 kbar (mean = 1.1±0.4 kbar) according to Hollister et al. (1987) and 1.1-2.9 kbar (mean = 2.2±0.4 kbar) according to Schmidt (1992) (Table 3).

The values obtained for pressure estimations for the Işıkdere Pluton varied from 0.8-3.9 kbar (mean

= 1.7±0.6 kbar) according to Hammarstrom and Zen (1986), 0.5-4.0 kbar (mean = 1.5±0.7 kbar) according to Johnson and Rutherford (1989), 0.5-3.1 kbar (mean = 1.2±0.5 kbar) according to Hollister et al. (1987) and 1.4-4.4 kbar (mean = 2.3±0.6 kbar) according to Schmidt (1992) (Table 3).

The amphibole-plagioclase and amphibole barometers used in this study similar reveals values (0.1-3.1 kbar) (Table 3), while the values obtained from the biotite barometer are slightly higher (0.4-3.8 kbar). In the literature, there are studies stating that the pressure values calculated for granitoids using the hornblende Al barometer are consistent with geological features and the emplacement depths of the plutons (Tulloch and Challis, 2000). In the light of the qualitative and quantitative data obtained in this study, the emplacement pressures for the plutons are limited to ~1-4 kbar. The hornblendes in the studied plutons are calcic hornblendes with $Al^{(t)}$ values lower than 2.0. This value ($Al^{(t)}$ <2.00) generally indicates shallow depth intrusion (Hammarstrom and Zen, 1986; Kaygusuz et al., 2018). Additionally, the textural properties like porphyritic and regrowth supporting the shallow intrusion of the plutons are noteworthy in the studied plutons (Figure 5).

The solidus temperature given by thermometers like amphibole-plagioclase is generally >700°C (Anderson, 1996). Considering the mineral associations in plutons, an attempt is made to determine a reasonable crystallization temperature interval using different thermometric approaches. As stated above, the values estimated with the hornblende-plagioclase (Holland and Blundy, 1994) thermometer are high and have a broad temperature interval (610-928°C) (Table

Table 2- The temperature estimates calculated using hornblende-plagioclase (Holland and Blundy, 1994), hornblende (Ridolfi et al., 2010; Ridolfi and Renzulli, 2012) and biotite (Luhr et al., 1984) for the plutons.

	T°C Holland and Blundy (1994)	**T°C Ridolfi et al. (2010)**	**T°C Ridolfi and Renzulli (2012)**	**T°C Luhr et al. (1984)**
Alemdar Pluton (n*)	**35**	**35**	**35**	**6**
Min.	754	741	662	541
Max.	931	814	791	741
Mean	829	785±16	757±38	645
Işıkdere Pluton (n*)	**31**	**31**	**31**	**16**
Min.	610	764	690	619
Max.	938	816	786	695
Mean	811±16	786±5	756±28	674

* n: the number of analyzes

Table 3- The pressure estimates for the plutons calculated using hornblende-Al, hornblende and biotite barometers.

	P1 (kbar) Hammarstrom and Zen (1986)	**P2 (kbar) Johnson and Rutherfort (1989)**	**P3 (kbar) Hollister et al. (1987)**	**P4 (kbar) Schmidt (1992)**	**P5(kbar) Ridolfi et al. (2010)**	**P6 (kbar) Ridolfi and Renzulli (2012)**	**P7 (kbar) Uchida et al. (2007)**
Alemdar Plütonu (n*)	**35**	**35**	**35**	**35**	**35**	**35**	**6**
Min.	0.4	0.1	0.2	1.1	0.6	0.7	2.2
Max.	2.3	2.2	1.7	2.9	1.1	1.2	3.8
Mean	1.5 ± 0.4	1.4 ± 0.5	1.1 ± 0.4	2.2 ± 0.4	0.9 ± 0.2	0.9 ± 0.3	2.8
Mean Depth (km)	5.7	5.0	4.2	8.0	3.3	3.3	10.3
Işıkdere Plütonu (n*)	**31**	**31**	**31**	**31**	**31**	**31**	**16**
Min.	0.8	0.5	0.5	1.4	0.7	0.6	0.4
Max.	3.9	4.0	3.1	4.4	1.1	1.0	1.9
Mean	1.7 ± 0.6	1.5 ± 0.7	1.2 ± 0.5	2.3 ± 0.6	0.9 ± 0.3	0.9 ± 0.2	0.8
Mean Depth (km)	6.1	5.5	4.5	8.4	3.3	3.3	2.9

* n: the number of analyzes, depth was taken as 1kbar=3.7 km for the continental crust (Tulloch and Challis. 2000).

2). Additionally, thermometer estimations calculated using calcic hornblende in chemical equilibrium with calcalkaline volcanic rocks (Ridolfi et al., 2010; Ridolfi and Renzulli, 2012) gave partially lower temperatures (662-816°C). In addition to hornblende-based thermometric calculations, the biotite-Ti thermometer (Luhr et al., 1984) was used and low temperature (541-741°C) values were estimated (Table 2). The low temperature values obtained from the biotite thermometer show reequilibration with subsolidus intracrystal variation during cooling of feldspars (Toksoy-Köksal, 2016). Additionally, the hornblende-plagioclase thermometer giving a broad interval may indicate re-equilibration in slowly-cooling rocks in the late stage.

5.1.2. Oxygen Fugacity and Water Content

Another important factor in crystallization processes in magmatic rocks is oxygen fugacity (fO_2) which is defined as partial pressure of oxygen. Oxygen fugacity controls the pressure-temperature correlations in melts and affects the stability intervals for rock-forming minerals. This value changes as a function of temperature, and generally increases linked to the increase in temperature (Wones, 1989; Ridolfi et al., 2010). Additionally, the amount of oxygen contained in silicate melts is controlled by the source of temperature and mixing rates of gases.

Due to slow cooling, the original oxygen fugacity of granitic magmas cannot be determined, so there are only relative approaches and calculations available (Wones, 1989; Anderson and Smith, 1995; Kemp, 2004). The oxygen fugacity values ($\log_{10}\ fO_2$) calculated with the approach proposed by Wones (1989), were between -20.0 to -15.5 (mean = -18.9) for Alemdar Pluton, -19.7 to -17.0 (mean = -17.7) for Işıkdere Pluton (Table 4). The oxygen fugacity values calculated according to Ridolfi et al. (2010), using the Mg content of hornblendes in the plutons are, respectively between -14.7 to -11.8 and between -14.1 to 11.9 (Table 4). The relative oxygen fugacity (ΔNNO) varies from 0.5-2.2 and 0.6-2.1, respectively. The (ΔNNO) values calculated according to Ridolfi and Renzulli (2012) vary between -2.1 to 0.3. The mean water (H_2O) content calculated according to Ridolfi et al. (2010) is 4.4 to 7.8 wt% for Alemdar Pluton, 4.5 to 5.9% for Işıkdere Pluton, while mean water content was 4.8-7.3% for Alemdar Pluton and 4.5-5.8% for Işıkdere Pluton according to Ridolfi and Renzulli (2012) (Table 4).

The water content of magma containing amphiboles is controversial with variations between 2-3% according to Luhr et al. (1984), mean 5% according to Eggler (1972), Helz (1973) and Naney (1983), and mean 6% according to Merzbacher and Eggler (1984). The water content calculated from amphiboles in the studied samples varies from 4.4-7.8%. The presence of hydrous mafic minerals (amphibole, biotite), titanite and apatite in the samples indicates high water and volatile contents in magma. The high temperature magmas in this content may rise to shallow depths in the continental crust without full crystallization (Helmy et al., 2004).

In conclusion, according to thermobarometric calculations based on mineral chemistry data, the studied rocks have estimations for pressure values from 1 to 4 kbar and temperature values from 541 to

Table 4- Oxygen fugacity and water content for plutons calculated using hornblende and biotite minerals.

	Ridolfi et al. (2010)			**Ridolfi and Renzulli (2012)**		**Wones (1989)**
	DNNO	fO_2	H_2O	**DNNO**	H_2O	fO_2
Alemdar Pluton (n*)	**35**	**35**	**35**	**35**	**35**	**6**
Min.	0.5	-14.7	4.4	-2.1	4.8	-23.0
Max.	2.2	-11.8	7.8	0.3	7.3	-15.5
Mean	1.6	-12.6	5.0	-0.4	5.3	-18.9
Işıkdere Pluton (n*)	**35**	**35**	**35**	**35**	**35**	**16**
Min.	0.6	-14.1	4.5	-2.1	4.5	-19.7
Max	2.1	-11.9	5.9	0.3	5.8	-17.0
mean	1.3	-12.8	5.1	-0.9	5.1	-17.7

* n: the number of analyses

938°C. Considering all these features, it is proposed that the investigated plutons were emplaced at mid to shallow depths (4-15 km) from hydrous magmas.

5.2. Disequilibrium Parameters

The composition of minerals and textural features observed in rocks are related to the different types of disequilibrium during evolution of magma. Cooling, decompression and/or magma mixing are among factors triggering variations in temperature, pressure and composition of magma. As a result of these factors, the magmas may come into disequilibrium (Nixon 1988; Rutherford and Hill, 1993; Simonetti et al., 1996; Perugini et al., 2003). Petrographic or textural criteria, which involve the disequilibrium of texture as sieved plagioclase crystals (Dungan and Rhodes, 1978), presence of normal and sieved plagioclases in the same sample (Stimac and Pearce, 1992; Venezky and Rutherford, 1997), and rounded and embayed crystals (Stimac and Pearce, 1992). Compositional criteria, which involve the determination of normally and reversely zoned crystals and the presence of these two types of crystals in the same sample (Sakuyama, 1981).

The textural, petrographic and mineral compositional features of the studied magmatic rocks which indicates the presence of disequilibrium and compositional zoning in the plagioclase (Figure 5b, f, 12). In addition to oscillatory zoning in plagioclases, the observation of occasional sieve texture may be another textural feature representing disequilibrium (Figure 5b, f). The reverse zoning observed in some plagioclase minerals, especially, and presence of both reverse and normal zoned plagioclase in the same sample indicate disequilibrium crystallization (Figure 12a-f). Additionally, K-feldspars containing poikilitic hornblende, plagioclase and opaque minerals and

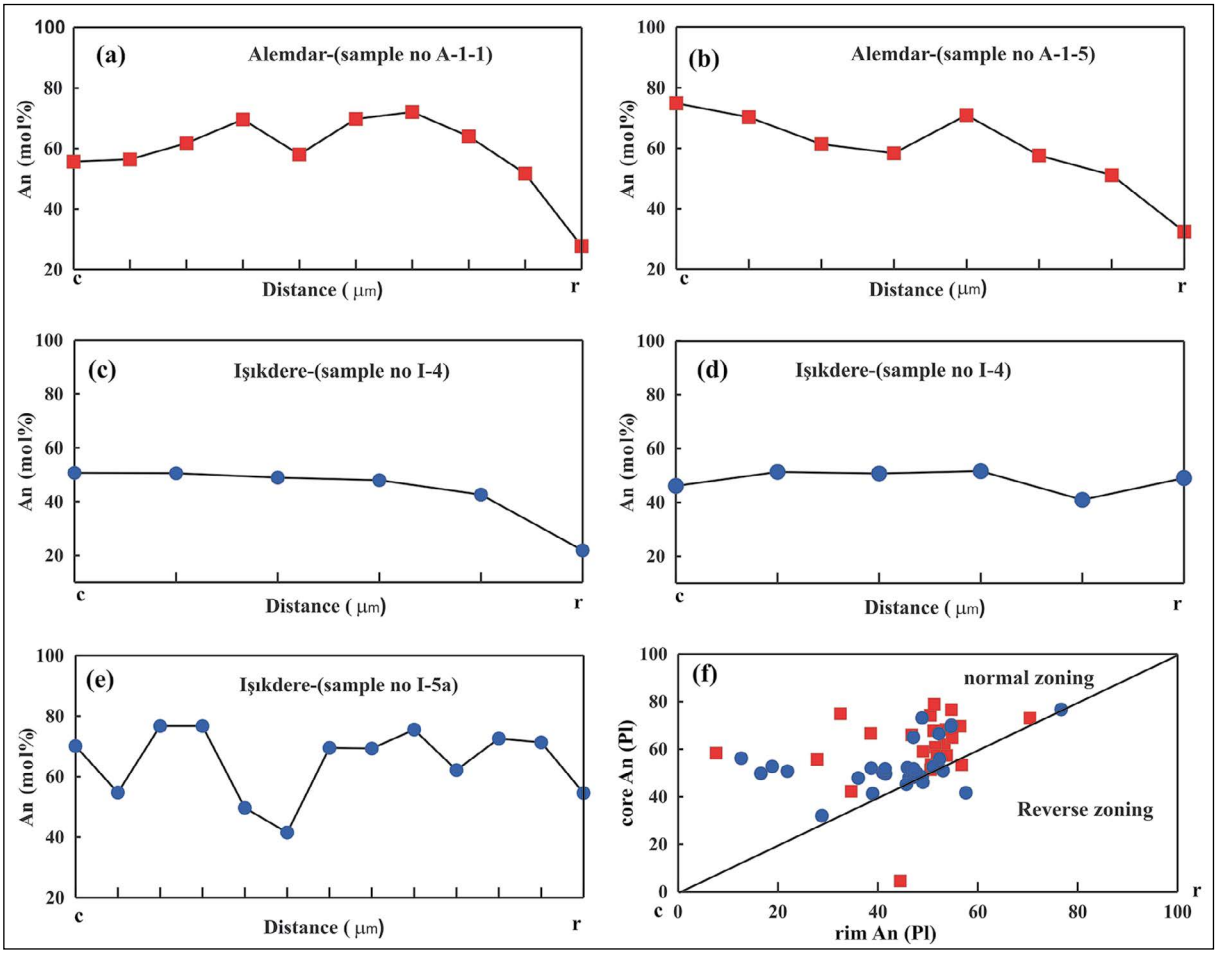

Figure 12- Core-rim An content variations in normally and reverse zoning in plagioclase of the studied plutons (c: core, r: rim).

this observed textural feature (Figure 5a) may be considered further data representing disequilibrium crystallization.

While normally zoning for plagioclases can be explained by fractional crystallization, reversely zoning there are differing views can be explained by using different views; (i) temperature and pressure increase under water-saturated conditions (Blundy and Cashman, 2001), (ii) temperature increases during ascent of water-saturated magmas (Blundy et al., 2006) and (iii) temperature increases because of back mixing (Couch et al., 2001) of magma to hotter, recharging magma (Streck, 2008). The rim of the plagioclases from studied commonly display a wide range of compositions (An_{8-77}). This wide compositional range of the plagioclase rims in a single sample indicates the complex origin of the plagioclase due to magma mixing (Wallace and Carmicheal, 1994).

5.3. Evolution of Magma within the Crust

According to pre-existing studies from the region, Lower-Middle Jurassic rocks originated in a back-arc extensional environment associated with the southward subduction of the Paleo-Tethyan oceanic lithosphere (Karslı et al., 2017). The extension occurring in the back-arc caused asthenospheric upwelling and due to this upwelling heat flow caused partial melting of the lithospheric mantle and formation of magmas leading to formation of Jurassic rocks. Again, thinning and fracture systems forming in the crust due to tectonic extension allowed movement of these melts upward within the crust. Petrographic and mineral chemical data show the presence of magma chambers at two different levels of moderate and shallow depths with evolving magma which formed Jurassic rocks under polybaric crystallization conditions. According to barometer estimations based on minerals (Table 3), the studied rocks indicate the presence of magma chambers at nearly 8-12 km (Figure 13). At these depths in addition to hornblende

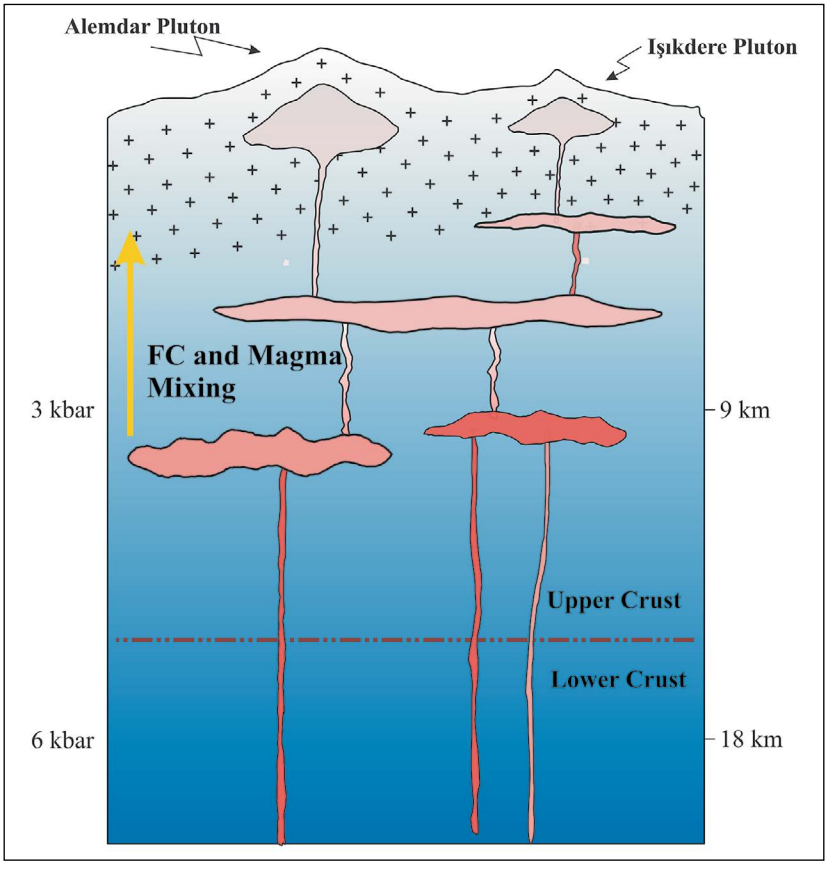

Figure 13- Schematic cross-section showing development of studied plutons within the crust.

crystallization, crystallization of plagioclase with high anorthite content and biotite is observed. Later the magma began to rise and was retained in different magma chambers at moderate levels of 4-5 km depth (Figure 13). In addition to fractional crystallization in the magma chambers, the magma mixing events occurred characterized by textural features like sieve texture and zoning. Magma rise occurred again and magma was stored in shallow magma chambers at 2-3 km depth (Figure 13). The dominant minerals in this magma chamber were biotite, plagioclase with low An content, K-feldspar and finally quartz crystalizing at relatively lower temperatures. Oxygen fugacity estimations indicate that crystallization at this level occurred under very high oxidation conditions. Finally, the fractionating magma was emplaced at shallow levels and cooled.

6. Conclusion

- The rocks of the Alemdar and Işıkdere Plutons outcropping around Gümüşhane in the south of the Eastern Pontide Orogenic belt are fine-moderate grained and quartz-diorite, quartz monzodiorite and tonalite composition.

- Petrographically, the studied plutons comprise of mainly plagioclase, hornblende, biotite, K-feldspar, quartz and Fe-Ti oxide minerals.

- There were also observed some textural features in these studied plutons indicating disequilibrium crystallization such as; sieve and oscillatory zoned plagioclase, presence of normally and reversely zoned plagioclase in the same sample, the poikilitic textures observed in K-feldspar minerals.

- According to thermobarometer estimations, the investigated plutons have pressures from 0.1 to 4.4 kbar, temperature from 541 to 938°C, oxygen fugacity values from -23 to -12 and water contents of 4.4-7.8%. Considering field, petrographic and thermobarometric data, the studied plutons were intruded at mid to shallow depts (~4-15 km) in continental crust.

Acknowledgements

This study was supported by Gümüşhane University Scientific Research Projects Coordinatorship (Project No: 17.F5114.01.01). The authors thank to İrfan Temizel and Fatma Toksoy Köksal for their constructive criticism and opinions about the manuscript.

Supplementary Data

Tables 1-4; Electronic Data for Appendices are available at https://dergi.mta.gov.tr/documents/2307_162_supplementary_tables_emre_aydincakir.pdf.

References

Ague, J.J. 1997. Thermodynamic calculation of emplacement pressures for batholithic rocks, California: implications for the aluminum-inhornblende barometer. Geology 25, 563-566.

Ağar, U. 1977. Demirözü (Bayburt) ve Köse (Kelkit) Bölgesinin Jeolojisi. Doktora Tezi, İstanbul Üniversitesi, İstanbul (unpublished).

Altherr, R., Topuz, G., Siebel, W., Şen, C., Meyer, H.P., Satır, M. 2008. Geochemical and Sr-Nd-Pb isotopic characteristics of Paleocene plagioleucitites from the Eastern Pontides (NE Turkey). Lithos 105, 149-161.

Anderson, J.L. 1996. Status of thermobarometry in granitic batholiths. Trans Royal Society Edinburgh, Earth Sciences 87, 125–138.

Anderson, J.L., Smith, D.R. 1995. The effects of temperature and $fO2$ on the Al-inhornblende barometer. American Mineralogist 80, 549–559.

Arslan, M., Aslan, Z. 2006. Mineralogy, petrography and whole-rock geochemistry of the Tertiary granitic intrusions in the eastern Pontides, Turkey. Journal of Asian Earth Sciences 27, 177-193.

Arslan, M., Temizel, İ., Abdioğlu, E., Kolaylı, H., Yücel, C., Boztuğ, D., Şen, C. 2013. 40Ar-Ar dating, whole-rock and Sr-Nd-Pb isotope geochemistry of post-collisional Eocene volcanic rocks in the southern part of the Eastern Pontides (NE Turkey): Implications for magma evolution in extension induced origin. Contribution to Mineralogy and Petrology 166, 113-142.

Aslan, Z. 2010. U-Pb zircon SHRIMP age, geochemical and petrographical characteristics of tuffs within calcalkaline Eocene volcanics around Gümüşhane (NE Turkey), Eastern Pontides. Neues Jahrbuch für Mineralogie Abhandlungen 187, 329-346.

Aslan, Z., Arslan, M., Temizel, İ., Kaygusuz, A. 2014. K-Ar dating, whole-rock and Sr-Nd isotope geochemistry of calc-alkaline volcanic rocks around the Gümüşhane area: implications for post-collisional volcanism in the Eastern Pontides, Northeast Turkey. Mineralogy and Petrology 108, 245-267.

Aydın, F. 2014. Geochronology, geochemistry, and petrogenesis of the Maçka subvolcanic intrusions: implications for the late Cretaceous magmatic and geodynamic evolution of the eastern part of the Sakarya zone, northeastern Turkey. International Geology Review 56, 1246-1275.

Aydın, F., Karslı, O., Chen, B. 2008. Petrogenesis of the Neogene alkaline volcanics with implications for post collisional lithospheric thinning of the Eastern Pontides, NE Turkey. Lithos 104, 249-266.

Aydınçakır, E. 2014. The Petrogenesis of Early-Eocene non adakitic volcanism in NE Turkey: Constraints on geodynamic implications. Lithos 208, 361–377.

Aydınçakır, E. 2016. Subduction-related Late Cretaceous high-K volcanism in the Central Pontides orogenic belt: Constraints on geodynamic implications, Geodinamica Acta 28(4), 379-411.

Aydınçakır, E. 2017. Taşlıyayla (Çaykara, Trabzon, KD Türkiye) Civarı Geç Kretase Yaşlı Kalk-alkali Volkanik Kayaçların Petrografik ve Jeokimyasal Özellikleri. GÜFBED 7 (1), 71-78.

Aydınçakır, E., Şen, C. 2013. Petrogenesis of the post collisional volcanic rocks from the Borçka (Artvin) area: Implications for the evolution of the Eocene magmatism in the Eastern Pontides. Lithos 172, 98-117.

Bacon, C. R., Hirschmann, M. M. 1988. Mg/Mn partitioning as a test for equilibrium between coexisting Fe-Ti oxides. American Mineralogist, 73, 57-61.

Blundy, J.D., Holland, T.J.B. 1990. Calcic amphibole equilibria and a new amphibole-plagioclase geothermometer. Contributions to Mineralogy and Petrology 104, 208-224.

Blundy, J., Cashman, K. 2001. Ascent driven crystallization of dacite magmas at Mount St. Helens, 1980–1986. Contributions to Mineralogy and Petrology 140, 631–650.

Blundy, J., Cashman, K., Humhreys, M. 2006. Magma heating by decompression-driven crystallization beneath andesite volcanoes. Nature 443, 76–80.

Couch, S., Sparks, R.S.J., Carroll, M.R. 2001. Mineral disequilibrium in lavaş explained by convective self-mixing in open magma chambers. Nature 411, 1037–1039.

Çimen, O., Göncüoğlu, M.C., Simonetti, A., Sayit, K. 2017. Whole rock geochemistry, zircon U-Pb and Hf isotope systematics of the Çangaldağ pluton: evidences for middle jurassic continental arc magmatism in the Central Pontides, Turkey. Lithos 290–291, 136-158.

Çimen, O., Göncüoğlu, M.C., Simonetti, A., Sayit, K. 2018. New zircon U-Pb LA-ICP-MS ages and Hf isotope data from the Central Pontides (Turkey): Geological and geodynamic constraints. Journal of Geodynamics 116, 23–36.

Çoğulu, E. 1975. Gümüşhane ve Rize Granitik Plütonlarnın Mukayeseli Petrojeolojik ve Jeokronometrik Etüdü. Doçentlik Tezi, İTÜ. Maden Fakültesi, İstanbul (unpublished).

Demir, Y. 2019. Geological, mineralogical and geochemical properties of the Dağbaşı skarn ores (Araklı-Trabzon, NE Turkey). Bulletin of the Mineral Research And Exploration 158, 167-196.

Dilek, Y. 2006. Collision tectonics of the Eastern Mediterranean region: Causes and consequences. Geological Society of America Special Paper 409, 1-13.

Dokuz, A. 2011. Slab Detachment and Delamination Model for the Generation of Carboniferous High Potassium I-type Magmatism in the Eastern Pontides, NE Turkey:The Köse Composite Pluton. Gondwana Research 19, 926-944.

Dokuz, A., Tanyolu, E. 2006. Geochemical constraints on the provenance, mineral sorting and subaerial weathering of lower Jurassic and upper Cretaceous clastic rocks from the Eastern Pontides, Yusufeli (Artvin), NE Turkey. Turkish Journal of Earth Sciences 15, 181-209.

Dokuz, A., Karslı, O., Chen, B., Uysal, İ. 2010. Sources and petrogenesis of Jurassic granitoids in the Yusufeli area, Northeastern Turkey: Implications for pre- and postcollisional lithospheric thinning of the Eastern Pontides. Tectonophysics 480, 259-279.

Dokuz, A., Uysal, İ., Meisel, W., Turan, M., Duncan, R., Akçay, M. 2013. Post-collisional adakitic volcanism in the eastern part of the Sakarya Zone, Turkey: evidence for slab and crustal melting. Contributions to Mineralogy and Petrology 166, 1443–1468.

Dokuz, A., Külekçi, E., Aydınçakır, E., Kandemir, R., Alçiçek, M.C., Pecha, M.E., Sünnetçi, K. 2017*a*. Cordierite-bearing strongly peraluminous Cebre Rhyolite from the eastern Sakarya Zone, NE Turkey: Constraints on the Variscan Orogeny. Lithos 278–281, 285–302.

Dokuz, A., Aydincakir, E., Kandemir, R., Karslı, O., Siebel, W., Derman, A.S., Turan, M. 2017*b*. Late Jurassic

magmatism and stratigraphy in the eastern Sakarya Zone, Turkey: evidence for the slab breakoff of Paleotethyan oceanic lithosphere. Journal of Geology 125, 1–31.

Dungan, M.A., Rhodes, J.M. 1978. Residual glasses and melt inclusions in basalts from DSDP Legs 45 and 46: evidence for magma mixing. Contributions to Mineralogy and Petrology 67, 417–431.

Eggler, D.H. 1972. Water-saturated and undersaturated melting relations in a Paricutin andesite and an estimate of water content in the natural magma. Contributions to Mineralogy and Petrology 34, 261–271.

Eyüboğlu, Y., Bektaş, O., Seren, A., Maden, N., Jacoby, W.R., Özer, R. 2006. Three axial extensional deformation and formation of the Liassic rift basins in the Eastern Pontides (NE Turkey). Geologica Carpathica 57 (5), 337-346.

Eyüboğlu, Y., Dilek, Y., Bozkurt, E., Bektaş, O., Rojay, B., Şen, C. 2010. Structure and geochemistry of an Alaskan-type ultramafic–mafic complex in the Eastern Pontides, NE Turkey. Gondwana Research 18, 230–252.

Eyüboğlu, Y., Dudas F.O., Santosh, M., Y.I.K., Kwon, S., Akaryalı, E. 2013. Petrogenesis and U-Pb zircon chronology of adakitic porphyries within the Kop ultramafic massif (Eastern Pontides Orogenic Belt, NE Turkey). Gondwana Research 24, 742–766.

Eyüboğlu, Y., Dudas, F.O., Santosh, M., Xiao, Y., Yi, K., Chatterjee, N., Wu, F.Y., Bektaş, O. 2016. Where are the remnants of a Jurassic Ocean in the Eastern Mediterranean Region? Gondwana Research 33, 63–92.

Eyüboğlu, Y., Dudas, F.O., Thorkelson, D., Zhu, D.C., Liu, Z., Chatterjee, N., Yi, K., Santosh, M. 2017. Eocene granitoids of northern Turkey: Polybaric magmatism in an evolving arc–slab window system, Gondwana Research 50, 311–345.

Eyüboğlu, Y., Dudas, F.O., Zhu, D.C., Liu, Z., Chatterjee, N. 2019. Late Cretaceous I- and A-type magmas in eastern Turkey: Magmatic response to double-sided subduction of Paleo- and Neo-Tethyan lithospheres. Lithos 326, 39-70.

Genç, Ş.C., Tüysüz, O. 2010. Tectonic setting of the Jurassic bimodal magmatismin the Sakarya Zone (Central and Western Pontides), northern Turkey: a geochemical and isotopic approach. Lithos 118, 95–111.

Gülmez, F., Genç, Ş.C., Prelevic, D., Tüysüz, O., Karacik, Z., Roden, M.F., Billor, Z. 2016. Ultrapotassic volcanism from the waning stage of the Neotethyan subduction: a key study from the İzmir– Ankara–Erzincan Suture Belt, Central Northern Turkey. Journal of Petrology 57, 561–593.

Güven, İ.H. 1993. Doğu Pontidler'in 1/250.000 Ölçekli Kompilasyonu, Maden Tetkik ve Arama Genel Müdürlüğü, Ankara.

Hammarstrom, J.M., Zen, E. 1986. Aluminum in hornblende: An empirical igneous geobarometer. American Mineralogist 71, 1297–1313.

Helmy, H.M., Ahmed, A.F., El Mahallawi, M.M., Ali, S.M. 2004. Pressure, temperature and oxygen fugacity conditions of calc-alkaline granitoids, Eastern Desert of Egypt and tectonic implications. Journal of African Earth Sciences 38, 255–268.

Helz, R. T. 1973. Phase relations of basalts in their melting ranges at PH2O=5 kb as a function of oxygen fugacity. Journal of Petrology 14, 249–302.

Holland, T.J.B., Blundy, J.D. 1994. Non-ideal interactions in calcic amphiboles and their bearing on amphibole-plagioclase thermometry. Contribution to Mineralogy and Petrology 116, 433-447.

Hollister, L. S., Grisson, G.C., Peters, E.K., Stowell, H.H., Sisson, V.B. 1987. Confirmation of the empirical correlation of Al in hornblende with pressure of solidification of calc-alkaline plutons. American Mineralogist 72, 231–239.

Johnson, M.C., Rutherford, M.J. 1989. Experimental calibration of the aluminiun-in amfibole geobarometer with application to Long Valley Caldera (California) volcanic rocks. Geology 17, 837–841.

Kandemir, R. 2004. Sedimentary characteristics and depositional conditions of Lower-Middle Jurassic Şenköy Formation in the around of Gümüşhane. Doktora Tezi, KTÜ, 274 s. Trabzon (unpublished).

Kandemir, R., Yılmaz, C. 2009. Lithostratigraphy, facies, and deposition environment of the lower Jurassic Ammonitico Rosso type sediments (ARTS) in the Gümüşhane area, NE Turkey: Implications for the opening of the northern branch of the Neo-Tethys Ocean. Journal of Asian Earth Sciences 34, 586-598.

Kandemir, R., Lerosey-Aubril, R. 2011. First report of a trilobite in the Carboniferous of Eastern Pontides, NE Turkey. Turkish Journal of Earth Sciences 20, 179–183.

Karslı, O., Chen, B., Aydın, F., Şen, C. 2007. Geochemical and Sr-Nd-Pb isotopic compositions of the Eocene Dölek and Sarıçiçek Plutons, Eastern Turkey: implications for magma interaction in the genesis of high-K calc-alkaline granitoids in a post-collision extensional setting. Lithos 98, 67-96.

Karslı, O., Dokuz, A., Uysal, İ., Aydın, F., Bin, C., Kandemir, R., Wijbrans, R.J. 2010. Relative contributions of crust and mantle to generation of Campanian high-K calc-alkaline I-type granitoids in a subdution setting, with special reference to the Harşit pluton, Eastern Turkey. Contributions to Mineralogy and Petrology 160, 467–487.

Karslı, O., Uysal, İ., Ketenci, M., Dokuz, A., Kandemir, R., Wijbrans, J. 2011. Adakite-like granitoid porphyries in the Eastern Turkey: potential parental melts and geodynamic implications. Lithos 127, 354-372.

Karslı, O., Dokuz, A., Uysal, İ., Ketenci, M., Chen, B., Kandemir, R. 2012. Deciphering the shoshonitic monzonites with I-type characteristic, the Sisdağı pluton, NE Turkey: magmatic response to continental lithospheric thinning. Journal of Asian Earth Sciences 51, 45-62.

Karslı, O., Uysal, İ., Dilek, Y., Aydın, F., Kandemir, R. 2013. Geochemical modelling of early Eocene adakitic magmatism in the Eastern Pontides, NE Anatolia: continental crust or subducted oceanic slab origin? International Geology Review 55, 16, 2083-2095.

Karslı, O., Dokuz, A., Kaliwoda, M., Uysal, I., Aydın, F., Kandemir, R., Fehr, K.T., Wijbrans, R.J. 2014. Geochemical fingerprints of late Triassic calc-alkaline lamprophyres from the Eastern Pontides, NE Turkey: a key to understanding lamprophyre formation in a subduction-related environment. Lithos 196-197, 181-197.

Karslı, O., Dokuz A, Kandemir, R. 2016. Subduction-related late Carboniferous to early Permian magmatism in the eastern Pontides, the Camlik and Casurluk plutons: Insights from geochemistry, whole-rock Sr-Nd and in situ zircon Lu-Hf isotopes, and U-Pb geochronology. Lithos 266-267, 98-114.

Karslı, O., Dokuz A, Kandemir, R. 2017. Zircon Lu-Hf isotope systematics and U-Pb geochronology, whole-rock Sr-Nd isotopes and geochemistry of the early Jurassic Gokcedere pluton, Sakarya Zone-NE Turkey: a magmatic response to roll-back of the Paleo-Tethyan oceanic lithosphere. Contributions to Mineralogy and Petrology doi: 10.1007/s00410-017-1346-0

Kaygusuz, A., Aydınçakır, E. 2009. Mineralogy, Whole Rock and Sr-Nd Isotope Geochemistry of Mafic Microgranular Enclaves in Cretaceous Dağbaşı Granitoids, Eastern Pontides, NE Turkey: Evidence of Magma Mixing, Mingling, and Chemical Equilibration. Chemie der Erde/Geochemistry 69, 247-277.

Kaygusuz, A., Aydınçakır, E. 2011. Petrogenesis of a Late Cretaceous composite pluton from the eastern Pontides: the Dağbaşı pluton, NE Turkey. Neues Jahrbuch Für Mineralogie 188, 3, 211-233.

Kaygusuz, A., Öztürk, M. 2015. Geochronology, geochemistry, and petrogenesis of the Eocene Bayburt intrusions, Eastern Pontide, NE Turkey: implications for lithospheric mantle and lower crustal sources in the high-K calc-alkaline magmatism. Journal of Asian Earth Science 108, 97–116.

Kaygusuz, A., Siebel, W., Şen, C., Satir, M. 2008. Petrochemistry and petrology of I-type granitoids in an arc setting: the composite Torul pluton, Eastern Pontides, NE Turkey. International Journal of Earth Sciences 97, 739-764.

Kaygusuz, A., Arslan, M., Wolfgang, S., Sipahi, F., İlbeyli, N. 2012. Geochronological evidence and tectonic signifi cance of Carboniferous magmatism in the southwest Trabzon area, eastern Pontides, Turkey. International Geology Review 54 (15), 1776–1800.

Kaygusuz, A,. Sipahi, F,. İlbeyli, N,. Arslan, M,. Chen, B., Aydınçakır, E. 2013. Petrogenesis of the Late Cretaceous Turnagöl intrusion in the eastern Pontides: Implications for magma genesis in the arc setting. Geoscience Frontiers 4, 423–438.

Kaygusuz, A., Arslan, M., Sipahi, F., Temizel, İ. 2016. U-Pb zircon chronology and petrogenesis of Carboniferous plutons in the northern part of the Eastern Pontides, NE Turkey: constraints for Paleozoic magmatism and geodynamic evolution. Gondwana Research 39, 327–346.

Kaygusuz, A., Yücel, C., Arslan, M., Sipahi, F., Temizel, İ., Çakmak, G., Güllüoğlu, Z.S. 2018. Petrography, mineral chemistry and crystallization conditions of Cenozoic plutonic rocks located to the North of Bayburt (Eastern Pontıdes, Turkey). The Bulletin of the Mineral Research and Exploration 157, 77-104.

Kemp, A.I.S. 2004. Petrology of high-Mg, low-Ti igneous rocks of the Glenelg River Complex (SE Australia) and the nature of their interaction with crustal melts. Lithos 78, 119-156.

Laird, J., Albee, A.L. 1981. Pressure, temperature, and time indicators in mafic schist: their application to reconstructing the polymetamorphic history of Vermont. American Journal of Science 281, 127-175.

Leake, E.B., Wooley, A.R., Arps, C.E.S., Birch, W.D., Gilbert, M.C., Grice, J.D., Hawthorne, F.C., Kato, A., Kisch, H.J., Krivovichev, V.G., Linthout, K., Laird, J., Mandarino, J., Maresch, W.V., Nickhel, E.H., Rock, N.M.S., Schumacher, J.C., Smith, D.C., Stephenson, N.C.N., Ungaretti, L.,

Whittaker, E.J.W., Youzhi, G. 1997. Nomenclature of amphiboles report of the subcommittee on amphiboles of the International Mineralogical Association Commission on New Minerals and Mineral Names. European Journal of Mineralogy 9, 623–651.

Luhr, J.F., Carmichael, I.S.E., Varekamp, J.C. 1984. The 1982 eruptions of El Chicón Volcano, Chiapas, Mexico: Mineralogy and petrology of the anhydrite bearing pumices. Journal of Volcanology and Geothermal Research 23, 69–108.

Merzbacher, C., Eggler, D.H. 1984. A magmatic geohygrometer: application to Mount St. Helens and other dacitic magmas, Geology 12, 587–590.

MTA, 2002. 1/500.000 ölçekli Türkiye Jeoloji Haritası, Samsun ve Trabzon Paftaları, Maden Tetkik ve Arama Genel Müdürlüğü, Ankara.

Naney, MT. 1983. Phase equilibria of rock-forming ferromagnesian silicates in granitic systems, American Journal of Science 283, 993–1033.

Nixon, G.T. 1988. Petrology of the younger andesites and dacites of Iztaccihuatl volcano, Mexico: disequilibrium phenocryst assemblages as indicators of magma chamber processes. Journal of Petrology 29, 213–264.

Okay, A.İ., Leven, E.J. 1996. Stratigraphy and paleontology of the upper Paleozoic sequences in the Pulur (Bayburt) region, Eastern Pontides. Turkish Journal of Earth Sciences 5, 145-155.

Okay, A.İ., Şahintürk, Ö. 1997. Geology of the Eastern Pontides. In: Robinson, A.G. (ed.), Regional and Petroleum Geology of the Black Sea and Surrounding Region. American Association of Petroleum Geologists Memoir 68, 291-311.

Okay, A.İ., Tüysüz, O. 1999. Tethyan sutures of northern Turkey. In: Durand, B., Jolivet, L., Hovarth, F., Séranne, M. (eds), The Mediterranean Basins: Tertiary Extension within the Alpine Orogen Tethyan Sutures of Northern Turkey. Geological Society London. Special Publications 156, 475-515.

Okay, A.I., Satır, M., Siebel, W. 2006. Pre-Alpide Palaeozoic and Mesozoic orogenic events in the Eastern Mediterranean region. In: Gee, D.G., Stephenson, R.A. (Eds.), European Lithosphere Dynamics. Geological Society, London, Memoirs 32, 389–405.

Özdamar, Ş., Roden, M.F., Billor, M.Z. 2017. Petrology of the shoshonitic Çambaşı Pluton in NE Turkey and implications for the closure of the NeoTethys Ocean: insights from geochemistry, geochronology and Sr–Nd isotopes. Lithos 284 (285), 477–492.

Pelin, S. 1977. Alucra (Giresun) Güneydoğu Yöresinin Petrol Olanakları Bakımından Jeolojik İncelenmesi. KTÜ Yayınları, 87, 103s, Trabzon (unpublished).

Perugini, D., Busa, T., Poli, G., Nazzareni, S. 2003. The role of chaotic dynamics and flow fields in the development of disequilibrium textures in volcanic rocks. Journal of Petrology 44, 733–756.

Ridolfi F., Renzulli, A. 2012. Calcic amphiboles in calcalkaline and alkaline magmas: thermobarometric and chemometric empirical equations valid up to 1,130°C and 2.2 Gpa. Contributions to Mineralogy and Petrology 163, 877–895.

Ridolfi, F., Renzulli, A., Puerini, M. 2010. Stability and chemical equilibrium of amphibole in calc-alkaline magmas: an overview, new thermobarometric formulations and application to subduction-related volcanoes. Contributions to Mineralogy and Petrology 160, 45–66.

Rutherford, M.J., Hill, P.M. 1993. Magma ascent rates from amphibole breakdown: an experimental study applied to the 1980–1986 Mount St. Helens eruptions. Journal of Geophysical Research 98, 19667–19685.

Sakuyama, M. 1981. Petrological study of the Myoko and Kurohime Volcanoes, Japan: crystallization sequence and evidence magma mixing. Journal of Petrology 22, 553–583.

Saydam Eker, Ç., Sipahi, F., Kaygusuz, A. 2012. Trace and rare earth elements as indicators of provenance and depositional environments of Lias cherts in Gumushane, NE Turkey. Chemie der Erde Geochemistry 72, 167–177.

Schmidt, M.W. 1992. Amphibole composition in tonalite as a function of pressure: An experimental calibration of the Al-in amfibole barometer. Contributions to Mineralogy and Petrology 110, 304–310.

Simonetti, A., Shore, M., Bell, K. 1996. Diopside phenocrysts from nephelinite lavas, Napak Volcano, Eastern Uganda: Evidence for magma mixing. Canadian Mineralogist 34, 411–442.

Sipahi, F., Kaygusuz, A., Saydam Eker, Ç., Vural, A., Akpınar, İ. 2017. Late Cretaceous arc igneous activity: The Eğrikar Monzogranite example. International Geology Review 60 (3), 382–400.

Smith, J.V., Brown, W.L. 1988. Feldspar minerals. 2nd review and extended edition Book (ISBN 0387176926), Springer-Verlag, Berlin.

Speer, J. A. 1984. Micas in igneous rocks. In S. W. Bailey (Ed.), Micas: Reviews in mineralogy and geochemistry (Vol. 13, pp. 299–356). Washington, DC: Mineralogical Society of America.

Stimac, J.A., Pearce, T.H. 1992. Textural evidence of mafic–felsic magma interaction in dacite lavas, Clear Lake, California. American Mineralogist 77, 795–809.

Streck, M.J. 2008. Mineral textures and zoning as evidence for open system processes. In: Putirka KD, Tepley III FJ (eds) Minerals, inclusions and volcanic processes. Miner Soc Am and Geochem Soc, Rev Mineral 595–622

Streckeisen, A. 1976. To each plutonic rock its proper name. Earth Sciences Review 12, 1–33.

Şahin, S.Y., Güngör, Y., Boztuğ, D. 2004. Comparative petrogenetic investigation of composite Kaçkar Batholith granitoids in eastern Pontide magmatic arc (Northern Turkey). Earth Planets Space 56, 429–446.

Şen, C. 2007. Jurassic volcanism in the Eastern Pontides: Is it rift related or subduction related?. Turkish Journal of Earth Sciences 16, 523-539.

Temizel, İ., Kurt., A. 2019. Geç Kretase yaşlı Bozat (Giresun, KD Türkiye) Plütonu'nun petrografik, jeokimyasal ve petrolojik Özellikleri. GÜFBED 9 (3), 454-472.

Temizel, İ., Arslan, M., Ruffet, G., Peucat, J.J. 2012. Petrochemistry, geochronology and Sr–Nd isotopic systematics of the Tertiary collisional and post-collisional volcanic rocks from the Ulubey (Ordu) area, eastern Pontide, NE Turkey: implications for extension-related origin and mantle source characteristics. Lithos 128, 126-147.

Temizel, İ., Abdioğlu-Yazar, Emel, Arslan, M., Kaygusuz, A., Aslan, Z. 2018. Mineral chemistry, whole-rock geochemistry and petrology of Eocene I-type shoshonitic plutons in the Gölköy area (Ordu, NE Turkey). The Bulletin of Mineral Research and Exploration 157, 123-155.

Temizel, İ., Arslan, M., Yücel, C., Abdioğlu-Yazar, E., Kaygusuz, A., Aslan, Z. 2019*a*. U-Pb geochronology, bulk-rock geochemistry and petrology of Late Cretaceous syenitic plutons in the Gölköy (Ordu) area (NE Turkey): Implications for magma generation in a continental arc extension triggered by slab roll-back. Journal of Asian Earth Sciences 171, 305-320.

Temizel, İ., Arslan, M., Yücel, C., Abdioğlu-Yazar, E., Kaygusuz, A., Aslan, Z. 2019*b*. Eocene tonalite–granodiorite from the Havza (Samsun) area, northern Turkey: adakite-like melts of lithospheric mantle and crust generated in a post-collisional setting. International Geology Review doi.org/10 .1080/00206814.2019.1625077.

Toksoy-Köksal, F. 2016. Ekecikdağ Magmatik Birliği (Orta Anadolu) Granitoyidlerinin Petrojenezi: Mineral Kimyası Perspektifi. Yerbilimleri 37(2), 139-178.

Topuz, G., Altherr, R., Kalt, A., Satir, M., Werner, O., Schwarz, W.H. 2004. Aluminous granulites from the Pulur Complex, NE Turkey: a case of partial melting, efficient melt extraction and crystallization. Lithos 72, 183–207.

Topuz, G., Altherr, R., Schwarz, W.H., Dokuz, A., Meyer, H. P. 2007. Variscan amphibolite-facies rocks from the Kurtoğlu metamorphic complex: Gümüşhane area, Eastern Pontides, Turkey. International Journal of Earth Sciences 96, 861-873.

Topuz, G., Altherr, R., Siebel, W., Schwarz, W.H., Zack, T., Hasözbek, A., Barth, M., Satır, M., Şen, C. 2010. Carboniferous high-potassium I-type granitoid magmatism in the Eastern Pontides: the Gümüşhane Pluton (NE Turkey). Lithos 116, 92–110.

Topuz, G., Okay, A.İ., Altherr, R., Schwarz, W.H., Siebel, W. Zack, T., Satır, M., Şen, C. 2011. Post-collisional adakite-like magmatism in the Ağvanis Massif and implications for the evolution of the Eocene magmatism in the Eastern Pontides (NE Turkey). Lithos 125, 131-150.

Tulloch, A.J., Challis, G.A. 2000. Emplacement depths of Paleozoic–Mesozoic plutons from western New Zealand estimated by hornblende-Al geobarometry. New Zealand Journal of Geology and Geophysics 43, 555-567.

Uchida, E., Endo, S., Makino, M. 2007. Relationship between solidification depth of granitic rocks and formation of hydrothermal ore deposits. Resource Geology 57, 47–56.

Ustaömer, T., Robertson, A.H.F. 2010. Late Palaeozoic Early Cenozoic tectonic development of the Eastern Pontides (Artvin area), Turkey: stages of closure of Tethys along the southern margin of Eurasia. Geological Society, London. Special Publications 340, 281-327.

Venezky, D.Y., Rutherford, M.J. 1997 Preeruption conditions and timing of dacite–andesite magma mixing in the 2.2 ka eruption at Mount Rainier. J Geophys Res 102, 20069–20086.

Wallace, P.J., Carmichael, I.S.E. 1994. Petrology of Volcan Tequila, Jalisco, Mexico: disequilibrium phenocryst assemblages and evolution of the subvolcanic magma system. Contrib Mineral Petrol 117, 345–361.

Wones, D.R. 1989. Significance of the assemblage titanite + magnetite + quartz in granitic rocks. American Mineralogist 74, 744–749.

Yılmaz, S., Boztuğ, D. 1996. Space and time relations of three plutonic phases in the Eastern Pontides (Turkey). International Geology Review 38, 935–956.

Yılmaz, Y. 1972. Petrology and structure of the Gümüşhane granite and surrounding rocks. NE Anatolia. PhD Thesis, Universty of London, 260s.

Yılmaz, Y., Tüysüz, O., Yiğitbaş, E., Genç, Ş.C., Şengör, A.M.C. 1997. Geology and tectonics of the Pontides. in Robinson, A.G. (eds.), Regional and Petroleum Geology of the Black Sea and Surrounding Region. American Association of Petroleum Geologists Memoir 68, 183-226.

Yücel, C. 2017. Akçaabat (Trabzon) Güneyi ve Çevresindeki Kampaniyen Yaşlı Volkanik Kayaçların Petrografisi, Jeokimyası, Jeokronolojisi ve Petrojenezi. Gümüşhane Üniversitesi Fen Bilimleri Dergisi 7 (1), 79-101.

Yücel, C., Arslan, M., Temizel, İ., Abdioğlu, E. 2014. Volcanic facies and mineral chemistry of Tertiary volcanics in the northern part of the Eastern Pontides, northeast Turkey: Implications for pre eruptive crystallization conditions and magma chamber processes. Mineralogy and Petrology 108, 439-467.

Yücel, C., Arslan, M., Temizel, İ., Abdioğlu, E., Ruffet, G. 2017. Evolution of K-rich magmas derived from a net veined lithospheric mantle in an ongoing extensional setting: Geochronology and geochemistry of Eocene and Miocene volcanic rocks from Eastern Pontides (Turkey). Gondwana Research 45, 65-86.

Bulletin of the Mineral Research and Exploration

http://bulletin.mta.gov.tr

Morphological parameters causing landslides: A case study of elevation

Seda ÇELLEK[a*]

[a]*Geology Engineering Department, Engineering and Architecture Faculty, Kırşehir Ahi Evran University, Kırşehir, Turkey*

Research Article

Keywords:
Landslide, Susceptibility, Morphology, Elevation, Parameter.

ABSTRACT

The history of landslide susceptibility maps goes back about 50 years. Hazard and risk maps later followed these maps. Inventory maps provide the source of all these. There are different parameters selected specially for each field in the literature as well as parameters selected because they are easy to produce and obtain data. This study tried to research the effect of elevation on landslides by reviewing the literature in detail. The used class ranges and elevation values were reviewed and applied to map sections selected from Turkey. By analyzing the results, the goal was to determine at which elevation ranges landslides occurred. The study tried to investigate the effect of the parameter of elevation using data from the literature. It works to compare the elevation values for map sections selected to compare with the literature. The study comprises two stages. The first step tried to acquire statistical data by researching the data from the literature. The data were investigated in the second stage. For this purpose, close to 1.500 studies prepared between 1967 and 2019 were reviewed. According to the literature, the parameter of was used in analyses because it is easy to produce and is morphologically effective.

Received Date: 27.06.2019
Accepted Date: 22.10.2019

1. Introduction

"Elevation is one of the most essential key factors that determine the stress distribution of slopes" (Althuwaynee et al., 2016; Hong et al., 2017*a, b;* Chen et al., 2018, 2019). There is strong evidence that elevation is an indicator for susceptibility to landslides. Elevation is also one of the simplest features of slopes (Kornejady et al., 2017*a, b*). For this reason, it is frequently preferred as a parameter in the preparation of landslides susceptibility maps. It is also a parameter chosen for danger maps. Many researchers around the world accept the importance of elevation in the formation of landslides (Juang et al., 1992; Pachauri and Pant 1992; Dai and Lee, 2001, 2003; Ercanoğlu and Gökceoğlu, 2002, 2004; Lee et al., 2002; Çevik and Topal, 2003; Gomez and Kavzoğlu, 2005; Gökçeoğlu et al., 2005; Mazman, 2005; Creighton, 2006; Duman et al., 2006; Lee and Pradhan, 2007; Chen and Wang, 2007; Dağ, 2007; Caniani et al., 2008; Ercanoğlu et al., 2008; Kamp et al., 2008; Yao et al., 2008; Özdemir, 2009; Akıncı et al., 2010; Balteanu et al., 2010; Bai et al., 2010; Park et al., 2010; Yılmaz, 2010; Oh and Pradhan, 2011; Rozos et al., 2011; Sezer et al., 2011; Yalçın et al., 2011; Dağ and Bulut, 2012; Kavzoğlu et al., 2012; 2014, Mashari et al., 2012; Pourghasemi et al., 2012*a, b, c, d, e*; Schicker and Moon, 2012; Xu and Xu XW, 2012; Yılmaz et al., 2012; Sabatakakis et al., 2013; Chen et al., 2013, 2015, 2016*a,b,* 2017, 2018, 2019; Devkota et al., 2013; Liu et al., 2013; Özdemir and Altural, 2013; Özşahin and Kaymaz, 2013; Akıncı et al., 2014; Avcı and Günek, 2014; Chalkias et al., 2014; Conforti et al., 2014; Jaafari et al., 2014; Jebur et al., 2015; Moradi and Rezaei, 2014; Nourani et al., 2014; Sujatha et al., 2014; Tazik et al.,

Citation info: Çellek, S. 2020. Morphological parameters causing landslides: A case study of elevation. Bulletin of the Mineral Research and Exploration 162, 197-224. https://doi.org/10.19111/bulletinofmre.649758

* *Corresponding author: Seda ÇELLEK, sedacellek@ahievran.edu.tr*

2014; Umar et al., 2014; Youssef et al., 2014*a, b, c*; Zhu et al., 2014; Akıncı and Kılıçoğlu, 2015; Dehnavi et al., 2015; Dragicevi et al., 2015; Goetz et al., 2015; Özşahin, 2015; Pradhan and Kim, 2015; Youssef, 2015; Youssef et al., 2015; Aghdam et al., 2016; Avcı, 2016*a, b, c*; Balamurugan et al., 2016; Demir, 2016; Liu and Wu, 2016; Myronidis et al., 2016; Wang et al., 2016, 2017; Wu and Ke, 2016; Wu et al., 2016; Zhang et al., 2016*a, b*; Dou et al., 2017; Kornejady et al., 2017*a, b;* Pawluszek and Borkowski, 2017; Raja et al., 2017). Zhang et al. (2017), connected the use of elevation in the preparation of generally landslide-susceptible maps to different elevations being correlated to different environmental factors. Some researchers found that landslide activity in a certain basin materialized at certain elevations (Dai et al., 2001; Çevik and Topal, 2003; Yılmaz et al., 2012). The effects of different elevations on landslide susceptibility is different (Çellek, 2013). Jimenez-Peralvarez et al. (2009) in their study reported that elevation wasn't the most commonly used determinant parameter according to the literature (Fernandez et al., 2008) and that the effect of the parameter was determinant for mountainous areas with different elevation values like their own working areas. Elevation affecting landslide susceptibility at different ranges obfuscates the relationship between landslide activity and elevation (Dai and Lee, 2002; Kavzoğlu and Çölkesen, 2010; Kavzoğlu et al., 2012; Tazik et al., 2014). Because determining the elevations of the landslides that have occured in any region can only be considered as preliminary data (Özşahin, 2015).

2. Elevation (Relative Elevation-Topographic Elevation)

The maximum and minimum elevations in the working area are determined with this parameter (Ramesh and Anbazhagan, 2015). Elevation can be defined as the height of a point from sea level or from a local reference point. Elevation in susceptibility maps is considered as either "topographic elevation" based on altitude values from sea level or as "relative elevation" based on elevation differences of topographic elements in the study area. Relative elevation is commonly used and is considered by some researchers (Ercanoğlu, 2003; Görüm, 2006). The general tendency among researchers is to use topographic elevation (Dağ, 2007; Dağ and Bulut 2012; Kavzoğlu et al., 2012; Çellek, 2013; Akıncı and Kılıçoğlu, 2015). The parameter was used as topographic elevation in 51 studies reviewed by Hasekioğulları (2011) and as relative elevation in seven studies. Süzen and Kaya (2011) stated that elevation was used as an input parameter in 34.27% of researchers in the studies they reviewed. Relative and topographical elevation being used together leads to repetition and causes the consideration of the same parameter twice. Only one of the topographic and relative elevation parameters is therefore used, or the analysis results are compared, used separately in the evaluation of landslide susceptibility (Ercanoğlu, 2003; Ayalew and Yamagishi 2005; Görüm, 2006; Yüksel, 2007).

Relative Elevation: It is the elevation based on the height differences of the topographical elements in the study area or it defines the height difference between a point and another point taken as a reference (Carrara et al., 1991; Anbalagan, 1992; Pachauri and Pant, 1992; Anbalagan and Singh, 1996; Nagarajan et al., 2000; Ercanoğlu, 2003, Görüm, 2006; Yüksel, 2007; Nefeslioğlu et al., 2008; Chauhan et al., 2010; Çellek, 2013; Raja et al., 2017). In other words, relative elevation describes the range of elevations between the lowest and highest points in a region. Generally, there are three ways to define the difference in relative elevation. The differences lie in the definition of base elevation. In the first, the smallest absolute elevation of the entire field is used as the base elevation; in the second, elevation is applied as the smallest elevation in each negative sub basin; and the third is based on a convolution process (Zhang et al., 2012).

Topographical Elevation: Topographical elevation is defined as the elevation from sea level or a local reference point (Moore et al., 1991; Ercanoğlu, 2003; Tangestani, 2003; Ercanoğlu and Gökçeoğlu, 2004; Lan et al., 2004; Süzen and Doyuran, 2004*a, b*; Ayalew and Yamagishi, 2005; Gomez and Kavzoğlu, 2005; Görüm, 2006; Dağ, 2007; Yüksel, 2007; Caniani et al., 2008; Gattinoni, 2009; Hasekioğulları, 2011; Dağ and Bulut, 2012; Kavzoğlu et al., 2012; Çellek, 2013; Nourani et al., 2014; Akıncı and Kılıçoğlu, 2015).

3. The Effect of Elevation on Other Parameters and Landslides

If we are to assess previously conducted research, the parameter of elevation is a widely used parameter

in the preparation of susceptibility maps, and the relationship between the formation of landslides (toppling, rock falls, rock slides, etc.) and the parameter is complex due to its effect over many parameters that cause the occurrence of landslides (morphology, soil type, tectonics, soil thickness, erosion-weathering, land cover, precipitation, etc.). As a result, elevation is evaluated as a parameter that has an indirect effect together with the variances of the other parameter and affects the entire system (Zolotraev, 1976; Dai and Lee 2002, 2003; Yüksel, 2007; Rozos et al., 2008; Park, 2010; Yılmaz, 2010; Hasekioğulları, 2011; Yalçın et al., 2011; Çellek, 2013; Pourghasemi, et al., 2013*a, b*; Moradi and Rezaei, 2014; Nourani et al., 2014; Kouli, et al., 2014; Umar et al., 2014; Youssef et al., 2015; Pradhan and Kim, 2017). Gritzner et al. (2001) emphasized that elevation could be considered as a guide for other variables that are directly related to elevation. Jimenez-Peralvarez et al., (2009) stated that elevation has a range that is wide enough to cause significant changes in climatic conditions, like precipitation and temperature also represents variable vegetation units. Aniya (1985), however, stated that different elevations being exposed to different climate and weather conditions would lead to the formation of different types of plants and soil (Pourghasemi et al., 2014). Dai and Lee (2001) reported that the rocks at much higher elevations disintegrated with the freezing-thawing effect, while rocks at much lower elevations were inclined to accumulate thick alluvion (Pourghasemi et al., 2014).

Gravity: Relative elevation demonstrates the potential gravitational energy for each unit (Zhang et al., 2012). The elevation difference is a measure of the potential energy of landslides. Generally, an increasing difference in elevation corresponds to the possibility of an increasing failure tied to an increase in sliding force (Fernandez et al., 2003).

Biological Elements: According to the literature biological elements, biophysical parameters, and natural-artificial factors have an effect on landslides triggered by elevation. Landslides (Dai and Lee, 2002; Kavzoğlu et al., 2012; Akıncı and Kılıçoğlu, 2015). It is therefore stated that the factor of elevation has effects that can lead to slope stability and slope breakup (Vivas, 1992; Dai and Lee, 2002; Ayelew et al., 2005; Hasekioğulları, 2011; Kavzoğlu et al., 2012, 2014; Akıncı et al., 2015).

Anthropogenic Activity: It is known that elevation affects anthropogenic activity and anthropogenic activity triggers landslides. Many high-altitude areas in their study area are desolate (devoid of human activity), the ground is covered in glaciers and snow and, thus, is rarely affected by human activities. There are fewer landslides and low susceptibility for this reason. Exactly the opposite, settlements, transportation, and consequently human activity is greater at altitudes (Vivas, 1992; Dai and Lee, 2002; Ayalew et al., 2005; Hasekioğulları, 2011; Kavzoğlu et al, 2014; Kouli et al., 2014; Yang et al., 2015; Aghdam et al., 2016; Meng et al., 2016; Wang et al., 2017).

Erosion - Disintegration - Degradation - Soil: Elevation can be evaluated as a parameter that controls the processes of erosion-disintegration-degradation and the type and degree of erosion in the formation of landslides (Zolotraev, 1976; Pachauri and Pant, 1992; Vivas, 1992; Dai and Lee, 2002; Lan et al., 2004; Ayelew et al., 2005; Yüksel, 2007; Rozos et al., 2008; 2010; 2011; Hasekioğulları, 2011; Jaafari et al., 2015*a, b*; Youssef et al., 2015; Aghdam et al., 2016; Ilia and Tsangaratos, 2016; Pham et al., 2016; Pham et al., 2017). He et al., (2011) and Erener and Lacasse (2007) connected the occurrence of landslides at low elevations in their study areas to erosion and flowing water corrosion. Hasekioğulları (2011) reported in a study that low topographical elevations in areas with landslides are composed of soil materials that are the mostly the products of degradation. The slopes steepening with erosion leads to increased elevation above the threshold value that is then followed by landslides (Raja et al., 2017). Typically, higher mountain elevations receive greater rainfall than areas at lower elevations (Coe et al., 2004*a, b*). This increases soil moisture in higher mountain elevations and can lead to the decrease of soil strength and the increase of stress in the soil matrix (Ray and Jacobs, 2007). Furthermore, slopes are inclined toward landslides due to a fine colluvium cover because erosion generally is seen in connection with accumulation in these regions. However, the frequency of landslides is low in low elevations because the terrain itself is soft and covered in thick colluvium and/or residual soil, and a higher settled water table will be necessary to instigate a landslide (Dai and Lee, 2002; Opiso et al., 2016). Elevation is a parameter that regulates soil depth and development along with physical erosion and chemical disintegration (Opiso et al., 2016).

Ochoa (1978) stated that elevation was related to the effect over the properties of the physical-chemical soil at Cordillera de Me'rida (Opiso, et al., 2016). Aniya, (1985) reported that weather and climate conditions vary greatly at different elevations and that this reflects on soil differences (Dou et al., 2017).

Precipitation: Elevation is used as a factor for frequent climatization for landslide susceptibility analyses (Wu et al., 2016). If we are to speak generally, they affect elevation, precipitation/snow (Koukis and Ziourkas, 1991; Nagarajan, 2000; Gökçeoğlu and Ercanoğlu, 2001; Görcelioğlu, 2003; Tangestani, 2004; Görüm, 2006; Rozos et al., 2008;2011; Yüksel, 2007; Hasekioğulları, 2011; Tazik et al., 2014; Yang et al., 2015; Dölek and Avcı, 2016*a, b, c*; Balamurugan et al., 2016; Chen et al., 2017). Climate conditions, however, do have potential influence over slope stability (Kavzoğlu et al., 2014; Meng et al., 2015; Wang et al., 2016). Yang et al. (2015) reported that numerous high-altitude regions are covered in glaciers and snow in their study area, that these areas are scant affected by earthquakes and human activities and therefore encounter fewer landslides and have low susceptibility. Elevation is greatly important in terms of affecting accumulated amounts of precipitation (Görcelioğlu, 2003; Yüksel, 2007; Avcı and Günek, 2014). Indeed, Yılmaz and Keskin (2009) reported that precipitation accumulated at the bottom of the slope due to the incline along with the decrease in elevation and, consequently, created a higher vacuum pressure and could lead to a greater risk of landslide at low elevations (on valley floors). Clerici et al. (2006) connected the observation of the loss of slope in their study area at different elevations between 401-600 m and 801-1000 m to the snow precipitation and the freeze-thaw cycle. Koukis and Ziourkas (1991) observed in their study landslides in areas with elevation values of at most 600-1000 m. Researchers have correlated this situation with the high sections in mountainous regions receiving greater precipitation. The literature features researchers who state that in their study areas heavy rainfall falls mostly on low elevations in causes an inverse relationship between landslides and elevation in this (Carrara, 1983; Gallart and Clotet, 1988; Baeza and Corominas, 2001; Wang and Li, 2017; Chen et al, 2017). "Gruber and Haeberli, (2007) noted that the hard precipitation rate increased with the decrease in elevation and that temperature dropped and contributed to the cooling of the slopes" (Chen et al., 2017). The relationship of these with landslides should be revealed with precipitation analyses to define relative elevation in detail. Landslide distribution based on morphology can be shown by not evaluating the factor of precipitation in situations where there are not enough precipitation stations in the study area, and the graphic of the density of landslides can be drawn based on the class of elevation. Elevation information isn't used most of the time in superficial flow conjectures in classic hydrological methods because the procurement of elevation data is an inconvenient process (Dölek and Avcı, 2016).

Temperature: Generally speaking, the increase of elevation affects all systems (Rozos et al., 2008; Rozos, et. al., 2010). Namely, elevation affects temperature (Tazik et al., 2014; Meng et al., 2016). Atmospheric heat decreases 0.5 C° every 100 m (Sancar, 2000; Yılmaz, 2009*a, b*; Kavzoğlu et al., 2012; Avcı and Günek, 2014; Avcı, 2016*a, b, c*). The rate of hard precipitation increases at increasing elevations and temperature drops. This leads to the cooling of rocks, the growth of different species of flora, and landslides (Zolotarev, 1976; Vivas, 1992; Nagarajan et al., 2000; Gruber and Haeberli, 2007; Kavzoğlu et al., 2014; Tazik et al., 2014; Meng et al., 2015; Balamurugan et al., 2016; Wang et al., 2016; Chen et al., 2017; Wang and Li, 2017; Dou et al., 2017).

Land Cover: Elevation has a significant effect over the topographic properties that explain the spatial variability of different landscaping processes like the distribution of flora. Thus, it creates an indirect effect in the ocurrence of landslides (Aniya, 1985; Moore et al, 1991; Vivas, 1992; Dai and Lee 2003; Tangestani, 2003; Ercanoğlu and Gökçeoğlu, 2004; Lan et al., 2004; Süzen and Doyuran, 2004*a, b*; Ayalew and Yamagishi, 2005; Goméz and Kavzoğlu, 2005; Gruber and Haeberli, 2007; Yüksel, 2007; Kamp et al., 2008; Park, 2010; Yılmaz, 2010; Oh and Pradhan, 2011; Yalçın, et al., 2011; Mohammady et al., 2012; Pourghasemi et al., 2012*a, b, c*; Kavzoğlu et. al., 2012; Kavzoğlu et al., 2014; Jaafari et al., 2015*a, b*; Meng et al., 2015, 2016; Wang et al., 2016; Chen et al., 2017; Ding et al., 2017; Dou et al., 2017). Decreases are seen in temperature and precipitation as elevation increases, and different vegetation zones form at the changing stages of elevation. Thus, variable elevation conditions in topography are influential over biological and natural elements (Vivas, 1992; Kavzoğlu et al.,

2012). Researchers think that, although there is no clear relationship between landslides and elevation, there is an effect related to forest density. Elevation has significant influence over the surface of the Earth and topographical properties. These properties demonstrate the spatial variability of different landscaping processes like flora distribution generally affected by topographical influences (Saadatkhah et al., 2014; Ding et al., 2017).

Lineament: Elevation does not directly contribute to the formation of a landslide but can cause landslides with other parameters like tectonic, and this affects the entire system (Zolotarev, 1976; Koukis and Ziourkas, 1991; Nagarajan et al., 2000; Görüm, 2006; Rozos et al., 2008; 2010; 2011; Yang et al., 2015; Dölek and Avcı, 2016*a, b, c*; Ilia and Tsangaratos, 2016). Researchers have reported that a relationship of relative elevation with landslides must emerge by considering its detailed study and definition and the seismic effects of these (Vivas, 1992; Nagarajan, 2000; Gökçeoğlu and Ercanoğlu, 2001; Görüm, 2006; Özdemir, 2009; Jaafari et al., 2015*a, b*; Avcı, 2016*a, b, c*; Dölek and Avcı, 2016). "Elevations in their working area extended along the Yinxiu - Beichuan Lineament line and, when the direction of incline is guided parallel to the Lineament, has an increasing susceptibility to landslides" (Zhang et al., 2012). Because the horizontal components of seismic acceleration in vertical sections for high segments in seismically active mountainous regions have a greater impact, these segments are more sensitive to landslides. The correlation of seismic analysis with landslides should be conducted in these areas. There was a requirement for this for seismographic stations (Gökçeoğlu and Ercanoğlu, 2001). It was reported that because the horizontal component of seismic acceleration in the vertical segments of mountainous areas have an effect that is 1.2 to 1.5 times greater than that of valleys, these areas were more susceptible to landslides (Zolotarev, 1976; Nagarajan et al., 2000; Görüm, 2006; Gökçeoğlu and Ercanoğlu, 2001; Avcı, 2016*a, b, c*). Bai et al. (2013) stated that most landslides in their study area (more than 84%) were triggered by earthquakes at elevations below 2100 m. Bai et al. (2014) reported in their study that most of all landslides triggered with earthquakes (more than 84.09%) took place at altitudes below 1900 m. Tanoli et al. (2017) reported that 86% of landslides occurred at elevations of 1000 to 3000 m before earthquakes in their study area and that 90% of earthquakes occurred at elevations of 1500 to 3500 m after earthquakes. They reported in this that there was proof that coseismic landslides occurred at higher altitudes compared with landslides before earthquakes.

Geology: Elevation is accepted as one of the significant parameters in the formation of landslides because it is controlled by various geological processes (Dai and Lee, 2001, 2002; Ayalew and Yamagishi 2005; Gorsevski et al., 2012; Pradhan and Kim, 2014; Jaafari et al., 2014). Landslide susceptibility increases as elevation increases but is different in increases at different geological levels (Dai and Lee, 2001; Zhu et al., 2014; Raja et al., 2017). Some researchers reported that the units at much higher elevations comprised rock-type materials and were less susceptible to landslides because they have greater durability compared with the materials at lower elevations (Caniani et al., 2008; Avcı, 2016). Ercanoğlu (2005) said that durable rocks belonging to the Ulus Formation have at high elevations an incline greater than 45 degrees and at low elevations a mild slope (0-20°). Liu et al. (2013) reported that landslides occurred in their study area in the middle section of hilly and mountainous areas and that few landslides occurred in peaks or the peaks of mountains because most rocks on peaks were worn and hard. Pachauri and Pant (1992) stated that their study area comprised resistant lithological units (Limestone) at high elevations, despite having reported that high areas were more sensitive to landslides. Kouli et al. (2014) reported that elevation indirectly caused landslides in their study area, that landslides that occurred at high elevations were composed of adhesive units, and that the unit was affected by poor climate conditions such as precipitation. They gave the highest score in their study area to vertical morphological areas that occurred from flysch and phyllite-quartzites between 700 and 1000 m. Çevik and Topal (2003) reported that landslides between 10-150 m in their study area occurred mostly (63.1%) due to the lithological character and structural control of the units. Rozos et al. (2010) reported that the density of landslides in their working area was not directly correlated to elevation but that Plio-Pleistosen sediments were influential in landslides that occurred between 250 and 500 m.

Geomorphology: Tangestani (2003) showed the elevation between geomorphic or terrain-based risk factors that increase susceptibility to landslides.

Drainage: The change in elevation for each region is one of the influential factors in the ocurrence of mass movement. This factor controls the direction of flow and the rate of drainage intensity (Abedini et al., 2017). Erener and Lacasse (2007) reported that landslides in the working area demonstrating high correlation at low elevations from 0 to 15 m originates from inclination into rivers and from erosion. On the contrary, He et al. (2011) reported that landslides that occurred at low elevations in their study area occurred because they were defenseless against corrosion and erosion by flowing water.

4. Elevation Classes

The literature contains research suggesting that landslides increase with the increase in elevation. In other words, it is shown that landslides tend to appear more in places of high altitude (Koukis and Ziourkas, 1991; Pachauri and Pant, 1992; Pachauri et al., 1998; Gökçeoğlu and Ercanoğlu, 2001; Gritzner et al., 2001; Ercanoğlu et al., 2004; Gökçeoğlu et al., 2005; Görüm, 2006; Lee and Pradhan, 2007; Caniani et al., 2008; Akıncı et al., 2010; 2011; Özdemir, 2009; Özşahin and Kaymaz, 2013; Pradhan and Kim, 2014, 2015; Özşahin, 2015; Avcı, 2016 *b*; Dölek and Avcı, 2016; Wu and Ke, 2016). On the contrary, there are studies in which landslide intensity decreases as elevation increases and in which landslides occur at low and medium elevations (Yüksel, 2007).

High Elevations: The literature contains research that asserts that landslides aren't frequently encountered at high elevations. Researchers connect this to units at very high elevations forming from rock-type materials and having high cutting resistance compared with disintegrated rocks at lower elevations (Dai and Lee, 2001; Ercanoğlu, 2003; Görüm, 2006; Dağ, 2007; Yüksel, 2007; Caniani et al., 2008; Dragicevic et al., 2015; Avcı, 2016*a, b, c*; Abedini et al., 2017; Pradhan and Kim, 2017). To the contrary, the literature contains views that assert that high elevations cause landslides together with other parameters. This view has two fundamental causes. The first is that high segments get much more precipitation (Nagarajan, 2000; Görüm, 2006). Typically, higher mountain elevations receive greater rainfall than areas at lower elevations (Coe et al., 2004*a, b*). This increases soil moisture in higher mountain elevations and can lead to the decrease of soil strength and the increase of stress in the soil matrix (Ray and Jacobs, 2007; Opiso et al., 2016). The second is that these have a 1.2 to 1.5 times greater impact for vertical components of seismic acceleration in the segments that are relatively more horizontal than valleys (Nagarajan, 2000; Görüm, 2006). Pradhan and Kim (2017) reported that the possibility of landslide formation is greater for high-altitude areas because of the existence of remaining soil cover on rocks. Kavzoğlu et al. (2012) in their study connected the landslides that occurred in the 600-1000 m field to these segments receiving greater precipitation compared to the literature review they conducted while some studies correlated the landslides to densely forested areas as the reason for the for their occurrence at >600 m. Clerici et al. (2006) connected the observation of the landslides in the study area in areas with much higher elevations to there being greater rain and snow precipitation in this area and the freezing-thawing cycle. Bai et al. (2013) reported in their study area that only 7.06% of all landslides occur at elevations greater than 2400 m. Bai et al. (2014) reported in their study that only 3.04% of all landslides triggered by earthquakes occurred at elevations above 2500 m. On the other hand, Bai et al. (2013) reported in their working area that most landslides (more than 84%) occurred at elevations below 2100 m, while Bai et al. (2014) reported in their study that most of all landslides (more than 84.09%) occurred at elevations below 1900 m. Tanoli et al. (2017) reported that 90% of coseismic landslides occurred at elevations of 1500 to 3500 m.

Medium Elevations: Fields at medium elevations are assessed as more susceptible to landslides because of the ground cover that forms due to accumulating of materials, weathering, and erosion coming from higher fields (Dai and Lee, 2001; 2002; Ercanoğlu, 2003; Lan et al., 2004; Ayalew and Yamagishi, 2005; Görüm, 2006; Dağ, 2007; Yüksel, 2007; Gorsevski and Jankowski, 2008; Hasekioğulları, 2011; Kavzoğlu et al., 2012; Çellek, 2013; Elkadiri et al., 2014; Wang et al., 2015; Dragicevic et al., 2015; Avcı, 2016*a, b, c*; Opiso et al., 2016; Abedini et al., 2017; Pradhan and Kim, 2017). Yüksel (2007) determined in a study that medium-elevation areas are more susceptible to landslides compared with lower or higher sections. On the contrary, Liu et al. (2013) reported in their study that landslides occurred in the middle section of hilly and mountainous areas and that few landslides occurred in the upper elevations of peaks or mountains because most rocks on peaks were worn and hard.

Low Elevations: Low elevations generally are considered as less susceptible to landslides because slope incline includes less and thicker cover material. Because the terrain itself is soft, low elevations have low inclines. It is thus covered with thick alluvion or residual soil, and the possibility of landslide is lower as long as the water table doesn't rise up to instigate a landslide (Dai and Lee, 2001; 2002; Ercanoğlu and Gökçeoğlu, 2002; Çevik and Topal, 2003; Ercanoğlu, 2003; Ayalew and Yamagishi, 2005; Chau and Chan, 2005; Görüm, 2006; Dağ, 2007; Caniani et al., 2008; Kavzoğlu et al., 2012; Çellek, 2013; Dragicevic et al., 2015; Avcı, 2016*a, b, c*; Opiso et al., 2016; Abedini et al., 2017). Ercanoğlu and Gökçeoğlu (2002) explained the occurrence of landslides in lower topographic elevations in their study area with the high regions in the working area being composed of stable units and these regions being covered by dense vegetation, Çevik and Topal (2003) connected this situation to the lithologic character and structural control of the units that constitute the study area. Chau and Chan (2005) and Ayalew and Yamagishi (2005), however, connected it to there being large sections of road cuts in these regions because the population is greater at these elevations (Hasekioğulları, 2011). Erener and Lacasse (2007) reported that landslides in the study area demonstrated high correlation at low elevations from 0 to 15 m because of proximity to rivers and erosion. Zhuang et al. (2015) separated their study area into three regions. They reported that a vast majority of landslides occurred on Qin Mountain at 50-90m (45.18%), on Li Mountain at 10-70m (87.30%), and in Loess Tableland at 10-30m (44.90%). They also revealed that landslide frequencies increased proportionally to the difference of elevation in the Qin and Li Mountains but that the frequency started to fall in the altittude otherwise that defeat 60 m. They showed that the reason for this is that terrain with elevation differences that exceed this value is generally used for terrace harvesting.

5. Class Interval Ranges

The class ranges selected in the study areas vary. Most studies used literature-based classification, and it was reported that very few studies selected unique class ranges. Özşahin (2015) prepared the elevation values that affect landslide susceptibility in the study area by considering the class ranges made in the literature. Myronidis et al. (2016) adapted class ranges in their study based on Chen and Wang (2007) and Sabatakakis et al. (2013). Pourghasemi and Kerle (2016) utilized the literature in their study (Lee and Pradhan, 2007; Pourtaghi et al., 2014) and used equal class ranges. Pourghasemi and Rossi (2017) selected equal class ranges in their study, using the literature (Pourtaghi et al., 2014; Pourghasemi and Beheshtirad 2015). The class range numbers selected for the evaluation were determined by reviewing 90 selected studies (Figure 1).

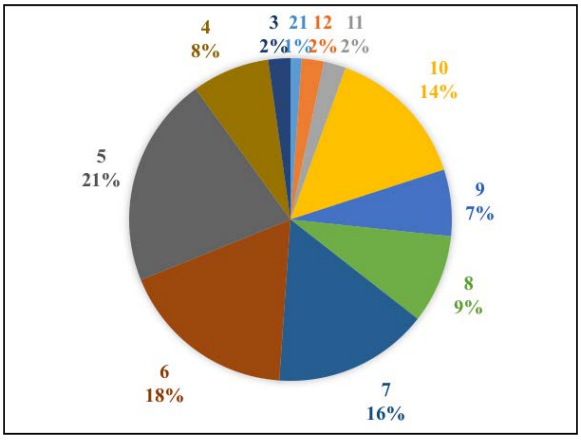

Figure 1- Class range numbers % distribution for 90 studies.

The number of class ranges selected in the studies was at most 21 and at least 3. Five class ranges in 19 studies, six class ranges in 16 studies, seven class ranges in 14 studies, and 10 class ranges in 13 studies were selected. Although not being selected as much as the others, the class ranges of 8, 4, and 9, respectively, were selected as well. The class ranges selected the least were 12, 11, and 3. While 21 class ranges were selected in only one publication, 13 class ranges weren't selected by any researcher.

Based on this, there was variance in the classifications selected in the studies. Table 1 provides the class ranges in 58 evaluated studies. The variable class ranges are notable when reviewing the table. While most researchers chose equal class ranges (Balamurugan et al., 2016; Chen et al., 2016*a, b*; 2017; Demir, 2016; Leonardi et al., 2016; Peng et al., 2014; Pradhan and Kim 2017; Pradhan et al., 2014; Rozos et al., 2010; Shrestha et al., 2017; Umar et al., 2014; Wang et al., 2015; Wu and Ke, 2016; Zhang et al., 2016*a, b*). While most researchers chose equal class ranges (Aghdam et al., 2016; Acharya and Pathak, 2017; Akıncı and Kılıçoğlu, 2015; Amirahmadi et

al., 2017; Ataol and Yeşilyurt, 2014; Avcı, 2016*a, b, c*; Chen et al., 2016; 2017; Çellek et al., 2015; Dağ and Bulut, 2012; Dou et al., 2017; Eker et al., 2012; Fenghuan et al., 2010; Hasekioğulları, 2011; Ilia and Tsangaratos, 2016; Kornejady et al., 2014; Lee and Pradhan 2007; Liu and Wu, 2016; Moradi and Rezaei, 2014; Pourtaghi et al., 2015; Raja et al., 2017; Sadr et al., 2014; Tazik et al., 2014; Tsangaratos and Ilia, 2016; Wang et al., 2016; 2017; Wu et al., 2016; Xu et al., 2013; 2016*a, b*; Zare et al., 2014; Zhao et al., 2014).

The class range selection distribution was determined when 42 publications that used equal class range were examined (Figure 2). The most preferred interval values based on this are 200 m (29%) and 500 m (24%). The least preferred were 100 m (12%), 150 m, 250 m (7%), 50 m, 300 m, and 400 m (5%). The

Table 1- Class intervals (meters) used by some researchers in the literature.

Researcher (s) /Year	Sınıf (metre)	Gaps
Aghdam et al., 2016	<200, 200–400, 400–600, 600–800, 800–1000, 1000–1200, 1200–1400, 1400–1600, 1600–1800, 1800-2000, 2000–2200, 2200–2400, 2400–2600, 2600–2800, 2800–3000, 3000–3200, 3200–3400, 3400–3600, 3600–3800, 3800–4000, >4000	200
Acharya and Pathak, 2017	<800, 800-1200, 1200-1600, 1600-2000, 2000-2400, 2400-2800, >2800	200
Akıncı et al., 2014	180-250, 250-500, 500-750, 750-1000, 1000-1278	250
Akıncı and Kılıçoğlu, 2015	0-100, 100-200, 200-300, 300-400, 400-500, 500-600, 600-700, 700-800, 800-900, 900-1300	100
Amirahmadi et al., 2017	0-559,7, 559,7-1000, 1000-1500, 1500-2000, 2000-2500, 2500-3000, 3000-3500, 3500-4000, 4000-4500, 4500-5597	500
Ataol and Yeşilyurt, 2014	<800, 800-1000, 1000-1200, 1200-1400, >1400	200
Avcı, 2016*a*	1140-1300, 1300-1500, 1500-1700, 1700-1900, 1900-2100, 2100-2300, >2300	200
Avcı, 2016*b*	1150-1200, 1200-1400, 1400-1600, 1600-1800, 1800-2000, 2000-2200, 2200-2400, 2400-2600, >2600	200
Balamurugan et al., 2016	819-1086, 1086-1340, 1340-1630, 1630-1953, 1953-2452	yok
Chen et al., 2016*a*	80–330, 330–620, 620–1000, 1000-2000	yok
Chen et al., 2017	561–800, 800–1050, 1050–1300, 1300–1550, 1550–1800, 1800–2074	250
Chen et al., 2018	632-1284, 1284-1773, 1773-2206, 2206-2680, 2680-3940	yok
Chen et al., 2016*b*	720–850, 850–1000, 1000–1150, 1150–1300, 1300–1560	150
Çellek et al., 2015	0-100, 100-200, 200-300, 300-400, 400-500, 500-600, 600-700, 700-800, 800-900, 900-1000, 1000-1100	100
Dağ and Bulut, 2012	0-100, 100-200, 200-300, 300-400, >400	100
Demir, 2016	500-750, 750-950, 950-1200, 1200-1450, 1450-1700	yok
Duo et al., 2017	<1000, 1000-1500, 1500-2000, 2000-2500, 2500-3000, > 3000m	500
Eker et al., 2012	<300, 300-600, 600-900, 900-1200, >1200	300
Fenghuan et al., 2010	500- 1000, 1000-1500, 1500-2000, 2000-2500, 2500-3000, 3000-3500, 3500-4000, >4000	500
Hasekioğulları, 2011	0-250, 250-500, 500-750, 750- 1000, 1000-1250, 1250-1500, 1500-1750	250
Ilia and Tsangaratos, 2016	<220, 221-440, 441-660, 661–880, 881–1100,> 1101	220
Kornejady et al., 2014	<1000, 1000-1200, 1200-1400, 1400-1614	200
Lee and Pradhan, 2015	<100, 100–500, 500-1000, 1000–1500, 1500–2000, 2000–2500, 2500–3000, >3000	500
Leonardi et al., 2016	0-150, 151-300, 301-600, >601	yok
Liu and Wu, 2016	> 2400, 2200-2400, 2000-2200, 1800-2000, 1600-1800, 1400-1600, <1400	200
Moradi and Rezaei, 2014	<1400, 1400-1600, 1600-1800, 1800-2000, 2000-2500, 2500-3000, >3000	200
Nourani et al., 2014	<1,300, 1,300–1,700, 1,700–2,100, 2,100, 2,500, 2,500–2,900	400
Padrones et al., 2017	0-176, 176-352, 352-528, 528-704, 704-880, 880-1056, 1056-1232, 1232-1408, 1408-1584, 1584-1760	176
Peng et al., 2014	80-330, 330-620, 620-1000, 1000-2000	yok
Pham et al., 2015	0 - 600, 600 - 750, 750 - 900, 900 - 1050, 1050 - 1200, 1200 - 1350, 1350 - 1500, 1500 - 1650, 1650 – 1800, > 1800	150
Pham et al., 2016	<600, 600–750, 750–900, 900–1050, 1050– 1200, 1200–1350, 1350–1500, 1500–1650, 1650–1800, >1800	150

Table 1- continue.

Pham et al., 2017	0-700, 700–900, 900–1100, 1100–1300, 1300–1500, 1500–1700, 1700–1900, > 1900 m	200
Pourghasemi and Kerle, 2016	<100, 100–500, 500-1000, 1000–1500, 1500–2000, 2000–2500, 2500–3000, >3000	500
Pourghasemi and Rossi, 2017	<500, 500–1000, 1000–1500, 1500–2000, >2000	500
Pourghasemi et al., 2014	<1,500, 1,500–2,000, 2,000–2,500, 2,500–3,000, 3,000–3,500, >3,500	500
Pourtaghi et al., 2014	<100, 100–500, 500-1000, 1000–1500, 1500–2000, 2000–2500, 2500–3000, 3000 m	500
Pradhan and Kim, 2017	<75, 75–100, 100-150, 150–200, 200-250, >250	yok
Pradhan et al., 2014	0–20, 20–25, 25–35, 35–65, 65–115, 115–252, 252–465, 465–705, 705–950, 950–2,000	yok
Raja et al., 2017	<50, 50–100, 100-150, 150–200, >200	50
Rozos et al., 2010	<250, 250–500, 501–800, 801–1200, >1200	yok
Saadatkhah et al., 2014	0-50, 50–100, 100–200, 200–300, >300	yok
Sadr et al., 2014	0-100, 100-200, 200-300, 300-425	100
Shrestha et al., 2017	<1281, 1281–1755, 1755-2254, 2254–3302, 3302–3850, 3850–4424, 4424– 4973, 4973-5621, 5621-6968> 6968	yok
Simon et al., 2017	<30, 30-60, 60-90, >90	30
Tazik et al., 2014	500-1000, 1000-1500, 1500-2000, >2000	500
Tsangaratos and Ilia, 2016	<400, 401–600, 601–800, >801	200
Umar et al., 2014	0-9.01, 9.01-18.02, 18.02-45.07, 45.07-90.14, 90.14-135,21, 135.21-198.31, 198.31-297.45, 297.46-458.73, 468.73-748.18, 748.18-2298.62	yok
Wang et al., 2015	20–850, 850–1000, 1000–1150, 1150–1300, 1300–1560	yok
Wang and Li, 2017.	<900, 900–1300, 1300–1700, 1700–2100, 2100–2500 ve> 2500	400
Wang et al., 2016	<150, 150–200, 200–250, 250–300, 300–350, 350–400, 400–450, 450–500, 500–550, >550	50
Wu et al., 2016	<1400, 1400–1600, 1600–1800, 1800-2000, 2000-2200, 2200–2400, > 2400	200
Wu and Ke, 2016	720-850, 851-1000, 1001–1150, 1151–1300 and 1301-1560	yok
Xu et al., 2013	<1000, 1000–1500, 1500–2000, 2000–2500, 2500–3000, 3000–3500, 3500–4000, 4000–4500, 4500–5000, 5000–5500, >5500	500
Xu et al., 2016*a*	2207-2300, 2300-2400, 2400-2500, 2500-2600, 2600-2700, 2700-2800, 2800-2900, 2900-3000, 3000-3100, 3100-3200, 3200-3340	100
Zare et al., 2014	<300, 300-600, 600-900, 900-1200, 1200-1500, 1500-1800, 2100-2400, 2400-2700, 3000- 3300, >3300	300
Zhang et al., 2016*a*	0-50, 50–200, 200–350, 350–500, >500 m	yok
Zhang et al., 2016*b*	<1000, 1000–1600, 1600-2200, 2200-2880 and >2800	yok
Zhao et al., 2014	60–80, 800–1000, 1000–1200, 1200– 1400, 1400–1600 m, 1600–1800, 1800– 2060	200

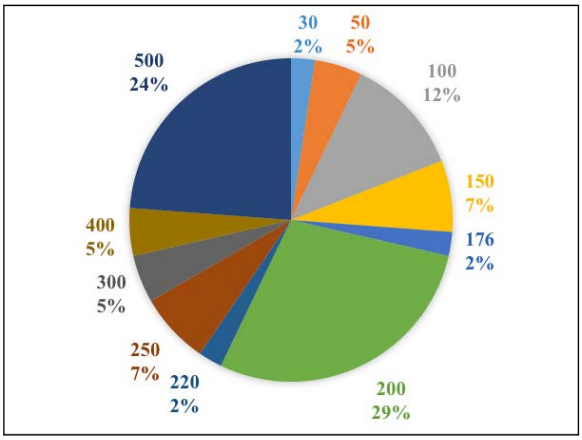

Figure 2- The preferred class range distributions in the literature.

least preferred interval values were 30 m, 176 m, and 220 m (2%). Intermediate values such as 350 m and 450 m weren't chosen.

6. Materials and Methods

It is accepted that elevation has influence over the formation of landslides, despite researchers not fully reaching a consensus. This study tried to research the influence of the parameter over landslides. For this purpose, close to 1500 studies prepared between 1967 and 2017 were reviewed. According to the literature, the parameter of elevation was used in analyses because of its effect on the formation of landslides, because

it's easy to produce, and because it is morphologically effective. A review of previous studies determines that landslides are encountered at various elevations. It was determined that any elevation triggers landslides, remaining under the influence of a different parameter.

For the purpose of comparison with the data in the literature, 64 out of 2945 landslide map sections at a scale of 1/25.000 prepared by Mineral Research and Exploration (MRE) were selected and were digitized by adjusting the cell size to 28 pixels. For elevation maps to be created, digitized topographic maps at a scale of 1/25.000 in which the contours belonging to the selected landslide regions pass once every 10 m were procured from the General Command of Cartography. Using the ArcGIS 10.4 software, the attributions of the numerical contours and TIN (Triangulated Irregular Network) model and numerical elevation models were acquired in the form of triangular networks. The numerical elevation model (NEM) was obtained with the prolongation from the acquired TIN models (TIN to Raster). This model is incredibly important in terms of constituting a base for the other data used as topographical data in the studies. Thus, procuring the elevation parameter from other secondary topographical data was more easily provided and was converted into a raster data format. Elevation classes were made considering the conditions of the terrain. These range distances can be increased and decreased based on the conditions of the terrain. Using the literature, the class ranges of 50 and 100 m were selected for elevation. By digitalizing inventory maps for 50 selected map sections, they were superposed with elevation maps. The result maps were produced with "reclassify" and "raster to polygon" by selecting the class ranges. At which elevation values landslides occurred was determined by analyzing the prepared maps, and they were compared with their corresponding values in the literature.

7. Findings

The selected map sections were classified with 100 m ranges, and a total of 32 ranges were procured. Figure 3 provides the results in percentage distributions.

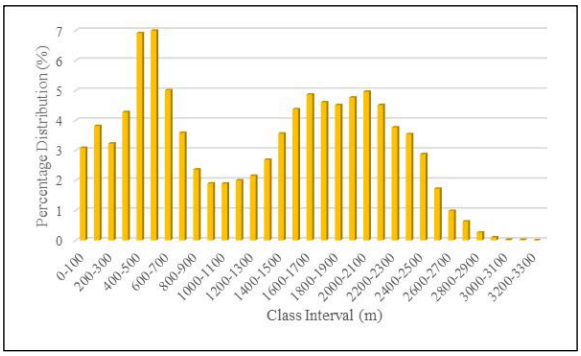

Figure 3- Distributions of the analyzed map sections in % based on 100 m class ranges.

As a result of the analysis of approximately 50 map sections, the range values were evaluated between 0 and 3300 because the areas had different elevation values. There are no significant differences between class ranges, and it was reported that about 20% of landslides occurred between 500-700 m. The lowest values were found in areas above 2600 m.

It was seen that range values increased in providing a stable value because class ranges are unique to each area. The 10 map sections selected have values that can be classified with 50 m ranges. The analysis values are seen in figure 4.

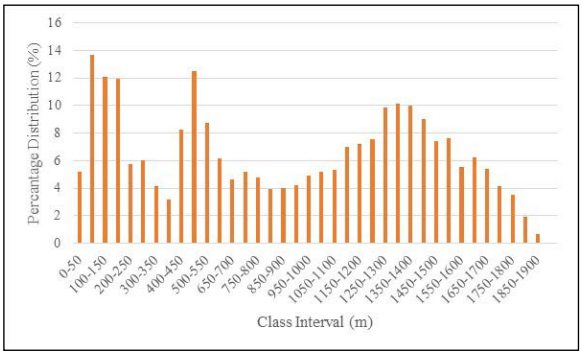

Figure 4- Distributions of the analyzed map sections in % based on 50 m class ranges.

The 50-100-meter range with 14% is the area at which the most landslides are seen. The 100-150 m range and the 450-500 m class range follow that with 12%. The lowest values are encountered after 1900 m. The reason for this is that elevations that allow for short ranges have comparatively low elevation values.

Finally, elevation distribution graphics were created for each area. The reason for this is that each

field will be unable to resort to generalization from there being unique elevation values but that how distribution changes based on the terrain is examined (Figure 5).

The graphics show that gradually increasing values decreases again gradually after reaching a peak point. A drop occurred after a regular increase in all areas. If we are to generalize, landslides occurred at the average elevation values for the study area.

Figure 5- Elevation class range-landslide field distribution for the map sections used in the study (km^2).

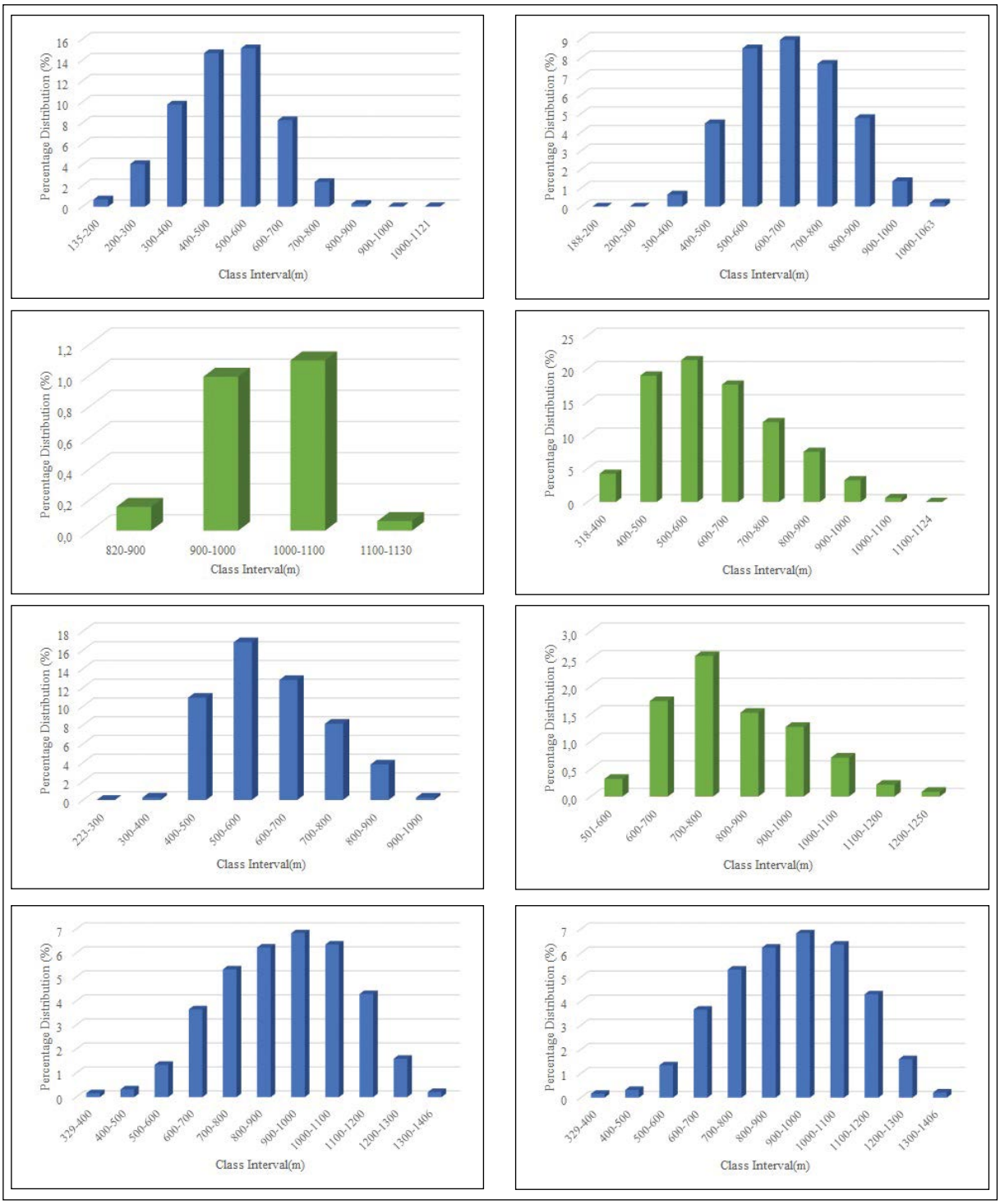

Figure 5- Continued.

Figure 5- Continued.

Figure 5- Continued.

Figure 5- Continued.

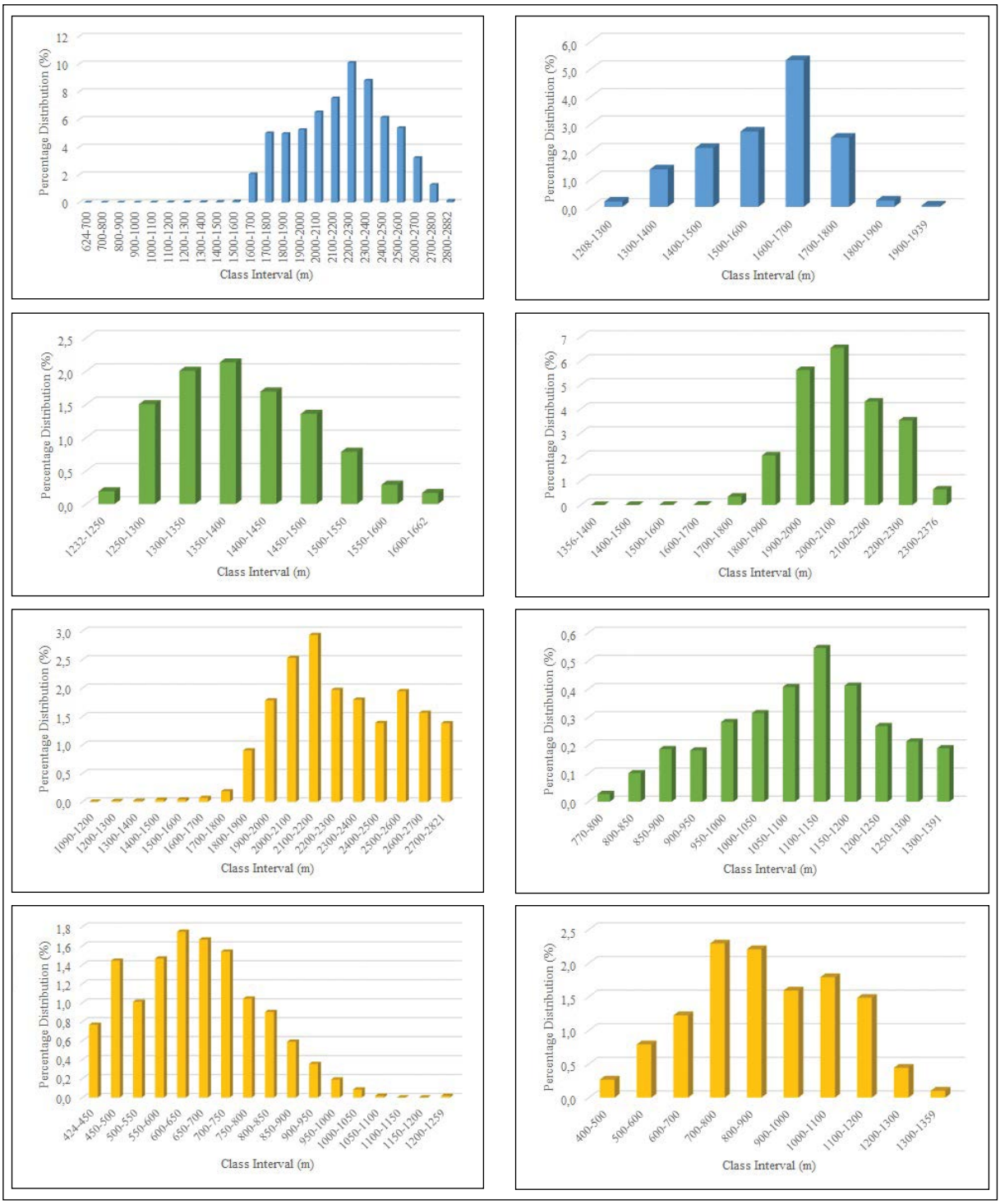

Figure 5- Continued.

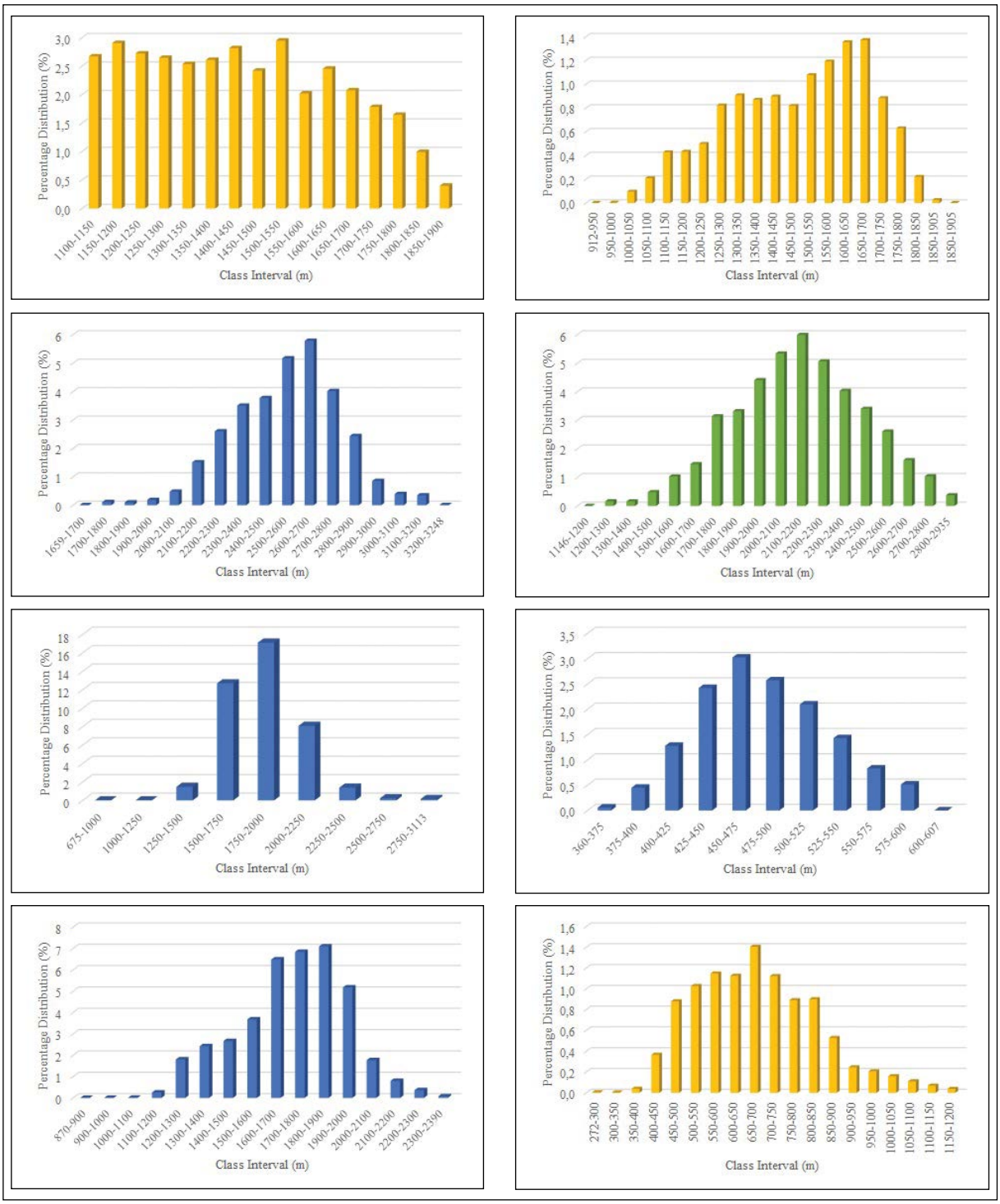

Figure 5- Continued.

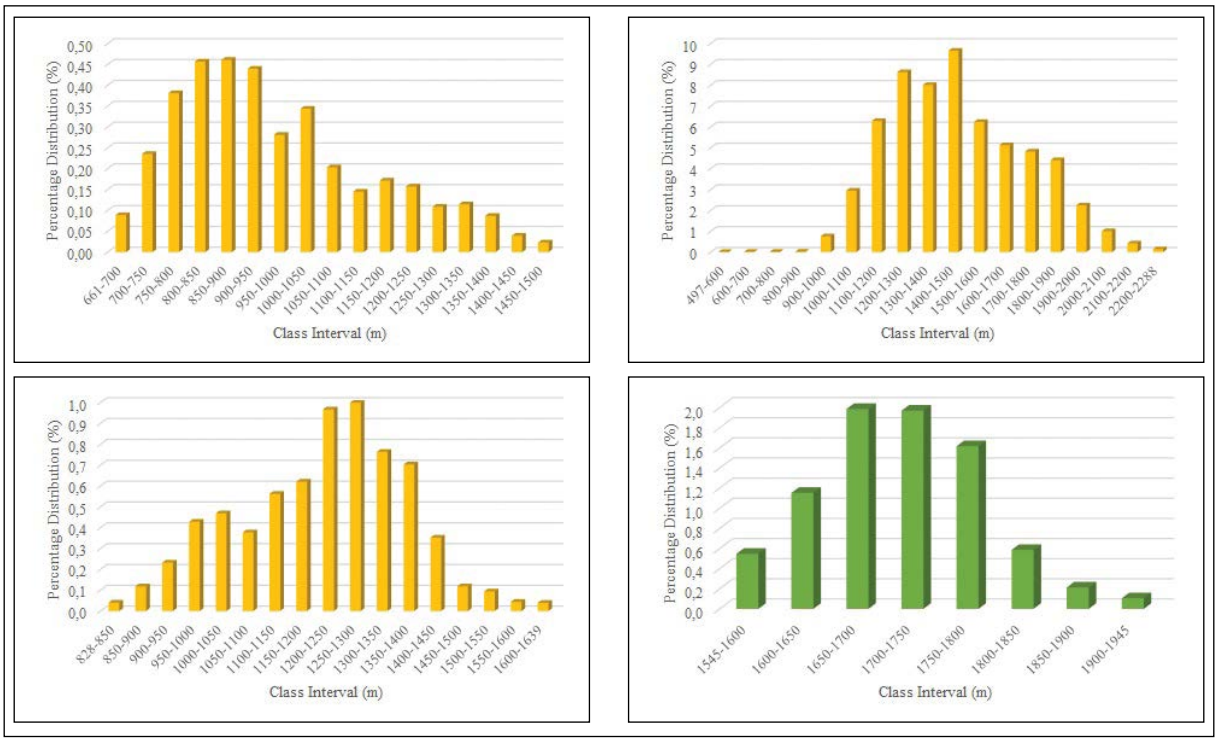

Figure 5- Continued.

8. Results and Discussion

The literature uses elevation values in two forms: relative and topographical. But topographical elevation is more commonly chosen. The most important reason that it is used as a parameter in susceptibility maps is that it is easy to access and produce.

When the parameter is evaluated by itself, an indirect effect from the influence of the other parameters becomes relevant, even if it is not influential. The effect of the parameter affects the entire system. The most affected parameter was the effect of precipitation, seismicity, temperature, flora and humans.

There is no clear elevation range at which landslides occur. Each area has unique properties. The increase of elevation in an area with seismicity also increases the severity of the formation of landslides. The change of climate conditions and flora with elevation concludes the same results. While terrain sometimes forms from lower elevations, it sometimes has higher elevations.

There are landslides that form in many different classes in the literature. Each area has its own unique elevation values. Therefore, elevation classes must reflect the character of the selected area. If this subject is to be assistance from the literature, determining the class range for the same areas is providing ideas about the effects of different areas but similar parameters (such as climate, terrain, anthropological effect, and temperature) as well as how they would be assessed.

Most studies in the literature assert that the intensity of landslides increases with the increase of elevation. Contrary to this, there are studies that assert that landslides cannot be seen at certain elevations. In addition to this, there are studies that assert that it is more susceptible to landslides at low and medium elevations. Some studies according to the literature say that landslides intensify at certain elevations while there are studies that assert that the effects of different elevations on susceptibility to landslides are also different.

It was seen in the selected map section analyses that each area has its own characteristics elevation values. Landslides varies based on the elevation values for their own study areas. Just as landslides can occur at very high elevations in other areas compared to one area, landslides can occur at low elevations. The

results of the analysis showed that landslide intensities increase gradually in any study area and reach a peak value at a certain point of elevation. If we are to generalize, while it cannot be envisaged that landslides will occur at a certain elevation value, landslides peak at average values at their own elevation values for the area for each area. This peak point, compared to other variables, is observed two or three more times in some areas.

Although it is not a determinant parameter for each area, the effect of elevation consequently is determinant if the study area comprises mountainous areas with different elevation values. The effect value also changes based on the parameter variables found for the same system. Landslides should be expected at the average elevation values of an area. It was reported that landslides occurred at certain elevation values for the study area (medium elevations for the field), although not at a certain elevation value.

Acknowledgement

This study was carried out within scope of MMF. A4.18.017 BAP project

References

Abedini, M., Ghasemyan, B., Mogaddam, M.H. 2017. Landslide susceptibility mapping in Bijar City, NW Province of Iran: A comparative study by logistic regression and AHP models. Environ Earth Science 292- 308.

Acharya, S., Pathak, D. 2017. Landslide hazard assessment between Besi Sahar and Tal area in Marsyangdi River Basin, West Nepal. Int. Journal of Advances in Remote Sensing and GIS 29-38.

Aghdam, I.N., Varzandeh, M.H.M., Pradhan, B. 2016. Landslide susceptibility mapping using an Ensemble Statistical İndex (Wi) and adaptive Neuro-Fuzzy Inference System (ANFIS) Model at Alborz Mountains (Iran). Environ Earth Sci 1-20.

Akıncı, H., Kılıçoğlu, C. 2015. Production of landslide susceptibility map of Atakum (Samsun) district. MÜHJEO'2015: National Engineering Geology Symposium, 3-5 September 2015, Trabzon.

Akıncı, H., Doğan, S., Kılıçoğlu, C., Keçeci, S.B. 2010. Production of landslide susceptibility map of Samsun province center. Electronic Journal of Map Technologies 13-27.

Akıncı, H., Doğan, S., Kılıçoğlu C. 2011. Production of landslide susceptibility map of Samsun City Center by using frequency ratio method. TMMOB Surveying Engineers, 13th Turkey Scientific and Technical Conference 18-22 April 2011, Ankara.

Akıncı, H., Özalp-Yavuz, A., Özalp, M., Temuçin-Kılıçer, S., Kılıçoğlu, C., Everan, E. 2014. Production of landslide susceptibility maps using bayesian probability theorem. 5. Remote Sensing-GIS Symposium (Uzal-GIS), 14-17 Oct., 2014, İstanbul.

Althuwaynee, O.F., Pradhan, B., Lee, S. 2016. A novel integrated model for assessing landslide susceptibility mapping using CHAID and AHP pair-wise comparison. International Journal of Remote Sensing 37-40.

Amirahmadi, A., Shiran, M., Zanganeh, Asadi, M., Keramati, F. 2017. Landslide susceptibility zonation using the fuzzy algebraic operators in GIS. Iran. J. Mater Environ Sci 50-59.

Anbalagan, R. 1992. Landslide hazard evaluation and zonation mapping in mountainous terrain. Engineering Geology 269-277.

Anbalagan, R., Singh, B. 1996. Landslide hazard and risk assessment mapping of mountainous terrains-a case study from Kumaun Himalaya, India. Engineering Geology 237-246.

Aniya, M. 1985. Landslide-susceptibility mapping in Amahata River Basin, Japan. Annals of the Association of American Geographers 102-114.

Ataol, M., Yeşilyurt, S. 2014. Identification of landslide risk zones along the Çankırı-Ankara (between Akyurt and Çankırı) state road. Istanbul University Faculty of Letters Department of Geography 51-69.

Avcı, V. 2016*a*. Analysis of landslide succeptibility of Manav Stream Basin (Bingöl). The Journal of International Social Research 42-49.

Avcı, V. 2016*b*. Landslide susceptibility analysis of Esence Stream Basin (Bingöl) by weight- of- evidence method. International Journal of Social Science 287-310.

Avcı, V. 2016*c*. The landslide susceptibility analysis of the Gökdere Basin and its surrounding region (The Southwest of Bingöl) according to the frequency ratio method. Marmara Geographical Review 160-177.

Avcı, V., Günek, H. 2014. The distribution of active landslides in Karlıova Basin and surrounding (Bingöl) according to lithology, elevation, slope, inspection and NDVI Parts. International Journal of Social Science 445-464.

Ayalew, L., Yamagishi, H. 2005. The application of GIS-based logistic regression for landslide

susceptibility mapping in the Kakuda-Yahiko Mountains, Central Japan. Geomorphology 15-31.

Ayalew, L., Yamagishi, H., Marui, H., Kanno, T. 2005. Landslides in Sado Island of Japan Part II. GIS-based susceptibility mapping with comparisons of results from two methods and verifications. Engineering Geology 432-445.

Baeza, C., Corominas, J. 2001. Assessment of shallow landslides susceptibility by means of multivariate statistical techniques. Earth Surface Processes and Landforms 251-1263.

Bai, S.B., Wang, J., Lü, G.N., Zhou, P.G., Hou, S.S., Xu, S.N. 2010. GIS-based logistic regression for landslide susceptibility mapping of the Zhongxian segment in the Three Gorges area, China. Geomorphology 23-31.

Bai, S.B., Xu, Q., Jian, W., Zhou, P. 2013. Pre-conditioning factors and susceptibility assessments of Wenchuan Earthquake landslide at the Zhouqu Segment of Bailongjiang Basin. China Journal of the Geological Society of India 82-95.

Bai, S.B., Wang, J., Thiebes, B., Cheng, C., Chang, Z.Y. 2014. Susceptibility assessments of the Wenchuan earthquake-triggered landslides in Longnan using logistic regression. Environmental Earth Sciences 731–743.

Balamurugan, G., Ramesh, V., Touthang, M. 2016. Landslide susceptibility zonation mapping using frequency ratio and fuzzy gamma operator models in part of NH-39, Manipur, India. Nat Hazards 465–488.

Balteanu, D., Chendes, V., Sima, M., Enciu, P. 2010. A country-wide spatial assessment of landslide susceptibility in Romania. Geomorphology 102–112.

Caniani, D., Pascale, S., Sdao, F., Sole, A. 2008. Neural networks and landslide susceptibility: A case study of the urban area of Potenza. Natural Hazards 55–72.

Carrara, A. 1983. Multivariate models for landslide hazard evaluation. Mathematical Geology 403–426.

Carrara, A., Cardinalı, M., Detti, R., Guzzetti, F., Pasqui, V., Reichenbach, P. 1991. GIS techniques and statistical models in evaluating landslide hazard. Earth Surface Processes and Landforms 427-445.

Chalkias, C., Ferentinou, M., Polykretis, C. 2014. GIS-based landslide susceptibility mapping on the Peloponnese Peninsula, Greece Geosciences 176-190.

Chau, K. T., Chan, J. E. 2005. Regional bias of landslide data in generating susceptibility maps using logistic regression: Case of Hong Kong Island. Landslides 280–290.

Chauhan, S., Sharma, M., Arora, M.K., Gupta, N. K. 2010. Landslide susceptibility zonation through ratings derived from artificial neural network. International Journal of Applied Earth Observation and Geoinformation 340-350.

Chen, Z., Wang, J. 2007. Landslide hazard mapping using logistic regression model in Mackenzie Valley, Canada. Natural Hazards 75-89.

Chen, C.W., Saito, H., Oguchi, T. 2015. Rainfall intensity–duration conditions for mass movements in Taiwan, Progress in. Earth and Planetary Science 1–13.

Chen, S.C., Chang, C.C., Chan, H.C., Huang, L.M., Lin, L.L. 2013. Modeling typhoon event-induced landslides using GIS-based logistic regression: A case study of Alishan Forestry Railway, Taiwan. Math. Prob. Eng. URL: https://www.hindawi.com/journals/mpe/2013/728304/.

Chen, W., Chai, H., Sun, X., Wang, Q., Ding, X., Hong, H. 2016*a*. A GIS-based comparative study of frequency ratio, statistical index and weights-of-evidence models in landslide susceptibility mapping. Arab J Geosci 204-215.

Chen, W., Wang, J., Xie, X., Hong, H., Trung Van N., Bui, D. T., Wang, G., Li, X. 2016*b*. Spatial prediction of landslide susceptibility using integrated frequency ratio with entropy and support vector machines by different kernel functions. Environ Earth Sci 1344-1350.

Chen, W., Pourghasemi, H. R., Kornejady, A., Zhang, N. 2017. Landslide spatial modeling: Introducing new ensembles of ANN, MaxEnt, and SVM machine learning techniques. Geoderma 314–327.

Chen, W., Pourghasemi, H. R., Kornejady, A., Xie, X. 2018. GIS-based landslide susceptibility evaluation using certainty factor and index of entropy ensembled with alternating decision tree models, In book: Natural Hazards GIS-Based Spatial Modeling Using Data Mining Techniques. Advances in Natural and Technological Hazards Research 48-57.

Chen, W., Sun, Z., Han, J. 2019. Landslide susceptibility modeling using ıntegrated ensemble weights of evidence with logistic regression and random forest models. Applied Sciences 17-29.

Clerici, A., Perego, S., Tellini, C., Vescovi, P. 2006. A GIS-based automated procedure for landslide susceptibility mapping by the conditional analysis method: the Baganza valley case study (Italian Northern Apennines). Environmental Geology 941-961.

Coe, J.A., Michael, J.A., Crovelli, R.A., Savage, W.Z., Laprade, W.T., Nashem, W.D. 2004*a*. Probabilistic assessment of precipitation triggered landslides

using historical records of landslide occurrence, Seattle, Washington. Environ Eng Geosc 103–122.

Coe, J.A., Godt, J.W., Baum, R.L., Bucknam, R.C., Michael, J.A., 2004*b*. Landslide susceptibility from topography in Guatemala, In: Lacerda WA et al. (ed) Landslides, evaluation and stabilization. Proceedings of the 9th International Symposium on Landslides, Rio de Janeiro, 69–79.

Conforti, M., Pascale, S., Robustelli, G., Sdao, F. 2014. Evaluation of prediction capability of the artificial neural networks for mapping landslide susceptibility in the Turbolo River catchment (northern Calabria Italy). Catena 236-250.

Creighton, R. 2006. A Report of the Irish Landslides Working Group. Geological Survey of Ireland 100-109.

Çellek, S. 2013. Landslide susceptibility analysis of Sinop-Gerze region. Doctora Thesis, KTU, Trabzon (unpublished).

Çellek, S., Bulut, F., Ersoy, H. 2015. Utilization and Application of AHP Method in Landslide Susceptibility Mapping Production (Sinop and its Surroundings), Research Article. Journal of Geological Engineering 59-90.

Çevik, E., Topal, T. 2003. GIS-based landslide susceptibility mapping for a problematic segment of the natural gas pipeline, Hendek (Turkey). Environmental Geology 949-962.

Dağ, S. 2007. Landslide Susceptibility Analysis of Çayeli (Rize) and its Surranding by Statistical Methods. Doktorate Thesis, KTU, Trabzon, (unpublished).

Dağ, S., Bulut, F. 2012. Preparation of GIS-based landslide susceptibility maps: Çayeli (Rize, NE Türkey) Research Article. Journal of Geological Engineering 35-62.

Dai, F.C., Lee, C.F. 2001. Terrain-based mapping of landslide susceptibility using a geographical information system: A case study. Can Geotech J 911–923.

Dai, F.C., Lee, C.F. 2002. Landslide characteristics and slope instability modeling using GIS, Lantau Island, Hong Kong. Geomorphology 213–228.

Dai, F.C., Lee, C.F. 2003. A spatiotemporal probabilistic modelling of storm induced shallow landsliding using aerial photographs and logistic regression. Earth Surf Process Landforms 527–545.

Dehnavi, A., Aghdam, I.N., Pradhan, B., Varzandeh, M.H.M. 2015. A new hybrid model using step-wise weight assessment ratio analysis (SWARA) technique and adaptive neuro-fuzzy ınference system (ANFIS) for regional landslide hazard assessment in Iran. Catena 122–148.

Demir, G. 2016. Landslide susceptibility assessment of the 1 part of the North Anatolian Fault Zone (Turkey) by GIS-based frequency ratio and index of entropy models. Nat. Hazards Earth Syst Sci 327-340.

Devkota, K.C., Regmi, A.D., Pourghasemi, H.R., Yoshida, K., Pradhan, B., Ryu, I.C., Dhital, M.R., Althuwaynee, O.F. 2013. Landslide susceptibility mapping using certainty factor, index of entropy and logistic regression models in GIS and their comparison at Mugling–Narayanghat road section in Nepal Himalaya. Nat. Hazards 135–165.

Ding, Q., Chen, W., Hong, H. 2017. Application of frequency ratio, weights of evidence and evidential belief function models in landslide susceptibility mapping, Geocarto International. URL:https://www.researchgate.net/publication/298425978_Application_of_frequency_ratio_weights_of_evidence_and_evidential_belief_function_models_in_landslide_susceptibility_mapping

Dou, J., Yamagishi, H., Xu, Y., Zhu, Z., Yunus, A.P. 2017. Characteristics of the torrential rainfall-ınduced shallow landslides by typhoon bilis, in July 2006, using remote sensing and GIS. In book: GIS Landslide Publisher: Springer Japan, URL:https://www.researchgate.net/publication/317041333_Characteristics_of_the_Torrential_RainfallInduced_Shallow_Landslides_by_Typhoon_Bilis_in_July_2006_Using_Remote_Sensing_and_GIS

Dölek, İ., Avcı, V. 2016. Determination of areas with landslide susceptibility in Arguvan district (Malatya province) and its surrounding by multi-criteria decision analysis method (MDAM). The Journal of Academic Social Science 106-129.

Dragicevi, C.S., Lai, T., Balram, S. 2015. GIS-based multicriteria evaluation with multiscale analysis to characterize urban landslide susceptibility in data-scarce environments. Habitat International 114–125.

Duman, T.Y., Çan, T., Gökçeoğlu, C., Nefeslioğlu, H.A., Sönmez, H. 2006. Application of logistic regression for landslide susceptibility zoning of Çekmece Area (İstanbul, Turkey). Environmental Geology 241-256.

Eker, A.M., Dikmen, M., Cambazoğlu, S., Akgün, H. 2012. Application of artificial neural network and logistic regression methods to landslide susceptibility mapping and comparison of the results for the Ulus district, Bartın. Journal of the Faculty of Engineering and Architecture of Gazi University 163-173.

Elkadiri, R., Sultan, M., Youssef, A.M., Elbayoumi, T., Chase, R., Bulkhi, A.B., Al-Katheeri, M.M. 2014. A remote sensing-based approach for debris-flow susceptibility assessment using artificial neural networks and logistic regression modeling. IEEE

Journal of Selected Topics in Applied Earth Observations and Remote Sensing 4818–4835.

Ercanoğlu, M. 2003. Production of landslide susceptibility maps by fuzzy logic and statistical methods: Western Black Sea Region (Kumluca-Yenice). Doctora Thesis, Hacettepe University, Ankara, (unpublished).

Ercanoğlu, M. 2005. Landslide susceptibility assessment of SE Bartin (West Black Sea region, Turkey) by artificial neural networks. Natural Hazards Earth System Science 979–992.

Ercanoğlu, M., Gökceoğlu, C. 2002. Assessment of landslide susceptibility for a landslide prone area (north of Yenice, NW Turkey) by fuzzy approach. Environmental Geology 720–730.

Ercanoğlu, M., Gökçeoğlu, C. 2004. Use of fuzzy relations to produce landslide susceptibility map of a landslide prone area (West Black Sea Region, Turkey). Engineering Geology 229–250.

Ercanoğlu, M., Gökceoğlu, C., Van Asch, Th. W.J. 2004. Landslide susceptibility zoning north of Yenice (NW Turkey) by multivariate statistical techniques. Natural Hazards 1–23.

Ercanoğlu, M., Kasmer, O., Temiz, N. 2008. Adaptation and comparison of expert opinion to analytical hierarchy process for landslide susceptibility mapping. Bulletin of Engineering Geology and the Environment 565–578.

Erener, A., Lacasse, S., 2007. Landslide Susceptibility Mapping Using GIS. TMMOB Chamber of Survey and Cadastre Engineers National Geographic Information Systems Congress, KTÜ, Trabzon.

Fenghuan, S., Peng, C., Jianqiang, Z., Lingzhi, X., 2010. Susceptibility assessment of landslides caused by the Wenchaun earthquake using a logistic regression model. Journal of Mountain Science 234-245.

Fernandez, T., Irigaray, C., El Hamdouni, R., Chacon, J. 2003. Methodology for landslide susceptibility mapping by means of a GIS. Application to the contraviesa area (Granada, Spain). Nat. Hazards 297–308.

Fernandez, T., Jimenez, J., Fernandez, P., El Hamdouni, R., Cardenal, F.J., Delgado, J., Irigaray, C., Chacon, J. 2008. Automatic detection of landslide features with remote sensing techniques in the Betic Cordilleras (Granada, Southern Spain). Int Soc Photogramme, 351-356.

Gallart, F., Clotet, N. 1988. Some aspects of the geomorphic processes triggered by an extreme rainfall event: The November 1982 flood in The Eastern Pyrenees. Catena 79–95.

Gattinoni, P. 2009. Parametrical landslide modeling for the hydrogeological susceptibility assessment: from the Crati Valley to the Cavallerizzo landslide (Southern Italy). Natural Hazards: Journal of the International Society for the Prevention and Mitigation of Natural Hazards 161-178.

Goetz, J.N., Brenning, A., Petschko, H., Leopold, P. 2015. Evaluating machine learning and statistical prediction techniques for landslide susceptibility modeling. Comput. Geosci. 1–11.

Gomez, H., Kavzoğlu, T. 2005. Assessment of shallow landslide susceptibility using artificial neural networks in Jabonosa River Basin, Venezuela. Engineering Geology 11–27.

Gorsevski, P.V., Jankowski, P. 2008. Discerning landslide susceptibility using rough sets. Computers, Environment and Urban Systems 53-65.

Gorsevski, P.V., Donevska, K.R., Mitrovski, C.D., Frizado, J.P. 2012. Integrating multi-criteria evaluation techniques with geographic information systems for landfill site selection: A case study using ordered weighted average. Waste Management 287-296.

Gökçeoğlu, C., Ercanoğlu, M. 2001. Uncertainties on the parameters employed in preparation of landslide susceptibility maps. Bulletin of Earth Sciences Application and Research Centre of Hacettepe University, 189-206.

Gökçeoğlu, C., Sönmez, H., Nefeslioğlu, H.A., Duman, T.Y., Çan, T. 2005. The 17 March 2005 Kuzulu landslide (Sivas, Turkey) and landslide–susceptibility map of its near vicinity. Engineering Geology 65–83.

Görcelioğlu, E. 2003. Flood and avalanche control. Istanbul University Publication Faculty of Forestry Publication, 473-490.

Görüm, T. 2006. Landslide susceptibility analysis with geographic information systems and statistical methods: Melen Gorge and near vicinty. İstanbul University, Master Thesis, Istanbul (unpublished).

Gritzner, M.L., Marcus, W.A., Aspinall, R., Custer, S.G. 2001. Assessing landslide potential using GIS, soil wetness modelling and topographic attributes. Payette River, Idaho, Geomorphology 149-165.

Gruber, S., Haeberli, W. 2007. Permafrost in steep bedrock slopes and its temperature-related destabilization following climate change. J Geophys Res 112-130, URL: https://agupubs.onlinelibrary.wiley.com/doi/10.1029/2006JF000547

Hasekioğulları, G.D. 2011. Assessment of parameter effects in producing landslide susceptibility maps. Master Thesis, Hacettepe University, Ankara (unpublished).

He, S., Li, D., Wu, Luo, Y. 2011. Study on the rainfall and aftershock threshold for debris flow of post-earthquake. J. Mountain Sci 750–756.

Hong, H., Chen, W., Xu, C., Youssef, A.M., Pradhan, B., Tien, Bui, D. 2017*a*. Rainfall-induced landslide susceptibility assessment at the Chongren area (China) using frequency ratio, certainty factor, and index of entropy. Geocarto Int 139–154.

Hong, H., Ilia, I., Tsangaratos, P., Chen, W., Xu, C. 2017*b*. A hybrid fuzzy weight of evidence method in landslide susceptibility analysis on the Wuyuan area, China. Geomorphology 1–16.

Ilia, I., Tsangaratos, P. 2016. Applying weight of evidence method and sensitivity analysis to produce a landslide susceptibility map. Landslides 379–397.

Jaafari, A., Najafi, A., Pourghasemi, H.R., Rezaeian, J., Sattarian, A. 2014. GIS-based frequency ratio and index of entropy models for landslide susceptibility assessment in the Caspian forest, northern Iran. Int J Environ Sci Technol 909–926.

Jaafari, A., Najafi, A., Rezaeian, J., Sattarian, A. 2015*a*. Modeling erosion and sediment delivery from unpaved roads in the north mountainous forest of Iran. International Journal on Geomathematics 343–350.

Jaafari, A., Najafi, A., Rezaeian, J., Sattarian, A., Ghajar, I. 2015*b*. Planning road networks in landslide-prone areas: A case study from the northern forests of Iran. Land Use Policy 198–208.

Jebur, M.N., Pradhan, B., Tehrany, M.S. 2015. Manifestation of LiDAR derived parameters in spatial prediction of landslides using a novel ensemble evidential belief functions and support vector machine models in GIS. IEEE J Sel Top Appl Earth Obs Remote Sens 674-689.

Jimenez-Peralvarez, J.D., Irigaray, C., El Hamdouni, R., Chacon, J. 2009. uilding models for automatic landslide-susceptibility analysis, mapping and validation in ArcGIS. Nat Hazards, 571 – 590.

Juang, C.H., Lee, D.H., Sheu, C. 1992. Mapping slope failure potential using fuzzy sets. Journal of Geotechnical Engineering ASCE 475–494.

Kamp, U., Growley, B.J., Khattak, G.A., Owen, L.A. 2008. GIS-based landslide susceptibility mapping for the 2005 Kashmir earthquake region. Geomorphology 631–642.

Kavzoğlu, T., Çölkesen, İ. 2010. Classification of Satellite Images Using Decision Trees: Kocaeli Case. Electronic Journal of Map Technologies 36-45.

Kavzoğlu, T., Çölkesen, İ., Şahin, E.K. 2012. Investigation of the Effects of Factors Used in Production of Landslide Susceptibility Maps: A Case Study in Düzköy. IV. Remote Sensing and Geographic Information Systems Symposium (UZAL-GIS), Oct., 2012, Zonguldak.

Kavzoğlu, T., Şahin, E.K., Çölkesen, İ. 2014. Factor Selection based on Chi-Square Test in Landslide Sensitivity Analysis. V. Remote Sensing and Geographical Information Systems Symposium (UZAL-GIS), 14-17 Oct.,2014, İstanbul.

Kornejady, A., Heidari, K., Nakhavali, M. 2015. Assessment of landslide susceptibility, semi-quantitative risk and management in the Ilam dam basin, Ilam, Iran Environ Resour Res 85–109.

Kornejady, A., Ownegh, M., Bahremand, A. 2017*a*. Landslide susceptibility assessment using maximum entropy model with two different data sampling methods. Catena 144–162.

Kornejady, A., Ownegh, M., Rahmati, O., Bahremand, A. 2017*b*. Landslide susceptibility assessment using three bivariate models considering the new topo-hydrological factor: HAND. Geocarto Int 1155–1185.

Koukis, G., Ziourkas, C. 1991. Slope Instability Phenomena in Greece: A Statistical Analysis. Bulletin of International Association of Engineering Geologists 47-60.

Kouli, M., Loupasakis, C., Soupios, P., Rozos, D., Vallianatos, F. 2014. Landslide susceptibility mapping by comparing the WLC and WofE mutli-criteria methods in the West Crete Island, Greece. Environ Earth Sci.

Lan, H.X., Zhou, C.H., Wang, L.J., Zhang, H.Y., Li, R.H., 2004. Landslide hazard spatial analysis and prediction using GIS in the Xiaojiang watershed, Yunnan, China Eng Geol 109–128.

Lee, S., Pradhan, B., 2007. Landslide hazard mapping at Selangor, Malaysia using frequency ratio and logistic regression models. Landslides 33–41.

Lee, S., Choi, J., Min, K. 2002. Landslide susceptibility analysis and verication using the bayesian probability model. Enviromental Geology 120-131.

Leonardi, G., Palamaraa, R., Ciriannia, F. 2016. Landslide Susceptibility mapping using a fuzzy approach procedia engineering, World Multidisciplinary Civil Engineering-Architecture-Urban Planning Symposium, WMCAUS, 380–387.

Liu, C., Li, W., Wu, H. 2013. Susceptibility evaluation and mapping of China's landslides based on multi-source data. Natural Hazards 1477–1495.

Liu, S., Wu, Y. 2016. Landslide susceptibility mapping in the Gangu County, China using artificial neural network and Gis. Bund 7614-7628.

Mashari, S., Solaimani, K., Omidvar, E. 2012. Landslide susceptibility mapping using multiple regression and gıs tools in Tajan Basin, north of Iran. URL:https://www.researchgate.net/publication/311921212_Landslide_Susceptibility_Mapping_ Using_Multiple_Regression_and_GIS_Tools_in_Tajan_Basin_North_of_Iran

Mazman, T. 2005. Landslide susceptibility assessment in Kumluca (SE Bartın) watershed by geoeraphic information systems and statistical analysis methods. Master Thesis, Çukurova University, Adana (unpublished).

Meng, Q., Miao, F., Zhen, J., Wang, X., Wang, A., Peng, Y., Fan, Q. 2015. GIS-based landslide susceptibility mapping with logistic regression, analytical hierarchy process, and combined fuzzy and support vector machine methods: A case study from Wolong Giant Panda Natural Reserve, China Bull Eng Geol Environ.

Meng, X., Pei, X., Liu, Q., Zhang, X., Hu, Y. 2016. GIS-based environmental assessment from three aspects of geology, ecology and society along the road from Dujiangyan to Wenchuan, Mt Res 110–120.

Mohammady, M., Pourghasemi, H.R., Pradhan, B. 2012. Landslide susceptibility mapping at Golestan Province Iran: A comparison between frequency ratio, Dempster-Shafer, andweights of evidence models. J Asian Earth Sci 221-230.

Moore, I.D., Grayson, R.B., Ladson, A.R. 1991. Digital terrain modelling: A review of hydrological, geomorphological and biological applications. Hydrological Processes 23-30.

Moradi, S., Rezaei, M. 2014. A GIS-based comparative study of the analytic hierarchy process, bivariate statistics and frequency ratio methods for landslide susceptibility mapping in part of the Tehran metropolis, Iran J Geope 45-61.

Myronidis, D., Papageorgiou, C., Theophanous, S. 2016. Landslide susceptibility mapping based on landslide history and analytic hierarchy process (AHP). Nat. Hazards 245–263.

Nagarajan, R., Roy, A., Vinod, Kumar, R., Mukherjee, A., Khire, M.V. 2000. Landslide hazard susceptibility mapping based on terrain and climatic factors for tropical monsoon regions. Bulletin of Engineering Geology and the Environment 275–287.

Nefeslioğlu, H., Gökceoğlu, C., Sönmez, H. 2008. An assessment on the use of logistic regression and artificial neural networks with different sampling strategies for the preparation of landslide susceptibility maps. Engineering Geology 171-191.

Nourani, V., Pradhan, B., Ghaffari, H., Sharifi, S.S. 2014. Landslide susceptibility mapping at Zonouz Plain, Iran using genetic programming and comparison with frequency ratio, logistic regression and artificial neural network models. Nat Hazards 523–547.

Ochoa, G. 1978. La influencia de la altitud sobre algunas propiedades fisico-qui´micas de los suelos de los Andes venezolanos. Revista Geograifica 56–72.

Oh, H.J., Pradhan, B. 2011. Application of a neuro-fuzzy model to landslide-susceptibility mapping for shallow landslides in a tropical hilly area. Computers&Geosciences 1264-1276.

Opiso, E.M., Puno, G.R., Alburo, J.L.P., Detalla, A.L. 2016. Landslide susceptibility mapping using GIS and FR method along the Cagayan de Oro-Bukidnon-Davao City route corridor, Philippines. KSCE Journal of Civil Engineering 2506–2512.

Özdemir, A. 2009. Landslide susceptibility mapping of vicinity of Yaka Landslide (Gelendost, Turkey) using conditional probability approach in GIS. Environ Geol 1675–1686.

Özdemir, A., Altural, T. 2013. A comparative study of frequency ratio, weights of evidence and logistic regression methods for landslide susceptibility mapping: Sultan Mountains, SW Turkey. J Asian Earth Sci 180–197.

Özşahin, E. 2015. Landslide susceptibility analysis by geographical information systems: the case of Ganos Mount (Tekirdağ). Electronic Journal of Map Technologies 47-63.

Özşahin, E., Kaymaz, Ç.K. 2013. Landslide susceptibility analysis of camili (Macahel) Biosphere Reserve Area (Artvin, NE Turkey). Turkish Studies - International Periodical for The Languages, Literature And History Of Turkish Or Turkic, 471-493.

Pachauri, A.K., Pant, M. 1992. Landslide hazard mapping based on geological attributes. Engineering Geology 81-100.

Pachauri, A.K., Gupta, P.V., Chander, R. 1998. Landslide zoning in a part of the Garhwal Himalayas. Env Geol 325-334.

Padrones, J. T., Ramos, N.T., Dimalanta, C.B., Queaño, K.L., Faustino-Eslava, D.V., Yumul, G.P. Jr., Watanabe, K. 2017. Landslide Susceptibility mapping in a geologically complex terrane: A case study from northwest Mindoro, Philippines Manila. Journal of Science 25–44.

Park, S., Jeon, S., Choi, C. 2010. Mapping urban growth probability in South Korea: Comparison of frequency ratio, analytic hierarchy process, and logistic regression models and use of the

environmental conservation value assessment. Landscape and Ecological Engineering.

Pawluszek, K., Borkowski, A. 2017. Impact of DEM-derived factors and analytical hierarchy process on landslide susceptibility mapping in the region of Rożnów Lake, Poland. Natural Hazards 919–952.

Peng, L., Niu, R., Huang, B., Wu, X., Zhao, Y., Ye, R. 2014. Landslide susceptibility mapping based on rough set theory and support vector machines: A case of the Three Gorges area, China. Geomorphology 287–301.

Pham, B.T., Tien, Bui, D., Indra, P., Dholakia, M. 2015. Landslide susceptibility assessment at a part of Uttarakhand Himalaya, India using GIS-based statistical approach of frequency ratio method. Int J Eng Res Technol 338–344.

Pham, B.T., Bui, D.T., Dholakia, M., Prakash, I., Pham, H.V. 2016. A comparative study of least square support vector machines and multiclass alternating decision trees for spatial prediction of rainfall-induced landslides in a tropical cyclones area. Geotech Geol Eng 1–18.

Pham, B.T., Bui, D.T., Prakash, I., Dholakia, M.B. 2017. Hybrid integration of multilayer perceptron neural networks and machine learning ensembles for landslide susceptibility assessment at Himalayan area (India) using GIS. Catena 52–63.

Pourghasemi, H.R., Gökçeoğlu, C., Pradhan, B., Deylami, Moezzi, K. 2012*a*. Landslide susceptibility mapping using a spatial multicriteria evaluation model at Haraz Watershed Iran, In: Pradhan B, Buchroithner M (eds) Terrigenous mass movements, Springer Berlin, 23–49.

Pourghasemi, H.R., Pradhan, B., Gökçeoğlu, C. 2012*b*. Application of fuzzy logic and analytical hierarchy process (AHP) to landslide susceptibility mapping at Haraz watershed Iran. Nat Hazards URL:https://www.researchgate.net/publication/230875072_Application_of_fuzzy_logic_and_analytical_hierarchy_process_AHP_to_landslide_susceptibility_mapping_at_Haraz_watershed_Iran

Pourghasemi, H.R., Mohammady, M., Pradhan, B. 2012*c*. Landslide susceptibility mapping using index of entropy and conditional probability models in GIS: Safarood Basin, Iran. Catena 97, 71–84.

Pourghasemi, H.R., Pradhan, B., Gökçeoğlu, C. 2012*d*. Remote sensing data derived parameters and its use in landslide susceptibility assessment using Shannon's entropy and GIS. AEROTECH IV–2012, Appl Mech Mater, 486–491.

Pourghasemi, H.R., Pradhan, B., Gökçeoğlu, C., Mohammadi, M., Moradi, H.R. 2012*e*. Application of weights-of-evidence and certainty factor models and their comparison in landslide susceptibility mapping at Haraz watershed, Iran. Arab J Geosci 2351–2365.

Pourghasemi, H.R., Moradi, H.R., Aghda, S.F. 2013*a*. Landslide susceptibility mapping by binary logistic regression, analytical hierarchy process, and statistical index models and assessment of their performances. Nat Hazards 749–779.

Pourghasemi, H.R., Pradhan, B., Gökçeoğlu, C., Mohammadi, M., Moradi, H.R., 2013*b*. Application of weights-of-evidence and certainty factor models and their comparison inlandslide susceptibility mapping at Haraz watershed, Iran. Arab J Geosci 2351.

Pourghasemi, H.R., Beheshtirad, M. 2015. Assessment of a data–driven evidential belief function model and GIS for groundwater potential mapping in the Koohrang Watershed, Iran. Geocarto Int 662–685.

Pourghasemi, H.R., Kerle, N. 2016. Random forests and evidential belief function-based landslide susceptibility assessment in Western Mazandaran province, Iran. Environmental Earth Sciences 185.

Pourghasemi, H.R., Rossi, M. 2017. Landslide susceptibility modeling in a landslide prone area in Mazandarn Province, north of Iran: a comparison between GLM, GAM, MARS, and M-AHP methods. Theor Appl Climatol 609–633.

Pourtaghi, Z.S., Pourghasemi, H.R., Rossi, M. 2014. Forest fire susceptibility mapping in the Minudasht forests, Golestan province, Iran. Environ Earth 1515–1533.

Pradhan, A.M.S., Kim, Y.T. 2014. Relative effect method of landslide susceptibility zonation in weathered granite soil: a case study in Deokjeok-ri Creek, South Korea. Natural Hazards 1189–1217.

Pradhan, A.M.S, Kim, Y.T. 2015. Application and comparison of shallow landslide susceptibility models in weathered granite soil under extreme rainfall events. Environ. Earth Sci 5761–5771.

Pradhan, A.M.S., Kim, Y.T. 2017. Spatial data analysis and application of evidential belief functions to shallow landslide susceptibility mapping at Mt. Umyeon, Seoul, Korea. Bull Eng Geol Environ 1263–1279.

Pradhan B, Abokharima, M.H., Jebur, M.N., Tehrany, M.S. 2014. Land subsidence susceptibility mapping at Kinta Valley (Malaysia) using, the evidential belief function model in GIS. Nat Hazards 112.

Raja, N. B., Çiçek, I., Türkoğlu, N., Aydın, O., Kawasaki, A. 2017. Landslide susceptibility mapping of the Sera River Basin using logistic regression model. Natural Hazards 1323-1346.

Ramesh, V., Anbazhagan, S. 2015. Landslide susceptibility mapping along Kolli hills Ghat road section (India) using frequency ratio, relative effect and fuzzy logic models. Environ Earth Sci 8009–8021.

Ray, R.L., Jacobs, J.M. 2007. Relationships among remotely sensed soil moisture, precipitation and landslide events. Natural Hazards 211–222.

Rozos, D.E.L., Skias, P.S., Tsangaratos, P. 2008. An implementation of rock engineering system for ranking the instability potential of natural slopes in Greek territory. An application in Karditsa County. Landslides 261-270.

Rozos, D., Bathrellos, G.D., Skilodimou, H.D. 2010. Landslide susceptibility mapping of the northeastern part of Achaia Prefecture using Analytical Hierarchical Process and GIS techniques. Bulletin of the geological society of Greece, Proceeding of the12th International Congress, Patras may, XLIII, 1637-1646.

Rozos, D., Bathrellos, G.D., Skilodimou, H.D. 2011. Comparison of the implementation of rock engineering system and analytic hierarchy process methods, upon landslide susceptibility mapping, using GIS: A case study from the Eastern Achaia County of Peloponnesus Greece. Environ Earth Sci 49–63.

Sabatakakis, N., Koukis, G., Vassiliades, E., Lainas, S. 2013. Landslide susceptibility zonation in Greece. Natural Hazards 523–543.

Saadatkhahi, N., Kassimi, A., Lee, M. L. 2014. Qualitative and quantitative landslide susceptibility assessments in Hulu Kelang area, Malaysia. EJGE, 545-563. URL: http://www.ejge.com/2014/Ppr2014.047mar.pdf

Sadr, M. P., Abbas, M., Bashir, S.S. 2014. Landslide susceptibility mapping of Komroud sub-basin using fuzzy logic approach. Geodyn Res Int Bull 14–27.

Sancar, C. 2000. Economy-ecology sensitive planning model and GIS for determination of urban development areas and planning. Phd Thesis, KTU, Trabzon (unpublished).

Schicker, R., Moon, V. 2012. Comparison of bivariate and multivariate statistical approaches in landslide susceptibility mapping at a regional scale. Geomorphology 40-57.

Sezer, E.A., Pradhan, B., Gökçeoğlu, C. 2011. Manifestation of an adaptive neuro-fuzzy model on landslide susceptibility mapping: Klang valley, Malaysia. Expert Systems with Applications 8208-8219.

Shrestha, S., Kang, T.S., Suwal, M. 2017. An Ensemble model for co-seismic landslide susceptibility using gıs and 29 random forest method. ISPRS International Journal of Geo-Information 365.

Simon, N. de Róiste M., Crozier, M., Rafek, A.G. 2017. Representing Landslides as Polygon (Areal) or Points? How Different Data Types Influence the Accuracy of Landslide Susceptibility Maps, Sains Malaysiana, 27-34.

Sujatha, E.R., Kumaravel, P., Rajamanickam, G.V. 2014. Assessing landslide susceptibility using Bayesian probability-based weight of evidence model. Bull Engg Geol Environ 147–161.

Süzen, M.L., Doyuran, V. 2004*a*. Data driven bivariate landslide susceptibility assessment using geographical information systems: a method and application to Asarsuyu catchment, Turkey. Engineering Geology 303-321.

Süzen, M.L., Doyuran, V. 2004*b*. A comparison of the GIS based landslide susceptibility assessment methods: Multivariate Versus Bivariate. Environmental Geology 665-679.

Süzen, M.L., Kaya, B.Ş. 2011. Evaluation of environmental parameters in logistic regression models for landslide susceptibility mapping. Int J Digit Earth 1–18.

Tangestani, M.H. 2003. Landslide susceptibility mapping using the fuzzy gamma operation in a GIS, Kakan catchment area, Iran. Map India Conference. URL:file:///C:/Users/Dekan/Downloads/Landslide susceptibility_mapping_using thefuzzyg.pdf

Tangestani, M. H. 2004. Landslide susceptibility mapping using the fuzzy gamma approach in a GIS, Kakan catchment area, southwest Iran. Australian Journal of Earth Sciences 439–450.

Tanoli, J. I., Ningsheng, C., Regmi, A. D., Jun, L. 2017. Spatial distribution analysis and susceptibility mapping of landslides triggered before and after Mw7.8 Gorkha earthquake along Upper Bhote Koshi, Nepal. Arabian Journal of Geosciences 10-13.

Tazik, E., Jahantab, Z., Bakhtiari, M., Rezae, A., Alavipanah, S. K. 2014. Landslide susceptibility mapping by combining the three methods Fuzzy Logic, Frequency Ratio and Analytical Hierarchy Process in Dozain Basin. International Conference on Geospatial Information Research (GI Research) 15-17 November 2014, Tehran, Iran.

Tsangaratos, P., Ilia, I. 2016. Comparison of a logistic regression and Naïve Bayes classifier in landslide susceptibility assessments: the influence of models complexity and training dataset size. Catena 164–179.

Umar, Z., Pradhan, B., Ahmad, A., Neamah, Jebur, M., Shafapour, Tehrany, M. 2014. Earthquake induced landslide susceptibility mapping using an integrated ensemble frequency ratio and logistic regression models in West Sumatera province, Indonesia. Catena 124–135.

Vivas, L. 1992. Los Andes Venezolanos, Academia Nacional de la Historia, Caracas.Wan, S., Lei, T. C., Chou, T.Y. 2012. Alandslide expert system: image classification through integration of data mining approaches for multi-category analysis. International Journal of Geographical Information Science 747-770.

Wang, H. Q., He, J., Liu, Y., Sun, S. 2016. Application of analytic hierarchy process model for landslide susceptibility mapping in the Gangu County, Gansu Province, China. Environ Earth Sci 422.

Wang, L., Guo, M., Sawada, K., Lin, J., Zhang, J. 2015. Landslide susceptibility mapping in Mizunami city, Japan: a comparison between logistic regression, bivariate statistical analysis and multivariate adaptive regression spline models. Geomorphology 271–282.

Wang, Y., Zhao, B., Li, J. 2017. Mechanism of the catastrophic June 2017 landslide at Xinmo Village, Songping River, Sichuan Province, China. Landslides 333–345.

Wu, Y., Ke, Y. 2016. Landslide susceptibility zonation using GIS and evidential belief function model. Arabian Journal of Geosciences 697.

Wu, Y., Li, W., Liu, P., Bai, H., Wang, Q., He, J., Liu, Y., Sun, S. 2016. Application of analytic hierarchy process model for landslide susceptibility mapping in the Gangu County, Gansu Province, China. Environ Earth Sci 422.

Xu, C., Xu, X.W. 2012. Spatial prediction models for seismic landslides based on support vector machine and varied kernel functions: a case study of the 14 April 2010 Yushu earthquake in China. Chin J Geophys 666–679.

Xu, C., Xu, X.W. 2013. Controlling parameter analyses and hazard mapping for earthquake triggered-landslides: an example from a square region in Beichuan County, Sichuan Province, China. Arab J Geosci 3827–3839.

Xu, C., Xu, X., Shen, L., Yao, Q., Tan, X., Kang, W., Ma, S., Wu, X., Cai, J., Gao, M., Li, K. 2016*a*. Optimized volume models of earthquake-triggered landslides. Scientific Reports 6, 29797.

Xu, C., Xu, X., Tian, Y., Shen, L., Yao, Q., Huang, X., Ma, J., Chen, X., Ma, S. 2016*b*. Two comparable earthquakes produced greatly different coseismic landslides: The 2015 Gorkha, Nepal and 2008 Wenchuan, China events. Journal of Earth Science 1008-1015.

Yalçın, A., Reis, S., Aydınoğlu, A.C., Yomralıoğlu, T. 2011. A GIS-based comparative study of frequency ratio, analytical hierarchy process, bivariate statistics and logistics regression methods for landslide susceptibility mapping in Trabzon, NE Turkey. Catena 274-287.

Yang, Z.H., Lan, H.X., Gao, X., Li, L.P., Meng, Y.S., Wu, Y.M. 2015. Urgent landslide susceptibility assessment in the 2013 Lushan earthquake-impacted area, Sichuan Province, China. Nat Hazards 2467–2487.

Yao, X., Tham, L.G., Dai, F.C. 2008. Landslide susceptibility mapping based on Support Vector Machine: A case study on natural slopes of Hong Kong, China. Geomorphology 572-582.

Yılmaz, Ç., Topal, T., Süzen, M.L. 2012. GIS-based landslide susceptibility mapping using bivariate statistical analysis in Devrek (Zonguldak-Turkey). Environmental Earth Sciences 2161-2178.

Yılmaz, I. 2009*a*. A case study from Koyulhisar (Sivas-Turkey) for landslide susceptibility mapping by artificial neural networks. Bull Eng Geol Environ 297–306.

Yılmaz, I. 2009*b*. Landslide susceptibility mapping using frequency ratio, logistic regression, artificial neural networks and their comparison: A case study from Kat landslides (Tokat—Turkey). Comput Geosci 1125–1138.

Yılmaz, I. 2010. Comparison of landslide susceptibility mapping methodologies for Koyulhisar, Turkey: conditional probability, logistic regression, artificial neural networks, and support vector machine. Environ Earth Sci 821–836.

Yılmaz, I., Keskin, İ. 2009. GIS based statistical and physical approaches to landslide susceptibility mapping (Şebinkarahisar, Turkey). Bulletin of Engineering Geology and the Environment 459-471.

Youssef, A.M. 2015. Landslide susceptibility delineation in the Ar-Rayth Area, Jizan, Kingdom of Saudi Arabia, by using analytical hierarchy process, frequency ratio,and logistic regression models. Environ Earth Sci 8499–8518.

Youssef, A.M., Al-Kathery, M., Pradhan, B. 2014*a*. Landslide susceptibility mapping at Al-Hasher Area, Jizan (Saudi Arabia) using GIS-based frequency ratio and index of entropy models. Geosci J 113–134.

Youssef, A. M., Al-Kathery, M., Pradhan, B., Elsahly, T. 2014*b*. Debris flow impact assessment along the Al-Raith Road, Kingdom of Saudi Arabia, using

remote sensing data and field investigations. Geomat Nat Hazards Risk 7-20.

Youssef, A. M., Pradhan, B., Jebur, M. N., El-Harbi, H. M., 2014*c*. Landslide susceptibility mappin gusing ensemble bivariate and multivariate statistical models in Fayfa area, Saudi Arabia. Environ Earth Sci 73-80.

Youssef, A.M., Al-Kathery, M., Pradhan, B. 2015. Landslide susceptibility mapping at Al-Hasher Area, Jizan (Saudi Arabia) using GIS-based frequency ratio and index of entropy models. Geosci J 113–134.

Yüksel, N. 2007. Usage of statistical techniques and artificial neural networks in producing landslide susceptibility maps based on geographical information systems: Kumluca-Ulus (Bartın) region. Phd Thesis, Hacettepe University, Ankara (unpublished).

Zare, M., Jouri, M.H., Salarian, T., Askarizadeh, D., Miarrostami, S. 2014. Comparing of bivariate statistic, AHP and combination methods to predict the landslide hazard in northern aspect of Alborz Mt. (Iran). Intl J Agri Crop Sci 543-554.

Zhang, J., Yin, K., Wang, J., Liu, L., Huang, F. 2016*a*. Evaluation of landslide susceptibility for Wanzhou district of three Gorges reservoir. Chinese Journal of Rock Mechanics and Engineering 35.

Zhang, J. Q., Liu, R. K., Deng, W., Khanal, N. R., Gurung, D. R., Sri, Ramachandra, Murthy, M., Wahid, S. 2016*b*. Characteristics of landslide in Koshi River Basin, Central Himalaya. Journal of Mountain Science 1711–1722.

Zhang, K., Wu, X., Niu, R., Yang, K., Zhao, L. 2017. The Assessment of landslide susceptibility mapping using random forest and decision tree methods in the Three Gorges Reservoir Area, China. Environ Earth Sci 405.

Zhang, M.S., Dong, Y., Sun, P.P. 2012. Impact of reservoir impoundment-caused groundwater level changes on regional slope stability: a case study in the Loess Plateau of Western China. Environ Earth Sci 1715–1725.

Zhao, W., Li, A., Deng, W. 2014. Surface energy fluxes estimation over the South Asia subcontinent through assimilating MODIS/TERRA satellite data with In Situ observations and GLDAS product by SEBS model. IEEE Journal of Selected Topics in Applied Earth Observations and Remote Sensing 3704–3712.

Zhu, H. H., Shi, B., Yan, J. F., Zhang, J., Zhang, C. C., Wang, B. J. 2014. Fiber Bragg grating-based performance monitoring of a slope model subjected to seepage. Smart Mater Struct 23, 095027. URL: https://iopscience.iop.org/article/10.1088/0964-1726/23/9/095027

Zhuang, J., Peng, C., Wang, G., Chen, X., Iqbal, J., Guo, X. 2015. Rainfall thresholds for the occurrence of debris flows in the Jiangjia Gully, Yunnan Province, China. Engineering Geology, 195. URL:https://www.researchgate.net/publication/281746840_Rainfall_thresholds_for_the_occurrence_of_debris_flows_in_the_Jiangjia_Gully_Yunnan_Province_China

Zolotraev, W.H. 1976. Present day problems in the engineering geological investigation of landslides, falls and mudflows in mountainous folded regions. In: Hutchinson JN (ed) Geological factors and mechanism involved in the development of landslides, falls and mudflows. UNESCO, Paris, 5-34.

Bulletin of the Mineral Research and Exploration

http://bulletin.mta.gov.tr

Physical modeling the formation of roof collapse zones in Vorkuta coal mines

Boris Yu ZUEV[a], Ruslan S. ISTOMIN[b], Stanislav V. KOVSHOV[a*] and Vyacheslav M. KITSIS[b]

[a]*Saint Petersburg Mining University, 21st Line, St Petersburg 199106, Russia*
[b]*National Research Mordovia State University 68/1 Bolshevistskaya St., Saransk, 430005, Russia*

Research Article

Keywords:
Coal mining, Roof collapse, Physical modeling.

ABSTRACT

Collapse of the roof during mining is a constant threat to the lives of miners and equipment performance. To predict it, different numerical and physical approaches are used. Physical modeling of the massif region from -951 m to -841 m using equivalent materials were undertaken in this investigation. Various options for mining the Vorkuta coal deposit were considered: mining only the upper industrial seam, mining the lower coal seam as a protective layer to the upper one, and assessing the impact on the collapse zone of the complex structure of the upper coal seam roof while maintaining an upward order of mining. The main results were as follows: calculated collapse zone is approximately 30% larger than theoretical; collapse zone decreased when using mining with lower protective coal seam; the largest collapse zone was observed when pinching the rocks in upward mining order. Therefore, the research has shown the need to adjust the project for a larger methane yield. Further large-scale modeling is needed for understanding the characteristics of the collapse zone.

Received Date: 29.06.2019
Accepted Date: 16.09.2019

1. Introduction

The collapse of the roof in the conditions of coal mines is a complex gas-dynamic and geomechanical phenomenon, accompanied by the release of a large amount of methane (Kazanin and Sidorenko, 2017*a*; Sidorenko et al., 2018). At this time, the most common emergencies occur during the underground mining of minerals, the most severe of which is accompanied by human and infrastructural losses (Gridina and Andreev, 2016). Most often, the collapse occurs in the intervals between mine working and support, or between the support racks, if the technological mode of their installation is not observed (Sidorenko and Sishchuk, 2016). The collapse mechanism is a complex process. As the face moves, the roof hangs behind the bottom, which leads to a gradual stretching of the coal seam and the formation of microcracks in the rock mass, gradually saturated with methane. At the moment of reaching the ultimate strength, the destruction begins with the subsequent splitting of the massif into micro blocks, and the roof caving occurs, under the influence of rock pressure with the formation of methane accumulations in the goaf, as well as in the face due to the unloading of the formation (Kazanin et al., 2017). The cracks formed in the zone of collapse beyond the stope, penetrate the roof for a considerable distance and due to them the flow of methane into the goaf from the accompanying beds increases. In subsequent collapses, this methane enters the face and increases in concentration, which is fixed by the aerogas control system and it stops the equipment in an emergency (Kazanin and Sidorenko, 2017*b*).

Citation info: Zuev, B.Y., Istomin, R.S., Kovshov, S.V., Kitsis, V. M. 2020. Physical modeling the formation of roof collapse zones in Vorkuta coal mines. Bulletin of the Mineral Research and Exploration 162, 225-234. https://doi.org/10.19111/bulletinofmre.620478

* *Corresponding author: Stanislav KOVSHOV, stanisl.kovsh@gmail.com*

Mathematical and computer modeling are widely used in the mining industry (Gao et al., 2014; Sidorov et al., 2018; Grigoriev et al., 2019). In order to predict the formation of zones of collapse, various methods of physical and computer modeling are applied (Andreev and Gridina, 2016; Sidorenko et al., 2019). It is also used computer modeling, e.g. 3D subsurface modeling for prediction and visualization of ore extraction in an optimal way (Akıska and Akıska, 2018). Finite Element Method as a variation of numerical analyses was successfully used for characterization of rock masses in the tunnel (Kanik et al., 2015). Nevertheless, both empirical and computational analyses should be combined with each other for the best tunnel project design (Kaya et al., 2011). Therefore, the virtue of physical modeling in its visibility. One of the main directions of physical modeling of such processes is modeling on equivalent materials (Wang et al., 2017; Gao et al., 2019; Pan et al., 2019). Having its drawbacks, such as labor and material intensity, the possibility of developing a small number of options, this method is suitable for obtaining data on the state of the simulated rock mass in a destroyed area, with the stochastic nature of the development of destruction processes. Physical modeling practices also help to verify technics for hard roof treatment (Bai et al., 2017). Physical field tests are used to find changes in roof bolt loading, roof separation and roadway deformation (Wang et al., 2019*b*). Physical modeling also can be applied for estimation of the backfilling strip mining method usage against surface collapse (Wang et al., 2019*a*). Acoustic emission can be used for monitoring rock bursts caused by hard roof failure (Li et al., 2015). Therefore, physical modeling was applied in simulation the processes of formation of the collapse zone for the Vorkuta coal deposit (Cherkai and Gridina, 2017). This method ensures the reproduction of the physicomechanical properties and structure of the rock mass, which plays a key role in solving all simulated geomechanical processes (Kang et al., 2018).

2. Materials and Methods

The relationship between full-scale materials and equivalent materials (EM) is established through linear scales α_l and the ratio of the weights α_γ.

For a detailed reproduction of the structure of the rock mass, the geometric scale of models no. 1, 2, and 3, α_l = 1: 100 was chosen. Considering the parameters of the mass, strength and deformation criteria - the main design parameters of the EM in models no. 1, 2, and 3, were determined (Table 1).

For further research, EM with a filler of fine-grained quartz sand (0.1-0.6 mm) and a binder based on DEG-1 and ED-20 resin was chosen as base materials. The main idea of selecting the required formulation of EM was to vary the percentage of the binder for ensuring the required strength parameters of EM in accordance with table 1.

EM manufacturing technology and testing consisted of 9 steps:

1. Evaluation of the particle size distribution of the filler.
2. Dosing and weighing of the filler and the binder were carried out on standard scales with an accuracy not exceeding 1-2%.
3. Mixing the mixture of filler and binder. Laying in a timbering.
4. Rolling was carried out in layers after leveling the surface of the mixture. The weight of the roller corresponded to the optimum specific load of 2.35 N/cm^2.
5. Storage for stabilizing the properties of EM. Storage time - 3 days, until full solidification.
6. Production of EM samples. The dimensions of the samples for testing on the press - 5x5x10 cm.
7. Testing the samples on the press was carried out on uniaxial compression to determine compressive strength. Comparison of obtained data with their desired values, the adjustment of the formulation. Predictive assessment of the influence of the percentage composition of the binder in accordance with the developed methodology was made.
8. The repetition of the technological cycle (steps 2-8) was carried out according to the next predictive adjustment. The cycles were ended after overlapping with the actual values of the required strength parameters.

As a result of the implementation of this technological research program, the following types

Table 1- Physical and mechanical properties in nature and model.

Stratum (m)	Layer thickness (m)	Rocks composition	Strength full-scale (Mpa)	Strength EM (Mpa)	Notice
110					
103	7	sandstone	80	0.44	
98	5	sandstone	80	0.44	
91	7	sandstone	90	0.50	
87	4	aleurolite	80	0.44	
84	3	sandstone	90	0.50	
80	4	aleurolite	60	0.33	
78	2	argillite	39	0.22	
76	2	aleurolite	55	0.31	
68	8	sandstone	90	0.50	
61	7	sandstone	97	0.54	
56	5	sandstone	96	0.53	
51	5	sandstone	85	0.47	
49	2	aleurolite	61	0.34	
47	2	sandstone	70	0.39	
44	3	aleurolite	60	0.33	
40	4	*coal*	15	0.08	productive formation H = -930 m
37	3	aleurolite	40	0.22	
33	4	sandstone	100	0.56	
30	3	aleurolite	60	0.33	
26	4	aleurolite	50	0.28	
23	3	sandstone	90	0.50	
18	5	aleurolite	50	0.28	
15	3	sandstone	100	0.56	
10	5	aleurolite	50	0.28	
9	1	*coal*	15	0.08	productive formation H = -960 m
6	3	aleurolite	60	0.33	
0	6	sandstone	90	0.50	

of equivalent materials and recipes were established: 1 - reproduction of coal based on DEG-1 resin (the condensation product of epichlorohydrin with diethylene glycol, contains at least 26% of epoxy groups), 2 - reproduction of sandstones based on ED-20 resin (oligomeric product based on diphenylolpropane diglycidyl ether, contains 20% of epoxy groups), 3 - reproduction of argillite and aleurolites based on ED-20 resin, providing reproduction of physical and mechanical characteristics of the massif (Table 1), presented in table 2.

Table 2- Characteristics of the EM main types and binder formulations.

Parameter / Name	Layer thickness (cm)	Strength (Mpa)	EM type
Coal	1.5- 4	0.08	DEG-1 Cs=0.7
Sandstone	2-12	0.39-0.68	ED-20 Cs=0.72-0.81
Argillite	1-2	0.22	ED-20 Cs=0.64
Aleurolite	2-12	0.22-0.36	ED-20 Cs=0.64-0.7

*Cs – resin content in EM

The physical model is manufactured on a stand with a simulated area of 5000x1100x200 mm, the scheme of which is shown in figure 1.

The physical model reproduced the region of massif from -951 m to -841 m. In this case, geomechanical processes depend on gravitational forces, the vertical components of which are determined by the weight of the overlying mass of the massif, and the horizontal ones - by passive lateral repulsion (according to Dinnik), which is provided by rigid stand side walls (Figure 1).

The loading of the model provides reproduction of the overlying mass of the massif on the simulated area, using a loading device with a pneumatic cushion.

The parameters of vertical and horizontal displacements were determined using reference marks of the "quadrant" type, installed on the front surface of models No. 1, 2, 3 on various horizons. Displacement parameters were determined using a Hasselblad H5D-200MS high-resolution photographic recorder with an accuracy of 15–33 mm on location. Low error rates were achieved due to the high-resolution shooting of 200 or 50 megapixels.

3. Results and Discussion

In model No. 1, the collapse zone was formed due to mining only the upper productive layer (H = -930 m). In this case, a clear dynamic nature of the collapse is observed - rock bump (Figure 2). This is confirmed by a similar characteristic of these layers in different mines of the Vorkuta coal basin. Such mining technique is unsafe.

In model No. 2, the lower coal seam was mined as protective to the upper one. Such mining technique reduces the rock-bump hazard of the layer, unloading it with cracks from the collapse of the roof of the lower

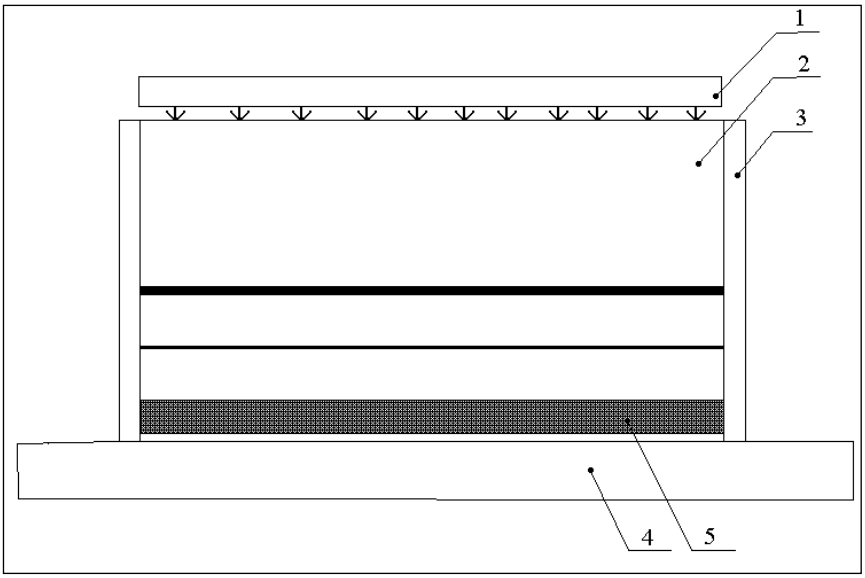

Figure 1- Schematic diagram of the stand (1 - loading device; 2 – model; 3 - side wall; 4 – stand base, 5 - sliding formwork).

Figure 2- Formation of the collapse zone in model no. 1.

layer. However, in this case, the flow of methane, into the bottom of the upper coal seam from the interlayer thickness and the emerging zone of collapse of the lower coal seam in the roof of the upper coal seam, increases (Figure 3).

In model no. 3, the impact on the collapse zone of the complex structure of the roof of the upper coal seam was estimated, while maintaining the ascending order of mining. This worsens the geomechanical state of mining of the upper coal seam (Figure 4).

The results of the distribution of vertical displacements of the rock layers at different horizons are presented in figures 5-9.

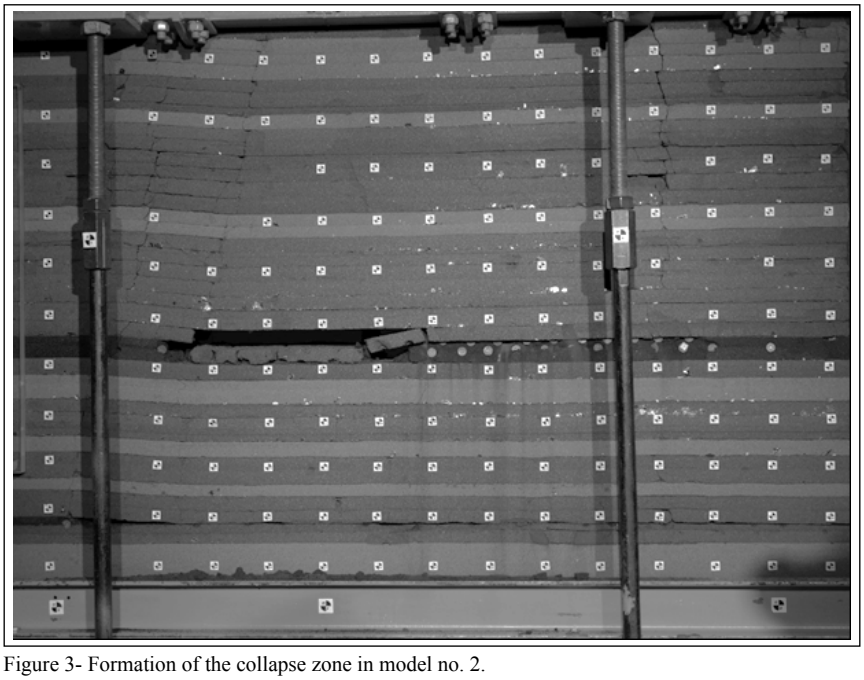

Figure 3- Formation of the collapse zone in model no. 2.

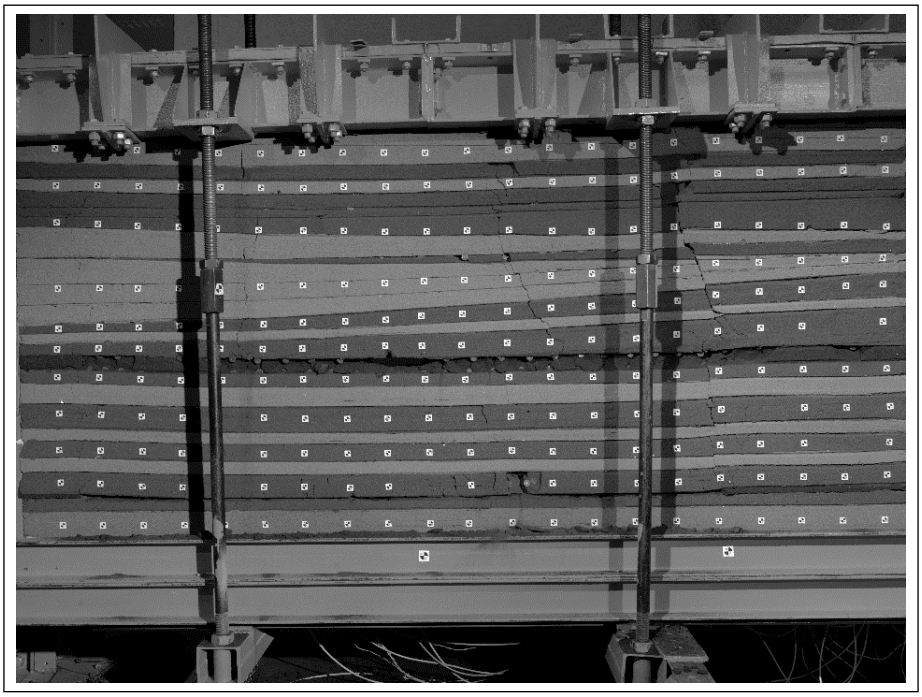

Figure 4- Formation of the collapse zone in model no. 3.

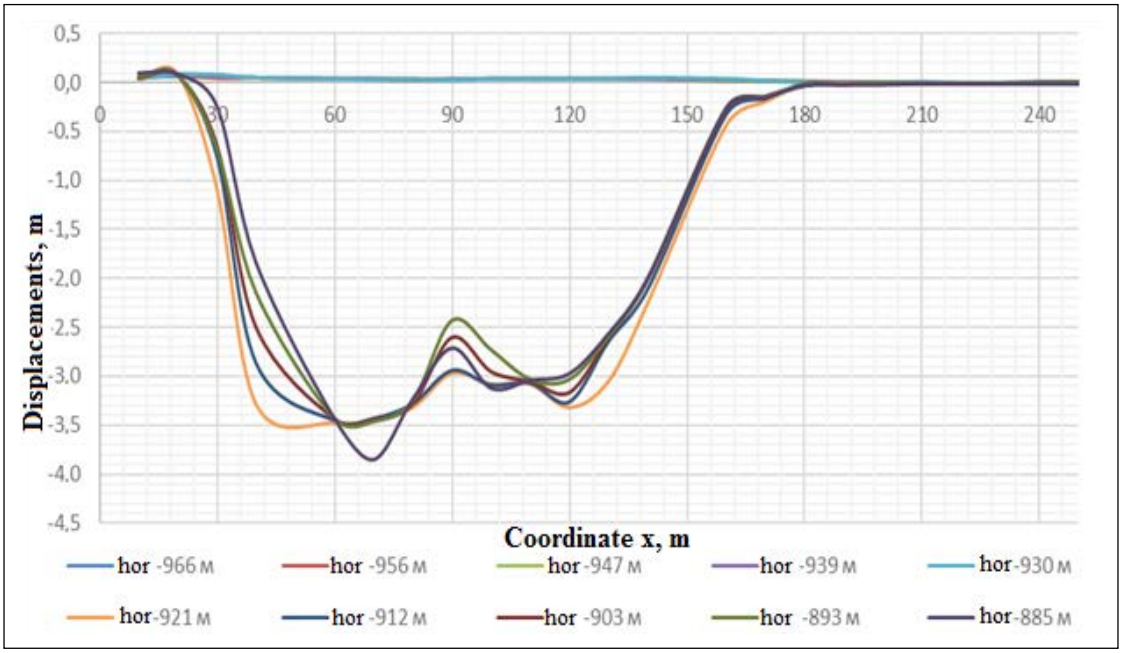

Figure 5- Vertical displacements in model No. 1 on horizons from -859 m to -969 m with a distance of the stope of 155 m.

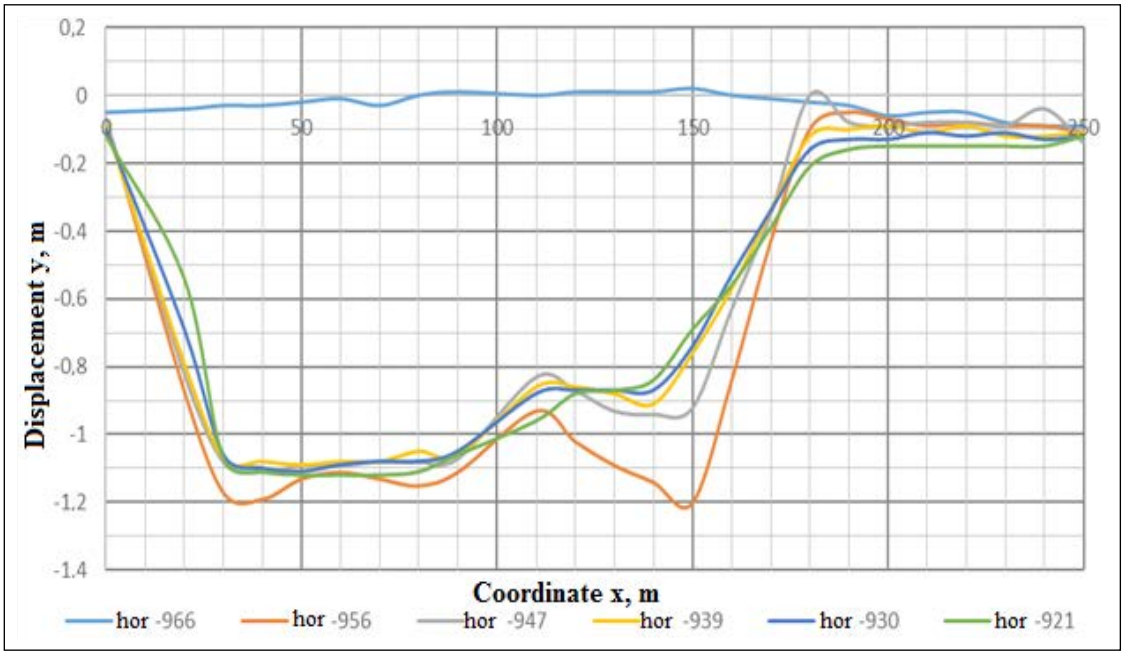

Figure 6- Vertical displacements in model no. 2, when mining the lower industrial formation at horizons from -921 m to -966 m with a span of 130 m.

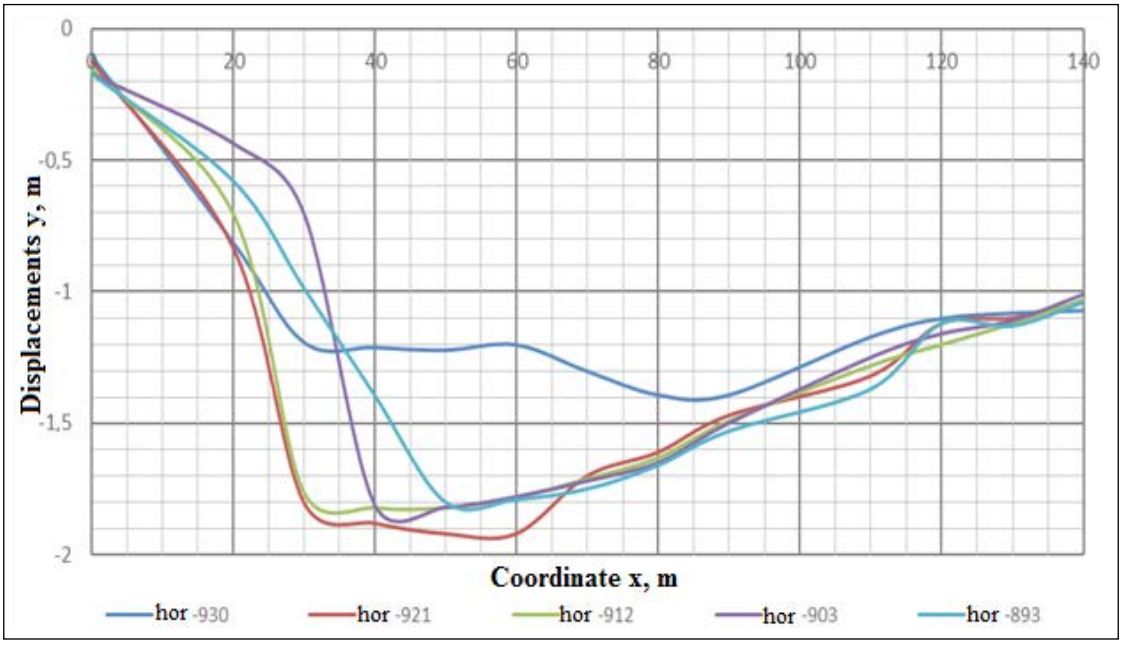

Figure 7- Vertical displacements in model no. 2, when mining the upper industrial formation at horizons from -893 m to -950 m with a span of 50 m.

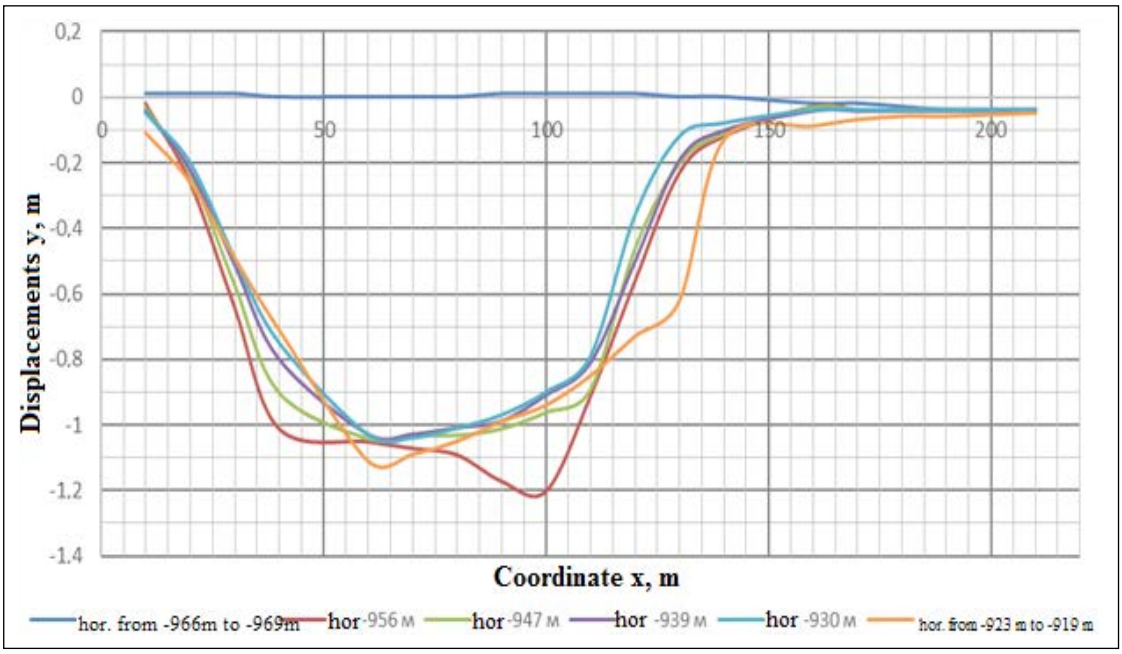

Figure 8- Vertical displacements at different horizons in model no. 3 in the horizon range from -969 to -919 m with a span of 160 m.

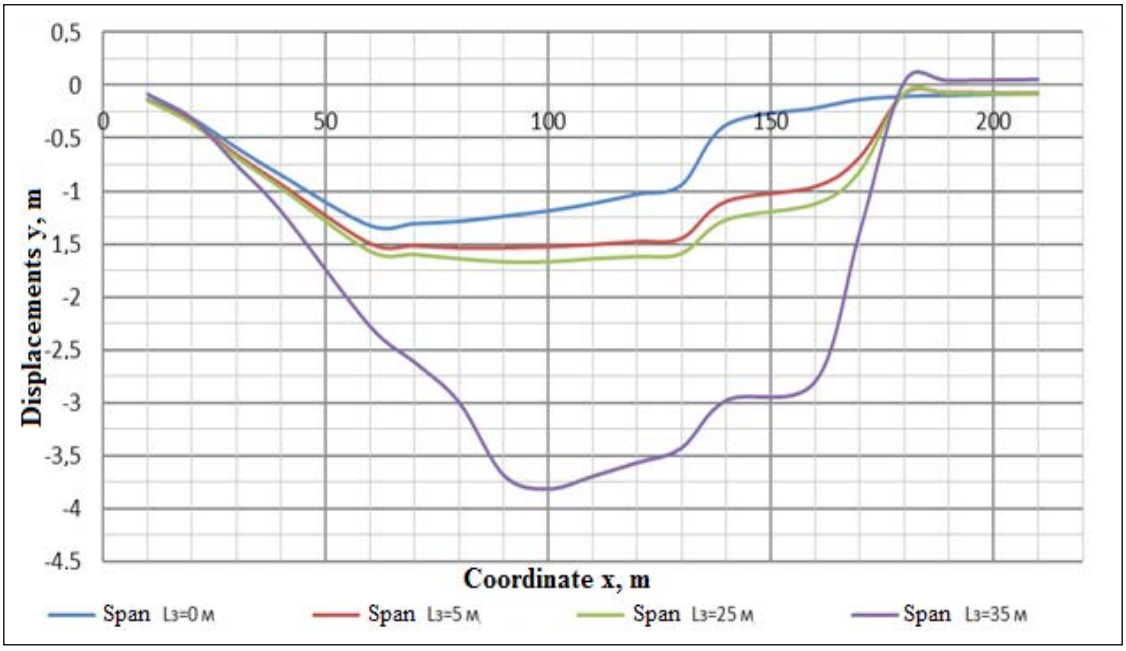

Figure 9- Vertical displacements in model No. 3 at the level of the immediate roof of the upper coal seam when wedging out a layer of sandstone in the rocks of the main roof at horizons -923 m -919 m.

Figures 5-8 show the displacements of different horizons during the collapse according to the reference marks on the surface. Displacements were recorded in each horizon above the developed layers, and their magnitude shows that the rock layers move together almost without decompaction. This means that these horizons are unstable and destroyed in reality. Sharp edges of the graphs reflect the roof caving behind the stope with a small step (10-30 m), and almost complete elimination of the voids of the goaf. Therefore, methane from there, except for small leaks, all goes to the bottom during the collapse.

Figure 9 shows the first roof caving, when mining the upper coal seam; initial displacements were formed after the lower seam was mined. The step size is 35 m. The collapse pattern corresponds to that in previous figures (sharp edges - without hanging the roof, the value corresponds to the thickness of the seam - no decompaction) was evident:

– When mining only the upper coal seam, the zone of the first collapse is 155 m.

– When mining sequentially, first the lower coal seam, then the upper coal seam, without considering the pinching-out of rocks, the collapse zone is 130 m.

– When mining sequentially, first the lower coal seam, then the upper coal seam, considering the pinching-out of rocks, the zone of collapse is 160 m.

In all models, the main width of the collapse zone is formed due to the mining of the upper coal seam and follows the stope. This is due to the thickness of the upper coal seam (4 m). A slightly smaller zone of collapse in model No. 2 shows the effectiveness of mining the lower coal seam as a protective one:

– The largest zone of collapse is observed when the rocks are pinching out. The nature of cracking and the width of cracks in model No. 3 indicates a positive effect of pinching on the expansion of the collapse zone. This is due to the large depth of mining, when even minor irregularities and bedding angles can lead to a change in the nature of the loading, from compression to tension and bending, reducing the strength and stability of rocks.

- The zone of collapse covers all simulated horizons and practically does not change along the mining width. The angle α showing the rock cavity is almost 90º. Without additional studies covering the simulated zone of not less than 100 layer thicknesses, it is not possible to predict the zone of influence.

4. Conclusions

The calculated collapse zone is approximately 30% larger than the project. This is due to the imperfection of computational techniques that do not consider a number of factors affecting the methane release from guiding beds. These factors include – the layers mining order, increased depth of mining, and the presence of violations in the roof of the developed seam.

The simulation confirmed the correctness of the design solution for mining the lower coal seam as a protective one. The collapse zone in this case has decreased. However, studies have shown the need to adjust the project for a larger methane yield. To clarify the characteristics of the collapse zone, it is necessary to conduct additional studies on a large scale modeling. The results of further research can be used to adjust the method for predicting methane inflow, into the stope from guiding beds; use of advance and preliminary degassing; the speed of the face movement and the required air volume.

References

Akıska, S., Akıska, E. 2018. An ore adit planning with the help of three dimensional ore body modeling: A case study from Çulfa Çukuru Pb-Zn-Cu-Ag deposit. Bulletin of the Mineral Research and Exploration 157, 201-217. DOI: 10.19111/bulletinofmre.372510.

Andreev, R.E., Gridina, E.B. 2016. A study of gas-dynamic processes in a charge chamber during the explosion of blasthole charges of various designs. Research Journal of Pharmaceutical, Biological and Chemical Sciences 7 (3), 2383-2392.

Bai, Q., Tu, S., Wang, F., Zhang, C. 2017. Field and numerical investigations of gateroad system failure induced by hard roofs in a longwall top coal caving face. International Journal of Coal Geology 173, 176-199.

Cherkai, Z.N., Gridina, E.B. 2017. Technological problems and fundamental principles of methods of engineering-geocryological exploration during construction and exploitation of wells in permafrost rock mass. Journal of Mining Institute 223, 82-85.

Gao, F., Stead, D., Coggan, J. 2014. Evaluation of coal longwall caving characteristics using an innovative UDEC Trigon approach. Computers and Geotechnics 55, 448-460.

Gao, F., Kang, H., Lou, J., Li, J., Wang, X. 2019. Evolution of local mine stiffness with mining process: Insight from physical and numerical modeling. Rock Mechanics and Rock Engineering 52(10), 3947-3958.

Gridina, E.B., Andreev, R.E. 2016. Principles of providing safety, comprehensive analysis of the injury risk and the targeted impact on the traumatic factors as the instruments of increasing the efficiency of integrated safety management systems at mining enterprises of the Russian Federation. Research Journal of Pharmaceutical, Biological and Chemical Sciences 7 (3), 2641-2650.

Grigoriev, B.S., Eliseev, A.A., Pogarskaya, T.A., Toropov, E.E. 2019. Mathematical modeling of rock crushing and multiphase flow of drilling fluid in well drilling. Journal of Mining Institute 235, 16-23.

Kang, H., Lou, J., Gao, F., Yang, J., Li, J. 2018. A physical and numerical investigation of sudden massive roof collapse during longwall coal retreat mining. International Journal of Coal Geology 188, 25-36.

Kanık, M., Gürocak, Z., Alemdağ, S. 2015. A comparison of support systems obtained from the RMR89 and RMR14 by numerical analyses: Macka Tunnel project, NE Turkey. Journal of African Earth Sciences 109, 224-238.

Kaya, A., Bulut, F., Sayın, A. 2011. Analysis of support requirements for a tunnel portal in weak rock: A case study from Turkey. Scientific Research and Essays 6(31), 6566-6583.

Kazanin, O.I., Sidorenko, A.A. 2017*a*. Interaction between gas dynamic and geomechanical processes in coal mines. ARPN Journal of Engineering and Applied Sciences, 12 (5), 1458-1462.

Kazanin, O.I., Sidorenko, A.A. 2017*b*. The best available technologies for horizon mining of flat-lying gaseous coal seams: Prospects for development in Russian mines. ARPN Journal of Engineering and Applied Sciences 12 (1), 227-23

Kazanin, O.I., Sidorenko, A.A., Vinogradov, E.A. 2017. Substantiation of the technological schemes of intensive development of gas-bearing coal beds. ARPN Journal of Engineering and Applied Sciences 12 (7), 2259-2264.

Li, N., Wang, E., Ge, M., Liu, J. 2015. The fracture mechanism and acoustic emission analysis of hard roof: a physical modeling study. Arabian Journal of Geosciences 8(4), 1895-1902.

Pan, W., Nie, X., Li, X. (2019). Effect of premining on hard roof distress behavior: a case study. Rock Mechanics and Rock Engineering 52(6), 1871-1885.

Sidorenko, A.A., Sishchuk, J.M. 2016. Stability of undermining seam panel entries at retreating longwall multiple mining. Research Journal of Pharmaceutical, Biological and Chemical Sciences 7 (2), 927-935.

Sidorenko, A.A., Sirenko, Yu.G., Sidorenko, S.A. 2018. Influence of face advance rate on geomechanical and gas-dynamic processes in longwalls in gassy mines. Eurasian Mining 1, 3-8.

Sidorenko, A.A., Ivanov V.V., Sidorenko S.A. 2019. Numerical simulation of rock massif stress state at normal fault at underground longwall coal mining. International Journal of Civil Engineering and Technology (IJCIET) 10, 844–851.

Sidorov, D.V., Potapchuk, M.I., Sidlyar, A.V. 2018. Forecasting rock burst hazard of tectonically disturbed ore massif at the deep horizons of Nikolaevskoe polymetallic deposit. Journal of Mining Institute 234, 604-611.

Wang, G., Wu, M., Wang, R., Xu, H., Song, X. 2017. Height of the mining-induced fractured zone above a coal face. Engineering Geology 216, 140-152.

Wang, F., Jiang, B., Chen, S., Ren, M. 2019*a*. Surface collapse control under thick unconsolidated layers by backfilling strip mining in coal mines. International Journal of Rock Mechanics and Mining Sciences 113, 268-277.

Wang, H., Shi, R., Lu, C., Jiang, Y., Deng, D., Zhang, D. 2019*b*. Investigation of sudden faults instability induced by coal mining. Safety Science 115, 256-264.

Bulletin of the Mineral Research and Exploration

http://bulletin.mta.gov.tr

Characteristic mollusc, larger foraminifera findings and environmental interpretations of the Middle Eocene Kocaçay formation deposits around Ayvalıca (Bayat, Çorum)

Müjde GÜRSOY[a] and Muhittin GÖRMÜŞ[b]

[a]*MTA General Directorate of Mineral Research and Exploration Şehit Cuma DAĞ Natural History Museum Paleontology Department 06800 Çankaya ANKARA*

[b]*Ankara University Engineering Faculty Geology Engineering Department 06830 Gölbaşı ANKARA.*

Research Article

Keywords:
Çankırı-Çorum Basin, Middle Eocene, Kocaçay formation, Ostrea, Velates, Nummulites.

ABSTRACT

Although the Çankırı-Çorum Basin was studied for various purposes such as geological, stratigraphical, tectonic, coal and oil exploration, studies on fossils are limited. Especially there have not been detailed studies on molluscs and larger foraminifera. The research area is located at the vicinity of Ayvalıca (north of Çankırı-Çorum basin). The Middle Eocene Kocaçay formation, which outcrops in the Çankırı-Çorum Basin, is widespread around Bayat Çorum in the north of the basin, Sulakyurt Kırıkkale in the west, Çiçekdağı Kırşehir in the south and Sungurlu Çorum in the middle of the basin. The formation is composed of conglomerate, carbonated sandstone, limestone and sandy marls and also includes rich larger foraminifera and molluscs. This study mainly focuses on taxonomy and environmental interpretations of *Ostrea roncaensis* (Partsch in coll. Bayan, 1870) de Gregorio, 1884, *Velates perversus* (Gmelin, 1791) species from *Mollusca and Nummulites beaumonti* d'Archiac and Haime, 1853, *N. aturicus* Joly and Leymerie,1848, *N. perforatus* (de Montfort, 1808) and *Assilina exponens* (Sowerby, 1840) species from larger Foraminifera. In addition, considering faunal features from bottom to top *Ostrea roncaensis*, *Velates perversus*, *Nummulites aturicus* and *Assilina exponens* Abundance Biozones were identified. The age range of the Kocaçay Formation is determined as Lutetian-Bartonian. Lithological and faunal contents indicate that sediments of the Kocaçay formation were deposited within lagoon to nummulitic sets in a shallow marine environment.

Received Date: 04.07.2019
Accepted Date: 03.02.2020

1. Introduction

Çankırı-Çorum basin where the field of study is carried out is one of the most important storage basins of Central Anatolia with a sedimentary thickness of 11,000 meters from Paleocene to Pliocene (Birgili et al., 1975). It is known that the Paleogene part of the sequence is composed of marine and Neogene part consists of terrestrial deposits. The basin is surrounded by the North Anatolian Fault (NAF) and Ophiolitic Melange in the north, Sakarya Massif in the east and Kırşehir Massif in the south. In this study, the mollusc and foraminiferal findings in the Middle Eocene Koçaçay formation were represented in the vicinity of Ayvalıca Village (Bayat, Çorum) located north of Çankırı-Çorum Basin (Figure 1).

There are studies about geology and stratigraphy (Lahn, 1939, 1943; Yücel, 1953; Erol, 1953, 1959; Ketin, 1955; Akarsu, 1959; Alpan, 1968; Norman,

Citation info: Gürsoy, M., Görmüş, M. 2020. Characteristic mollusc, larger foraminifera findings and environmental interpretations of the Middle Eocene Kocaçay formation deposits around Ayvalıca (Bayat, Çorum). Bulletin of the Mineral Research and Exploration 162, 235-267. https://doi.org/10.19111/bulletinofmre.685461

* *Corresponding author: Müjde GÜRSOY, mujde.gursoy@mta.gov.tr*

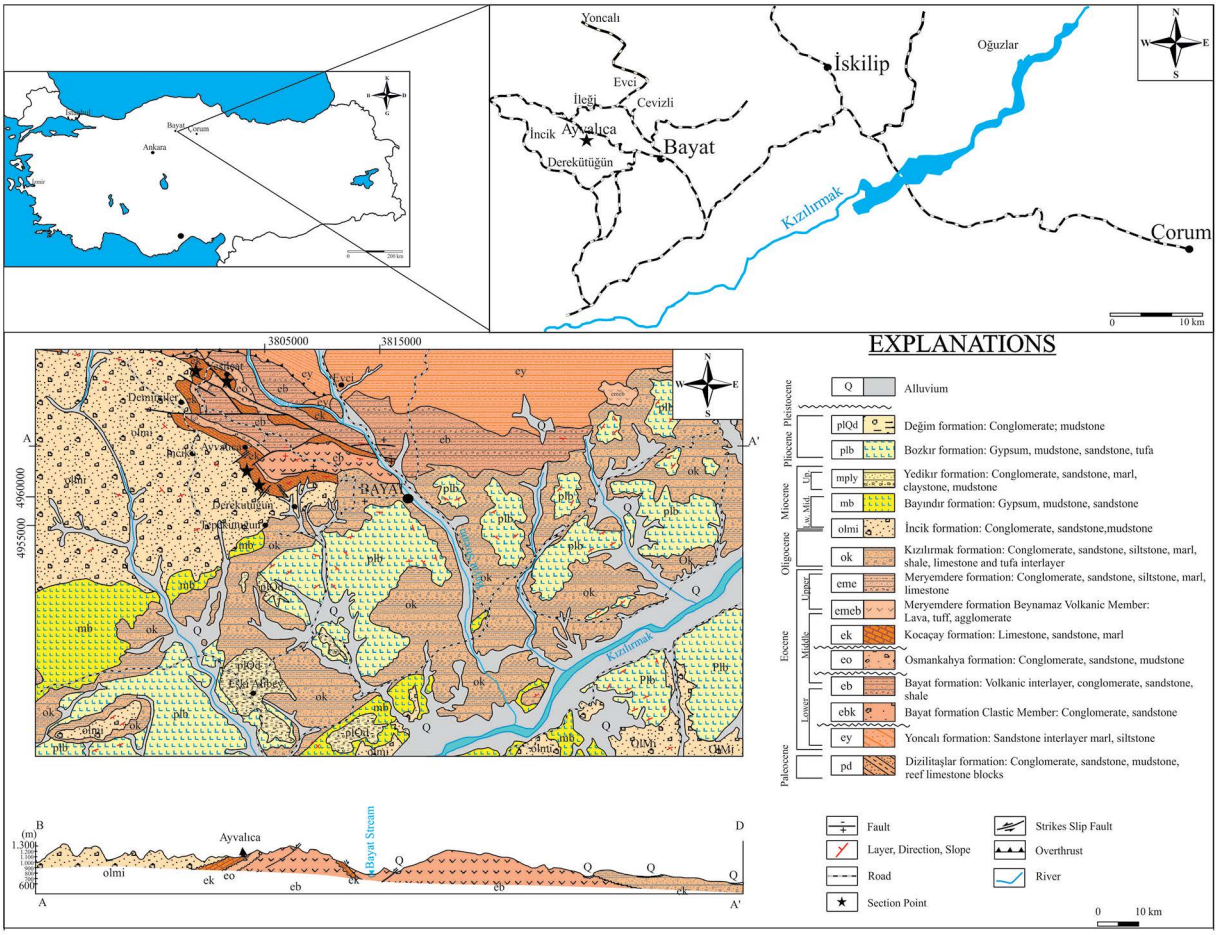

Figure 1- Location and geology map of Bayat (Çorum); it was revised from MTA Çorum G32 sheet at 1/100.000 scale (Sevin and Uğuz, 2011).

1972, 1975*a, b*; Çalgın et al., 1973; Birgili; et al., 1975; Çapan and Buket, 1975; Ergun, 1977; Yoldaş, 1982; Hakyemez et al., 1986; Bilgin et al., 1986; Erdoğan et al., 1996; Ateş et al., 2010; Bilgiç, 2012), sedimentology (Şenalp, 1974, 1980; 1981; Karadenizli, 1999; Karadenizli and Kazancı, 2000; Karadenizli et al., 2003 and 2004) and detailed the North Anatolian Fault (NAF) tectonism (Tüysüz and Dellaloğlu, 1992, 1994; Görür et al., 1998; Seyitoğlu et al., 1997; 2000; Kaymakçı, 2000; Kaymakçı et al., 2001; 2009). Due to the thick storage and salt content in the basin, oil exploration and coal geology investigations were carried out (Maucher, 1937; Blumental, 1938; 1948; Erol, 1953; 1959; Reckamp and Özbey, 1960; Savajo, 1961; Aziz, 1973; Tanrıverdi, 1973*a, b*,1974; Akyol, 1978 and Keskin, 1992). However, there are limited studies in the Çankırı-Çorum basin that contain environmental interpretations based on molluscs, large foraminifera systematics and these fossils (Okan and Hoşgör, 2009). Accordingly, the aim of this study is to investigate the association of mollusc and coarse foraminifera found in Kocaçay formation which is outcropping around Ayvalıca Village and to reveal the age and environmental characteristics of the formation.

2. Material and Method

This study was conducted by MTA General Directorate Şehit Cuma Dağ Natural History Museum (2018-08-16-01, 2017-08-16-01, 2016-08-16-01 project code number) within the frame of the Project "Çankırı-Çorum Basin Eocene -Oligocene Stratigraphy and Paleogeography". During this study one measured section and samples from 26 levels were collected. The mollusc samples were cleaned with hydrogen peroxide in the laboratories of the Museum and necessary measurements were made with vernier caliper measuring instrument.

Clean samples were selected and photographed. Thin sections of foraminifera samples were prepared at the Paleontology and thin section laboratories of Ankara University Geological Engineering Department, and photographed in Leica microscope in the laboratories of the Museum. Systematic determinations were made according to Bouchet et al. (2010) for bivalves, Bouchet et al. (2005) for gastropods and Loeblich and Tappan (1988) for Foraminifera systematics. All fossils identified were recorded in the Museum inventories and are conserved in the Museum archives.

3. Stratigraphy

3.1. Lithostratigraphy

Çankırı-Çorum Basin is a basin where Paleogene aged marine and Neogene terrestrial sediments are deposited on the basement developed as a result of the collision of Kırşehir and Sakarya continents in the Late Paleocene - Early Eocene age range (Tüysüz and Dellaloğlu, 1992;1994).

The basin begins with the Cretaceous aged Boğazkale Ophiolite consisting of radiolarite, serpentinite and limestone blocks at the bottom. Paleocene aged Dizilitaşlar formation, which contains conglomerate, sandstone, siltstone, marl and limestone, is deposited in the convergent and middle parts of the submarine spectrum. On the Dizilitaşlar formation, the Ypresian aged Hacıhalil formation is deposited in a fluvial environment with conglomerate and sandstone intercalations containing coal veins in the north. It is represented by Lutetian Karabalçık, Bayat, Osmankahya and Kocaçay formations in the region. Karabalçık is conglomerate and sandstone alternation and it's most prominent feature is that it contains good quality lignite veins. The volcano-sedimentary Bayat formation presents a sequence of tuff, agglomerate and lava flows at the base and coarse sandstone and conglomerates at the top; formation is important in terms of coal potential. Osmankahya, consisting of red coloured pebble, sandstone and siltstone, reflects the deposition in the fluvial environment. The shallow marine Kocaçay formation is overlain by a graded transition. Oligocene fluvial İncik formation consisting of red-burgundy and characteristic clastic terrestrial sediments, over Kocaçay with angular unconformity. Subsequently, the Kızılırmak formation, consisting of lacustrine Bayındır formation and meandering stream sediments, is composed of Oligo-Miocene aged gypsum. The age of Kızılırmak formation was found to be Late Oligocene by micromammals and vertebrate (Giant Rhino - *Paraceratherium* n.sp.) fossil studies (Karadenizli et al., 2004; Vural et al., 2010; Oyal, 2016; Oyal et al., 2017). The Kızılırmak formation is overlain by the Pliocene Değim formation. The youngest formation of the basin ends with Bozkır formation and Plio-Quaternary Değim formation consisting of sediments deposited by rivers in terrestrial environment (Figure 2).

Stratigraphic section of the study area and it's vicinity is found in the Ayvalıca village: The Bayat formation is represented by gray, brown andesite and conglomerate, sandstone and siltstone. It continues with the Kocaçay formation consisting of red coloured conglomerate, sandstone, siltstone and marls and yellowish gray shallow marine sandstone, siltstone, limestone and marls. İncik formation unconformably covers the underlying units. The boundary between Kocaçay and İncik formation sediments is very clear because of the colour difference (Figure 3a-b and Figure 4). The Kocaçay formation contains a large amount of macro and micro fossils (Figure 5).

Ayvalıca measurement stratigraphic section: Ayvalıca measured stratigraphic section, was revised from Çankırı-G32 sheet at 1/100.000 scale. The starting coordinates of the section are X: 97660 Y: 501102 Z: 1132 m and the ending coordinates are X: 97197 Y: 500804 Z: 1043 m. Thickness of 480 m was measured by systematic sampling at 26 points. The section starts at the bottom with sandstones and mudstones, mainly dominated by *Ostrea roncaensis*. At this level, the presence of cerithides and ampullunides is noticeable in addition to significant algal aggregates (Figure 5c). A thin layer with red silt is consequent to marl and *Ostrea roncaensis* horizon with a thickness of 20-25 cm. The conglomerate level of 30 cm thick with round radiolarite and serpentinite pebbles is consequent to sandy silty unit with abundant fossils. This unit is succeeded by a second ostreid accumulation. Above this, there is a thick layer of fossiliferous limestone containing 30-40 cm thick ostreid, cerithid, ampullinide. The sandstone, siltstone alternation is succeeded by the ostreid horizon for the third time. After the marly level, there is a 20 cm thick *Velates perversus* limestone layer. Beginning from the *Velates*

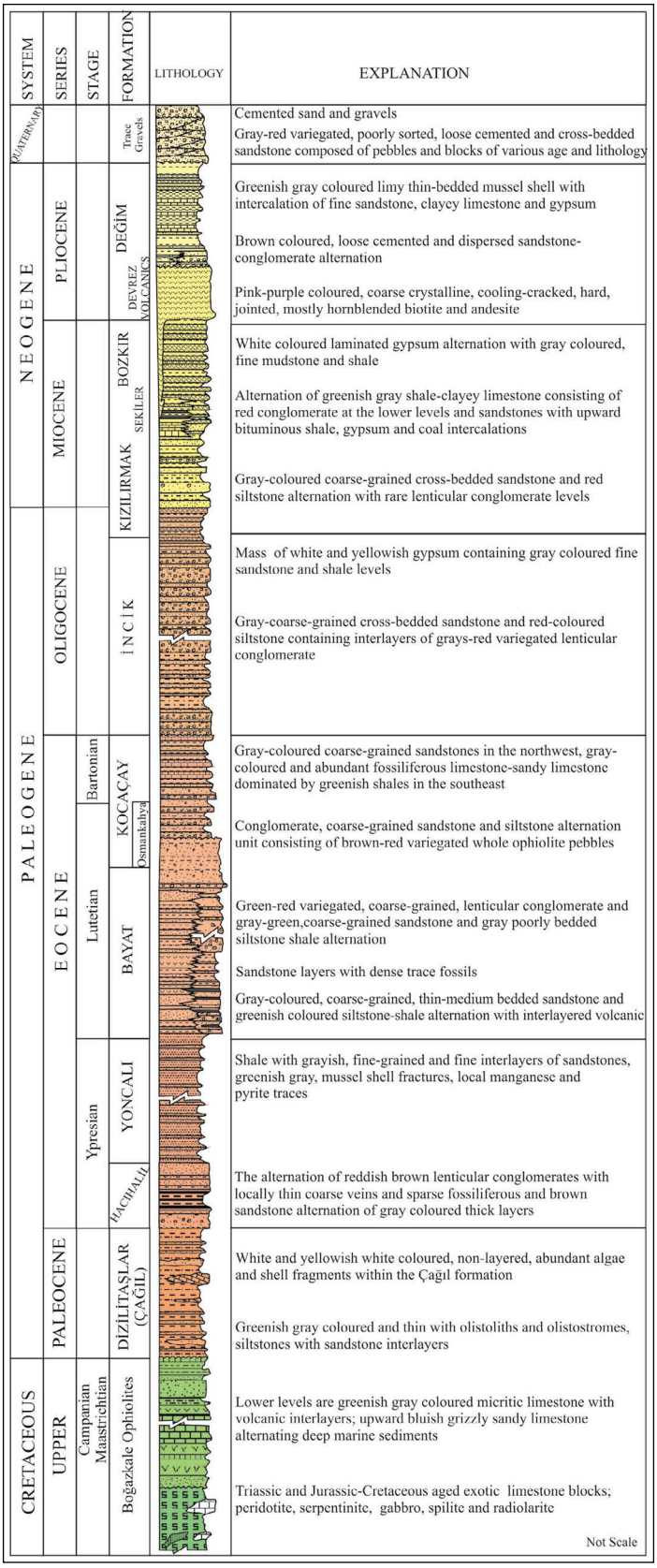

Figure 2- Generalized stratigraphic section of the Çankırı-Çorum Basin (Yoldaş, rearranged from 1982; the red frame shows the formations outcrop in the village of Ayvalıca).

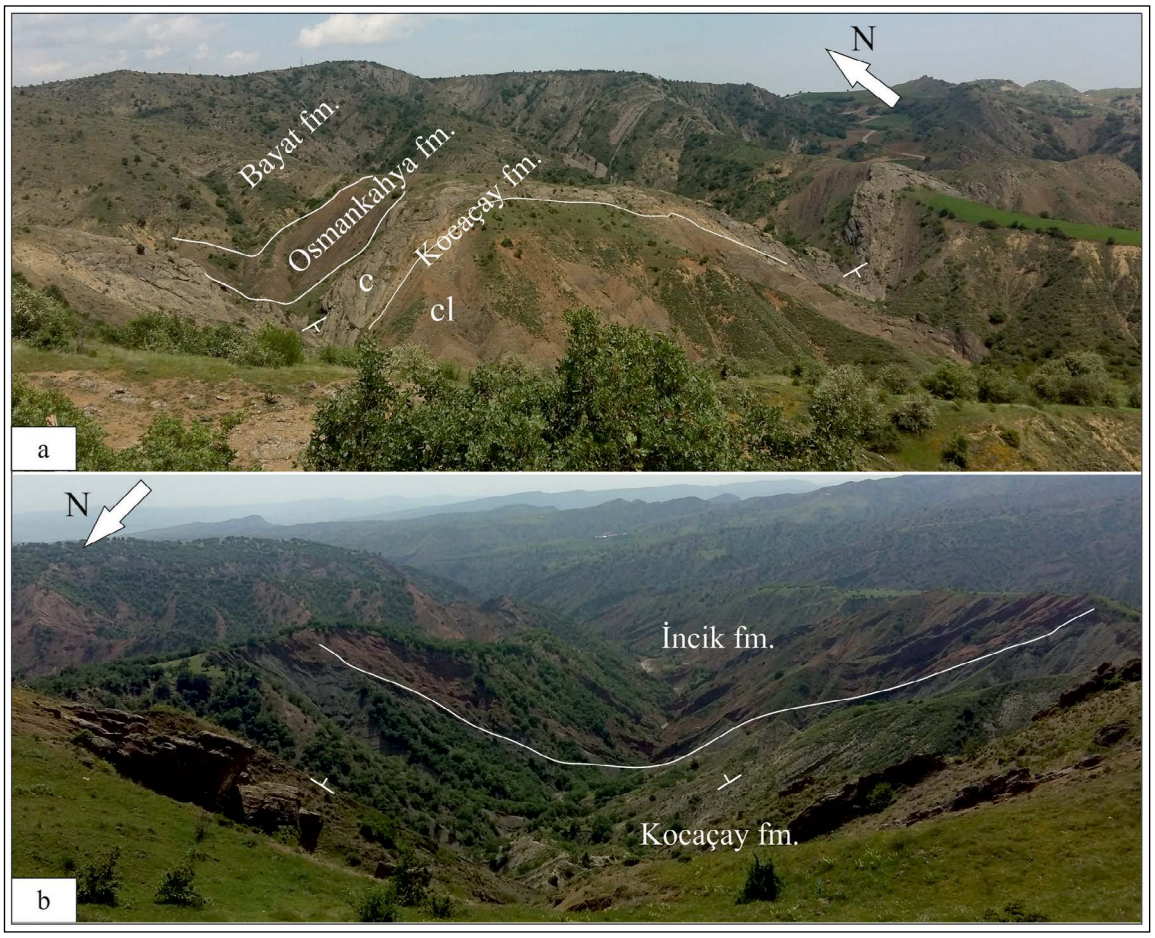

Figure 3- Land views of lower a) and upper, b) boundary relations of Kocaçay formation, east and south of Ayvalıca village, c) carbonate dominant levels, cl. clastic carbonate levels.

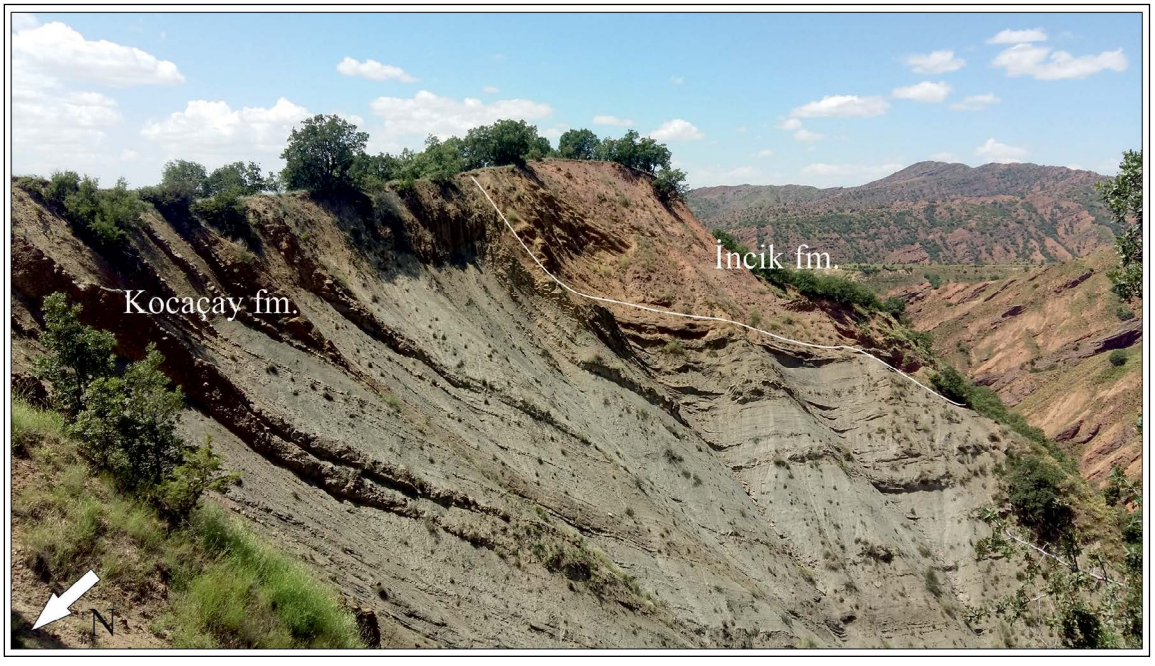

Figure 4- Top of the section, unconformity of Kocaçay and İncik formations.

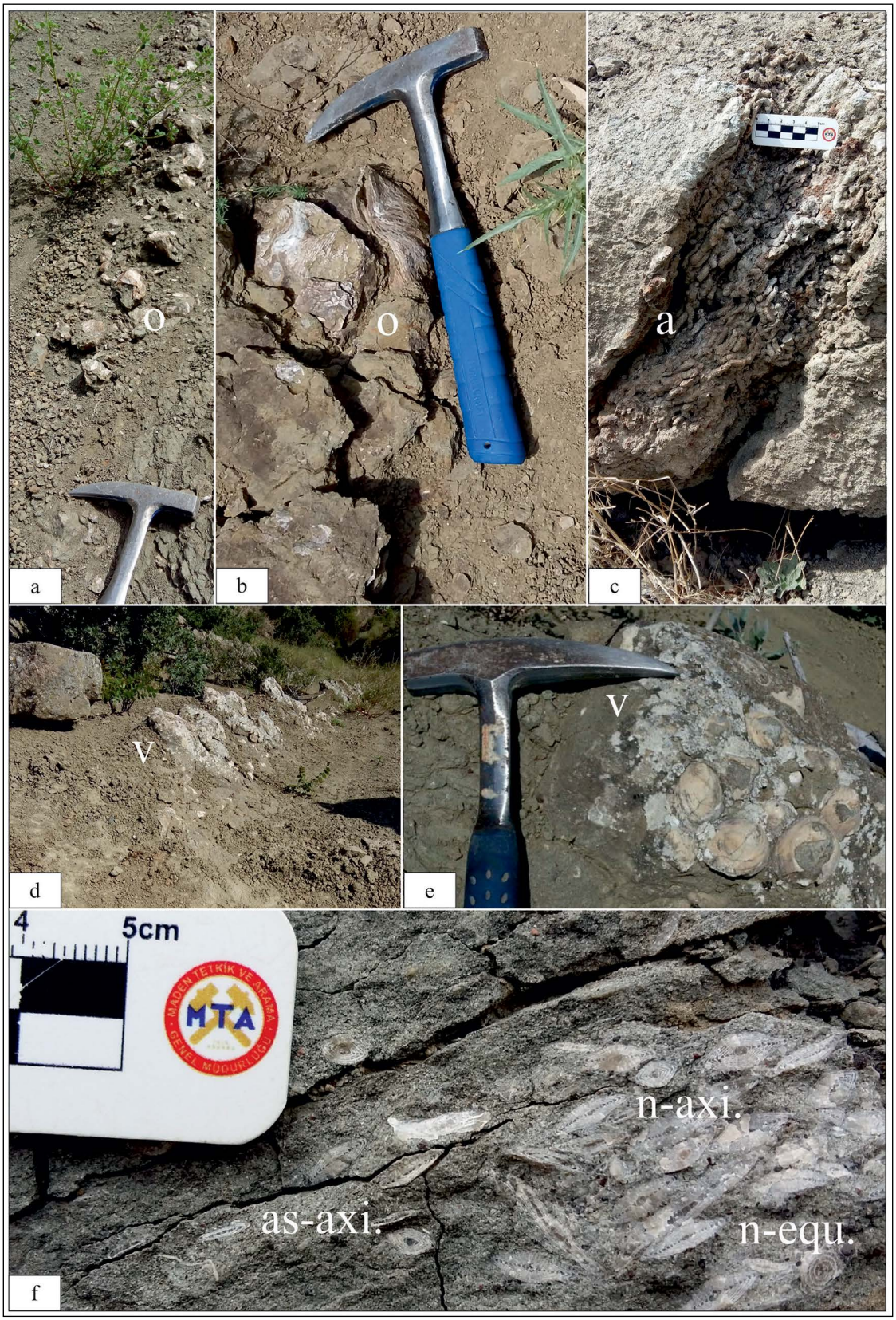

Figure 5- Ayvalıca section fossil views; a-b) *Ostrea roncaensis* (o) accumulations, a) General view, b) detail view; c) view from algae (a) containing levels; d-e) *Velates perversus* (v) level, d) general view, e) detail view; f) view from Nummulitic sandstone, *Nummulites* sp. (n-axi.) axial and (n-equ.) equatorial and *Assilina* sp. (as-axi.) axial.

level, the nummulite set, which is approximately 250 m long, contains plenty of coarse sandy marly nummulite. The Nummulite set ends with a 20 cm thick yellow limestone layer at the top. At this level, the abundance of *Nummulites perforatus* is replaced by the *Assilina exponens* species. Fossil content decreases in the upper part of the sequence. The transition to İncik formation is angular unconformable (Figure 6).

3.2. Biostratigraphy

Abundance zones have been identified in the deposits of Koçaçay formation around Ayvalıca and these are the abundance zones of *Ostrea roncaensis, Velates perversus, Nummulites aturicus* and *Assilina exponens*.

Ostrea Abundance Zone: It forms a distinct horizon especially at the basement level of the Koçaçay formation. Overlapping aggregates are evident. There are abundant *Ostrea* at marly levels. The dimensions of the individuals were width: 4-10 cm, height: 7-11 cm; thickness: 1-4 cm in width and average dimensions are width: 6 cm, height: 11 cm, thickness: 2.5 cm. The sludge matrix ratio is about 20-30% at the horizon level. *Ostrea*'s double-valved preserved ones are the majority. The *Ostrea* agglomerated horizon begins

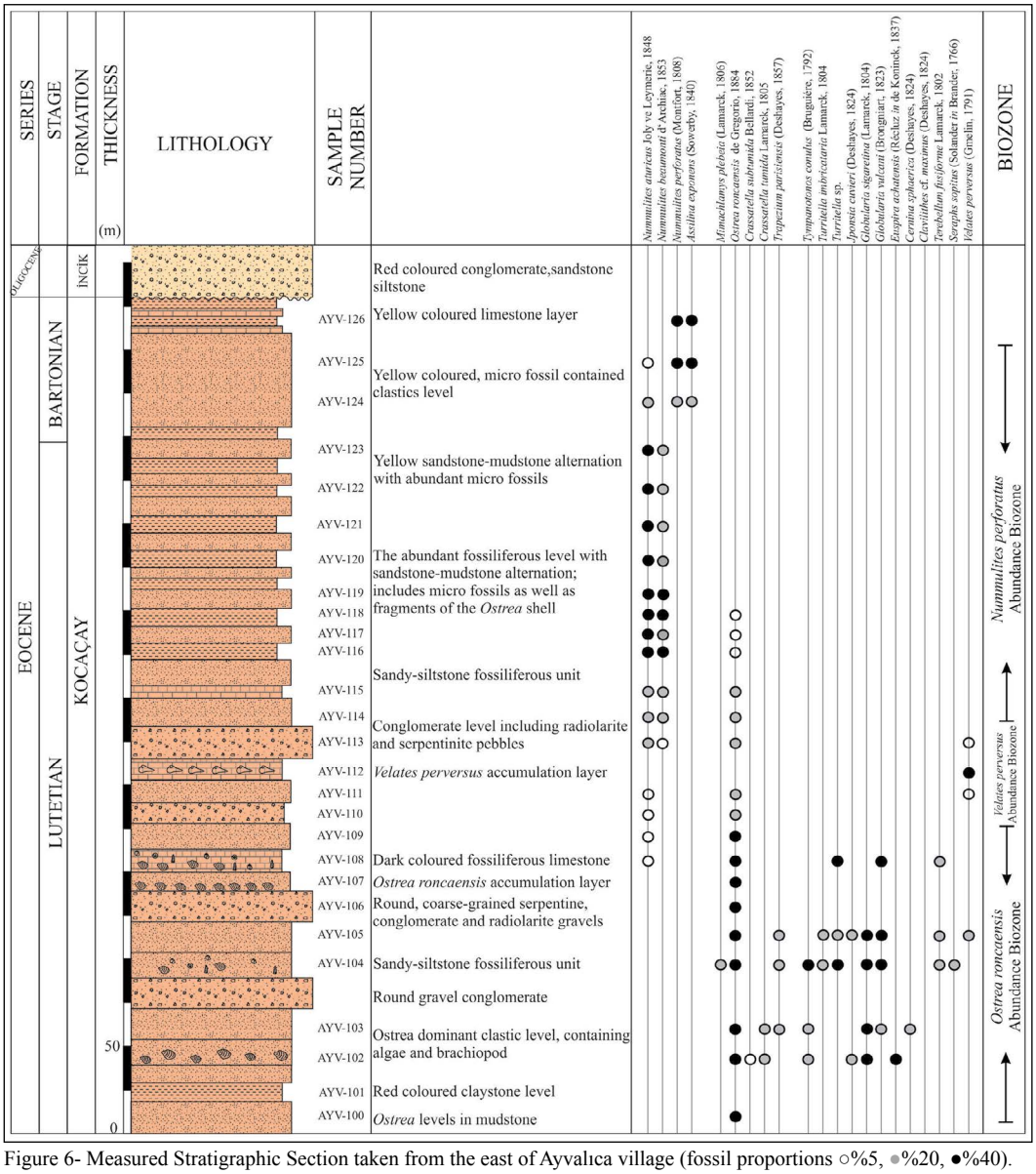

Figure 6- Measured Stratigraphic Section taken from the east of Ayvalıca village (fossil proportions ○%5, ●%20, ●%40).

with a thickness of about 1 meter at the bottom, and the next two horizons are 20-25 cm thick. Nummulitic marls are very low in number and are mostly observed as broken pieces. Ostreids generally live in estuaries or lagoons where eutrophic conditions prevail, abundant nutrients supply from land and algal growth occur (Volety, 2013). *Ostrea roncaensis* determines the Lutetian level in Ayvalıca (Figure 5a-b).

Velates Abundance Zone: The *Velates* abundance zone which succeeded the following three *Ostrea* zones is observed just in front of the nummulite set. Between the two marly levels, only the *Velates perversus* accumulation is evident in the limestone layer of approximately 20 cm in thickness. *Velates perversus*, first described by Gmelin (1791), is a characteristic neritid gastropod with a flat cone-shaped shell, short spiry of one or two rounds and a smooth and shiny outer surface that is not visible in other epifaunal gastropods. Measurements of samples collected from the study area; width: 5-5.5 cm, height: 2-3.5 cm and mouth opening varies between 2.6-2.8 cm. *Velates* generally live epifaunal in coarse grained shallow ponds, medium and high energy environments (Savazzi, 1992). In Ayvalıca, *Velates perversus* shows the Lutetian level (Figure 5d-e).

Nummulites Abundance Zone: The *Nummulites perforatus* species, which started to be seen in the range of 150-200 m, form a large set after the *Velates* level. Marns contain abundant and large samples. Towards the top of the embankment, the yellow limestone layer, 20-30 cm in thickness, becomes again fossiliferous (Figure 7). Continuation of this level increases the remarkableness rate of *Assilina exponens*. The diameter of the *Nummulites* shells is 6-20 mm and their thickness is 3-8 mm, with an average diameter of 12 mm and a thickness of 5 mm. *Nummulites* are generally known to live in reef margins and shallows (Tuzcu and Karabıyıkoğlu, 1991). However, especially in Lutetian massiveness and plenty of carbonate deposits in different parts of Turkey, *Nummulites* set formations are striking. It is observed that the *Nummulites* in the Ayvalıca area are up to 60-70% in the carbonates developed as a set feature. It is stated in the literature that *Nummulites* generally continue their whole lives slowly on seaweeds on leaking carbonate soils, immobilized or by using pseudopots and spend their lives in oligotrophic regions (Kopaevich et al., 2008). Their abundance is explained by the existence of suitable conditions throughout the Eocene series and the formation of autochthonous, allochthonous, semi-autochthonous communities with some hydrodynamic conditions (Aigner, 1986).

Assilina Abundance Zone: An increase of *Assilina exponens* is observed in front of the nummulit set. In front of the embankment, which is dominated by lenticular *Nummulites*, clay carbonate comes after around 25 cm yellow hard limestone layer, contains

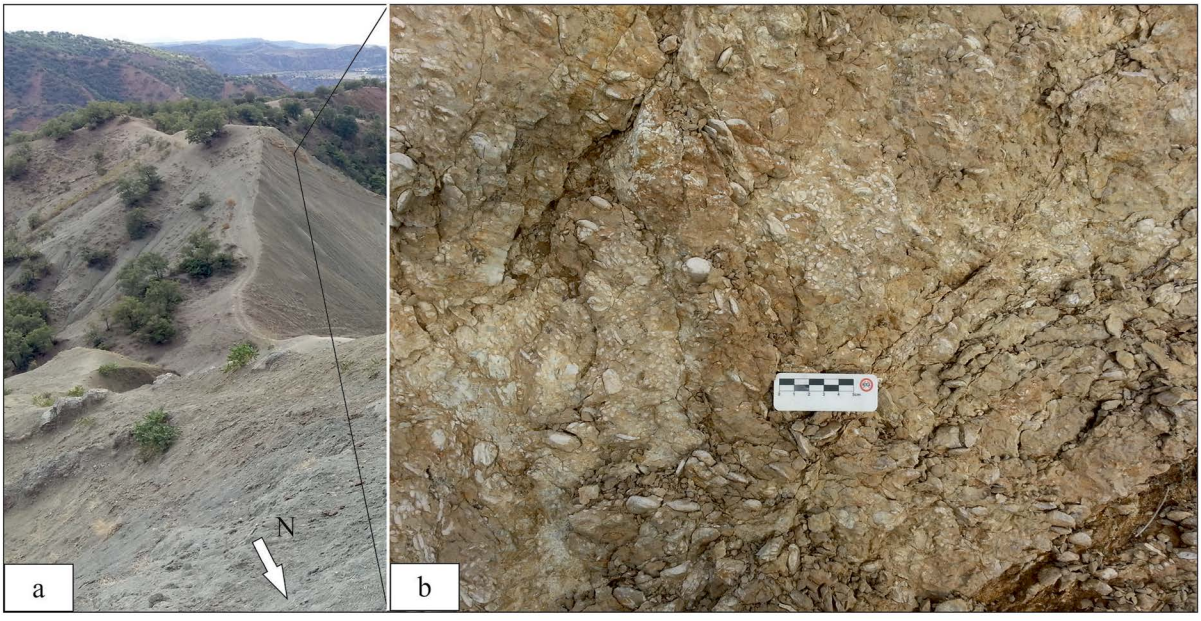

Figure 7- a) General and b) detailed land views belonging to the Nummulit bank.

abundant *Assilina* fossils. The diameters of the samples are between 18-25 mm in average and 2-3 mm in thickness. In addition, very large *Assilina* microspheric individuals with a diameter of 3-4 cm and very small macrospheric individuals of 1-2 mm in diameter are also present in the community.

4. Systematic

In this section, systematic descriptions of mollusc and benthic species forming biozones are given. Systematic determinations are made according to Bouchet et al. (2010) for bivalves, Bouchet et al. (2005) for gastropods and Loeblich and Tappan (1988) for Foraminifera systematics.

Class : Bivalvia Linnaeus, 1758

Subclass Pteriomorphia Beurlen, 1944

Ordo : Ostreida Férussac, 1822

Family : Ostreidae Rafinesque, 1815

Subfamily : Ostreinae Rafinesque, 1815

Genus : *Ostrea* Linnaeus, 1758

***Ostrea roncaensis* (Partsch *in coll.* Bayan, 1870) De Gregorio, 1884**

Figures 5a-b; Plate 1, Figures 1-5

1870 *Ostrea roncana* Partsch *in coll.*(?) Bayan, p. 484, no. 42.

1884 *Ostrea roncaensis* De Gregorio, p. 197.

1896 *Ostrea roncaensis* De Gregorio, p. 109, pl. 21, fig. 19; pl. 22, figs. 1-3; pl. 23, fig. 1.

1912*a Ostrea roncaensis* De Gregorio, Vogl, p. 90.

1912*b Ostrea* cfr. *roncaensis* De Gregorio, Vogl, p. 77.

1944 *Ostrea roncana* Partsch, Stchépinsky, p. 90.

1953 *Ostrea roncana* Partsch, Szöts, p. 211, 232, pl. 9, figs. 1-4.

1956 *Ostrea roncana* Partsch, Szöts, p. 22, 207, pl. 9, figs. 1-4.

1964 *Ostrea roncana* Partsch, Kopek and Kescskemétiné, p. 341-342.

1967 *Ostrea roncaensis* De Gregorio, Malaroda, p. 21.

1972 *Ostrea roncana* Partsch, Kescskemétiné-Körmendy, p. 204.

1980 *Ostrea roncana* Partsch, Kopek, p. 115.

1988 *Ostrea roncana* Partsch, Abate et al., p. 147, pl. 3, fig. 15.

1999 *Ostrea roncana* Partsch *in coll*.(?), Ozsvárt, p. 103, pl. 11, figs. 3-7; pl. 12, figs. 1-3; pl. 13, figs. 1-2.

2011 *Striostrea (Parastriostrea) roncana* (Partsch *in coll.,* Bayan, 1870), Abad-Garcia, p. 632-635, pl. 25, figs. 1-4; pl. 26, figs. 1-3.

2012 *Ostrea roncana*? Partsch, Abouessa et al., p. 76, fig. 5E.

Description: The sample has a medium-sized thickened shell. Shell plate or mug type; traces of residual komata on the edges of the shell and growth coverslips or traces on the upper surface of the lid are evident. Muscle scar is in the middle, crescent or kidney shape. The ligament site is of Ostreoid type. The left cover is slightly convex and the large, right cover is straight or slightly concave. The gripping area is nearly circular. With these characteristics, the sample belongs to the Ostreinae subfamily.

Similarities and Differences: For the sample identified for the first time by Bayan (1870), even though other sources used it as Partsch in coll., no information was found on behalf of Bayan (1870) dePartsch. Therefore it is considered as Ostrea roncana Partsch in coll. (?) Bayan. There is no picture related to the species described in the literature. De Gregorio (1896) argued that there is no picture in the description made by the Bayan and that the species should be "O.roncaensis" with reference to the name of the place. De Gregorio emphasized that the shell shape and thickness of the sample, which reached larger dimensions, differed individually and did not have limited features. The similarities of our specimens with the figures mentioned in the 3 plates in the study of De Gregorio (1896) are quite compatible. Studies of Szöts (1953, 1956), Abate et al. (1988), Ozsvárt (1999) and Abad-Garcia (2011) show similarities with the figures mentioned in the synonymous list.

Location and Stratigraphic Level: The measured stratigraphic sections taken from Bayat Ayvalıca village, it is the most abundant sample from the lowest levels (AYV 100-109), decreasing considerably after the nummulite bank. Archive numbers are 2018/1 and 2018/6.

Paleogeographic Distribution and Stratigraphic Level: Bayan (1870) found *O.roncana* species in Roncá northern Italy; De Gregorio (1884 and 1896) stated that the *O.roncaensis* in the Veneto region of Roncá was spread in the Middle Eocene. Vogl (1912*a, b*) emphasized that it was the same species as *O.roncana* Bayan and *O.roncaensis* De Gregorio within the Eocene identified fauna in Drvenik, Croatia. Oppenheim (1918) evaluated fossil findings from studies in Samsun, Yozgat, Sivas, Malatya, Maraş and Antep in his article with the title "Fossils from Asia Minor"; *O.roncana* with thick shells, which is known to be unique to Roncá, was identified in Merzifon at the Auversian level. Stchépinsky (1944) stated that *O.roncana* species, which he defined in his studies in Malatya region, spread in Lutetian. Szöts (1953) stated that they were identified in the Transdanub basin, Tatabánya, Pusztavám, Mór, Kisgyón in the Early Eocene, in Vicenzo (Roncá) and Egyptian Middle Eocene rocks outside Hungary. Szöts (1956) found that one of the most common fossils in the Middle Eocene limestones and marls in the southern Bakony basin was *Ostrea roncana* and reported from the Early Eocene to the early Bartonian. Kopek and Kescskemétiné (1964) described it at the base of the late Lutetian in Bakony, Hungary; transition to *Nummulites perforatus* was observed at the upper levels of the section. Kescskemétiné-Körmendy (1972) identified numerous mollusc fossils in the coal-fired units in the Hungarian Dorog basin. The author identified the spread of *O.roncana* as Early-Middle Eocene in the Bakony region. It was recorded as *Nummulites perforatus* biozone, mentioning that the fauna consisted of corals and molluscs living at a distance up to 10 m from the seaside. Kopek (1980) stated that *O. roncana* species, which he defined as "coral-mollusc level in the Middle Eocene, is very abundant in the plates below the *Nummulites perforatus* level in the Bakony mountain range in western Hungary. Abate et al. (1988) stated that the species they identified in their studies in northeastern Italy spread in the Middle Eocene in Roncá, Soave and Castelcerino, and added that the best preserved specimens of the species are in Hungary. Ozsvárt (1999) stated that the species spread in the Middle Eocene in his studies in Csordakút basin in Hungary. Abad-Garcia (2011) in his doctoral study on the Catalan Eocene mollusks *Striostrea (Paraostrea) roncana* species in the north of Barcelona Castellterçol, stated that they spread in the Middle Eocene. The author, Szöts (1953) emphasized that the Hungarian samples and the Catalan samples were compatible with each other, but should be included in the *Paraostrea* (Harry, 1985) sub-genus because of the overlapping growth lines. Abouessa et al. (2012) described the recurrent *Ostrea roncana* deposits at the Priabonian base levels in their study in the Libya Sirt basin. They stated that *O. roncana* shells, which had grown to form reefs on each other, were filled with cavities formed by sponges and bivalves of the Pholadidae family (Figure 8).

Class : Gastropoda Cuvier, 1795

Subclass : Neritimorpha Golikov and Starobogatov 1975

Ordo : Neritoina Rafinesque, 1815

Superfamily : Neritadea Rafinesque, 1815

Family : Neritidae Rafinesque, 1815

Subfamily : Neritinae Rafinesque, 1815

Genus : *Velates* Montfort, 1810

***Velates perversus* (Gmelin, 1791)**

Figures 5d-e; Plate 2, Figures 1-5

1786 *Nerita schmideliana sinistrosa* Chemnitz, p. 130, pl. 114, figs. 975-976.

1791 *Nerita perversa* Gmelin, t. 1, p.6, p. 3686, no. 329/72.

1824 *Nerita conoidea* Deshayes, t. 2, p. 149, pl. 18, figs. 1-8.

1834 *Velates perversa* Cuvier, v. 3, p. 62, pl. 22, fig. 7.

1883 *Nerita (Velates) schmideliana*, Chemnitz, Koch, p. 128.

1894 *Velates schmideliana* Chemnitz, De Gregorio, p. 31, pl. 6, fig. 181.

1896 *Velates schmideliana* Chemnitz, De Gregorio, p. 54, pl. 6, fig. 1-3; pl. 7, figs. 1-8.

1901 *Velates schmidelianus* Chemnitz, Oppenheim, p. 182-183.

1904 *Velates schmidelianus* Chemnitz, Dainelli *in* Canavari, p. 155.

1905 *Velates schmidelianus* Chemnitz, Dainelli *in* Canavari, p. 14-16.

1910-13 *Velates schmiedeli* Chemnitz, Cossmann and Pissarro, pl. 6, fig. 40-1.

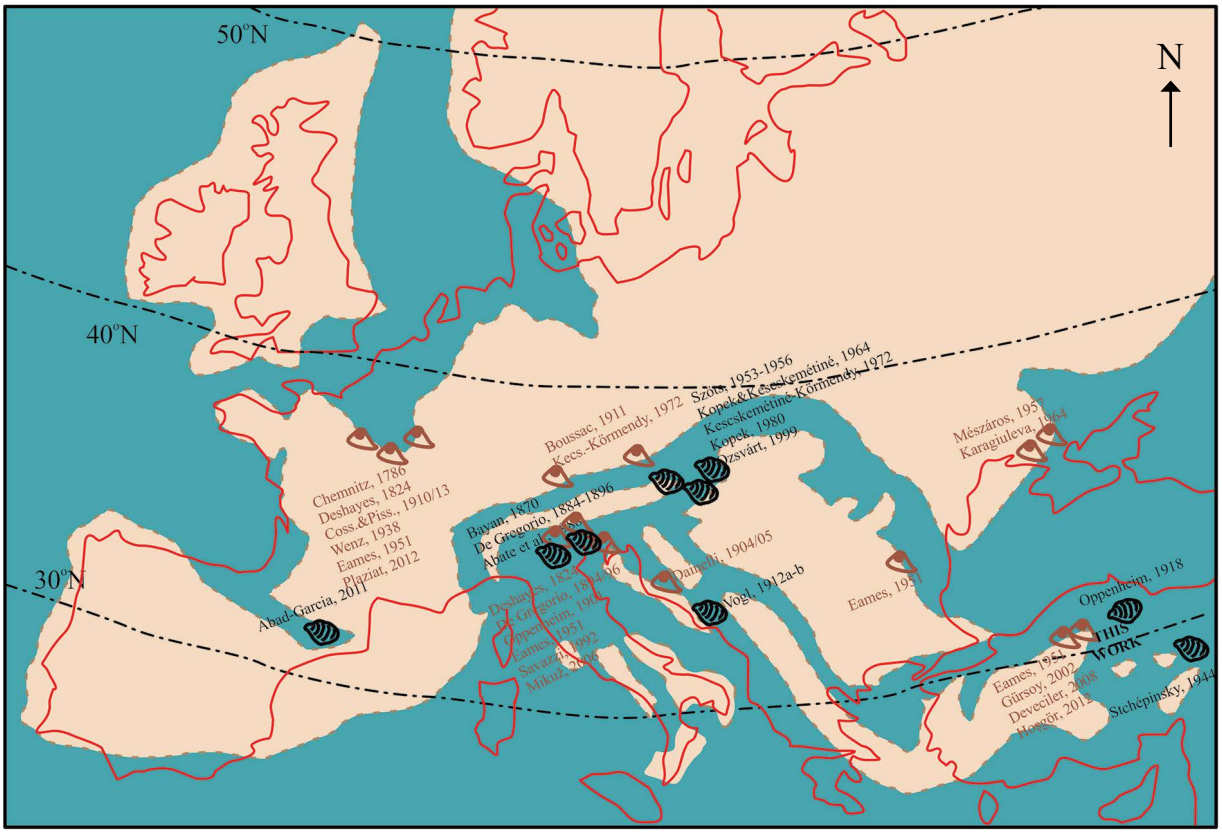

Figure 8- The paleogeographic distribution of *Ostrea roncaensis* ( ) and *Velates perversus* ( ) species throughout the Lutetian in Europe (it was revised from Plaziat, 1981 and Payros et al., 2015).

1912 *Velates schmiedeli* Chemnitz, Boussac, p. 321.

1918 *Neritina perversa* Gmelin, Favre, pl. 4, figs. 58a-c; pl. 5, figs. 59a-c, 60a-c, 61a-c.

1938 *Velates perversus* (Gmelin), Wenz, p. 417, fig. 1016.

1952 *Velates perversus* (Gmelin), Eames, p. 12-16.

1953 *Velates schmideli* (Chemnitz), Szöts, p. 143, pl. 1, figs. 41-56.

1957 *Velates (V.) schmidelianus* Chemnitz, Mészáros, p. 37, pl. 6, figs. 1, 1a.

1963 *Velates schmiedelianus* (Chemitz), Vlaicu-Tătărîm, p. 163-164.

1964 *Velates perversus* (Gmelin), Karagiuleva, p. 132, pl. 40, figs. 3a, b; 10.

1972 *Velates schmidelianus* Chemnitz, Kecskemétiné-Körmendy, p. 220, pl. 5, fig. 7; pl. 6, figs. 1-2.

1992 *Velates perversus* (Gmelin), Savazzi, p. 350, figs. 1A-G.

1992 *Velates perversus* (Gmelin), Squires and Demetrion, p. 26, figs. 55-56.

1994 *Velates perversus* (Gmelin), Squires and Demetrion, p. 126.

2002 *Velates perversus* (Gmelin), Gürsoy, pl. 1, figs. 2a, 2b.

2006 *Velates perversus* (Gmelin), Mikuž, p. 54, pl. 1, figs. 1a-1b; pl. 2, fig. 1; pl. 3, figs. 1a-1c.

2008 *Velates perversus* (Gmelin), Deveciler, p. 20, pl. 1, figs. 1-3.

2012 *Velates perversus* (Gmelin), Gürsoy and Taner, p. 64, figs. 2a, 2b.

2012 *Velates perversus* (Gmelin), Hoşgör, p. 40, pl. 3, figs. 7-9.

2012 *Velates perversus* (Gmelin), Plaziat, pp. 3-50, figs. 1-15.

Description: The shell is flat and wide. Spir is very short and consists of 1-2 rounds. The protocol is

downward and slightly curled to the right. The last lap has grown quite fast and swollen. The mouth opening is wide and half-moon shaped. There are notches along the inner lip. The shell is decorated with very thin growth lines.

Similarities and Differences: It is fully compatible with Chemnitz (1786) figures 975 and 976 and Cuvier (1834) drawing 7. Deshayes (1824) included *N. perversa* and *N. schmideliana* species in the synonymous list of the species he defined as *Nerita conoidea*, which is similar to our example. It fully conforms to the figures in De Gregorio (1896)'s plates 6 and 7. Cossmann and Pissorro (1910-13)'s pictures are very similar to the one in figure 40-1. The mouth shape, notches on the inner lip, growth lines on the shell are completely similar with Wenz (1938)'s figure 1016. Our samples are fully compatible with Szöts (1953) 41-56 and Kecskemétiné-Körmendy (1972)'s figures. Squires and Demetrion (1992) and Savazzi (1992) show similarities with the shapes mentioned in the synonymous list in terms of shell form, growth lines and notches in aperture opening. Gürsoy (2002) and Gürsoy and Taner (2012), is similar to the form given in the synonymous list, although in the Çorum basin *Velates* forms, the coils in the first rounds are more prominent. Mikuž (2006) shows a similarity within the plates 1 and 2 in terms of shell form, growth lines and notches in aperture. Deveciler (2008) and Hoşgör (2012) show similarities with the forms indicated on the plates, which are mostly core forms and their apical tours are not significant. It is similar to the figures given in the Plaziat (2012)'s study in which he examined the morphological structure of *Velates* species.

Location and Stratigraphic Level: Bayat formed a horizon (AYV-112) during the transition from *Ostrea roncaensis* horizons to nummulite set in Ayvalıca. Archive numbers are 2018/35 and 2018/36.

Paleogeographic Distribution and Stratigraphic Level: Chemnitz (1786) stated it's spread in Ypresian in Paris basin; Deshayes (1824) stated that it was very abundant in Rethissuil, Guise, Soissonnais in the north east of Paris and also it was observed in Vicentin in Ronca. Koch (1883) stated that well-preserved echinoids and mollusks were found in the limestones where the Middle Eocene fossilization was very rich, from Hungary to Romania (Magyarokereke and Marótlaka). Other fossils found with *Nerita (Velates) schmideliana* are *Natica caepacea, N. cigaretina, Cerithium giganteum, Xenophora agglutinans, Echinolampas giganteus, Euspatangus crassus*. The author stressed that all the fossils studied show the Middle Eocene and are also present in the Paris basin. De Gregorio (1894) noted that it is rarely seen in Mt. Postale, but it is more common in S.G.Ilarione in the Vicentin region, where he studied the Parisien level, which corresponds to the Lutetian level in northern Italy. He emphasized that the *Velates schmideliana* species, which he described in his study in Roncá in Lower and Middle Eocene sediments in northern Italy in 1896, showed a wide spread in the region and the climatic conditions were effective in this spreading. Oppenheim (1901), stated it in Italy, Vicenza in Grancona, Mossano, St. Nicola and St. Priabonian in Giovanni; Koch (1883), asserted the coexisting species such as *Terebellum* sp., *Natica caepacea*, *Nerita (Velates) schmideliana* and especially the giant cerithides characterizing Middle Eocene (Parisien=Lutetian) sharply in his article evaluating the studies conducted in 1882 in the north-east of Budapest. Dainelli (1904, 1905) described it in the Middle Eocene strata of Bribir, Ostroviza and Zazvic. For the sample described by Cossmann and Pissorro (1910-13) in Laon in northern France, the stratigraphic extension is given as Cusian (Thanetian-Lutetian). Boussac (1912) described in the Nummulitic limestones in Diablerets, Switzerland. Wenz (1938) stated that it spread in Ypres in Belgium and Saint Gobain in France during the Upper Eocene. Eames (1952), in his study on Western Pakistan and Western India Eocene, mentioned that the *Velates perversus* species had a wide spread throughout the Eocene, Ypresian in Tibet, Egypt, Iran, Somalia, Pyrenees, Sudan; early Lutetian in France, Italy, Anatolia and Egypt Mokattam; Lutetian in Italy, the Alps, France, Hungary and the Balkans, Iran, Iraq, Armenia; it was also discovered in the French Alps, Northern Italy, Croatia in the Priabonian stage and throughout the Eocene in Niger, Chat, Sicily, Russia. Szöts (1953) stated it spread in the Early Eocene around Mór, Kisgyón, Dudar, Zirc, Úrkút in the Transdanube basin; in the Middle Eocene in Esztergom, Bajót, Tatabánya, Dudar, Bakony; in Paris Basin in the Early-Middle Eocene. Mészáros (1957) stated that the spread of *Velates (V.) schmidelianus* existed during the first marine cycle in the Lower and Middle Eocene in Transylvania and in the Upper Eocene in the secondary marine cycle. In addition, it has spread in the Lower-Middle

Eocene in the Paris and Loire basins in France; during the Eocene in Hungary; Eocene in Bulgaria; Eocene in Egypt; Middle Eocene in Morocco and Tunisia; Lower Eocene in Crimea; Eocene in Switzerland and Bavaria; Eocene-Oligocene in Northern Italy; Eocene in southern France; Upper Eocene in Transcaucasia. Mészáros stated the spread of the species is at the Eocene-Oligocene interval in general. Vlaicu-Tătărîm (1963) described the species, which was observed in all mesogenic areas from the Paris basin to Burma, late Lutetian in Cluj, Romania. Karagiuleva (1964) has summarized in a table that it spreads in the Eocene-Oligocene in Bulgaria; Paleocene and Lower-Middle Eocene in England-France Basin; Paleocene-Eocene in North Africa; Eocene in Pyrenees and Southern France; Eocene-Oligocene in the Alps and Northern Italy; Upper Eocene in Yugoslavia; Eocene in Northwest Transylvania; Lower and Upper Eocene in Ukraine and Crimea. Kecskemétiné-Körmendy (1972) described the mollusc-bearing Middle Eocene sandstone benches in the Doroger basin of Hungary. Squires and Demetrion (1992, 1994) reported the stratigraphic distribution of the *Velates perversus* species Thanetian (Late Paleocene) -Bartonian (late Middle Eocene) in Europe and India. Savazzi (1992) described the species in Verona, Roncá' in the Middle Eocene is equivalent to the Mollusk layers called "Capay" and "Domengine", which correspond to the Early Eocene-early Middle Eocene interval on the Pacific coast of North America. The geographical distribution of the species was determined in Pakistan, India, Myanmar, Tibet, Middle East, North Africa, Western Europe, Florida, Panama and Southern California Baja, Mexico. In the studies around Ankara, Gürsoy (2002) reported that it spread in the Paleocene-Eocene in Temelli Polatlı; Deveciler (2008) stated it's extension in Lutetian-Bartonian in Haymana; Hoşgör (2012) determined it's extension in Early-Middle Eocene in Haymana-Polatlı. Mikuž (2006) made a comparison of two *Velates perversus* from Early and Middle Eocene areas. He noted that the *Velates* from the Goriška brda region were the largest and well-preserved *Velates* in Slovenia, while those in Gračišće near Istria Pazin had only the core parts left. Plaziat (2012) studied the morphology, stratigraphic and paleogeographic distribution of the *Velates* species, which is known as *V.perversus* or *V.schmidelianus,* he emphasized that is the most characteristic species found in subtropical seas in the whole northern hemisphere from Thanatian to Early Oligocene. He indicated that the Tetis or Mesogen type species is not only observed in France, Italy and northern Spain, but also spread from the Himalayas to the island of California and Java (Figure 8).

Phyllum : Foraminifera d'Orbigny, 1826

Class : Globothalamea Pawlowski, Holzmann and Tyszka, 2013

Ordo : Rotaliida Delage and Hérouard, 1896

Super Family : Nummulitoidea Blainville, 1827

Family : Nummulitidae Blainville, 1827

Genus : *Nummulites* Lamarck, 1801

***Nummulites aturicus* Joly and Leymerie, 1848**

Plate 3, Figures 1a, 2-4

1848 *Nummulites aturica* Joly and Leymerie, p. 187, pl. 2, figs. 9, 10.

1911*b Nummulites atacicus* Leymerie, Boussac, p. 28, pl. 2, fig. 26; pl. 3, fig. 15; pl. 5, fig. 14.

1981 *Nummulites aturicus* Joly and Leymerie, Schaub, p. 95, pl. 15, figs. 20-26; pl. 16, fig. 1-30.

2007 *Nummulites aturicus* Joly and Leymerie, Görmüş et al., p. 6, pl. 2, figs. 1-4.

2011 *Nummulites aturicus* Joly and Leymerie, Less et al., p. 821, figs. 38 q, r, t, u.

Description: Species have been identified from microspheric individuals in the study area. The valve is bulging and lenticular. The edges are less sharp looking. The average diameter is between 15-20 mm and the thickness is 2-3 mm. On the surface of the shell, the partition network is radial, slightly wavy, and in some others granular. In the granular species, the granules are larger in the central part. Equatorial cross-sections are slow-winding and the number of turns is high. 20 turns were counted in the sample with the diameter of 20 mm and 26 turns were counted in the sample with the diameter of 25 mm. The wall is thicker than in the other types. The compartments are slightly curved. The compartment width is greater than the height. It has a rectangular appearance. The first chamber is very small. Round heights reach to 1 mm in the middle sections. The most prominent feature of the species is that the shape of the shell is lenticularly bulged, the edges are sharp, the chambers

are rectangular and the winding is regular and frequent. Macrospheric individuals of the species have smaller diameters of 5-6 mm. Thickness is 2-3 mm.

Similarities and Differences: Avşar (1991, 1994) made a description of macrospheric individuals belonging to the species from Yozgat and Malatya areas. Örçen (1986) defined both macrospheric and microspheric individuals in the Malatya area. The dimensions of the microspheric individuals described by Örçen (1986) were found to be slightly smaller. It is separated from the *N.perfaratus* by the sharpness of the shell edges and the arrangement of the chambers from the center to the edge.

Location: It is one of the most abundant samples found in the section. The most abundant sample points are between AYV 116-123.

Stratigraphic Level: The paleogeographic distribution of the species is extensive. The age range is also known as Lutetian and according to Serra-Kiel et al. (1998) it is a species observed in the the SBZ16 biozone. Kenawy et al. (1993) described it in the Middle Eocene (late Lutetian) in the Nile valley in Egypt, Less et al. (2011) described it in the Early-Middle Bartonian in the Thrace basin, Örçen (1986) described it from Lutetian around Malatya, Avşar (1991, 1994) described it from late Lutetian around Yozgat and Malatya, Görmüş et al. (2007) described it in Lutetian again around Dinar and Avşar (2012) described it in the Upper Lutetian-Bartonian sediments around Darende, Less et al. (2011) described it in the late Bartonian (SBZ18) in the Thrace basin.

Nummulites cf. *beaumonti* d'Archiac and Haime, 1853

Plate 3, Figures 10-12

1853 *Nummulites beaumonti* d'Archiac and Haime, p. 133.

1981 *Nummulites beaumonti* d'Archiac and Haime, Schaub, pl. 53, figs. 17-19, 22-25.

2006 *Nummulites beaumonti* d'Archiac and Haime, Eraslan, p. 36, pl. 2, figs. 8-15.

2019 *Nummulites beaumonti* d'Archiac and Haime, Al Menoufy, p. 154, figs. 3G-Q.

Description: The shell is lenticular with sharp edges. Species have been identified from the macrospheric individuals. In these individuals, the diameter was measured as 5-6 mm and the thickness as 1-2 mm. The number of laps is between 6-8. Microspheric individuals are slightly larger and their diameter varies between 7-9 mm. In equatorial sections, the chambers are rectangular and their height is more than their width. Compartments are thin, slightly curved and flat.

Similarity and Difference: *N. beaumonti*'s smallness in size, and the greater height of the chambers than the width, shows its difference from other nummulite species.

Location: With *Nummulites aturicus,* they were detected only to a lesser extent, near the upper levels of the section (AYV 116-119).

Stratigraphic Level: Örçen (1986) made definition in the late Lutetian around NW Malatya Medik-Ebreme , Eraslan (2006) described it in middle-late Lutetian in Ankara Bağlum-Kazan. Al Menoufy (2019) described it in the SBZ19 biozone from the United Arab Emirates, Avşar (1991, 1994) described it in the late Lutetian around Yozgat and Malatya; it was described in the middle Lutetian in the SBZ15 biozone in Aydıncık (Yozgat) by Avşar et al. (2010); Örçen (1986, 1992) described it in the Late Lutetian in Malatya and Bursa.

Nummulites perforatus (De Montfort, 1808)

Plate 4, Figures 1-4

1808 *Egeon perforatus* de Montfort, t. I, pp. 166-167.

1911*a Nummulites perforatus* (Montfort), Boussac, pp. 15-16, pl. 6, figs. 5, 8.

1911*b Nummulites perforatus* (Montfort), Boussac, p. 21, pl. 3, figs. 1-7, 13, 14, 16.

2010 *Nummulites perforatus* (Montfort), Deveciler, p. 193, pl. 1, figs. 1-6, pl. 2, figs. 1-8.

2019 *Nummulites perforatus* (de Montfort, 1808), Al Menoufy, p. 149, figs. 3A-F.

Description: Illustrated samples were identified from microspheric individuals. The shell is lenticular. Very swollen and rounded edges are the characteristics of the species. The diameter and thickness of the shell are 18-30 mm and 6-8 mm respectively. The partition network is light meandered. The arrangement of the

chambers in the equatorial sections is also among the most descriptive features of the species. In advanced microspheric individuals, the initial 6-7 rounds are tight, It is rare in the next 8-15 rounds and very tight in three-phase coiling in the laps towards the last edges.. The number of tours is between 30-45. The chambers are rectangular in shape and the width of the chambers is higher than their height. Macrospheric individuals are smaller. The partition network is radial, slightly wavy. Between the chamber lines there are small granules.

Similarity and Difference: It is similar to *Nummulites aturicus* species. In contrast, the *Nummulites perfaratus* type is easily differentiated from other nummulite species by its bulging shell, rounded margins and the difference of coiling in three-phase equatorial chambers.

Location: It is found intensely at the top levels of the Ayvalıca section (AYV 125-126).

Stratigraphic Level: Avşar (1989, 1991, 1994) determined it in his research in the vicinity of Elazığ, Yozgat and Malatya in the Late Lutetian, Deveciler (2010) made a description in Bartonian in the Haymana field and Al Menoufy (2019) determined it in SBZ19 biozone from United Arab Emirates. According to Serra-Kiel et al. (1998), it is a species belonging to the SBZ17 biozone.

Family : Nummulitidae Blainville, 1827

Genus : *Assilina* d'Orbigny, 1839

***Assilina exponens* (Sowerby, 1840)**

Plate 4, Figures 5-11

1837-1840 *Nummulites exponens* Sowerby *in* Sykes, 2(5), p. 719, pl. 12, fig. 14.

1879 *Assilina exponens* Sowerby, De La Harpe, t. 16, p. 212.

1911*b Assilina exponens* Sowerby, Boussac, p. 100.

1976 *Assilina exponens* (Sowerby), Sirel and Gündüz, p. 39, pl. 10, fig. 9; pl. 11, fig. 1-9.

2006 *Assilina exponens* (Sowerby), Eraslan, p. 35.

2012 *Assilina exponens* Sowerby, Dinçer and Avşar, p. 46, pl. 2, figs. 1-12.

Description: The shape of the shell is thin lenticular in microspheric individuals; and it is flat and very flat. Partition traces are common and evident. The shell diameter reaches 30-40 mm. The shell thickness is between 1-2 mm. The coils in the equatorial section are regular and more loosely coiled towards the edges than the first coils. The chambers are rectangular, the width of the chambers is more than it's height. In axial sections, the tours cover each other, especially in the final sections. Macrospheric individuals are lenticular and traces of chambers are also evident. Several granules are observed in the center of the shell. The diameter of the shell varies between 5-6 mm and the thickness varies between 1-2 mm. The first chamber is round, oval shaped. In equatorial sections, the sections are vertical, slightly radial.

Similarity and Difference: It is easily distinguished from other genera and species due to the flattened shell of *Assilina exponens* species, U shaped tours, the presence of splitting traces on the shell.

Location: It is found intensely at the top levels of the section (AYV 125-126).

Stratigraphic Level: Sirel and Gündüz (1976) determined it aroun Polatlı in the Cuisian-Lutetian; Örçen (1986, 1992) determined it around KB Malatya Medik-Ebreme and Bursa in the late Lutetian, Avşar (1992) determined it around Mersin Namrun in the Lutetian; Özgen (1998) determined it around Çölmekçiler, Hacıgüzel, Çukurca (Bolu) and Safranbolu, Alparslan, İnözü, Ahmetoğlu (Kastamonu) in the Lutetian aged sediments. Örçen (1986, 1992) determined it around Malatya and Bursa in the late Lutetian; Avşar vd. (2010) determined it in the Aydıncık (Yozgat) SBZ16 biozone in the late Lutetian; Dinçer and Avşar (2012) determined *A.exponens* species around Malatya Darende in the SBZ16 biozone in the Late Lutetian.

5. Discussion

Living environments, life styles and life cycles of mollusks observed in the form of agglomeration are important for the interpretation of past environments. Therefore, it is necessary to analyze today's mollusc lives. According to Volety's (2013) study on the properties and habitats of ostreids, ostreids generally live in brackish shallow waters such as estuaries with

lower salinity than ocean water, forming beds or reef-like colonies. The larvae begin their lives by clinging to a hard surface, preferably other ostreid shells. They are hermaphrodites, that is, they start their lives as male individuals, sometimes turning to female and sometimes male. If the temperature of the water rises, they pass to the breeding period. They mostly live in eutrophic environments where food is abundant; they use their gills to take up oxygen in the water, feed themselves with algae and plankton. An adult ostreid can filter water up to 1500 times its volume daily. Ostreids survive in intertidal reefs by tightly closing their lids until the water returns when exposed to outdoor conditions during low tide. Thanks to this adaptation, the organism is kept away from other organisms, air and temperature changes. Volety (2013) suggested that the healthy formation of ostreid reefs should be supported in order to clean the estuaries naturally due to these characteristics.

In the study area, the dimensions, abundance and repetition of the ostreid individuals in the horizons suggest that too much nutrients come to the environment from the land and that it is a eutrophic paleoenvironment rich in algae. Although determined at marly levels, it was observed that larvae preferred other ostreid individuals as hard ground, thus stacking one another and forming several horizons. In the area under tidal influence, *Ostrea roncaensis* individuals in the estuary when the water is drawn may be affected by changing environmental conditions by closing their lids tightly. Because of their physical structure, they have a higher chance of survival compared to other organisms in the environment and therefore showed a higher population than other organisms. The maximum level of viability may have led to a reduction of oxygen in the environment after a while, leading to the death of organisms.

Nummulites, which are prominent in the study area with their dominant character, have been described by Purton and Brasier (1999) as the dinosaurs of the unicellular world. *Nummullites millecaput* as being the largest species in Lutetian, with a diameter of 160mm, due to their extinction only in the Late Eocene-Oligocene range, they were reduced in size and diversity. In their study on the giant Eocene *Nummulites* in the Hampshire basin, they put forward that the abundant and large-sized Middle Eocene *Nummulites* grow rapidly under eutrophic conditions with high nutrient intake, and as individuals grow and their shells become more calcified, the risk of prey decreases.

The nature and distribution of foraminifera are important in determining the different generations of the nummulite sets. Since the Cretaceous, the milliolids have characterized the reef lagoon, the *Nummulites* have been characterized by their reef margin, front and shallows (Tuzcu and Karabıyıkoğlu, 1991). Racey (2001) emphasized that *Nummulites* have more than 300 species but only 5% of them can form nummulite sets. He pointed out that the species forming this embankment are stratigraphically limited to the Late Early-Middle Eocene interval. *Nummulites* sets are often less associated with other micro- or macro-fossils, suggesting that the deposition develops in the nutrient-poor oligotrophic environment. Kopaevich et al. (2008) found that *Nummulites* generally live symbiotically with photosynthetic algae and therefore prefer warm (~ 25 ° C), clear and shallow waters (<120 m) in the euphotic zone. In the symbiotic relationship, the *Nummulites* provided shelter for algae, while algae produced nutrients and oxygen for the *Nummulites*. Light intensity and energy of water are the two most important factors controlling foraminifera distribution. Our field observations about the *Nummulites* show that the peak of the nummulit set, which forms a hill, is closer to the theory, that the paleodepth is between 10-30 m and that they live in shallow and warm euphoric zones and eutrophic environments. It is thought that by the abundance of nutrients from the estuary they increase in large number and size of development and form the nummulite set.

When all of the above mentioned informations and field observations are taken into consideration, the storage environment modeling developed by Catuneanu is thought to be constructed in Ayvalica Village as the land model. Catuneanu (2006) classified storage in sea-to-land transition systems in three broad categories: These are: 1. nonmarine (areas out of reach of sea floods); 2. coastal (intermittently under the influence of seawater); 3. marine (areas permanently covered with seawater) (Figure 9).

Ostreids are known to live in the estuary or lagoon and *Nummulites* in the reef edge or in front of the reef. When these informations are evaluated together with our land findings, transgressive river mouth

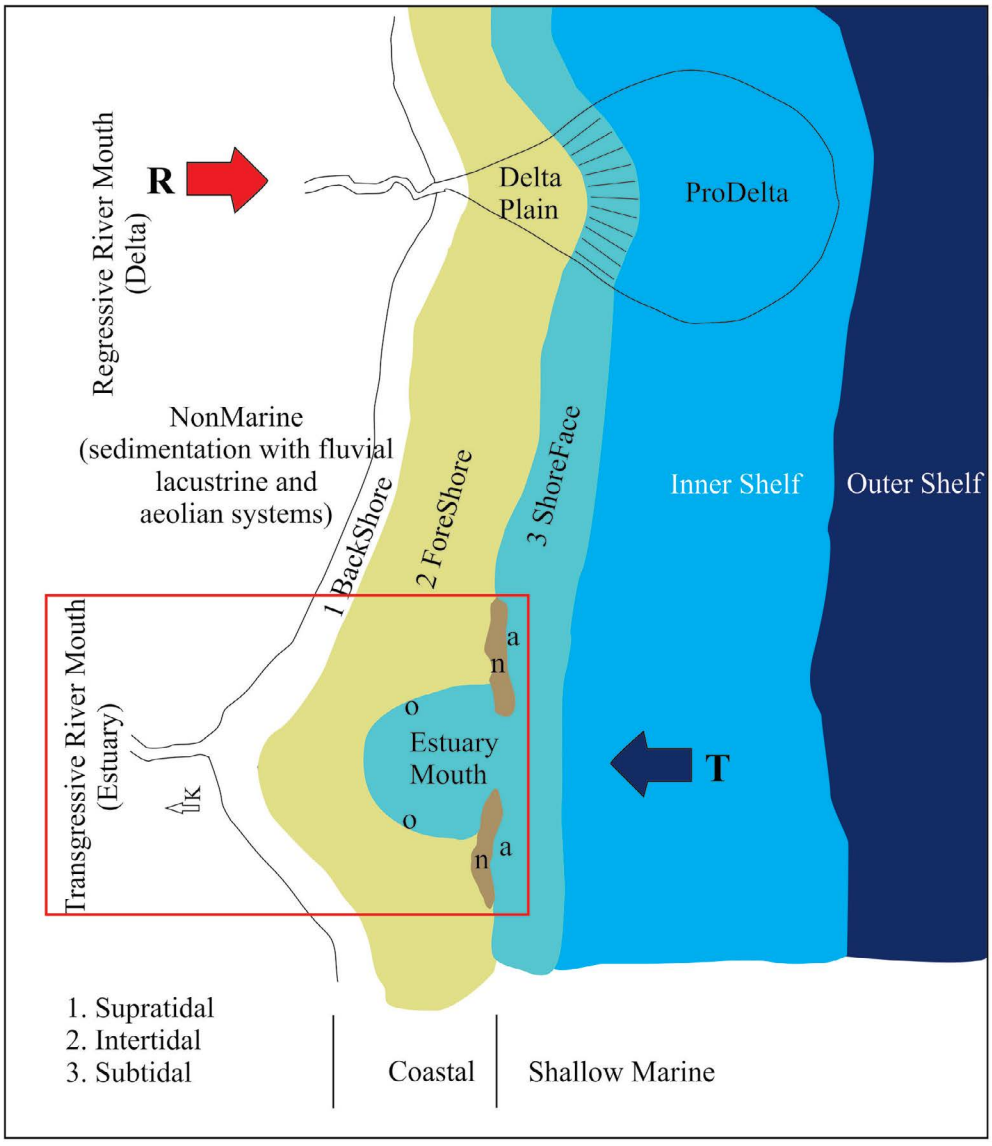

Figure 9- Transition from marine to non-marine environments; Regressive (R) and Transgressive (T) area and the coastline is an open shoreline (rearranged from Catuneanu, 2006). The estimated study area is indicated by a red frame (o-*Ostrea*, n-*Nummulites*, a-*Assilina*).

modeling is striking in the classification of the storage environment given by Catuneanu (2006).

6. Conclusions

In this study, two molluscs *Ostrea roncaensis, Velates perversus* and four foraminifers *Nummulites aturicus, N. beamunti, N. perfaratus* and *Assilina exponens* which are most abundant in Ayvalıca area, were identified and also *Ostrea*, *Velates*, *Nummulites* and *Assilina* abundance biozones were determined. According to the macro and microfauna content observed in the Koçaçay formation sediments, the age range is determined as Lutetian-Bartonian.

Environmental interpretations were performed with the obtained data. Ostreids are generally bivalves living in brackish water in the estuary environment (Volety, 2013). *Nummulites* are known as euphotic shallow, warm water foraminifera (Purton and Brasier, 1999). Field studies and living environments of the mentioned organisms show a transgressive river mouth environment where water is drawn from time to time (Figure 8 and 9). *Ostrea roncaensis* accumulations, which are repeated several times,

constitute the clue to the established theory. The abundance and size of ostreids, which develop with intense nutrient flow from the land, as well as the presence of cerithid, ampullinide and especially algae indicate transgressive river mouth environment. The absence of ostreids outside the estuary is evident in the development of a thick nummulite set. All data lead us to the conclusion that the Kocaçay formation in Ayvalıca was deposited in a sedimentary environment starting from the estuary conditions and continuing with shallow warm sea (Figure 10).

Acknowledgements

This study was supported by MTA Şehit Cuma Dağ Natural History Museum and it was carried out in the scope of "Çankırı-Çorum Basin Eocene-Oligocene Stratigraphy and Paleogeography" project (project no: 2018-08-16-01, 2017-08-16-01, 2016-08-16-01). The authors thank to Assoc. Prof. Huriye Demircan for the scientific help during the field studies and for her scientific contributions; Dr. İbrahim K. Ertekin, Prof. Dr. Cemal Tunoğlu and Assoc. Prof. Levent Karadenizli for their scientific help during the field studies in 2016; Prof. Dr. Güler Taner for supporting this article with her suggestions.

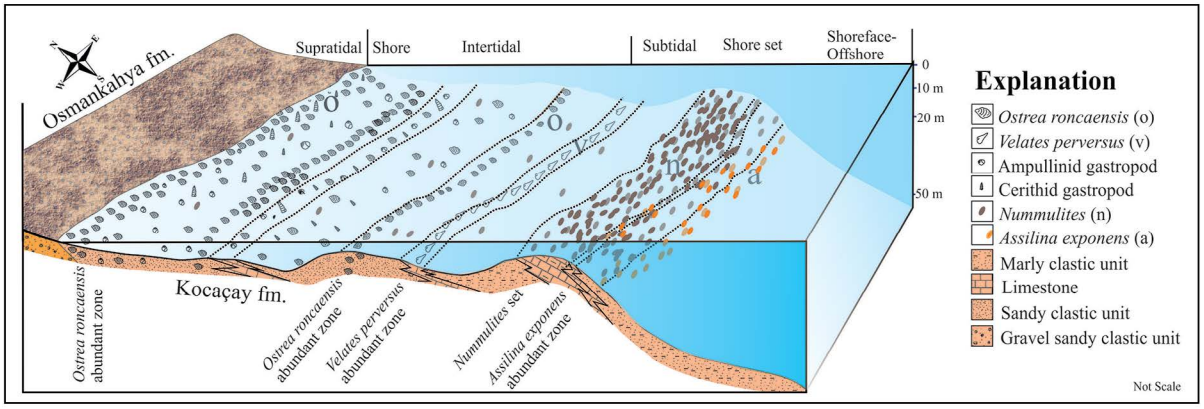

Figure 10- Study area, depositon model of Kocaçay formation.

References

Abad-Garcia, A. 2011. Paleotaxodonta y Pteriomorphia del Eoceno del Margen sur de la Depresión Central Catalana. Tesis Doctorals en Xarxa. Universitat Autónoma de Barcelona. 795 p., 28 lam.

Abate, A., Baglioni, A.,R., Bimbatti, C., Piccoli, G. 1988. Rassegna di Molluschi Marini Bentonici e Nectonici del Cenozoico Triveneto. Memorie di Scienze Geologiche 11: 135-171. Padova.

Abouessa A., Pelletier J., Duringer P., Schuster, M., Schaeffer, P., Métais E., Benammi, M., Salem, M., Hlal, O., Brunet, M., Jaeger, J.J., Rubino, J.L. 2012. New insight into the Sedimantology and Stratigraphy of the Dur At Talah tidal-fluvial sequence (Eocene-Oligocene, Sirt Basin, Libya). Journal of African Earth Sciences 65: 72-90.

Aigner, T. 1986 Bio. abrics as Dynamic Indicators in Nummulitik Accumulations, Discussions Journal of Sedimentary Petrol 56 (2): 317-320.

Akarsu, İ. 1959. Çorum Bölgesinin Jeolojisi. Türkiye Jeoloji Kurumu Bülteni 7(1) 19-29.

Akyol, E. 1978. Etude Palynologique De L'eocene De Bayat (Çorum-Turquıe) Et Essai De Correlation Entre Karakaya Et Emirşah. Bulletin of The Mineral Research and Exploration 91: 39-53.

Al Menoufy, S. 2019. *Nummulites perforatus* (de Montfort, 1808) and *N.beaumonti* d'Archiac and Haime, 1853: a new record from Gebel Hafit, United Arab Emirates. Alcheringa: An Australasian Journal of Palaeontology 43(1): 146-156.

Alpan, T. 1968. Bayat (Çorum) Kuzeybatısının Jeoloji Etüdü. Maden Tetkik ve Arama Genel Müdürlüğü Rapor No: 6822, Ankara (unpublished).

Ateş, M., İmik, M., Ulu, Ü., Arbas, A., Gök, L., Genç, Ş., Poyraz, N., Cevher, F. 2010. Boğazkale Osmancık (Çorum)-Gümüşhacıköy (Amasya) Dolayının Jeolojisi. Maden Tetkik ve Arama Genel Müdürlüğü Rapor No: 11246, Ankara (unpublished).

Avşar, N. 1991. Systematic study of the some species of the *Nummulites* of Uzunlu (Boğazlıyan-Yozgat) Region. Yerbilimleri/Geosound 19: 17-33.

Avşar, N. 1992. Namrun (İçel) Yöresi Paleojen Bentik Foraminifer Faunası. Bulletin of the Mineral Research and Exploration 114: 127-144.

Avşar, N. 1994. Kaçadağ-hasanağa Deresi (B Malatya) Civarının bazı *Nummulites* Türlerinin Sistematik İncelemesi. Çukurova Üniversitesi Mühendislik-Mimarlık Fakültesi 15.yıl Sempozyumu. 277-290.

Avşar, N., Özser, E., Dinçer, F., Aksoy, E., İç, Z. 2010. Aydıncık (Yozgat) Yöresi Tersiyer (Lütesiyen) İstifinin Bentik Foraminiferleri. Çukurova Üniversitesi Mühendislik-Mimarlık Fakültesi Dergisi 25 (1-2): 17-32.

Aziz, A. 1973. İskillip civarı ile güney ve güneybatısın detay jeolojisi ve petrol olanakları. Maden Tetkik ve Arama Genel Müdürlüğü Rapor No: 6132, Ankara (unpublished).

Bayan, F. 1870. Sur les Terrains Tertiaires de la Vénetie. Bulletin de la Société Géologique de France 1869-1870. 27(2): 444-486, Paris.

Beurlen, K. 1944. Beiträge zur Stammesgeschichte der Muscheln. Mathematisch-Naturwissenschaftlichen Abteilung der Bayerischen Akademie der Wissenschaften zu München, Sitzungsberichte (1–2): 133–145.

Bilgiç, T. 2012. Çankırı-Çorum Tersiyer Havzasının Doğu Kesiminin Jeolojisi. Maden Tetkik ve Arama Genel Müdürlüğü Rapor no: 11567, Ankara (unpublished).

Bilgin, Z.R., Esentürk, K., Güner, E., Kara, H., Akarsu, B., Arbas, A., Elibol, E., Yaşar, T. 1986. Kırıkkale-Kesikköprü-Çiçekdağ Alanının Jeolojisi. Maden Tetkik ve Arama Genel Müdürlüğü Rapor No: 7876, Ankara (unpublished).

Birgili, Ş., Yoldaş, R., Ünalan, G. 1975. Çankırı-Çorum Havzasının Jeolojisi ve Petrol Olanakları. Maden Tetkik ve Arama Genel Müdürlüğü Rapor no: 5621, Ankara (unpublished).

Blainville, H. M., Ducrotay de. 1827. Manuel de malacologie et de conchyliologie (1825). Paris: F. G. Levrault.

Blumental, M.M. 1938. Kızılırmak ve Yeşilırmak arasındaki mıntıkada bulunan linyit, hidrokarbür ve bitümlü şist yatakları. Maden Tetkik ve Arama Genel Müdürlüğü Rapor No: 164, Ankara (unpublished).

Blumental, M.M. 1948. İskilip, Osmancık ve Tosya arasındaki mıntıka ve bu mıntıkanın linyitleri hakkında jeolojik mülahazalar. Maden Tetkik ve Arama Genel Müdürlüğü Rapor No: 676 Ankara (unpublished).

Bouchet, P., Rocroi, J.P., Hausdorf, B., Kaim, A., Kano, Y., Nützel, A., Parkhaev, P., Schrödl, M., Strong, E. 2005. Revised Classification, Nomenclator and Typification of Gastropod and Monoplacophoran Families. Malacologia 61 (1–2): 1–526.

Bouchet, P., Rocroi, J.P., Bieler, R., Carter, J.G., Coan, E.V. 2010. Nomenclator of Bivalve Families with a Classification of Bivalve Families. Malacologia 52 (2): 1–184.

Boussac, J. 1911*a*. Études Stratigraphiques et Paléontologiques sur le Nummulitique de Biarritz. Ann. Hébert, 5, 1-96.

Boussac, J. 1911*b*. Études Paléontologiques sur le Nummulitique Alpin. Texte et Planches, Paris.

Boussac, J. 1912. Mémoires Pour Servir à l'Explication de la Carte Géologique Détaillée de la France Études Stratigraphiques sur le Nummulitique Alpin. 386 p. Paris.

Catuneanu, O. 2006. Principles of Sequence Stratigraphy. Elsevier 387 p.

Chemnitz, J. H. 1786. Neues system atisches Conchylien-Cabinet, 9: 1-194. Nürnberg.

Cossmann, M., Pissarro, G. 1910-1913. Iconographie Complete des Coquilles Fossiles de L'Eocene des Environs de Paris. T.II – Scaphopodes, Gastropodes, Brachiopodes, Cephalopodes, 65 lev., Paris, France.

Cuvier, G. 1795. Second Mémoire sur l'organisation et les rapports des animaux à sang blanc, dans lequel on traite de la structure des Mollusques et de leur division en ordre, lu à la société d'Histoire Naturelle de Paris, le 11 prairial an troisième. Magazin Encyclopédique, ou Journal des Sciences, des Lettres et des Arts 2: 433-449. Paris.

Cuvier, G. 1834. The Animal Kingdom: Arranged According to its Organization, Serving as a Foundation for The Natural History of Animals, and an Introduction to Comparative Anatomy. Vol. 3: Mollusca, Annelides, Crustacea, Arachnides and Insecta London.

Çalgın, R., Pehlivanoğlu, N., Ercan, T., Şengün, M. 1973. Ankara Civarının Jeolojisi. Maden Tetkik ve Arama Genel Müdürlüğü Rapor No: 6487 Ankara (unpublished).

Çapan, U.Z., Buket, E. 1975. Aktepe-Gökdere Bölgesinin Jeolojisi ve Ofiyolitli Melanj. Türkiye Jeoloji Kurumu Bülteni 18(1): 11-16.

Dainelli, G. 1904. La Fauna Eocenica di Bribir in Dalmazia *in* Canavari, M., Palaeontographia Italica Memorie di Paleontologia 10: 141-275, Pisa.

Dainelli, G. 1905. La Fauna Eocenica di Bribir in Dalmazia *in* Canavari, M., Palaeontographia Italica Memorie di Paleontologia 2, 11: 1-92, Pisa.

D'Archiac, A., Haime J. 1853. Description des animaux fossiles du groupe nummulitique de l'Inde : Essai d'une Monographie des *Nummulites*. 373, 36 pls. Paris.

De Gregorio, M.A. 1884. Studi Su Talune Conchiglie Mediterranee Viventi e Fossili. Siena. 458 s.

De Gregorio, M.A. 1894. Description des Faunes Tertiaires de la Vénétie Fossiles des Environs de Bassans Surtout des Tertiaire Inférieur de L'Horizon a Conus diversiformis Desh. et Serpula spirulaea Lamk. Annales de Géologie et de Paleontologie. Turin-Palerme.

De Gregorio, M.A. 1896. Description des Faunes Tertiaires de la Vénétie Monographie de la Faune Eocenique de Roncá. Annales de Géologie et de Paleontologie. Turin-Palerme.

De Montfort, D.P. 1808. Conchyliologie Systématique, et Classification Méthodique de Coquilles. F. Schoell, 409 p., Paris.

Deshayes, G.P. 1824-1837. Description des Coquilles Fossilles des Environs de Paris. Tome Premier. Conchiféres. Text. 392 p., Tome Second. Mollusques. 814 p., (1837) Tome Premier. Atlas, 28 p., 65 pls., (1837) Tome Second. Atlas. 51 p., 101 pls., Paris.

Deveciler, A. 2008. Haymana Çevresindeki Eosen Yaşlı Çayraz Formasyonu Pelecypoda ve Gastropoda Faunalarının Paleontolojisi. Ankara Üniversitesi Yüksek Lisans Tezi, 57 s., 3 lev., Ankara (unpublished).

Deveciler, A. 2010. The first appearance of the Bartonian benthic foraminifera at the Çayraz Section (north of Haymana, south of Ankara, central Turkey). Yerbilimleri 31 (3), 191-203.

Dinçer, F., Avşar, N. 2012. Darende Havzası (KB Malatya) Üst Lütesiyen-Bartoniyen Birimlerinin Bentik Foraminifer Biyostratigrafisi ve Ortamsal Yorumu. Yerbilimleri. 33 (1): 31-58.

Eames, F.E. 1951. A Contribution to the Study of the Eocene in Western Pakistan and Western India. B. The description of the Lamellibranchia from standard sections in the Rakhi Nala and Zinda Pir areas of the Western Punjab and in the Kohat district. 313-476.

Eraslan, A. 2006. Bağlum-Kazan (KB Ankara) Yöresinin Eosen Stratigrafisi ve Bentik Foraminiferleri. Çukurova Üniversitesi YL Tezi. Adana. 75 s.

Erdoğan B., Akay, E., Uğur, M.S. 1996. Geology of the Yozgat Region and Evolution of the Collisional Çankırı Basin. International Geology Review, 38: 788-806.

Ergun, O.N. 1977. Sedimantology of Tertiary Evaporites, Uğurludağ Area, Çankırı-Çorum Basin, Turkey. Imperial College of Science and Technology. London. 260 s.

Erol, O. 1953. Çankırı-Sungurlu-Tüney Arasındaki Kızılırmak Havzasının ve Şabanözü Civarını Jeolojisi Hakkında Rapor. Maden Tetkik ve Arama Genel Müdürlüğü Rapor no: 2026, Ankara (unpublished).

Erol, O. 1959. Ankara Civarını Jeolojisi Hakkında Rapor. Maden Tetkik ve Arama Genel Müdürlüğü Rapor No: 2491, Ankara (unpublished).

Favre, J. 1914-1918. Catalogue illustre de la collection Lamarck. Museo d'Historia Naturales de Genéve, pl 112, Genéve.

Férussac, A.E. 1822. Tableaux systématiques des animaux mollusques classés en familles naturelles, dans lesquels on a établi la concordance de tous les systèmes; suivis d'un prodrome général pour tous les mollusques terrestres ou fluviatiles, vivants ou fossils. Paris. 110 s.

Gmelin, J.F. 1791. Caroli A Linné Systema Naturae per Regna Tria Naturae. Regnum Animalium. T. 1 (6): 3021-3909.

Golikov, A.N., Starobogatov, Y.I. 1975. Systematics of Prosobranch Gastropods. Malacologia 15(2):185-232.

Görmüş, M., Avşar, N., Dinçer, F., Uysal, K., Köse-Yeşilot, S., Kanbur, S., İç, Z. 2007. Dinar (Afyon) yöresi Eosen (Lütesiyen) sedimanlarının bentik foraminifer biyostratigrafisi. Yerbilimleri 28(1): 1-13.

Görür, N., Tüysüz, O., Şengör, A.M.C. 1998. Tectonic Evolution of the Central Anatolian Basins. International Geology Review 40: 831-850.

Gürsoy, M. 2002. Temelli-Haymana Yöresi Tersiyer Mollsuk Faunası ve Stratigrafisi Ankara Üniversitesi Yüksek Lisans Tezi, 75 s., 10 lev., Ankara.

Gürsoy, M., Taner, G. 2012. Kuşçu ve Macun köyleri arası Paleojen Mollusk Faunası ve Biyostratigrafisi, Temelli (GB Ankara). Türkiye Jeoloji Bülteni c. 55(2): 57-85.

Hakyemez, Y., Barkut, M.Y., Bilginer, E., Pehlivan, Ş., Can, B., Dağer, Z., Sözeri, B. 1986. Yapraklı-Ilgaz-Çankırı-Çandır Dolayının Jeolojisi. Maden Tetkik ve Arama Genel Müdürlüğü Rapor no:7966, Ankara (unpublished).

Harpe, P. de la. 1879. Les *Nummulites* du compté de Nice: leur espèces et leur distribution stratigraphique:

et échelle de *Nummulites*. Bulletin de la Société Vaudoise des Sciences Naturelles 16 (82): 201-243.

Harry, H. 1985. Synopsis of the supraspecific classification of living oysters (Bivalvia: Grypheidae and Ostreidae). Veliger, 28: 121-158.

Hoşgör, İ. 2012. Haymana-Polatlı Havzası Paleosen Mollusklarının Taksonomik Tanımlanması, Paleoekolojisi, Paleocoğrafyası ve Bentik Foraminiferlerle Biyostratigrafik Deneştirilmesi. Ankara Üniversitesi Doktora Tezi, 109 s., 11 lev., Ankara (unpublished).

Joly, N., Leymerie, A. 1848. Mémoire sur les *Nummulites*, considérées zoologiquement et géologiquement. Mémoire de l'Académie des Sciences de Toulouse 3(4): 149– 218.

Karadenizli, L. 1999. Çankırı-Çorum Havzasındaki Orta Eosen – Erken Miyosen Tortullarının Sedimantolojisi. Doktora Tezi. Ankara Üniversitesi.

Karadenizli, L., Kazancı, N. 2000. Çankırı-Çorum Havzasındaki PaleoYükselti ve Alt Havzalar. Cumhuriyetin 75.Yıldönümü Yerbilimleri ve Madencilik Kongresi, Maden Tetkik ve Arama Genel Müdürlüğü, Ankara.

Karadenizli, L., Seyitoğlu, G., Saraç, G., Kazancı, N., Şen, Ş., Hakyemez, Y., Savaşçı, D. 2003. Çankırı-Çorum Havzası Batı Kenarı Erken-Orta Miyosen Paleocoğrafik Evrimi. Bulletin of the Mineral Research and Exploration 126: 69-86.

Karadenizli, L., Saraç, G., Şen, Ş., Seyitoğlu, G., Antoine, P.O., Kazancı, N., Varol, B., Alçiçek, C., Gül, A., Ertan, H., Esat, K., Özcan, F., Savaşçı, D., Antoine , A., Filoreau, X., Hervet, S., Bouvrain, G., Bonis, L., Hakyemez, Y. 2004. Çankırı-Çorum Havzasının Batı ve Güney Kesiminin Memeli Fosillere Dayalı OligoMiyosen Biyostratigrafisi ve Dolgulanma Evrimi. Maden Tetkik ve Arama Genel Müdürlüğü Rapor No: 10706, Ankara (unpublished).

Karagiuleva, J. D. 1964. Les fossiles de Bulgarie. Fosilite na Blgarija VI a. Paléogene Mollusca. Blgarska Akademija na naukite (Sofija): 1-270 str., lev. 1-58.

Kaymakçı, N. 2000. Tectono-stratigraphical evolution of the Çankırı basin (Central Anatolia, Turkey), PhD Thesis, Universiteit Utrecht Geologica Ultraiectina, no. 190.

Kaymakçı, N., Özçelik, Y., White, S.H., Van Dijk, P.M. 2001. Neogene tectonic development of the Çankırı basin (Central Anatolia, Turkey). The Bulletin of Turkish Association of Petroleum Geologists 13: 27-56.

Kaymakçı, N., Özçelik, Y., White, S.H., Van Dijk, P.M. 2009. Tectonostratigraphy of the Çankırı Basin: Late Cretaceous to Early Miocene evolution of the Neotethyan Suture Zone in Turkey. Collision and Collapse at the Africa-Arabia-Eurasia Subduction Zone, The Geological Society of London, Special Publications 311: 67-107, London.

Kecskemétiné-Körmendy, A. 1972. A Dorogi-Medence Eocén Mollusca Faunája. Annales Ins. Geo. Pub. Hungarica. A Magyar Állami Földtani Intézet Évkönyve, 55(2): 147-287, Budapest.

Kenawy, A.I., Mohamed, H.K., Mansour, H.H. 1993. Biostratigraphic Zonation of the Middle Eocene on the Nile Valley. Zitteliana, 20: 301-309.

Keskin, E. 1992. Çiçekdağ (Kırşehir)-Yerköy-Şefaatli-Yozgat dolayının jeolojisi ve kömür olanakları. Maden Tetkik ve Arama Genel Müdürlüğü Rapor No: 9363, Ankara (unpublished).

Ketin, İ. 1955. Yozgat Bölgesinin Jeolojisi ve Orta Anadolu Masifinin Tektonik Durumu. Türkiye Jeoloji Kurumu Bülteni.6 (1): 1-40.

Koch, A. 1883. Bericht über die im Klausenburger Randgebirge und in dessen Nachbarschaft im Sommer 1882 Ausgeführte Geologische Special-Aufnahme. Földtani Közlöny. 117-140. Budapest.

Kopaevich, L.F., Lygina, E.A., Nikishin, A.M., Yakovishina, E.V. 2008. The Crimean Eocene Nummulite Bank. Moscow University Bulletin 63 (3): 195-198.

Kopek, G. 1980. A Bakony Hegység Ék-I Részének Eocénje. A Magyar Állami Földtani Intézet Évkönyve 63(1): 1-154. Budapest.

Kopek, G., Kescskemétiné T. 1964. A Bakonyi Eocén Köszéntelepek Keletkezési Körülményeiröl. Földtani Közlöny v. 94 (1-4): 340-348. Budapest.

Lahn, E. 1939. Kızılırmak ve Yeşilırmak Arasındaki Bölge Hakkında Rapor. Maden Tetkik ve Arama Genel Müdürlüğü Rapor no: 1026, Ankara (unpublished).

Lahn, E. 1943. Sungurlu, İskilip ve Kalecik Arasındaki Bölge Hakkında Muhtıra. Maden Tetkik ve Arama Genel Müdürlüğü Rapor no: 1498, Ankara (unpublished).

Lamarck, J. B. 1801. Système des animaux sans vertèbres, ou tableau général des classes, des ordres et des genres de ces animaux; Présentant leurs caractères essentiels et leur distribution, d'apres la considération de leurs rapports naturels et de leur organisation, et suivant l'arrangement établi dans les galeries du Muséum d'Histoire Naturelle, parmi leurs dépouilles conservées; Précédé du discours d'ouverture du Cours de Zoologie, donné dans le Muséum National d'Histoire Naturelle l'an 8 de la République. Published by the author and Deterville, Paris: 8tv + 432 pp.

Less, G., Özcan, E., Okay, A.İ. 2011. Stratigraphy and larger Foraminifera of the Middle Eocene to Lower Oligocene Shallow-Marine Units in the Northern and Eastern Parts of the Thrace Basin, NW Turkey. Turkish Journal of Earth Sciences, vol. 20: 793-845.

Linnaeus, C. 1758. Systema Naturae per regna tria naturae, secundum classes, ordines, genera, species, cum characteribus, differentiis, synonymis, locis. Editio decima, reformata. Laurentius Salvius: Holmiae, vol. 1, 824 ss.

Loeblich, A.R.Jr., Tappan, H. 1988. Foraminiferal Genera and Their Classification. Department of Earth and Space Sciences and Center for the Study of Evolution and the Origin of Life University of California, Los Angeles s. 2114.

Malaroda, R. 1967. Calcari Nummulitici. Note Illustrative della Carta Geologica d'Italia. F. 49 Verona. 21-23 pp. Servizio Geologico D'Italia. Roma.

Maucher, A. 1937. Çankırı, Tosya ve İskilip Tetkikine ait Raporlar. Maden Tetkik ve Arama Genel Müdürlüğü Rapor No: 340, Ankara (unpublished).

Mészáros, N.1957. Biblioteca de Geologie şi Paleontologie - I, Fauna de Molluşte a Depozitelor Paleogene din Nord-Vestul Transilveniei, 174 p., 33 pl., Bucureşti, Romine.

Mikuž, V., 2006. The new findings of *Velates* snail from Eocene flysch in Goriških brd in Gorišće in Istria. Geologija 49 (1): 53-60. Ljubljana.

Montfort, P. D. de. 1808-1810. Conchyliologie Systématique et Classification Méthodique des Coquilles. Paris: Schoell. Vol. 1: pp. 87+ 409 (1808). Vol. 2: pp. 676 + 16 (1810).

Norman, T. 1972. Ankara-Yahşihan bölgesinde Üst Kretase-Alt Tersiyer istifinin stratigrafisi: Türkiye Jeoloji Kurumu Bülteni, 15:180-276.

Norman, T. 1975*a*. Kuzey Kızılırmak Havzasının ERTS-A uydusu tarafından çekilmiş görüntülerinde bazı yeni tektonik gözlemler ve bunların yorumlanması. Türkiye Jeoloji Kurumu Bülteni, 18: 41-66.

Norman, T. 1975*b*. Çankırı-Çorum-Yozgat Bölgesinde Alt Tersiyer Yaşta Sedimentlerde Paleoakıntılar ve Denizaltı Heyelanları. Türkiye Jeoloji Kurumu Bülteni 18: 103-110.

Okan, Y., Hoşgör, İ. 2009. Early Eocene (middle-late Cuisian) Molluscs Assemblage from the Harpactocarcinid Beds, in the Yoncalı Formation of the Çankırı Basin, Central Anatolia, and Implications for Tethys Paleogeography. Türkiye Jeoloji Bülteni c. 52(1): 1-30.

Oppenheim, P. 1901. Über Enige Alttertiäre Faunen der Österreichischen-Ungarischen Monarchie. Beitr. Pälaont. Geol. Öst.-Ung. Orients (Wien) 13: 145 (1) 1- 277 (133), Taf. 11 (1) - 19 (9).

Oppenheim, P. 1918. Das Neogen in Kleinasien. Zeitschr, Deutsch Geol Ges Bd. 70, Berlin.

Orbigny, A. d'. 1826. Tableau méthodique de la classe des Céphalopodes. Annales des Sciences Naturelles 7: 245-314.

Orbigny, A. D. d'. 1839. Foraminifères, in de la Sagra R., Histoire physique, politique et naturelle de l'ile de Cuba. A. Bertrand. 1-224.

Oyal, N. 2016. Çankırı-Çorum Havzasındaki Oligosen Yaşlı Dev Gergedanın (*Paraceratherium*, Rhinocerotoidea, Mammalia) Tanımı, Evrimi ve Paleocoğrafyası. Hacettepe Üniversitesi Doktora Tezi (unpublished).

Oyal, N., Şen, Ş., Karadenizli, L., Saraç, G., Antoine, P.O., Metais, G., Özer Kayseri, M.S., Tunoğlu, C. 2017. Çankırı-Çorum Havzası ve Çevresinde, En Büyük Kara Memelisi Olan Baluchitherium 'un ve Eşlik Eden Diğer Omurgalıların Bulgu Yerlerinin Araştırılması ve Bölgenin Paleocoğrafyası. Maden Tetkik ve Arama Genel Müdürlüğü Rapor No: 13600, Ankara (unpublished).

Ozsvárt, P. 1999. Middle Eocene foraminifer, mollusc and ostracod fauna from the Csordakút basin (Gerecse Mountains, Hungary): palaeoenvironments recorded in a transgressive sequence. Annales Universitatis Scientiarum Budapestinensis, Sectio Geologica 32: 73-135. Budapest.

Örçen, S. 1986. Biostratigraphy and Paleontology of the Medik-Ebreme (NW Malatya) Area. Bulletin of The Mineral Research and Exploration 105 (105-106): 15-53.

Örçen, S. 1992. Gemlik (Bursa) Güney-Güneydoğusunun Nummulites'leri: Tanımlamaları, Stratigrafik Yayılımları ve Evrimi. Türkiye Jeoloji Kurumu Bülteni 7: 33-49.

Özgen, N. 1998. Batı Pontidler'in Paleosen-Eosen Bentik Foraminifer Toplulukları. Türkiye Jeoloji Bülteni 41 (2): 63-78.

Pawlowski, J., Holzmann, M., Tyszka, J. 2013. New supraordinal classification of Foraminifera: Molecules meet morphology. Marine Micropaleontology 100: 1-10.

Payros, A., Dinarés-Turell, J., Monechi, S., Orue-Etxebarria, X., Ortiz, S., Apellaniz, E., Martinez-Braceras, N. 2015. The Lutetian/Bartonian transition (middle Eocene) at the Oyambre section (northern Spain): Implications for standard chronostratigraphy. Palaeogeography, Palaeoclimatology, Palaeoecology 440: 234– 248.

Plaziat, J.C. 1981. Late Cretaceous to Late Eocene Palaeogeographic Evolution of Southwest Europe. Palaeogeography, Palaeoclimatology, Palaeoecology 36: 263--320.

Plaziat, J.C. 2012. Le genre *Velates* (Gastropoda, Neritoidea): études des caractéristiques morphologiques et structurales des espèces et perspectives taxinomiques. Répartition stratigraphique et paléogéographique du genre. Cossmanniana 14: 3-50, Antwerpen.

Purton, L.M.A., Brasier M.D. 1999. Giant Protist *Nummulites* and its Eocene Environment: Life span and Habitat Insights from d18O and d13C data from *Nummulites* and Venericardia, Hampshire Basin, UK. Geology 27 (8): 711-714.

Racey, A. 2001. A Review of Eocene Nummulite Accumulations: Structure, Formation and Reservoir Potential. Journal of Petroleum Geology 24 (1): 79-100.

Rafinesque, C.S. 1815. Analyse de la Nature ou Tableau de l'Univers et des Corps organisés. Palerme. 1-224.

Reckamp, J.U., Özbey, S. 1960. Çankırı sahasının petrol imkanları hakkında tamamlayıcı rapor (AR/TGO/11/471-472 nolu ruhsat sahalarına ilişkin). Petrol İşleri Genel Müdürlüğü Arşivi.

Savajo, A. 1961. Sungurlu (Çorum) Batı Bölgesinin Detay Jeolojisi ve Petrol İmkanları. Maden Tetkik ve Arama Genel Müdürlüğü Rapor no: 4216, Ankara (unpublished).

Savazzi, E. 1992. Shell construction, life habits and evolution in the gastropod *Velates*. Palaeogeography, Palaeoclimatology, Palaeoecology 99, 349-360.

Schaub, H. 1981. *Nummulites* et *Assilines* de la Tethys Paléogène. Taxonomie, phylogenèse et biostratigraphie. Mémoires de la Société Paléontologique Suisse. 104: 1-236; 105: pl. 1-48; 106: pl. 49-97; pp. 193-194 pl. 70 fig. 1-13.

Serra-Kiel, J., Hottinger, L., Caus, E., Drobne, K., Ferrandez, C., Jauhri, A. K., Less, G., Pavlovec, R., Pignatti, J., Samso, J. M., Schaub, H., Sirel, E., Strougo, A., Tambareau, Y., Tosqella, J., Zakrevskaya, E. 1998. Larger foraminiferal biostratigraphy of the Tethyan Paleocene and Eocene. Bulletin Geological Society of France 169: 281-299.

Sevin, M., Uğuz, M.F. 2011. 1:100.000 Ölçekli Türkiye Jeoloji Haritaları Çankırı G32 paftası. Maden Tetkik ve Arama Genel Müdürlüğü Yayınları No: 148.

Seyitoğlu, G., Kazancı, N., Karakuş, K., Fodor, L., Araz, H., Karadenizli, L. 1997. Does continuous compressive tectonic regime exist during Late Palaeogene to Late Neogene in NW Central Anatolia, Turkey? Preliminary observations. Turkish Journal of Earth Sciences 6, 77–83.

Seyitoğlu, G., Kazancı, N. Karadenizli, L., Şen, Ş., Varol, B., Karabıyıkoğlu, T. 2000. Rock–fall avalanche deposits associated with normal faulting in the NE of Çankırı basin: implication fort the post collisional tectonic evolution of the Neo-Tethyan suture zone: Terra Nova 12(6): 245-251.

Sirel, E., Gündüz, H. 1976. Haymana (G. Ankara) yöresi İlerdiyen, Küziyen ve Lütesiyen'deki *Nummulites*, *Assilina* ve *Alveolina* cinslerinin bazı türlerinin tanımlamaları ve stratigrafik dağılımları. Türkiye Jeoloji Kurumu Bülteni 19(1): 31-44.

Sowerby, J. de C. *in* Sykes, W.H. 1837-1840. Transactions of the Geological Society of London. Plates and Maps in Illustration. 2 (5), 754 p., 61 pls. London.

Squires, R.L., Demetrion R.A. 1992. Paleontologyof the Eocene Bateque Formation, Baja California Sur, Mexico. Contributions in Science. Number 434: 1-55.

Squires, R.L., Demetrion R.A. 1994. New Reports of Eocene Mollusks from the Bateque Formation, Baja California Sur, Mexico. The Veliger 37 (2): 125-135.

Stchépinsky, V. 1942. Bursa ile Tercan arasındaki bölgenin mukayeseli stratigrafisi. Bulletin of The Mineral Research and Exploration 27: 290-321.

Stchépinsky, V. 1944. Malatya Bölgesinin Jeolojisi and Mineral Varlıkları. Bulletin of The Mineral Research and Exploration 31: 79-104. Ankara.

Szöts, K.E. 1953. Magyarország Eocén puhatestúi. I. gantkörnyéki eocén puhatestúek. [Mollusques Éocénes de la Hongrie. I. Les Mollusques Éocénes des Environs de Gant]. Geologica Hungarica, Series palaeontologica 22, 1-270.

Szöts, K. E. 1956. Eocene Units of Hungary. Geologica Hungarica Series Geologica 9:1-320.

Şenalp, M. 1974. Tertiary sedimentation in part of the Çankırı-Çorum Basin, Central Anatolia: Doktora Tezi, Imperial College of Science and Technology, London, 366 (unpublished).

Şenalp, M. 1980. Çankırı-Çorum Havzasının Sungurlu Bölgesindeki Eosen Yaşlı Türbidit, Olistostrom ve Olistolit Fasiyesileri. Bulletin of the Mineral Research and Exploration 93/94: 27-53.

Şenalp, M. 1981. Çankırı-Çorum Havzası'nın Sungurlu Bölgesindeki Karasal Formasyonlarının Sedimantolojik İncelenmesi. Türkiye Jeoloji Kurumu Bülteni 24: 65-74.

Tanrıverdi, K. 1973*a*. Çankırı-Çorum Havzası Sulakyurt güneyi ile Balışeyh kuzeyi arasında kalan

yörelerin jeolojisi ve petrol olanakları. Maden Tetkik ve Arama Genel Müdürlüğü Rapor No: 5916, Ankara (unpublished).

Tanrıverdi, K. 1973*b*. Çankırı (Yapraklı) ve Kızılırmak Yöresinin Jeolojisi ve Petrol Olanakları. Maden Tetkik ve Arama Genel Müdürlüğü Rapor No: 6240, Ankara (unpublished).

Tanrıverdi, K. 1974. Çankırı-Çorum Havzası Sulakyurt Güneyi ile Balışıh Kuzeyi Arasında Kalan Yörelerin Jeolojisi ve Petrol Olanakları. Maden Tetkik ve Arama Genel Müdürlüğü Rapor No: 5916, Ankara (unpublished).

Tuzcu, S., Karabıyıkoğlu, M. 1991. Resifler: Genel Karakterleri, Fasiyesleri, Evrimi ve Ekonomik Önemi. Jeoloji Mühendisliği Dergisi 38: 5-38.

Tüysüz, O., Dellaloğlu, A.A. 1992. Çankırı Havzasının Tektonik Birlikleri ve Havzanın Jeolojik Evrimi. Türkiye 9. Petrol Kongresi Bildirileri Özeti, 333-349.

Tüysüz, O., Dellaloğlu, A.A. 1994. Orta Anadolu'da Çankırı Havzası ve Çevresinin Erken Tersiyer'deki Paleocoğrafik Evrimi. Türkiye 10. Petrol Kongresi ve Sergisi Bildiriler Kitabı 57-76.

Vlaicu-Tătărîm, N.V. 1963. Stratigrafia Eocenului din Regiunea de la Sud-Vest De Cluj. Editura Academiei Republicii Populare Romine 244 s. Bucureşti.

Vogl, V. 1912*a*. Die Fauna der Eozänen Mergel im Vinodol in Kroatien. Mittellungen aus dem Jahrbucheder Kgl. Ungarischen Geologischen Reichsanstalt. Bd. 20(2): 79-114.

Vogl, V. 1912*b*. A Vinodol Eocén Márgáinak Faunája. Földtani İntézet Évkönyve. 20(2): 69-100.

Volety, A.K. 2013. Southwest Florida Shelf Coastal Marine Ecosystem - Habitat: Oyster Reefs. Atlantic Oceanographic and Meteorological Laboratory National Oceanic and Atmospheric Administration. (https://www.aoml.noaa.gov/ocd/ocdweb/docs/MARES/MARES_SWFS_ICEM_20130913_Appendix_OOysterReefs.pdf).

Vural, A., Karadenizli, L., Şen, Ş. 2010. Çankırı-Çorum Havzasındaki En Büyük Kara Memelisi Olan Baluchitherium'un ve Eşlik Eden Diğer Omurgalıların Bulgu Yerlerinin Araştırılması ve Bölgenin Paleocoğrafyası (Ön Rapor). Maden Tetkik ve Arama Genel Müdürlüğü Rapor No: 11276, Ankara (unpublished).

Wenz, W. 1938. Handbuch der Palaozoologie. Band.6, Gastropoda. 1505 s., Berlin, Germany.

Yoldaş, R. 1982. Tosya (Kastamonu) ile Bayat (Çorum) Arasındaki Bölgenin Jeolojisi. Doktora Tezi. İstanbul Üniversitesi Fen Fakültesi, 311s.

Yücel, T. 1953. Kızılırmak - Yeşilırmak Arasında Kalan Bölgenin Jeolojisi Hakkında Rapor, Maden Tetkik ve Arama Genel Müdürlüğü Rapor No: 2001, Ankara (unpublished).

PLATES

Plate 1

(1-6) *Ostrea roncaensis* (Partsch *in coll*. Bayan, 1870) De Gregorio, 1884

Left (lower) valv (1)inside; (2) outside and (3) side profile view

Right (upper) valv (4) inside view; left and right valves (5) profile view; (6) left (lower) valv inside view.

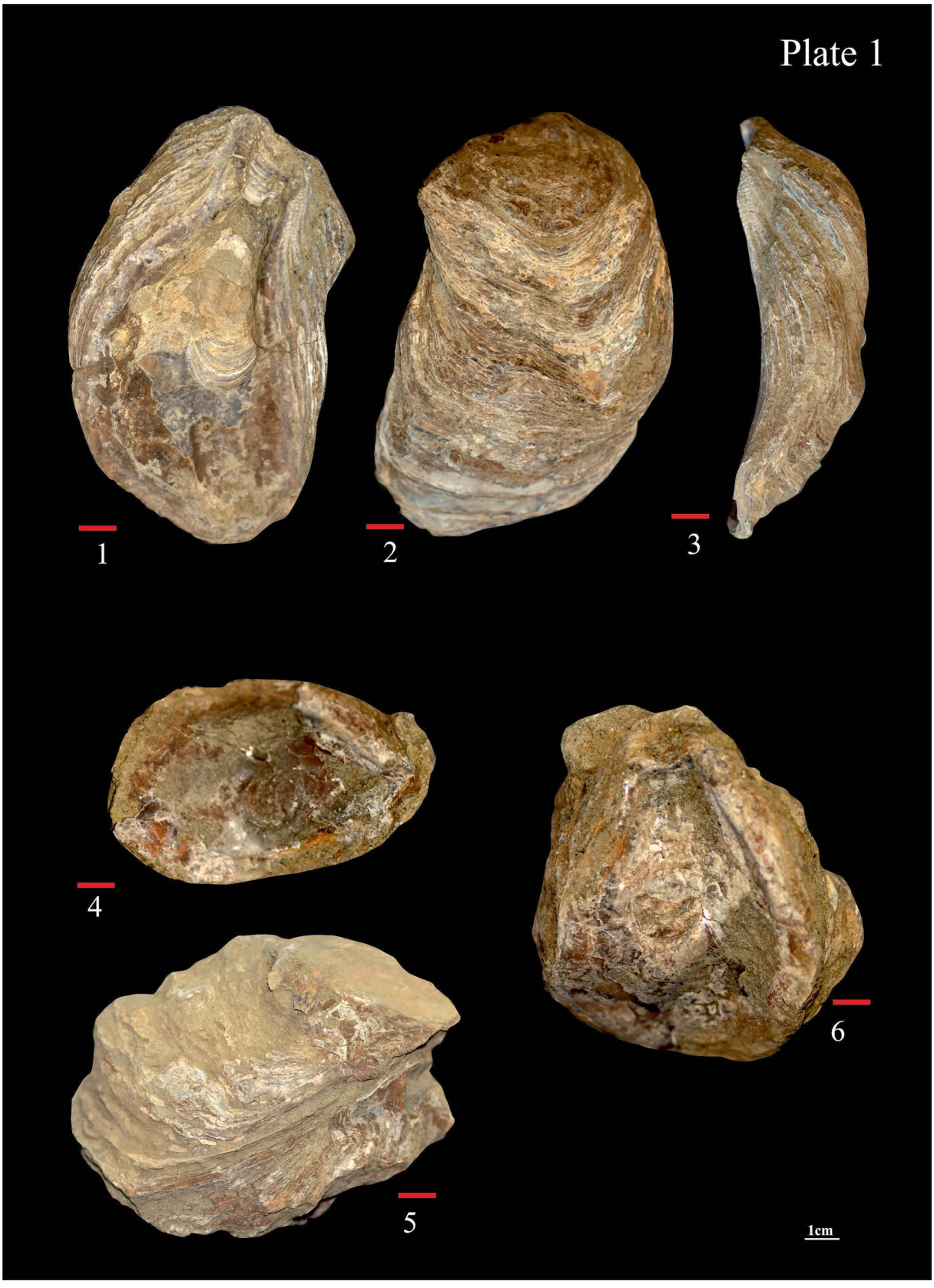
Plate 1
1
2
3
4
5
6
1cm

Plate 2

(1-5) *Velates perversus* (Gmelin, 1791)

(1) Top-abapertural view, (2) bottom-apertural and (3) side-whorl profile view

(4) Protoconk detailed view; (5) side-whorl profile view.


Plate 2
1
2
3
4
5

Plate 3

(1) *Nummulites* and *Assilina* external view

a *Nummulites aturicus* Joly and Leymerie, 1848

b *Nummulites beaumonti* d'Archiac and Haime, 1853

c *Assilina exponens* (Sowerby, 1840) form A

d *Assilina exponens* (Sowerby, 1840) form B

(2-4) *Nummulites aturicus* Joly and Leymerie, 1848

2-3 equatorial sections

4 axial section

(5) *Nummulites* sp., axial section

(6) *Nummulites* sp., equatorial section, form A

(7-8) *Nummulites* sp., equatorial sections, form B

(9-12) *Nummulites* cf. *beaumonti* d'Archiac and Haime, 1853

(9) equatorial section, form B

(10) equatorial section, form A (11-12) axial sections

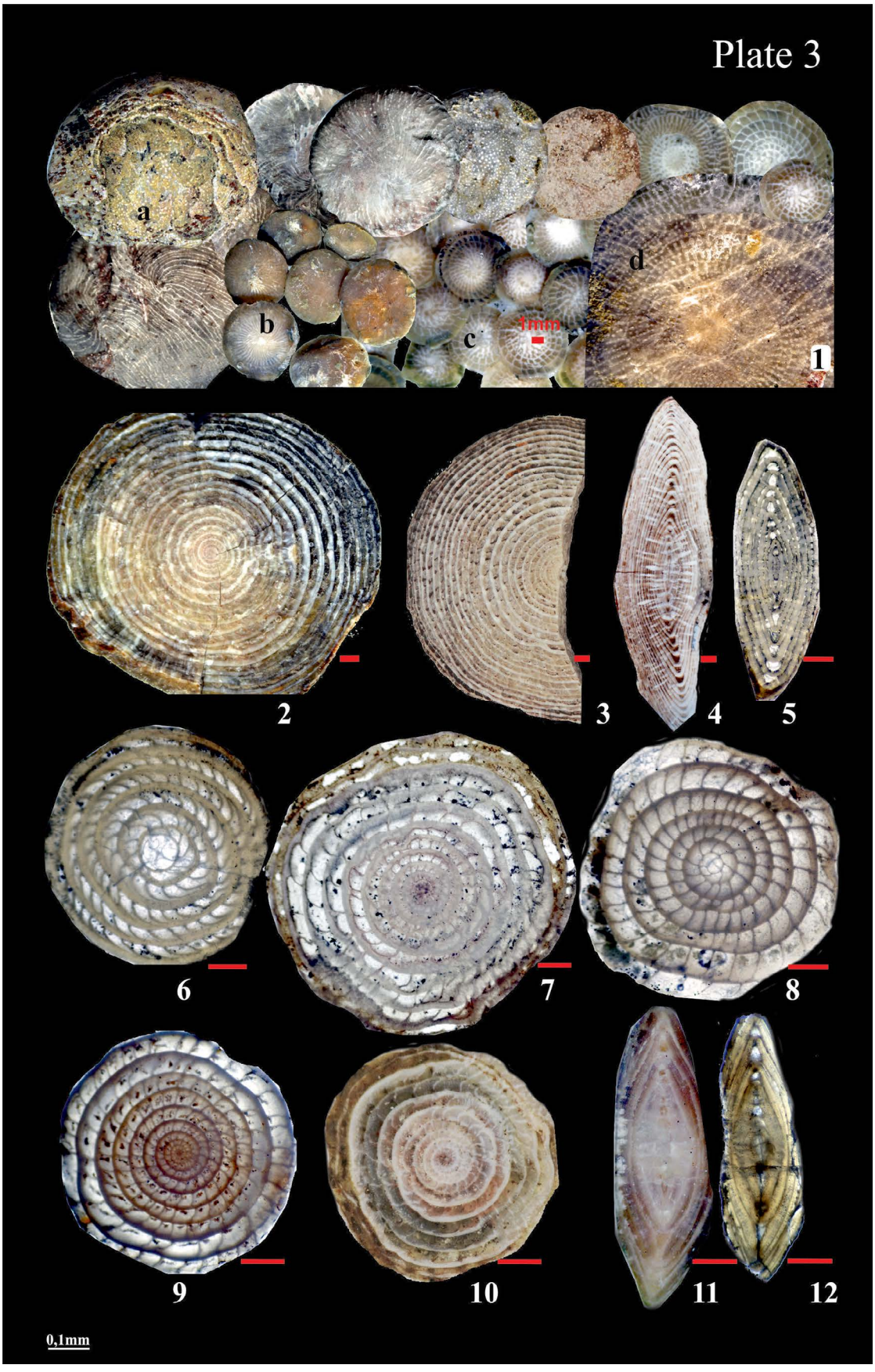
Plate 3
a
b
c
d
1mm
1
2
3
4
5
6
7
8
9
10
11
12
0,1mm

Plate 4

(1-4) *Nummulites perforatus* (De Montfort, 1808)

(1-2) equatorial sections, form B

(3-4) axial sections, form B

(5-6, 8-11) *Assilina exponens* (Sowerby, 1840)

(5) equatorial section, form B

(6) axial section, form B

(8) equatorial section, form A (contains micro trace)

(9) equatorial section, form A

(10-11) axial sections

(7) *Nummulites* sp.

(12) *Nummulites millecaput* Boubée, 1832 equatorial section, form A

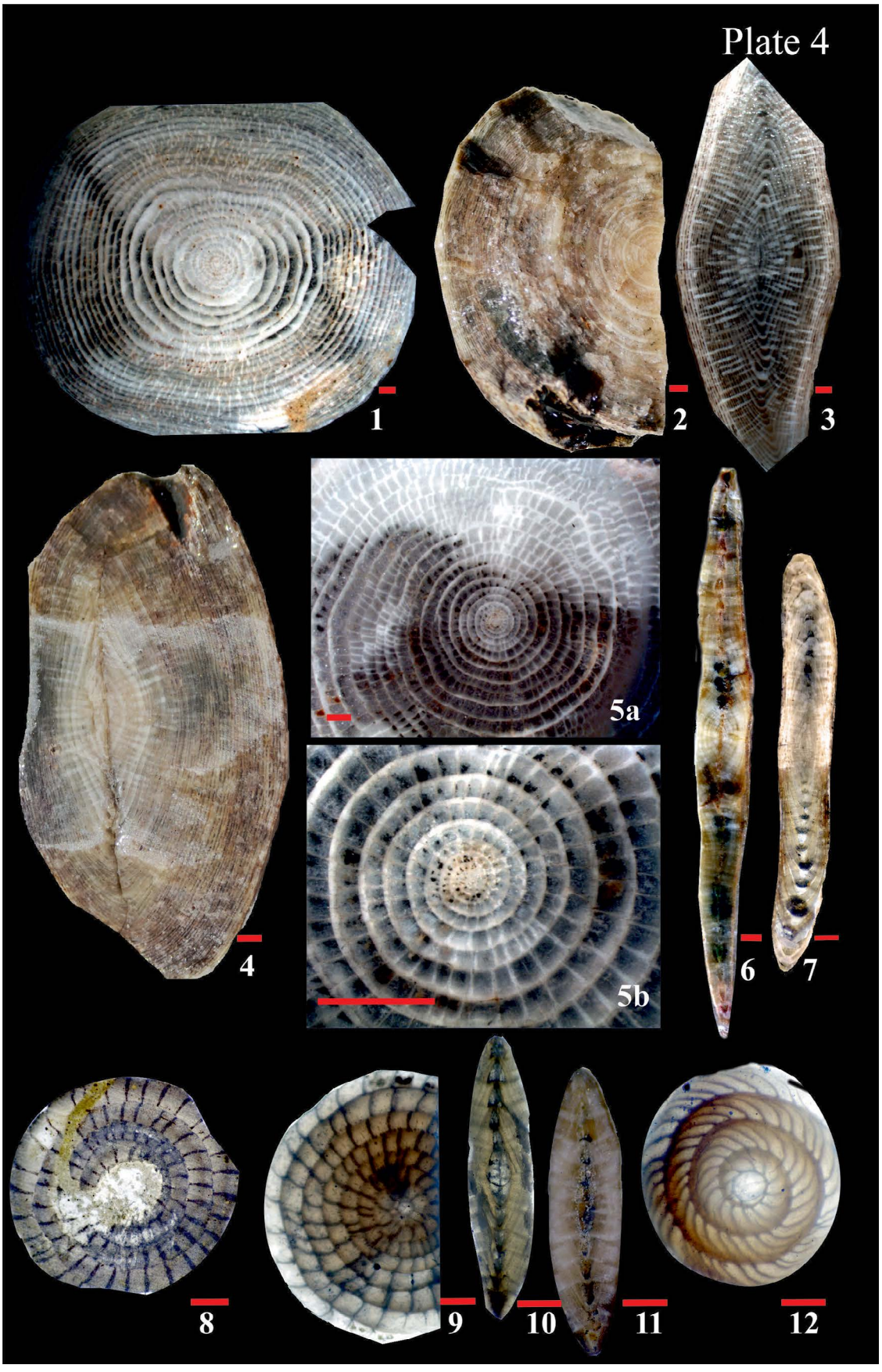
Plate 4
1
2
3
4
5a
5b
6
7
8
9
10
11
12

1. Aims of Publication

- To announce and share researches in all fields of geoscientific studies in Turkey with geoscientists worldwide.
- To announce scientific researches and practices on geoscientific surveys carried out by the General Directorate of Mineral Research and Exploration (MTA) to the public.
- To use the journal as an effective media for international publication exchange by keeping the journal in high quality, scope and format.
- To contribute to the development of Turkish language as a scientific language.

2. Scope

At least one of the following qualifications is required for publishing the papers in the Bulletin of Mineral Research and Exploration.

2.1. Research Articles

2.1.1. Original Scientific Researches

- These articles cover and contribute to the main subjects of the earth sciences, the original scientific researches and its results related to all aspects of disciplines in geoscience like exploration and evaluation of the underground sources and environmental problems, and
- The studies, which apply new aspects and methods for the solution of problems about the earth sciences and researches, which apply new aspects and methods for the solution of the problems, in the engineering sciences carried out in MTA.

2.1.2. Review Articles

These papers include comphrehensive scholarly review articles that summarize and critically assess previous geoscientific researches with a new perspective and reveal a new approach.

2.2. Discussion/Reply

- This type of article is intended for the discussion of papers that have already been published in the latest issue of the Bulletin. The discussion/reply type articles, which criticize all or a part of a recently published article, are published in the following first issue if it is submitted within six months after the publication of the Bulletin.
- The discussions are sent to the corresponding author of the original paper to get their reply before publication. The discussions abut the paper with two or more authors are sent only to the corresponding author.
- If the review article is not published within the prescribed preiod then it is published alone. Later sent replies are not published. Re-criticising of the replies is not allowed.
- The authors should obey the rules of scientific ethics and discussions in their discussion/reply papers. The papers in this category should not exceed four printed pages of the journal including figures and tables etc. The format of the papers should be compatible with the "Spelling Rules" of the Bulletin.

2.3. Short Notes

- The short notes part of the Bulletin covers short, brief and concisely written research reports for papers including the data obtained from ongoing and/or completed scientific researches and practices related to geoscience and new and/or preliminary factual findings from Turkey and worldwide.
- The short notes will follow a streamlined schedule and will normally be published in the following first or second issue shortly after submission of the paper to the Bulletin.
- This type of articles should not exceed four printed pages of the journal including figures, tables and an abstract.

3. Submission and Reviewing of Manuscripts

- Manuscript to be submitted for publishing in the Journal must be written clearly and concisely in Turkish and/or English and prepared in the Bulletin of Mineral Research and Exploration style guidelines. All submissions should be made online at the http://dergi.mta.gov.tr website.
- The manuscript submitted for reviews must not have been published partially or completely previously in another journal.
- The rejected manuscripts are not returned back to

author(s) whereas a letter of statement indicating the reason of rejection is sent to the corresponding author.

- Submitted manuscripts must follow the Bulletin style and format guidelines. Otherwise, the manuscript which does not follow the journals' style and format guidelines, is given back to corresponding author without any reviewing.
- Every manuscript which passes initial Editorial treatise is reviewed by at least two independent reviewers selected by the Editors. Reviewers' reports are carefully considered by the Editors and associated editors.
- The manuscript that need to be corrected with the advices of reviewer(s) is sent back to corresponding author(s) to assess and make the required corrections suggested by reviewer(s) and editors. The authors should prepare a letter of well-reasoned statement explaining which corrections are considered or not.
- If there are any suggestions given by editors and referees that are not accepted and corrected by the author, then it should be sent to the Editor's Office with corrected copies of the report explaining the reason for not accepting these suggestions and corrections.
- Figures and tabless should be 1/3 of the main text.
- To be published in the Bulletin of Mineral Research and Exploration, the printed lenght of the manuscript should not exceed 30 printed pages of the journal including an abstract, figures and tables. The publication of longer manuscripts will be evaluated by Editorial Board if it can be published or not.
- The authors must do the reviewer's corrections and proposals in 60 days and must upload to the system.
- At the printing stage after the last control, the first print of the manuscript are sent to the author/ authors in pdf version and asked from the author/ authors to make the press control.

4. Publication Language and Periods

- The Bulletin of Mineral Research and Exploration is published at least twice a year and each issue is published both in Turkish and English. Thus, the manuscripts are accepted in Turkish or English. The spelling and punctuation guidelines of Turkish Language Institution are preferred for the Turkish issue. However, the technical terms related to geology are used in accordance with the decision of the Editorial Board.

5. Spelling Draft

Manuscripts should be written in word format in A4 (29,7 x 21 cm) size and double-spaced with font size Times New Roman 10-point, margins of 25 mm at the sides, top and bottom of each page.

The formulas requiring the use of special characters and symbols must be submitted by the symbols part of the Microsoft Office Word Program on computer.

Initial letters of the words in sub-titles must be capital. The first degree titles in the manuscript must be numbered and left-aligned, 10 point bold Times New Roman must be used. The second degree titles must be numbered and left-aligned, they must be written with 10 point normal Times New Roman. The third degree titles must be numbered and left-aligned, they must be written with 10 point italic Times New Roman. The fourth degree titles must be left-aligned without having any number; 10 point italic Times New Roman must be used. The text must continue placing a colon after the title without paragraph returns (See: Sample article: http://bulletin.mta.gov.tr).

One line spacing must be left after paragraphs within text.

Paragraphs must begin with 0,5 mm indent.

The manuscript must include the below sections respectively;

o Title Page

o The Name and Surname of the author and * sign (Adress, e-mail adres must be given at the bottom of the page)

o Abstract

o Key Words

o Introduction

o Body

o Discussion

o Conclusion

o Acknowledgements

o References

5.1. Title Page

The title must be short, specific and informative and written with small letters font size Times New Roman 12-point bold. The title mustn't contain the subjects insufficiently processed in the article.

5.2. Author(S)'S Name, Addresses and Email Address

- The name and surname of the author/authors must be written without affiliations. Name must be written in small letters, the surname must be written in capital letters.
- At the affiliation (work adres) written after the name and the surname of the author/authors only the name of the company must be written, the author's job mustn't be written.
- Information about the adresses must be given at the next line as 10-point and italic.
- ORCID number should be taken from www.orcid.org and placed below the address.
- At the articles with two or more than two authors, the numbers must be written above the surnames of the authors, the informations about their adresses must be given at the next line by leaving one space line. Also, at this part the corresponding author must be indicated by the (*) symbol and the telephone, FAX and e-mail address of the corresponding author must be given.
- Abbreviations must not be made while writing the name of the uthor and the affiliation adres. Adresses must be given in Turkish in the Turkish version, in English in the English version.
- At the end of the article the name of the corresponding author and contact informations must be added.

5.3. Abstract

- The abstract must be understandable before having a look at the text.
- The abstract should state briefly the overall purpose of the research, the aim of the article, its contributions to the known theories, new data, principle results and major conclusions.
- Tha abstract must contain short and brief sentences.
- Addressing other sections and illustrations of the text or other writings must be avoided.
- The information, which have not been mentioned in the text, must not be in the abstract.
- The article must be written as one paragraph, preferably. Please provide an abstract which doesn't exceed 200 words.
- The abstract must be written with 10-point, normal Times New Roman in single-spaced lines.
- "Abstract" must not be given for the writings that will be located in "Short Notes" section.
- The English abstract must be under the title of "Abstract".

5.4. Key Words

Immediately after the abstract, please provide up to 5 key words and with each words seperated by comma. These key words will be used for indexing purposes.

5.5. Introduction

- The introduction section should state the objectives of the work, research methods, location of the study area and provide an adequate and brief background by avoiding a detailed literature survey.
- Non-standard or uncommon classifications or abbreviations should be avoided. But if essential, then they must be defined at their first mention and used consistently thereafter. Seperate paragraphs could be organized for each of the subjects at the introduction part. If it is necessary, the subtitle can be given for each of them (for example method, material, terminology etc.).
- When pre-information is needed for facilitating the understanding of the text, this section can also be used (for example, statistical data, bringing out the formulas, experiment or application methods, and others).

5.6. Body

- In this chapter, there must be data, findings and opinions that are intended to convey to the reader about the subject. The body section forms the main part of the article.
- The data used in other sections such as "Abstract", "Discussions", and "Results" are caused by this section.
- While processing the subject, the care must be taken not to go beyond the objective highlighted in the "Introduction" section. The knowledge, which

do not contribute to the realization of the purpose of the article or are useless for conclusion, must not be included.

- All data used and the opinions put forward in this section must prove the findings obtained from the studies or they must be based on a reference by citation.
- The guidance and methods to be followed in processing subjects vary according to the characteristics of the subjects mentioned. Various topic titles can be used in this section as many as necessary.

5.7. Discussions

- Discussion of the data and findings that are objectively transferred in the Main Text section of the article should be done in this section. This must be written as a seperate section from the results section.

5.8. Conclusions

- The main conclusion of the study provided by data and findings of the research should be stated concisely and concretely in this section.
- The subjects that are not mentioned sufficiently and/or unprocessed in the body section must not be included in this section.
- The conclusions can be given in the form of substances in order to emphasize the results of the research and to make the expression understandable.

5.9. Acknowledgements

- In this section, the significant contributions made in the realization of investigation that form the topic of the paper is specified. While specifying contributions, the attitude diverted the original purpose of this section away is not recommended. Acknowledgements must be made according to the following examples.
- This study was carried out within scope of .....project.
- I/we would like to thank to …… for contributing to the development of this article with his/her critiques.
- Academic and/or authoritorial affiliations are written for the contributions made because of requirement of ordinary task.
- For example:
- “Prof. Dr. İ. Enver Altınlı has led the studies”.
- “The opinions and warnings of Dr. Tandoğan Engin are considered in determining the chemistry of chrome minerals.”
- The contributions made out of the requirement of ordinary task:
- For example:
- “I would like to thank to Professor Dr. Melih Tokay who gives the opportunity to benefit from unpublished field notes”; “I would like to thank to the preliminary-Plan Chief Engineer Ethem Göğer, State Hydraulic Work, 5th Zone”. Academic and / or task-occupational titles are indicated for such contributions.
- The contributions, which are made because of requirement of ordinary task but do not necessitate responsibility of the contributor mustn’t be specified.
- For example:
- Sentences such as “I would like to thank to our General Manager, Head of Department or Mr. / Mrs. President ……who has provided me the opportunity to research” must not be used.

5.10. References

- All references cited in the text are to be present in the reference list.
- The authors must be sure about the accuracy of the references. Publication names must be written in full.
- Reference list must be written in Times New Roman, 9-point type face.
- The reference list must be alphabetized by the last names of the first author of each work.
- If an author’s more than one work is mentioned, ranking must be made with respect to publication year from old to new.
- In the case that an author’s more than one work in the same year is cited, lower-case alphabet letters must be used right after publication year (for example; Saklar, 2011*a, b*).
- If the same author has a publication with more than one co-author, firstly the ones having single author

are ranked in chronological order, then the ones having multiple authors are ranked in chronological order.

- In the following examples, the information related to works cited is regulated in accordance with different document/work types, considering punctuation marks as well.
- If the document (periodic) is located in a periodical publication (if an article), the information about the document must be given in the following order: surnames of the author/authors, initial letters of author's/ authors' first names. Year of publication. Name of the document. Name of the publication where the document is published, volume and/ or the issue number, numbers of the first and last pages of the document.

For example:

Pamir, H.N. 1953. Türkiye'de kurulacak bir hidrojeoloji enstitüsü hakkında rapor. Türkiye Jeoloji Bülteni 4, 1, 63-68.

Barnes, F., Kaya, O. 1963. İstanbul bölgesinde bulunan Karbonifer'in genel stratigrafisi. Maden Tetkik ve Arama Dergisi 61,1-9.

Robertson, A.H.F. 2002. Overview of the genesis and emplacement of Mesozoic ophiolites in the Eastern Mediterranean Tethyan region. Lithos 65, 1-67.

- If more than one document by the same authors is cited, firstly the ones having single name must be placed in chronological order, then the ones having two names must be listed in accordance with chronological order and second author's surname, finally the ones having multiple names must be listed in accordance with chronological order and third author's surname.
- If the document is a book, these are specified respectively: surnames of the author/authors, initial letters of author's/authors' first names. Year of publication. Name of the book (initial letters are capital). Name of the organization which has published the book, name of the publication wherethe document is published, volume and/ or the issue number, total pages of the book.

For example

Meriç, E. 1983. Foraminiferler. Maden Tetkik ve Arama Genel Müdürlüğü Eğitim Serisi 23, 280p.

Einsele, G. 1992. Sedimentary Basins. Springer-Verlag, p 628.

- If the document is published in a book containing the writings of various authors, the usual sequence is followed for the documents in a periodic publication. Then the editor's surname andinitial letters of their name /names are written. "Ed." which is an abbreviation of the editor word is written in parentheses. Name of the book containing the document (initial letters are capital). Name of the organization which has published the book. Place of publication, volume number (issue number, if any) of the publication where the document is published, numbers of the first and last page of the document.

For example:

Göncüoğlu, M.C., Turhan, N., Şentürk, K., Özcan, A., Uysal, Ş., Yalınız, K. 2000. A geotraverse across northwestern Turkey. Bozkurt, E., Winchester, J.A., Piper, J.D.A. (Ed.). Tectonics and Magmatism in Turkey and the Surrounding Area. Geological Society of London Special Publication 173, 139-162.

Anderson, L. 1967. Latest information from seismic observations. Gaskell, T.F. (Ed.). The Earth's Mantle. Academic Press. London, 335-420.

- If name of a book where various authors' writings have been collected is specified, those must be indicated respectively: book'seditor/editors' surname/surnames, and initial letters of their name/ names. "Ed." which is an abbreviation of the editor word must be written in parentheses. Year of Publication. Name of the book (initial letters are capital). Name of the organization which has published the book, total pages of the book.

For example:

Gaskel, T.F. (Ed.) 1967. The Earth's Mantle. Academic Press, 520p.

- If the document is an abstract published in a Proceedings Book of a scientific activity such as conference/symposium/workshop …etc. , information about the document must be given in the following order: surnames of the author/authors, initial letters of author's/authors' first names. Year of publication. Title of the abstract. Name, date and place of the meeting where the Proceedings Book is published, numbers of the first and last pages of the abstract in the Proceedings Book.

For example:

Yılmaz, Y. 2001. Some striking features of the Anatolian geology. 4. International Turkish Geology Symposiums 24-28 September 2001, London, 13-14.

Öztunalı, Ö., Yeniyol, M. 1980. Yunak (Konya) yöresi kayaçlarının petrojenezi. Türkiye Jeoloji Kurumu 34. Bilim Teknik Kurultayı, 1980, Ankara, 36

- If the document is one of the unpublished documents as report, lecture notes, and so on., information about the document must be given by writing the word "unpublished" in parentheses to the end of information about the document after it is specifiedin accordance with usual order which is implemented for a document included in a periodic publication.

For example:

Özdemir, C. Biçen, C. 1971. Erzincan ili, İliç ilçesi ve civarı demir etütleri raporu. General Directorate of Mineral Research and Exploration Report No: *4461*, 21 p. Ankara (unpublished).

Akyol, E. 1978. Palinoloji ders notları. EÜ Fen Fakültesi Yerbilimleri Bölümü, 45 p., İzmir (unpublished).

- The followings must be specified for the notes of unpublished courses, seminars, and so on: name of the document and course organizer. Place of the meeting. Name of the book, corresponding page numbers.

For example:

Walker, G. R. Mutti, E. 1973.Turbidite facies and facies associations. Pacific Section Society for Sedimentary Geology Short Course. Annaheim. Turbitides and Deep Water Sedimantation, 119-157.

- If the document is a thesis, the following are written: surname of the author, initial letter of the author's first name. Year of Publication. Name of the thesis. Thesis type, the university where it is given, the total number of pages, the city and "unpublished" word in parentheses.

For example:

Seymen, İ. 1982. Kaman dolayında Kırşehir Masifi'nin jeolojisi. Doçentlik Tezi, İTÜ Maden Fakültesi, 145 s.İstanbul (unpublished).

- Anonymous works must be regulated according to publishing organization.

For example:

MTA. 1964. 1/500.000 ölçekli Türkiye Jeoloji Haritası, İstanbul Paftası. Maden Tetkik ve Arama Genel Müdürlüğü, Ankara.

- The date, after the name of the author, is not given for on-printing documents; "in press" and / or "on review" words in parenthesis must be written. The name of the article and the source of publication must be specified, volume and page number must not be given.

For example:

- Ishihara, S. The granitoid and mineralization. Economic Geology 75th Anniversary (in press).

- Organization name, web address, date of access on web address must be indicated for the information downloaded from the Internet. Turkish sources must be given directly in Turkish and they must be written with Turkish characters.

For example:

- ERD (Earthquake Research Department of Turkey). **http://www.afad.gov.tr**. March 3, 2013.

- While specifying work cited, the original language must be used; translation of the title of the article must not be done.

6. Illustrations

- All drawings, photographs, plates and tables of the article are called "illustration".
- Illustrations must be used when using of them is inevitable or they facilitate the understanding of the subject.
- While selecting and arranging the illustrations' form and dimensions, page size and layout of the *Bulletin* must be considered, unnecessary loss of space must be prevented as much as possible.
- The pictures must have high quality, high resolution suitable for printing.
- The number of illustrations must be proportional to the size of the text.
- All illustrations must be sent as separate files independent from the text.

- While describing illustrations in the text, abbreviations must be avoided and descriptions must be numbered in the order they are mentioned in the text.
- Photographs and plates must be given as computer files containing EPS, TIFF, or JPEG files in 600 dpi and higher resolutions (1200 dpi is preferred) so that all details can be seen in the stage of examination of writing.

6.1. Figures

- Drawings and photos (except for the plates in the text) will be evaluated together as "Figure" and they must be numbered in the order they are mentioned in the text.
- The figures published in the Bulletin of Mineral Research and Exploration must be prepared in computer considering the dimensions of single-column width 7.4 m or double-column width 15.8 cm. Figure area together with the writing at the bottom should not exceed 15.8x21in maximum.
- Unnecessasry details must not be given in figures or care must be taken not to use much space for information transfer.
- Figures must be arranged in such a way to be printed in black/white or colored.
- The figure explanations being justified in two margins must be as follows:

Figure 1- Sandıklı İlçesinin (Afyon); a) güneybatısının jeolojik haritası, b) İnceleme alanının genel dikme kesiti (Seymen 1981), c) Türkiye'nin önemli neotektonik yapıları (Koçyiğit 1994'den değiştirilerek).

Figure 1- a) Sandıklı ilçesinin güneybatısının jeolojik haritası, b) İnceleme alanının genel dikme kesiti (Seymen, 1981), c) Türkiye'nin önemli neotektonik yapıları (Koçyiğit 1994'den değiştirilerek).

- Drawings must be made by well-known computer programs painstakingly, neatly and cleanly.
- Using fine lines, which can disappear when figures shrinks, must be avoided. Symbols or letters used in all drawings must be in Times New Roman and not less than 2 mm in size when shrink.
- All standardized icons used in the drawings must be explained preferably in the drawing or with figure caption if they are too long.
- Linear scale must be used for all drawings. Author's name, figure description, figure number must not be included into the drawing.
- Photos must be in quality and quantity that will reflect the objectives of the subject.

6.2. Plates

- Plates must be used when needed a combination of more than one photo and the publication on a special quality paper.
- Plate sizes must be equal to the size of available magazine pagespace.
- Figure numbers and linear scale must be written under each of the shapes located on the Plate.
- The original plates must be added to the final copy which will be submitted if the article is accepted.
- Figures and plates must be independently numbered. Figures must be numbered with Latin numerals and plates with Roman numerals (e.g., Figure1, Plate I).
- There must be no description text on Figures.

6.3.Tables

- All tables must be prepared preferably in word format in Times New Roman fonts.
- Tables together with table top writing must not exceed 15x8 cm in size.
- The table explanations being justified in two margins must be as follows:

Table 1- Hydrogeochemical analysis results of geothermal waters in the study area.

7. Nomenclature and Abbreviations

- Non-standard and uncommon nomenclature abbreviations should be avoided in the text. But if essential, they must be described as below: In cases where unusual nomenclatures and unstandardized abbreviations are considered to be compulsory, the followed way and method must be described.
- Full stop must not be placed between the initials of words for standardized abbreviations (MER, SHW, etc.).
- Geographical directions must be abbreviated in English language as follows: N, S, E, W, NE …etc.
- The first time used abbreviations in the text are presented in parenthesis, the parenthesis is not used for subsequent uses.

- The metric system must be used as units of measurement.
- Figure, plate, and table names in the article must not be abbreviated. For example, "as shown in generalized stratigraphic cross-section of the region (Figure 1……..."

7.1. Stratigraphic Terminology

Stratigraphic classifications and nomenclatures must be appropriate with the rules of International Commision on Stratigraphy and/or Turkey Stratigraphy Committee. The formation names which have been accepted by International Commision on Stratigraphy and/or Turkey Stratigraphy Committee should be used in the manuscript.

7.2. Paleontologic Terminology

Fossil names in phrases must be stated according to the following examples:

o For the use of authentic fossil names;

e.g. Limestone with *Nummulites*

o When the authentic fossil name is not used;

o e.g. nummulitic Limestone

o Other examples of use;

e.g. The type and species of *Alveolina / Alveolina* type and species

- Taxonomic ranks must be made according to the following examples:
- The names of the fossils should be stated according to the rules given below:

o For the first use of the fossil names, the type, spieces and the author names must be fully indicated;

Alveolina aragonensis Hottinger, 1960, not reference

Alveolina cf. *aragonensis* Hottinger, 1960, not reference

Alveolina aff. *aragonensis* Hottinger, 1960, not reference

o When a species is mentioned for the second time in the text;

A.aragonensis

*A.*cf.*aragonensis*

*A.*aff. *aragonensis*

It is accepted as citiation if stated as *Alveolina aragonensis* Hottinger (1960). Cited Hottinger (1960), stated in the Reference section.

- The statement of plates and figures (especially for the articles of paleontology):

a for the statement of species mentioned in the body text; ***Borelis vonderschmitti*** (Schweighauser, 1951)

(Plate, Figure, Figure in the body text).

b. When cited for other articles;

1951 ***Neoalveolina vonderschmitti*** Schweighauser, page 468, figure 1-4, figure in body text.

1974 ***Borelis vonderschmitti*** (Schweighauser), Hottinger, page 67, plate 98, figure 1-7.

c. For the citation in the text

(Schweighauser, 1951, page, plate, figure, figure in the body text)

(Hottinger, 1974, page, plate 97, figure 67, plate 98, figure 1-7, figure in the body text).

Ordo: Foraminiferida Eichwald, 1830 Super family: Alveolinacea Ehrenberg, 1939 Family: Borelidae Schmarda, 1871 Type genus: *Borelis* de Montfort, 1808 Type species: *Borelis melenoides* de Montfort, 1808; *Nautilus melo* Fitchel and Moll, 1789	Not reference, Not stated in the Reference section
Borelis vonderschmitti (Schweighauser, 1951) (Plate, Figure, Figure in Body Text)	Schweighauser, 1951 not reference
1951 *Neoalveolina vonderschmitti* Schweighauser, page 468, figure 1-4	Cited Scweighauser (1951), stated in the Reference section.
1974 *Borelis vonderschmitti* (Schweighauser), Hottinger, page, 67, plate 98, figure 1.7	Cited Hottinger (1974), stated in the Reference section.

8. Citations

All the citiations in the body text must be indicated by the last name of the author(s) and the year of publication, respectively. The citations in the text must be given in following formats.

- For publications written by single author:

- It is known that fold axial plain of Devonian and Carboniferious aged units around Istanbul is NS oriented (Ketin, 1953, 1956; Altınlı, 1999).

- Altınlı (1972, 1976) defined the general characteristics of Bilecik sandstone

- For publications written by two authors:

- The upper parts of the unit contain Ilerdian fossils (Sirel and Gündüz, 1976; Keskin and Turhan, 1987, 1989).

- For publications written by three or more authors:

According to Caner et al. (1975) Alıcı formation reflects the fluvial conditions.

The unit disappears wedging out in the East direction (Tokay et al., 1984).

- If reference is not directly obtained but can be found in another reference, cross-reference should be given as follows:

- It is known that Lebling has mentioned the existence of Lias around Çakraz (Lebling, 1932: from Charles, 1933).

9. Reprints

The author(s) will receive 2 two hard copies of the related issues.

10. Copyright and Conditions of Publication

- It is a condition of publication that work submitted for publication must be original, previously unpublished in whole or in part.

- It is a condition of publication that the authors who send their publications to the Bulletin of Mineral Research and Exploration hereby accept the conditions of publication of the Bulletin in advance.

- All copyright of the accepted manuscripts belong to MTA. The author or corresponding author on behalf of all authors (for papers with multiple authors) must sign and give the agreement under the terms indicated by the Regulations of Executive Publication Committee. Upon acceptance of an article, MTA can pay royalty to the authors upon their request according to the terms under the "Regulations of Executive Publication Committe" and the "Regulations of Royalty Payment of Public Office and Institutions"

All the information and forms about the Bulletin of Mineral Research and Explorations can be obtained from http://bulletin.mta.gov.tr